Gary M. Glazer, M.D.
*Emma Pfeiffer Merner Professor
in the Medical Sciences
Professor and Chairman
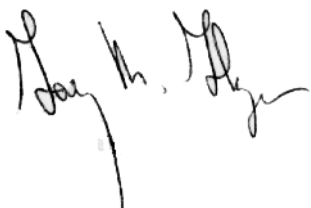Department of Radiology*

On May 21, 2005 the Stanford University Department of Radiology celebrated one hundred years of making radiology history. The centennial celebration began with historical and scientific exhibits presented by the faculty. A symposium was held to explore the potential of biomedical imaging and targeted therapies to lead the way in making personalized medicine a reality.

Looking back over the past century, we feel immense pride in the stunning achievements of our Department. These legacies include harnessing the power of the linear accelerator to treat cancer, developing a cure for Hodgkin's disease, and advancing non-invasive imaging using x-ray and magnetic resonance methods to better understand the structure and function of living systems.
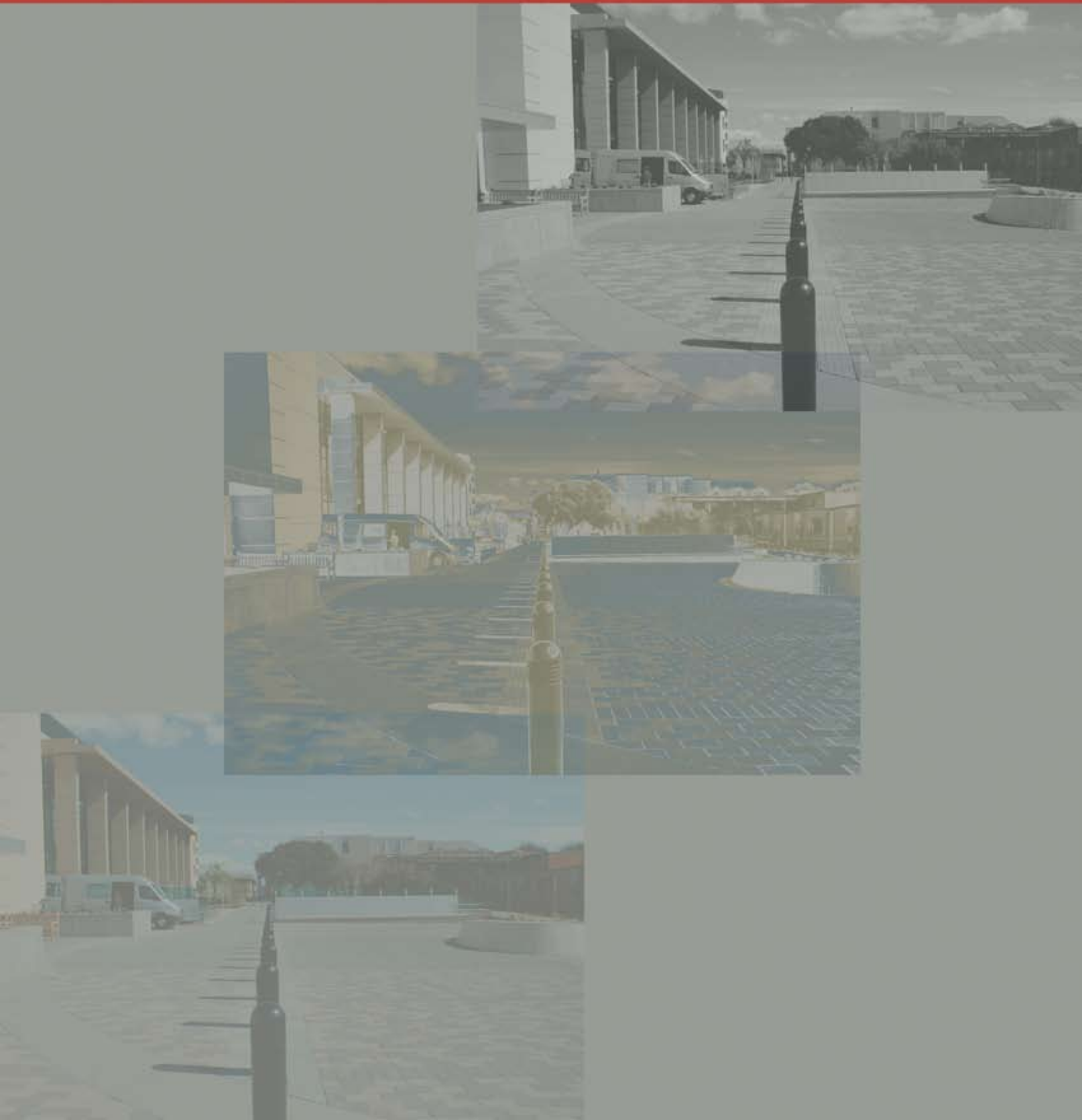
Our second century began on a high note with the opening of the expansion of the Lucas Center for Imaging. Together with the original Lucas Center, completed in 1992, both buildings constitute one of the world's largest centers for imaging located on a University campus. The expansion involved the addition of two underground stories: the approximately 20,000 square feet of new space more than doubled the size of the Lucas Center. The expansion houses faculty and equipment associated with the Radiological Sciences Laboratory and Radiology's Molecular Imaging Program. Major new installations include a 7T whole body magnet, a cyclotron and associated radiochemistry facilities, wet labs for biology and chemistry and a unique education center with the latest technology for fully interactive learning. These exceptional facilities have facilitated recruitments of key scientists representing a variety of disciplines.

We are delighted that our current work is well recognized. Our investigations have graced the covers of three major scientific publications this year and our faculty are competing very effectively for federal funding. I am particularly proud that we have NIH-funded Centers for both MR Technology development and for in-vivo Cellular and Molecular Imaging. These Center grants are important because they support a core infrastructure as well as provide recognition for our excellence in these key areas. We intend to develop more national centers in the years ahead.

I believe we now have the team in place at Stanford to create the quality of advances that our faculty created in the past century. Recognizing that today diseases are detected late in their natural history, we have a tremendous opportunity to improve human health through earlier diagnosis thereby enhancing therapy. Indeed some even dream that disease, once better understood, can be prevented by appropriate methods before it becomes macroscopic or clinically evident. We could not ask for better supporters and partners as we begin our second century.

LUCAS ANNUAL REPORT

STANFORD UNIVERSITY
100
A Century of Discovery, Diagnosis and Treatment
RADIOLOGY & RADIATION ONCOLOGY

Acknowledgements

Lucas Annual Report 2005

Table of Contents

Stanford Radiology 2005

In looking back over 2005, we commemorate not only the past year, but the past 101 years of making radiology history. On Saturday, May 21, 2005, Stanford Radiology celebrated its centennial anniversary. The day began with an interactive presentation of historical and scientific exhibits showcasing the future promise of imaging and personalized medicine. In the afternoon symposium, leaders from academia and industry discussed the potential of personalized medicine and its economic costs. The day's festivities also included the dedication of the Richard M. Lucas Center II. This expansion adds approximately 20,000 square feet of new space and contains Stanford Radiology's Molecular Imaging Program. The Richard M. Lucas Center and its expansion strongly position Stanford Radiology as a world leader in the field of imaging.

Like the Lucas Center II expansion, *The World of Stanford Radiology: 1901-2005* by Otha W. Linton, MSJ, is a legacy of one-hundred years of discovery, diagnosis, and treatment. Published in 2005, this book chronicles the unique story of Stanford Radiology as we expanded from a very small facility with one staff person to two departments with more than 50 full-time faculty members and a large number of fellows and residents. The dreams of the early pioneers of Stanford Radiology fill the pages of *The World of Stanford Radiology: 1901-2005* and, from cover to cover, they slowly materialize before our eyes. One common theme resonating throughout the book is that of Stanford Radiology as the site of many monumental "firsts." In 1956, the first medical linear accelerator in America was installed at Stanford Hospital. We were the first in the world to perform an acute, type-B aortic dissection with a stent graft in 1996. This was the same year we created the first 3-D Medical Imaging Laboratory for research, clinical, and teaching activities. In 1998, we housed the first multidetector CT outside of the factory environment.

In 2005, we continued our premier tradition by scanning a mummy for the first time in Stanford Radiology's history. For the last 75 years, the mummy had been housed at

Professor and Chairman Gary Glazer, Dean Phillip Pizzo, and Jeffrey Immelt, Chairman of the Board and CEO of General Electric Corporation, share a light moment during the Radiology Centennial Celebration, May 21, 2005.

the Rosicrucian Egyptian Museum in San Jose, California. Stanford Medical Center was the first to acquire the high-end AXIOM Siemens scanner used to scan the mummy who has recently been named "Sherit"—ancient Egyptian for "little one." With its powerful arm that rotates around the patient, the AXIOM Siemens scanner was able to produce 60,000 highly detailed images without ever disturbing "Sherit." These high-resolution images revealed that "Sherit" was a 4 to 5 year-old girl with black curls and a receding chin. Using the technology of the future, we looked into the past to unveil a mystery of antiquity.

Today, we are able to achieve sub-mm resolution of human organs within seconds using multiple, complementary methods such as CT scanning, MR imaging, or ultrasound. Computer-based graphics methods allow us to display data in innovative ways by converting anatomic sections into 3D images. Stanford Radiology is the leader in the development of the most innovative technology. Moving into 2006 and a new century of radiology, we anticipate improving our patient-care imaging facilities, expanding our important educational goals, and continuing our successful research efforts. We look forward to leading the revolution in radiology and molecular medicine.

3D reconstruction of scans performed in the Radiology AXIOM lab in May 2005 reveals a 2,000 year-old child encased in an Egyptian mummy.

Collaborating Stanford Departments

Almost three hundred faculty, postdoctoral fellows, students and research staff from across the university are affiliated with research programs in the Department of Radiology representing the following departments:

Anesthesia	Medicine/Oncology
Applied Physics	Nephrology
Bioengineering	Neurobiology
Cancer Biology	Neurology
Cardiovascular Medicine	Neurosurgery
Chemistry	OB/GYN
Computer Sciences	Orthopedics/Orthopedic Surgery
Electrical Engineering	Pediatrics/Neonatology
ENT	Psychiatry
Functional Restoration	Psychology
Infectious Diseases	Stroke Center
Materials Science	Surgery
Mechanical Engineering	Urology
Medical Informatics	Vascular Surgery

Outside Collaborators

Active collaborations are in place with researchers from outside Stanford representing the following institutions:

Aneurex	M.D. Anderson
ART Inc.	Millenium Pharmaceuticals
Bresagen	NexRay
Brown University	Novartis
Chiron	Nycomed
Cordis	Palo Alto Veterans Administration
CRI Inc.	R2 Technology, Inc.
Dana Ferber	Siemens Medical Systems
Diadexus	Smith Kettlewell Eye Institute
Elbit	SRI International
Endius	Stanford Center for Biomedical Ethics
Ethicon	Sterling
FeRx, Inc.	University of California, Berkeley
Fred Hutch Cancer Center	University of California, Davis
Galil Medical	University of California, Irvine
Genentech, Inc.	University of California, Los Angeles
Genetics	University of California, San Francisco
GE Medical Systems	University of California, San Diego
Intronn Inc.	Visualsonics
Lunar Corporation	

RSL Overview

Radiological Sciences Laboratory and the Center for Advanced MR Technology

GARY H. GLOVER

DIRECTOR, RADIOLOGICAL SCIENCES LABORATORY

The Lucas Center is home to the Radiological Sciences Laboratory, a section of the Radiology Department, and in conjunction with the Electrical Engineering Department is host to the *Center for Advanced MR Technology*, an NIH-funded National Research Resource. Its state of the art imaging facilities support hundreds of on-campus and extramural researchers as a core facility.

THE RADIOLOGICAL SCIENCES LABORATORY

The RSL has seen exciting growth this year with the addition of new faculty and students and with the occupation of offices and lab space in the beautiful, new Lucas Expansion. We are now comprised of 12 faculty, approximately 50 graduate and postdoctoral students, 28 scientific staff and 7 administrative assistants, as well as the Lucas Center/RSL Administrative Director, Donna Cronister. Dr. Daniel Fiat is a visiting scholar, who is here for about 9 months to perform research in imaging of 17O.

The faculty serve in a wide variety of advisory roles to government and foundation agencies, such as the NIH, and in policy-making positions for international scientific societies, such as the ISMRM and RSNA. A number of our faculty, scientific staff and students have garnered prestigious awards for their exceptional research achievements. Some of the Lab's honors of the past year are noted here.

Kim Butts reached an important milestone this year, with the graduation of her first PhD student, **Viola Rieke**. To our great delight, Viola has stayed in the lab as a postdoc. Kim continues to serve on the ISMRM Board of Trustees.
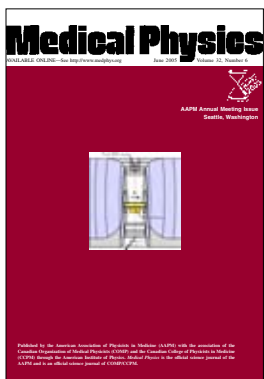
Rebecca Fahrig has been very much in the news lately with her pioneering work on the development of digital tomosynthesis, having an article in the American Association of Physics journal *Physics Today* as well as a front cover illustration on the journal *Medical Physics*. She also was featured for assisting with CT studies of a mummy.

Brian Hargreaves, our newest faculty member, was senior or co-author on two award-winning posters:

Best Poster -- Pulse Sequences, International Society of Magnetic Resonance in Medicine (2005). Wideband SSFP: SSFP with imaging bandwidth greater than 1/TR. (K.S. Nayak, B.S. Hu and B.A. Hargreaves).

Lauterbur Award, Society of Computed Body Tomography and Magnetic Resonance (2005). Rapid body MRI using IDEAL water-fat separation and parallel imaging. (S.B. Reeder, H. Yu, N. Rofsky, C. McKenzie, A. Brau, B.A. Hargreaves, J.W. Johnson, R. Herfkens, G.E. Gold and J.H. Brittain.)

Mike Moseley was a Co-Organizer for the "Update on DTI Cognitive Neuroscience" conference, New York Academy of Sciences, August 2004. He continues service on a standing study section for the NIH and several additional ad hoc committees.

Sandy Napel and **Geoff Rubin** were awarded an R01 grant for their study, "Improving Radiologist Detection of Lung Nodules with CAD."

Moriah Thomason, a graduate student in the Neurosciences program, was honored by the journal *NeuroImage* in selecting a figure from her paper for it's front cover (Thomason ME; Burrows BE; Gabrieli JDE; Glover GH. Breath holding reveals differences in fMRI BOLD signal in children and adults. *NeuroImage* 25:824-837 (2005). Moriah just concluded service as Chair of the Graduate Student Council.
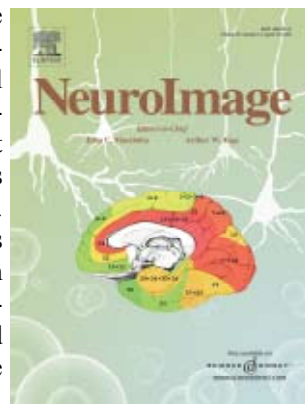
RSL FACULTY RECRUITMENT

This year the RSL recruited **Brian Hargreaves** to join the faculty to augment our expertise in imaging of the body with MR. Brian was a research associate in the MRSRL laboratory and has strong expertise in the basic sciences of imaging physics and applications to cardiovascular and other aspects of whole body imaging. In addition, **David Paik** will be joining the faculty in September to fill a new role in the burgeoning use of computer aided detection (CAD) methods in diagnostic radiology. David was a graduate student and then research associate in Sandy Napel's lab.

We are delighted to have attracted such exceptional candidates to the lab and look forward to the advancements they will make. Finally, we are concluding a search for a faculty member to head our new effort in very high field MRI, which will center on the 7T magnet still being installed.

THE NATIONAL CENTER FOR ADVANCED MR TECHNOLOGY AT STANFORD (CAMRT)

The Center is now in its eleventh year of operation as a National Research Resource of the NIH's National Center for Research Resources, having obtained renewal of the grant this spring for another five years with the somewhat amazing priority score of 118. In fact, California Senator Barbra Boxer called to provide her congratulations. Outstanding progress has been made in all six of the core technology development areas that include reconstruction methods (Dwight Nishimura, EE Department, core director), imaging of brain activation (Gary Glover, core director and PI), diffusion and perfusion weighted imaging methods (Mike Moseley, core director), imaging of cardiovascular struc-

ture and function (Norbert Pelc, core director and CAMRT co-PI), spectroscopic imaging development (Dan Spielman, core director) and interventional MRI technique development (Kim Butts, core director). Some of this research is chronicled in the scientific reports that follow.

Lucas Center Facilities

Completion of the Center's major expansion was celebrated in conjunction with the Department's Century celebration and symposium on May 21, 2005. The new addition has nearly doubled laboratory and office space, and includes a new whole body 7T magnet, cyclotron, wet labs, hot labs for molecular biology and chemistry, a 1000 sq. foot learning center and offices for faculty and students as well as visiting scholars. The cyclotron, under the direction of **David Dick**, is undergoing final calibrations but has already been delivering routine clinical FDG as well as experimental radioisotopes. The 7T magnet was recently cooled to liquid helium temperature in preparation for ramp up and installation of the electronics.

Plans are nearly completed for a renovation of the existing 3D lab and animal magnet space for installation of a second 3T magnet. The 4.7T magnet will be replaced by a new "micro-Signa" 7T magnet to be installed under the direction of **Mike Moseley** in the Clark Center's Small Animal Imaging Facility.

Gary Glover takes a well-deserved rest following the installation of the 7T magnet in the Lucas Center Expansion.

Molecular Imaging Program at Stanford

SANJIV SAM GAMBHIR
DIRECTOR, MIPS

The MIPS is an inter-departmental program (http://mips.stanford.edu) that continues to rapidly grow. This program brings together faculty from different disciplines to advance the field of molecular imaging. Development of new molecular probes, novel instrumentation, assays for living subjects, and translation of strategies for clinical imaging are all goals of the MIPS.

The first annual MIPS retreat at the San Francisco Exploratorium was held this year with over 60 faculty/staff and students in attendance. A chance to present brief research updates by students as well as many fun planned activities around the Exploratorium took place (view slideshow at http://mips.stanford.edu/public/events.adp).

The completion of the Lucas Expansion allowed several new faculty (Drs. J. Rao, X. Chen, S. Biswal, S. Guccione) to move into their shared laboratories. New facilities for cell/molecular biology as well as synthetic organic chemistry are now in place and critical to the growth of the MIPS. The MIPS was able to go live with the cyclotron facility in Lucas Expansion in mid 2005 and the cyclotron is now routinely producing several isotopes including Flourine-18. Dr. David Dick, head of Cyclotron Physics, has been able to bring the facility on-line and will continue to streamline operations for clinical and research isotope production. We have recently also recruited Dr. Fred Chin, Head of Cyclotron Chemistry, formerly at the NIH, to help build our infrastructure for routine clinical and research radiochemistry. Architectural plans for the new Nuclear Medicine/Molecular Imaging clinic have also been finalized and ~15,000 square feet of new space on the second floor of Stanford Hospital will start renovation in 2006 and be completed in 2008. This will be key for translating many of the discoveries in MIPS to clinical applications in the near future. This new facility will consolidate PET-CT, SPECT-CT, SPECT, as well as newer generation molecular imaging instrumentation.

The MIPS was recently awarded a National Cancer Institute (NCI) In Vivo Cellular Molecular Imaging Center (ICMIC) P50 grant for $10,000,000. The other investigators include Dr. C. Contag (co-PI), D. Felsher, X. Chen, R. Negrin, F. Blankenberg, J. Rao, G. Nolan, C. Levin, D. Paik, M. Schnitzer, T. Graves, as well as many other faculty. Stanford University was the only new center in the entire country funded this year. This grant will help MIPS to leverage the existing infrastructure on campus in order to continue to expand molecular imaging research on campus. Research projects for several faculty in the Department of Radiology as well as other Departments will be funded. Support for the small animal imaging center in the Clark Building as well as the Cyclotron/Radiochemistry facility are included in this grant. Developmental projects will also be funded through this grant and will help to seed new research that can become competitive for further extramural funding.

The MIPS has also finalized plans to work with several companies on various molecular imaging research projects that will help fuel industry-academic partnerships. General Electric is one such key partner actively involved in helping to set up various fa-cilities in the new Lucas Expansion and will now be actively involved in specific research projects. Other companies which are also involved in specific research projects include Pfizer, Amgen, and Chiron. It is hoped that the acceleration of drug validation will be made possible through methods being developed and validated in the MIPS.

This was the first year that MIPS educational activities went into full gear. The faculty taught Bioengineering 222 for the first time highlighting all the different facets of molecular imaging to graduate students (http://mips.stanford.edu/public/classes/). We expect that this one quarter class will grow to a two quarter class in the near future. The molecular imaging seminar series also continued to invite speakers from around the world. These lectures are webcast (http://mips.stanford.edu/public/mi_seminar.adp) and have covered topics that include molecular imaging research with bioluminescence tomography, magnetic resonance imaging, positron emission tomography, as well as many other important areas.

The MIPS continues to expand its active small animal imaging resource (http://mips.stanford.edu/public/sci3.adp) with multiple small animal imaging instruments located in the Clark Center. These technologies play critical roles in helping to validate new molecular imaging probes and many different types of pre-clinical models. Most recently, a new GE Vista MicroPET and a new small animal SPECT-CT have been installed.

Many new faculty have been recruited to the program in the last two years, primarily through the Department of Radiology. Over 80 faculty, research scientists, post-doctoral fellows, and graduate students are now in place as part of the MIPS. A full list of faculty may be found on the MIPS web site, but the recent accomplishments of MIPS faculty with Radiology as their primary Department are described next.

Sandip Biswal M.D. and members of his lab, Drs. Parasuraman Padmanabhan, PhD, Sheen-Woo Lee, MD, Ray Lertvaranurak, MD and Bao Do, MD are interested in using multimodality molecular imaging techniques to study musculoskeletal diseases. Dr. Padmanabhan specializes in building novel genetic constructs to study the expression of specific genes and understanding protein-protein interactions in vivo. He is developing methods to see estrogen receptor-mediated signaling and calmodulin folding in vivo. Dr. Lee has developed protocols to monitor the trafficking of mesenchymal stem cells in living, longitudinal models of long bone fracture. She has found that bone healing can be augmented with the addition of stem cells to a fracture environment. She is also developing and validating the use of clinically-relevant magnetic resonance imaging and computed tomography methods for the early detection of rheumatoid arthritis. Dr. Lertveranurak is interested in monitoring the trafficking and integration of neural stem cells into central nervous system tumors. Dr. Bao has made significant inroads in understanding glucose metabolism in the human spinal cord. We have been fortunate to receive the Donald E. and Delia B. Baxter Foundation Research Scholar Award and to present our work at a number of national conferences.

Francis Blankenberg M.D. is supported by NCI/NIBIB RO1 EB000898-04A1 (PI-Blankenberg) and NCI/NIBIB R01 CA102348-1-01 (PI-Jonathan F. Tait, CoPI-Blankenberg). The first grant, Imaging Apoptosis In Vivo with Technetium 99m, focuses on the sensitivity and specificity of radiolabeled annexin V uptake, a marker of programmed cell death, following stroke and in tumors in response to chemotherapy in rodent and murine models, respectively. The second grant, Membrane Binding and Imaging Applications of Annexins examines the biodistribution and imaging characteristics of a dozen mutated forms of self-chelating annexin V to better understand the in-vivo binding characteristics and mechanisms of annexin V localization in vivo. Dr. Blankenberg is also a PI on a developmental project for the NCI ICMIC grant, Development of VEGF-driven PET imaging of tumor vasculature. Accomplishing these specific aims of the VEGF project will determine the feasibility of targeted PET imaging of tumor angiogenesis in oncology patients. In addition, this type of imaging might provide the basis for rational selection of patients for anti-angiogenic therapies.

Xiaoyuan (Shawn) Chen Ph.D. is supported by the NCI ICMIC grant, PET Imaging of Brain Tumor Angiogenesis and Anti-Angiogenic Treatment; NIBIB grant, MicroPET and NIR Fluorescence Imaging Tumor Angiogenesis; DOD BCRP IDEA award, Alpha-v Integrin Targeted PET Imaging of Breast Cancer Angiogenesis and Low-Dose Metronomic Anti-Angiogenic Chemotherapy Efficacy; DOD PCRP NIA award, Imaging Primary Prostate Cancer and Bone Metastasis; American Lung Association Research Award, Vasoactive Intestinal Peptide Receptor Targeted Imaging of Lung Cancer. Postdoctoral fellow Weibo Cai received both the Dean's Fellowship and the 2005 Society for Molecular Imaging (SMI) Travel Award. Eight papers were either published or are in press; another 5 papers have been submitted. Over 15 abstracts have been submitted to AMI 2005, SNM 2005, SMI 2005, and other conferences.

Sam Gambhir M.D., Ph.D. received the NCI ICMIC P50 grant for $10,000,000 for which he serves as the Principal Investigator. He received the Doris Duke Distinguished Clinical Scientist Award which includes $1,500,000 in funding for work on novel PET imaging agents for cancer. Work from his lab on PET imaging of patients undergoing gene therapy was featured on the cover of the *Journal of Gastroentorology* and work on quantum dots was featured on the cover of *Science* this year. His students, Dr. Andreas Loening, Olivier Gheysens, and Yingbing Wang all received fellowships this year. Dr. Gambhir gave the Henry Wagner Lectureship at the Society of Nuclear Medicine to over 4000 people on multimodality molecular imaging this year. Work from his lab in collaboration with Drs. Andy Quon, Sandy Napel, and Chris Beaulieu received the Society of Nuclear Medicine (SNM) Image of the Year for 2005. Dr. Gambhir is working on several new educational projects including the Advanced Residency Training at Stanford (ARTS), which is a new initiative to allow residents to work on a Ph.D. in order to build stronger academic physician-scientists.

SNM 2005 Image of the Year

Dr. Gambhir also serves as the President of the Academy of Molecular Imaging (AMI), and is on the National Cancer Institute Scientific Advisory Board.

Craig Levin Ph.D. joined the Radiology Department in Spring of 2004. He was awarded two research grants from the National Institutes of Health (NIH): one from the National Cancer Institute (NCI) for the development of a new positron emission tomography (PET) camera dedicated to breast cancer imaging, and the other from the National Institute of Biomedical Imaging and Bioengineering (NIBIB) to build an ultra-high resolution research PET system for pre-clinical molecular imaging research of small animal disease models. Dr. Levin was also awarded a research grant from the Whitaker Foundation to develop a sensitive gamma ray imager for surgical cancer staging. He received NIH and Susan G. Komen Foundation funding to organize and direct a Breast Cancer Workshop. He organized and chaired a symposium on Technologies for In-Vivo Small Animal Imaging, the first of its kind, at the American Association for Physicists in Medicine annual meeting in Seattle, Washington. He has also chaired sessions at international conferences and has served on grant proposal review panels for NIBIB and the US Army Breast Cancer Research Program. His students Angela Foudray, Dr. Jin Zhang, and Peter Olcott were awarded research fellowships to conduct research in his laboratory and/or travel fellowships to attend various international conferences and workshops to present their research results. Dr. Levin is currently organizing the first Small Animal Imaging Symposium to be held at Stanford to teach international researchers the science of molecular imaging in small animal models of disease.

Jianghong Rao, Ph.D. and his lab members are working at the interface of chemistry and biology with an emphasis on the development of methods and techniques to image biological events of interest in normal and diseased states in their native physiological environments. Combining expertise from organic chemistry, biochemistry, molecular biology, and optical imaging, we are taking a synergic effort towards developing these imaging tools and techniques. Dr. Rao's research is supported by awards from the NIBIB, NCI, and the Burroughs Wellcome Fund. Dr. Yan Zhang from his lab has been awarded the Dean's Fellowship, and Dr. Nga-Wai (Tiffany) Chung was awarded the Bio-X Interdisciplinary Postdoctoral Fellowship. Dr. Bengang Xing has been selected for a 2005 Young Investigator Travel Award by the Academy of Molecular Imaging.

Joseph Wu, M.D., Ph.D. received the American Heart Association Beginning Grant in Aid for $140,000 for cardiac imaging of stem cell therapy. He won the Best Drug Development Award at the Academy of Molecular Imaging meeting. Dr. Wu is an invited moderator for scientific sessions at this year's upcoming American Heart Association meeting. He is currently involved in many aspects of molecular imaging research related to stem cell therapy. Dr. Wu's student, Dr. Feng Cao, received a cardiovascular molecular imaging fellowship from the American Society of Nuclear Cardiology.

Research Overview

Strategic Research Development

NORBERT PELC, SUSAN KOPIWODA

2005 has been a record-breaking year for research at the Richard M. Lucas Center, and for the Stanford Radiology Department as a whole, thanks to the tremendous accomplishments of our faculty, staff, and students. During this past year, we have pioneered new programs and secured renewed funding for our long-standing programs. Radiology now directs four highly competitive NIH-supported research and education programs: 1) The Center for Advanced Magnetic Resonance Technology (CAMRT), in its eleventh year of continuous funding; 2) The Center for Advanced Cancer Imaging, in its thirteenth year of continuous funding; 3) The In Vivo Cellular and Molecular Imaging Center (ICMIC), in its initial year of funding; and 4) The Computational Modeling of Cancer Biology, also in its initial year of funding. A major goal is to train the next generation of world-renowned imaging scientists. To accomplish this, we have made education and training the primary focus in these large programs. Each relies almost exclusively on the Lucas Center space and facilities.

The Department of Radiology had a remarkably successful research year as indicated by the number of projects held by the department and the number of faculty leading funded projects. More than 60% of our faculty are principal investigators for various sponsored projects, and 40% direct more than one project while 38% lead NIH projects. More than 60% of all funded projects within the department are government supported, and more than 80% of our research dollars are generated by government projects. During fiscal year 2005, government funding totaled $15M: a record for our department. NIH funded projects comprised $13.4M of that amount (Figure 1). Total funding for all projects in 2005, including federal, industry, and foundation dollars, was $17M. Congratulations to everyone in the department for this phenomenal research year!
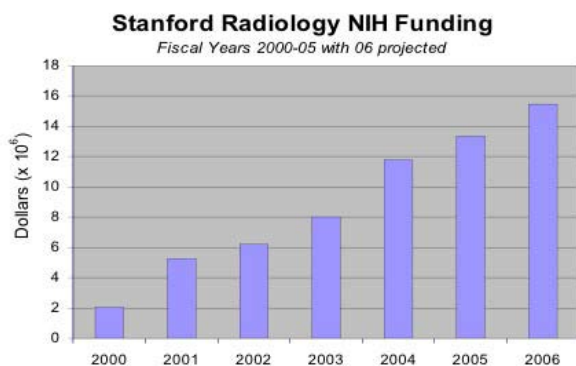

Figure 1. Illustrates Stanford Radiology NIH funding history from 2000 to 2005 with a conservative projection for 2006.

The Department's research activity is facilitated by Norbert Pelc, Associate Chair of Research, Susan Kopiwoda, Director of Strategic Research Development, with strategic oversight from Department Chair, Gary Glazer. Along with other departmental leaders, this key group provides guidance in establishing new research directions and aiding faculty to attain their research goals. We work with our experienced researchers to provide assistance in transforming their research visions to vibrant, well-funded projects.

Our research group continues to grow in size and scope, expanding with the growing volume of research activity within the department. With the addition of 6 new research faculty since 2003 (from 12 to 18), we have added an equal number of labs and an average of 6 to 7 research people per faculty. Figure 2 illustrates department research personnel growth including faculty, postdoctoral trainees, graduate students, and research staff.
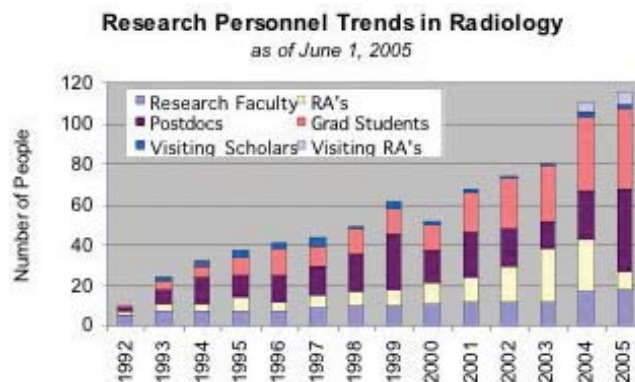

Figure 2. Illustrates the history of department growth in research personnel since 1992.

2005 RANK AND EXPECTED 2006 FUNDING

The NIH proposals we are submitting reflect the extraordinary breadth of activities of our faculty in the areas of MRI, CT, nanotechnology and multimodality imaging (including MRI/CT, PET/CT) as well as our continued efforts to develop disease-specific imaging techniques/devices and interventional image-guided techniques.

The increase in our NIH funding from 2004 to 2005 improved our NIH ranking among U.S. radiology departments. For the NIH 2005 fiscal year, we are the 5th highest NIH funded Radiology department in the country (Figure 3). Because of pressures on the federal budget and essentially no growth in the NIH appropriation, the outlook for NIH funding in 2006 is unclear, but not optimistic. Nonetheless, based on current proposals in the pipeline and anticipated submissions, we expect to reach ~$15-17M in government funding in 2006 (see Figure 1 for 2006 and NIH projection).
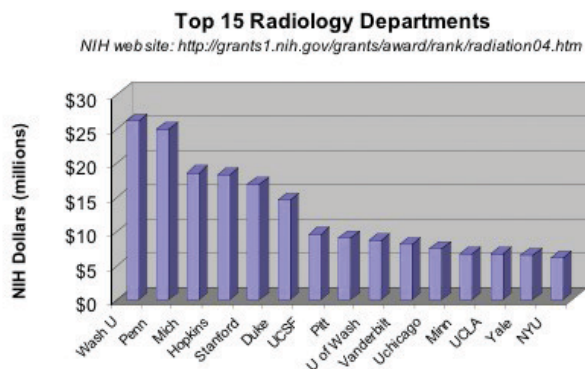

Figure 3. This data is taken from the NIH website and shows the top ranking radiology departments in the country. NIH data combines radiology and radiation oncology funding.

Government Sponsored Research

PI	Sponsor	Title
Chen X	DOA	Alpha-v Integrin Targeted PET Imaging of Breast Cancer Angiogenesis
Chen X	DOA	Molecular Imaging of Ovarian Carcinoma Angiogenesis
*Chen X	DOD	Imaging Primary Prostate Cancer and Bone Metastasis
Gambhir	DOE	Molecular Imaging of Stem Cell Survival, Apoptosis, and Differentiation in Myocardium
Bammer	NIH	Improving SENSE MRI for Spiral and Echo-Planar Imaging
Beaulieu	NIH	Three-Dimensional CT Colonography
Blankenberg	NIH	Imaging Apoptosis in vivo with Technetium 99m Annexi
Butts	NIH	Improved Open MRI for Image-Guided Breast Procedure
Butts	NIH	iMRI Methods for Cancer Diagnosis and Treatment
Butts	NIH	iMRI Methods for Cancer Diagnosis and Treatment
*Chen X	NIH	MicroPET and NIR Flourescence Imaging of Tumor Angiogenesis
Daniel	NIH	Magnetic Resonance Imaging of Breast Cancer
Daniel	NIH	Techniques for MRI-Guided Cryosurgery of Prostate Cancer
Fahrig	NIH	Hybrid X-Ray/MR Systems for Image-Guided Procedures
Fahrig	NIH	Improved C-Arm CT for Interventional Procedures
Gabrieli	NIH	Cognitive Analysis of Working Memory Development
Gambhir	NIH	In Vivo Cellular and Molecular Imaging Center at Stanford
*Gambhir	NIH	Multimodality Imaging of Cell Mediated Gene Transfer
Gambhir	NIH	Reporter Imaging of Protein-Protein Interactions
Glazer/Pelc	NIH	Advanced Techniques for Cancer Imaging
Glover	NIH	Center for Advanced Magnetic Resonance Technology at Stanford
Gold	NIH	Rapid MRI for Evaluation of Osteoarthritis
Guccione	NIH	Correlative Imaging of Tumor Angiogenesis
*Levin	NIH	A New Photon Sensor to Improve Molecular Cancer Imaging
Levin	NIH	New Scintillation Light Detection Concepts for PET
Moseley	NIH	DWI Assessment of Clinical Acute Stroke
Moseley	NIH	Improved PWI Methodology in Acute Clinical Stroke
Napel	NIH	Efficient Implementation of 3D Vascular Image Data
Plevritis	NIH	Breast Cancer Trend Analysis Using Stochastic Simulation
Plevritis	NIH	Computational Modeling of Cancer Biology
*Plevritis	NIH	Cost-Effectiveness Analysis of Lung Cancer Screening
Rao	NIH	Unified Reporter Gene for Multi-Modality Imaging
*Rubin	NIH	Improving Radiologist Detection of Lung Nodules with CAD
Rubin	NIH	Volumetric Analysis of the Aorta and Its Branches
Sommer	NIH	MRI of Renal Anatomy and Function in Chronic Ischemia
*Sommer	NIH	Precise MRI-Directed Sonic Ablation of Prostate Cancer
Spielman	NIH	Magnetic Resonance Spectrosopic Neoplasm Imaging
Spielman	NIH	MR Spectroscopic Imaging in Alzheimer's Disease
*Wu	NIH	Molecular Imaging of Cardiac Cell Transplantation
*Napel	BioEng/NIH	SIMBIOS - Physics-Base Simulation of Biological Structures
Blankenberg	U of Wash/NIH	Membrane Binding and Imaging Applications of Annexins
Glover	UCSD/NIH	Functional Imaging Research in Schizophrenia Testbed
*Gold	UCSF/NIH	Data Coordinating Center for Osteoarthritis Initiative
Gold	VA PAIRE/NIH	Biomechanical Modeling of Muscle Function Following Tendon Transfer Surgery
Glazer	VA	Department of Veteran Affairs Mammography Screening Contract
Glazer	VA	Solicitation Agreement
Glazer	VA	Solicitation Agreement for IR and Cardiovascular Imaging
Glazer	VA	Solicitation Agreement for Musculoskeletal Services

Foundation Sponsored Research

Chan	American Lung Assn	Vasoactive Intestinal Peptide Receptor Targeted Imaging of Lung Cancer
Chan	The Whitaker Foundation	Optimized 4-D Magnet Resonance Flow Imaging for Congenital Heart Disease
Chen, Ian	American Heart Assn	Multimodality Imaging of Cardiac Therapy
*Do	Stanford	A Novel Non-Invasive Device for Occluding Cerebral Aneurysms
Fahrig	Sunnybrook & Women's College Fd	Low Cost Digital X-ray Detectors Using Liquid Crystals
Fahrig	The Whitaker Foundation	Ultrafast Tomosynthesis for the Detection of Lung Cancer
Gambhir	Doris Duke Charitable Fd	Molecular Imaging of Cancer with a Voltage Sensor
Gold	Stanford	Modeling Muscles in Contact
*Gold	Wallenberg Fd.	Learning Radiology in Simulated Environments
*Herfkens/ Hellinger	Stanford-OTL	Solution Encoder for Diagnostic Radiological Imaging

Levin	The Whitaker Foundation	Novel Impact of Gamma Ray Imager for Improved Surgical Staging of Cancer
Mazin	American Heart Assn	Fast Volumetric Cardiovascular CT Scanner
Pineda	American Heart Assn	Task-Based Reconstruction of Ultrafast Tomosynthesis for Guidance of Lung-Nodule Biopsy
Rao	The Burroughs Wellcome Fund	Career Award at the Scientific Interface
Rubin	RSNA	Fellowship in Cardiovascular Imaging
Rubin	Stanford	Undergraduate Research Support
*Wu	American Heart Assn	In Vivo Tracking of Stem Cells in the Ischemic Myocardium
Wu	American Soc of Nuclear Cardiology	PET Imaging of Cardiac Stem Cell Transplant Survival
Yaghoubi	RSNA	PET Imaging of Cell Trafficking in Adoptive Immune Cell Gene Therapy of RA

Industry Sponsored Research

Bammer	Endius, Inc.	Evaluation of Minimally Invasive vs Open Posterolateral Lumbar Fusion with MRI
*Biswal	Roche Laboratories	MRI of Treated and Control Non-Stanford Murine Models of Rheumatoid Arthritis
*Frisoli	Cook Incorporated	The Zilver PTX Drug Eluding Vascular Stent in the Above the Knee Femoralpopliteal Artery
Frisoli	Vivant Medical, Inc.	Microwave Ablation of Metastatic Bone Tumors for Palliation of Pain
Frisoli	W.L. Gore & Associates	Comparing Use of Thoracic EXCLUDER Endoprosthesis to Open Surgical Repair in Descending Thoracic Aneurysms
Frisoli	W.L. Gore & Associates	A Feasibility Study Using a Transluminally Placed Self-Expanding Stentgraft
Frisoli	W.L. Gore & Associates	Evaluation of the GORE TAG Thoracic Endoprothesis for Treatment of Descending Thoracic Aneurysms
Frisoli	W.L. Gore & Associates	Use of the GORE TAG Thoracic Endoprosthesis in Subjects with Descending Thoracic Aortic Aneurysms
*Gambhir	AMGEN	In Vivo Effects of Amgen Compounds Using PET (Compound D)
*Gambhir	AMGEN	In Vivo Effects of Amgen Compounds Using PET (Compound E)
*Gambhir	Chiron Corporation	Assessing Tumor Response to Therapy
*Gambhir	diaDexus, Inc.	Pilot Antibody Tumor Imaging Study in Mice
Gambhir	Pfizer Central Research	Molecular Imaging of the Effects of New Anti-Tumor Pharmaceuticals
Glazer	General Electric	Destination Digital Agreement
Glazer	General Electric	GE PACS System
Glazer	General Electric	Magnetic Resonance Imaging (MRI) Systems
Glover	SRI International	CVD Risk Factors and Brain Morphology in Twins
Guccione	Varian	Local Drug Delivery Using External Radiation
*Ikeda	U-Systems	3-D Full Field Whole Breast Ultrasound: Development
Kee	Cook Incorporated	Zilver Vascular Stent in the Iliac Arteries
Kee	W.L. Gore & Associates	Evaluating the Thoracic EXCLUDER Endoprosthesis in the Treatment of Descending Thoracic Aortic Diseases
Marks	Concentric Medical, Inc.	A Multinational Controlled Registry to Evaluate the Concentric Merci Retriever System
Marks	Diversified Diagnostic Products	A Prospective Collection of Safety Data to Measure Cerebral Blood Flow (CBF)
Moseley	Nihon Medi-Physics	Comparison of Fast Imaging Techniques for MRI of H20-17
Napel	Siemens Corporate Research	Interventional Room of the Future
Pelc	GE Med Systems	CT XRAY
Rubin/Napel	R2 Technology, Inc.	Computer Aided Tracking and Analysis of Pulmonary Nodules Over Time
Spielman	SRI International	In Vivo Diffusion and Spectroscopic Brain Imaging in Alcoholism
*Sze	Cook Incorporated	Zenith TX2 Thoracic TAA Endovascular Graft
Sze	W.L. Gore & Associates	Use of the Modified Bifurcated EXCLUDER Endoprosthesis vs Open Surgical Repair in the Treatment of Infrarenal Abdominal Aortic-Aneurysms
Sze	W.L. Gore & Associates	Use of the Bifurcated EXCLUDER Endovascular Prosthesis vs Open Surgical Repair in the Treatment of Infrarenal Abdominal Arotic Aneurysms
Wu	GlaxSmithKline R & E Foundation	Molecular Imaging of Cardiac Cell Transplant
*Wu	Pfizer Pharmaceuticals	The Role of Statins in Cardiac Stem Cell

* indicates newly sponsored project

Radiology Scientific Research Personnel

Faculty and Staff

Faculty

Gary M. Glazer, M.D.
Gary H. Glover, Ph.D.
Roland Bammer, Ph.D.
Mark Bednarski, M.D., Ph.D.
Kim Butts, Ph.D.
Xiaoyuan (Shawn) Chen, Ph.D.
Rebecca Fahrig, Ph.D.
Sam Gambhir, M.D., Ph.D.
Samira Guccione, Ph.D.
Brian Hargreaves, Ph.D.

Robert J. Herfkens, M.D.
Craig Levin, Ph.D.
Michael E. Moseley, Ph.D.
Sandy Napel, Ph.D.
David Paik, Ph.D.
Norbert J. Pelc, Sc.D.
Sylvia K. Plevritis, Ph.D.
JianHong Rao, Ph.D.
Daniel M. Spielman, Ph.D.

Scientific Staff

Marcus Alley, Ph.D.
Wendy Baumgardner, RVT, LATg
Bonnie Bell
Robert Bennet, Ph.D.
Jenea Boshart, M.A.
Thomas Brosnan, Ph.D.
Ian Chen, M.D., Ph.D.
Danye Cheng
Zhen Cheng, Ph.D.
Frederick Chin
Garry Chinn
Steven Choi, B.S.
David Clayton, Ph.D.
Mangal Dandekar, M.D.
Abhijit De
David Dick, Ph.D.
Tim Doyle, Ph.D.
Mary Draney, Ph.D.
Arundhuti Ganguly, Ph.D.
Diane Howard, RVT, LATg
William Johnsen
Keshni Kumar, R.T.

Andreas Loening, Ph.D.
Dirk Mayer, Ph.D.
Linda Novello, R.T.
Peter Olcott
Laura Pierce, B.S., R.T.
Bhargav Raman
Ruminder Samra, R.T.
Manish Patel
Pritha Ray, M.S.
Viola Rieke, Ph.D.
Sandra Rodriguez, R.T.
Anne Sawyer-Glover, B.S., R.T. (R)(MR)
Greig Scott
Bronislava Sigal, Ph.D.
Stefan Skare, Ph.D.
Marc Sofilos, R.T.
Yingyun Wang, B.S.
Lars Wigstrom, Ph.D.
Joseph Wu, M.D., Ph.D.
Yishan Yang, Ph.D.
Marowan Zakhour, M.D.

Administrative and Support Staff

Phoebe Abt
Mary Bobel, M.B.A.
Maggie Bos
Nancy Bucy
Michelle Christierson
Donna Cronister
Debra Frank
Susan Kopiwoda, M.S., M.P.H,
Suzi Kosher
Marlys Lesene

Laura Lotfy
Kevin Murphy
Sharon Pollio
Kala Raman
John Reuling
Lanzie Rivera
Julie Ruiz, Ph.D.
Susan Singh
Susie Spielman
Lakeesha Winston

Students and Visitors

POSTDOCTORAL FELLOWS

Weibo Cai, Ph.D.
Feng Cao, Ph.D.
Qizhen Cao, Ph.D.
Carmel Chan, Ph.D.
Nga-Wai (Tiffany) Chung, Ph.D.
Bao Do, M.D.
Daniel Ennis, Ph.D.
Tony Faranash, Ph.D.
Nadine Gaab, Ph.D.
Olivier Gheysens, Ph.D.
Gayatri Gowrishankar, Ph.D.
Frezghi Habte, Ph.D.
Jung-Jin (Jason) Hsu, Ph.D.
Thies Jochinsen
Shay Keren, Ph.D.
Manikam Krishnan, Ph.D.
Malika Larabi, Ph.D.
Sheen-Woo Lee, M.D.
Michael Lim, Ph.D.
Chunlei Liu, Ph.D.

Erin Liu, Ph.D.
Aiming Lu, Ph.D.
Michael McDonald, Ph.D.
Scott Nagle, M.D.
Rex Newbold, Ph.D.
Parasuraman Padmanabhan, Ph.D.
Angel Pineda, Ph.D.
Laura Pisani, Ph.D.
Paulmurugan Ramasamy, Ph.D.
Cesar Rodriguez, Ph.D.
Justus Roos, Ph.D.
Meike Schipper, Ph.D.
Cindy Shi, Ph.D.
Jeffery Tseng, Ph.D.
Yun Wu, Ph.D.
Bengang Xing, Ph.D.
Shahriar Yaghoubi, Ph.D.
Xinrui Yan, M.D.
Hequan Yao, Ph.D.
Yan Zhang, Ph.D.

GRADUATE STUDENTS

Murat Aksoy, M.S.
Jongduk Baek, M.S.
Priti Balchandani
Regina Bouwer, M.S.
Jean Chen, M.S.
Yen-Lin Chia, M.S.
Angela Foudray, M.S.
Taly Gilat, M.S.
Anjia Gu, M.S.
Meng Gu, M.S.
Misung Han, M.S.
Andrew Holbrook, M.S.
Yanle Hu, M.S.
Elena Kaye, M.S.
Susan Shu-An Lin, M.S.
Cyrus Jame, M.S.
Sonal Josan, M.S.
Ajay Joshi, M.S.
Christine Law, M.S.
Yakir Levin, M.S.
Calvin Lew, M.S.
Sam Mazin, M.S.

Michael Padilla, M.S.
Bini Pankhudi, M.S.
Rebecca Rakow, M.S.
Tejas Rakshe, M.S.
Anthony Sherbondy, M.S.
Leroy Sims, M.S.
Gaurav Srivastra, M.S.
Jared Starman
Shaohua Sun, M.S.
Padma Sundaram, M.S.
Moriah Thomason, M.S.
Chardonnay Vance, M.S.
Zachary Walls, M.S.
Yingbing Wang, M.S.
Zhifei Wen, M.S.
Jung Ho Won, M.S.
Yao-Hung Yang, M.S.
Sung-Won Yoon, M.S.
Huanzhou Yu, M.S.
Jian Zheng, M.S.
Lei Zhu, M.S.

VISITING RESEARCHERS AND SCHOLARS

Daniel Fiat, Ph.D.
Jinha Mark Park, M.D., Ph.D.
Min Kyung So, Ph.D.
Zhengming Xiong , M.D., Ph.D.
Xianzhong Zhang, Ph.D.

UNDERGRADUATES

Tom Hope

Awards and Honors

Patrick D. Barnes, Outstanding Senior Faculty of the Year for Contributions to Resident Education, Compassionate Patient Care, and Research. Department of Radiology. Stanford University Medical Center, May 2005

Sandip Biswal, Outstanding Junior Faculty of the Year for Contributions to Resident Education, Compassionate Patient Care, and Research. Department of Radiology. Stanford University Medical Center, May 2005

Kim Butts, International Society of Magnetic Resonance in Medicine, Board of Trustees

Weibo Cai, Dean's Fellowship, 2005

Feng Cao, cardiovascular molecular imaging fellowship, The American Society of Nuclear Cardiology

Frandics Chan, Overall Outstanding Faculty for Contributions to Resident Education, Compassionate Patient Care, and Research. Department of Radiology. Stanford University Medical Center, May 2005

Nga-Wai (Tiffany) Chung, Bio-X Interdisciplinary Postdoctoral Fellowship

Rebecca Fahrig, Cover of journal *Medical Physics*, Performance of a static-anode/flat-panel x-ray fluoroscopy system in a diagnostic strength magnetic field: A truly hybrid x-ray/MR imaging system, 2005

Dominik Fleischmann, Editor's recognition award, *Radiology* for Reviewing, 2004

Nancy Fischbein, Lysia Forno Award for Teaching Excellence, Department of Neurology, Stanford University Medical Center, 2005

Angela Foudray, P.E.O. International Scholar Award, 2005

Angela Foudray, Molecular Imaging Summer School Scholarship, 2005

Sam Gambhir, Henry Wagner Lectureship at the Society of Nuclear Medicine, 2005

Sam Gambhir, President, Academy of Molecular Imaging (AMI), 2005-06

Sam Gambhir, National Cancer Institute (NCI), Board of Scientific Advisors, 2004-08

Sam Gambhir, First Prize, Clinical Abstract; Imaging Gene Therapy in Humans; AMI, 2005

Sam Gambhir, Presidential Lecture, Memorial Sloan Kettering Cancer Center, 2005

Sam Gambhir, Pendergrass Lecture, Vanderbilt University, 2005

Sam Gambhir, Cover of journal *Science*, Molecular Imaging with Quantum Dots, 2005

Gary M. Glazer, President, International Society for Strategic Studies in Radiology, 2003-2005

Gary Glover, National Institutes of Biological Imaging and Bioengineering National Advisory Council

Garry Gold, Kaiser Award for Outstanding and Innovative Contributions to Medical Education, 2005

Garry Gold, ASB Pre-doctoral research award (Co-Author) 2005

Brian Hargreaves, Best Poster. ISMRM. Nayak KS, Hu BW, Hargreaves BA. Wideband SSFP: SSFP with imaging bandwidth greater than 1/TR

Michael Lim, Gianini Family Foundation Award

Michael Marks, ASNR Outstanding Presentation Award in Interventional Neuroradiology, ASITN's Michael Brothers Memorial Award, 43rd. Annual Meeting of the American Society of Neuroradiology, Toronto, Ontario, Canada, May 2005, Marks MP, Wojak JC, Al-Ali F, Jayaraman MV, Marcellus ML, Connors JJ, Do HM. Angioplasty for symptomatic intracranial stenosis: Long-term clinical outcome

William Northway, J.E. Wallace Sterling Lifetime Alumni Achievement Award, Stanford University for pioneering work in the field of pediatric radiology and his ongoing commitment to impart his expertise to students, residents, and fellows

Andrew Quon, Sandy Napel, Chris Beaulieu, Sam Gambhir, Society of Nuclear Medicine (SNM) Image of the Year, 2005

Norbert Pelc, National Institutes of Biological Imaging and Bioengineering National Advisory Council

Scott B. Reeder, Lauterbur Award for Outstanding MRI Paper. Society of Computed Body Tomography and Magnetic Resonance (SCBT/MR), 28th Annual Meeting, Miami Beach, March 20, 2005. Reeder SB, McKenzie CA, Brau ACS, Hargreaves BA, Yu H, Shimakawa A, Brittain JH, Gold GE, Johnson JW, Rofksy NM, Herfkens RJ, Rapid body MRI using IDEAL water-fat separation and parallel imaging

Scott B. Reeder, Radiological Society of North America (RSNA) Fellow Research Trainee Prize (Physics), December 2004

Viola Rieke, Poster Award, 5th Interventional MRI Symposium. October 2004. Rieke V, Ganguly A, Scott GC, Daniel BL, Pauly JM, Pelc NJ, Fahrig R, Butts K. X-ray compatible RF-coil for integrated x-ray/MR imaging systems

Hans Ringertz, Gold Medalist of the European Association of Radiology and the European Congress of Radiology, March 2005

Leroy Sims, Howard Hughes Medical Institute Scholarship, 2004

Leroy Sims, Howard Hughes Medical Institute Research Training Fellowship, 2005

Daniel Spielman, Outstanding Teacher Award, International Society of Magnetic Resonance in Medicine, 2005

Moriah Thomason, cover of journal *NeuroImage*. Breath holding reveals differences in fMRI BOLD signal in children and adults.

Laura Varich, Outstanding Clinician Educator for Contributions to Resident Education, Compassionate Patient Care, and Research. Department of Radiology. Stanford University Medical Center, May 2005

Joseph Wu, Best Drug Development Award, Academy of Molecular Imaging

Jin Zhang, Stanford University Medical School Dean's Fellowship, 2004-2005

Yan Zhang, Dean's Fellowship

RESEARCH GROUP UPDATES

RSL GROUP UPDATES

MAGNETIC RESONANCE RESEARCH

Functional Imaging - Technology Development

GARY GLOVER

The functional MRI group continues to develop new methods for acquisition of functional imaging data. Projects include development of faster spiral-in/out methods, 3D fMRI acquisitions, calibration of fMRI using breathholding and hemodynamic response measurements, and development of fetal fMRI methods. In addition, the Center continues an active role in the FIRST BIRN schizophrenia testbed funded by the NCRR.

Christine Law continues to examine approaches using spiral-in/out trajectories that provide advantages in terms of either temporal resolution, spatial resolution or reduced "drop-out" artifacts. These methods use a multi-shot acquisition and variants on the UNFOLD reconstruction technique developed here several years ago by Bruno Madore (now at Brigham and Womens Hospital). By reversing the direction of the trajectories periodically, artifacts from imperfect gradient hardware can be removed from the final image timeseries.

The real-time fMRI projects include collaborations between Sean Mackey (Director of the Stanford Pain Center, Anesthesiology), Chris deCharms (Omnion) and our group, which continue to demonstrate exciting results. It has been found that, like normal subjects, chronic pain subjects can learn to control their perception of pain using biofeedback that is developed by the processing of brain activation during the scan. Apparently this control ability persists for months after the scanning sessions have ended. In addition, Sean's NIH R01 grant application to study fMRI in the spinal cord recently received the wonderful priority score of 138.

Graduate student Yanle Hu is studying the noise propagation in 3D spiral fMRI acquisitions. Theoretically, the 3D method should have improved BOLD CNR, but noise that stems from basal metabolism in the brain is greater in 3D methods than the counterpart 2D techniques. Yanle is exploring the basics of this phenomenon and has developed several methods for its mitigation. Signal to noise ratio improvements of 80% have been demonstrated.

Jung Jiin (Jason) Hsu has further advanced his localized shim coil approach for fMRI, that improves the homogeneity of the magnetic field in the vicinity of the frontal orbital region of the brain. Most recently, he has developed a dynamic method that changes the shim characteristics for each imaging slice, thereby reducing the signal loss over a larger region of the brain. He has developed a set of hardware and software to control his new coils.

Nadine Gaab, a postdoc in Gabrieli's lab, has submitted several papers on the use of sparsely sampled methods to alleviate the influence of scanner noise on auditory processing. She has found a surprisingly large effect, and her method is very effective. Furthermore, she has found that the scanner noise has a significant effect on the basal metabolism in the brain.

Postdoc Laura Pisani has begun a new project on the use of neuronal activity measured by fMRI as a surrogate marker for fetal viability in cases of intra-uterine growth retardation (IUGR). This is a challenging project because of the issues of fetal motion and difficulty in stimulating the fetus. She proposes the use of an oxygen challenge to the mother as a way of observing the changes in vascular reactivity in the fetal brain. She will be submitting an NIH fellowship grant application. This is a collaboration with Richard Barth, pediatric radiology section chief, OB clinicians and Roland Bammer in the RSL.

In a related project, Chardonnay Vance is a grad student at UC-Berkeley and Stanford, who is studying aging processes as well as the biochemistry of placental membranes. Using measurements of NMR relaxation times and other parameters in vitro and in vivo, she wants to understand the various transport mechanisms in the placenta in health and IUGR.

Rebecca Rakow-Penner, a grad student in Biophysics, is continuing the use of functional methods to characterize breast cancer and is finishing a paper on the relation properties of breast tissue. She was accepted into medical school at Stanford and will be very busy, indeed.

Moriah Thomason, past Chair of the Stanford Graduate Student Council, continues her study of working memory in children and adults, and has recently published a paper on the differences in cerebral vascular response in the two age groups using breath-holding as a probe. Paradoxically, she found that children's brains are more reactive but also "noisier" than those of adults. Her article was featured on the front cover of the journal *NeuroImage*, a prestigious accomplishment for a graduate student (or faculty!).

I am incredibly proud of my students; they are not only wonderful scientists but also delightful people to be with and an honor to mentor.
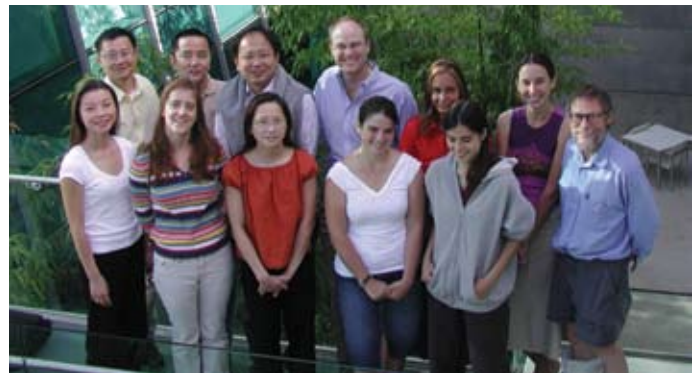
fMRI group (l-r) front row: Fumiko Maeda, Laura Pisani, Christine Law, Rebecca Rakow-Penner, Catie Chang; Back row: Jung-Jiin Hsu, Yanle Hu, Takefumi Ueno, Sean Mackey, Nadine Gaab, Chardonnay Vance, Gary Glover. Not shown: Moriah Thomason.

Functional "Microvascular" Neuroimaging
Roland Bammer and Michael Moseley

Magnetic resonance imaging (MRI) continues to advance the state-of-the-art in adult and pediatric neuroimaging. This last year has further advanced functional MRI which can map and measure brain tissue water diffusion rates and direction, perfusion of blood, and the brain's response to many functional activation tasks (such as vascular responses to mild reversible stresses) in a large number of diseases. We are planning to use the new 7 Tesla MRI scanner to refine new tools of high-field and high-speed MRI to focus on disease processes in "brain attacks" (cerebral stroke) using diffusion MRI (DWI), tissue perfusion mapping (PWI), as well as the new field of mapping the brain and white matter connectivity in both adults and in children (DTI). During the past year we've made significant progress in developing functional imaging technologies in several key areas under the general title of "Microvascular" imaging. These include diffusion and perfusion techniques for both imaging of acute stroke and for

The "neuroimaging" team includes (l-r) Mike Moseley, Thies Jochimsen, Jian Zhang, Roland Bammer, Chunlei Liu, Scott Nagle, Murat Aksoy, Rexford Newbould, David Clayton, Lanzie Rivera, and Stefan Skare.

imaging of white matter structure and integrity. By responding to the needs of our collaborators and colleagues here at Stanford and worldwide, we have found that diffusion and perfusion techniques have significantly advanced far beyond the experimental arena into everyday, routine clinical applications in a wide variety of fields where they are being actively and effectively used in numerous self-initiated and collaborative studies. The coming year will further advance our MR imaging tools and sharpen our focus on the critical clinical issues of detecting brain attacks with new experimental and clinical MR methods to predict eventual brain injury, to further map how the brain and spine are "wired," to understand the complex physiological stresses and changes that the brain experiences during stroke, and to extend these tools to better evaluate evolving therapies.

Roland Bammer has established several key collaborations with the Departments of Neurology and Pediatrics and has already initiated an active pediatric DTI program on the Lucille Packard Children's Hospital MRI scanner. Roland is also a "Docent" at the University of Graz, Austria and teaches there for 3 weeks per year. Currently Roland has two peer-reviewed grants from the NIH and has been named as "key personnel" on eight others. Mike Moseley is the Past President of the International Society of Magnetic Resonance in Medicine (ISMRM) and has had two key grants funded recently, including an NCRR grant for a $2M experimental GE 7T MRI scanner. He also sits on 6 different NIH study sections and is currently organizing an international meeting on DTI funded by the NSF and the NY Academy of Sciences. The neuroimaging team remains involved in white matter tensor "fiber-tracking" neuroimaging projects as well as building collaborative programs.

## Magnetic Resonance Spectroscopy
Daniel Spielman

During the past year, we have continued our research focus on the development of optimized in vivo magnetic resonance spectroscopic imaging (MRSI) techniques, with particular emphasis on high field systems ($\geq$ 3T). Increased information becomes available with the stronger field as the signal-to-noise ratio increases and coupling patterns are simplified. To date, the majority of in vivo proton (1H) MRSI has been performed in the brain due to minimal motion artifacts and low levels of overlapping lipid signals. In particular, ^{1}H MRSI is an important new tool for the noninvasive assessment, diagnosis, and treatment monitoring of brain disorders as well as general studies of interrelationships among brain development, structure, and function. In this year's Lucas Annual Report, improved methods for reducing gradient imperfections in spiral MRSI, volumetric brain imaging using a dualband spectral-spatial excitation pulse, and a spiral MRSI method incorporating effective homonuclear decoupling are presented.

^{1}H MRSI has also been shown to have an important role in oncology by providing unique measurements of metabolic markers for the early detection, grading, and treatment planning of tumors throughout the body. Progress on these technically challenging applications is discussed in terms of new optimized RF pulse designs for breast cancer spectroscopy.

Finally, this year, we have launched an exciting new research project in the development of methodology for the efficient imaging of hyperpolarized 13C-labeled compounds. In particular, with SNR enhancements on the order of the 100,000-fold, dynamic nuclear polarization (DNP) of metabolically active substrates (e.g. 13C-labeled pyruvate or acetate) theoretically

permits in vivo imaging of not only the injected agent, but also downstream metabolic products. This feature of hyperpolarized MRS provides a unique chance to noninvasively monitor critical dynamic metabolic processes in vivo under both normal and pathologic conditions. This year's Lucas Report contains a discussion of our initial work in the development of a high-speed 13C MRSI technique which, when combined with the administration of hyperpolarized substrates, has the potential to measure key in vivo metabolic fluxes (e.g. TCA-cycling) at a 5 mm spatial resolution with imaging times under 200 ms.

With respect to personnel, Dong-Hyun Kim has left the Lucas Center to take an Assistant Professor position in the Department of Radiology, UCSF. Good luck Dong-Hyun! In addition, a new Electrical Engineering Ph.D. graduate student, Priti Balchandani, joined the group to work.
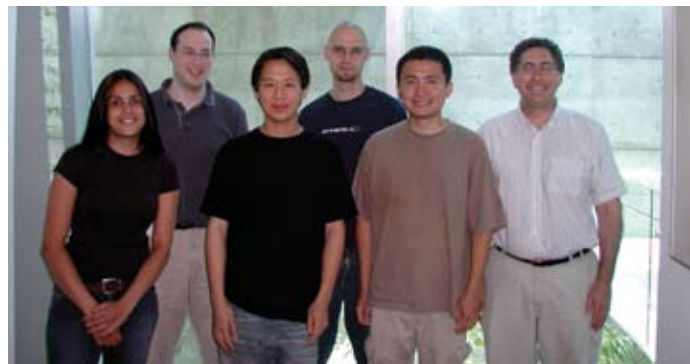
MR Spectroscopy Group L-R: Priti Balchandani, Yakir Levin, Calvin Lew, Dirk Mayer, Meng Gu, Dan Spielman.

Interventional and Open MRI
Kim Butts

Major achievements for the group include Viola Rieke graduating from her Electrical Engineering PhD program. We are delighted that she has stayed as a research associate. She continues to refine her referenceless MR thermometry method for liver and prostate applications. We are pleased other groups are duplicating and verifying her method. Aiming Lu has joined the group as a postdoctoral fellow. With a solid background in pulse sequence programming from the University of Wisconsin, he is heading up the effort to achieve robust T2* maps of short T2* tissues (including frozen tissue). Erin Liu came from Case Western Reserve University to join the lab as a postdoctoral fellow. She will be contributing to thermal modeling as well as comparing temperature images with histology in collaboration with Donna Bouley in Comparative Medicine.

Jing Chen continues her PhD work for the improvement of breast interventions. She demonstrated that one can tradeoff the improved CNR efficiency of SSFP for flexibility in application of the contrast agent. This can allow for a significant extension of the period of enhancement for biopsy. Sonal Josan continues to work in the area of imaging of short T2 tissues. Elena Kaye has joined the group as a PhD student. She has developed a series of coils for imaging of the mouth and neck for our collaborative studies with Otolaryngology. In addition, she will be analyzing the MR parameters in a variety of frozen tissues. Andrew Holbrooke joined the group as a PhD student from the new BioEngineering Department. He will be working on HIFU of liver and renal tumors. Most recently, Serena Wong joins the group to work between our lab and that of Professor Khuri-Yakub in Electrical Engineering. Serena comes with a background in developing HIFU devices with piezoelectric crystals, but will be exploring the use of capacitive micromachined ultrasound transducers for HIFU.

Interventional and Open MRI group: Front row (l-r): Jean Chen, Kim Butts-Paul, Viola Reike; Back row (l-r): Aiming Lu, Erin Liu, Andrew Holbrook, Elena Kaye

In addition, our collaborations are also making progress. The prostate thermal ablation project with Graham Sommer and Chris Diederich's group at UCSF is continuing to build and test new transurethral and interstitial applicators. The prostate cryoablation project with Bruce Daniel was recognized by an invitation to Kim to speak at the Society of Cryobiology. The XMR projects are continuing with an increase in the number of pediatric voiding cystography studies. Garry Gold and collaborators are continuing dynamic knee and spine studies. Lastly, we began a new collaboration with Gerald Popelka in Otolaryngology for MR imaging of swallowing and speech. It's been a productive year for the group, and we are looking forward to another productive year to come.
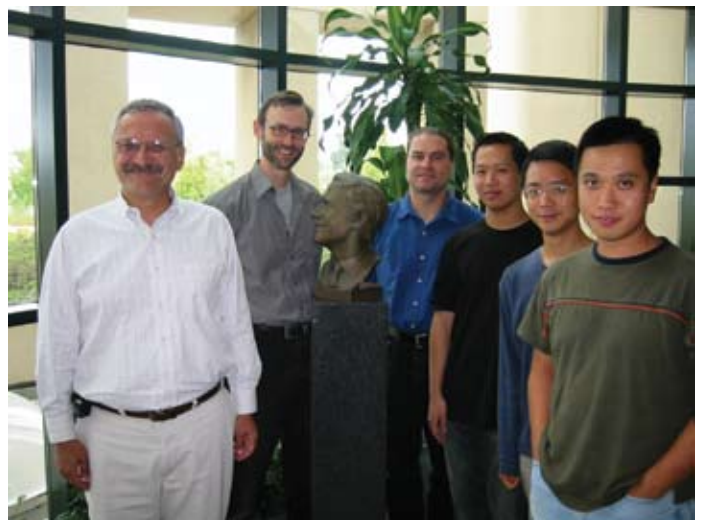
Cardiovascular Imaging
Robert J. Herfkens and Norbert Pelc

Dynamic imaging, including time resolved 3D (i.e. 4-D) velocity imaging, continues to be a major area of work, and a source of a great deal of collaboration. This year, we continued to make improvements in the acquisition methods (abstracts by Alley and Yu).

We also continue to make improvements to our techniques for Magnetic Resonance Angiography (MRA) (abstract by Alley). 4-D velocity imaging generates a wealth of data, the analysis and visualization of which can be complex. We are developing techniques to help visualize physiologically important flow features (abstract by Wigström).

Our collaborators are using all these methods to study a number of vascular regions and disorders, such as the thoracic aorta (abstract by Elkins) and congenital diseases (abstract by Nagle). In conjunction with Prof. Charles Taylor's lab, we are exploring the use of MR data to study the biology of the aorta under rest and exercise (abstract by Tang), as a function of age and gender (abstract by Draney), and in patients with pathologic conditions (abstracts by LaDisa and Kim), and in the superficial femoral artery (abstract by Cheng). We are also continuing to develop methods to use MR imaging data for physiological modeling (abstract by Bekkers). In addition, the techniques are being adapted to study animal models, for example, for use in preclinical studies (abstracts by Les and Greve).

Cardiovascular imaging: Norbert Pelc, Marc Alley, Michael Markl, Calvin Lew, Zhifei Wen, Huanzhou Yu.

ADVANCED X-RAY TECHNIQUES
X-Ray Guidance of Interventional Procedures
REBECCA FAHRIG

Work led by Dr. Fahrig in the area of x-ray guidance of interventional procedures and x-ray system development continues in both the Axiom Lab and the Advanced X-ray Imaging Lab.

New algorithms to improve the image quality of C-arm CT systems were developed, with work on reducing truncation artifacts (abstract by Starman) and 3D image artifacts (abstract by Strobel). A detailed investigation led to a significant improvement in low contrast detectibility, and C-arm CT image quality is starting to approach that of clinical CT (abstract by Fahrig). Dose optimization to ensure the highest quality for minimal patient dose is also underway (abstract by Fahrig). The next step is to provide acquisition protocols for the broad range of 3D imaging applications in the interventional suite, such as assessment of renal artery stenosis and kidney function (abstract by Fahrig),

Combined Advanced X-ray Techiques Labs. Standing (l-r): Norbert Strobel, Marlys Lesene, Sung-Won Yoon, Lei Zhu, Jongduk Baek, Sam Mazin, Arun Ganguly, Zhifei Wen, Jayant Chakravarthy, Vishnu Vyas, Abhik Kumar, Taly Gilat Schmidt, Huanzhou Yu; Seated (l-r): Angel Pineda, Rebecca Fahrig, Norbert Pelc, Robert Bennett

visualization of stents in the superficial femoral artery (abstract by Bonita Song) and imaging during TIPS. We acquired the very first retrospectively-gated cardiac images on a C-arm system just two months ago (abstract by Fahrig). The possibilities for 3D imaging during cardiac interventions are legion and represent an exciting new direction for us and for the field. This work is funded by the NIH, and benefits from a close collaboration with Siemens Medical Solutions, AX Division.

Our work in fast tomosynthesis for lung nodule detection continues. An observer performance study showed that dramatic improvements in nodule detection can be achieved even for small tomosynthesis angles (abstract by Pineda). Initial experimental studies using the NexRay Inc. technology (large area scanned x-ray source with a small detector) are also very encouraging, and support the results of the observer study (abstract by Yoon).

The X-ray/MR project, incorporating a digital flat panel fluoroscopy system into the bore of an interventional MR system, continues. A recent review article in *Physics Today* highlighted the innovations in x-ray tube design and system integration that we carried out. Work on the system continues, with investigation of fundamental physics (abstract by Wen) and development of new applications (abstract by Ganguly). The next phase of the project has been planned, and we hope to receive continued funding from NIH to develop configurations applicable to widely available closed-bore systems, with a flat-panel C-arm fluoroscopy system placed directly adjacent to a 3.0T magnet.

Finally, we were pleased to be involved in a project that exploited the very high resolution of the Siemens Axiom C-arm CT system to image a child mummy from the Rosicrucian Museum. In collaboration with Dr. Paul Brown, Dr. Amy Ladd and other Stanford clinicians, SGI, VolumeGraphics and the Museum, we were able to peek underneath bandages without disturbing the little girl to build a story about both her life and her death.

Inverse Geometry CT and Conventional CT
NORBERT PELC

Work led by Dr. Pelc in the area of conventional and inverse-geometry CT is aimed at understanding the basic limitations in current systems and the development of an advanced CT platform that uses an inverted imaging geometry, and is therefore called inverse-geometry CT (IGCT).

As the CT radiation dose is reduced, increases in noise level are expected. However, with conventional systems, a point is reached where the system performs far more poorly than the statistics of x-ray detection dictate. Our system avoids this "noise floor" by using photon counting detectors. To understand the potential impact, we developed a technique to measure the noise floor of clinical scanners and to provide data related to dose efficiency (abstract by Dormo). The method is able to handle varying spatial resolution, which is important since CT systems automatically adjust spatial resolution as the dose is reduced.

Our main thrust is to develop an IGCT system that can image a thick object in one fast rotation with high spatial resolution and dose efficiency, and with no cone-beam artifacts (abstracts by Baek, Mazin, and Schmidt). The proposed system uses a wide, distributed array of x-ray sources that illuminate the smaller

array of photon counting x-ray detectors. We developed a method to calibrate the system geometry using small beads and a least-squares fitting approach (abstract by Baek). The new method is more precise than our previous one. We acquired experimental IGCT data in collaboration with NexRay, Inc. We built a prototype table top IGCT system by adding a computer controlled rotating stage and our calibration and reconstruction algorithms to NexRay's source, detector, and data acquisition technology, and used this system to validate previous results from analytical studies and computer simulations (abstract by Schmidt). Among the studies performed, we imaged an inner ear from a human cadaver, and showed that the image quality is excellent, with sharper images than available from conventional scanners. One disadvantage of the simplest form of IGCT is that a large source array is needed to image a large object. We developed the idea of using multiple detector arrays to increase the field of view by roughly the number of detector arrays (abstract by Mazin). We collected data using multiple scans and a single detector to mimic a multi-detector system. The results are quite positive.

IMAGE ANALYSIS, STATISTICAL MODELING & OUTCOMES ANALYSIS

Imaging Analysis
SANDY NAPEL

Sandy Napel's group addresses the field of image analysis, which has become increasingly important because the number of images per patient scan has increased dramatically and now numbers in the thousands. The group focuses on volumetric visualization, structure segmentation, quantitative analysis, and computer-aided detection of lesions. Although his group works with many colleagues in the Radiology Department, notably Chris Beaulieu, Dominik Fleischman, and Geoff Rubin are active participants in the group's endeavors. This year saw the successful funding of their NIH proposal entitled, "Improving Radiologist Detection of Lung Nodules with CAD," which seeks to imrpove the accuracy, reproducibility, and efficiency for the detection and follow up of lung nodules using CT scans. They continued work on existing projects, namely "Efficient Interpretation of Vascular Images and Three-Dimensional Spiral CT Colonography," funded by the NIH; "Computer-aided Detection of Lung Nodules," funded by R2 Technology Inc.; and the "Interventional Room of the Future," funded by Siemens Medical Solutions, Inc. Six new papers are in press and nine abstracts have been submitted to RSNA 2005. The group is also beginning their active participation in a second year of funding for an NIH Roadmap Award entitled Physics-based Simulation of Biological Structure; the new Center is charged with developing a simulation toolkit to enable scientists worldwide to model biological systems ranging from molecules to whole organisms.
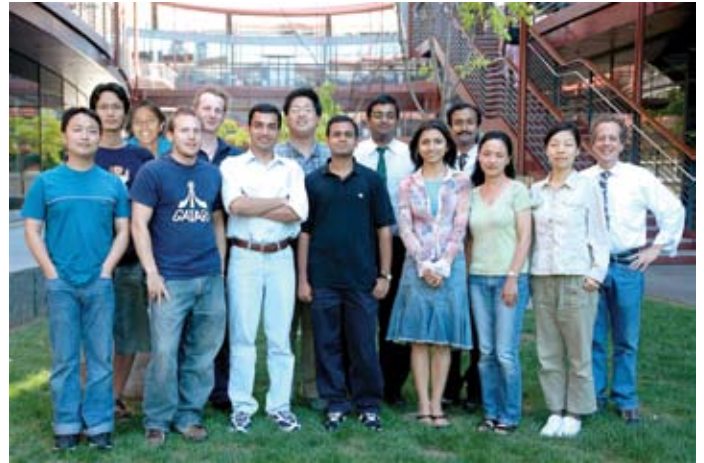

Image analysis group - Bottom row (l-r): Feng Zhuge, Anthony Sherbondy, Teja Rakshe, Ajay Joshi, Bindi Pankhudi, Cindy Shi, Shaohua Sun; top row (l-r): Johann Won, Padma Sundaram, Markus Kukuk, David Paik, Bhargav Raman, Raghav Raman, Sandy Napel

Model-Based Outcomes Analysis of Screening
SYLVIA K. PLEVRITIS

Sylvia Plevritis' research program is best known for producing computer simulation models that yield predictions on the impact of new image-based cancer screening technologies on long-term patient outcomes and health-care costs. These computer models have been applied to evaluate the impact screening for breast cancer with mammography in the US population trends from 1975 to 2001; currently, they are being applied to evaluate the cost-effectiveness of screening for breast cancer with magnetic resonance imaging (MRI) in the high risk population, and the cost-effectiveness of screening with computerized tomography (CT) in current and former smokers. The National Cancer Institute (NCI) has been our main funding agency and recently awarded us with two new grants, one which is a 5-year grant from the NCI's "Cancer Intervention and Surveillance Modeling Network" and the other is a 3-year grant from the NCI program "Economics of Cancer."

The core elements underlying our screening simulation models are mathematical models that describe the progression of cancer and the mechanisms of tumor detection in the absence or presence of screening. In developing natural history models of cancer progression from clinical data, we have been increasingly asking unanswered questions about cancer progression, with one of the most fundamental scientific questions being: If a primary tumor is detected early, has the disease process been arrested? We have begun exploring answers to questions of this type from a variety of avenues, including the knowledge being gained from genomic, proteomic and signaling pathway analysis. This activity is being funded bu the NCI Integrated Cancer Biology Program with the ultimate goal to develop a center in cancer biocomputation.

Thankfully to our latest round of NIH funding, we are currently expanding our group with two new research student positions in modeling screening programs and three postdoctoral positions in biocomputational modeling. Recently, we graduated our first PhD candidate, Peter Salzman, who is currently a postdoctoral fellow in the Department of Biocomputation at the University of Rochester. Our second PhD candidate, YenLin Chia, passed her PhD Dissertation defense with targetted graduation in Fall 2005. Allison Kurian, MD, one of the newer members of our Group, was recently awarded a two-year Postdoctoral Fellowship from the California Breast Cancer Research Foundation for research on evaluating the cost and utility of breast MRI screening.

Statistical modeling and outcomes analysis group (l-r): YinLin Chia, Bronislava Sigal, Sylvia Plevritis and Allison Kurion

RESEARCH IN PROTEOMICS

Proteomics, Biomarkers, and Nanoparticle Platforms for Imaging and Therapeutics
SAMIRA GUCCIONNE

The completion of the initial draft of the human genome and the rapid growth in high throughput assays, has opened a new era in translational research in medicine. The focus of our laboratory is translational research leading to agents for clinical use in detection, diagnosis, treatment, monitoring, and prognosis of clinical pathologies.

We take a comprehensive approach in the design of agents that can span the "bench to bedside" timeline efficiently with our primary focus in development of novel agents for cancer. The research

Proteomics group - Back row (l-r): Leroy Sims, Regina Bower, Michael Lim, Yingyun Wang; Front row (l-r): Amanda Chu, Yishan Yang, Samira Guccione, Steven Choi; Inset: Malika Larabi; Not shown: Maggie Bos

in our laboratory uses high throughput genomic and proteomic analysis on clinical pediatric and adult tissue samples to identify molecular targets. Ligands that bind these molecular targets are used to develop molecular imaging and therapeutic agents. We have developed a nanoparticle-based platform for attaching these ligands; thus creating targeted imaging and/or therapeutic agents. These targeted nanoparticles are first tested in vitro and used in in-vivo animal models, as molecular imaging probes. We have developed multimodality probes for MRI, gamma, fluorescent, and CT imaging. Visualization and quantitative evaluation of these targeted nanoparticles in vivo through molecular imaging, will provide information on the bio-distribution and accumulation of probes at the site of interest. Subsequently, we design therapeutic approaches including delivery of targeted chemo or radioactive agents, or non-viral-based genes for gene therapy. This is a powerful new approach that uses molecular imaging for identifying patients that will respond to treatment prior to choosing the best treatment regiment. We have successfully used this approach to image tumor vasculature in models of primary brain tumors, melanoma, and metastatic colon cancer to the liver and lung. A modified form of these nanoparticles was then successfully used for an antiangiogenic therapeutic approach to the tumor vasculature. We are currently performing toxicity studies as the preclinical requirement for clinical trials.

Other research areas include tissue engineering applications in revascularization to enhance wound healing and vascularly compromised tissue; localized drug delivery systems; and biomarker development.

MIPS GROUP UPDATES
MOLECULAR IMAGING RESEARCH

Multimodality Molecular Imaging
SAM GAMBHIR

The multimodality molecular imaging lab is developing imaging assays to monitor fundamental cellular events in living subjects. Technologies such as micro positron emission tomography (microPET), bioluminescence optical imaging with a charge coupled-device (CCD) camera, fluorescence optical imaging, micro computerized axial tomography (microCAT) are all being actively investigated in small animal models. Our goals are to marry fundamental advances in molecular/cell biology with those in biomedical imaging to advance the field of molecular imaging. We have a particular focus on cancer biology and gene therapy. We have developed several reporter genes/reporter probes compatible with all of the above imaging modalities. These reporter genes are being used in cell trafficking models, gene therapy models, as well as in transgenic models for studying cancer biology. Assays to interrogate cells for mRNA levels, cell surface antigens, and protein-protein interactions are also under active development. We are also extending many of these approaches for human clinical applications.
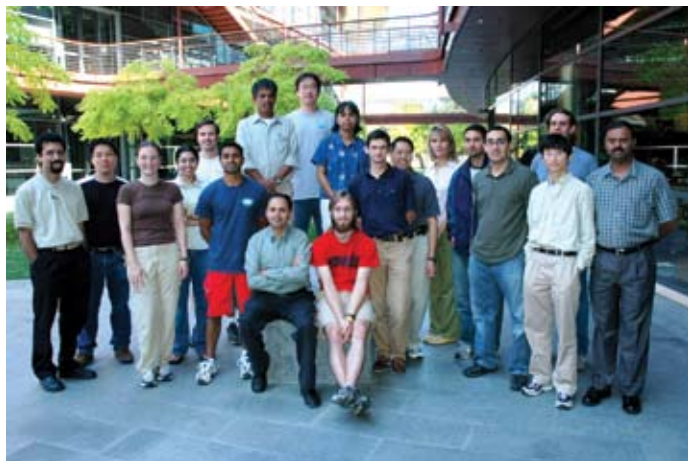
Multimodality molecular imaging group. Seated (l-r): Sam Gambhir, Zac Walls; Standing (l-r): Abijt De, Carmel Chan, Meike Schipper, Sunetra Ray, Andreas Loening, Manish Patel, Ramasamy Palmuragan, Ian Chen, Pritha Ray, Olivier Gheysens, Jeffrey Tseng, Jelena Levi, David Yerushalmi, Shahriar Yaghoubi, Shay Keren (behind), Zhen Cheng, Gobalakrisnan Sundaresan; Not Shown, Mangal Dandekar, Ashot Khanamaryan, Cesar Rodriguez, Martin Rodriguez-Porcel

Molecular Imaging Instrumentation Lab
CRAIG LEVIN

The molecular imaging instrumentation lab develops novel imaging tools for in-vivo imaging of molecular-based signals of disease in humans and small laboratory animals. New camera hardware is under development to efficiently image radiation emissions in the form of positrons, annihilation photons, gamma rays, and light from molecular probes developed to target molecular processes from deep within tissue of live subjects. Our goal for the new imaging instrumentation is to push the sensitivity and spatial, spectral, and temporal resolutions as far as physically possible. In conjunction, software algorithms are being developed to understand the physical system comprising the subject tissues, radiation transport, and imaging system and to provide the best available reconstructed image quality and quantitative accuracy. The activities in the lab involve computer modeling and the development and characterization of position sensitive sensors, readout electronics, data acquisition systems, and image formation, image processing, and data/image analysis algorithms that can be incorporated into practical imaging devices. Our ultimate goal is to introduce new imaging tools for studying molecular mechanisms and guiding treatment of disease in the clinic and in small animal research.

Molecular imaging instrumentation lab - Bottom row (l-r): Jin Zhang, Frezghi Habte, Garry Chinn; Top row (l-r): Angela Foudray, Peter Olcott, Craig Levin, Guillem Pratx, Billie Robles

## Cellular and Molecular Imaging Lab
Jianhong Rao

Cellular and molecular imaging lab (l-r) Hequan Yao, Chenjie Xu, Gayatri Gowrishankar, Min-Kyung So, J Rao, Bengang Xing, Yan Zhang, Xinrui Yan, Tiffany Chung

The cellular and molecular imaging lab is working at the interface of chemistry and biology with the emphasis on the development of methods and techniques to image biological events of interest in normal and diseased states in their native physiological environments. Combining expertises from organic chemistry, biochemistry, molecular biology, and optical imaging, we are making a synergic effort towards developing these imaging tools and techniques. Dr. Rao's research is supported by awards from the NIBIB, NCI, and the Burroughs Wellcome Fund. Dr. Yan Zhang from his lab has been awarded the Dean's Fellowship, and Dr. Nga-Wai (Tiffany) Chung was awarded the Bio-X Interdisciplinary Postdoctoral Fellowship. Dr. Bengang Xing has been selected for a Young Investigator Travel Award at the Academy of Molecular Imaging 2005 annual conference.

Molecular Imaging Probe Laboratory (MIPL)
Xiaoyuan (Shawn) Chen
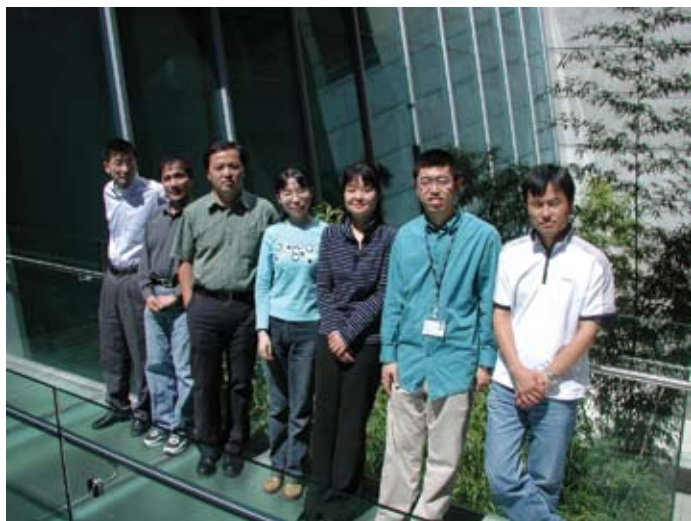
Molecular imaging probe laboratory (l-r): Xiaoyuan (Shawn) Chen, Zhengming Xiong, Kai Chen, Qizhen Cao, Yun Wu, Weibo Cai, Xianzhong Zhang

The molecular imaging probe laboratory is interested in developing and validating novel molecular imaging probes (monoclonal antibodies, minibodies, proteins, peptides and peptidomimetics) for visualization and quantification of molecular targets that are aberrantly expressed during tumor growth, angiogenesis and metastasis. We are trying to combine both anatomical (microMRI and microCT) and molecular (microPET, microSPECT, and NIR fluorescence) imaging techniques to pinpoint molecular and functional information related to tumor growth and dissemination,

and monitor specific molecular therapeutic efficacy. In particular, we are currently working closely with cell surface adhesion and signaling receptor integrin αvβ3, which is highly expressed in tumor cells of various origins and activated endothelial cells in growing tumors but not on normal cells and quiescent endothelial cells, for diagnostic and therapeutic applications. Specific projects include:

- Multimodality imaging of integrin αvβ3 expression in vivo;
- Integrin targeted internal radiotherapy via antibody and RGD peptides;
- Integrin specific delivery of gene therapeutics and chemotherapeutics.

The existing grant support include: the NCI P50 ICMIC grant (Research Project #4, PET Imaging of Brain Tumor Angiogenesis and Anti-Angiogenic Treatment); the NIBIB R21 grant, MicroPET and NIR Fluorescence Imaging Tumor Angiogenesis; the DOD BCRP IDEA award, Alpha-v Integrin Targeted PET Imaging of Breast Cancer Angiogenesis and Low-Dose Metronomic Anti-Angiogenic Chemotherapy Efficacy; DOD PCRP NIA award, Imaging Primary Prostate Cancer and Bone Metastasis; and the American Lung Association Research Award, Vasoactive Intestinal Peptide Receptor Targeted Imaging of Lung Cancer. Postdoctoral fellow Weibo Cai received both the Dean's Fellowship and the 2005 Society for Molecular Imaging (SMI) Travel Award. Eight papers were either published or in press, and another five papers have been submitted. Over 15 abstracts have been submitted to AMI 2005, SNM 2005, SMI 2005, and other conferences.

Molecular Imaging of Musculoskeletal Illnesses
Sandip Biswal

Dr. Sandip Biswal, MD and members of the lab, Drs. Parasuraman Padmanabhan, PhD, Sheen-Woo Lee, MD, Ray Lertvaranurak, MD and Bao Do, MD are interested in using mulitimodality molecular imaging techniques to study a variety of musculoskeletal diseases. Dr. Padmanabhan specializes in building novel genetic constructs to study the expression of specific genes and understanding protein-protein interactions in vivo. He is developing methods to see estrogen receptor-mediated signaling and calmodulin folding in vivo. He has been able to show that the activity of the human telomerase gene can be controlled by semi-selective chemotherapeutic agents. Dr. Lee has developed protocols to monitor the trafficking of mesenchymal stem cells in living, longitudinal models of long bone fracture. She has found that bone healing can be augmented with the addition of stem cells to a fracture environment. She is also developing and validating the use of clinically-relevant magnetic resonance imaging and computed tomography methods for the early detection of rheumatoid arthritis. Dr. Lertveranurak is interested in monitoring the trafficking and integration of neural stem cells into central nervous system tumors. Dr. Bao has made significant inroads in understanding glucose metabolism in the human spinal cord. We have been fortunate to receive the Donald E. and Delia B. Baxter Foundation Research Scholar Award and to present our work at a number of national conferences.

Molecular Imaging of Musculoskeletal Illness group (l-4): Sheen-Woo Lee, Sandip Biswal, Parasuraman Padmanabhan.

Cardiovascular Molecular Imaging
Joseph Wu

Ischemic heart disease is the number one cause of morbidity and mortality in the United States. The repeated ischemic insults can lead to congestive heart failure, which is the leading cause of hospital admissions for people aged 65 years and over. With the advent of the human genome project, cardiovascular diseases will likely be targeted at the basic cellular and molecular levels. The cardiovascular molecular imaging lab is a multi-disciplinary team that combines expertise in molecular and cell biology, cardiovascular physiology, and molecular imaging. To better understand stem cell biology in vivo, we use novel molecular markers that enable us to follow the fate of transplanted stem cells noninvasively. These include monitoring survival, proliferation, and differentiation as related to embryonic stem cells and bone marrow stem cells. The highly sensitive imaging devices we use include bioluminescence, fluorescence, positron emission tomography, and magnetic resonance scanners. We also work on gene expression profiling of stem cell markers as well as optimizing cardiac gene therapy protocols. The eventual goal is to establish molecular imaging as a platform for translational research in cellular and gene therapies for ischemic heart disease in the 21st century.

Cardiovascular Molecular Imaging Group (l-r): Feng Cao, Gwendolen Chang, Yao-Hung Yang, Joseph Wu, Manickam Krishnan, Susan Lin.

EDUCATION AND FACILITIES
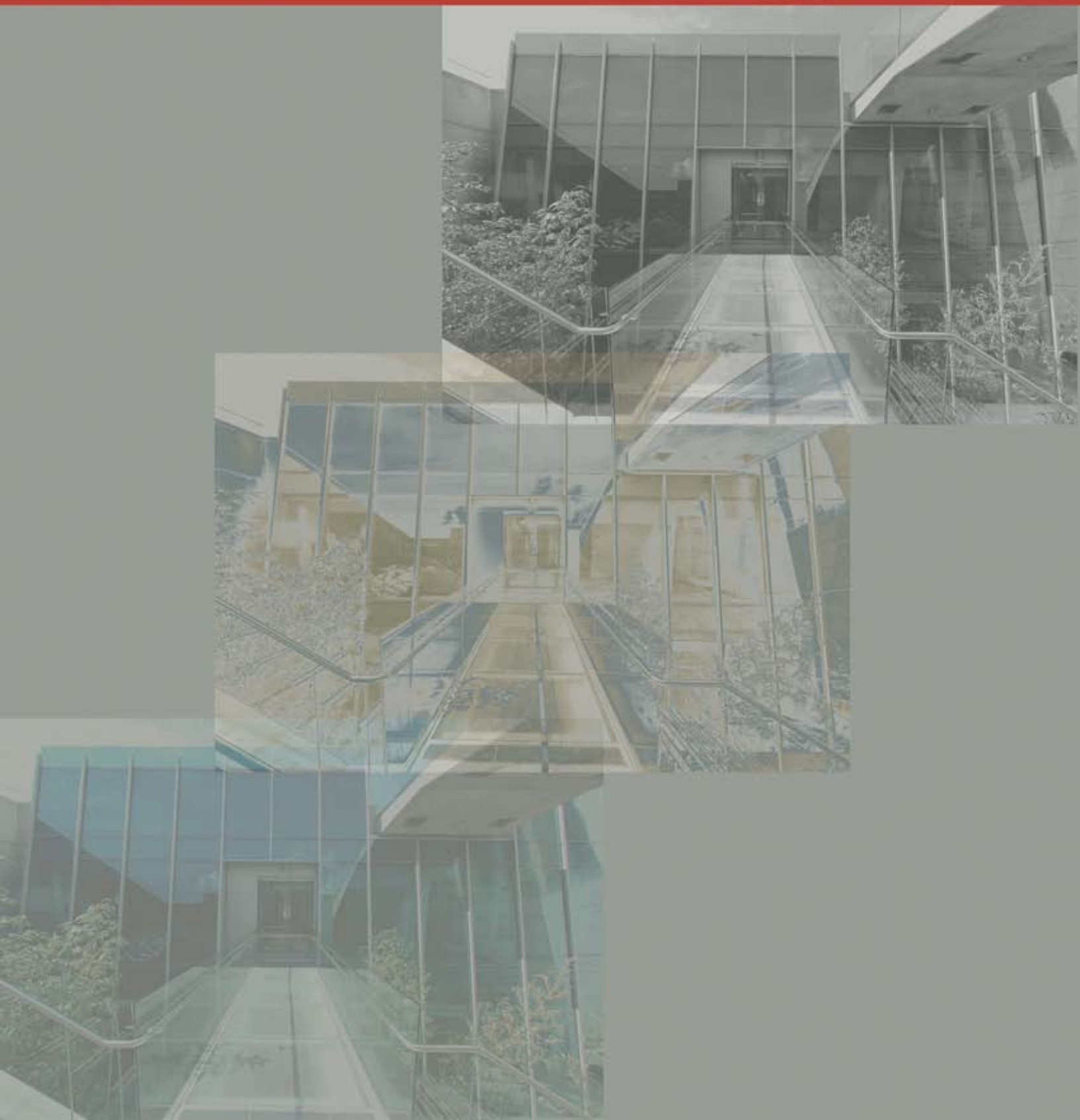
Education Updates
Postgraduate Education
Susie Spielman

Stanford is the leader in Radiology continuing medical education. In 2005 we offered 10 courses to over 2,700 healthcare professionals from 25 countries. With a 17% increase in registration vs. 2004, our program continues to grow in reputation and influence.

We are committed to optimizing medical care for patients through the highest quality CME courses. We craft our programs to ensure the latest advances from our department and within our field are broadly disseminated. Many of our meetings are singly focused and the first to educate the medical imaging community about impending transitions to new and emerging technologies. As imaging research and technology rapidly advances, we offer physicians the forum to maintain clinical competency and update their knowledge and skills. Courses are directed by the leading faculty in our Department and speakers include our distinguished faculty along with the finest academic radiologists known for their teaching abilities and expertise. The inclusion of 177 world renowned speakers at our courses has been a key element of differentiation. We are able to bring together multiple leading experts in a single forum on a focused topic. It is a rare opportunity for our registrants, industry supporters and even our own faculty to learn, network and discuss the key issues in our field.

Our 2005 breast courses had incredible attendance, each with over four hundred registrants, due to their focus on much needed education in Breast MR and Digital Mammography. Further, our International Symposium on Multidetector Row CT (MDCT) is now in its seventh year and, with over 845 attendees (175 of which were international) and innovative content, the program again surpassed our earlier efforts. This year, 59 speakers presented highly focused lectures in a new nine minute format. The shorter format provided an intensive program which was rich in the latest scientific information and trends. The course received incredible ratings and we were truly complemented when leading clinicians in the world told us they came to our course to learn.

An additional focus to our post-grad program are meetings that are co-hosted by strategic partners in Japan and Europe which build international relationships for our faculty and extend our international reach and reputation. We are currently planning for a program in China in 2006 and Europe in 2007. In 2006 we will be adding courses on Venous Therapy, PET/CT and Molecular Imaging, and a Small Animal Imaging Workshop.

We look forward to continued growth and innovation in the years ahead.

2005 International Symposium on Multidetector Row CT: Geoff Rubin introduces the Workstation Face Off

NCI Training Program in Cancer Imaging

DONNA CRONISTER

Our thirteenth year of training began on February 1, 2005. Thus far, we have graduated 21 trainees from our program, Advanced Techniques in Cancer Imaging, thus far. A specific aim of this training program is to position our trainees for a career in academic radiology. Ten of the postdoctoral fellows who have completed the program are actively performing research as faculty or academic staff in major universities. Our trainees continue to be extremely productive and we often collaborate with them in their new positions both locally and throughout the country.

We have four fellows participating in the project: Drs. Daniel Ennis, Tony Faranesh, Michael McDonald and Lewis Shin. Drs. Ennis and Faranesh are working with Dr. Norbert Pelc. Dr. Lewis Shin, M.D. started in July 2005 and is currently working his clinical rotation. Dr. Michael McDonald is with the Molecular Imaging Program at Stanford. We have one open position to be filled before January 31, 2006.

NCI Fellow	Graduated	Mentor	Current Position	Institution
Daniel Margolis, M.D.	2005	R. Brooke Jeffrey	Radiologist	Bay Area Imaging Consulants
Laura Pisani, Ph.D.	2004	Gary Glover	Postdoctoral Fellow	Stanford Department of Radiology
Jon Levin, M.D.	2004	Robert Herfkens and Graham Sommer	Radiologist & Clinic	St. Luke's Medical Center, Minneapolis, MN
Charles Liu, M.D.	2003	Robert Herfkens and Graham Sommer	Radiologist	La Jolla Radiology
Susan Hobbs, M.D., Ph.D.	2003	Mark Bednarski	Resident	University of Minnesota
Karl Vigen, Ph.D.	2003	Kim Butts	Research Scientist	University of Wisconsin-Madison
Lawrence Chow, M.D.	2002	Graham Sommer	Assistant Professor	University of Oregon
Yishan Yang, Ph.D.	2002	Mark Bednarski	Research Associate	Stanford Department of Radiology
Samira Guccione, Ph.D.	2002	Mark Bednarski	Assistant Professor	Stanford Department of Radiology
Curtis Coulam, M.D.	2001	Graham Sommer	Radiologist	Gem State Radiology Group, Boise, Idaho
Martin Blum, M.D.	2000	Brooke Jeffrey	PET/Nuclear Medicine Researcher	Palo Alto VA Health Care System
Steven G.Heiss, M.D.	1999	King Li	Radiologist	Radiology Imaging Associates, Denver,CO
Roger Shifrin, M.D.	1998	Norbert Pelc & Robert Herfkens	Radiologist	Radiology Associates, Daytona Beach, FL
Esther Yuh, Ph.D.	1998	King Li & Sandy Napel	Medical Student	Stanford University School of Medicine
Yi-Fen Yen, Ph.D.	1997	Gary Glover	Assistant Professor	University of Western Ontario, London, Ontario
Garry Gold, M.D.	1997	Albert Macovski	Assistant Professor	Stanford Department of Radiology
Bruce Daniel, M.D.	1997	Robert Herfkens	Assistant Professor	Stanford Department of Radiology
Susan Lemieux, Ph.D.	1996	Gary Glover	Assistant Professor	Diagnostic Imaging, University of Western Virginia
Ian Ch'en, M.D.	1996	King Li	Staff Radiologist	Southwest Washington Medical Center, Vancouver, WA
John Strang, M.D.	1995	Robert Herfkens	Assistant Professor	University of Rochester, Rochester, NY

MIPS Training Program
SANJIV SAM GAMBHIR

The "In Vivo Cellular and Molecular Imaging Center at Stanford" (ICMIC@Stanford) program (NCI P50) has recently been funded and is still in the early stages of being established. The career development component of this P50 is designed to be as flexible as possible to attract highly qualified candidates with the passion and ability to make an impact on cancer research that will benefit patient care in terms of diagnosis, therapy, and monitoring. This overarching theme will guide the process of candidate selection and lead to successfully trained individuals who will be capable of leading their own independent research teams in the field of molecular imaging cancer research. For the first year of the ICMIC@Stanford we expect to fund 2 trainees with plans of

retaining four trainees each year through the life of the grant. We are currently in the process of submitting an NCI R25T training grant that will allow us to support an additional 2-3 trainees per year for a combined total of 4-5 trainees each year.

Selected candidates will be expected to attend various educational activities in the Molecular Imaging Program at Stanford (MIPS) and will be expected to bridge activities between a minimum of two laboratories. The candidates invited to join the ICMIC@Stanford program will be well trained in basic science or in imaging science and will have the energy and drive to impact the growing field of molecular imaging cancer research.

Integrated Cancer Biology Program at Stanford
Sylvia Plevritis

The "Integrated Cancer Biology Program at Stanford" (ICBP@Stanford) has recently been funded by the National Cancer Institute (NCI) as a Planning Center, under the NCI U56 funding mechanism, to create a multidisciplinary program in the system biology of cancer. The career development component of this U56 is designed to attract highly qualified candidates with outstanding analytical skills and the desire to apply their skills to the study of cancer biology. Candidates are being cross-trained not only in the basic principles of cancer biology, but also in the

basic mechanisms underlying novel biotechnologies, measuring genomic and proteomic signatures of molecular processes. Our goal is to produce the first generation of thought leaders who can seamlessly integrate molecular biology with biocomputation. We have been and will continue to enrich our environment to train individuals who will be capable of leading their own independent research teams in biocomputational modeling of cancer biology. Over the next two years, we will extend three additional postdoctoral training fellowships in th ICBP@Stanford.

Research Facilities Updates

Radiology Clinical Informatics

RICK KONG AND ROBERT HERFKENS

Radiology utilizes various application systems that provide for clinical patient and image management services, including: Cerner Radnet Millenium Radiology Information System (RIS) at LPCH; Dictaphone Digital Dictation; General Electric Healthcare Technology Centricity Picture Archiving and Communication System (PACS); IDXrad Radiology Information System (RIS) at SHC; and Siemens Medical Systems KinetDx Ultrasound PACS.

The Radiology Clinical Informatics team provides and supports the integration of digital imaging modalities, the workflow associated with digital imaging, application training, and the 24x7 operation of these systems.

Over the past year, the digitization of Radiology has made tremendous progress. With the opening of the Stanford Advanced Medicine Center, Radiology is now 99.9% digital from an acquisition perspective. Older generation modalities used for Interventional Radiology, and new DICOM conformant modalities are now integrated with RIS and PACS. Digital acquisition modalities integrated with RIS/PACS at both facilities include: 11 Computed Radiography systems; 5 CT systems; 3 Digital Fluoroscopy systems; 4 Direct Radiography systems; 2 Film Digitizers; 3 Full Field Mammography systems; 5 MRI systems; 1 MRT system; 1 PET/CT system; 1 SPECT/CT system; 10 Ultrasound systems and other post-processing systems.

The Cerner Radnet Millenium RIS is part of the new electronic medical record initiative at LPCH and has just recently moved into production operation.

The IDXrad RIS utilized by SHC, includes HP AlphaServer with OpenVMS and IDXrad Version 9.9.2. SHC has completed a RIS vendor evaluation and is moving forward to replace the existing proprietary RIS platform.

GE Centricity PACS is used by both SUH and LPCH. With an annual exam volume of ~240,000 exams, PACS now archives 9+ terabytes (TB) of new data per year with more than 50 TB of total clinical patient images archived.

PACS activity is carried out on 90 PACS workstations and includes implementation of a new generation of Sun servers, the EMC Centera storage system for archiving, Sybase database replication, and multiple application releases – all improvements to performance and functionality.

Radiology Learning Center (RLC)

JOHN REULING AND SUSIE SPIELMAN

The Radiology Learning Center was developed as part of the Lucas Center Expansion and opened in July, 2005. The RLC is comprised of three distinct spaces: a conference room, a small breakout room and "hotel" space for visiting faculty. The vision for our project was to create a unique educational learning center which will be used to advance radiology education and foster changes in the nature of learning, teaching and learning environments through the intelligent use of technology.

The RLC conference room is located at the entrance to Lucas II and will serve as a show site for the department's achievements. It is a desirable teaching space for faculty and an inspiring resource which will draw talented students to Stanford for their education. It will further serve as a hub for faculty and visiting scholars.

The room was designed to support interactive, collaborative group learning. It is a technology-intensive learning space, with multiple projection and plasma displays and an audio-video routing system that allows the instructor to work with a number of computer and video "sources" in a number of different configurations. The room will seat approximately 40 students in a classroom configuration, but can easily be reconfigured to facilitate various seating styles. The technological sophistication of this space is unmatched in the school of medicine. As our faculty begin to teach in this new facility it is evident that the opportunity to create unique curriculum and new tools for teaching will provide a great advantage to our students in the years to come.

Visitors from around the world are already coming to teach and do research in partnership with our faculty. Space for up to eight visiting faculty has been held to accommodate our visitors. The hotel office provides them with the essentials for a productive working environment as well as an adjacency to our research efforts and teaching facilities.

Radiology Learning Center Conference Room in Lucas II
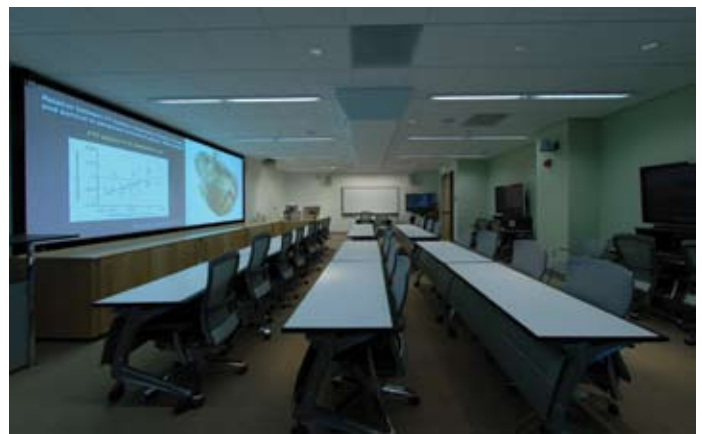
3D Visualization and Quantitation, Clinical Applications

Laura J. Pierce, MPA, RT (CT) and Geoffrey D. Rubin, MD

Introduction

The Stanford 3D medical imaging laboratory continues to pursue its mission of developing and applying innovative techniques for efficient analysis and display of medical imaging data through interdisciplinary collaboration. Our clinical goal is to deliver these advances as rapidly as possible following validation as services to the Stanford and worldwide healthcare communities. Our educational goal is to disseminate knowledge and duplicate our 3D services at other institutions by providing training for physicians and technologists locally and worldwide in the latest developments in 3D imaging.

Figure 1. 3D imaging specialists at work in the Lucas 3D Lab.

Progress

Over the past year, the 3D laboratory has continued its operations simultaneously in two locations: the first floor of the Lucas Center as well as the third floor of the James H. Clark Center, a new building dedicated to interdisciplinary science. This May we passed the 30,000 milestone for the number of clinical exams processed since our inception in 1996. We continue to provide 3D service for every clinical department at the Stanford Medical Center. The majority of our referrals come from vascular surgery, cardiothoracic surgery, gastroenterology, cardiology, urology, and neurosurgery. With our expansion into the Clark Center, opportunities for increased interactions between radiologists, technologists, clinicians, and researchers have grown. Projects are not limited to radiology personnel—other biomedical science departments who seek to extend volumetric analyses into their practices and research programs collaborate with our technologists and researchers. For example, this past year reconstructive surgeons analyzed facial bone CT data in 3D to determine changes in angles of facial structures that occur from aging. As demand for 3D imaging has moved into mainstream medicine, the 3D lab has sponsored an increasing number of visiting radiologists and
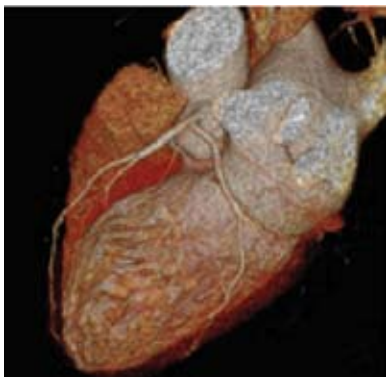
Figure 2. Coronary arteries depicted in 3D from images acquired with new Siemens Somatom Sensation 64 scanner.

technologists who have sought training through our 3D clinical fellowship program. With the introduction of the Siemens Somatom Sensation 64 slice CT scanner last November at Stanford Health Services, our CT datasets have increased in speed of acquisition resulting in an increase in range of anatomical coverage. This exciting technology has resulted in isotropic

Figure 3. This image created in the 3D lab is a merged or "fused" picture of the body's metabolism and structure. This image was named the 2005 Image of the Year at the Society of Nuclear Medicine's 52nd Annual Meeting in Toronto.

CT resolution below 4 mm voxel size, within the ability to create 3D images with ultra sharp detail in areas that normally would be limited due to motion, such as cardiac imaging (see figure 2). We look forward to combining 3D and molecular imaging techniques in the next year to display molecular pathology in 3D anatomical models for improved disease representation and treatment planning (see figure 3).

Infrastructure

Both labs include space for our 3D imaging specialists: Laura Pierce (3D lab manager), Marc Sofilos, Linda Novello, and our newest technologists Keshni Kumar and William Johnsen. The labs are also attended by a rotation of our radiology body fellows and residents. Our administrative assistant (Lakeesha Winston) and software engineer (Kala Raman) are located in the Lucas 3D lab, which is also occupied by our cardiovascular radiology fellows, visiting MDs and international scholars. Both labs include a central area table that invites collaboration and accommodates eight advanced 3D workstations for processing clinical cases and for research and development. We have excellent relationships with corporate developers of 3D workstations (e.g., GE Healthcare, TeraRecon, and Vital Images) who site their hardware and software in the 3D lab in anticipation of our valuable feedback and market exposure to our scholars, researchers, and visitors. These relationships ensure that we are able to provide the latest technology available to our patients and researchers. We anticipate establishing new relationships this year with Merge eFilm and Siemens Medical Solutions, which will result in the acquisition of the latest in coronary artery calcium scoring and cardiac functional software. We also provide imaging services for medical device developers, who use our expertise to evaluate their current and future products, in anticipation of FDA approval.

Conclusion

The 3D Medical Imaging Lab continues to function as a major clinical, teaching, and research facility and to advance the Department and the Lucas Center as leaders in this aspect of medical imaging science. The confluence of talented clinical, medical, and engineering expertise as well as the most up-to-date 3D equipment has resulted in a steady stream of innovation and new developments of diagnostic and treatment planning approaches.

Experimental Animal Model Care
DIANE HOWARD, RVT, LATG, WENDY BAUMGARDNER, RVT, LATG

The mission of the veterinary technical staff at the Lucas Center is to provide research support to all investigators from the Department of Radiology, as well as from collaborating departments to further knowledge in the detection and treatment of disease using imaging techniques. Our mission is to provide appropriate care and use of all the animals entrusted to us. Currently our modalities include MRI, CT, PET, MRT, fluoroscopy, and fluoroscopy/CT. With these various methods of imaging we are able to study all systems of the body including such specific diseases as alcoholism, stroke and cancer of the liver, breast, and prostate. We also study neuroimaging of the brain, and stent/graft implantation.

We are now in the planning stages of renovating our current fluoroscopy suite to include a sterile surgical suite and patient preparation and recovery areas and outfitted with state-of-the-art equipment. This will vastly improve our ability to plan long-term chronic studies on our animal species in an approved USDA and AALAC animal facility. As always, our goal is to diligently provide support to our animal subjects with the utmost respect, compassion and professional care, while insuring compliance to all government and university regulations and policies. All studies are carried out under IACUC approved animal use protocols that are reviewed by the APLAC panel yearly. Protocols are very explicit in terms of detailed procedures and approved personnel, and deviation from the protocol is not permitted. All personnel are required to attend appropriate seminars in the use of animal subjects given by the Department of Comparative Medicine as required by Stanford University. In addition to our technical support we have instituted a rodent use-training program that all personnel working with rodents in the Lucas Center are required to successfully complete.

Animals used to assist in the development of new technology, such as the c-arm flat panel CT in the Siemens Axiom lab, are cared for by the veterinary technical staff in the Department of Radiology.

We look to the future with the hope that through quality biomedical research the necessity for animal use will decrease with the increased use of computerized models or other non-living research systems. With this in mind we realize the privilege we are granted and strive for continued excellence in all research taking place within the Department of Radiology.

A licensed veterinary nurse attends to anesthesia and imaging equipment in a non-aseptic study.

Vital signs are recorded by a licensed RVT using a multifunctional monitoring system, in conjunction with arterial blood gases and activated clotting times to maintain homeostasis.

Lucas Center MR Systems Updates, Education and Systems Support: 1.5T and 3.0T Whole Body Magnets

Anne Marie Sawyer-Glover, B.S., R.T.(R)(MR), Romi Samra, R.T.(R), Sandra Rodriguez, R.T.(R)(MR) - Department of Radiology

Systems Updates 2004 - 2005

The 1.5 Tesla G.E. Medical Systems Echospeed LX CV/i MR system (11.0 M4 systems revision) was upgraded to a research version of software that allows maximum gradient amplitudes of 50 milliTesla per meter (5 Gauss per centimeter) and a maximum slew rate of 150 milliTesla per meter per second. This improvement will allow faster imaging, shorter echo times, higher temporal and spatial resolution, and the capacity to remain on the leading edge of MR imaging applications.

A multitude of functional brain imaging studies (fMRI) investigating diseases, congenital disorders and conditions such as chronic pain, are being conducted in adults and children as well as studies focused on advancing neuroscience knowledge. Body and musculoskeletal imaging applications are in development at the 3.0T including knee, ankle/foot, wrist, elbow, shoulder, breast, pelvis, prostate, and cervical spine (Figure 1). Research studies utilizing hydrogen and multi-nuclear spectroscopy and imaging spectroscopy are also being conducted in several areas of the brain and body.

MR research studies in the detection and characterization of breast disease and prostate cancer continue at both 1.5T and 3.0T as well as stroke, cardiovascular disease, kidney disease, cystic fibrosis, muscle damage, cartilage of the knee, cancer of the head and neck, aging, Alzheimer's disease, schizophrenia, depression, obesity, post-traumatic stress disorder, bipolar disorder, attention deficit hyperactive disorder, dyslexia, memory and language disorders, vision, mood disorders, psychotic disorders, concussion, autism, chronic and intractable pain, alcoholism, Fragile X syndrome, obsessive compulsive disease, mental retardation, Williams syndrome, uterine leiomyomata, lumbar spine fusion, AIDS and HIV.

A new 7.0 Tesla magnet was installed in the new extension of the Lucas Center that was completed this past spring (Figure 2).

Radio Frequency Imaging Coil Updates 2004 - 2005

The investigation and testing of new designs and concepts in RF imaging coils for use in MR imaging and spectroscopy is ongoing at the Lucas Center whole body scanners, both 1.5 Tesla and 3.0 Tesla. Of primary focus currently is improved imaging in the brain, breast, abdomen, musculoskeletal and prostate. We are working with coil manufacturers and independent researchers building coils at the Lucas Center and at other academic research facilities. As part of the Excite II upgrade to the 1.5T MR system, eight-channel RF coils provide higher signal-to-noise ratio that allows increased resolution and faster imaging. The new eight-channel coils are designed to image the brain, neurovascular system, cardiac system, spine, breast and chest-abdomen or abdomen-pelvis (Figures 3 through 8).

Equipment Updates 2004 - 2005

Several new imaging devices and accessories have been added over the last year including a MR compatible infusion pump that provides continuous infusion drug therapy delivery during the scan. This will be used at the 1.5T system in development of new techniques to detect and characterize breast disease and cancer. The infusion pump will also be used at the 3.0T system in brain research in individuals with chronic pain.

Safety Training and System Instruction 2004 - 2005

Safety training and system instruction have been provided to ninety-four new researchers conducting experimental MR studies at the Lucas Center. Magnet safety training is provided twice a month and is a requirement for all researchers assisting or conducting studies on any of the magnet systems at the Lucas Center. Safety training is a yearly requirement for all researchers. A magnet safety refresher course will be provided to 155 researchers. This ensures that all users and assistants are qualified to operate the system and satisfies Lucas Center and University

Figure 1. Romi Samra and Sandra Rodriguez prepare a female subject for a MR scan of the pelvis using the four-channel torso phased array coil.

Figure 2. The new 7.0T magnet is lowered through the hatch during installation into the MR suite of the recent Lucas expansion.

Figure 3. The new eight-channel cardiac phased array RF coil is shown. This coil is used to image the heart, coronary arteries and aorta (G. E. Healthcare, Milwaukee, WI, USA)
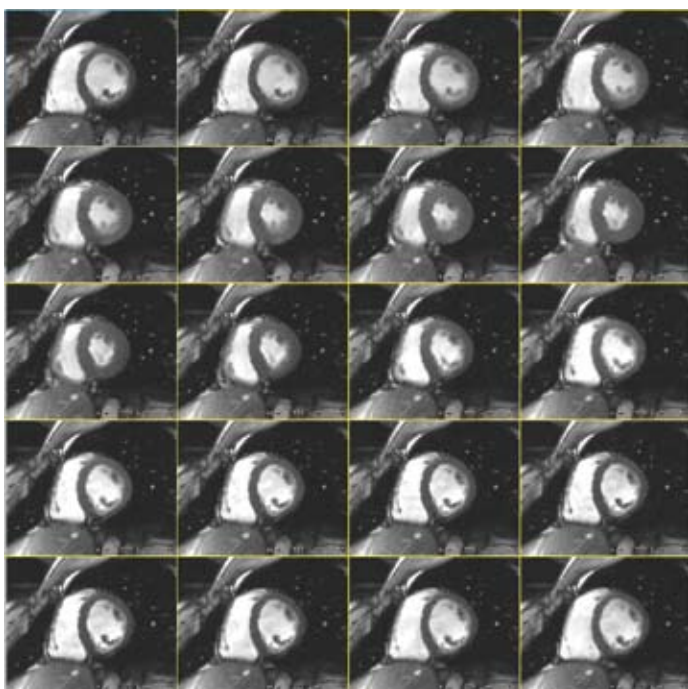

Figure 4. These images demonstrate multiple phases of the cardiac cycle acquired in a short axis view to visualize the left and right ventricles.

Figure 5. Shown here is the new seven-channel breast phased array RF coil used to detect and characterize breast disease and cancer (Invivo/MRI Devices, Inc., Waukesha, WI, USA).
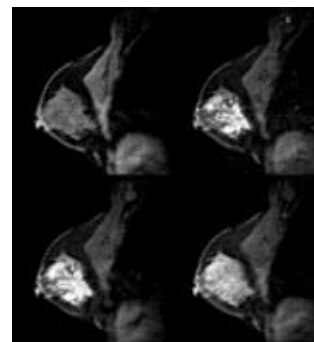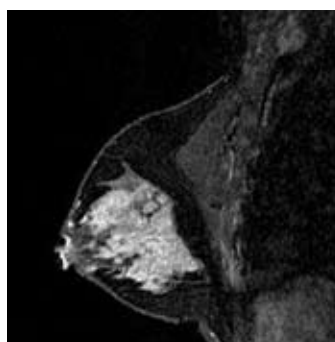

Figure 6. Ductal and lobular breast cancer is shown in these gadolinium contrast enhanced images acquired with the new seven-channel phased array breast coil at the 1.5T system. (a) A high resolution image acquired with the 3dssmt research imaging sequence. (b) Four images taken from a dynamic scan of 46 images using a 3D spiral research imaging sequence.

Figure 7. The new eight-channel RF coil shown here is used for high resolution imaging of the spine including cervical, thoracic and lumbar regions (G. E. Healthcare, Milwaukee, WI, USA).
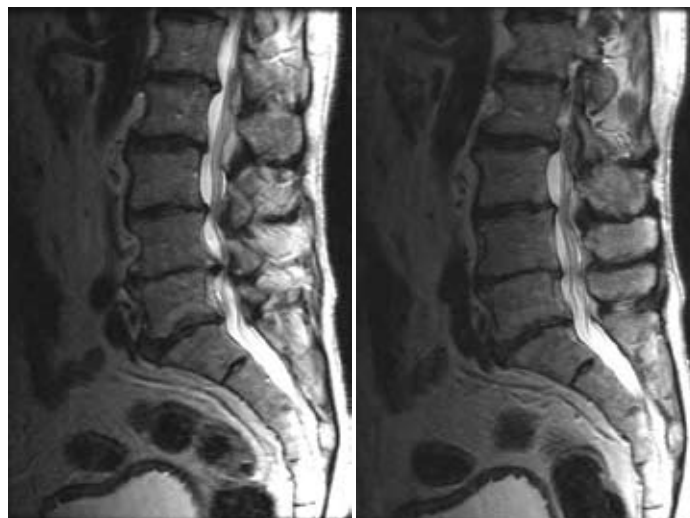
Figure 8. Two images showing the lumbar spine in the sagittal plane acquired with the eight-channel phased array spine coil (G.E. Healthcare, Milwaukee, Wisconsin, USA).

Figure 9. Shown here are pictures of the new MR compatible infusion pump system for continuous drug therapy delivery (Medrad Continuum System, Indianola, Pennsylvania, USA).

requirements for safety. System and safety support is provided to the researchers 7 days a week, 24 hours a day to ensure that research endeavors are successful, generate valuable data, and, above all, are safe for the researchers, the human subjects and the MR system and its components. Magnet safety is an on-going concern as the MR environment can be a potentially lethal setting without continuing education and persevering support. The research environment generates many new, yet prototype designs in RF imaging coils, imaging accessories, monitoring and response devices such as button boxes, eye trackers, and electroencephalogram (EEG) recorders, and sensory devices. Evaluation of these new devices is on-going to ensure that neither the image data, the safety of the human subject, nor the integrity of the MR system is compromised by the presence of these devices in the magnet room, in the bore of the magnet, or in the presence of an RF coil.

MR Systems Support 2004 - 2005

Daily support is provided to all researchers including faculty, post-doctoral fellows, graduate students, and visiting scholars in the Lucas Center and Department of Radiology; researchers from other University departments such as Psychology, Psychiatry, Neurology, Neurosurgery, and Nephrology; and service center users from outside of the University. Scan support was provided for multiple research studies including:

- MR Imaging of Breast Disease and Cancer; R. Herfkens, B. Daniel, D. Ikeda, and G. Glover (Radiology)
- Identification of Ductal Atypia with MR Galactography; B. Daniel (Radiology); A. Hartman (Oncology)
- MRI/MRS of Prostate at 3.0T; B. Daniel, G. Sommer (Radiology)
- MRI of Renal Anatomy and Function in Chronic Ischemia; G. Sommer and N. Pelc (Radiology); B. Myers (Nephrology)
- Development of 3T Scan Protocols for the Musculoskeletal System; C. Beaulieu and G. Gold (Radiology)
- 3T Imaging of 3D Joint Models in Cadavers; A. Ladd (Orthopedic Surgery); P. Brown (NASA Biocomputational Center); C. Beaulieu and G. Gold (Radiology)
- Fat Redistribution and Metabolic Change in HIV; A. Zolopa (Infectious Diseases)
- Diabetes Therapy to Improve Muscle Mass and Clinical Status in Cystic Fibrosis Patients with Abnormal Glucose Tolerance; R. Moss (Pediatrics)
- MRI Study to Measure Operative Muscle Damage; T. Alamin (Orthopedic Surgery), R. Bammer, K. Stevens (Radiology)
- Trial on Efficacy and Safety of Long-Term Treatment with ICL670 in Comparison with Deferoxamine in B-thalassmeia Patients with Transfusional Hemosiderosis; M. Jeng (Pediatric Oncology)
- Phase III Double Blind Study to Evaluate Efficacy and Safety of Two Doses of J867 vs. Placebo in Subjects with Uterine Leiomyomata; L. Swiersz (Obstetrics and Gynecology)
- Women's Health Initiative Memory Study; M. Stefanick (Medicine – Stanford Prevention Research Center)
- Computer Modeling and MRI of Hemodynamic Conditions in the Aorta; In-Vivo Quantification of Hemodynamic Conditions in the Human Abdominal Aorta During Lower Limb Exercise; Hemodynamic and Geometric Study of the Lower Extremity Vessels with Respect to Body Posture, External Compression, and Muscle Contraction; C. Taylor, C. Zarins (Vascular Surgery); N. Pelc, R. Herfkens (Radiology)
- Comparison of Vascular Development in Human Cancer Cell Line Xenographs in Mice Models with Vascular Development Syngeneic Mice Models; Development of Antiangiogenic Nanoparticles for Imaging and Therapy; Dual Modality Imaging Agents; Synthesis and Characterization of T1-weighted Macromolecular Contrast Agents; In Search of Tumor Stem Cells; S. Guccione (Radiology)
- Image Based Computational Blood Flow Modeling of the Pulmonary Tree as Applied to Problems in Congenital Heart Disease; J. Feinstein (Pediatric Cardiology), C. Taylor (Vascular Surgery)
- Cerebral Perfusion (Deep Hypothermic Circulatory Arrest); K. Riemer (Cardiology)
- A Model for Hypercortisolism for Major Depression; Functional MRI of the Brain; HPA Axis/Dopamine Interactions in Psychotic Depression; D. Lyons and A. Schatzberg (Psychiatry)
- Cortical Processing of Visual Motion in Primates; W. Newsome (Neurobiology)
- Physiologic Basis of Visual Cognition in Primates; T. Moore (Neurobiology)

Cyclotron Suite Update
DAVID DICK

The past year has resulted in an enormous growth in the ability to provide radiotracers for use in molecular imaging. A GE PETtrace cyclotron had been lowered into place in the Lucas Expansion during the initial phase of construction in 2004, and 2005 started off with the placement of radiation shielding in the Cyclotron Suite. The Comecer shielding equipment consists of three "hot cells," six "mini cells" and four shielded fume hoods, with a combined weight of 130,000 lbs. Once the equipment was in place, the mechanical and electrical installation of the cyclotron and ancillary equipment started and all of the equipment needed to perform radiochemistry was interconnected with the cyclotron. These processes have consumed the better part of 2005, but the pieces are now in place for the radiopharmaceutical arm of MIPS to start growing.

CYCLOTRON

A GE PETtrace cyclotron (Fig. 1) was lowered into place at the Lucas Expansion during April of 2004, but the mechanical and electrical installation was not performed until May of 2005. The PETtrace is a dual particle machine, capable of producing a particle beam of either 16.5 MeV protons or 8.4 MeV deuterons. In its current configuration, the PETtrace can switch between production of C-11, N-13, O-15 or F-18 in a matter of minutes. The machine is unshielded, so it resides in a concrete vault and all loading and unloading of the targets is done remotely. Typical production yields are shown in the table below.

Figure 1: David Dick stands by the newly installed GE PETtrace cyclotron.

Radiochemical	Yield EOB	Bombardment time
^{18}F-Fluoride	4.5 – 5.0 Ci	120 minutes
^{18}F-F$_2$	300 mCi	60 minutes
^{13}N-NH$_3$	450 mCi	30 minutes
^{11}C-CO$_2$	3.0 Ci	30 minutes
^{15}O-H$_2$O	1.2 Ci	6 minutes

RADIATION SHIELDING

In order to keep the radiation exposure to the radiochemists low, Comecer shielding equipment was installed (Figure 2). There are three "hot cells" that feature a 30.5 cubic foot work area surrounded by three inches of lead shielding on all sides. A large lead glass window allows the radiochemist to see inside the cell and manipulators allow the chemist to move things inside the cell. These cells are used for dispensing and semi-automated chemistry. Six "mini cells" feature a 9.2 cubic foot work area surrounded by three inches of lead shielding on all sides. Top units have a lead glass window and all units have CCD cameras and flat panel displays to allow the radiochemist to see what is occurring inside the cell. Computer-controlled automated chemistry

systems are housed in these cells. Finally, there are four shielded fume hoods that have two inches of lead shielding on all sides with open access on the top half of the fume hood front face for manual radiochemistry syntheses. All of the radiation shielding equipment is connected to a vast network of underground piping that allows for the remote transfer of radioactive material to or between cells.

*Figure 2: FDG synthesis module.*

SYNTHESIS MODULES

Five GE automated synthesis modules have been installed in the Comecer shielding equipment for the synthesis of PET radiopharmaceuticals. There are two modules for general purpose ^{18}F-fluoride chemistry, one for general purpose ^{11}C-CO$_2$ chemistry, one for general purpose ^{18}F-F$_2$ chemistry and a module dedicated for the synthesis of ^{18}F-FDG (Figure 3). These modules allow for the complete automation of routine production of clinical and research radiopharmaceuticals, such as ^{18}F-FDG, ^{18}F-FHBG and ^{18}F-FLT. In addition, there is an ammonia process module for the production of ^{13}N-NH$_3$ for both clinical and research use.

CYCLOTRON SUITE GOING FORWARD

The majority of 2005 has been spent installing equipment and verifying the proper operation of all the components of the Cyclotron Suite. The tools are now in place to allow for research of novel compounds to be developed as radiopharmaceuticals for PET imaging. Automated synthesis modules allow for the routine production of clinical and research radiopharmaceuticals. Shielded fume hoods allow radiochemists to develop novel compounds that will be used to further understand physiology and biological pathways through molecular imaging.

Figure 2: Comecer shielding equipment keeps radiation exposure to the radiochemists low.

ABSTRACTS
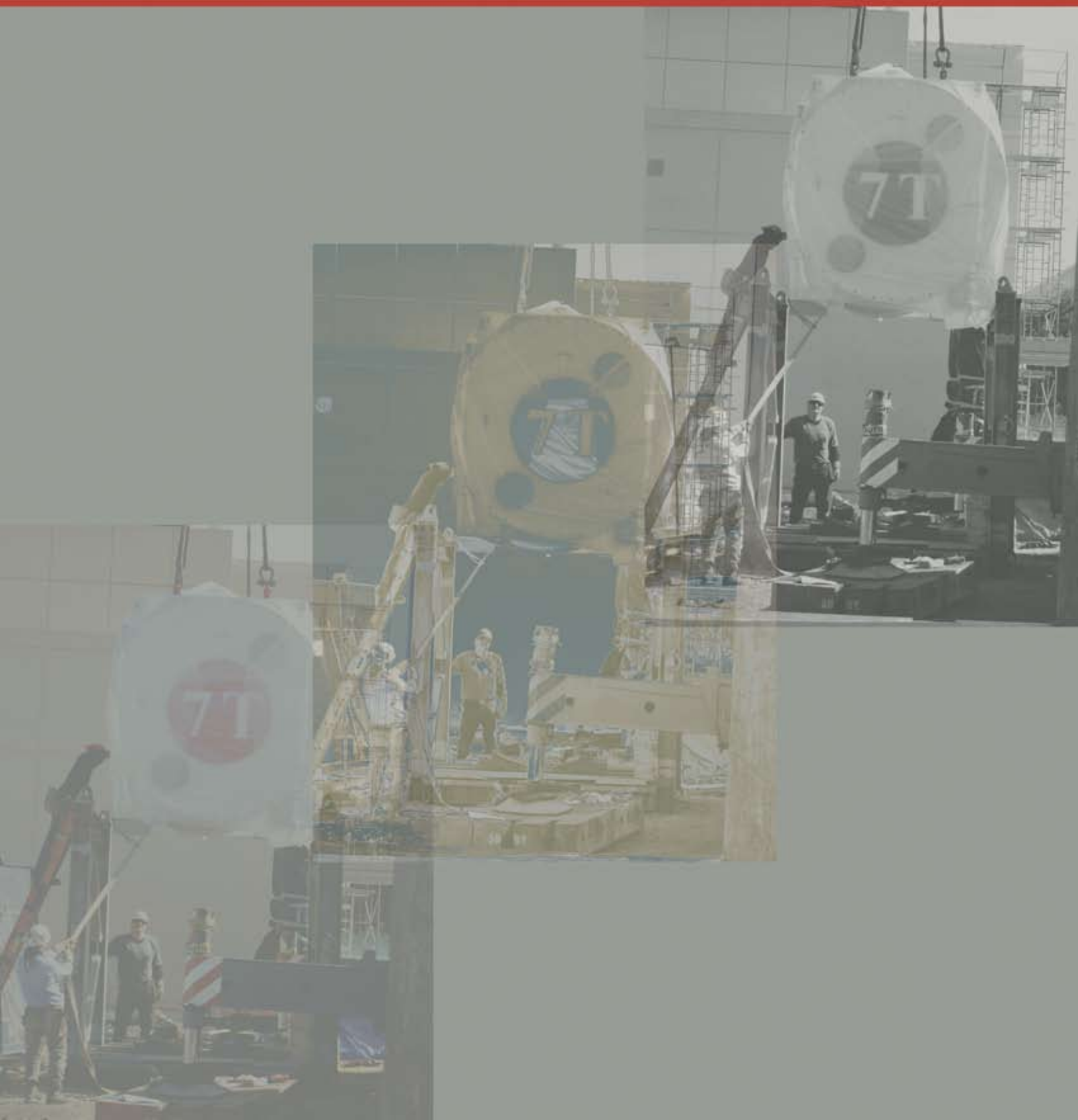
Interleaved Spiral-In/Out for BOLD fMRI

Christine Law[1,2], Gary Glover[2] – [1]Department of Electrical Engineering, [2]Department of Radiology

INTRODUCTION

The spiral in/out imaging sequence has been shown to reduce susceptibility signal drop-out and increase fMRI sensitivity in frontal and lower temporal regions [1]. Each half (in & out) is sufficiently sampled to produce an alias-free image which causes readout time to be long, thereby increasing signal dropout. We propose a new sequence using a two-interleaf spiral trajectory with the first interleaf gathered as spiral-in and the second as spiral-out (Fig. 1). The entire sequence critically samples the desired k-space. This proposed sequence allows fMRI of the frontal and lower temporal regions with better spatial or temporal resolution, and reduced susceptibility induced signal drop-out.

MATERIALS AND METHODS

Compared with standard spiral-out, the proposed sequence is equal in readout duration covering the same k-space but in two interleaves (Fig. 1). The spiral-in trajectory covers the first interleaf, and is immediately followed by the spiral-out half (the second interleaf). Images reconstructed using data from this new proposed sequence typically suffer from artifacts due to eddy current, off-resonance, and trajectory imperfection. Two methods for image reconstruction are used to eliminate
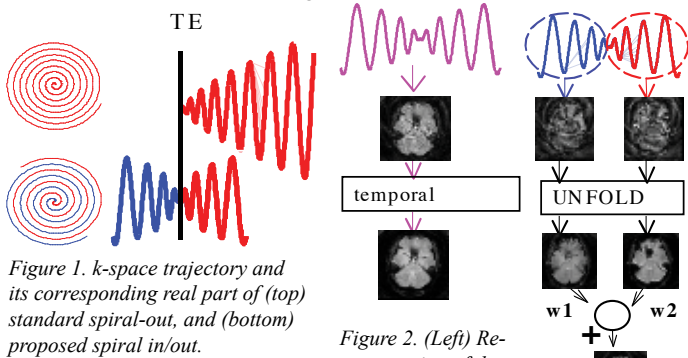
Figure 1. k-space trajectory and its corresponding real part of (top) standard spiral-out, and (bottom) proposed spiral in/out.

these artifacts. In the first method, direction of the trajectory is reversed in alternate frames. Images are reconstructed using both interleaves and filtering in the temporal domain [2,3] (Fig. 2).

Figure 2. (Left) Reconstruction of the new spiral in/out with standard technique: artifact is removed by temporal filtering. (Right) Using UNFOLD to un-alias images from spiral-in half and spiral-out half. Each is multiplied by its weight and the two are added.

In the second method, we separately reconstruct an image from each interleaf. Since each is undersampled, we use UNFOLD [4] to remove aliasing artifacts. These two images are then combined according to their relative signal strength and correlation coefficient ratio [1,5] (Fig. 2). We compare these two methods of reconstruction using the proposed sequence with the standard spiral-out having temporal filtering identical to that in the first method of reconstruction. The result is an alias-free image with reduced susceptibility drop-out compared to standard spiral-out.

A breath-holding activation experiment was carried out at a GE 1.5T. This task consists of 15s normal breathing and 15s breath-holding after inspiration, visually cued and repeated for 8 cycles. This causes a systemic hypoxia and results in BOLD signal modulation, independent of cognition, having a trough during breath-holding epochs [6]. Ten oblique slices (96 X 96) were gathered using a standard head coil (TR/TE/α /TH/FOV = 1s, 30ms, 70°, 5mm, 20cm). Eight volunteers participated, each scanned four times: twice with standard spiral-out, and twice with the new spiral in/out sequence. The sequence order used for each volunteer was counter-balanced to reduce biasing.

DISCUSSION

Although only two imaging sequences are used, four image sets are created using data processing procedures mentioned above (Fig. 3): images using (a) new spiral in/out sequence with standard reconstruction technique, (b) spiral-out sequence, (c) new spiral in/out sequence reconstructed with the second method: combination of spiral-in half image and spiral-out half image with signal magnitude weighting, and (d) same as (c) but with correlation coefficient weighting. Correlation analysis is performed on each set of images.
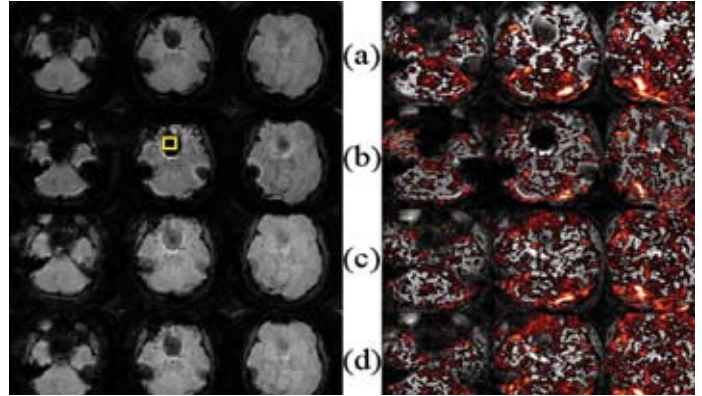

Figure 3. Left: Images using (a) new spiral in/out, (b) spiral-out, (c) combination of spiral-in half & spiral-out half using signal weighting, (d) same as (c) but with correlation weighting. Right: Correlation coefficient maps corresponding to those in the left.

Figure 3 (left) shows these four sets of images near frontal and parietal regions from one volunteer; notice, more signal is recovered with the new spiral in/out than with standard spiral-out. Figure 3 (right) shows the activation maps corresponding to those in the left. The new spiral in/out reveals activation area that spiral-out misses. Figure 4 shows the median number of activated pixels in an ROI in Fig. 3.
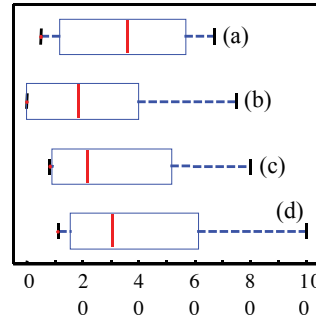

Figure 4. Number of activated pixels inside frontal & parietal regions corresponding to those in Fig 3. The box outlines the lower & upper quartile, and the red is the median. The dotted lines show the extent of the rest of the data.

CONCLUSION

We developed a new spiral in/out sequence that allows fMRI in susceptibility sensitive regions. Unlike EPI where these susceptibility-induced drop-out regions suffer from geometric distortion, this new technique is superior, only suffering from the more tolerable blurring artifacts [7]. While the existing spiral in/out is also susceptibility-tolerant, this new sequence allows image acquisition with higher resolution and the same amount of data acquisition-time. Where temporal resolution is critical, one can therefore take advantage of shorter sequence duration (as compared to spiral-out) to reduce repetition time.

REFERENCES

1. Glover GH, Law CS, Magn Reson Med. 2001; 46(3):515-22.
2. Madore Magn Reson Med. 2002; 48(3):493-501.
3. Chen NK, Yoo SS, Chou YH, Oshio K, Panych LP, Proc Intl Soc Magn Reson Med. 2004; 11:514.
4. Madore B, Glover GH, Pelc NJ, Magn Reson Med. 1999; 42(5):813-28.
5. Glover GH, Thomason ME, Magn Reson Med. 2004; 51(4):863-8.
6. Kastrup A, et. al. Magn. Reson. Med. 1999; 42(3):608-611.
7. Nishimura DG, Irarrazabal P, Meyer CH, Magn. Reson. Med. 1995; 33(4):549-56.

Intensity Encoding of Pain in the Human Cervical Spinal Cord

DEEPAK SONEJI[1], TAKEFUMI UENO[1], KIM KAPLAN[1], DAVID LUDLOW[1], GARY GLOVER[2], SEAN MACKEY[1] - [1]DEPARTMENT OF ANESTHESIA, [2]DEPARTMENT OF RADIOLOGY

AIM OF INVESTIGATION

Functional imaging studies of pain in humans have primarily dealt with the brain. Though previous work in electrophysiology and imaging1 has shown intensity encoding of pain in the spinal cord of animals, this has not yet been demonstrated in humans. We investigated spinal cord activations with fMRI in order to elucidate the mechanisms by which pain intensity is encoded in the human spinal cord.

METHODS

Nine (9) healthy adults were scanned with a 3T magnet to measure fMRI BOLD activation of the spinal cord in response to noxious thermal stimuli. Twelve axial images (4 mm thickness, 0 mm skip) were collected from each subject in the area of C5 to C7. Four(4) subjects were presented with a stimulus on the right thenar eminence, and 5 subjects were given the stimulus on the right forearm. Each subject was presented with 3 psychophysically-adjusted temperatures (low, moderate, and high), with each stimulus lasting 30s. Functional images were retrospectively corrected to filter noise created by the respiratory cycle and cardiac pulsatility. The data were then analyzed to measure both voxel significance and percent BOLD changes.

RESULTS

We observed expected pain-related activation of the ipsilateral dorsal
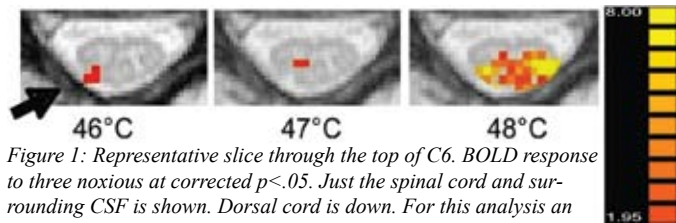
Figure 1: Representative slice through the top of C6. BOLD response to three noxious at corrected p<.05. Just the spinal cord and surrounding CSF is shown. Dorsal cord is down. For this analysis an ROI of just the spinal cord was drawn.

horn, with some subjects also having activation in the contralateral side. Several subjects showed slight changes in the spread of activation or percent BOLD between the low pain and moderate pain states. However, the highest temperature consistently produced both a significantly greater spatial extent, both within and among slices, of activation in the dorsal horn and also greater percent BOLD changes compared to the other two temperatures.

CONCLUSIONS

Our results suggest that both population coding and changes in individual voxel activation in the spinal cord play a role in encoding pain intensity in humans. This data can be used to investigate further central changes that may play a role in acute and chronic pain.

REFERENCES

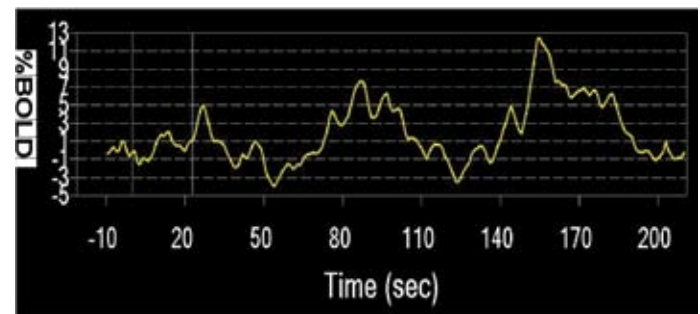1. Coghill R. et al. Pain(1993)53:293-305.

Figure 2: Single subject event averaged time course of single superficial dorsal horn voxel from Figure 1 above (voxel at location of arrow in 46°C image). Stimulus onsets are at: 0 sec (46°C), 70 sec (47°C) and 140 sec (48°C). Data was low pass filtered with a 5 sec kernel.

Reorganization of the Somatosensory Cortex in Patients with Complex Regional Pain Syndrome (CRPS)

TAKEFUMI UENO[1], DEEPAK SONEJI[1], KIM KAPLAN[1], DAVID LUDLOW[1], CAMILLE PALMA[1], EVA PATIL[1], GARY GLOVER[2], SEAN MACKEY[1] [1]DEPARTMENT OF ANESTHESIA, [2]DEPARTMENT OF RADIOLOGY

AIM OF INVESTIGATION

Complex regional pain syndrome (CRPS) is a debilitating chronic neuropathic pain that affects millions of people worldwide and is thought to involve central neural mechanisms. In this study, we used fMRI to investigate somatosensory cortex reorganization in CRPS patients.

Methods: We recruited 8 healthy subjects and 7 chronic pain patients who met IASP criteria for CRPS. We used fMRI to map the somatotopic location of their hands in the primary somatosensory cortex (S1) with stimulation of the thumb for both the affected and unaffected hands, delivered via computer-controlled pneumatic plungers embedded in a foam glove. High-resolution anatomical and functional scans were collected on a 3T scanner. SPM2 software was used for co-registration and detection of activation areas in S1 (P<0.05 corrected).

RESULTS

All healthy subjects showed that tactile stimulation of the left and right thumb activated areas in S1 that were located at the same height. However, 4 patients' brain activation demonstrated proper somatotopic localization of the unaffected hand but significant cephalad shifting of the affected hand. One patient had the activation area of unaffected side thumb more cephalad. Additionally, two patients underwent subsequent successful inpatient treatment and were scanned post-treatment. The fMRI results demonstrated that the affected S1 activation area relocated closer to the height of the unaffected side.
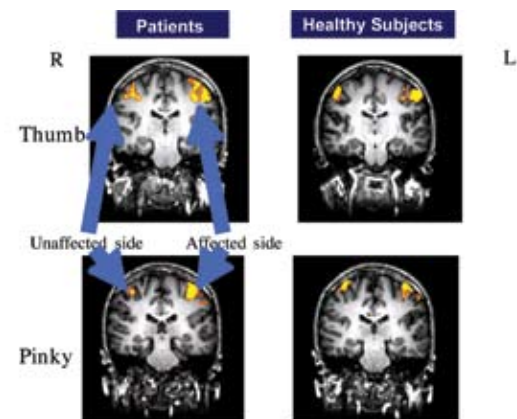

CONCLUSIONS

Two studies using MEG have reported different somatotopic locations of hand sensation in affected/unaffected side in CRPS patients. Such reorganization was not present in our healthy subjects and occurred in 4 of our 7 patients. The reorganization may depend on clinical condition. These results indicate that cortical reorganization of S1 may play a role in the pathophysiology of CRPS and that short-term treatment can reverse some of those changes.

Assessing the Influence of Scanner Background Noise on Auditory Processing: An fMRI Study Comparing Auditory Processing in the Absence and Presence of Recorded Scanner Noise Using a Sparse Design

Nadine Gaab[1,2], John D.E. Gabrieli[2], Gary H. Glover[1] – [1]Department of Radiology, [2]Department of Psychology

This study demonstrates the influence of recorded scanner background noise (RecSBN) on signal intensities within primary and higher order auditory regions by directly comparing two experimental sessions with the same auditory stimulation, which was presented either with or without RecSBN. Ten subjects listened to a series of four one-syllable words and had to decide whether two of the words were identical. The words were either presented with a silent background (WoSil) or with added RecSBN (WoRecSBN) during the auditory stimulation. This was contrasted with either silence (Sil) or RecSBN. A sparse temporal sampling method was used in both sessions which enabled us to directly assess the influence of RecSBN without varying scanning parameters, acquisition quantities or auditory stimulations. Results show previously reported neural masking effects when comparing WoSil>Sil with WoRecSBN>RecSBN. Furthermore, we found signal decreases in response to a "noisy" baseline (WoSil>Sil vs. WoSil>RecSBN) as well as effects of nonlinearity within auditory cortices. Confirming Talavage&Edmister (2004), our results suggest that neural masking in experimental designs that employ continuous scanner background (SBN) noise might be caused by an interaction between increased baseline levels and nonlinearity effects within auditory cortices. Adding SBN to an experimental condition does not enhance signal intensities to the same degree than SBN does when presented with a silent background, and therefore a comparison between the two may lead to neural masking. In addition, our study shows this effect is greatest in Heschl's gyrus but can also be observed to a lesser degree in higher order auditory areas.
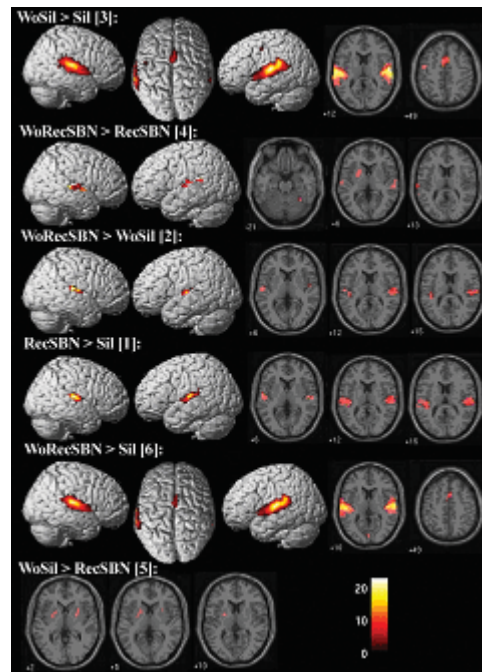
Imaging results for the 6 different contrasts (p<0.05, corrected for multiple comparisons).

Abnormal Brain Morphology in Patients with Complex Regional Pain Syndrome (CRPS)

Takefumi Ueno[1], Deepak Soneji[1], Kim Kaplan[1], David Ludlow[1], Camille Palma[1], Eva Patil[1], Gary Glover[2], Sean Mackey[1] - [1]Department of Anesthesia, [2]Department of Radiology

Aim of Investigation

CRPS is a debilitating chronic neuropathic pain condition that is poorly understood. Recent evidence suggests that supraspinal mechanisms may play a role in the generation and maintenance of CRPS. Previous work has demonstrated abnormalities in gray matter density of the prefrontal cortex and thalamus in chronic back pain patients. In this study, we investigated gray matter density differences between CRPS patients and controls using voxel-based morphometry (VBM).

Methods

Twelve healthy subjects and nine patients who met the IASP criteria for CRPS were recruited. High-resolution anatomical scans were collected on a 3T MRI scanner. SPM2 and MRIcro were used for skull stripping, normalization, segmentation, and detection of volume differences between the patients and healthy subjects. We performed ANOVA to detect gray matter density differences between the two groups. Furthermore, t-statistics were applied to interrogate whether these differences were due to increases or decreases in patients compared to controls.

Results and Conclusions

In CRPS patients compared to controls, we found gray matter increases in bilateral thalamus and the cerebellum, while there were decreases in the insular, orbitofrontal, and anterior cingulated cortices. The regions reported here have been previously implicated in pain processing. The increase in thalamic and cerebellar volumes may be due to repeated painful stimuli being processed through the cerebello-thalamo-cortical pathway. This abnormal processing may have induced synaptic changes leading to an increase in gray matter density. In turn, reduction in the insular and frontal regions may have resulted in loss of inhibition on the pain processing networks in CPRS patients.

References

1. Apkarian, A. et al. Chronic Back Pain Is Associated with Decreased Prefrontal and Thalamic Gray Matter Density. J. Neurosci, 2004.
2. Merskey, H. et al. Classification of Chronic Pain, 2nd edn., IASP Press, Seattle, WA, 1994.
3. Price, D. Psychological and Neural Mechanisms of the Affective Dimension of Pain., Science, 2000.
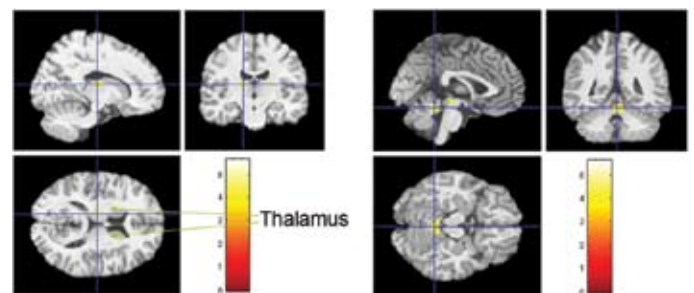
Areas which showed greater gray matter density in CRPS patients
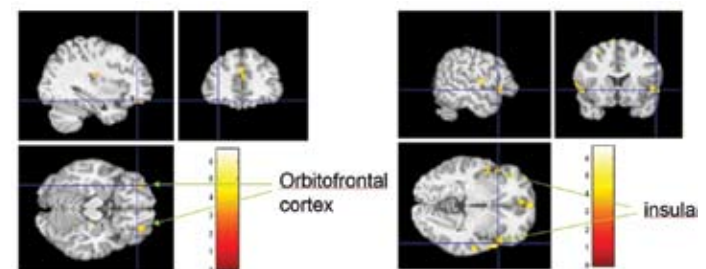
Areas which showed less gray matter density in CRPS patients

Dynamic Shimming for fMRI

Jung-Jiin Hsu and Gary H. Glover – Department of Radiology.

Introduction

The imaging magnetic field in the human inferior portion of the frontal lobe (IFL) is seriously distorted due to the change (9 ppm) in the magnetic susceptibility across boundaries of the brain, the nasal cavity, and the sinuses. The shims of conventional clinical scanners are not able to correct the field to a satisfactory level. To compensate the shimming deficiency, there is increasing interest [1-3] in local shimming in which the shimming fields have a smaller scale of spatial variation, comparable to the target region. Previously, we have shown [4,5] that local shimming for IFL can be achieved by using the fields generated by current carrying coils held in the subject's mouth. It is found [5] that the improved field homogeneity can recover signal loss and enhance the sensitivity in time-series analysis in functional MRI (fMRI), thus increasing the extent of neuronal activity detected by fMRI. It is also noted [5] that the distance between the IFL and the location that the shim coil is held is about twice larger than the maximum diameter of a coil that can be comfortably held in the mouth, so the field generated by the oral shim coil of simple geometry is relatively uniform in comparison with the complex, small-scale structured field distortion in the IFL. Nevertheless, it is possible to obtain better results by dividing the ROI into smaller regions and shim and acquire each region's image separately. In this work, we discuss this problem and develop a solution of dynamical shimming.

Materials and Methods

The details of the localized shimming are given in Ref. [5]. In short, a set of circular coils are held in the subject's mouth; then, in turn, each coil is given a test current and a magnetic field (B0) map is obtained to determine the field the test current generates. A background B0 map without any current is also acquired. The scanner operator prescribes a region of interest (ROI) and the pixels in the ROI are used to compute the shim currents through a linear least-square fitting to zero the background B0 map. Thus the shimming field is optimized for the ROI of the operator's choice. To assess the effectiveness of applying the divided-ROI scheme for local shimming, a volume in the IFL which involved three slices was prescribed. Separate experiments were carried out with shim currents optimized for the whole ROI (volum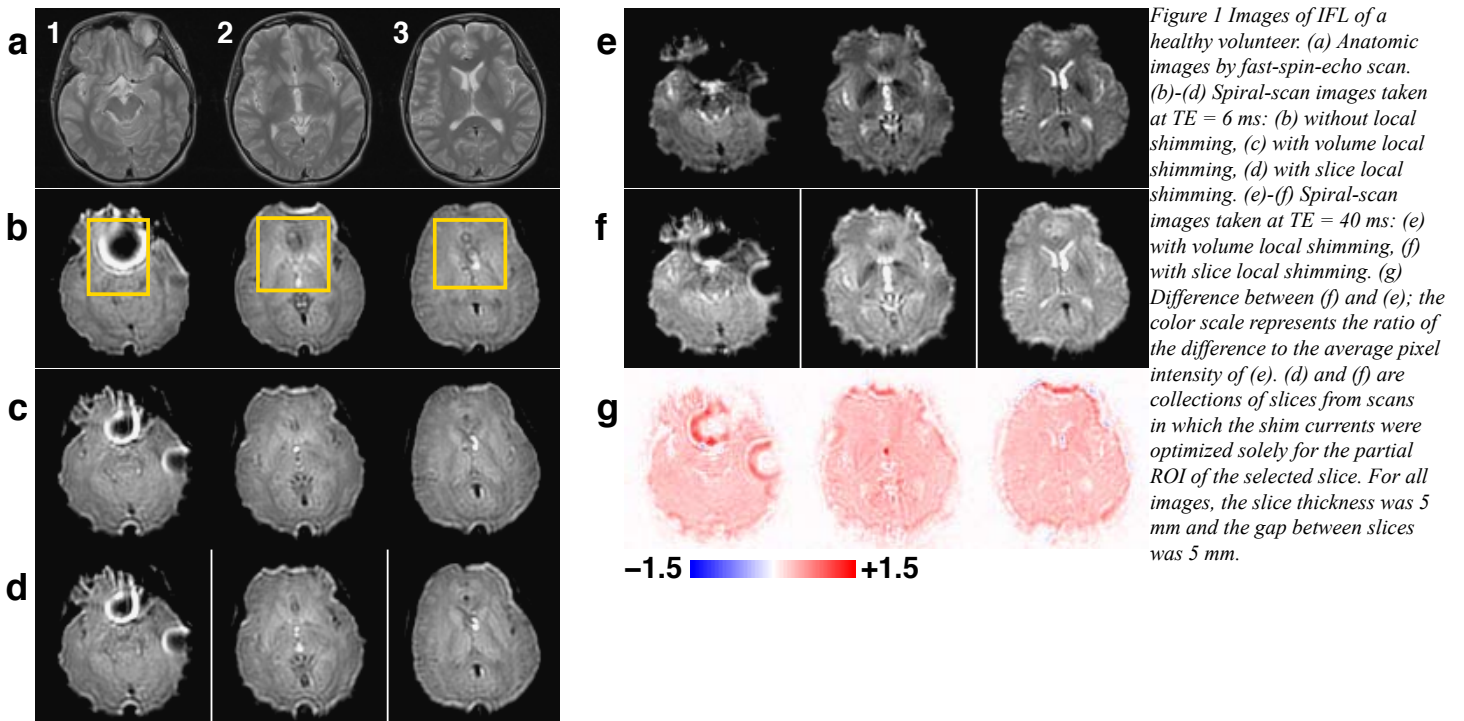e shimming) and for each partial ROI in the three slices (slice shimming). The experiment was carried out at 1.5 T. A spiral pulse sequence [6] was used for fast data acquisition. The B0 maps were acquired at TE = 6 ms.

Results and Discussion

The results are collected in Figure 1. The boxes in Fig. 1b indicate the ROI. The slice shimming (Fig. 1d) improves the images over the volume-shimmed ones subtly for TE = 6 ms (Fig. 1c). However, long TE is preferred in fMRI for ideal BOLD contrast; and at TE = 40 ms, slice shimming (Fig. 1f) improves over volume shimming (Fig. 1e) considerably. The improvement (Fig. 1g) includes an overall signal intensity increase and signal recovery at the boundaries. The present results suggest that one can take advantage of the better shimming results of smaller ROIs and vary the ROI location dynamically according to the slice selection during a multi-slice MRI scan. This will be very useful in fMRI, in which the data are usually acquired slice-wise. Implementing dynamic shimming with conventional linear shims has been successful in the past [7,8]. Utilizing the existing hardware and software at the Lucas Center, we have successfully integrated a functional prototype for dynamic shimming for fMRI. During an fMRI time-series data acquisition, the MRI scanner triggers a personal computer each time before a slice is acquired. The personal computer then sends commands to a multi-channel shim power supply to update the shim current outputs before the image data of the slice is acquired. Optimizing the determination of the shim currents is currently under study by the authors.

References

[1] JL Wilson et al., Magn Reson Med 48, 906 (2002); Neuroimage 19, 1802 (2003).
[2] V Roopchansingh et al., In: Proc 12th ISMRM, 1650 (2004).
[3] EC Wong and Y Mazaheri, In: Proc 12th ISMRM, 520 (2004).
[4] J-J Hsu and GH Glover, In: Proc 11th ISMRM, 734 (2003); In: Proc 12th ISMRM, 994 (2004).
[5] J-J Hsu and GH Glover, Magn Reson Med 53, 243 (2005). [6] GH Glover and S Lai, Magn Reson Med 39, 361 (1998).
[7] AM Blamir et al., Magn Reson Med 36, 159 (1996).
[8] G Morrell and D Spielman, Magn Reson Med 38, 477 (1997).

Figure 1 Images of IFL of a healthy volunteer. (a) Anatomic images by fast-spin-echo scan. (b)-(d) Spiral-scan images taken at TE = 6 ms: (b) without local shimming, (c) with volume local shimming, (d) with slice local shimming. (e)-(f) Spiral-scan images taken at TE = 40 ms: (e) with volume local shimming, (f) with slice local shimming. (g) Difference between (f) and (e); the color scale represents the ratio of the difference to the average pixel intensity of (e). (d) and (f) are collections of slices from scans in which the shim currents were optimized solely for the partial ROI of the selected slice. For all images, the slice thickness was 5 mm and the gap between slices was 5 mm.

−1.5 ▬▬ +1.5

Feasibility of Outer Volume Suppression and Reduced Field of View Imaging for Fetal fMRI (f-fMRI)
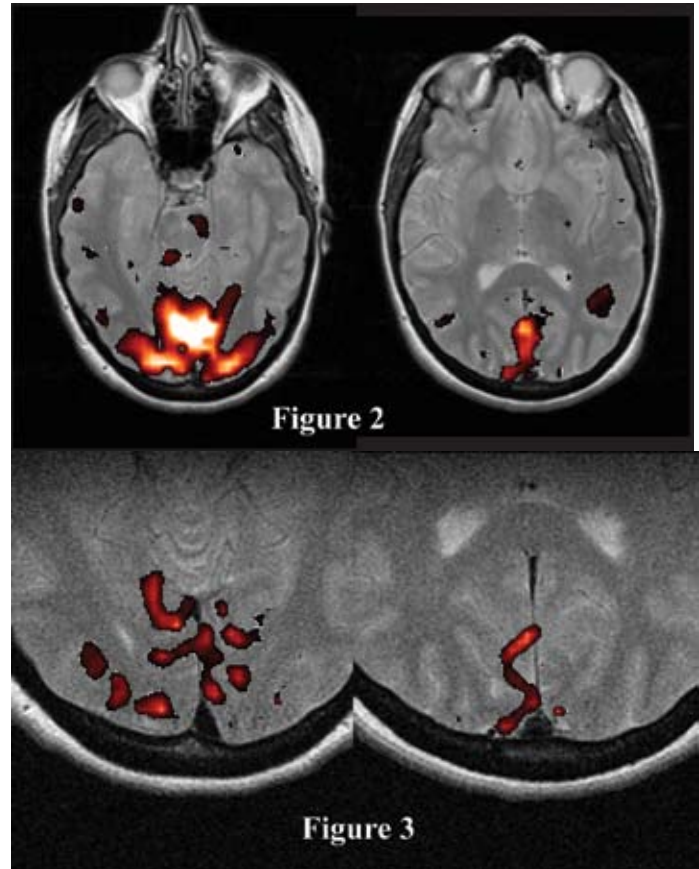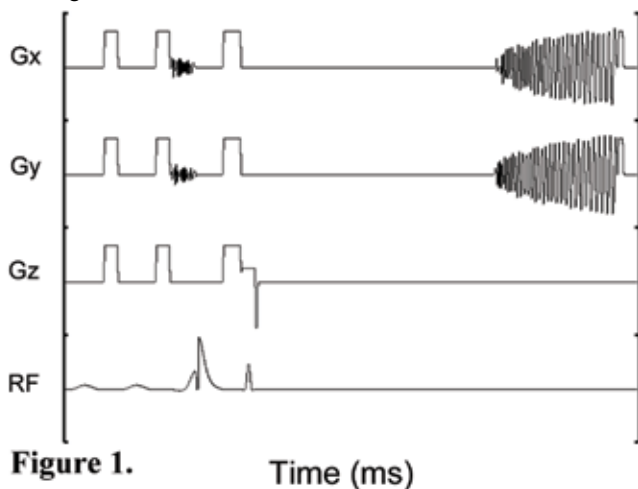
L. J. Pisani, R. Bammer, G. H. Glover – Department of Radiology

Introduction

Fetal functional MRI (f-fMRI) may be useful for differentiating between normal and compromised fetal well-being in pregnancies at risk for intrauterine growth restriction (IUGR). In designing an f-fMRI pulse sequence, one must consider the large girth of the maternal abdomen, motion of the maternal abdomen and fetal head, susceptibility effects, and specific absorption rate [1]. Despite the relatively small size of the fetal head, in order to avoid aliasing conventional pulse sequences require long readouts for a field of view (FOV) that encompasses the maternal abdomen. We demonstrate the feasibility of f-fMRI with an outer volume suppression and reduced readout FOV pulse sequence, by presenting fMRI of the visual cortex in an adult brain.

Materials and Methods

Our reduced FOV pulse sequence (Fig. 1) begins with two fat saturation radio frequency (RF) pulses and crusher gradient sets (Gx, Gy, and Gz). Next, a two dimensional (2D) spatially selective pulse and an adiabatic pulse achieve outer volume suppression before slice selective excitation. The 2D spatially selective 90° RF pulse [13] affects a cylinder of magnetic dipole spin states along the z axis rather than the more commonly selected slice of spins. The subsequent half-sech adiabatic fast passage pulse is insensitive to inhomogeneity in transmitted RF deposition across the subject and is spatially non-selective. Spins within the cylinder selected by the first 90° pulse are realigned with the main magnetic field, and spins outside that cylinder are brought into the transverse plane, then dephased by the following crusher gradient set. The slice selective 90° is followed after 40ms by the spiral readout to provide T2*-weighted BOLD contrast in an adult brain.

Figure 1. Time (ms)

Sagittal images were acquired in order to prescribe the image volume so that it included the visual cortex. fMRI images (64x64 pixels) were acquired with:

1. Conventional spiral GRE fMRI (TE = 40ms, FOV = 24cm) acquisition (Fig. 2), and

2. Reduced readout FOV outer volume suppression (FOV = 12cm) acquisition (Fig. 3).

Figure 2

Figure 3

High-resolution anatomic images (256x256 pixels) were acquired of the same volumes, on which to superimpose activation estimates. The fMRI stimulus consists of a 20s block of a contrast-reversing (3Hz) checkerboard pattern alternating with a 20s block of a small white fixation cross at the center of a black screen. 120 time frames are acquired with TR=2s, resulting in a 4min. protocol on a 1.5T GE scanner.

Results

Activation maps (thresholded at p < 0.02) demonstrate that the higher resolution achieved with reduced readout FOV (Fig. 3) provides more punctate regions of activation than that obtained with conventional fMRI (Fig. 2). With the decreased SNR at this resolution, such regions may predominantly correspond to venules draining the surrounding capillary bed, although details of the BOLD contrast mechanisms are still under investigation.

Conclusion

The achievement of increased resolution by a factor of four in the visual cortex of an adult brain fMRI is encouraging. The outer volume suppression and reduced FOV readout allow good fMRI resolution and reasonable readout duration, independent of the size of the maternal abdomen or orientation of the fetal head.

References

1. Fulford, J., S. H. Vadeyar, et al. (2004). "Fetal brain activity and hemodynamic response to a vibroacoustic

Correction of 3D Truncation Artifacts in Knee and Breast Imaging

Rebecca Rakow-Penner[1], Bruce L. Daniel[1], Garry Gold[1], John M. Pauly[2], Sam R. Mazin[1], Gary H. Glover[1] -- [1]Department of Radiology, [2]Department of Electrical Engineering

Introduction

Three-dimensional magnetic resonance imaging often requires long acquisition times. Scan durations are commonly shortened to accommodate breath-hold sequences, data acquisition during a contrast bolus, and limited scanner availability. Consequently, a minimum amount of data is collected to reduce scan time. In decreasing the amount of data collected, artifacts may result manifesting in Gibbs ringing in the direction of truncation. This study focuses on results from truncation in the slice encode (kz) direction. Rather than zero filling truncated k-space, a modified linear prediction (LP) algorithm proposed by Martin et. al. [1] can be used to interpolate uncollected lines. Although originally intended for 2D imaging, the algorithm can be applied in a third dimension to diminish truncation artifacts in the z direction. Potential 3D truncation artifacts include wrapping between the beginning and ending slices, residual Gibbs ringing from the in-plane direction, and apparent ghosting artifacts from adjacent image ringing. Clinical applications that can benefit from this artifact reduction include knee cartilage imaging and breast imaging with gadolinium contrast. Phantom data was analyzed using a 3D breast protocol, and in-vivo data was analyzed from 3D imaging of a healthy volunteer's knee.

Methods

Our method of linear prediction is modified from Martin, et. al. [1] for 3D imaging. Our technique works in four steps. (1) K-space is multiplied by a ramp in the direction of truncation that weights k-space based on each line's distance from the origin. For our 3D application, x and y remain on one axis and are plotted against kz. Each kz line is then weighted accordingly. This now high-pass filtered data can more readily and accurately be used as inputs into an LP algorithm. (2) Each (x,y) line is independently autocorrelated in the kz direction. (3) These autocorrelated lines are then entered, along with the recursion order (number of pre-

data was truncated to 30 kz lines and then predicted back out to 50. Data was collected using a 1.5T scanner (GE Healthcare, Waukesha, WI), with designated breast and knee coils (MRI Devices, Waukesha, WI).

Results

In Figures 1 and 2, image A is the reconstruction of the full kz acquisition without any truncation or prediction. Image B is the reconstruction when kz , the slice encode direction, has been truncated from 32 to 20 kz lines for the phantom images and 50 to 30 kz lines for the knee images. Figure 1 is data collected using the 3D breast protocol.

Notice the bar artifacts in the truncated image (B, arrow). This is a ringing artifact from an adjacent slice that has strong signal in that position. The prediction algorithm significantly reduces this artifact. The difference signal is notably stronger in the truncated/original difference image (D) than in the LP/original difference image (E). Linear prediction effectively corrected truncation artifacts caused by the clinically applied breast protocol. In Figure 2, which is windowed to show the artifact, notice the ringing effects from truncation near the cartilage (B,arrows). Since truncation is in kz, the ringing is not from the x-y plane but rather from adjacent slices. Image C is the linearly predicted data in which the ringing noted in B is corrected.

Discussion

Linear prediction can significantly reduce Gibbs ringing in the slice en-

Figure 1. Phantom data collected using a 3D breast protocol. (A) full kz data (B) image from truncated kz (C) predicted image from truncated data. A,B,C are on the same windowing scale. (D)subtraction image of truncated data image from original image. (E) subtraction image of predicted image from original image. E,D are windowed on the same scale.

Figure 2. In-vivo knee data collected with 3D protocol. (A) image from full kz data (B) image from truncated kz (C) image from predicted kz. A,B,C are on the same windowing scale.

vious kz lines used to predict the new line) into the Levinson-Durbin recursion algorithm. The predicted kz lines are added to the original kz lines. (4) The ramp multiplied previous to prediction is divided out of all the data. Finally, kz is Fourier transformed into image space providing the augmented number of images.

We applied this technique to a 3D breast imaging protocol using a phantom as well as to a 3D knee protocol in-vivo. Full kz data was collected to provide a standard for ideal data. Truncation followed by prediction occurred in post processing. The contrast breast protocol [2] includes: 3D spectral-spatial spiral acquisition, 32 slices/slab (full 32 kz acquisition), 256x256, FOV 20cm, flip angle 40, BW +/-125kHz, TE minimum, TR 38ms. For clinical use, only 20 kz lines are collected with this protocol and the remaining 12 are zero filled for a 32-slice reconstruction. Instead of zero filling, the lines were linearly predicted. The knee protocol [3] includes: 3D fat-saturated SPGR, 50 slices/slab, 256x256, FOV 14cm, flip angle 10, TE 4.2ms, TR 20.7 ms. The

code direction. In 3D breast imaging, not all kz lines are collected due to contrast enhancement time constraints. As demonstrated by phantom imaging, resultant ringing in the z direction may be corrected with the proposed 3D linear prediction algorithm. In cartilage imaging, a tri-laminar appearance of cartilage has been noted as an effect of Gibbs ringing [4]. Linear prediction in kz, significantly reduces this artifact. Future research entails applying the algorithm to clinical 3D breast MR and knee imaging. The algorithm will also be applied to 3D functional MR, MRCP and MRA imaging.

References

[1] Martin, et al. J Magn Res. 82: 392-399 (1989) [2] Agoston, et al. Radiographics. 21(1):217-226 (2001). [3] Gold, et. al. Radiographics. 23(5):1227:1242 (2003). [4] Frank, et al. Am J Roentgenol. 168(2):547-554 (1997). Funding provided by NIH P41-RR09784.

Breath Holding Reveals Differences in fMRI BOLD Signal in Children and Adults.

Thomason M.E. [1], Burrows B.E. [1], Gabrieli J.D.E. [1,2], & Glover G.H. [1,3] – [1]Neurosciences Program, [2]Department of Psychology, [3]Department of Radiology

Introduction

Interpretation of fMRI results in children is presently based on vascular dynamics that have been studied primarily in healthy adults. Comparison of the neurological basis of cognitive development is valid to the extent that the neurovascular responsiveness between children and adults is equal.

Materials and Methods

The present study was designed to detect age-related vascular differences that may contribute to altered BOLD fMRI signal responsiveness. We examined BOLD signal changes in response to breath holding, a global, systemic state change in brain oxygenation. Children exhibited greater percent signal changes than adults in grey and white matter, and this was accompanied by an increase in noise. Consequently, the volume of activation exceeding statistical threshold was reduced in children. The reduced activation in children was well modeled by adding noise to adult data.

Discussion

These findings raise the possibility that developmental differences in
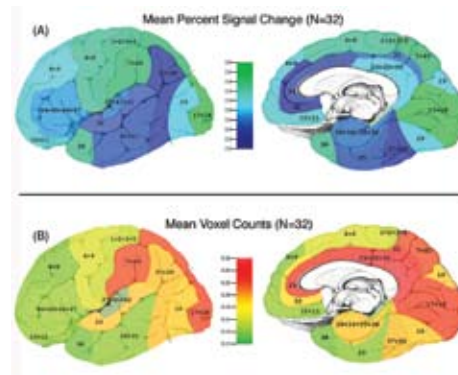
Mean BOLD response to breath-holding, averaged across 16 children and 16 adults shows regional variability across subjects.

fMRI findings between children and adults could, under some circumstances, reflect greater noise in the BOLD response in the brains of children than adults. BOLD responses varied across brain regions, but showed similar regional variation in children and adults.

Conclusion

Future BOLD investigations comparing children and adults should take noise information into account when estimating effect size.

Amygdala Reactivity to Emotional Faces Predicts Improvement in Major Depression.

Canli T. [1], Cooney R.E. [2], Goldin P. [2], Shah M. [2], Sivers H. [2], Thomason M.E. [2], Whitfield-Gabrieli S. [2], Gabrieli J.D.E. [2], Gotlib I.H. [2], [1]Department of Psychology, Stony Brook University [2]Department of Psychology, Stanford University

Introduction

Depression is associated with abnormalities in frontal and limbic neural circuits including the amygdala, which is more strongly activated at rest and in response to emotional stimuli in depressed patients than in controls. Individual differences in response to emotional stimuli can predict subsequent treatment outcome.

Materials and Methods

We conducted a prospective study of 16 individuals diagnosed with major depressive disorder (MDD). Participants viewed emotional and neutral faces in a gender discrimination task as they underwent functional magnetic resonance imaging (fMRI) during a depressive episode at Time 1 (T1). We examined the relationship between degree of amygdala activation at T1 and improvement in level of depressive symptomatology an average of 8 months later at Time 2 (T2). We show that greater amygdala activation to emotional facial expressions among depressed patients predicts symptom reduction 8 months later, controlling for initial depression severity and medication status.
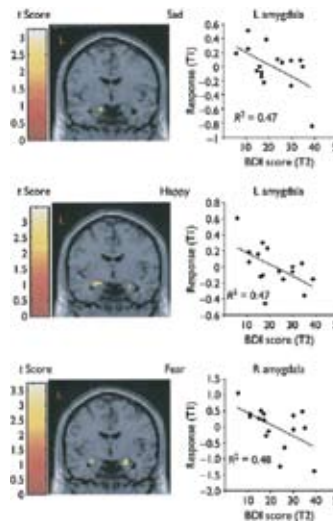
Amygdala activation across individuals at Time 1 (T1) correlated with Beck Depression Inventory (BDI) symptom improvement at Time 2 (T2). Scatterplots depict fitted and adjusted responses for the maximally significant voxels.

Discussion

This is the first study to show that amygdala reactivity to emotional facial expressions in a sample of MDD participants predicted the degree of symptom improvement 8 months later.

Conclusion

Functional magnetic resonance imaging may thus be used as a method to identify neural markers in depressed patients at risk for poor outcome.

## Brain Activation to Emotional Words in Depressed vs Healthy Subjects.

Canli T.[2], Sivers H.[1], Thomason M.E.[1], Whitfield-Gabrieli S.[1], Gabrieli J.D.E.[1], Gotlib I.H.[1]. [1]Department of Psychology, Stony Brook University; [2]Department of Psychology, Stanford University

Introduction

Depression can be conceptualized as enhanced processing of negative emotional stimuli or diminished processing of positive emotional stimuli. Using fMRI and samples of healthy control subjects and participants diagnosed with major depressive disorder (MDD), we identified specific brain regions that may be implicated in these forms of dysfunctional processing.

Materials and Methods

Fifteen participants diagnosed with major depressive disorder and 15 controls were scanned during a lexical decision task involving neutral, happy, sad, and threat-related words. In group-comparisons of patterns of brain activation in response to happy-neutral words, depressed participants showed consistently blunted reactivity, relative to normal controls, in a number of brain regions associated with language-related processes, affective and visceral states, and motor systems.
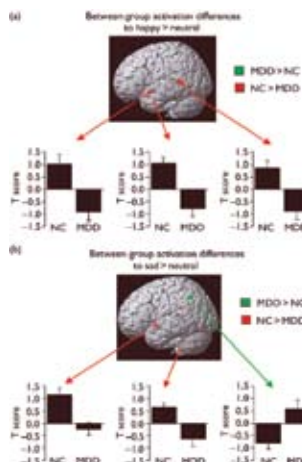
Between-group activation differences to happy-neutral (a, top) and sad-neutral (b, bottom) words.

Discussion

We observed a complex pattern of decreased activation in MDD subjects in superior temporal and cerebellar regions and increased activation in the parietal cortex in response to sad stimuli.

Conclusion

Using fMRI and a lexical decision task, we found that, relative to control subjects, depressed patients exhibit decreased activation to positive stimuli throughout the brain, supporting a theory of diminished processing of stimuli.

SNR Dependence of DTI Fiber Tracking Protocols

Murat Aksoy[1,2], Barak Acar[3], Roland Bammer[2] - [1]Department of Electrical Engineering, [2]Lucas Center, Department of Radiology, Stanford University; [3]Department of Electrical & Electronics Engineering, Bogazici University, Istanbul, Turkey

Introduction

DTI based tractography promises to become a useful tool in basic clinical neuroscience and studying abnormalities in various diseases like schizophrenia, multiple sclerosis, and neoplasms. Current imaging protocols that produce high fidelity DTI data for tracking are prohibitively long for clinical settings. The objective of this study was to determine whether or not DTI protocols that are fast enough to be used for routine clinical work-up provide results that are comparable to a gold standard defined by a high SNR DTI protocol.

Methods

We defined two outcome measures: 1) The deviation of the closest tracking endpoint between the gold standard and the protocol proposed for clinical use, and 2) A metric that characterizes the overall deviation between fibers computed with the gold standard and the clinical protocol. Specifically, we used "Closest Point Euclidean Distance", "Closest Point Harmonically Summed Euclidean Distance", "Closest Point Hausdorff Distance" and "Curve Fitting to Closest Point Distance" as the similarity measures between the fibers derived from the gold standard and the proposed clinical protocol.

Whole brain DTI scanning was conducted on a 1.5T unit with 50mT/m maximum gradient strength. The scanning parameters were as follows: FOV=25cm, slice thickness/gap=3mm/0mm, 24 encoding directions, b=850s/mm2. The total scanning time per average was less than 2.5min. To study the influence of SNR on the tracking results the protocol was repeated six times. For DTI post-processing repetitions were averaged that correspond to a NEX range from 1 to 6 (gold standard [GS]). Fibers from the corpus callosum (CC) and the cortico-spinal tract (CST) were selected for further analysis.

Results

The results for these 6 different types of measures are summarized in Table 1 and Figure 2. With increasing SNR the endpoint and similarity measures increase to match the GS. The parameters extracted from these models give an intuition about the speed of the deviation, which of course is expected to be higher for low SNRs due to an increased uncertainty in the eigenvector estimation. Table 1 shows the results for 5 different types of metric used, averaged over all the fibers emanating from the seed regions in Corpus Collosum and Corticospinal Tract, for different number of averages used
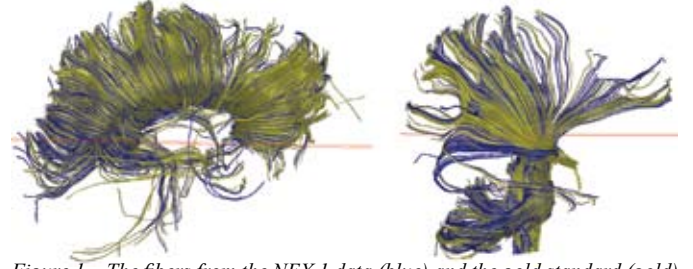
Figure 1 – The fibers from the NEX 1 data (blue) and the gold standard (gold) in the same visualization window for Corpus Collosum (left) and Corticospinal Tract (right)

In this study, it has been found that increasing the number of scans and thus increasing the SNR indeed helps in constructing more accurate fiber trajectories. In the endpoint distance analysis used, it is found that there is a 50% decrease in the average distance between the endpoints of the fibers in GS and the proposed clinical protocol. The same is also true for the similarity between the fibers, where the error decrease in most of the similarity measures is on the order of 50% or more. In order to get more accurate results about the exact minimum affordable SNR for a reliable fiber tracking, more measures are warranted that take into account the behavior of fibers in different regions of interest.
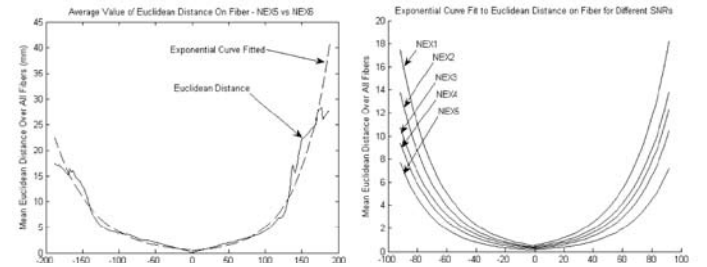

Figure 2 – Left: The Euclidean Distance between the points on fibers from the NEX1 data set and the gold standard The dotted line shows the Exponential curve fitted to this data. Right: The Results of the Exponential Curve fit using different number of averages for tracts in Corticospinal Tract

	Endpoint Distance (mm)		Closest Point Euclidean Distance (mm)		Closest Point Harmonically Summed Euclidean Distance (mm)		Closest Point Hausdorff Distance (mm)		Line Fitting Analysis – Slope of line	
	CC	CST	CC	CST	CC	CST	CC	CST	CC	CST
NEX1	2.3680	2.0016	2.4683	6.9410	0.6638	0.9433	8.2347	20.7605	0.0516	0.1261
NEX2	1.5525	1.3941	2.3742	5.6961	0.5629	0.6777	8.4741	17.8812	0.0466	0.1017
NEX3	1.0048	1.0001	1.9163	4.9331	0.3897	0.5370	7.3479	15.7320	0.0405	0.0875
NEX4	0.8310	0.6820	1.6710	4.2479	0.3168	0.4316	6.5830	13.9338	0.0348	0.0736
NEX5	0.4554	0.2211	1.2702	3.1833	0.1441	0.2710	5.3535	10.6699	0.0259	0.0549

Table 1 – Resultant Mean Metric Values for Fibers Starting from Corpus Collosum (CC) and Corticospinal Tract (CST) for different number of averages used

Time-resolved 3D Quantitative Flow MRI of the Major Intracranial Arteries

Roland Bammer[1], Murat Aksoy[1], Maarten A. Lansberg[2], Tom Hope[1], Michael M. Moseley[1], Robert J. Herfkens[1], Marcus T. Alley[1].
[1]Lucas Center, Department of Radiology; [2]Stroke Center, Department of Neurology

Introduction

3D Time Resolved MRA is a technique used to measure blood flow at different time instances by exploiting motion induced phase shifts. This technique provides a complete vector field in 3D, which enables a deeper understanding of the physiology of the blood flow and further investigation of hemodynamic abnormalities such as in stenoses or intracranial aneurysms. In this study, we aim to optimize and investigate the potential of this method for measuring the ICA, Circle of Willis, ACA, PCA, MCA and basilary and vertebral arteries (Fig. 1).
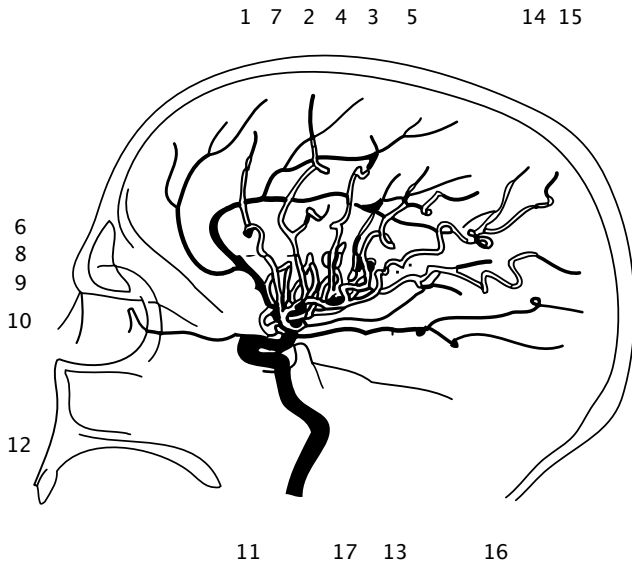
Fig. 1 - Angiography of the internal carotid artery and its major branches. (1) orbitofrontal artery, (2) precentral artery, (3) artery of the central sulcus, (4) calloso-marginal artery, (5) postcentral artery, (6) frontopolar artery, (7) pericallosal artery, (8) insular arteries, (9) anterior cerebral artery, (10) ophthalmic artery, (11) siphon, (12) siphon-incisivum-line, (13) anterior choroidal artery, (14) artery of the angular gyrus, (15) posterior temporal artery, (16) posterior cerebral artery, and (17) middle cerebral artery. (modified from Krayenbühl & Yasargil et al.)

Materials and Methods

Cine 3D PC MRI was optimized to cover the major intracranial arteries of volunteers on a 1.5T scanner with high performance gradients (50 mT/m, SR = 150) using a dedicated 8-channel head coil: FOV = 180mm, slice thickness=2.5mm, TR=4.5ms, TE=1.9ms, matrix 192x160, ZipX2, bandwidth ±62.5kHz, NEX=1, views per segment=4 slice encodes x 4 phase encodes (temporal resolution= 4·4·4.5ms=73.6ms), velocity encoding (venc) = 70cm/s (all directions). All procedures performed were approved by our institution's review board. Using the 3D vector field, it is possible to construct streamlines that emanate from user specified seed points by linear interpolation methods such as Euler or Runge Kutta. The existence of time information also enables a very intuitive streamline visualization method, which is called the particle trace. In this method, imaginary particles that start from specific seed points go through a trajectory defined by the vector field information at different times. This type of visualization is further developed to include particle traces starting from the same seed locations but at different time frames. To demonstrate this concept, a software package developed in-house for DTI-based fiber-tracking (smartTRACK) was modified to allow a visualization of the major cranial vessels.
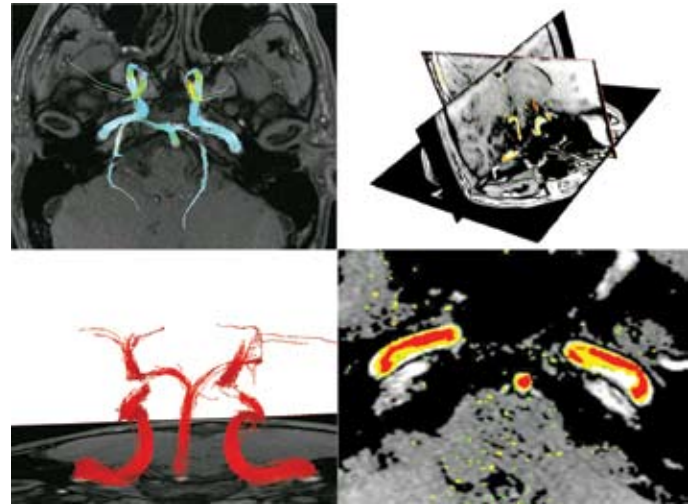
Fig. 2 – An illustration of the VTK Interface and streamline visualization of the flow-vector field at different points in time and from four different viewing perspectives. The magnitude of the flow is represented by the color of the streamlines (red=high, blue=low flow)

Results

Our preliminary results demonstrate the feasibility to measure the components of intracranial blood flow using 3D PC MRI at multiple time points. Compared to 2D methods, the 3D PC MRI used in this study provides higher SNR which provides better absolute flow quantification and diminished orientation uncertainty. Quantitative flow values measured from the 3D PC MRI were in good agreement with what one usually finds with Doppler flow measurements (carotid siphon = 44±14cm/s, MCA = 80±13cm/s, PCA = 54±11cm/s, ACA = 67±14cm/s, vertebral arteries = 50±12cm/s). The fidelity of the vector fields generated from these data is sufficient to support streamline computations even in vessels with rapid orientation changes, such as in the siphon of the ICA at the level of the Sella Turcica (Figure 2), which is impressive insofar that the vessel calibers in the brain are considerably small and susceptible to partial volume artifacts. If the voxel size is chosen too big, flow in the opposite direction will cancel but this effect was never observed in this study. Significant improvements in streamline tracking with smartTrack could be made by adaptive changes in maximum tolerable angular deviations between tracking steps and spline interpolation of the vector field. The VTK environment used for smartTrack allows for 3D rendering of the tracks and interactive viewing from essentially all perspectives.

Conclusion

3D PC MRI in the major intracerebral arteries is possible and provides flow vector fields of useful quality. DTI methods, previously used for tract tracing, can be applied to increase the sensitivity of flow visualization in 3D PC MRI. One limitation of the technique used is related to the fixed velocity encoding value over the entire cardiac cycle. At certain instances during the cardiac cycle the full dynamic range of flow encoding could not be fully utilized. Along these lines further investigation is warranted and adaptive flow-encoding gradients that adjust optimal encoding during the RR interval are desired. From the T1 shortening of contrast material, we anticipate further improvements in terms of SNR. Future improvements include developing a method to avoid confounding effects from venous overlay.

Methods for SENSE Reconstruction with Partial k-Space Acquisition

David Clayton, Roland Bammer – Department of Radiology

Introduction

Partial k-space acquisition capitalizes on the conjugate symmetry of hermitian data and allows for faster image formation with fewer phase-encode steps. However, MR data are not fully hermitian because images contain spatially-varying phase. As a result, slightly more than half of the k-space is required to correct for this incidental phase variation and an estimate of a low-resolution phase image from the symmetric portion around the origin of k-space can be used. Calculation of final full k-space data is usually accomplished either by direct conjugate synthesis, such as homodyne reconstruction (ref 1), or by an iterative algorithm, such as the method of projection onto convex sets (POCS) (ref 2). A further acquisition speed-up can be achieved by combining partial k-space acquisitions with parallel imaging. It is intuitive that the k-space-based GRAPPA or SMASH formalisms are compatible with all partial k-space methods since the synthesis of the full-FOV image is done in k-space prior to homodyne or POCS. It has been shown, however, that direct use of homodyne reconstruction in conjunction with SENSE fails because of the loss of phase information and needs to be performed in two steps (ref 3). Here, we demonstrate that this two step approach is only necessary for homodyne but not for POCS and evaluate the performance of the different methods with a numerical phantom and in vivo data.

Materials and Methods

Sensitivity maps for 6 circularly-arranged coils were made with a Biot-Savart calculation and were used to modulate a Shepp-Logan phantom. Aliased images with a reduction factor of 4 were made by keeping every fourth phase-encoding line (taken to be in the y-direction) and fractional k-space was achieved by removing all but 8 phase-encoding lines prior to the center line. T2w-FSE images (2562) were acquired with full k-space acquisition from a human volunteer with a GE Signa 1.5T scanner using an 8-channel head array (MRI Devices). A 3D FGRE (32x1282) scan was performed for the coil sensitivity estimates. Manipulations similar to those done with the numerical phantom were performed on phase-encoding lines so that a reduction factor of 4 was achieved and 8 lines prior to the center of k-space were kept. Three methods of reconstructing partial k-space were investigated. (i) A straightforward zero-fill of the missing k-space data prior to SENSE reconstruction. (ii) Homodyne reconstruction with SENSE was implemented as described in ref 3: the k-space was split into symmetric (low-pass) and asymmetric (double conjugate) parts by filter operations, SENSE reconstruction was applied to each of the resulting images, the complex data from the double conjugate image was phase-corrected using the low-pass image, and the final image was taken as the real part of the latter. (iii) POCS reconstruction was performed on the undersampled, fractional k-space data using 10 iterations (which is more than sufficient for convergence), and then SENSE reconstruction is applied directly to the result.
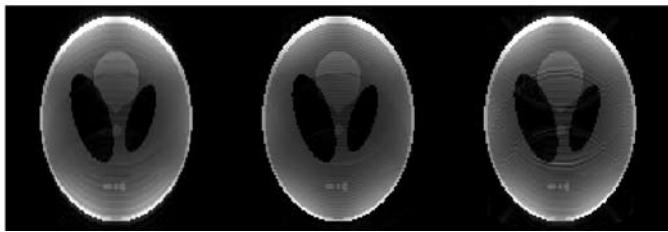
Discussion

Phantom results are shown in fig 1 and in vivo images are shown in fig 2. In each case, the zero-filled data appears blurred (as would be expected from the effective sharp filter transition between the acquired data and the additional zeros), the POCS data has the most significant residual aliasing, and the homodyne data has the least aliasing and the best SNR performance. The critical issue for successful SENSE reconstruction is the preservation of phase information. Partial or complete loss of complex signal yields considerable reconstruction artifacts. Intuitively, then, because POCS reconstructs complex data and includes phase information, it would seem natural to use this method in conjunction with SENSE. It might also be preferred over the hybrid homodyne-SENSE reconstruction in ref 3 because the latter involves two separate SENSE steps for each image and therefore doubles the time of the total reconstruction. However, from the results shown here, when POCS is applied prior to SENSE, there is a greater level of residual aliasing artifacts. A possible explanation for this has to due with the order of the low-resolution phase-correction step that is performed in both procedures. The POCS-SENSE algorithm applies a low-resolution phase correction prior to the SENSE reconstruction, while the homodyne-SENSE reconstruction waits until after the full-FOV images are formed. Therefore, any errors produced by the low-resolution phase estimate in the POCS step will get propagated by the SENSE reconstruction and should appear as residual aliasing, but this is not the case for the homodyne-SENSE combination. POCS, however, is still required if phase information in the final image is important.

Conclusion

In order to traverse k-space as quickly as possible, it is often desired to use fractional k-space acquisition in conjunction with parallel imaging. In the case of Cartesian SENSE acquisitions in which a further reduction of k-space lines is achieved by collecting asymmetric data (e.g., fractional-echo single-shot FSE), an accurate method of generating this missing lines prior to k-space center is required. We have compared two methods: applying POCS prior to SENSE and a hybrid homodyne-SENSE combination. Simulation and in vivo data suggest that the SENSE-homodyne combination produces less residual aliasing.

References

(1) Noll DC, et al. IEEE Tr Med Imaging 1991;10:154.
(2) Lindskog ED, et al. J Magn Reson 1991;92:126.
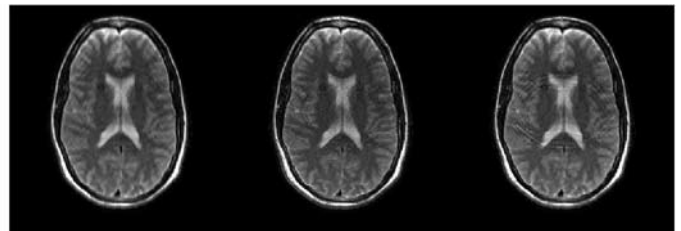(3) King KF and Angelos L. Proc ISMRM 8th Meeting 2000;153.

Fig 1. Reconstructed images from an undersampled (reduction factor of 4) fractional ky (8 lines prior to ky =0) mathematical phantom (6 coils): (A) Zero-filled, (B) homodyne-SENSE, and (C) POCS-SENSE. Significant residual aliasing is apparent in (C).

Fig 2. Reconstructed images from an undersampled (reduction factor of 4) fractional ky (8 lines prior to ky =0) in vivo acquisition (8 coils): (A) Zero-filled, (B) homodyne-SENSE, and (C) POCS-SENSE. Significant residual aliasing is apparent in (C).

Augmented SENSE Reconstruction by an Improved Regularization Approach

David Clayton[1], Stefan Skare[1], Gene Golub[2], Majid Modarresi[2], Roland Bammer[1] – [1]Department of Radiology, [2]Department of Computer Science

Introduction

Image reconstruction from undersampled k-space data acquired with parallel receivers, such as SENSE, can severely suffer from a poor conditioning of the design matrix. One major determinant is the geometrical properties of the receiver coil elements relative to size and location of the desired FOV and the degree of aliasing. Poor conditioning leads to residual aliasing and more noise in the final image. Ill-conditioned systems can be solved using regularization methods in which the solution is stabilized by including appropriate additional information. SENSE reconstruction has become the focus for a variety of regularization techniques (refs 1-4). In its original implementation, Cartesian SENSE reconstruction is typically done by traversing the aliased image and separating the aliased pixels based on coil sensitivities (ref 5). For each set of n_a aliased pixels, the problem can be cast into an $n_c \times n_a$ matrix system (n_c is the number of coils), which is generally very small. Regularizing the solution vector is limited by the paucity of singular values. Moreover, the solution vector is usually comprised of pixels from distant and therefore unrelated positions and does not allow advanced penalty terms to take advantage of the continuous physical nature of the system. In this work, we present a more physically meaningful regularization method in which an entire line of pixels is unfolded at once using a single matrix inversion so that the solution vector represents an image profile.

Materials and Methods

Sensitivity maps for 6 circularly-arranged coils were made with a Biot-Savart calculation and were used to modulate a Shepp-Logan phantom. Noise (SNR=50) was added and phase-encoding lines were eliminated to achieve desired reduction factors from 2 to 6. An additional reference image was generated from the original phantom by blurring with a 2-pixel kernel, shifting by 1 pixel in the x-direction, and adding one anterior feature (ellipse). T2w-FSE images (256²) were acquired with full k-space acquisition from a human volunteer with a GE Signa 1.5T scanner using an 8-channel head array (MRI Devices). A 3D FGRE (32x128²) scan was performed for the coil sensitivity estimates. Desired aliasing was again achieved by eliminating the corresponding number of phase-encode lines. Four methods of SENSE reconstruction were used: (i) the pixel-wise method (ref 5): at each pixel location in the undersampled data, S, a vector of n_a pixels, x, in the unfolded image, U, is found by solving the linear system, Ax=b, using a least-squares method where the vector b is formed from the pixels of the coil components in S, and A is formed from the coil sensitivity estimates; (ii) similar to (i) but using Tikhonov regularization with L-curve analysis to determine the optimum regularization parameter; (iii) similar to (ii) but includes prior information from a reference scan (ref 2); and (iv) performs column-wise unfolding, described as follows. For each pixel in a column (fixed frequency-encoding index) of S, the matrix A and vector b are formed,

then a block-diagonal matrix D=diag(A1, A2, …, An) is made, where n is the number of rows in S, and a corresponding composite vector c is formed, c=(b1, b2, …, bn). The solution vector x, of the augmented system Dx=c now gives an entire column in U. However, the index mapping from x to the U is not monotonic and so the columns in D need to be sorted. This step is essential for using regularization methods that assume a relatively continuous set of values in the solution vector. For this column-wise method, we used a damped-SVD algorithm with the first-order derivative as the penalty term, L, and generalized cross-validation to find the optimum regularization parameter.

Discussion

The effects of regularization are most obvious with decreased conditioning of the design matrix. Pixel-wise regularization tends to over-regularize and noise-reduction has to be paid off by increased residual aliasing. With reduced conditioning and stronger regularization the solution of methods that rely on regularization images can become dominated by the regularization image. Our new column-wise method takes advantage of the continuity of data and is virtually immune to such influences (fig 1). Such an artifact is clearly apparent in the result of method (iii) by the inclusion of the ellipse feature in the unfolded image (fig 1c) which only exists in the regularization image. In vivo images with a reduction factor of 6 using 8 coils show a clear SNR improvement made by the column-wise method (fig 2d) over the unregularized pixel-wise method (fig 2a). In addition, there is significant residual aliasing artifact reduction as compared to the regularized pixel-wise methods (figs 2b and 2c). Given the high reduction factor, the potential of this new approach is clearly apparent.

Conclusion

We have presented a line-by-line SENSE reconstruction technique that exploits the continuous behavior of the solution vector by incorporating derivative constraints into the regularization. Significant improvements in eliminating residual aliasing artifacts and noise enhancement are shown for phantom and in vivo data for severely ill-posed cases, i.e. when the reduction factor approaches the number of coils. Operating on a larger design matrix and using a more appropriate penalty term clearly outperforms previous methods. Therefore, this method shows promise in allowing for greater scan acceleration for a fixed receiver system.

References

(1) Bammer R, et al. MRM 2002;48:128.
(2) Lin F-H, et al. MRM 2004;51:559.
(3) Liang Z-P, et al. ISMRM 10th Meeting 2002;2388.
(4) Eggers H. and Boesiger. ISMRM 11th Meeting 2004;2409.
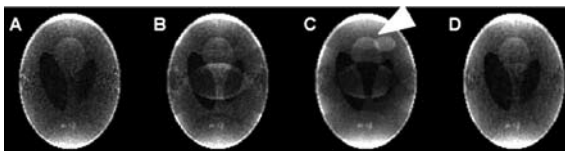(5) Pruessmann KP, et al. MRM 1999;42:952.

Fig 1. Phantom data (R=3, nc=6) reconstructed using conventional SENSE (A), conventional SENSE with Tikhonov (B), conventional SENSE with Tikhonov and a regularization image (C), and column-wise SENSE with damped generalized SVD and generalized cross-validation (D). Tikhonov (B) reduces noise at the cost higher residual aliasing. In (C) the regularization image strongly affects the final solution (arrow). Regularized column-wise SENSE (D) gives the most optimal solution with regard to artifact power and noise amplification.
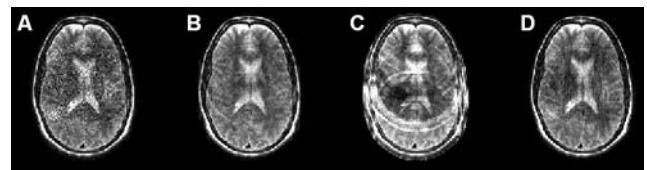

Fig 2. T2w-FSE data (R=6, nc =8) reconstructed using conventional SENSE (A), conventional SENSE with Tikhonov (B), conventional SENSE with Tikhonov and a regularization image (C), and column-wise SENSE with damped generalized SVD and generalized cross-validation (D) (from left to right). The regularized column-wise SENSE clearly outperforms all other methods at these high reduction factors.

Improved TurboSENSE with Iterated Conjugate Gradient Phase Refinement

Calvin Lew[1], Dan Spielman[2], Frandics Chan[2], Roland Bammer[2] – [1]Department of Electrical Engineering, [2]Department of Radiology

Introduction

Phase-constrained parallel imaging has been shown to have better SNR characteristics compared to SENSE (1) at the same reduction factor. These techniques double the number of SENSE equations by separating the real and imaginary components and consequently narrows the solution vector for the minimal least-squares solution. In effect, the g-factor is lowered. Having an accurate phase estimate is key to obtaining a good reconstruction. Problems arise when the phase requires high resolution to capture sharp phase profiles such as air-tissue or water-fat interfaces. The residual phase errors can leave aliasing artifacts in the turboSENSE reconstruction. Since the phase is incorporated into the real and imaginary equations in the turboSENSE matrix, phase errors directly translate into errors in the magnitude reconstruction. Field map inhomogeneity issues in least squares estimation of multi-point Dixon imaging are similar to the phase errors with turboSENSE. Reeder, et al (2), have demonstrated an iterative method for least squares estimation of field map inhomogeneity in multi-point Dixon imaging. Here, we present a similar method to improve the phase estimate.

Figure 1

Materials and Methods

The proposed method employs an iterative conjugate gradient method similar to Reeder's method to update the phase estimate for turboSENSE reconstruction. Initially, a turboSENSE reconstruction is performed with the coil calibrations obtained from a separate scan or internal self-calibration. The initial phase estimate has already been absorbed into the calibration measurement. For a reduction factor of n (R=n), turboSENSE reconstruction is performed on each set of n aliased pixels for the entire image. Next, the residual error is computed. The error is approximated to be the total derivative of the SENSE equations with respect to the set of aliased magnitude and phase pixels. The derivative is separated into phase and magnitude changes. Omitting higher order terms, this error represents a new set of equations that can be solved via least squares. The phase error for the n pixels is solved and used to update the phase in the original turboSENSE reconstruction matrix. A new turboSENSE reconstruction is performed. This process repeats until convergence of the residual error to a minimum.
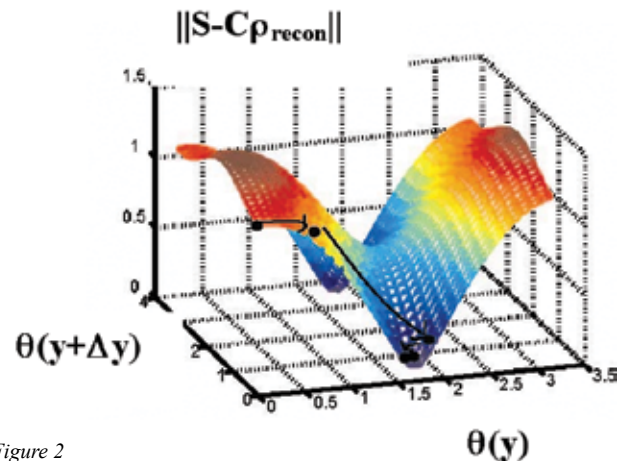
The coil calibrations were acquired with an in-vivo phase-contrast gradient echo sequence from a GE Signa 1.5T scanner with a 256x160 imaging matrix in Cartesian k-space with 6 views per segment. The calibrations were performed on a separate scan with a 4-channel torso coil. The sensitivity matrix was calculated by dividing the individual coil calibrations by the sum-of-squares image. The undersampled acquisition was also performed with the same sequence. Reduction factors of 2, 3, and 4 were used. Iterations were performed until there was a less than 1% change in the residual norm from the previous iteration.

Discussion

Figure 1 shows the magnitude images for reduction factors of 2, 3, and 4 for SENSE, the initial turboSENSE reconstruction, and the final iterated turboSENSE reconstruction. Specifically for R=2, figure 2 shows a mesh plot of the residual error norm as a function of phase perturbations for pixel (140,90) and its aliased counterpart at (140,186). Since the error is periodic over π, only the range from 0 to π is shown. The trajectory of the (140,90) pixel during iterated turboSENSE is shown as well. Refer to the red arrows on figure 1 for the pixel location.

It is clearly shown that the iterated turboSENSE improves upon the initial turboSENSE reconstruction. Iterated turboSENSE removed many of the aliasing chest wall artifacts and cleaned up areas in the aorta and pulmonary artery. Compared to SENSE, iterated turboSENSE is visually at least as good for R=2 and R=3. In R=4, it has a clear performance gain over SENSE in terms of residual aliasing and noise enhancement. The chest wall in iterated turboSENSE is more clearly delineated than those of SENSE and turboSENSE. Future work would be to improve the iterative approach to exploit the lower g-factor of turboSENSE further.

References

1. Pruessman, K.P., et al. MRM, 42:952-962, 1999. 2. Reeder, S., et al. MRM, 51:35-45, 2004.

$$\|S-C\rho_{recon}\|$$

$\theta(y+\Delta y)$

$\theta(y)$

Figure 2

Challenges with Coil Calibrations in In-Vivo Phase Contrast SENSE

Calvin Lew[1], Roland Bammer[2], Dan Spielman[2], Frandics Chan[2] – [1]Department of Electrical Engineering, [2]Department of Radiology

Introduction

Phase contrast imaging, or PC, is a useful tool for clinicians to diagnose diseases such as myocardial shunts. PC employs a flow-encoding technique that encodes the velocity of the blood flow onto the phase of the MRI image. PC unfortunately requires considerably longer duration to scan due to the extra acquisition. Parallel imaging methods such as SENSE (1) offer a way to reduce the scan time. Breathheld scans are more manageable for patients. SENSE requires accurate coil sensitivity maps to obtain a feasible image reconstruction. This abstract examines different choices for selecting coil sensitivity maps for phase-contrast SENSE.

Materials and Methods

A phase-contrast scan with 20 cardiac phases was performed with a reduction factor of 2 on a 4-coil torso coil on GE Signa 1.5T scanner. A VENC of 150cm/sec was used. The scan was acquired with 6 views per segment. A separate torso-coil calibration and a body-coil calibration were performed. These calibrations were done with flow encoding as well. 5 calibration cases were performed for each calibration type. Case 1 synchronizes each flow image of the calibration scan with that of the SENSE acquired scan. Case 2 synchronizes the first flow image of each cardiac phase as calibration for the corresponding pair of flow images for the SENSE scan. Case 3 uses the first flow image of the first cardiac phase as the calibration for the entire set of cardiac phases. Case 4 uses the first flow image of the fifth cardiac phase as the calibration for the entire set. Case 5 uses a standard cine GRE sequence with flow compensation as the calibration scan and synchronizes the cardiac phases together. Finally, another phase contrast scan was performed with a 3d calibration scan. Sum-of-squares was used as the calibration method for the SENSE reconstruction. The 3d sequence was a spoiled GRE sequence with 5 deg flip angle, 128x128x32 imaging matrix, nongated, and non-flow-encoded. All flow measurements were calculated using the complex phase-difference.
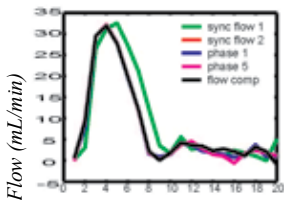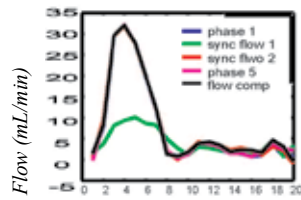

Figure 1   Cardiac phase

Figure 2   Cardiac phase

Case 1: sync flow 1
Case 2: sync flow 2
Case 3: phase 1
Case 4: phase 5
Case 5: flow comp

Figure 3

Discussion

Fig. 1 shows the flow measurements for all the cases performed with the body coil calibration. Fig 2 shows the flow measurements for the sum-of-squares calibration. Fig 3 shows an image of the magnitude and phase difference

Figure 4

reconstruction. Fig. 4 shows the flow measurements with and without SENSE for the 3d calibration. The flow measurements acquired through SENSE almost all agreed well. The case 1 calibration gave an incorrect flow measurement because each flow-encoded calibration image cancels out the flow-encoded phase of the SENSE acquired scan. For the body coil, this is not as significant because the flow-encoded phase of the body scan has canceled out most of the torso coil calibration flow-encoded phase. Although the flow measurements for case 3 and case 4 agree with the others, there may be misregistration between coil calibration and SENSE acquisition scans due to cardiac motion and flow in future scans. The flow-compensation calibrations also agreed with the other cases. Self-calibration scans would be important for future research. The 3D scan shows reasonable agreement between the non-SENSE and SENSE acquired scan. The lack of gating has not apparently caused a difference in this particular scan. There is residual chest wall aliasing in the reconstruction due to misregistration between the calibration scan and SENSE acquisition scan. Future work would include situations when the chest wall has aliased onto the aorta. This would demand more robust SENSE calibration measurements.

References

1. Pruessman, K.P., et al. MRM, 42:952-962, 1999

Implementation of a 3D IR-trueFISP Tissue Relaxation Mapping Sequence

Rexford D Newbould, Marcus T Alley, Roland Bammer – Department of Radiology

Introduction

An inversion recovery prepared balanced SSFP sequence, known as IR-trueFISP, has recently been presented as a method to quantify tissue parameters from a single acquisition [1]. Analytical expressions for the signal recovery curve as a function of T1, T2, proton density (PD), and the flip angle α have been determined in previous work [1][2]. The IR-trueFISP sequence requires the sampling of the magnetization curve for each voxel in the volume of interest as it progresses from the initial inverted value towards its final, steady-state value. This method has now been adapted for rapid use in clinical studies of several tissue types. Further, once parameters have been mapped, the image contrast from several common imaging routines may be simulated.
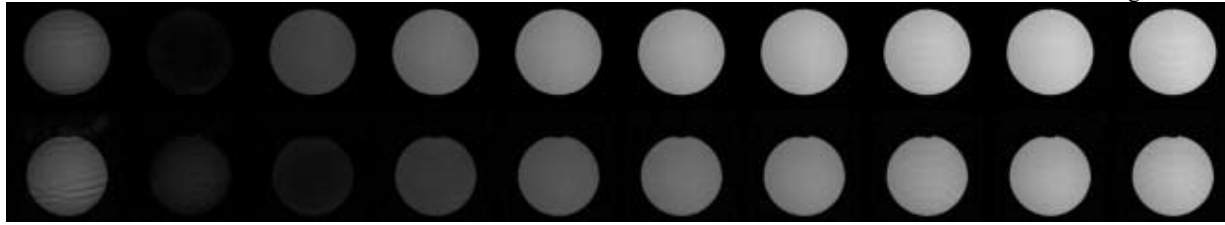
Figure 1. Magnetization magnitude of two slices from a 3D slab of a uniform phantom taken at 100ms intervals. A train of unoptimized 600us SSFP pulses was used; note the difference in value with time between the two.

Materials and Methods

A novel 3D CINE version of the IR-trueFISP sequence was implemented on a 1.5T GE EXCITE clinical MR scanner (GE Medical Systems, Waukesha, WI) with high strength 50mT/m gradients using receive-only 8-channel phased array coils (MRI Devices, Waukesha, WI). Each cardiac interval consists of an inversion pulse, followed by an $\alpha/2$ SSFP preparation pulse [2], which is followed by a train of SSFP α pulses. As the inversion time does not affect the SSFP TR, an adiabatic inversion pulse was implemented to give full inversion even in the presence of B1 field inhomogeneity. The SSFP pulses, however, do greatly influence the TR, which influences the amount of off-resonance effects. The use of a 3-D slab aided the ability to reduce pulse length without sacrificing slice profile, however, the use of a short, standard RF pulse yielded unacceptable variation in magnetization, as shown in Figure 1. Even small variations in flip angle across the slices resulted in pronounced variations in the relaxation curve. For this reason, a short-time scale (600us) minimum phase profile-optimized SLR pulse was implemented.
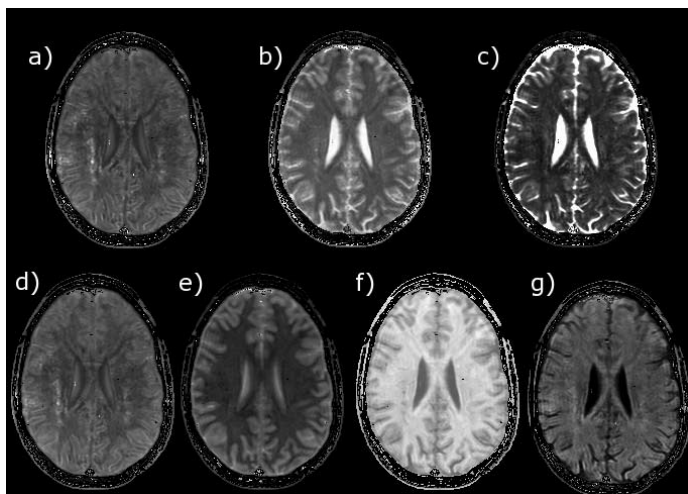

Figure 2. a) PD, b) T1, and c) T2 maps in the brain. From these images, d) PDw, e)T2w, f) T1w, and g)FLAIR images may be produced.

Slice encoding in the 3D slab occurs after each readout period. Once a readout line in each slice has been acquired, the pattern is repeated. This readout set is repeated as quickly as possible until the magnetization has entered its steady-state value. A lack of fixed phase encodes influences only the time resolution of the sampling, rather than the number of locations sampled. This is allows an arbitrary resolution and number of slices in a fixed time period: additional slices only reduce the curve sampling. For a reasonable number of slices (up to 100), the curve is sampled enough to attain nominal fit values. This slice-sampling process is then repeated for the next phase encode in the next cardiac period. The entire data collection scheme is encapsulated in a respiratory compensating, cardiac-gated CINE sequence [3]. The relaxation mapping can thus occur in motion-free tissues in a straightforward manner, yet can also occur in areas with motion by simply enabling the gating control.

The relaxation curves were fit to a three-parameter expression [1] using a nonlinear least-squares fitting routine implemented in IDL (Research Systems Inc., Boulder, CO). Once parameter maps have been obtained, in-house software allows the construction of image contrast from standard imaging routines, such as PD-weighted, T1-weighted, T2-weighted, and FLAIR images.
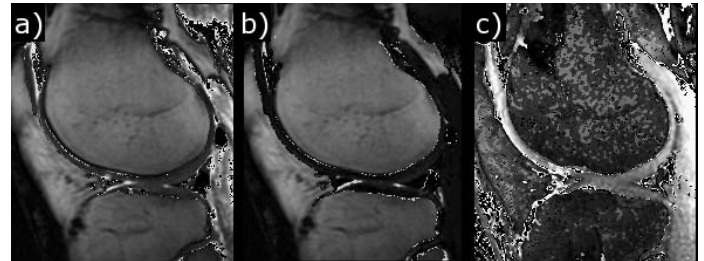

Figure 3. a) T1, b) T2, and c) PD maps of human knee cartilage.

Discussion

The sequence is implemented as a slab-selective 3D SSFP sequence, using a novel CINE-based approach which varied sampling of the recovery curve, rather than scan timing parameters. The sampling of the relaxation curve at a number of points allows decreased SNR without reduced fidelity of the fitted tissue parameters. Furthermore, the relaxation curve is only scaled by off-resonant banding artifacts. That is, areas of characteristic banding were consistent through the time course. The relaxation curve was therefore only scaled by the passband value. This does not affect the estimated T1 and T2 values, though does scale the pseudo-PD. The resultant estimated tissue parameters have been noted to be extremely sensitive to the achieved SSFP flip angle. Attaining exact flip angles, with only small variation across the volume can be problematic. The angle achieved is a function of both the excitation slice profile as well as the B1 field homogeneity. Furthermore, flatter slice profiles require longer excitation pulses, which can lengthen the TR, enhancing off-resonance effects. The use of the body coil to transmit, and multi-channel phased-array coils for reception was noted to alleviate these problems.

Quantified T1, T2, and PD Mapping in Cartilage with 3D IR-trueFISP

Rexford D Newbould, Garry E Gold, Marcus T Alley, Roland Bammer – Department of Radiology

Introduction

MRI has been shown to be an effective non-invasive method for cartilage imaging. T1 [1] and T2 [2] relaxation times have been correlated with cartilage matrix status. Current quantitative mapping schemes usually determine one tissue parameter at a time, and suffer from long scan times. Morphologic cartilage imaging routines involve proton density weighted (PDw) and T2-weighted (T2w) fast spin-echo sequences, as well as a T1-weighted (T1w) gradient-echo sequence [3]. Recently, an inversion recovery prepped balanced SSFP sequence, known as IR-trueFISP, has been proposed as a fast method to quantify T1, T2, and spin density (PD) from a single steady-state recovery curve [4]. In this work, cartilage relaxation parameters have been determined from a single examination, using a 3D version of this IR-trueFISP approach. These parameters may then be used to simulate image contrast in common imaging sequences.
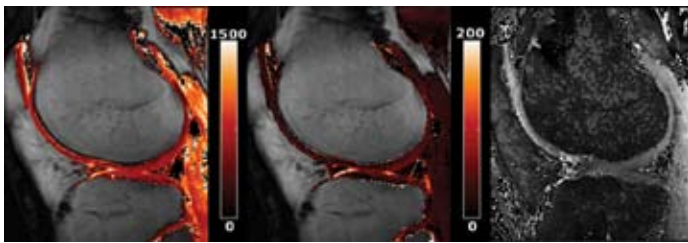
Figure 1. Colorized T1 map overlay, color scale in ms. *Figure 2. Colorized T2 map overlay, color scale in ms.* *Figure 3. Calculated pseudo- spin density map.*

Materials and Methods

A novel 3D inversion recovery prepared balanced SSFP sequence was implemented on a 1.5T GE EXCITE clinical MR scanner (GE Medical Systems, Waukesha, WI) and applied to healthy volunteers using an 8-channel phased-array receive only knee coil (MRI Devices, Waukesha, WI). An adiabatic non-slice selective inversion was followed by an $\alpha/2$ steady-state preparation pulse, which was followed by a train of slab-selective profile optimized pulses ($\alpha = 40o$, TR = 3.47ms, TE = 1.73ms). Magnetization values were sampled at twenty time points (Δt = 100ms) from each slice in the 3D slab, taken across 2 seconds in the initial curve as magnetization approached a steady-state value. Afterwards, a 3 second dead time was implemented to allow full longitudinal relaxation before repeating the inversion for the next phase encode. Total scan time to acquire a 128x128x32 3D volume (FOV = 16cm, NEX = 1, slice = 3mm) with in-plane resolution of 1.25mm was 8:03s. Tissue relaxation parameters were calculated from these curves via a nonlinear least-squares fitting routine implemented in IDL (Research Systems Inc., Boulder, CO).
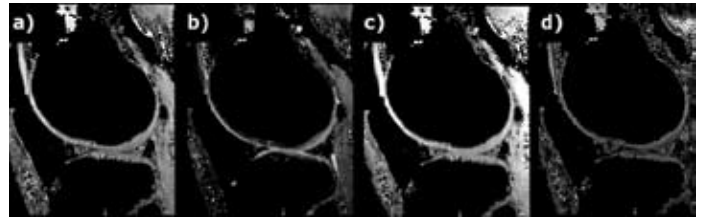

Figure 4. a) T1w, b) T2w, c) PDw, and d) FLAIR images as determined by the calculated T1, T2, and PD maps. Values were omitted for voxels containing fluids.

Discussion

Calculated T1, T2, and PD maps of a healthy knee are shown in Figures 1, 2, and 3 respectively. A region of interest was taken of the cartilage, which showed a mean T1 value of 821.354ms (SD: 35.746) and a mean T2 value of 45.354ms (SD: 6.927). This is in agreement with accepted values for knee cartilage for T1 [5] and T2 [6]. From these quantitative maps plus a calculated PD map, T1w (TR = 500ms, TE = 5ms), T2w (TR = 10000 ms, TE = 50 ms), PDw (TR = 10000 ms,TE = 5ms), and FLAIR-weighted (TR = 10000ms, TE = 5 ms, TI = 1000ms) sequences were simulated, and are shown in Figure 4. As joint fluid was determined not to be of interest to this particular study, these values have been selectively masked from the maps.

Conclusion

IR-trueFISP relaxometry has shown to be a rapid method to quantify T1, T2, and PD values. As implemented, slice count affects sampling time resolution rather than acquisition time. Here, 32 slices were acquired in just over 8 minutes. For short T1 species, the protons fully relax more quickly, and thus the required "dead" time for relaxation can be shortened, accelerating scan time.

Determined tissue parameters have been noted to be sensitive to applied B1 inhomogeneity. Improved homogeneity using optimized excitation pulses transmitted using the body coil aided the determination of correct tissue values.

Quantitative determination of relaxation values is important for diagnostic decisions and therapeutic monitoring. A fast, precise measurement technique incorporating the advantages of 3D scanning was presented. This sequence can thus be used to map both the structural and functional status of cartilage

Flip Angle Sensitivity in IR-trueFISP T1 and T2 Mapping

Rexford Newbould, Roland Bammer – Department of Radiology

Introduction

An inversion recovery prepared balanced SSFP sequence, known as IR-trueFISP, has recently been proposed as a fast method to quantify T1, T2, and spin density (PD) from a single acquisition. Analytical expressions for the signal recovery curve as a function of T1, T2, PD, and the flip angle α have been previously determined. In this work, we examine the dependence of the fitted values of T1, T2, and PD upon the difference between desired flip angle, α, and achieved flip angle. The angle achieved is a function of both the excitation slice profile as well as the B1 field homogeneity. Exact flip angles are difficult to achieve in practice, and often vary over the volume of interest. Furthermore, flat slice profiles require longer excitation pulses, which can lengthen the TR, enhancing off-resonance effects.

Materials and Methods

Bloch equation simulations of the SSFP sequence, using a variety of achieved flip angles versus desired flip angles over a range of T1 and T2 values were performed. Analytical expressions were additionally derived from the signal recovery equations for the change in the experimentally determined values.

An optimized 3-D version of the IR-trueFISP sequence was implemented on a 1.5T GE EXCITE clinical MR scanner using a body coil and a quadrature head coil (GE Medical Systems, Waukesha, WI). Adiabatic non-slice selective inversion and an SSFP preparation period was followed by a train of slab-selective (α=40) profile optimized RF pulses (TR = 3.84ms, TE = 1.9ms, FOV=24, matrix=64x64, acq. time=4:03s). Identical coil and phantom setups were also used with a single echo gradient-echo sequence (TR = 5000ms, TE = 4.5ms), for the double-angle

method to determine the relative flip angle distribution. Here, a single 60o pulse was repeated with a 120o pulse.

Discussion

The analytical expressions for the change in the fitted values agree well with the results found via the Bloch simulations. Both the simulations and derived expressions show that the estimated T2 is extremely sensitive to changes in flip angle. The estimated T1, however, is relatively insensitive, especially at lower flip angles. An interesting result is that the errors in the T1 and PD values are not related to the actual T1 and T2 values of the medium. Though not readily apparent from the form of (3), the variation in T2 is sensitive to the T1/T2 ratio, though not the absolute values of each.

Parameter fitting was performed on a uniform ball phantom from each IR-SSFP dataset using a nonlinear least squares fitting routine implemented in IDL (Research Systems Inc., Boulder, CO). Additionally, relative flip angle mapping for each was performed using the double angle method (DAM) using the gradient echo data from the same phantom and coil setup. Shown in Figure 2 are the resultant parameter maps from the quadrature head coil, with the relative flip angle map from the DAM on the upper left. A somewhat increased flip angle was noted in an area of the phantom with this setup, which corresponded to increased estimated T1 and PD values, and markedly decreased estimated T2 value. Figure 3 contains the results from using the body coil, which is more homogeneous over the same FOV. Improved fits are noted in all parameter maps.

Conclusion

The extreme sensitivity to the achieved flip angle can be problematic yet overcome when implementing an IR-trueFISP sequence. While some gain in profile can be attained by using a 3D sequence with optimized slab profile pulses, B1 sensitivity remains. A transmit and receive quadrature coil tends to have poor transmit B1 homogeneity. The use of the body coil for transmit and receive greatly improved the homogeneity, though at the penalty of SNR and possible absolute scaling of the flip angle. The mapping process was noted to be robust to poor SNR. The use of receive-only coils can restore the SNR, though coil coupling / dielectric resonance can be a concern. At higher field strengths, SAR can also become a problem when using the body coil to transmit. From the results of this study, the use of receive-only phased-array coils has been adopted for in-vivo tissue parameter mapping with this sequence.

As a secondary note, the dependence of the derived T1 and PD values solely upon flip angle would in fact give the ability to determine flip angles from the changes in the fits, at least in uniform phantoms. In heterogeneous environments, such as those clinically of interest, the near linear PD variation gives a simple way to map changes in derived PD with changes in flip angle. The achieved flip angle can then be used to fit the other parameters, including T2. The incorporation of a gradient echo readout after the SSFP period for an inherent DAM calculation, or the repetition of the experiment with two different flip angles should be be explored as a method to additionally map the flip angle, to fully correct the fits.

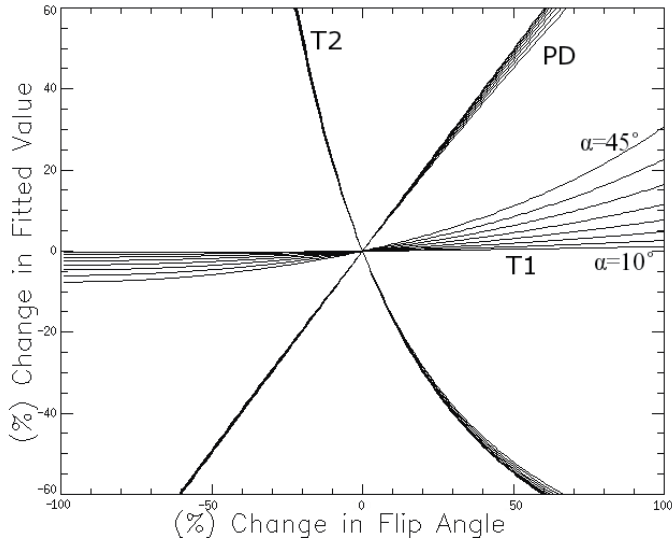Figure 1. Percent change in fitted value as determined by the Bloch simulations for the three intrinsic parameters as a function of flip angle variation.

$$(1) \quad \Delta \hat{PD} = \frac{\sin(\frac{\hat{\alpha}}{2})}{\sin(\frac{\alpha}{2})}$$

$$(2) \quad \Delta \hat{T}_1 = \frac{2 \cdot \sin(\frac{\hat{\alpha}}{2})\cos(\frac{\alpha}{2})}{\sin(\hat{\alpha})}$$

$$(3) \quad \Delta \hat{T}_2 = \frac{(\sin^2 \hat{\alpha})}{\left[\frac{\cos^2(\frac{\hat{\alpha}}{2})}{T_1} + \frac{\sin^2(\frac{\hat{\alpha}}{2})}{T_2}\right]\left[1 - \frac{\cos(\frac{\alpha}{2})\sin(\hat{\alpha})}{\sin(\frac{\hat{\alpha}}{2})(\frac{T_1}{T_2} + 1 - \cos(\hat{\alpha})(\frac{T_1}{T_2} - 1))}\right]}$$

Spatial Modeling of the GRAPPA weights

Stefan Skare, Roland Bammer – Department of Radiology

Introduction

Compared to earlier k-space methods such as (VD)-AUTO-SMASH, GRAPPA[1,2] fits Nsrc×Ncoils acquired "source" lines to each single coil ACS line. As for VD-AUTO-SMASH, tricks to make the weight estimation problem overdetermined are 1) "sliding" in ky and 2) grouping kx points (or rather "x"-points since Fourier transformation along kx is normally applied initially) together into blocks. Ultimately, a single set of weights could potentially be used across the entire x-FOV, yet, this is likely to be sub-optimal because the coil sensitivity normally changes significantly over the FOV. In this work, the artifact power for various block sizes have been investigated, for completeness with and without prior FFT in kx (denoted here as "FFTx"), and compared with a new proposed method for determining the GRAPPA-weights in x/ky space. In the latter, the key point is that each weight in the weight-set is a smooth parameterized function across all x values, rather than a scalar applicable to a given block of x-values. Let y = Aw, where y is a Nx×1 column vector containing the entire Fourier transformed ACS line. First assume we have independent weights for each x, then w is a (Nsrc×Ncoils×Nx)×1 vector of weights to be reconstructed. Ignoring sliding in ky (in this derivation), the A matrix to be inverted is now sparse and heavily under-determined by a factor of Nsrc×Ncoils.

$$\mathbf{y} = \begin{bmatrix} y_1 \\ y_2 \\ y_3 \\ \vdots \\ y_{Nx} \end{bmatrix}_{\text{coil } j} = \underbrace{\begin{bmatrix} \mathbf{a}_1 & 0 & \cdots & 0 \\ 0 & \mathbf{a}_2 & 0 & \vdots \\ \vdots & & \ddots & 0 \\ 0 & \cdots & 0 & \mathbf{a}_{Nx} \end{bmatrix}}_{\mathbf{A}} \underbrace{\begin{bmatrix} \mathbf{w}_1 \\ \mathbf{w}_2 \\ \vdots \\ \mathbf{w}_{Nx} \end{bmatrix}}_{\mathbf{w}}, \text{ where} \begin{cases} \mathbf{a}_m = [S_{src1, coil1} \ S_{src1, coil2} \cdots S_{src1, Ncoils} \ S_{src2, coil1} \ S \\ m = 1 \rightarrow Nx \end{cases}$$

and where wm is a (Nsrc×Ncoils)×1 vector corresponding to the mth x-position. Now, define the matrix W (size = (Nsrc×Ncoils)×Nx), where w = vec(W) (NB: The vec-operator forms a matrix into a vector, column-by-column). For most scenarios, the coil sensitivity will vary smoothly along x, and so should the weights across the columns of W. To enforce this, the coil weights are now modeled by a cosine basis set of order Norder, contained in a Nx×Norder matrix C. We have W = (CH)T, where H is the coefficient matrix for the cosine basis set, C, forming W. Instead of estimating the weights, vec(W), directly we want to estimate H containing a total of Norder×Nsrc×Ncoils unknowns. Combining Eqs. [1] and [2], gives

$$\mathbf{y} = \mathbf{A}\,\text{vec}\big((\mathbf{CH})^T\big) = \mathbf{A}\,\text{vec}\big(\mathbf{H}^T\mathbf{C}^T\big) = \begin{bmatrix} \text{Algebra rule:} \\ \text{vec}(\mathbf{XY}) = (\mathbf{Y}^T \otimes \mathbf{I})\text{vec}(\mathbf{X}) \end{bmatrix} = \mathbf{A}\underbrace{(\mathbf{C} \otimes \mathbf{I})}_{\mathbf{Q}}\underbrace{\text{vec}(\mathbf{H}}_{\mathbf{h}}$$

where, Q is the Kronecker product of C and the identity matrix INsrc×Ncoils, and h is the vectorized representation of HT. Thanks to that both A and Q are very sparse, their product is easily calculated. Now we have arrived at the final least squares expression for the estimation of the cosine coefficients of the GRAPPA weights

$$\underset{[(Ncoils*Nsrc*Norder)\times1]}{\mathbf{h}} = \underset{[(Ncoils*Nsrc*Norder)\times Nx]}{(\mathbf{AQ})^+} \underset{[Nx\times1]}{\mathbf{y}} \qquad [4]$$

where "+" denotes the pseudo-inverse. To reconstruct a missing ky line, the acquired nearby source lines, formed as A in Eq 1, is simply multiplied with Qh.

Material and Methods

A brain phantom was scanned with 256×256 resolution and 4 mm axial slices using an FSE sequence on a 1.5T GE EXCITE scanner. An 8-channel brain RF-coil was used. A single slice was first reconstructed using all k-space data. Then 75% of the ky lines was removed (i.e. ORF=4) outside of the center 20 lines used for estimating the weights. The weights were estimated using the standard block method (with and without Fourier transformation along kx) and with the method proposed in this work. Two "ACS blocks" were used for both approaches, forming the pattern [src-acs-acs-acs-src].
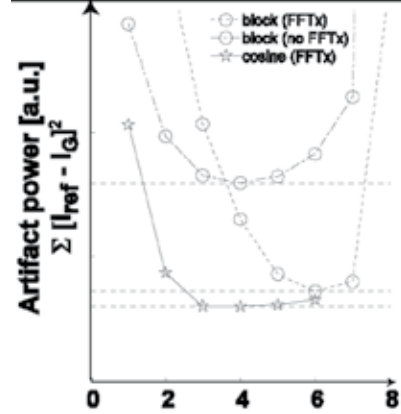

Figure 1

Results

The artifact power, measured as the sum-of-squares difference between the GRAPPA reconstructed images and the fully sampled reference image, is shown in Figure 1. Without FFTx (dashed-dotted line), the fits fall far from the optimal solution due to the unresolved coil sensitivity in kx and the lowest artifact power is twice that of the block approach with FFTx.
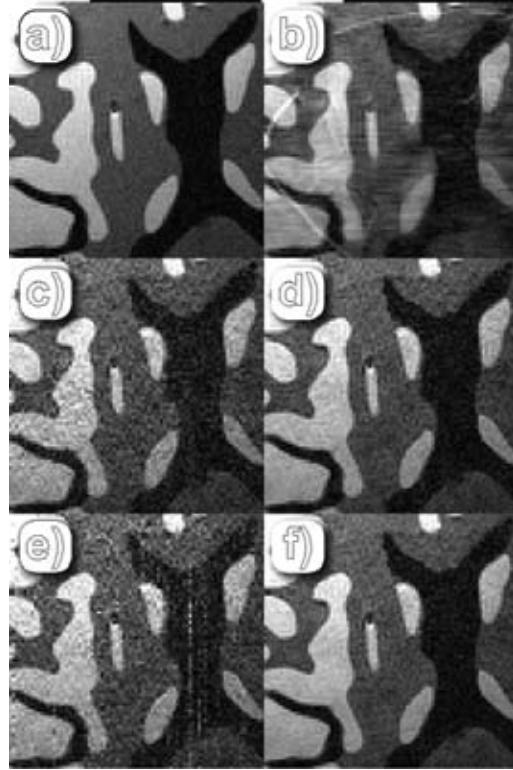

Figure 2

Using few blocks, the problem is highly overdetermined, yet producing more artifacts than the optimal 26=64 blocks (with FFTx). For the proposed basis set approach, 23 = 8-order set (see Fig. 1) seems to be sufficient to model the variation of the weights in x. Most interestingly, one obtains 20% less artifact power with the proposed method than with the optimal blocked one. In Figure 2, a cropped part of one of the coil-images is shown, with a) the fully sampled reference, b) 16-block (no FFTx), c) 16-block, d) 64-block, and e) 256-block GRAPPA. Finally, in f), a 16-order cosine GRAPPA is shown. b), d) and f) show images at optimum settings for the compared techniques, where the noise is markedly lowest in f).

Discussion

A new GRAPPA reconstruction algorithm has been developed, which has better artifact characteristics than the standard blocked approach, at least on the coil tested in this work. A low order cosine model works well, but this could easily be replaced in Eq. 3 by some other basis set depending on the coil configuration. Other coil configurations and k-space sampling strategies will be investigated.

Limitations of ADC-Based Models in Characterizing Non-Gaussian Diffusion

Chunlei Liu, Roland Bammer, Michael E. Moseley – Department of Radiology, Stanford University

Introduction

Several new methods have been introduced to address the issue of non-gaussian diffusion in neural fiber systems. Some of them are based on apparent diffusion coefficient (ADC) analysis; and some are based on **q**-space analysis. We demonstrate that although ADC-based approaches can qualitatively detect the existence of non-Gaussian diffusion, their ability to characterize non-Gaussian diffusion is fundamentally limited. In addition to the mathematical proof, Monte Carlo (MC) simulation for restricted diffusion is also applied to illustrate the poor data fitting of these ADC models in the presence of non-Gaussian diffusion. Specific comparisons are performed between two GDTI methods: one introduced by Liu et al (which will be referred to here as GDTI-1) (3,4) and one introduced by Özarslan et al (referred to as GDTI-2 here) (2). Finally, we investigate the possibility of imaging asymmetrical fiber structures with GDTI-1.

Materials and Methods

Methods based on ADC measurements, such as HARD and GDTI-2, assume that MR signal decays monoexponentially as a function of the b-value. These methods tend to analyze the distribution of measured ADC profiles and use the distribution to characterize the underlying non-Gaussian diffusion process. For example, in GDTI-2, an ADC profile is described by the elements of a higher order tensor. Although higher order terms extracted from ADC distributions are thought to be able to characterize the non-Gaussian diffusion pattern in multi-fiber systems, the mere existence of these parameters contradicts the assumption of the model.

First, the assumption of a monoexponential signal behavior implies that the underlying diffusion is Gaussian. Specifically, write the diffusion gradient $\mathbf{G} = (G,\theta,\phi)$ in the spherical coordinate, and the random displacement $\mathbf{r} = (x,y,z)$ in the Cartesian coordinate. Let r_g be the projection of $\mathbf{r}$ along the direction of the diffusion gradient $\mathbf{G}$. Assuming that the signal measured along the direction of $\mathbf{G}$ is an exponential function of the b-value, it can be shown that r_g is a one-dimensional Gaussian random variable. To show $\mathbf{r}$ is a three-dimensional Gaussian random variable, we observe the relationship shown in Eq.[1].

$$[1] \quad \begin{aligned} &\sigma_x^2 \cos^2\phi \sin^2\theta + \sigma_y^2 \sin^2\phi \sin^2\theta + \\ &\sigma_z^2 \cos^2\theta + 2\sigma_{xy}\cos\phi\sin\phi\sin^2\theta + \\ &2\sigma_{xz}\cos\phi\sin\theta\cos\theta + 2\sigma_{yz}\sin\phi\sin\theta\cos\theta = \sigma_{r_g}^2 . \end{aligned}$$

$$[2] \quad \Sigma = \begin{bmatrix} \sigma_x^2 & \sigma_{xy}^2 & \sigma_{xz}^2 \\ \sigma_{yx}^2 & \sigma_y^2 & \sigma_{yz}^2 \\ \sigma_{zx}^2 & \sigma_{zy}^2 & \sigma_z^2 \end{bmatrix}$$

Here, σ_x^2 is the variance of x; σ_{xy}^2 is the covariance of x and y; and so on. Since $\sigma_{r_g}^2 > 0$, and Eq. [1] is true for any direction defined by (θ, ϕ), the matrix Σ shown in Eq.[2] is positive definite and it forms the covariance matrix of the random vector $\mathbf{r}$. Furthermore, since all higher-order cumulants of r_g are zero, higher-order cumulants of $\mathbf{r}$ are also zero due to the linear relationship between r_g and $\mathbf{r}$ (5). Therefore, $\mathbf{r}$ is a Gaussian random vector with covariance matrix Σ.

Second, since a Gaussian distribution has only six degrees of freedom, it is not necessary to include higher-order terms in spherical harmonic decomposition which requires more than six free variables, or in the signal equation of GDTI-2.

Discussion

To demonstrate the limitations of ADC-based models, MC simulations were performed on two phantoms: 1) a perpendicularly crossing tube (Phantom-1); and 2) a Y-shaped tube (Phantom-2).

Figure 1a plots a representative set of simulated data and curves fitted by both GDTI methods. The diffusion-weighted signal is not an exponential function of the b-value. Figure 1b shows the corresponding distribution of the displacement is non-Gaussian. Figure 2 compares the root mean square error (RMS) of both GDTI fittings over all 400 diffusion directions for Phantom-1. The mean RMS over all the directions is 0.029 and
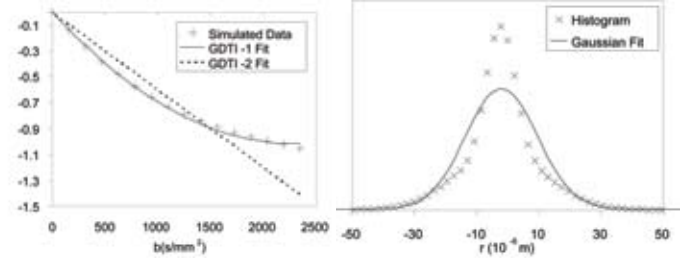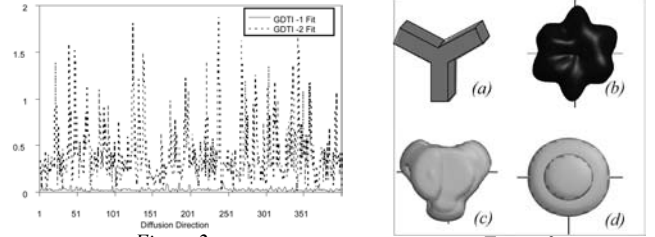

Figure 1a

Figure 1b

Figure 2

Figure 3

0.41 for GDTI-1 and GDTI-2, respectively. Figure 3 shows the structure of Phantom-2, the diffusivity profile generated using GDTI-2 (2) (Fig. 3b) and skewness maps generated using GDTI-1 with (Fig. 3c) and without (Fig. 3d) considering the phase of the signal (3,4).

Conclusion

The issue of resolving multiple fiber orientations in regions where fibers cross or merge has become increasingly important in fiber tractography (6). In principle, GDTI-1 is a physically correct formalism and has the capability to resolve the orientations of an asymmetric structure (Fig 3c). In real experiments, however, the accuracy of GDTI-1 is limited by signal to noise ratio (SNR) and the ability of MRI systems to accurately measure the phase of the signal. Our study shows that the phase of the signal is crucial in the reconstruction of an asymmetric PDF (Fig 3c and d).

Because of its ability to characterize non-Gaussian diffusion processs, GDTI-1 provides a mathematical framework for studying complex diffusion processes in neural fiber systems. Based on GDTI-1, we understand that the limitation of an ADC-based model stems from the assumption of an exponentially decaying signal. Simulations based on GDTI-1 have demonstrated that higher-order b-tensors and higher-order diffusion tensors are required to characterize a non-Gaussian signal behavior (Figure 1).

References

1) Frank LR. Magn Reson Med 2002; 47:1083-1099.
2) Özarslan E, et al. Magn Reson Med. 2003; 50:955-65.
3) Liu C, et al. ISMRM, 2003, p242.
4) Liu C, et al. Magn Reson Med. 2004; 51:924-37.
5) Kendall MB, Stuart A. The Advanced Theory of Statistics. Vol. 1, New York: Halsted Press, 1994.
6) Basser PJ, et al. Magn Reson Med 2000; 44: 625-632.

Iterative Phase Correction for Multi-Shot DWI Using Conjugate Gradient Method

Chunlei Liu, Roland Bammer, Michael E. Moseley – Department of Radiology, Stanford University

Introduction

A common problem encountered in multi-shot image acquisition is phase variation from shot to shot (1,2,3,4). This phase error is usually caused by patient motion during diffusion encoding periods. Typically this error is corrected for by subtracting a low resolution phase map from each shot. However, in most practical situations, this simple method cannot correct the phase completely. For example, when each shot undersamples the **k**-space, effect of aliasing causes the phase error at one location appearing at other locations. The resulting non-localized phase error can no longer be corrected through a simple phase subtraction. Here, we present a method that performs phase correction simultaneously with image reconstruction. This novel method combines the conjugate gradient (CG) method with a least-square estimation of the image to be reconstructed. Successful phase correction is demonstrated for multi-shot DWI with self-navigated interleaved spirals (SNAILS) (3).

Materials and Methods

Considering the motion-induced phase errors, data acquired with a multi-shot sequence can be expressed as,

$$\mathbf{d} = \mathbf{E}\,\mathbf{m} \qquad [1]$$

Here, **d** is the **k**-space data stored in a column vector; **m** is the image space data stored in the same fashion; and **E** is the encoding matrix. The size of **E** is $N_k \times N^2$, where N_k the total number of **k**-space sampling points and N is the image size. For the n-th shot, the elements of matrix **E** are

$$\mathbf{E}_{(k,n),\rho} = \exp(-i\,\mathbf{k}_{k,n}\mathbf{r}_\rho)\,p_n(\mathbf{r}_\rho) \qquad [2]$$

Here, $\mathbf{k}_{k,n}$ is the k-th sampling point of the n-th shot, and $\mathbf{r}_\rho$ is the ρ-th pixel of an image.

The image **m** can be effectively estimated using a least-square estimation:

$$\mathbf{m} = (\mathbf{E}^H\mathbf{E})^{-1}\mathbf{E}^H\,\mathbf{d} \qquad [3]$$

Typically E is a very large matrix. As a result, it is numerically impractical to estimate the image through direct matrix inversion and multiplication. However, this equation can be solved iteratively. For the efficiency of numerical evaluation, Eq. [3] can be rewritten as,

$$(\mathbf{E}^H\mathbf{E})\,\mathbf{m} = \mathbf{E}^H\,\mathbf{d} \qquad [4]$$

Various techniques have been developed to solve large systems of linear equations. Here, we apply the conjugate-gradient (CG) method by exploring the similarity between Eq [4] and the equation of sensitivity encoding (SENSE) (5). We observe that Eq.[4] is equivalent to the SENSE reconstruction problem when $p_n(\mathbf{r}_\rho)$ is treated as a pseudo "coil sensitivity" that varies from shot to shot (Figure 1).

In vivo diffusion-weighted images were acquired using SNAILS (3) on a GE Signa 1.5T whole-body system. The parameters were: number of interleaf = 28, FOV = 22cm, TR = 2.5s, TE = 67ms, and b = 800s/mm^2.

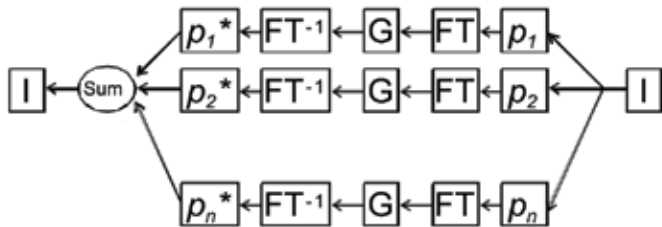Figure 1: Algorithm flow chart to be incorporated into the CG iteration. p_n: phase error of n-th shot. **G**: gridding and inverse gridding. **I**: intensity correction.

Six diffusion-encoding directions were applied to measure the diffusion tensor. Low resolution phase maps were estimated using the center k-space data from each interleaf.

Results

Figure 2 shows estimated initial images and phase-corrected final images after 5 iterations. The initial images suffer from various degrees of signal cancellation because the motion-induced phase can not be completely subtracted from each interleaf. The signal loss is clearly restored in the corrected final images, resulting in a much higher signal to noise (SNR) ratio. Figure 3 shows the computed fraction anisotropy (FA) map and color coded FA map.
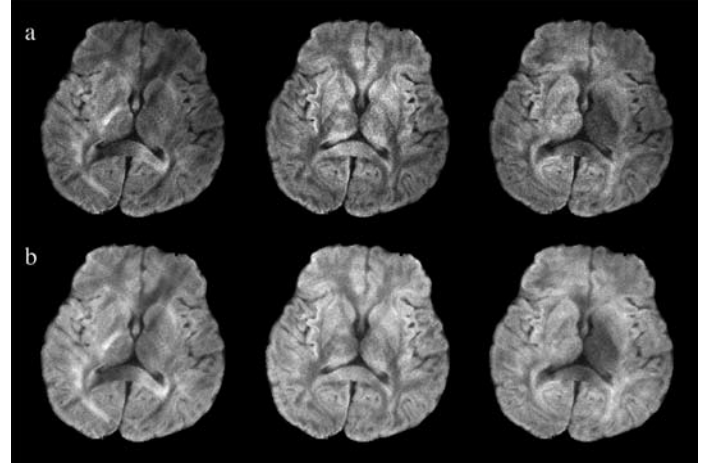

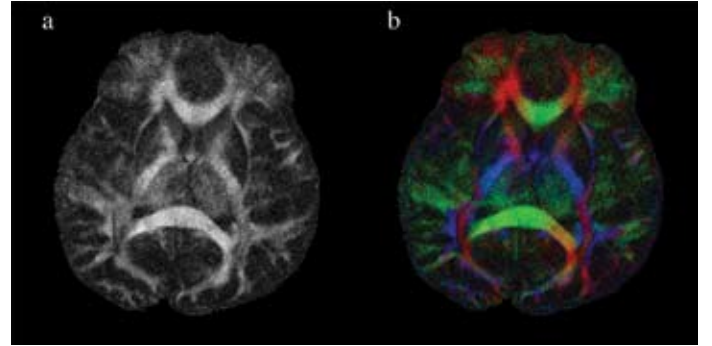Fig 2 – (a) initial and (b) final images for 3 diffusion directions.

Fig 3 – (a) FA; (b) color FA. Red: A/P; green: L/R; blue: S/I.

Discussion

We have established a mathematical framework for simultaneous image reconstruction and phase correction for multi-shot DWI. The image is computed iteratively using the CG method. In vivo experiments demonstrate that the signal cancellation caused by phase error can be successfully recovered using this algorithm (Fig 2). Due to the enhanced SNR, the number of signal averages required for high resolution DTI can be reduced, thus improving the acquisition speed.

References

1) Butts K, et al. Magn Reson Med 1996; 35:763-770.
2) Pipe JG, et al. Magn Reson Med 2002; 47:42-52.
3) Liu C, et al. Magn Reson Med, in press.
4) Miller KL, Pauly JM. Magn Reson Med 2003; 50:343-353.
5) Pruessmann KP et al. Magn Reson Med 2001; 46:638-651.

Simultaneous Off-Resonance and Phase-Correction for Multi-Shot DWI

Chunlei Liu, Roland Bammer, Michael E. Moseley – Department of Radiology, Stanford University

Introduction

Self-navigated interleaved spirals (SNAILS) (1) have been used for high resolution diffusion weighted imaging (DWI). Although spiral trajectories have many advantages for fast image acquisition, they normally suffer from image blurring caused by off-resonant spins. Many techniques have been developed for off-resonance correction (2). However, few studies have been reported for off resonance correction for multi-shot DWI. One difficulty in this situation originates from the **k**-space data distortion caused by motion-induced phase errors. Here, we integrate multi-frequency off-resonance correction with SNAILS image reconstruction. Using the proposed technique, off-resonance correction and phase correction are achieved simultaneously for multi-shot DWI.

Materials and Methods

Phase navigation is crucial for multi-shot DWI. In SNAILS, phase navigation is achieved by oversampling the center of **k**-space. For each interleaf of a variable-density (VD) spiral (3), a low resolution phase map is estimated and iteratively applied to correct for the phase error (2). To incorporate off-resonance correction, the phase correction iteration needs to be performed at different frequency bands.

Given one interleaf of VD spiral, we first grid the raw data onto Cartesian grids. For each **k**-space sampling points, the corresponding time delay from the beginning of the acquisition is calculated. A Cartesian time map is generated through gridding. The field map is measured at the beginning using two calibration scans. Following the multifrequency reconstruction algorithm (2), a finite set of frequencies are selected to cover the whole range of off-resonant frequencies. For each frequency level, the gridded k-space data is demodulated using the precomputed time map. Following the demodulation step, a phase map is estimated using the center **k**-space data. This low resolution phase map is then used to correct for the motion-induced phase error in the image domain. The resultant images are then masked using a mask that corresponds to each particular frequency level. Finally, images reconstructed at different frequecy levels are summed together to form the final image. This process can be iterated several times to achieve better phase correction. However, the demodulation steps can be neglected if the field map is not updated. The flow chart is shown in Figure 1.

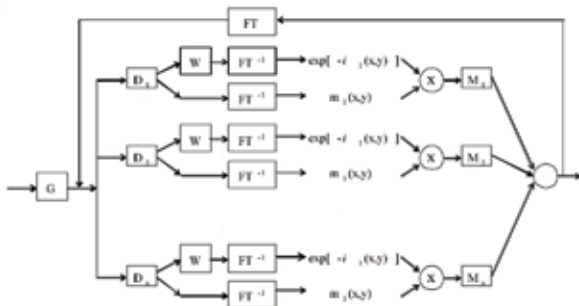The combined off-resonance and phase correction algorithm was tested using both phantom and in vivo data. The data were acquired on a healthy volunteer with a GE Signa 1.5T whole-body system using the SNAILS sequence (TR = 2.5s and TE = 68ms). The field map was measured in two separate calibration scans at the beginning of the study.
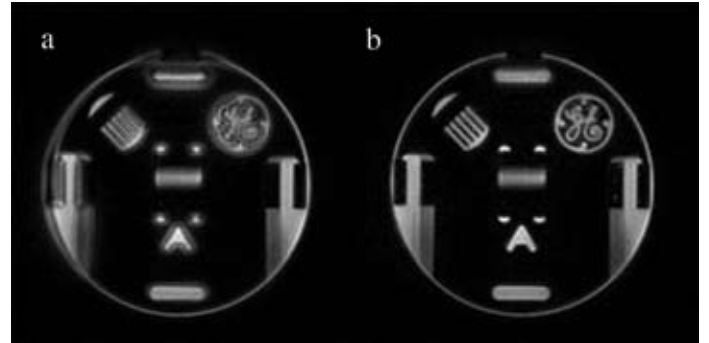

Fig 2 – Phantom images: (a) without off resonance correction; (b) with correction.
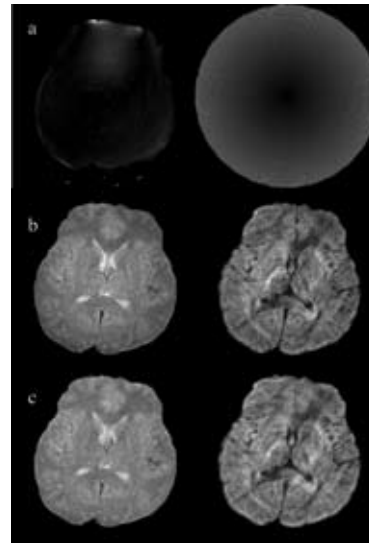

Fig 3 – In vivo results: (a) field map and time map; (b) without off resonance correction; (b) with correction. Left images are non-diffusion weighted.

Results

Figure 2 compares phantom images reconstructed with and without off-resonance correction. Figure 3 shows in vivo results. Fig 3a and b shows the measured field map and the corresponding time map associated with **k**-space trajectory. Fig 3b and c shows in vivo images both with and without diffusion weighting. Fig 3b shows images without off-resonance correction. Fig 3c shows images after correction.

Discussion

We have proposed an algorithm for simultaneous off-resonance and phase correction in high resolution DWI. Successful off resonance correction has been demonstrated on both phantom and in vivo images. With successful off-resonance correction, this algorithm allows a reduction of the number of interleaves required (4). Reducing the total number interleaves is important for fast acquisition of high resolution diffusion tensor data, where multiple averages are usually needed for sufficient signal to noise ratio (SNR).

Besides sharpening the image, off-resonance correction also enhances image intensity as shown in Fig 3b and c. In particular, great signal improvement appears in areas of strong off-resonance. This is because by demodulating the signal at the correct frequencies, signal cancellation is eliminated.

Fig 1 – Flow chart for simultaneous off-resonance and phase correction. This applies to each interleaf data separately. G: gridding; D_n: demodulation using n-th frequency level. W: Gaussian windowing; M_n: mask corresponding to the n-th

High-Resolution Multi-Shot SENSE DTI Using Self-Navigated Interleaved Spiral (SNAILS)

Chunlei Liu, Michael E. Moseley, Roland Bammer – Department of Radiology, Stanford University

Introduction

Multi-shot sequence is one approach for high-resolution diffusion weighted imaging (DWI) (1,2). Another approach for high-resolution DWI combines single-shot EPI with sensitivity encoding (SENSE) (3). In this work, we combine SENSE with multi-shot DWI to speed up data acquisition. One difficulty for multi-shot SENSE DWI is to perform phase correction on data modulated by complex-valued coil sensitivity of each receiver coil element. We have developed a technique that simultaneously performs SENSE reconstruction and phase correction. Using this technique, SNAILS with multiple receiver coils are implemented to acquire high resolution diffusion tensor imaging (DTI) data. We show that SNAILS offers great property for multi-shot SENSE DWI. High resolution diffusion-weighted images and FA maps are obtained with SENSE reduction factor up to four.

Methods

Under the weak voxel condition, SENSE data acquired in **k**-space can be expressed in a matrix and vector format as (4),

$$\mathbf{d} = \mathbf{E}\,\mathbf{m} \qquad [1]$$

Here, **d** is **k**-space data stored in a column vector; **m** is image space data stored in the same fashion; and **E** is the encoding matrix of size $N_c N_k$ x N^2. N_c is the number of receiver coils, N_k is the number of k-space sampling points, and N is the image size. For the γ-th coil, the entries of matrix **E** are

$$\mathbf{E}_{(\gamma,k),\rho} = \exp(-i\,\mathbf{k}_k \mathbf{r}_\rho)\,s_\gamma(\mathbf{r}_\rho) \qquad [2]$$

where $\mathbf{k}_k$ is the k-th sampling point in **k**-space, $\mathbf{r}_\rho$ is the ρ-th pixel of an image, and $s_\gamma(\mathbf{r}_\rho)$ is the complex spatial sensitivity of the γ-th coil.

A diffusion-weighted image is usually corrupted by an extra phase term. By including this phase, the encoding matrix can be modified as,

$$\mathbf{E}_{(\gamma,k,n),\rho} = \exp(-i\,\mathbf{k}_{k,n}\,\mathbf{r}_\rho)\,s_\gamma(\mathbf{r}_\rho)\,p_n(\mathbf{r}_\rho) \qquad [3]$$

Here, $\mathbf{k}_{k,n}$ is the k-th sampling point of the n-th interleaf, and $p_n(\mathbf{r}_\rho)$ is the motion-induced phase. Comparing to Eq. [2], we observe that $s_\gamma(\mathbf{r}_\rho)p_n(\mathbf{r}_\rho)$ is a composite sensitivity profile of the γ-th coil during the n-th interleaf. Under this treatment, image reconstruction for multi-shot SENSE DWI is equivalent to traditional SENSE reconstruction.

In vivo DTI data were acquired with SNAILS on a GE Signa 1.5T whole-body system using an 8-channel head coil. The sequence parameters were: number of interleaf = 20, FOV = 22cm, matrix size = 256x256, TR = 2.5s, TE = 67ms, b = 800s/mm², and NEX = 2. Six diffusion encoding directions were applied to measure the diffusion tensor. Reduction factors up to four were obtained by skipping a number of interleaves; and for each reduction factor diffusion tensors were calculated.

Results

Figure 1 shows a representative set of diffusion-weighed images and corresponding FA maps with reduction factors ranging from one to four. The diffusion encoding direction is [1 0 1]. Row (a) shows the initial estimation of the image. Row (b) shows corresponding images reconstructed with the conjugate gradient method. Compared to the initial images, signal intensity is greatly improved in the final images. Row (c) shows FA maps. Row (d) shows corresponding color-coded FA maps. The color coding is: red (A/P), green (R/L), and blue (S/I).
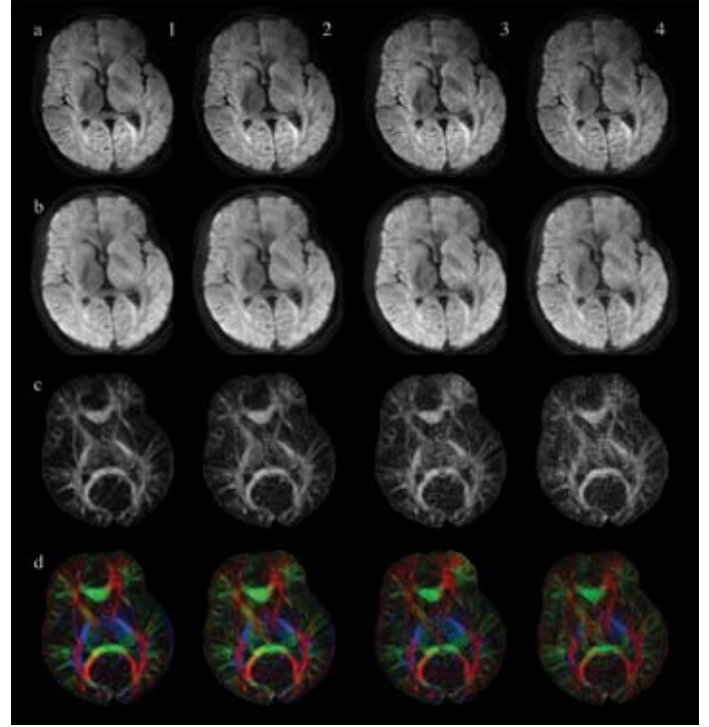

Figure 1: High resolution (256x256) multi-shot SENSE DTI using SNAILS. Reduction factor ranges from 1 to 4. (a) initial images; (b) corrected final images; (c) FA maps; (d) color-coded FA maps.

Discussion

We have shown that phase errors from multi-shot DWI can be incorporated very easily into the SENSE formulation. We have also successfully performed multi-shot SENSE DWI with SNAILS. By oversampling the center of **k**-space, SNAILS provides the capability of both sensitivity self-calibration and motion navigation. With SENSE SNAILS, high resolution DTI data can be acquired at a faster speed. The readout time of each interleaf can be shortened, thus reducing image blurring caused by off-resonance.

In multi-shot SENSE DWI, reliable sensitivity information is important for accurate image reconstruction. For single-shot acquisitions, the motion-induced phase error $p(\mathbf{r}_\rho)$ is a common factor for all coils, thus can be absorbed into vector **m** and neglected in image reconstruction. For multi-shot acquisitions, however, the phase error varies from shot to shot and can not be separated from the encoding matrix. Therefore it is crucial to dynamically update the composite sensitivity maps. This estimation can be readily achieved by using SNAILS. With SNAILS, each interleaf of variable-density spirals oversamples the center of **k**-space. For each interleaf, a low-resolution composite sensitivity map can be directly measured using the center portion of k-space data.

Fast SENSE Reconstruction Using Linear System Transfer Function

Chunlei Liu, Michael E. Moseley, Roland Bammer – Department of Radiology

INTRODUCTION

Reconstructing images from sensitivity encoded (SENSE) data acquired on arbitrary k-space trajectories is computationally demanding (1,2). With the conjugate gradient (CG) method, a matrix-vector product has to be calculated during each iteration. To improve the reconstruction efficiency, this multiplication is replaced with two gridding steps (2). However, gridding can still be computationally intensive for high resolution applications and for a large number of receiver coils. Here, we present a fast SENSE reconstruction algorithm by utilizing the property of system linearity. We show that a system transfer function can be derived and used to realize the matrix-vector multiplication, which dramatically improves the reconstruction efficiency.

Materials and Methods

In each iteration step of the SENSE reconstruction, the product of $(\mathbf{E}^H\mathbf{DE})\mathbf{x}$ has to be computed (2). Here $\mathbf{E}$ is an encoding matrix; $\mathbf{H}$ represents Hermitian operation; $\mathbf{D}$ is the k-space density correction function; $\mathbf{x}$ is an intermediate image weighted by coil sensitivities. Specifically, one needs to compute,

$$\mathbf{f}(\mathbf{r}_\rho) = (\mathbf{E}^H\mathbf{DE})\mathbf{x} = \sum\sum D(\mathbf{k}_k)\exp(i\mathbf{k}_k(\mathbf{r}_\rho - \mathbf{r}_{\rho'}))\,\mathbf{x}(\mathbf{r}_{\rho'}) \qquad [1]$$

Here $\mathbf{r}_\rho$ is a position vector in the image domain and $\mathbf{k}_k$ is a sampling position in the $\mathbf{k}$-space, which may not be located on a regular Cartesian grid. Eq.[1] describes a 2D linear shift invariant system (LSI) with $\mathbf{x}(\mathbf{r}_\rho)$ as input and $\mathbf{f}(\mathbf{r}_\rho)$ as output. Its transfer function can be found in the spatial frequency domain. Since $\mathbf{x}(\mathbf{r}_\rho)$ and $\mathbf{f}(\mathbf{r}_\rho)$ are sampled on regular Cartesian grids, the discrete Fourier transform (DFT) can be applied to find their spectrums on a Cartesian grid $\mathbf{k}$:

$$\mathbf{F}(\mathbf{k}) = \sum\sum\sum \exp(-i\mathbf{k}\mathbf{r}_\rho)\,D(\mathbf{k}_k)\exp(i\mathbf{k}_k(\mathbf{r}_\rho - \mathbf{r}_{\rho'}))\,\mathbf{x}(\mathbf{r}_{\rho'}) \qquad [2]$$

Let , and multiply Eq.[2] with $\exp(-i\mathbf{k}\mathbf{r}_{\rho'})\exp(i\mathbf{k}\mathbf{r}_{\rho'})$. Eq. [2] can be rewritten as:

$$\mathbf{F}(\mathbf{k}) = \left[\sum_{_q}\exp(-i\mathbf{k}\mathbf{r}_q)\sum_{_k}D(\mathbf{k}_k)\exp(i\mathbf{k}_k\mathbf{r}_q)\right]\sum_{_{\rho'}}\exp(-i\mathbf{k}\mathbf{r}_{\rho'})\mathbf{x}(\mathbf{r}_{\rho'}) = \left[\sum_{_q}\exp(-i\mathbf{k}\mathbf{r}_q)\sum_{_k}D(\mathbf{k}_k)\exp(i\mathbf{k}_k\mathbf{r}_q)\right]\mathbf{X}(\mathbf{k})$$
$$[3]$$

Therefore, the system transfer function can be expressed as:

$$\mathbf{H}(\mathbf{k}) = \sum\exp(-i\mathbf{k}\mathbf{r}_q)\sum D(\mathbf{k}_k)\exp(i\mathbf{k}_k\mathbf{r}_q) = \sum D(\mathbf{k}_k)\sum\exp(-i(\mathbf{k}-\mathbf{k}_k)\mathbf{r}_q) = \sum D(\mathbf{k}_k)G(\mathbf{k}-\mathbf{k}_k) \qquad [4]$$

Since $\mathbf{r}_q$ is on Cartesian grids, $G(\mathbf{k}\text{-}\mathbf{k}_k)$ can be computed analytically. When $\mathbf{k}_k$ fully samples $\mathbf{k}$-space, $G(\mathbf{k}\text{-}\mathbf{k}_k)$ can be approximated by a delta function, $\delta(\mathbf{k}\text{-}\mathbf{k}_k)$. For this special case, we find that $\mathbf{H}(\mathbf{k}) = D(\mathbf{k})$, where $D(\mathbf{k})$ is the $\mathbf{k}$-space density correction function evaluated on a Cartesian grid. For general cases, $\mathbf{H}(\mathbf{k})$ can be computed using Eq.[4]; and $\mathbf{H}(\mathbf{k})$ only needs to be computed once along with the initial image.

Overall, the product of $(\mathbf{E}^H\mathbf{DE})\mathbf{x}$ can be computed as $\text{FFT}^{-1}(\mathbf{H}(\mathbf{k})\mathbf{X}(\mathbf{k}))$, where $\mathbf{H}(\mathbf{k})\mathbf{X}(\mathbf{k})$ represents an element-by-element multiplication and FFT^{-1} is the inverse fast Fourier transform (Fig 1). Compared to the gridding steps, the transfer function approach reduces the number of multiplications from $2(2N)^2w^2$ to N^2. Here N is the image size and w is the size of the convolution kernel chosen in the gridding procedure. The resulting speed-up factor is thus around $8w^2$.

The transfer-function SENSE algorithm was tested both on simulated and in vivo data. In both cases, an 8-channel receiving coil was used.
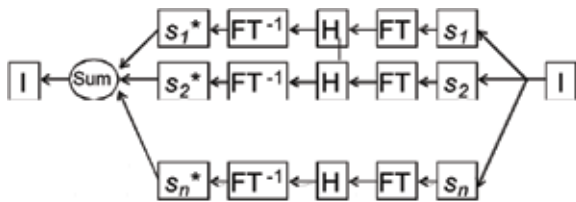

Fig 1 – Flow chart of the transfer function based SENSE. This part is to be incorporated into the conjugate gradient iteration. s_n is the coil sensitivity of the n-th coil. H represents transfer function multiplication in k-space. I is intensity correction.
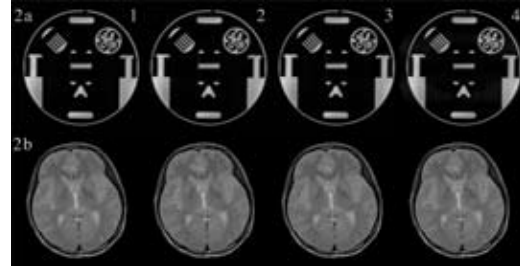

Figure 2: Images reconstructed using transfer function SENSE with Cartesian trajectories: (a) simulated data; (b) in vivo data
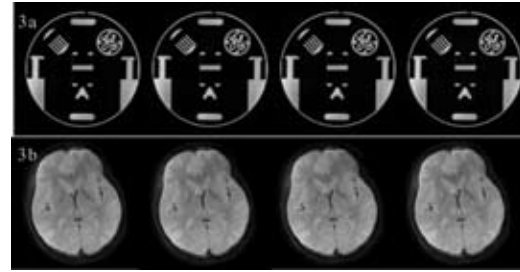

Figure 3: Images reconstructed using transfer function SENSE with VD spirals: (a) simulated data; (b) in vivo data.

Two types of trajectories were designed: a Cartesian grid and a variable-density (VD) spiral (3). The spiral trajectory contained 20 interleaves; and each interleaf had 4484 sampling points. The trajectory was designed with a field of view (FOV) of 22 cm for an acquisition matrix of 256x256.

RESULTS

Figure 2 shows images reconstructed from Cartesian data. Reduction factor ranges from one to four. The reduction factor is shown in the upper right corner of each image. Fig 2a shows simulated phantom images. Fig 2b shows in vivo results. Figure 3 shows images reconstructed from VD spiral data. Similarly, images in Fig 3a are reconstructed from simulated data; and images in Fig 3b are reconstructed from in vivo data.

DISCUSSION

We have shown that fast SENSE reconstruction can be achieved by utilizing the linearity property of the system. In this algorithm, the transfer function is equivalent to a k-space resampling function expressed in a Cartesian coordinate. Comparing to the traditional SENSE reconstruction, the transfer-function based algorithm gains a speed-up factor around $8w^2$ for non-Cartesian trajectories. For example, for the VD spiral trajectory with a reduction factor of two, the transfer-function algorithm takes 3.8s to complete 3 iterations; whereas the gridding based algorithm needs 308.4 s. This computation time is measured based on a Matlab program running on a PC with a 3.06GHz Pentium CPU. The transfer-function algorithm is related to the convolution approach (4) in the sense that both utilize the linearity property. Here, this formulation is treated more generally and the proposed algorithm does not require twice data support.

Although Eq.[1] describes an LSI, the original SENSE implementation with backward and forward gridding results in a shift variant system. The corresponding transfer function is thus location dependent and can be written as $\mathbf{H}(\mathbf{k}, \mathbf{k}')$. In other words, the transfer-function algorithm is not completely equivalent to the gridding approach. Using the transfer-function algorithm, successful image reconstruction has been demonstrated on both simulated and in vivo data. Overall image quality is good, though small residual artifacts remain on in vivo images with high reduction factors.

Orthogonal Tensor Invariants and the Analysis of Diffusion Tensor Magnetic Resonance Images

Daniel Ennis[1], Gordon Kindlmann[2] – [1]Department of Radiology, Stanford University; [2]Laboratory of Mathematics in Imaging, Harvard University

Introduction

Diffusion tensor magnetic resonance imaging (DTMRI) is a technique that maps the three-dimensional orientation of tissue structure. Such structural orientation information can be used, for example, to map the direction of nerve fibers in the brain or muscle fibers in the heart, tongue or skeletal muscles. Diffusion tensors can be mathematically decomposed into orientation (eigenvectors) and shape (eigenvalues) information. Our theoretical developments mathematically decompose tensor shape using a set of three orthogonal invariants that characterize the magnitude of isotropy, the magnitude of anisotropy, and the mode of anisotropy (linear, orthotropic, or planar anisotropy). When invariants have application-specific significance (as they do in DTMRI imaging), orthogonality is a useful property of an invariant set, because it isolates the measurement of variation in one physiological property from variations in another. The inclusion of the mode of anisotropy is useful for resolving an anisotropic region is linear anisotropic or planar anisotropic. The results are applied to the analysis and visualization of DTMRI in a healthy volunteer.

Theory

Theoretical extensions of the work by Criscione [1] in the field of hyperelastic strain energy functions resulted in the development of a spherical set of orthogonal tensor invariants. The cylindrical set of orthogonal invariants defined by Criscione are shown in Eqns. 1-3 and the spherical set we define is shown in Eqns. 4-6.

$$K_1 = \text{tr}(\mathbf{A}),\ K_1 = \text{tr}(\mathbf{A}),\ K_1 = \text{tr}(\mathbf{A}) \qquad [1\text{-}3]\ ;$$

$$R_1 = \text{norm}(\mathbf{A}),\ R_1 = \text{norm}(\mathbf{A}),\ R_2 = \text{FA}(\mathbf{A}) \qquad [4\text{-}6]$$

Note that the K_i invariants contain the tensor trace (tr) as a member of the set and that the R_i invariants contain fractional anisotropy (FA) as a member of the set. Though commonly used together in the analysis of DTMRI the invariants tr($\mathbf{A}$) and FA($\mathbf{A}$) are not contained within the same set, because they are not mutually orthogonal.

Methods

To improve the qualitative understanding of the theory a map of the space of tensor invariants is shown in Fig. 1. The theory can then be used to enhance the visualization of DTMRI data as shown in Figs. 2-3. Fig. 2 uses a colormap to encode areas of high fractional anisotropy with the underlying tensor mode. Fig. 3 shows a directionally encoded colormap (DEC) that is encoded without (3A) and with (3B) the use of tensor mode.

Results

Fig. 1 graphically demonstrates that low to moderately high levels of fractional anisotropy can be associated with any kind of tensor mode. Fig. 1 motivates the incorporation of tensor mode, to resolve the mode of the underlying anisotropy, into any visualization that incorporates fractional anisotropy. The use of tensor mode in Figs. 2 and 3 results in improved maps of DTMRI data. Fig. 2 is an improved fractional anisotropy map that indicates the mode of anisotropy within regions of high fractional anisotropy. Note that the full range of tensor mode is evident within areas of high fractional anisotropy. Fig. 3 compares a standard DEC with a mode-enhanced DEC. The use of tensor mode in 3B results in a map of the direction of linearly anisotropic structures rather than a map of highly anisotropic structure (3A).

Conclusion

The theoretical development of orthogonal tensor invariant sets provides an improvement in the visualization and analysis of DTMRI data.

Reference:

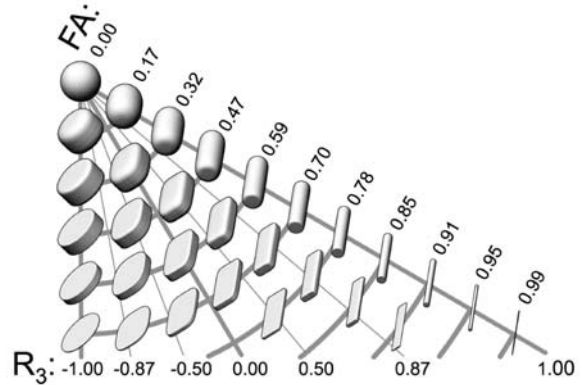Criscione JC, et al. J. Mech. Phys. Solids 2000; 48:2445-2465.

Figure 1. Demonstration of the space of anisotropy decomposed into two orthogonal channels: fractional anisotropy (FA) and mode (R_3). Each glyph represents the shape of diffusion tensors with constant tensor norm rendered with superquadric glyphs.
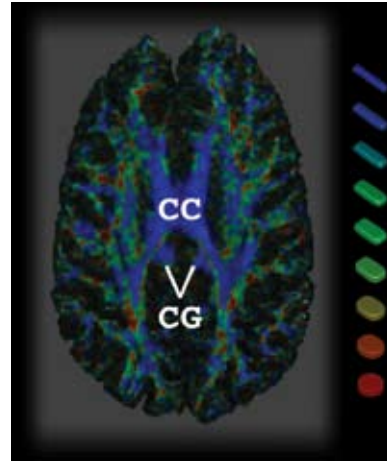

Figure 2. Enhanced fractional anisotropy map. Blue structures are indicative of linear anisotropy, green of orthotropy, and red of planar anisotropy. The corpus callosum and the cingulum are observed to be a largely linear anisotropic structures, but other structures with high fractional anisotropy are a mix of linear, orthotropic, and planar anisotropy.
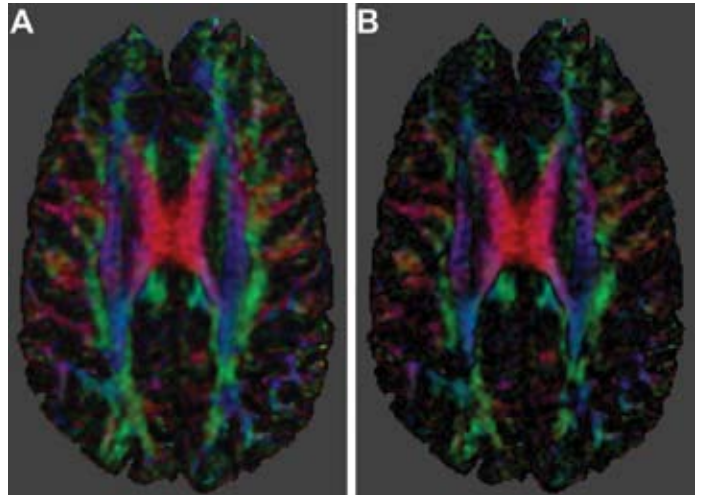

Figure 3. Directionally encoded colormaps of the primary eigenvectors (e_1). (A) highlights the orientation of e_1 regardless of tensor mode. Structures with high planar anisotropy are displayed equivalently as those with high linear anisotropy. (B) highlights the orientation only of structures with high linear anisotropy, structures for which e_1 is well determined. Low intensity structures indicate low fractional anisotropy or planar anisotropy and ambiguous e_1 directions. Note the intensity difference along the border of the corpus callosum and the cingulum and the general decrease in the colored extent of most structures.

Migration and Integration of Magnetically Labeled Human Neural Progenitor Cells After Transplantation in the Naïve Neonatal and Injured Adult Rat Brain

Guzman R[1], Uchida N[4], Bliss TM[1], He D[4], Greve JM[3], Palmer TD[1], Sun GH[1], Moseley ME[2], Steinberg GK[1] - Departments of [1]Neurosurgery, [2]Radiology, [3]Bioengineering, Stanford University; [4]Stem Cells Inc., California

Introduction

Cell replacement has the potential to become an important modality in the therapy of central nervous system injuries and diseases. Transfection of stem cells with iron oxide particles (SPIO) for non-invasive MRI tracking has been suggested. It is however not known whether transfection with SPIO impairs stem cell migration and integration in the host brain.

Methods

To test for the biological effects of iron labeling, human CNS-SC were incubated overnight with SPIO (Feridex) and protamine sulfate. Neonatal NOD-SCID mice received bilateral intraventricular transplants of either unlabelled or iron-labeled cells (2 x 10^5). Animals were imaged (4.7T MRI) at 0 hr, 1 hr, and 3, 9, 12 and 18 weeks after transplantation. Male SD rats were subjected to permanent distal middle cerebral artery occlusion and transplanted one week later with iron-labeled hCNS-SC (1 x 10^5l). MRI was acquired before, 1 and 5 weeks after transplantation.

Results

In NOD-SCID mice intraventricular distribution and migration of hCNS-SC along the rostral migratory stream towards the olfactory bulb was morphologically similar for unlabelled and iron-labeled cells and could be followed with MRI up to 18 weeks post-transplantation. When iron-labeled hCNS-SC were transplanted into Male SD rats with permanent distal middle cerebral artery occlusion, serial MR images after stroke showed robust targeted migration towards the lesioned area at 5 weeks but not at 1 week after transplantation. Migration and integration was confirmed by immunohistochemistry and did not differ for unlabelled vs. iron-labeled hCNS-SC in the naïve neonatal and injured adult rodent brain.

Conclusions

Magnetic labelling of hCNS-SC derived neurosphere cells prior to transplantation seems safe, allows non-invasive monitoring with MRI and could be considered for future clinical trials.

Magnetic Labeling of Human Neural Progenitor Cells for in vivo MRI Migration Analysis Following Transplantation in Stroke

Guzman R[1], Bliss TM[1], Uchida N[4], Greve JM[3], Palmer TD[1], Sun GH[1], Moseley ME[2], Steinberg GK[1] - [1]Department of Neurosurgery, [2]Department of Radiology, [3]Department of Bioengineering, Stanford University; [4]Stem Cells Inc.; California

Introduction

Stroke remains the leading cause of serious long-term adult disability in western countries. Recent attention has focused on restoring brain function through neural stem cell transplantation. Neural stem cells transplanted into the brain have been shown to undergo long-range, targeted migration towards lesion sites. The ability to non-invasively monitor stem cell migration is of great importance for future transplantation studies. Here we demonstrate that human neurosphere cells derived from CNS stem cells (hCNS-SC) can safely be labeled with FDA-approved paramagnetic iron oxide particles (SPIO) and that their migration following stroke can be analyzed using magnetic resonance imaging (MRI).

Methods

Human hCNS-SC-derived neurosphere cells were incubated overnight with SPIO (5µg/ml) (Feridex, Advanced Magnetics, USA) complexed to Protamine Sulfate (2.5µg/ml). Cell viability after transfection was assessed by Trypan blue dye exclusion assay. Male SD rats (300 ± 10 g, n=7) were subjected to permanent distal middle cerebral artery occlusion (dMCAo) with carotid artery occlusion for 1 hr. One week later the iron-labelled human neurosphere cells (1 x 105 cells/µl) were injected into 3 peri-infarct sites (1 µl/site) ventromedially on the A-P axis. All rats received daily intraperitoneal injection of cyclosporine A (10 mg/kg). MRI (4.7T) was performed before and several times after transplantation for up to 5 weeks. Histochemistry for iron (Prussian blue) and immunohistochemistry with a human-specific nuclear antibody was done thereafter.

Results

Mean cell viability was 93.6% (± 3.5 SD). Pre-transplantation MRI showed the stroked area on T2-weighted images and served as a reference image for post-transplantation comparison. At 1 week post-transplantation grafts were identified on T2*- and T2-weighted MR images as hypointense areas adjacent to the stroke without clear evidence of migration (Figure A). Subsequent MR images revealed progressive loss of infarcted cortex and migration of iron labeled human cells towards the lesioned area (Figure B). Targeted migration of NPC was confirmed by immunohistochemistry (Figure C). The hypointense signal as seen on MRI was correlated with Prussian blue stained coronal brain sections.
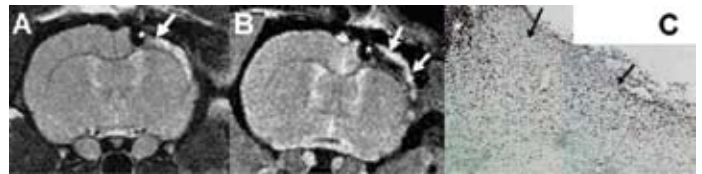

Figure 1: MRI at 1 (A) week and 5 (B) weeks after transplantation of iron-labeled human NPC (asterisk) adjacent to the cortical stroke. No migration was seen at 1 week, but a hypointense area extended towards the lesion at 5 weeks post-transplantation (white arrows). Corresponding immunohistochemistry (C) showing targeted migration of NPC (arrows) away from the graft (asterisk).

Conclusions

These preliminary results indicate that hCNS-SC-derived neurpshere cells can safely be transfected with FDA-approved SPIO. Targeted migration of human cells could be followed by means of MRI up to 5 weeks. Magnetic labeling of human stem cells prior to transplantation allows non-invasive monitoring with MRI and could be considered for future clinical trials.

High-resolution MR Imaging of Paraspinal Muscle Injury following Minimally Invasive and Conventional Open Posterolateral Lumbar Fusion

Kathryn Stevens[1], Karen Griffiths[1], Todd Alamin[2], Roland Bammer[1] – [1]Department of Radiology, [2]Department of Orthopedics

Introduction

The purpose of this study was to evaluate the feasibility of using MRI to evaluate and quantify paraspinal muscle damage resulting from posterolateral lumbar fusion, and to compare the minimally invasive Endius Atavi System with conventional open fusion.

Materials and Methods

Four patients with a minimally invasive Endius Atavi fusion, and 4 patients with an open single level posterolateral lumbar spinal fusion were imaged approximately 6 months post-surgery in a 1.5T GE scanner. Axial T1-weighted SE and T2-weighted FSE sequences were obtained for high resolution imaging. Axial short-tau inversion recovery (STIR) T2-weighted FSE and spectrally selective saturation (SPIR) T2-weighted FSE sequences were performed in order to differentiate between edema and fatty atrophy. Coronal T2 FSE sequences allowed overall assessment of the multifidus. Edema and atrophy within multifidus (MF) were scored on a visual scale of 0 to 3. Quantitative MRI was performed using a rapid two-point T2 mapping technique and line scan diffusion imaging (LSDI). An axial dual spin-echo sequence was used to measure

Figure 1. Coronal T2 FSE and axial STIR images of the paraspinal muscles in a female patient 6 months after having open posterior L4-5 spinal fusion, showing severe edema in multifidus

Fig2. Coronal T2 FSE and axial STIR images in a male patient 4 months after having a minimally invasive L3-4 fusion, showing mild edema in multifidus

T2 relaxation times in the 3 individual bundles of MF at each intervertebral level. LSDI was used to determine quantitative differences (ADC) in muscle damage from the two surgical techniques. T2 maps and apparent diffusion coefficient (ADC) maps were reconstructed at a remote LINUX workstation, and a region of interest measuring a minimum of 10 mm2 was placed on the three bundles of the multifidus muscles bilaterally, taking measurements in the region of maximal signal intensity.

Results

There was a striking visual difference in overall muscle edema between the open and minimally invasive group (Figs 1 and 2), and the visual estimate of edema at each site on axial images correlated well with the corresponding T2 values (r = 0.74, p < 0.0001). The mean T2 relaxation time was 90ms (± 23.3) in the open group, and 47ms (± 8.4) in the minimally invasive group (p = 0.013)(Fig 3). The mean ADC was 1626 (± 132) x 10 -6 mm2/s, compared to 1357 (± 104) x 10 -6 mm2/s (p = 0.0184) respectively. In most patients, edema was seen in a chevron configuration on coronal images, following the anatomy of MF fibers. Edema, T2, and ADC measurements were also analyzed in this distribution, incorporating measurements from the medial bundles at the level above the fusion, the medial and central bundles at the level of the fusion and from all three muscle bundles at the level below the fusion. Again, the results were statistically significant. The mean T2 was 99ms (± 20.5) in the open group and 51ms (± 8.9) in the Atavi group (p = 0.005), with a mean ADC of 1656 (± 119) x 10 -6 mm2/s and 1332(± 100) x 10 -6 mm2/s respectively (p=0.0059).
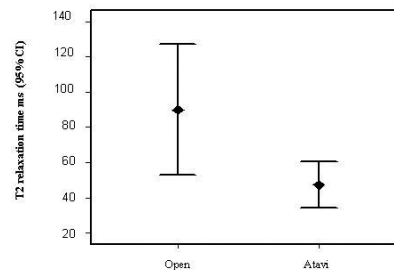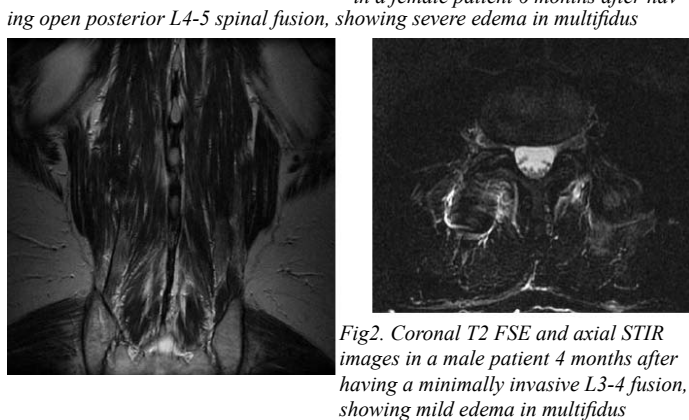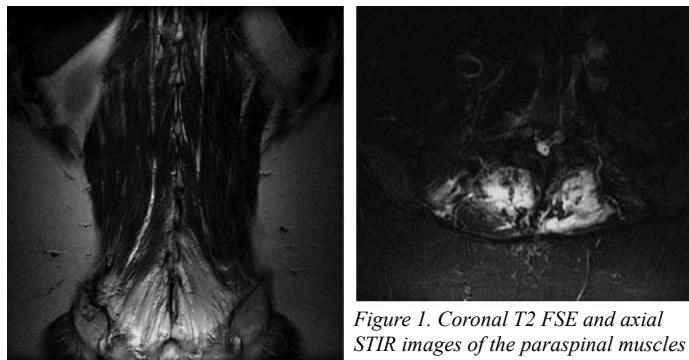

Fig 3. Comparison of mean T2 relaxation times at level of fusion

Discussion

Spinal fusions do not always have a satisfactory outcome, and one contributing factor is postulated to be the dissection and retraction of paraspinal muscles needed to perform a standard posterior instrumented spinal fusion. Minimally invasive techniques have recently been developed to minimize such damage. The T2 relaxation time is a quantitative measure of edema within the muscle, and has been shown to correlate with the severity of muscle damage. The mean T2 and ADC measurements were significantly lower in the Atavi group, suggesting that less muscle damage occurs using a minimally invasive approach.

Stroke Initiates Targeted Migration of Transplanted Iron-Labeled Neural Progenitor Cells as Revealed by Magnetic Resonance Imaging

Guzman R[1], Bliss TM[1], Greve JM[3], Palmer TD[1], Sun GH[1], Moseley ME[2], Steinberg GK[1] - [1]Department of Neurosurgery, [2]Department of Radiology, [3]Department of Bioengineering

INTRODUCTION

Several studies have demonstrated that labelled, transplanted cells can be monitored in the brain using magnetic resonance imaging (MRI). Migration of transplanted cells toward an existing lesion has been reported. We assessed the hypothesis that stroke following transplantation could initiate targeted cell migration in rats.

METHODS

Neural progenitor cells (NPC) derived from adult Fisher rats were incubated overnight with FDA-approved paramagnetic iron oxide particles (SPIO) (12.5μg/ml) (Feridex, Advanced Magnetics, USA) complexed to Protamine Sulfate (2.5μg/ml). Cell viability and proliferative capacity after transfection was assessed by Trypan blue dye exclusion assay. Fisher rats received an intrastriatal transplant of $1 \times 10E5$ iron-labeled cells in 1μl medium 14 days prior to contra-lateral permanent distal occlusion of the middle cerebral artery with 1hr carotid artery occlusion. Transplanted non-stroked rats served as controls. MRI was performed 7 days before and 3, 7 and 21 days after stroke. Thereafter serial coronal brain sections were stained for Prussian blue to detect transplanted cells.

RESULTS

Mean cell viability was 95,5% (±1.5 SD) for SPIO doses up to 200μg/ml and 94,6% (±3.2) for Protamine Sulfate doses up to 20μg/ml. Cell proliferation 72 hours after transfection was equal in treated vs. untreated cells. Transplanted iron-labeled cells were identified on gradient-echo and T2-weighted MR images 7 days after transplantation. At 3 days after stroke, respectively 17 days after transplantation, the left-sided cortical stroke was clearly visible on T2-weighted images without evidence of graft morphology changes. At 7 days after stroke, hypointense areas became visible adjacent to the infarcted area. No signal changes over time were observed in control animals. Prussian-blue-stained cells were found at the site of transplantation and at the infarct perimeter. In control animals iron containing cells were confined to the transplantation site.

CONCLUSIONS

These preliminary results indicate that NPC's can safely be transfected with FDA-approved SPIO and transfection agent for in vivo MR visualization. Targeted migration of transplanted NPC's is initiated by stroke and can be monitored with MRI.

Relating Medial Temporal Lobe Volume to Frontal fMRI Activation for Memory Encoding in Older Adults

Allyson Rosen[1,4,5], John Gabrieli[1], Travis Stoub[2], Matthew W. Prull[3], Ruth O'Hara[4], Jerome Yesavage[4,5], Leyla deToledo-Morrell[2] – [1]Department of Psychology, Stanford University; [2]Department of Neurological Sciences, Rush-Presbyterian-St. Luke's Medical Center; [3]Department of Psychology, Whitman College; [4]Department of Psychiatry and Behavioral Sciences, Stanford University; [4]Palo Alto Veterans Affairs Health Care System

INTRODUCTION

This study examines the relationship between two lines of neuroimaging research in older adults: structural changes in the medial temporal lobe and functional changes in the frontal lobe. Specifically, Structural imaging studies have found that smaller medial temporal lobe (MTL) volumes are associated with lower memory performance. Functional imaging studies have found that older adults often exhibit bilateral frontal-lobe activation under conditions where young adults exhibit unilateral frontal activation. As yet, no one has examined whether these MTL structural and frontal-lobe functional findings are associated.

METHODS

In this study, we tested whether these findings were correlated in a population of healthy older adults in whom we previously demonstrated verbal memory performance was positively associated with left entorhinal cortex volume in the MTL and right frontal lobe activation during memory encoding. Thirteen, non-demented, community-dwelling older adults participated both in a functional MRI (fMRI) study of verbal memory encoding and structural imaging. MRI-derived left entorhinal volume was measured on structural images and entered as a regressor against fMRI activation during verbal memory encoding.

CONCLUSION

Right frontal activation (Brodmann's Area 47/insula) was positively correlated with left entorhinal cortex volume. These findings indicate a positive association between MTL volume and right frontal-lobe function that may underlie variability in memory performance among the elderly.

a)

b)
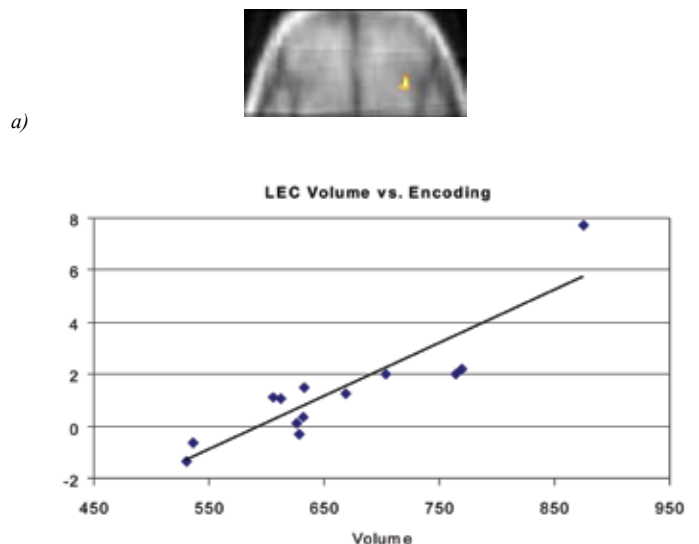
a) Region correlated with left entorhinal cortex activation; b) Scatterplot of relationship (r=0.89) between fMRI activation and entorhinal cortex volume. Note the correlation changed minimally with removal of the participant with the largest volume.

A Neuroimaging Approach to Reading Difficulties in Young Children: Characterization and Plasticity

Arvel Hernandez[1], Fumiko Maeda[1,2], Glenn McMillon[1], Jennifer Martindale[1], Heather Taylor[1], Ann Meyler[3], Marcel A. Just[3], John D. E. Gabrieli[1] – [1]Department of Psychology, [2]Department of Psychiatry, Stanford University; [3]Dept of Psychology, Carnegie Mellon University, PA

Introduction

Functional imaging studies have provided converging evidence that dyslexic individuals exhibit differential responses in left posterior and frontal language areas and their right hemisphere homologues when compared to healthy controls. Anatomical studies have contributed to this evidence using measures of gray matter volume and white matter structure. Further studies have revealed that these differences can be ameliorated through reading remediation. The novelty of this study was that we 1) included a 2nd control group (Reading-Matched Group): younger normal readers but with matched reading ability to dyslexics, 2) combined fMRI and VBM with the same subjects, and 3) Time1 reading ability AND changes (Time2-1) in reading ability were matched between dyslexics and controls.

Materials and Methods

Subjects 30 healthy, right-handed, native English speakers between the ages of 8-12 years old (mean = 10.35, standard deviation = 1.26). Reading Assessment Woodcock Johnson Reading Master Tests – Revised (WRMT): Word Identification (WID), Word Attack (WA), and Passage Comprehension (PC). Grouping Participants were assigned to one of three groups – dyslexic readers (WIDss(age) < 85), age-matched controls (WIDss(Age) > 85), and reading-matched controls matched to the dyslexic readers by their WID raw scores and to age-matched controls by their WIDss(age) scores. Real-Word Rhyme Task Participants judged whether two visually presented words rhymed (e.g., bait, gate) or not (e.g., price, miss) in the scanner. Each trial lasted a total of 6-sec (4-sec stimulus, 2-sec fixation cross). The entire scan consisted of 2 practice trials, 4 task blocks and 5 rest/fixation blocks lasting a total of 234 seconds. MRI fMRI and high-resolution anatomical images were collected.

Discussion

We identified six regions showing significantly greater recruitment in age-matched controls than in young dyslexic readers. All six of these ROIs showed similar effects when dyslexic readers were compared with controls matched for reading ability, indicating that the differences were not due to differences in reading skill. There were associated brain volume differences identified using VBM. Dyslexic readers showed increased activity in left and right posterior brain regions along with a right frontal region, potential sites for normalizing and compensatory changes, after 6 mos. of schooling. Reading-matched controls showed different patterns of change in activity even when matched for amount of behavioral improvement on three different measures of reading skill.

Conclusion

We hope that such findings can be used to unify scientific approaches toward the study and remediation of reading spectrum disorders.
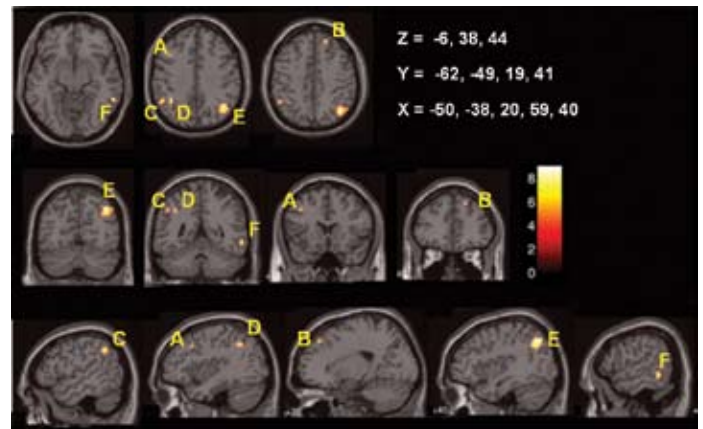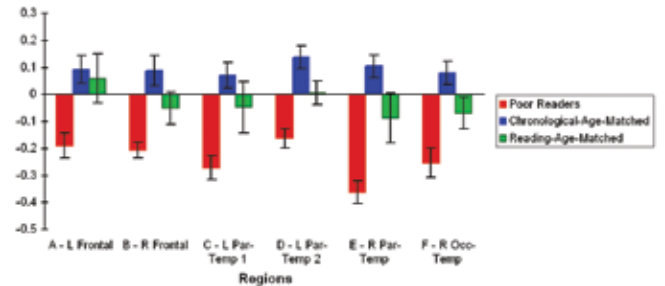

Fig 1: Activity in the six ROIs for the three groups. Y-axis: Mean contrast values of the six ROIs in Fig1 above. Error bars: Standard error of the mean.
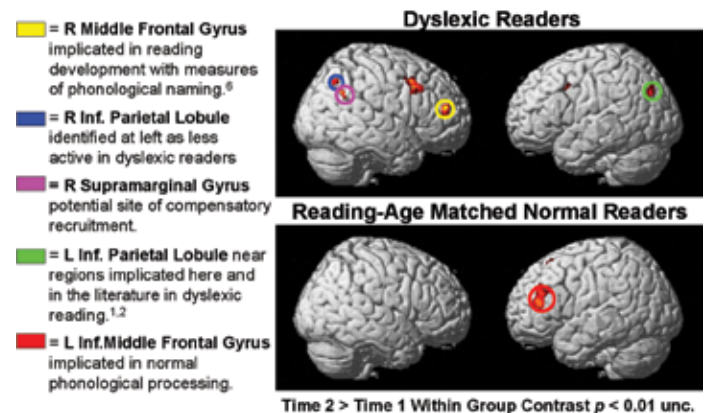

= R Middle Frontal Gyrus implicated in reading development with measures of phonological naming.[6]

= R Inf. Parietal Lobule identified at left as less active in dyslexic readers

= R Supramarginal Gyrus potential site of compensatory recruitment.

= L Inf. Parietal Lobule near regions implicated here and in the literature in dyslexic reading.[1,2]

= L Inf.Middle Frontal Gyrus implicated in normal phonological processing.

Dyslexic Readers

Reading-Age Matched Normal Readers

Time 2 > Time 1 Within Group Contrast p < 0.01 unc.

Fig 2: Increase in brain activation after 6 months.

Reward-motivated Learning: Correlated Mesolimbic and Hippocampal Activation Prior to Encoding Predicts Successful Memory Formation

R. Alison Adcock[1,2], Arul Thangavel[1,2], Brian Knutson[2], John D. E. Gabrieli[2] – [1]Department of Psychiatry, UCSF; [2]Department of Psychology, Stanford University

We examined reward-motivated intentional memory formation using event-related functional magnetic resonance imaging. Brain regions reflecting reward anticipation were localized using the Monetary Incentive Delay (MID) task. In a novel task, Monetary Incentive Encoding, cues signaled a high- or low-value reward for memorizing an upcoming scene. High-confidence recognition memory was tested twenty-four hours later. Prior to scenes later remembered, high- but not low-value cues evoked greater activation in anterior hippocampus and mesolimbic reward-anticipation regions (ventral tegmental area and nucleus accum- bens, also localized with the MID). These activations antecedent to the scene were inter-correlated and predicted recognition memory scores across individuals. In parahippocampal cortex, activation was greater on all high-value trials (remembered and forgotten), and predicted memory only during scene presentation. These results demonstrate memory-predicting functional coupling of anterior hippocampus and mesolimbic reward regions. They show that mesolimbic activation by reward antici- pation can enhance memory for immediately subsequent experience.

Phonological Processing & Rapid Temporal Processing in Dyslexia

Fumiko Maeda[1,2], Jessica Black[1], Galena Kolchugina[1], Afrooz Faizi[1], Arvel Hernandez[1], Glenn McMillon[1], Jennifer Martindale[1], Heather Taylor[1], Ann Meyler[3], Marcel A. Just[3], John D. E. Gabrieli1 – [1]Department of Psychology, [2]Department of Psychiatry

INTRODUCTION

THEORIES OF DYSLEXIA

1. PHONOLOGICAL DEFICIT HYPOTHESIS Impairment in phonological processing. (i.e.; Temple et al. Neuroreport (2001), PNAS (2003) - Lt Parieto-Temporal Region; Shaywitz et al. Biol Psychiatry (2002) - Occipito-Temporal Region).

2. LOW-LEVEL RAPID TEMPORAL PROCESSING DEFICIT

• RAPID AUDITORY DEFICIT HYPOTHESIS Inability to process rapid acoustic information. (i.e.; Temple et al. PNAS (2000) - Lt Prefrontal Area and Poldrack et al. JCNS – Lt Inferior Frontal Gyrus).

• MAGNOCELLULAR DEFICIT HYPOTHESIS Inability to process rapid visual motion information. (i.e.; Eden et al. Nature (1996))

MAIN RESEARCH QUESTION

How does LOW-LEVEL RAPID TEMPORAL PROCESSING contribute to PHONOLOGICAL PROCESSING?Materials and Methods

SUBJECTS

19 DYSLEXIC CHILDREN INCLUSION CRITERIA Normal IQ > 40 Performance IQ (WASI-T), Poor Reading Skills < 90 Real-Word Reading (Word ID-ss[age]) < 85 Spelling (WJS-ss[age]) or Comprehension (WRMTPC-ss[age])

19 NORMAL READING CONTROL CHILDREN INCLUSION CRITERIA Normal IQ > 40 Performance IQ (WASI-T), Normal Reading Skills > 90 All tests (ss[age] scores) Matched with individual dyslexics for age and genderRAPID AUDITORY TEMPORAL PROCESSING PSYCHOPHYSICAL TASK

(Tallal et al. 1996 Science, Merzenich et al. Science 1996)

Stimuli Two 75ms tones at 1.0kHz (Low Tone) and 1.4kHz (High Tone) presented in sequence. Variable Inter-stimulus interval between the 2 tones (1 – 1838ms) Task Are the tones ascending or descending? Methods Dual independant adaptive stair-case (1-up 3-down, 6 reversals, last 4 reversals for threshold determination designed to converge to 79.4% correct performance).

RAPID VISUAL MOTION PROCESSING PSYCHOPHYSICAL TASK

Stimuli Two spatially (1.08 deg) and temporally (600 ms) enveloped concentric gratings with eccentricity of the center of the stimuli being 3.9 deg, and with a spatial frequency 25-30 cycles/deg, presented simultaneously on left and right sides of screen. Speed of reference stimuli was 5.4 deg/sec. Variable Speed of target stimuli which appears either on left or right (0.12 – 30Hz). Task Which one is moving faster, left or right? Methods Dual independant adaptive stair-case (1-up 3-down, 6 reversals, last 4 reversals for threshold determination designed to converge to 79.4% correct performance).

REAL-WORD RHYME FMRI TASK

Participants judged whether two visually presented words rhymed (e.g., bait, gate) or not (e.g., price, miss) in the scanner. Each trial lasted a total of 6-sec (4-sec stimulus, 2-sec fixation cross). The entire scan consisted of 2 practice trials, 4 task blocks and 5 rest/fixation blocks lasting a total of 234 seconds. FMRI data was collected at the 3T.

RESULTS

Control children showed greater recruitment of the left prefrontal cortex than dyslexic children during the rhyming task. Activity in this area showed a strong negative correlation with better performance on both
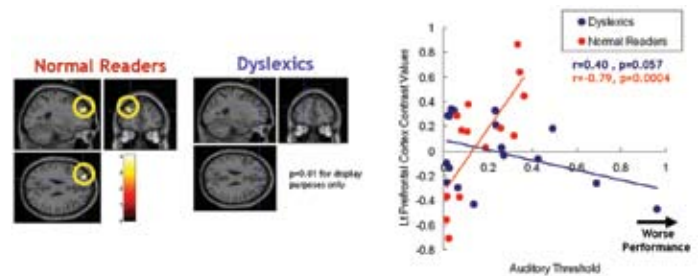

Fig1. Correlation between rapid auditory temporal processing threshold and contrast values in the left superior/middle frontal gyrus (BA 10; TC: x –24, y 46, z 23) during the real-word rhyme task showed significant positive correlation (p=0.005 small-volume corrected).
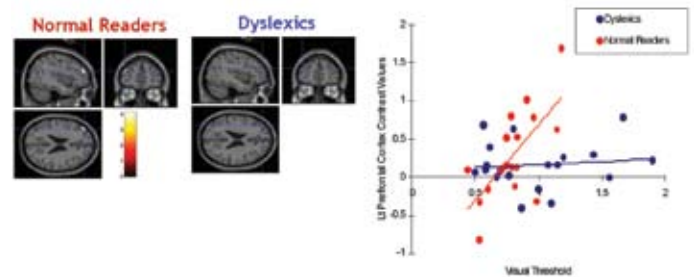

Fig2. Correlation between rapid visual motion perception threshold and contrast values in the left superior/middle frontal gyrus (BA 10; TC: x –40, y 50, z 20) during the real-word rhyme task showed significant positive correlation (p=0.005 small-volume corrected).

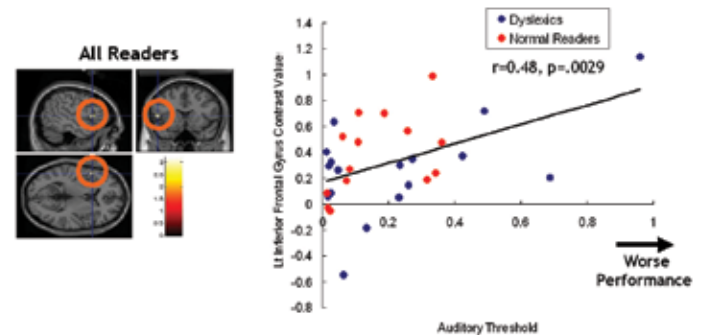

Fig3. Correlation between rapid auditory temporal processing threshold and contrast values in the left inferior frontal/central gyrus. (BA 44; TC: x –50, y 16, z 5) during the real-word rhyme task showed significant positive correlation (p=0.005 small-volume corrected)

visual and auditory rapid temporal processing tasks for control children. No significant correlation was observed for dyslexic children.

In addition, it was found that activity in the left inferior frontal gyrus during phonological processing was inversely correlated with performance on a rapid auditory processing task in both Control and Dyslexic children.Conclusion

The LEFT PREFRONTAL CORTEX and LEFT INFERIOR FRONTAL GYRUS may be involved in supra-modal rapid temporal processing, which in turn are involved in phonological processing.

Word Response Functions in Occipito-temporal Sulcus are Modulated by Age and Reading Skills in 7-12y Children

Michal Ben-Shachar, Robert F. Dougherty, Gayle K. Deutsch, Polina V. Potanina, Brian A. Wandell – Department of Psychology

Introduction

It has been suggested (e.g., Cohen et al., 2000, 2002) that the left ventral Occipito-Temporal Sulcus (OTS) takes a crucial part in the recognition of visual words. This region has been shown to be invariant to case, font, size as well as spatial position (left/right) of words. Furthermore, lesions that include this area are related to a specific deficit in reading (pure alexia). In an earlier study, we have demonstrated that the amplitude of BOLD responses in left and right occipito-temporal sulcus (OTS) covaries with word visibility in adults. Here we examine the development of this visual sensitivity to words in children.

Materials and Methods

Fifty children ages 7-12y participated in four testing sessions, including comprehensive neuropsychological assessment, high resolution MRI scans, diffusion tensor imaging and functional MRI scans. MRI scans were performed in the Lucas Center at Stanford University. In fMRI scans we presented visual words masked by phase-scrambled noise, while children were engaged in a fixation judgment task (implicit reading). Noise level was manipulated parametrically, resulting in 4 activation conditions, which were interleaved with fixation blocks.

Functional data were acquired using a 3T signa GE scanner, with spiral acquisition. 26 oblique slices (3x3x3 mm voxel size) were prescribed roughly along the ac-pc plane and covering the entire temporal and occipital lobes. Inplane anatomy was acquired with the same prescription, and was later aligned to the high resolution volume anatomical data (acquired in 3-4 short scans in a 1.5T GE scanner, averaged and resliced to 1x1x1 mm voxel size). Functional acquisition spanned 6 scans of 2:48 min, with a TR of 2000. Functional data were overlaid on the high resolution volume anatomy. In some cases (10 subjects) the volume anatomy was further segmented (using mrGray software, see http://white.stanford.edu/software/) into white and gray matter, and reconstructed into a 3D mesh for presentation purposes (see Fig. 1A). Functional analysis was performed with the mrVista suite of tools. ROIs in OTS and early visual cortex were defined functionally in individual brains by contrasting the word conditions against fixation and anatomically using sulcal landmarks. Within ROIs, the relative amplitude of the BOLD signal was computed separately for each noise level, resulting in a word visibility response function per ROI.

Results

Word-visibility response functions were present in bilateral OTS in children as young as 7y. Such sensitivity to word-visibility was not evident in early visual cortex (V1/2/3 foveal confluence). BOLD signals in OTS
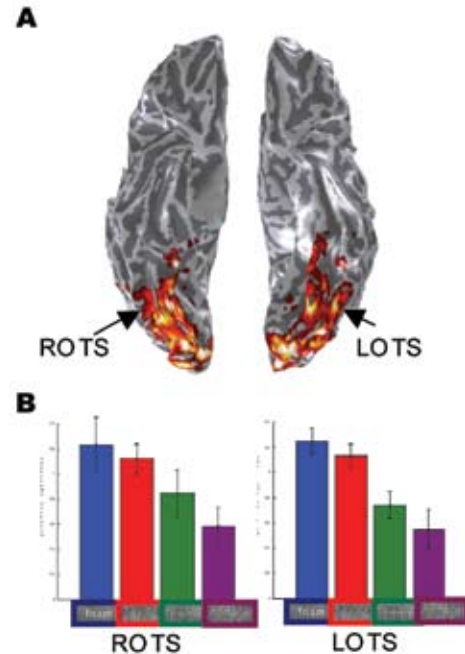

Figure 1: A. Activation for all word conditions (functional localizer) in an 11y child's brain. B. Word visibility response functions measured in left and right OTS in the same child.

were higher for the most visible words, and decreased with noise (see figure 1B). The steepness of the OTS response function depended on age and reading skills. Older children (age>10y) showed a steeper response function. Also, better readers (word ID standard score >100) showed higher BOLD signal for low-visibility words.

Conclusions

BOLD responses in left and right OTS are related to word-visibility in children. The quantitative form of this relationship changes between the ages of 7-12. Preliminary results from adult studies we have preformed suggest that the OTS response functions are not specific to word stimuli, but generalize to line drawings of common objects. As a whole, these results suggest that the OTS is part of a visual form recognition system in ventral occipitotemporal cortex. Specialization for words might have evolved on top of the existing sensitivity for contours and shapes in this piece of cortex.

New Subdivisions of the Human VO Cluster Derived from Visual Field Mapping and Stimulus Selectivity

Alyssa A. Brewer[1], Junjie Liu[2], Alex R. Wade[4], Brian A. Wandell[1,3] - [1]Neuroscience, [2]Applied Physics, [3]Psychology, Stanford University; [4]Smith-Kettlewell Eye Research Institute, San Francisco

Introduction

Human visual cortex is organized into a set of distinct visual field maps. There is consensus on the organization of several human maps, including V1, V2, and V3, but there is disagreement about the presence and organization of visual field maps in other locations1-4. Here, we report measurements in human ventral occipital cortex. We also describe the first coordinated measurements of color, object and face responsivity in and near these maps.

Materials and Methods

We measured visual field maps in ventral occipital cortex using phase-encoded fMRI mapping methods. The rotating wedge and expanding ring stimuli consisted of 3deg and 16deg black and white, drifting radial checkerboard patterns. Temporal phase-encoded BOLD signals were analyzed with an automated, atlas-fitting algorithm to define the visual area boundaries. Color, face, and object-selective responses were measured by performing separate color-luminance and object-face exchange experiments.

Results

The data support a model of ventral visual field map organization that includes a hemifield map, hV4, which abuts the central field representation of ventral V3. In addition, the measurements reveal two hemifield maps (VO-1 and VO-2) located anterior to hV4. The eccentricity representation of these maps begins in a distinct foveal representation on the fusiform gyrus and becomes increasingly peripheral as it extends medially across the collateral sulcus and approaches the peripheral representation of V3v. The hV4 and VO maps modulate during color-luminance exchange experiments. The VO maps modulate during object-face exchanges, in phase with objects. Cortex lateral to these maps modulates to object-faces exchanges as well, but in phase with faces.

Conclusion

Human VO contains at least three hemifield representations with differential stimulus selectivity. The map organization and stimulus respon-
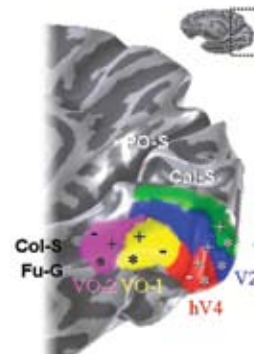

Figure 1. Summary of hV4, VO-1, and VO-2 field map [properties. The positions of the ventral-occipital visual field maps V2v (green, 0-16°), V3v (blue, 0-16°), hV4 (red), VO-1 (yellow) and VO-2 (magenta) are shown. The + and - indicate upper and lower visual field representations, respectively. The asterisk indicates the most central visual field representation within each map. PO-S: Parietal-occipital sulcus. Cal-S: Calcarine sulcus. Col-S: Collateral sulcus. Fu-G: Fusiform gyrus.

Area	Color	Faces	Objects
hV4	+	-	-
VO-1	+	-	+
VO-2	+	-	+
Lateral to hV4	-	+	-
Lateral to VO-1	- (L) + (R)	-	-
Lateral to VO-2	-	+	-

Table 1. Differential stimulus selectivity in VOT. Stimulus selectivity was measured in 3 mm radius disks placed at corresponding eccentricities in each of the listed regions. Significant selectivity for a stimulus type is indicated with a '+'. Note the asymmetry of color responses between the left and right (R) hemispheres in the region of interest lateral to VO-1.

sivity support a general organization of visual cortex based on clusters of maps that serve distinct computational functions5.

References

1. Wade, A.R., et al., Philos Trans R Soc Lond B Biol Sci, 2002. 357(1424): p. 963-73.
2. Bartels, A. and S. Zeki, Eur J Neurosci, 2000. 12(1): p. 172-93.
3. Hadjikhani, N., et al., Nature Neuroscience, 1998. 1(3): p. 235 - 241.
4. Malach, R., et al., Proc Natl Acad Sci U S A, 1995. 92(18): p. 8135-9.
5. Wandell B.A., et al., Philos Trans R Soc Lond B Biol Sci, 2005. 360(1456):693-707.

Working Memory and Long-term Memory for Faces: Evidence from fMRI and Global Amnesia for Involvement of the Medial Temporal Lobes

Elizabeth A. Nichols, Yun-Ching Kao, Mieke Verfaellie, John D. E. Gabrieli – Department of Psychology

Behavioral studies with amnesic patients and imaging studies with healthy adults have suggested that medial temporal lobe (MTL) structures known to be essential for long-term memory (LTM) may also be involved in some working memory (WM) tasks. To examine whether MTL structures are involved in WM for faces, and the nature of that involvement, WM and LTM for faces were examined in normal participants via functional magnetic resonance imaging (fMRI) and in amnesic patients behaviorally. In Experiment 1, participants were scanned while performing a WM task in which they determined if two novel faces, presented 7 seconds apart, were the same or different. Later, participants' LTM for the faces they saw during the WM task was measured in an unexpected recognition test. During WM maintenance, the hip-

pocampus was activated bilaterally. LTM analysis further revealed that bilateral hippocampal regions were more activated during the maintenance of faces that were later remembered than forgotten. The strong overlap in hippocampal activations across the tasks suggested that the same regions were recruited for WM and LTM. In Experiment 2, amnesic and control participants were tested on similar WM and LTM tasks. Amnesic patients, as a group, had intact performance with a 1-second maintenance period, but were impaired after a 7-second maintenance period and on the LTM task. Taken together, these findings suggest that hippocampal memory processes support WM for intervals as short as 7 seconds and LTM for faces.

Functional Organization of Human Occipital-callosal Fiber Tracts

Robert F. Dougherty[1,2], Michal Ben-Shachar[1,2], Gayle K. Deutsch[1,2], Roland Bammer[3], Polina Potanina[1,2], Brian A. Wandell[1,2]
[1]Department of Psychology, [2]Stanford Institute for Reading and Learning, [3]Department of Radiology

Introduction

Diffusion tensor imaging (DTI) and fiber tracking (FT) were used to measure the occipital lobe fiber tracts connecting the two hemispheres in individual human adults and children. These tracts are important for normal vision. Also, damage to portions of these tracts is associated with alexia and their integrity may be important for normal reading development.

Materials and Methods

DTI data were acquired on 1.5T Signa LX and fMRI data were acquired on a GE 3T Signa LX scanner, both located at the Lucas Center. DTI data were pre-processed using a custom program based on normalized mutual information that removed eddy current distortion effects using a constrained non-rigid image registration algorithm (Bammer & Auer, 2001). The fiber-tracking analyses and visualization were performed with custom software. Fiber tracts were estimated using a streamlines tracking algorithm with a 4th order Runge-Kutta path integration method and 1 mm fixed step size. A continuous tensor field was estimated using trilinear interpolation of the tensor elements. FMRI and DTI data were combined by considering all fibers with an end point within 2 mm of the gray matter - white matter surface and associating these fibers with the gray matter voxels (and thus functional properties) closest to their end points (see Dougherty et. al., 2005 PNAS for details). We performed detailed analysis on four adult subjects (shown here) and validated the basic findings on six other adult subjects and 54 children.
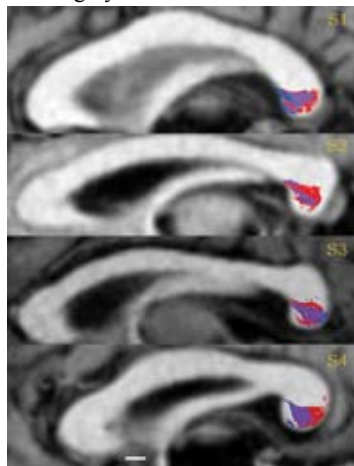
Figure 1. Left-right agreement. Red indicates fibers originating from the left occipital lobe; blue those from the right
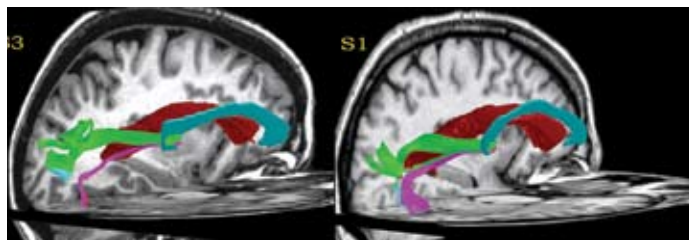

Figure 3. Splenial fiber tracts shown in two subjects with respect to the left lateral ventricle (red) and the corpus callosum region of interest (cyan).

Discussion

To assess the reliability of the DTI-FT measurements, occipital-callosal projections were estimated from each subject's left and right hemispheres independently. The left and right estimates converged onto the same positions within the splenium (Figure 1). We further characterized the properties of the estimated occipital-callosal fiber tracts by combining them with functional MRI. Using fMRI, we identified visual field maps in cortex and labeled fibers by the cortical functional response at the fiber endpoint. This labeling reveals a regular organization of the fibers within the splenium (Figure 2). The dorsal visual maps (dorsal V3, V3A, V3B, V7) send projections through a large band in the middle of the splenium, while ventral visual maps (ventral V3, V4) send projections through the inferior-anterior corner of the splenium.

The DTI-FT analysis also estimates the path followed by the occipital-callosal fiber tracts between the splenium and cortex (Figure 3). The bundles projecting to dorsal and ventral cortex course around the lateral ventricle in different positions. Fibers projecting to dorsal cortical regions (green) tend to fall on the superior aspect of the occipital horn of the lateral ventricle. Fibers projecting to ventral cortex separate and follow a route medial and inferior to the ventricle (magenta).
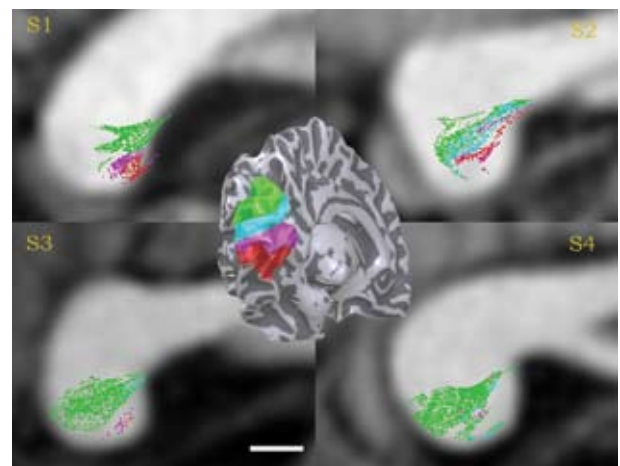

Figure 2. Splenial fibers colored by their cortical origin. Cortical ROIs are show in in the left hemisphere for one subject (inset).

Conclusion

The agreement between the independent left/right estimates, further supported by previous descriptions of homologous tracts in macaque, validates the DTI-FT methods. However, a principal limitation of these methods is low sensitivity: a large number of fiber tracts that connect homotopic regions of ventral and lateral visual cortex were undetected. We conclude that most of the estimated tracts are real and can be localized with a precision of 1-2 mm, but many tracts are missed due to data and algorithm limitations.

Color- and Luminance-preferring Stripes in Human Secondary Visual Cortex (V2)

Junjie Liu[1], David Ress[2,3], Brian A. Wandell[2] – Departments of [1]Applied Physics, [2]Psychology, [3]Radiology

Introduction

The visual cortex often comprises orderly patterns of responses to certain visual features; these patterns help us understand the functional architecture of visual pathways. Regarding to color, the luminance (light-dark) and color-opponent (red-green and blue-yellow) signals are represented in distinct layers in the primary visual cortex (V1). Several studies suggest that this segregation of color signals continues in cortical regions beyond V1 ("extrastriate"), but the underlying architecture, particularly in human, is unclear. We measured responses to color in human secondary visual cortex (V2) and other extrastriate regions using functional magnetic resonance imaging (fMRI).

Materials and Methods

We used the 3T magnet at Lucas center for fMRI measurements. In each scan we prescribed either 20 slices at 2.5 mm iso-voxel resolution that covers the entire visual cortex, or 15 slices at 1.6 mm iso-voxel resolution that covers only the most posterior portion near the occipital pole. First, we measured the visual eccentricity and polar angle that elicit strongest responses in each voxel, a standard procedure known as visual field mapping. Cortical regions were delineated based on these results: V1, V2, V3 and hV4 share a common foveal representation, whereas each of VO, MT+ and V3A regions belongs to a distinct, well-separated foveal representation (Wandell, Brewer and Dougherty, 2005). Figure 1 gives an example of the eccentricity mapping result, where boundaries of dorsal portions of V1 and V2 are shown.

Next, we made color measurements using a block design in which each cycle comprises a block (12 s) of luminance contrast [light-dark, (L+M)-cone] followed by a block of color-opponent contrast [red-green, (L-M)-cone; or blue-yellow, S-cone]. A variety of contrast levels were used for each type of stimulus. All stimuli were radial sinusoidal gratings (0.8 cycle/deg) covering the central 5 deg. Subjects engaged in a demanding fixation task that aims to divert their visual attention away from the gratings stimuli.

Results

We titrated the luminance and color contrasts for individual subjects. At certain contrast levels, V1 has somewhat stronger response to color than to luminance, yet V2, V3 and hV4 contain significant and spatially localized responses that are either in phase with the luminance (luminance-preferring) or color (color-preferring) stimuli. The color- and luminance-preferring regions interleave with each other (Figure 2).

In V2, we find a periodic pattern of color- and luminance-preferring stripes that parallel the iso-eccentricity direction and are perpendicular to the V1/V2 border (compare Figures 1 and 2). In individual subjects, this pattern is significant and stable across sessions in different days. The human V2 stripe periodicity is 8-16 mm (variable across subjects); each stripe covering 1-2 deg of eccentricity. Although similar V2 stripes were reported in rhesus monkey by optical imaging, we report the human V2 stripes for the first time using a non-invasive method (fMRI).

Beyond hV4, responses are color-preferring throughout ventral occipital (VO) regions, and luminance-preferring throughout regions MT+ and V3A (data not shown). This agrees with the critical roles that VO and MT+/V3A play in color and motion perception, respectively.

Conclusion

Color- and luminance-preferring cortical regions are interleaved in V2, V3 and hV4, with a stripe-like pattern identified in V2. These measurements help clarify how color information is distributed to human extrastriate cortex.
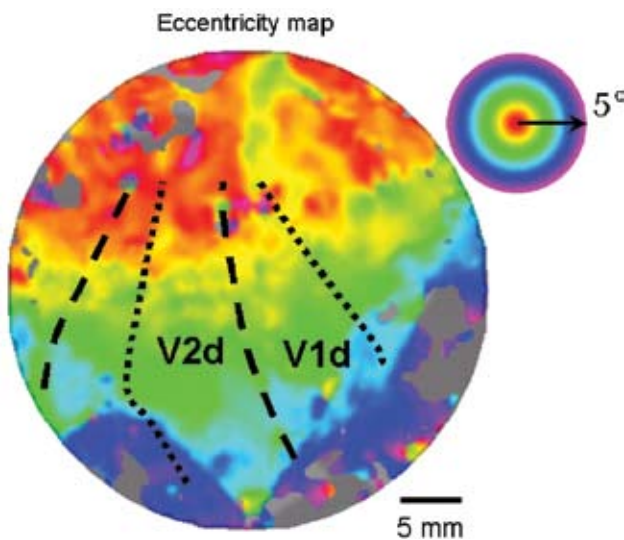

Figure 1: Eccentricity map on a flattened surface of part of visual cortex. The pseudo-color encodes central (red) to peripheral (blue) eccentrici-ties (see legend). Also shown are the borders of V1 and V2 (dorsal).
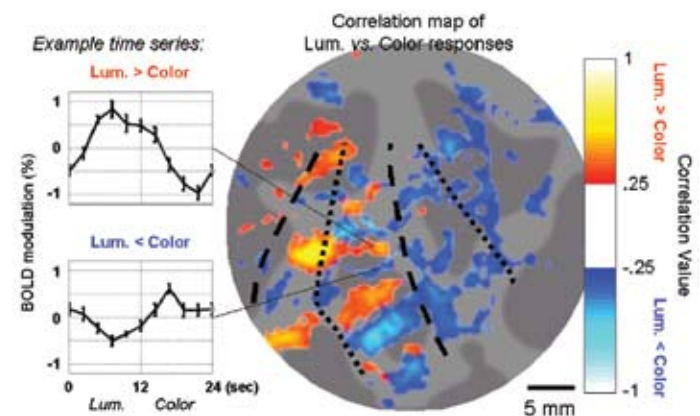

Figure 2: Responses to a luminance-color exchange stimulus shown on the same flatten surface as in Figure 1. Correlation value describes the significance of stronger BOLD response to luminance (red) or color (blue) stimuli. In the V2 dorsal (V2d) region, a pattern of interleaved responses is found.

An Optimized Amygdala Localizer for FMRI

Bryan T. Denny, Brian Knutson – Department of Psychology

Introduction

Several functional magnetic resonance imaging (FMRI) studies of emotional processing have focused on activation of the amygdala, a subcortical structure implicated in emotional learning (LaBar et al., 1998). Block design FMRI probes of amygdala activation have been developed. For instance, Hariri and colleagues (2000) have designed a probe that contrasts identification of fearful faces versus simple shapes. However, many of these probes do not control for: (1) performance, (2) expectation, or (3) habituation. These confounds could attenuate statistical power to detect activation. Here, we redesigned the Hariri and colleagues (2002) paradigm (e.g., effect size in amygdala for n=12, Z=3.64 for right amygdala peak) to control for these potential confounds and observed activation in amygdalar volumes of interest (VOIs).

Materials and Methods

During scanning (GE 1.5 T scanner, voxel size = 4 mm cubic, TR = 2000 msec, spiral in/out pulse sequence), six healthy subjects (one female, age range 20-30) judged the similarity of either faces or oval shapes. Face similarity criteria included either expression or identity (each face montage included at least one fear expression), while oval similarity criteria included either inscribed line or overall shape orientation. To control for performance, shape discriminability was minimized to approximate performance on the face-matching task. To control for expectation and habituation, stimulus presentation (4 sec each) was pseudorandomly jittered within each 60 sec block (2-6 sec ITI). Subjects engaged in four interleaved blocks of each type (i.e., oval or face matching), for a total of 8 min. FMRI data was analyzed with AFNI software and preprocessed with corrections for slice timing and motion, as well as including a slight spatial blur (4 mm FWHM) and bandpass filtering (6-90 sec). Preprocessed data were submitted to multiple regression with control regressors modeling residual head motion, baseline, linear, and nonlinear trends over the experimental session. Regressors of interest contrasted face versus oval matching. Volume of interest data was extracted from peak amygdala voxels for this contrast for each subject. Statistical maps of this contrast were spatially normalized, merged using a meta-analytic formula, and thresholded at p<.001, uncorrected (Knutson et al., 2000).
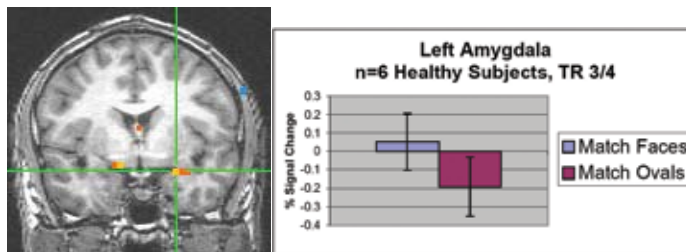

Figure 1a (Left). Group map for contrast of face versus oval matching, left amygdala focus (n=6, y= 0 mm, Z=3.55, TC: -23,0,-14, thresholded at Z=3.26, p<.001). Figure 1b (Right). Mean percent signal change in peak left amygdala voxel (n=6, TR=3/4 averaged) are significantly different for face vs. oval matching (F(1,5)=17.24, p<.01).

Discussion

Within-subjects ANOVAs of reaction time estimates indicated that subjects responded faster to the ovals than to the faces (F(1,5)=23.62, p<.01), indicating a slight difference in performance. Group statistical maps of the contrast of face versus oval matching yielded significant activation foci in both left amygdala (Z=3.55, TC: -23,0,-14) and right amygdala / parahippocampal gyrus (Z=6.22, 16,-5,-11), revealing comparable or greater effect size to that documented in prior research, which included a similar number of observations but twice as many subjects (Hariri et al., 2002; see Figure 1). Volume of interest analyses of peak amygdala voxels indicated that mean percent signal change values for face and oval matching were significantly different (F(1,5)=17.24, p<.01, see Figure 2). Further VOI analyses suggested that event-related signal did not habituate across blocks by repetition (F(1,5)=1.09, p=n.s.), indicating removal of the habituation observed in prior research utilizing block designs without pseudorandomized interstimulus intervals (Hariri et al., 2002).

Conclusion

These results suggest that the optimized amygdala localizer provides a short task (~8 min) that evokes robust amygdala activation on an individual basis. Perhaps as a result of controlling for expectation and habituation effects, the task elicits stronger activations than existing block designs. Future research may further minimize the performance discrepancy between face and shape discrimination and explore the responsiveness of amygdala activation in patients with affective disorders such as those with unipolar major depression.

References

Hariri, A. R., Bookheimer, S. Y., & Mazziota, J. C. (2000). Modulating emotional responses: Effects of a neocortical network on the limbic system. *NeuroReport, 11(1),* 43-48.

Hariri, A. R., Tessitore, A., Mattay, V. S., Fera, F., & Weinberger, D. R. (2002). The amygdala response to emotional stimuli: A comparison of faces and scenes. *NeuroImage, 17,* 317-323.

Knutson, B., Westdorp, A., Kaiser, E., & Hommer, D. (2000). FMRI visualization of brain activity during a monetary incentive delay task. *NeuroImage, 12,* 20-27.

LeBar, K. S., Gatenby, J. C., Gore, J. C., LeDoux, J. E., & Phelps, E. A. (1998). Human amygdala activation during conditioned fear acquisition and extinction: A mixed-trial fMRI study. *Neuron, 20(5),* 937-945.

View-dependent Visual Object Representations in Human Object-selective Visual Cortex

David Andresen, Kalanit Grill-Spector – Department of Psychology

Introduction

Humans can instantly recognize a familiar object even though that object can appear dramatically different when viewed from various viewpoints. How are objects represented in the human cortex such that they can be recognized from any viewpoint?

Methods

Experiment 1: View-Preference. We first examined the neural response in human visual cortex to objects in 4 viewpoints: 15°, 75°, 135°, and 195° (Figure 1) in a blocked paradigm using a 3.0T scanner. Subjects categorized each image as an animal, vehicle, or neither.

Experiment 2: View-Adaptation. We next used an adaptation paradigm to examine the selectivity of neural responses. Adaptation is the reduction in neural response of a cortical area when a stimulus is repeatedly presented. When a completely new stimulus is presented, the neural response returns to initial levels. By adapting visual cortex to one view of an object and then testing rotations away from that view, we assessed the degree of rotation that elicited a response similar to a novel object (i.e., the amount of rotation to which the cortical area no longer recognized the image as the adapted object; Figure 1). We examined the effect of adaptation to the front views (i.e., the 15° views) as well as the back views (i.e., the 195° view) of all objects.

Results

Experiment 1 revealed that there is a greater neural response for front views than rear views (Figure 2). Experiment 2 revealed a hierarchy across visual cortex, with lateral occipital visual areas very sensitive to viewpoint (i.e., complete recovery from adaptation after 60° rotation), and fusiform areas more invariant to viewpoint (i.e., recovery after 120° rotation; Figure 3, left). Experiment 2 also revealed an asymmetry that depended upon adapting view. When adapted with the front view, the tuning curve was flatter suggesting invariance to viewpoint. However, when adapted with the back view, the tuning curve was steep, suggesting sensitivity to viewpoint (Figure 3, right).

Conclusions

Object-selective visual cortex shows a preference for front views over back views of objects that can be assessed directly using standard fMRI techniques.
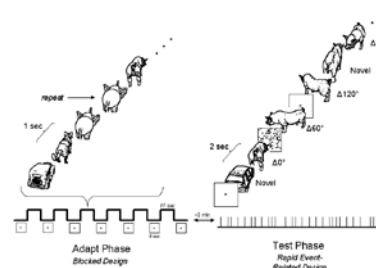

Figure 1. Adapt phase (left) and test phase (right) for Experiment 2. Experiment 1 did not have an adapt phase.
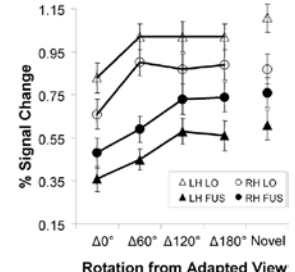

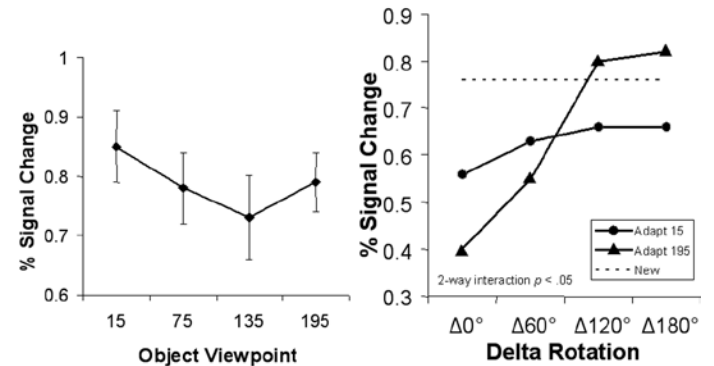Figure 2. Hierarchy of increasing view-invariance in visual cortex.

Figure 3. fMR response to views of objects without adaptation (left), and with adaptation (right)in the right fusiform. Note the asymmetry in recovery from adaptation depending upon adapting view (right).

Furthermore, this asymmetry in view representation interacts with adaptation to produce apparently differential view sensitivity depending adapting view. However, this apparent asymmetry is explained by a common recovery from adaptation for both adapting views that is modulated by the increased or decreased response to preferred and non-preferred views respectively. Finally, a hierarchy of increasing invariance is revealed across human visual cortex.

Spatio-temporal Properties of Repetition Effects in the Human Cortex: EEG and fMRI Combined

Sven P. Heinrich, Kalanit Grill-Spector – Department of Psychology

Introduction

Repetition of the same object typically yields a reduction of the fMR signal in object-selective cortex. However, not much is known about what stage of processing yields this reduced neural activity. EEG has a higher temporal resolution than fMRI and can provide additional insights, e.g. whether adaptation occurs bottom-up or top-down. Previous EEG studies report earliest repetition effects at various times ranging from 170–400 ms and at different locations with both increasing and decreasing activity. To better understand the spatial-temporal pattern of adaptation, we measured both EEG and fMRI activation in the same subjects and the same stimulus paradigm.

Methods

We obtained 61-channel EEG recordings from 10 subjects and fMRI measurements from 7 subjects. Subjects viewed repeated images of the same dog (18 repetitions), the same bird (18 repetitions), or non-repeated images of dogs and birds. Images were presented in an event-related

design for 150 ms followed by a blank interval of 1850 ms. Conditions appeared in random order and were intermixed with scrambled images and fixation trials. Subjects participated in 10 blocks of 108 trials and were asked to categorize images to "bird", "dog" or "other" while fixating. In each block, a different set of images was used.

Discussion & Conlusion

Consistent with previous fMRI studies, in 5 out of 7 subjects the response decreased in the lateral occipital complex. 9 out of 10 subjects showed increased EEG signal around 160 ms for repeated vs. non-repeated animals. This early difference suggests differential bottom-up processesing of repeated objects. A dipole fit indicates the lateral occipital cortex as the source of this differential activity. There was no difference in latencies, suggesting that processing speed in unchanged at this early stage. In summary, we conclude that adaptation in the lateral occipital cortex is a local process rather than the result of feedback from higher cortical areas.

Identifying Representations of Single Objects in Human Extrastriate Cortex using High-Resolution fMRI

Rory Sayres[1], David Ress[2], Kalanit Grill-Spector[1,3] – [1]Department of Neuroscience, Stanford University; [2]Department of Neuroscience, Brown University; [3] Department of Psychology, Stanford University

Introduction

The category of visual stimuli has been reliably decoded from patterns of neural activity in extrastriate visual cortex. It has yet to be seen whether object identity can be inferred from this activity. To address this question, we used high-resolution fMRI imagingat 3.0 T to measure responses in human extrastriate cortex to a set of 12 distinct object images (Figure 1a).

Materials and Methods

We used a custom-built receive-only surface coil to obtain high resolution fMRI images. This coil was small and flexible, with a 7.5 cm diameter, and could be placed on a subject's skull directly over the region to be imaged. Because of the restricted field of view of this coil, we imaged only right hemisphere cortex for these experiments. We imaged 4 subjects (1 female), each of whom participated in multiple recording sessions. For each recording session, we imaged 12 oblique slices, with voxel dimensions of 1 x 1 x 1 mm. (More typical fMRI resolutions are around 3 x 3 x 3 mm–3x3x6 mm, at least 27 times lower in resolution.), collecting a full volume every two seconds.

We used a simple event-related design for our experiments. For each trial, we presented one of the 12 object images to the subject for 2 s, then masked the image with a scrambled image baseline for 10 s.We ran 10-15 event-related scans for each scanning session. This allowed us to analyze trial-by-trial variations in response to different images.

Results

We observed a large number of object-selective voxels (illustrated in Figure 1b), with a large heterogeneity in responses to different stimuli. We summarized the response of each voxel to the different object images by computing the mean response amplitude to that object compared to the scrambled stimulus. As illustrated in Figure 2a, each image produced a range of response amplitudes across voxels. We examined whether this heterogeneous response was reliable by applying a classifier, for which we divided each data session into a training set (odd scans) and a test set (even scans). We computed the cross-correlation of responses between the training and test set for every possible image pairing (Figure 2b). Based on the training data, the classifier "guessed"

what image was present in the test set by choosing the stimulus that produced the highest correlation in each row. For some sessions, the same image always produced the highest correlation in each row, and so the classifier performed at 100%. This indicates the identity of each object can be decoded by examining visually responsive voxels.

For other data sets, noisy voxels contributed unreliable information to the classifier. We were able to identify voxels which could distinguish our stimuli, by sorting visually-responsive voxels according to a reliability criterion (Figure 2c). Using this criterion, we found surprisingly small subsets of the data, sometimes as few as a dozen voxels, could distinguish different object images. Conversely,large subsets of the data, usingthousands of voxels, could also perform well, indicating that only a small proportion voxels were unreliable or unrelated to object representation. However, reverse-sorting voxels did not produce performance above chance—not all voxels contribute equal information about object identity.

Conclusions

Our data show that object-selective cortex can discriminate individual objects. This implies that category-related fMRI responses are not the result of each member of a category producing an identical response. However, category-related responses may result from visual features which are correlated with different categories, but which can also be used to discriminate individual identity. Ongoing research is aimed at identifying redundant representation of information within these regions, and relating fMRI responses to the presence of particular visual information.
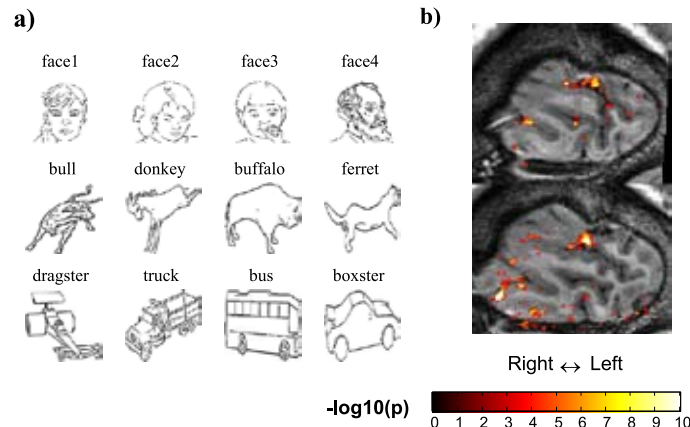

Figure 1: Experimental Design and data. (a) The 12 object stimuli used. (b) Results of a statistical contrast (all objects > scrambled baseline) superimposed over T1-weighted anatomical images from one session. Map is thresholded at log10(p) < -3.
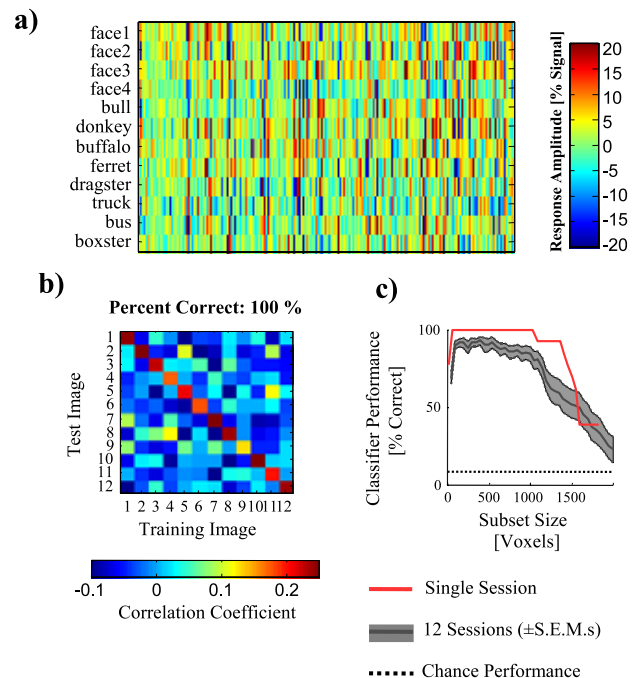
Figure 2: Reliability of object representation across voxels. (a) Response amplitudes across visually-responsive voxels to each image in our stimulus set.(b) Correlation matrix between a test (even scans) and training set (odd scans) from one session. High diagonal values indicate consistent response patterns for the same image compared to other images. (c)Results of the reliability analysis for different subsets of voxels, from one session (red) and across 12 sessions (gray). Voxels were ranked by reliability of responses across the session.

Prefrontal, Parietal, and Medial Temporal Contributions to Item and Temporal-Recency Recognition

Nicole Dudukovic, Anthony Wagner – Department of Psychology and Neurosciences Program

Declarative memory supports remembering what events occurred as well as when they were experienced. Few imaging studies have investigated the neural processes supporting retrieval of temporal information, and extant studies have tended not to match test conditions when comparing item and temporal-recency recognition. Some data suggest that recency decisions recruit left prefrontal and parietal regions typically involved in attempts to recollect or retrieve source information, whereas other evidence suggests that recency decisions recruit right prefrontal regions implicated in orienting to item familiarity. While carefully matching test conditions, the present study sought to investigate the neural processes underlying temporal-order retrieval and item recognition.

In the present study, functional magnetic resonance imaging (fMRI) was conducted while eighteen participants made item recognition and temporal-recency decisions. Functional data were acquired on a 3.0 Tesla GE Signa scanner at the Lucas Center using a gradient echo spiral in-out pulse sequence. During each study phase, participants made an abstract/concrete decision for each word in a series. Subsequently, a brief retention interval was filled through engagement in a spatial working memory task. Event-related fMRI data were then collected while participants encountered three-alternative-forced-choice memory retrieval trials, each consisting of two words from the preceding study phase and one novel word. Participants were to either identify the novel item (Novelty trials) or the more recently presented study item (Recency trials). Relative to correct Novelty decisions, correct Recency decisions elicited greater activation in left frontopolar, dorsolateral prefrontal cortex (PFC), and intraparietal sulcus, suggesting that participants attempted to recollect contextual details to guide their recency decisions. Recency decisions also recruited right superior PFC, indicating a putative reliance on visuo-spatial attention in the service of orienting to familiarity. Correct Recency decisions were further associated with greater left ventral precuneus activation than incorrect Recency decisions, which could either reflect more successful attempts to recollect and retrieve contextual information or an enhanced familiarity signal. By contrast, correct Novelty decisions activated right hippocampus to a greater extent than did correct Recency decisions, which may reflect increased novelty encoding. Temporal-order retrieval appears to activate a distributed network of PFC and parietal regions, suggesting that both recollective and familiarity processes may play a role in determining the relative recency of an event.

Forgetting and Remembering During Competitive Memory Retrieval: Prefrontal and Parietal Cortical Mechanisms Impact Episodic Memory Suppression and Recovery

Brice Kuhl[1], Anthony Wagner[1,2] – [1]Department of Psychology, [2]Neurosciences Program

Episodic retrieval often involves selection of a target amidst interference from competing memories. While selection of target memories facilitates later retrieval of those targets (a benefit of memory rehearsal), there are often adverse consequences for memories which are selected against—namely, forgetting. To explore the neurobiological mechanisms recruited during retrieval in the face of competition and the mechanisms that contribute to the suppression, or forgetting, of selected-against competitors, we used fMRI to study retrieval-induced forgetting (Anderson, Bjork, & Bjork, 1994). Participants (n=13) initially studied cue–associate word pairs, learning multiple associates for each cue. Subsequently, participants performed retrieval practice for some of the associates of some of the cues. Specifically, participants practiced retrieving half of the associates for half of the cue words. Finally, a cued recall test was administered for all items.

Behavioral data replicated the standard retrieval-induced forgetting effect: practiced associates were better recalled than unpracticed associates of an unpracticed cue, whereas unpracticed associates of a practiced cue (competitors) were less likely to be recalled than unpracticed associates of an unpracticed cue (baseline items). The impaired recall of competitors relative to baseline items provides critical behavioral evidence for suppression of competing memories. Initial fMRI analyses targeting the neural processes associated with suppression and the recovery of selected-against memories revealed two main findings. First, fMRI data collected during retrieval practice revealed a correlation between the magnitude of activation in intraparietal sulcus (IPS) and the extent of forgetting (suppression) of competing memories, suggesting a role of IPS in internally guiding selective attention to target memory representations. Second, successful retrieval of selected-against competitors on the final test was associated with increased activity in dorsolateral prefrontal cortex (DLPFC), suggesting that DLPFC is involved in overcoming suppression such that competitors can be successfully recovered. Taken together, these data provide evidence for a consequence of IPS selective attention mechanisms for memory suppression during competitive retrieval, and of DLPFC in overcoming interference in service of remembering.

The Neural Bases of Amusement and Sadness: A Comparison of Block Contrast and Subject-Specific Emotion Intensity Regression Approaches

PHILIPPE R. GOLDIN, CENDRI A.C. HUTCHERSON, KEVIN N. OCHSNER, GARY H. GLOVER, JOHN D.E. GABRIELI, JAMES J. GROSS
DEPARTMENTS OF PSYCHOLOGY, RADIOLOGY

Neuroimaging studies have made substantial progress in elucidating the neural bases of emotion. However, few studies to date have directly addressed the subject-specific, time-varying nature of emotional responding. In the present study, we employed functional magnetic resonance imaging to examine the neural bases of two common emotionsˆamusement and sadnessˆusing both (a) a stimulus-based block contrast approach and (b) a subject-specific regression analysis using continuous ratings of emotional intensity. Thirteen women viewed a set of nine 2-min amusing, sad, or neutral film clips two times. During the first viewing, participants watched the film stimuli. During the second viewing, they made continuous ratings of the intensity of their own amusement and sadness during the first film viewing. For sad films, both block contrast and subject-specific regression approaches resulted in activations in medial prefrontal cortex, inferior frontal gyrus, superior temporal gyrus, precuneus, lingual gyrus, amygdala, and thalamus. For amusing films, the subjectspecific regression analysis demonstrated significant activations not detected by the block contrast in medial, inferior frontal gyrus, dorsolateral prefrontal cortex, posterior cingulate, temporal lobes, hippocampus, thalamus, and caudate. These results suggest a relationship between emotion-specific temporal dynamics and the sensitivity of different data analytic methods for identifying emotion-related neural responses. These findings shed light on the neural bases of amusement and sadness, and highlight the value of using emotional film stimuli and subject-specific continuous emotion ratings to characterize the dynamic, time-varying components of emotional responses.

Attention and Emotion: Does Rating Emotion Alter Neural Responses to Amusing and Sad Films?

C.A. HUTCHERSON, P.R. GOLDIN, K.N. OCHSNER, J.D. GABRIELI, L. FELDMAN BARRETT, J.J. GROSS – DEPARTMENT OF PSYCHOLOGY

Functional neuroimaging of affective systems often includes subjective self-report of the affective response. Although self-report provides valuable information regarding participants' affective responses, prior studies have raised the concern that the attentional demands of reporting on affective experience may obscure neural activations reflecting more natural affective responses. In the present study, we used potent emotion-eliciting amusing and sad films, employed a novel method of continuous self-reported rating of emotion experience, and compared the impact of rating with passive viewing of amusing and sad films. Subjective rating of ongoing emotional responses did not decrease either self-reported experience of emotion or neural activations relative to passive viewing in any brain regions. Rating, relative to passive viewing, produced increased activity in anterior cingulate, insula, and several other areas associated with introspection of emotion. These results support the use of continuous emotion measures and emotionally engaging films to study the dynamics of emotional responding and suggest that there may be some contexts in which the attention to emotion induced by reporting emotion experience does not disrupt emotional responding either behaviorally or neurally.

Amygdala Reactivity and Mood-Congruent Memory in Individuals at Risk for Depressive Relapse

WIVEKA RAMEL[1], PHILIPPE GOLDIN[1], LISA EYLER[2], IAN GOTLIB[1], JOHN MCQUAID[2] – [1]STANFORD UNIVERSITY, [2]VA SAN DIEGO HEALTHCARE SYSTEM & UNIVERSITY OF CALIFORNIA SAN DIEGO

INTRODUCTION

Cognitive diathesis-stress theories posit that individuals with a history of major depression have a latent cognitive vulnerability, which makes them susceptible to relapse. This vulnerability can manifest as mood-congruent memory biases in sad mood. A potential neural substrate of mood-congruent memory is the amygdala, as this structure is implicated in memory for emotionally arousing stimuli. The goal of the current study was to examine the role of the amygdala in retrieval of negatively valenced words before and after a sad mood induction in individuals with or without a history of recurrent major depression.

METHOD

A matched sample of 14 healthy remitted depressed (RD) and 14 never depressed (ND) individuals were scanned using functional magnetic resonance imaging (fMRI) while performing a self-referent encoding/ evaluation task (SRET) preceding and following a sad mood induction procedure. After each SRET, participants did a free recall test on the words in the SRET.

RESULTS

The results indicated that following a sad mood induction, bilateral amygdala response to valenced words during encoding was associated with increased recall of negative self-referent words for RD participants only. This relationship was not present before the sad mood induction and was not seen in individuals without a history of depression regardless of mood state. The relationship was exhibited by a subgroup of female RD individuals with a specific psychiatric history and cognitive-affective profile.

DISCUSSION

These results are consistent with cognitive diathesis-stress theories and suggest a role for the amygdala in mediating mood-congruent and self-referent retrieval during transient sad mood in individuals vulnerable to depression relapse.

Detection and Repair of Transient Artifacts in fMRI Data

PAUL K. MAZAIKA, SUSAN WHITFIELD, JEFF COOPER - DEPARTMENT OF PSYCHOLOGY

INTRODUCTION

Large data artifacts can make true activations disappear or cause false activations to arise. Artifacts may arise from sudden motions, deep breaths, or electrical noise. One approach to correct outliers is to diagnose abnormal events in the data and demonstrate they can be safely removed (Luo and Nichols, Neuroimage (2003)). Another method is purely statistical, namely to screen outliers on a voxel-wise basis and repair them automatically (Cox, AFNI 3dDespike program (2002)). Our objective is to automatically detect physically-based artifacts, and provide user-friendly tools to repair large amounts of data.

MATERIALS AND METHODS

Automated and semi-automated algorithms were built to detect and repair volume and slice artifacts. Visualization with contrast images helps identify physical sources of the artifacts. Movie viewing of the contrast images allows user to review of intensity changes in every voxel over time.

DISCUSSION

Transient artifacts (large amplitude and short duration noise bursts) occur in many data sets. They cause 1.5% fluctuations of the global mean, and over 10% fluctuations in the intensity measured on an individual voxel. Contrast images showed sharp spikes in the global mean from sudden subject motion, and dips in the global mean associated with unusual breathing patterns. Other common artifacts include motion, eye movement and normal physiological noise. "Normal" fluctuations in the global mean are within 0.5% of the time series mean. Software was developed to screen volume and slice artifacts from the data. The algorithms automatically remove the spiral alias, create a head mask, and set up a GUI for a user to adjust thresholds for volume and slice repair.
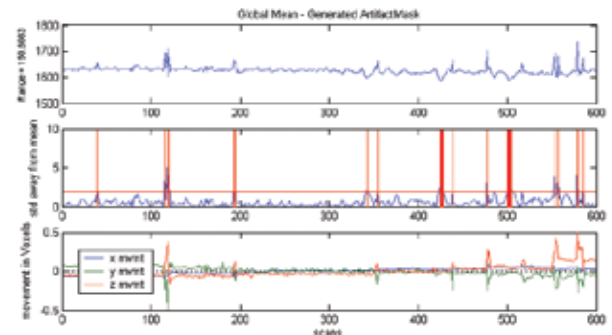
Global time history used to detect unusual scan volumes. Data was collected from Lucas Center 3T magnet, with TR = 1.4 sec. Subject was an 8 year old child using a bite bar. Second graph shows volumes with unusual intensities. Bottom graph shows correlation with subject motion.

Default thresholds were set bases on analyses of more than 100,000 volumes of data. Artifact detection and repair is applied before any preprocessing. The software has been applied to numerous data sets to improve the statistical confidence of activation measurements.

CONCLUSION

Physically-based outliers can be removed without compromising data integrity. Automated detection and repair methods were developed to clean up physically-based transient artifacts to improve statistical analysis. The software is compatible with SPM and user-friendly for bulk data processing. Software and documentation are available for download from http://gablab.stanford.edu/tools.htm.

The Effects of Perceptual Similarity on Item Recognition and Repetition Suppression in the Medial Temporal Lobe

R. K. OLSEN[1]; B. D. GONSALVES[1]; A. R. PRESTON[1]; T. CURRAN[2]; K. A. NORMAN[3]; A. D. WAGNER[1] - [1]DEPT. PSYCHOLOGY & NEUROSCIENCES PROGRAM, STANFORD UNIVERSITY; [2]DEPT. OF PSYCHOLOGY, UNIV. OF COLORADO, BOULDER; [3]DEPT OF PSYCHOLOGY, PRINCETON UNIVERSITY

INTRODUCTION

Declarative memory permits an organism to recognize stimuli as previously encountered. One basis for recognition is item memory strength, which may support the perception of stimulus familiarity. Recognition memory models posit that stimulus familiarity depends on the global similarity between a test probe and studied items. Though the medial temporal lobes are known to be critical for declarative memory, at present the neural mechanisms supporting differences in memory strength remain poorly specified. In this experiment, high-resolution functional MRI (fMRI) indexed correlates of graded memory strength in the human brain, focusing on the medial temporal lobe cortex (parahippocampal and perirhinal cortex).

MATERIALS AND METHODS

At study, faces were incidentally encoded during performance of a similarity judgment task. At test (scanned), a subsequent recognition memory test varied study-test perceptual similarity across three classes of memory probes: studied faces, faces that were morphs between a studied and an unstudied face, and unstudied faces. Subjects responded using a five-point confidence scale, indicating whether they recognized the face as old or new (1= sure new, 5= sure old).

RESULTS

Behavioral results showed that item strength was modulated by study-test perceptual similarity. fMRI analyses revealed a decrease in medial temporal cortical activation that was sensitive to similarity and that varied with perceived item strength.

CONCLUSION

Memory strength is affected by study-test similarity and is associated with repetition suppression in medial temporal cortex.

Atypical Brain Development : Neuroanatomical and Neurofunctional Studies

CENTER FOR INTERDISCIPLINARY BRAIN SCIENCES RESEARCH, DEPARTMENT OF PSYCHIATRY AND BEHAVIORAL SCIENCES

INTRODUCTION

The Center for Interdisciplinary Brain Sciences Research includes a major research component dedicated to structural and functional neuroimaging in individuals with brain disorders as well as typically developing individuals. In this report, we summarize several recent structural and functional MRI studies conducted at the Lucas Center on individuals with fragile X syndrome, Turner syndrome, autism, and ADHD that illustrate how magnetic resonance imaging has helped bridge our understanding of associations between gene, brain, and behavior in atypical development.

MATERIALS AND METHODS

Images in these studies were acquired at the Lucas Center: for structural studies, images were acquired on the 1.5T GE Signa scanner and analyzed using BrainImage (SPNL) and SPM99 software; functional studies were performed on either the 1.5T GE scanner using a custom built whole head coil or the 3T GE Signa scanner.

RESULTS

FRAGILE X SYNDROME

Michael D. Greicius,[1,2] Jesse M. Boyett-Anderson,[2] Vinod Menon,[2,3,4] Allan L. Reiss[2,3,4] - Departments of [1]Neurology and Neurological Sciences; [2]Psychiatry and Behavioral Sciences; [3]Program in Neuroscience; [4]Stanford Brain Research Institute

Fragile X syndrome (fraX), the most common heritable cause of developmental disability, is associated with IQ, memory, and visuospatial processing deficits. The fragile X gene (*FMR1*) is prominently transcribed in two regions critical to memory encoding and attention: the hippocampus and the basal forebrain. To probe functional MRI activation abnormalities associated with the disorder, girls with fraX and age-matched, typically-developing girls were scanned during a test of visual memory encoding. While there were considerable similarities in activation patterns between the two groups, the girls with fraX showed significantly less activation in the hippocampus and the basal forebrain. This is the first study, to our knowledge, demonstrating functional deficits in fraX subjects in brain regions known to have the highest *FMR1* transcription. The basal forebrain deficit will be particularly important to confirm because it raises the possibility of treating

Fig. 1. Group activation during visual encoding. Axial images showing group activation during the visual encoding task for the FraX group (a) and control group (b). Functional images are overlaid on the respective group-averaged structural scans. The left side of the image corresponds to the left side of the brain.
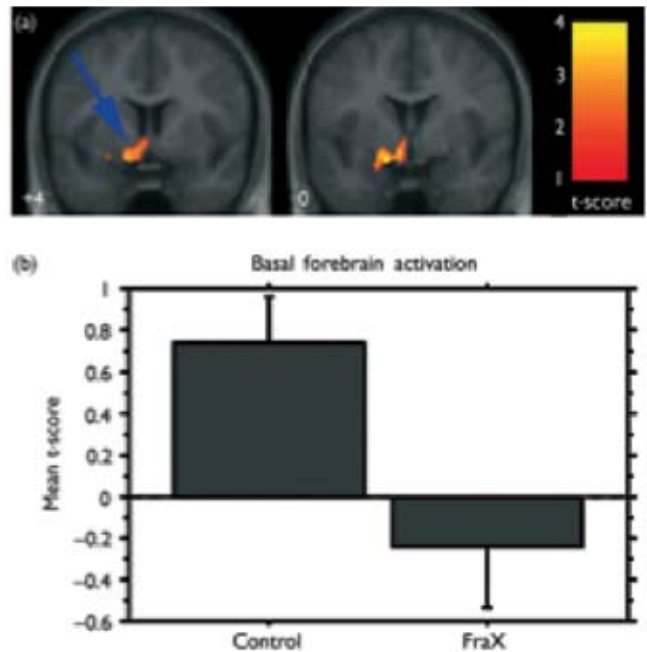

Fig. 2. Deficient basal forebrain activation in FraX. Coronal images showing regions activated more in the control group vs the FraX group after covarying for FSIQ and performance on the recognition task (a). The functional map was overlaid on the average structural map from the control group. The blue arrow indicates the approximate location of a 29 voxel subcluster in the region of the nucleus basalis whose average activation in the two groups is shown in (b). A two- sample t-test demonstrated a significant difference in the average activation for the nucleus basalis ROI after (and before) co-varying for IQ and performance (df1/426, t1/42.79, p1/40.01). After controlling for IQ and performance, the mean tscore was 0.74 (s.e. 0.22) for the control group and ^ 0.25 (s.e. 0.29) for the FraX group. The black bars in (b) indicate s.e.

this prevalent disorder with currently available medicines such as the acetylcholinesterase inhibitors.

TURNER SYNDROME (TS)

Shelli R. Kesler[1], Amy Garrett[1], Bruce Bender[3], Jerome Yankowitz[4], She Min Zeng[4], Allan L. Reiss[1,2] [1]Department of Psychiatry and Behavioral Sciences, [2]Program in Neuroscience, [3]Brain Research Institute, Stanford University; [4]Department of Pediatrics, National Jewish Medical and Research Center, Denver

Turner syndrome (TS) results from partial or complete X-monosomy and is characterized by deficits in visuospatial functioning as well as social cognition and memory. Neuroimaging studies have demonstrated volumetric differences in the parietal region of females with TS compared to controls. In the present study, we scanned 30 females with TS and 29 age-matched controls to examine amygdala and hippocampus morphology in an attempt to further understand the neural correlates of psychosocial and memory functioning in TS. Volumetric analyses of the MRI scans included whole brain segmentation and manual delineation of the amygdala and hippocampus. Compared to controls, participants with TS demonstrated significantly larger left amygdala gray matter volumes, irrespective of total cerebral tissue and age. Participants with TS also showed disproportionately reduced right hippocampal volumes, involving both gray and white matter. Amygdala and hippocampal volumes appear to be impacted by X-monosomy. Aberrant morphology in these regions may be related to the social cognition and memory deficits often experienced by individuals with TS. Further investigations of changes in medial temporal morphology associated with TS are warranted.
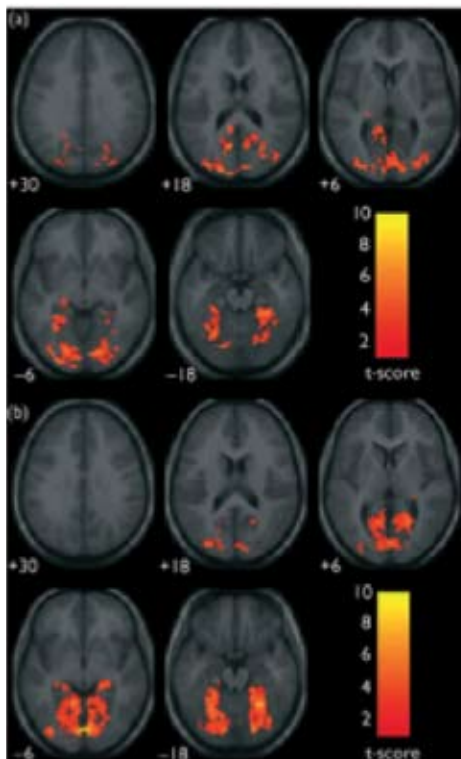
AUTISM SPECTRUM DISORDERS – WHITE MATTER STRUCTURE IN AUTISM

Naama Barnea-Goraly, Hower Kwon, Vinod Menon, Stephan Eliez, Linda Lotspeich, Allan L. Reiss

Individuals with autism have severe difficulties in social communication and relationships. Prior studies have suggested that abnormal connections between brain regions important for social cognition may contribute to the social deficits seen in autism. In this study, we used diffusion tensor imaging to investigate white matter structure in male children and adolescents with autism and age-, gender-, and IQ-matched control subjects. Reduced fractional anisotropy (FA) values were observed in white matter adjacent to the ventromedial prefrontal cortices and in the anterior cingulate gyri as well as in the temporoparietal junctions. Additional clusters of reduced FA values were seen adjacent to the superior temporal sulcus bilaterally, in the temporal lobes approaching the amygdala bilaterally, in occipitotemporal tracts, and in the corpus callosum. These findings suggest that disruption of white matter tracts between regions implicated in social functioning may contribute to impaired social cognition in autism.
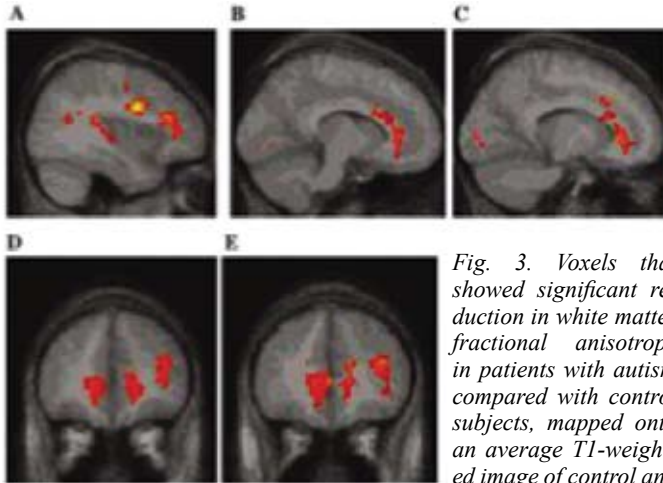
Fig. 3. Voxels that showed significant reduction in white matter fractional anisotropy in patients with autism compared with control subjects, mapped onto an average T1-weighted image of control and autism *brains. (A, B, C) Sagittal view, significant clusters shown in the ventromedial prefrontal region (A, B), the anterior cingulate and subgenual area (C), the corpus callosum(B, C), the superior temporal gyrus (A), centrumsemiovale (A), and temporoparietal junction (A). (D) Coronal view, significant clusters shown in the ventromedial prefrontal region bilaterally and along the middle frontal sulcus (D, E).*
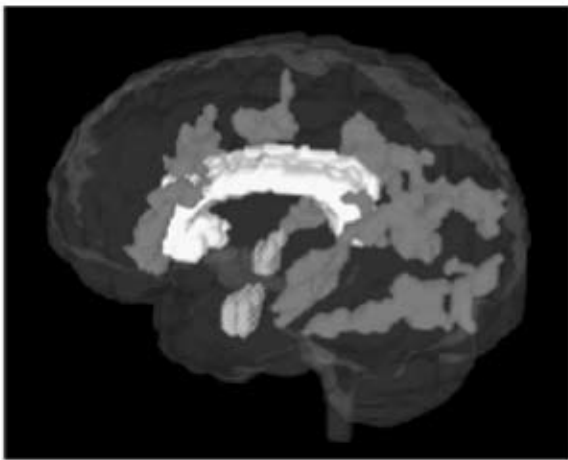
Fig. 4. A three-dimensional representation of the aberrant white matter (dark gray) in relation to the corpus callosum (white), and the amygdala (checkered gray).

AUTISM SPECTRUM DISORDERS – EMOTIONAL ATTRIBUTION IN HIGH-FUNCTIONING INDIVIDUALS

Judith Piggot, Hower Kwon, Dean Mobbs, Christine Blasey, Linda Lotspeich, Vinod Menon, Susan Bookheimer, Allan Reiss.

High-functioning autism spectrum disorders (ASD) include Asperger's syndrome and high-functioning autism. Despite normal intelligence, high-functioning individuals with ASD have marked deficits in social understanding. Although individuals with high-functioning ASD are able to attribute emotion from basic facial expressions, many of the deficits in social cognition are consistent with reduced expertise in the attribution of emotion. Individuals with ASD have particular difficulty attributing emotion from more subtle facial expressions and multiple facial expressions in actual social situations. In this study, high-functioning individuals with ASD and controls attributed emotion from basic facial expressions in two tasks (the perceptual emotion match [EM] task and the linguistic emotion label [EL] task) while fMRI scans were acquired. Accuracy, response time, and average activation were measured for each ROI. There was no significant difference in accuracy, response time, or ROI activation between groups performing the EL task. The ASD group was as accurate as the control group performing the EM task but had a significantly longer response time and lower average fusiform activation.

The principal finding of this study was that the expertise in the attribution of emotion from basic facial expressions is task-dependent in individuals with ASD. Explanation of the difference in expertise in the ASD group requires consideration of the differences between task demands. The presentation of a single facial expression and affective labels may facilitate expertise in the attribution of emotion in the EL task. Individuals with ASD may have similar expertise in the EL task because they use a language-based strategy to facilitate the attribution of emotion. Reduced expertise in the perceptual (EM) task may be explained by the absence of affective labels and/or the increased number of facial stimuli presented, constituting an increased global processing load. Individuals with ASD have been suggested to have reduced expertise in the global processing of facial stimuli and during the processing of facial stimuli to activate the ITG, an area associated with feature-based analysis of objects. The use of a feature-based strategy supported outside the fusiform offers a possible explanation for the reduced expertise and reduced fusiform activation when individuals with ASD attribute emotion from basic facial expressions in the perceptual (EM) task.

ADHD

Leanne Tamm, Vinod Menon, Allan Reiss

Directed attention, the ability to allocate and direct attention toward a salient stimulus, is impaired in Attention Deficit Hyperactivity Disorder (ADHD). This construct is often assessed with target detection or Oddball tasks, and individuals with ADHD perform poorly on such tasks. However, to date, the specific brain structures or neural mechanisms underlying dysfunction in target detection of individuals with ADHD have not been identified. This study investigated the neural correlates of target detection dysfunction in ADHD using event-related fMRI.

Behavioral and brain activation data were collected from 14 adolescent males with ADHD-Combined Type and 12 typically developing age matched male controls while the subjects performed a visual Oddball task. Individuals with ADHD made significantly more errors of commission than controls. Further, compared with controls, individuals with ADHD showed significantly less activation bilaterally in the parietal lobes (including superior parietal gyrus, and the supramarginal, and angular gyri of the inferior parietal lobe), right precuneus, and thalamus. Adolescents with ADHD demonstrated significant impairments in their ability to direct and allocate attentional resources. These difficulties were associated with significant aberrations in the parietal attentional system, which is known to play a significant role in attention shifting and detecting specific or salient targets. Thus, dysfunction in the parietal attentional system may play a significant role in the behavioral phenotype of ADHD.
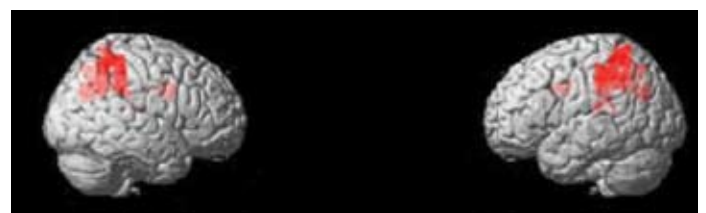

Fig. 5. Surface rendering of regions in which the control group activated more

Conclusion

These results illustrate how structural and functional MRI combined with genetic analyses and behavioral/cognitive measures, an approached called "behavioral neurogenetics" can provide insights into our understanding of how both genetic and environmental factors contribute to complex variations in atypical human development.

References

1. Greicius MD, Boyett-Anderson JM, Menon V, Reiss AL (2004). "Reduced basal forebrain and hippocampal activation during memory encoding in girls with fragile X syndrome." Neuroreport 15(10):1579-83.

2. Kesler SR, Garrett A, Bender B, Yankowitz J, Zeng SM, Reiss AL. (2004). "Amygdala and hippocampal volumes in Turner syndrome: a high-resolution MRI study of X-monosomy." Neuropsychologia 42(14):1971-8.
3. Barnea-Goraly N, Kwon H, Menon V, Eliez S, Lotspeich L, Reiss AL (2004). "White matter structure in autism: preliminary evidence from diffusion tensor imaging." Biol Psychiatry 55(3):323-6.
4. Piggot J, Kwon H, Mobbs D, Blasey C, Lotspeich L, Menon V, Bookheimer S, Reiss AL (2004). "Emotional attribution in high-functioning individuals with autistic spectrum disorder: a functional imaging study." 43(4):473-80.
5. Tamm L, Menon V, Reiss AL: Parietal attentional system aberrations during target detection in adolescents with attention deficit hyperactivity disorder: Event-related fMRI evidence. American Journal of Psychiatry (in press).

Neural Basis of Human Territoriality

Fumiko Maeda, Christa L. Watson, Shelli R. Kesler, Keith E. Bettinger, Allan L. Reiss - Center for Interdisciplinary Brain Sciences Research, Department of Psychiatry and Behavioral Sciences

Introduction

Territoriality is a fundamental human behavior that exists everywhere, whether at an individual- or a nation-level. Despite its importance, the neural correlates of human territoriality are virtually unknown. In this study, we used functional magnetic resonance imaging (fMRI) to examine the neural processes underlying territoriality. If theories concerning linkages between animal and human territoriality are true, i.e. that human behaviors are much driven by the "territorial imperative" just like any other animal, then areas such as the nucleus accumbens (NAc), hypothalamus (HYPT), amygdala (AMYG) and thalamus (THAL) may be involved in human territoriality, similar to what has been shown in animals. A second goal of the study was to investigate whether there were gender differences in the neural processes underlying human territoriality. In humans, it is known that, compared to women, men are more territorial and tend to guard spatial boundaries and social power more fervently. Our final goal was to investigate whether there were links between personality traits and neural processes underlying human territoriality.

Materials and Methods

Images in these studies were acquired at the Lucas Center on the 1.5T GE Signa scanner using a custom built whole head coil. Subjects performed a simple computer game devised to elicit human territorial behavior in the form of space-related dominance.

Results

Brain regions that showed significant activation during Territory vs. Rest, and Control vs. Rest conditions included areas known to be involved in visual processing, visuo-spatial attention, motor function, and sensori-motor transformation. Territory and Control conditions were then contrasted by focusing on regions most frequently implicated in animal territorial behavior: bilateral NAc (NAc_{bil}), $THAL_{bil}$, $HYPT_{bil}$, and $AMYG_{bil}$. There was significant activation in NAc_{left} and $THAL_{bil}$, with a trend for significance in $AMYG_{bil}$ and $HYPT_{bil}$, consistent with studies of animal territoriality. Direct comparisons between males and females revealed significantly greater activation in males in the NAc_{bil}, $THAL_{bil}$, $AMYG_{right}$ and $HYPT_{left}$, in which the greater $AMYG_{right}$ activation was driven by deactivation in females. Based on the animal literature, it appears that this region is more generally related to aggression, which can occur under many conditions including defense of offspring or predatory behavior. Activity in the AMYG can be mediated through testosterone, which is consistent with the marginal activation of the AMYG during the territory condition in males - during which no explicit aggressive behavior was elicited.

We used the NAc_{left} as an initial seed region to investigate the functional connectivity of the selected ROIs. All ROIs showed significant correlation with the time course of NAc_{left}. When direct comparisons were performed examining areas with *greater* correlation in males than females, there was a significant effect in $THAL_{bil}$. Territorial performance correlated significantly with functional connectivity between NAc_{left} and $THAL_{bil}$ for both males and females. Only males, however, showed significant correlation between territorial performance and functional connectivity between NAc_{left} and $AMYG_{right}$. Together with the finding of reduced activation of the AMYG in females, it is tempting to speculate that the AMYG, as the gateway to the limbic system, plays an important gender-specific role in territorial behavior beyond aggression.

Finally, we examined correlations between brain activation and the personality traits of extraversion (NEO-E) and neuroticism (NEO-N). There was no significant correlation between brain activation and NEO-E or NEO-N. When gender was examined separately, males showed a significant correlation between NEO-E and activation in $AMYG_{right}$. Females showed no significant correlation or statistical trend between the NEO-E score and activation in any of these areas. None of the ROIs showed significant correlations with NEO-N in either males or females. The absence of personality-brain correlations in females could be partly attributable to the lack of significant AMYG activation in females for the Territory vs. Control contrast and the relatively small sample size.

Conclusion

Taken together, the results presented here provide evidence of a putative neural basis underlying territorial behavior in humans. These findings reinforce the concept of an intimate relation between reward, emotion, motivation, threat and goal-directed behavior underlying territorial behavior. Further, it supports the view that animals and humans share similar processes underlying territoriality. These studies may eventually lead to a better understanding of human behavioral variation within the broader contexts of work, socialization and politics.
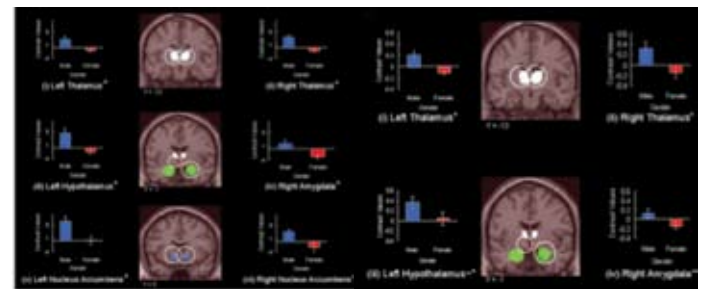

Fig. 1a   Fig. 1b

Fig. 1. *Gender Difference in Neural Responses to Territory Task. ROIs used for analyses (center column in figure) -- THAL-white, HYPT–red, AMYG–green, NAc–blue. Contrast values from the ROIs that were significant when compared between genders (p_{svc}=0.01) are extracted. Error bars represent s.e.m. *: p<0.01, ~*: p0.05 (a) Contrast values of brain activation are compared. Peak Tal coordinates -- (i)–12 –16 1, (ii) 22 –33 5, (iii) -8 -6 –6, (iv) 34 0 –14, (v) -8 8 –4, (vi) 10 9 -6. (b) Contrast values of functional connectivity are compared. Peak Tal coordinates -- (i) -10 –5 13, (ii) 8 –13 10, (iii) -8 -6 –6, and (iv) 30 -8 –13.*

Delayed Hemodynamic Responses in Schizophrenia

Judith M. Ford[1], Matthew B. Johnson[1], Susan L. Whitfield[2], Daniel H. Mathalon[1] – [1]Department of Psychiatry, Yale University, [2]Department of Psychology, Stanford University

Introduction

While there are many reports of reduced amplitude of hemodynamic responses in schizophrenia, there are no reports of delayed hemodynamic responses, in spite of event-related brain potential (ERP) evidence of slowed neural responses. Recently, Henson et al (2002) proposed a new method for testing small latency effects (<2 sec) in hemodynamic responses.

Materials and Methods

fMRI data were collected during a visual oddball task with infrequent (12%) targets (K) and frequent standards (X), presented every 1-3 sec pseudorandomly, with 7-24 sec between targets. SPM99 yielded parameter estimates for the hemodynamic response and its temporal derivative (TD). Beta images reflecting hemodynamic response magnitude to target stimuli were minimally thresholded (p<.05, uncorrected), and latencies were estimated for surviving voxels using TD and hemodynamic response beta values. DSM-IV schizophrenia patients (n=12) and sex- and age-matched healthy control subjects (n=12) were recruited from the community.

Results and Discussion

Although groups differed only mimimally in activation height, hemodynamic responses were significantly delayed in patients, in basal ganglia, thalamus, and cerebellum, as well as, superior parietal, anterior
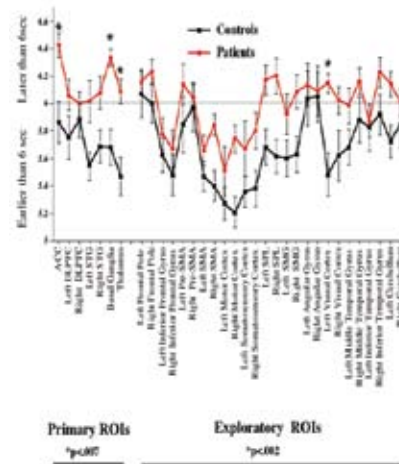
Figure 2: The average latency in seconds for activation at each ROI listed in Table 2 is plotted separately for controls and patients. The line at 6 sec marks the boundary between activations occurring earlier and later than expected. Asterisks over the Primary ROIs indicate the necessary p<.007 level of significance was achieved, and asterisks over the Exploratory ROIs, indicate the necessary p<.002 level of significance was achieved.

cingulate, auditory, somatosensory, motor, and visual cortices. Psychomotor slowing reflected in reaction times to targets recorded outside the magnet was related to hemodynamic slowing in basal ganglia, anterior cingulate, thalamus, and left cerebellum in controls.

Conclusion

Delays in the hemodynamic response have far-reaching implications for understanding the pathophysiology of schizophrenia from slowed neural responses to slowed substrate delivery. In addition, this report raises methodological issues regarding modeling hemodynamic responses in patients and controls.
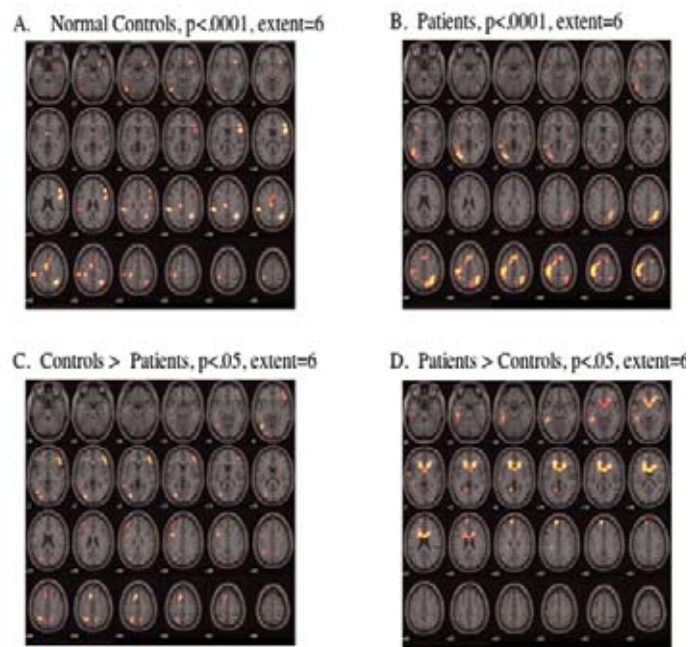

Figure 1: Beta images are shown in successive 4mm axial images from bottom to top of the brain for controls (a) and patients (b) illustrating location of activations to correctly detected target Ks, thresholded at p<.0001, with an extent threshold of 6 contiguous voxels. Contrast images (thresholded at p<.05, extent=6) for controls > patients (c) and patients > controls (d) for correctly detected target Ks.
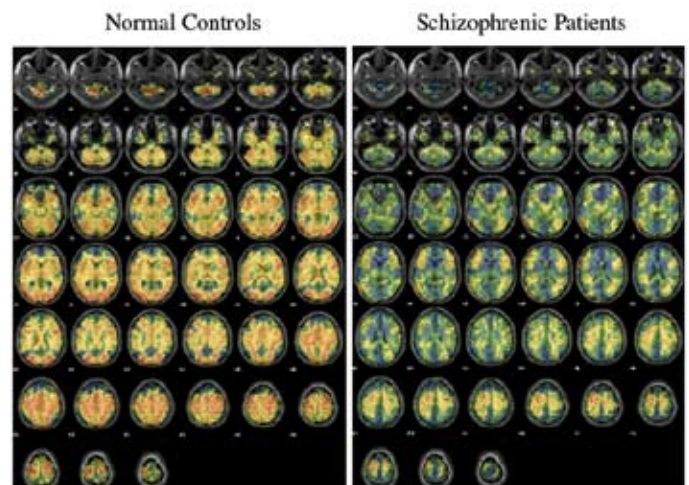

Figure 3. Average relative latencies for each voxel for both groups are shown in successive 4mm axial images from bottom to top of the brain. Each average latency value is based on data from all the subjects with activated voxels (p<.05). Not all voxels for each subject are included in the calculation of the averages. Voxels with an earlier than expected (6 sec) hemodynamic response appear in red/yellow tones, with red being even earlier than yellow. Voxels with a later than expected (6 sec) hemodynamic response appear in blue/green, with blue being even later than green.

Functional Disconnectivity in Schizophrenia Is Related to Severity of Auditory Hallucinations

Judith M. Ford[1], E. Max Gray[2], Susan L. Whitfield[2], Gary Glover[3] Daniel H. Mathalon[1] – [1]Department of Psychiatry, Yale University; [2]Department of Psychology, Stanford University; [3]Department of Radiology, Stanford University

Introduction

Communication between frontal lobes, where speech and verbal thoughts are generated, and temporal lobes, where they are perceived, may be dysfunctional in schizophrenia. This disconnection may underlie the failure of patients with schizophrenia to recognize inner speech and thoughts as self-generated, resulting in the misattribution of internal language-related experiences to external "voices". The efference copy/corollary discharge mechanism may be the basis for frontal-temporal communication during talking and inner speech. For example, as you begin to speak, an efference copy of the motor command is sent to auditory cortex, resulting in a corollary discharge. This mechanism acts to suppress cortical responses to self-produced sounds. Auditory event-related potentials (ERPs) from the temporal lobe confirm its dysfunction in schizophrenia. We performed a functional magnetic resonance imaging (fMRI) study to localize more precisely the temporal lobe regions involved in this process.

Materials and Methods

FMRI data were collected while 21 patients with schizophrenia (DSM-IV) and 21 age- and gender-matched healthy adults uttered the syllable [a] aloud and then listened to it played back through headphones. Both talking and listening were timed to occur only during the silent periods of clustered acquisition sequences. Analysis of event-related fMRI data focused on superior (STG), middle (MTG), and inferior temporal gyri (ITG) activations in the talking-listening and listening-talking contrasts.

Results and Discussion

There was less bilateral temporal lobe activation during talking than listening in healthy controls (Figure 1, top). This was the expected pattern, consistent with the action of a corollary discharge mechanism suppress-

Controls

Patients with Schizophrenia
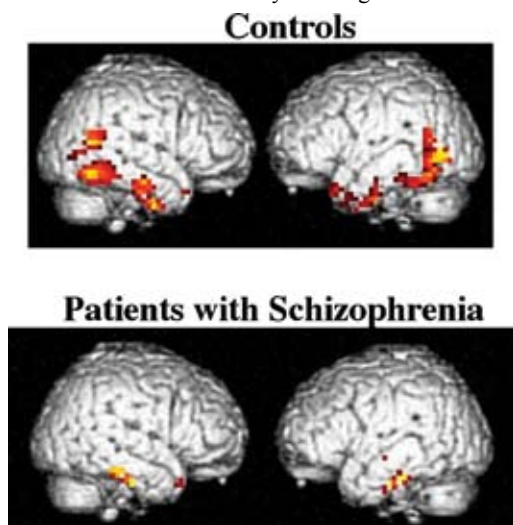
Figure 1: Temporal lobe suppression during Talking compared to Listening (Listening – Talking).
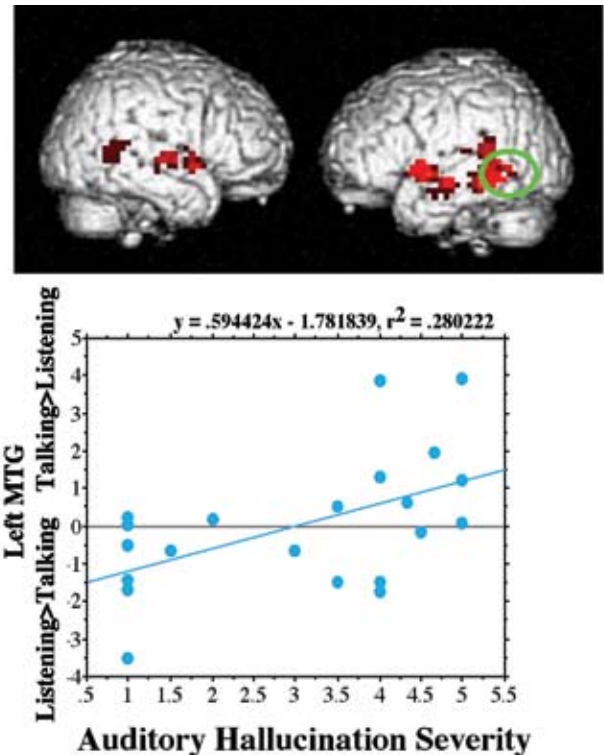

$$y = .594424x - 1.781839, r^2 = .280222$$

Figure 2: Correlation between Talking-Listening and severity of auditory hallucinations in schizophrenic patients.

ing auditory cortex during talking. In patients, there was no suppression of STG or MTG activation during talking, but there was some ITG suppression (Figure 1, bottom). Instead, patients had more activation for the Talking-Listening contrast than did controls (not shown here).

Figure 2 (upper) displays the correlation Statistical Parametric Maps (SPMs) indicating temporal lobe regions where activation height is correlated with hallucination severity for the Talking – Listening contrast. Figure 2 (lower) shows each patient's average activation height for the left MTG plotted against his hallucination severity score. Patients with the most severe auditory hallucinations had the least suppression in STG and MTG (p<.03) during talking (i.e., these patients had more activation during talking than listening). There was no region of the temporal lobe, or the whole brain, which showed the opposite correlation with hallucinations.

Conclusion

These data suggest that the corollary discharge mechanism that works to suppress temporal lobe activity during talking, and perhaps during thinking and internal language-related experiences, is dysfunctional in patients with schizophrenia. This is most true in those who experience the most severe auditory hallucinations.

Dysmorphology and Microstructural Degradation of the Corpus Callosum: Interaction of Age and Alcoholism

[1,2]Adolf Pfefferbaum, M.D., [3]Elfar Adalsteinsson, Ph.D., [1]Edith V. Sullivan, Ph.D. – [1]Neuroscience Program, SRI International, Menlo Park, CA; [2]Department of Psychiatry and Behavioral Sciences, [3]Department of Radiology, Stanford University

Introduction

Chronic alcohol abuse is a universal health and societal problem, with a growing prevalence in the older population. Alcoholism is a source of substantial deterioration in brain tissue and has been most consistently observed in vivo and postmortem in white matter.

Materials and Methods

To quantify the potential compounded effect of age and alcoholism, we used conventional structural MRI and diffusion tensor imaging (DTI) to examine the macrostructural and microstructural integrity the corpus callosum, one of the most prominent white matter structures of the brain, in 131 adults, age 27 to 75 years. Microstructural integrity was measured with DTI as fractional anisotropy (FA), an index of intravoxel orientational coherence of white matter fibers, and bulk mean diffusivity <D>, an index of intravoxel water motility.

Results

Compared with the 74 controls, the 40 alcoholic men and 17 alcoholic women, who were abstinent from alcohol for an average of 3 months, showed similar patterns and extents of callosal shrinkage, which was greatest in the genu and body and less prominent in the splenium. The macrostructural shrinkage was accompanied by abnormalities in anisotropy and diffusivity of the microstructural environment of these callosal regions, indicative of disruption of structural constituents of local brain white matter. Correlational analyses revealed an age-alcohol interaction, where older alcoholics had smaller genu and splenium and higher diffusivity in these regions than younger alcoholics. Significant correlations between regional MRI and DTI measures and performance on working memory, visuospatial ability, and gait and balance provided evidence for the functional ramifications of the callosal abnormalities.

Grand average images after nonlinear alignment of the midline sagittal SPGR (left) and FA (right) data for 32 control men, 42 control women, 40 alcoholic men, and 17 alcoholic women. The bright area inferior to the genu of the corpus callosum on the FA images is caused by B0 inhomogeneity artifact and is excluded from analysis.
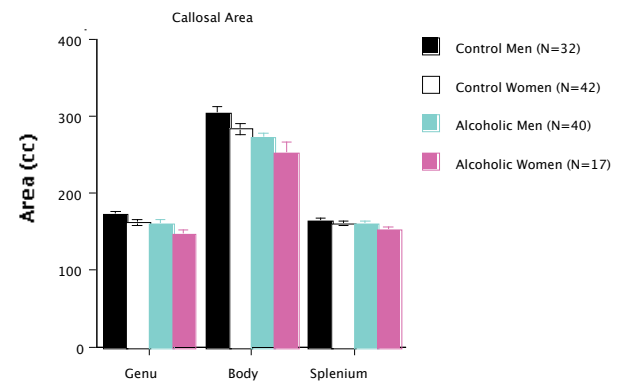
Conclusion

Despite abstinence from alcohol, the interaction of age and recent alcoholism history exerted a compounded untoward effect on callosal macrostructure and microstructure.
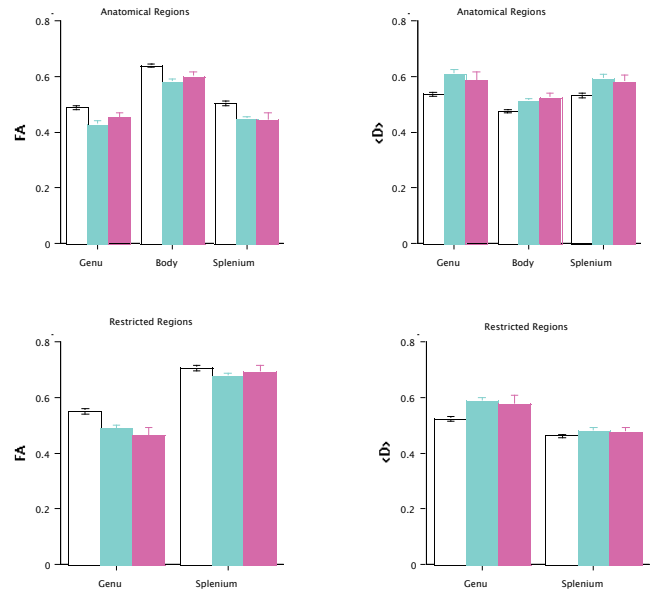
Mean (±S.E.M.) regional FA and <D> values of the corpus callosum in the total group of 74 controls (32 men plus 42 women), 40 alcoholic men, and 17 alcoholic women. These values are not corrected for normal variation in age.

Mean (±S.E.M.) regional midsagittal areas (cc) of the corpus callosum in the control men and women and alcoholic men and women. These values are not corrected for normal variation in intracranial volume or age.

Corpus Callosal Microstructural Integrity Influences Interhemispheric Processing: A Diffusion Tensor Imaging Study

[1]Tilman Schulte, [2]Edith V. Sullivan, [2]Eva M. Mueller-Oehring, [3]Elfar Adalsteinsson, [1,2]Adolf Pfefferbaum, – [1]Neuroscience Program, SRI International, Menlo Park, CA, [2]Department of Psychiatry and Behavioral Sciences; [3]Department of Radiology, Stanford University

Introduction

Normal aging and chronic alcoholism result in disruption of brain white matter microstructure that does not typically cause complete lesions but may underlie degradation of functions requiring interhemispheric information transfer. We used diffusion tensor imaging (DTI) to assess microstructural integrity of the corpus callosum and related it to behavioral measures of interhemispheric processing speed.

Materials and Methods

We used DTI to measure fractional anisotropy (FA), orientation and intravoxel coherence of water diffusion usually in white matter fibers, and bulk mean diffusivity ($<D>$), the amount of intracellular and extracellular fluid diffusion, in 11 men and women meeting DSM-IV criteria for alcohol dependence and 13 age and sex-matched controls. We tested the hypothesis that FA and $<D>$ in the corpus callosum would be correlated with (i) the crossed--uncrossed difference (CUD), testing visuomotor interhemispheric transfer; and (ii) the redundant targets effect (RTE), testing parallel processing of visual information presented to each cerebral hemisphere.

Results

Callosal FA was lower and $<D>$ higher in alcoholics than in controls. Older age was correlated with lower FA and greater diffusivity in controls but not in alcoholics. In controls but not alcoholics, large CUDs correlated with low FA and high $<D>$ in total corpus callosum and regionally in the genu and splenium. In alcoholics but not controls, small RTEs correlated with low FA in genu and splenium and high $<D>$ in the callosal body.

Discussion

We coupled DTI, a sensitive in vivo measure of the integrity of the microstructure of white matter, with tests of interhemispheric processing
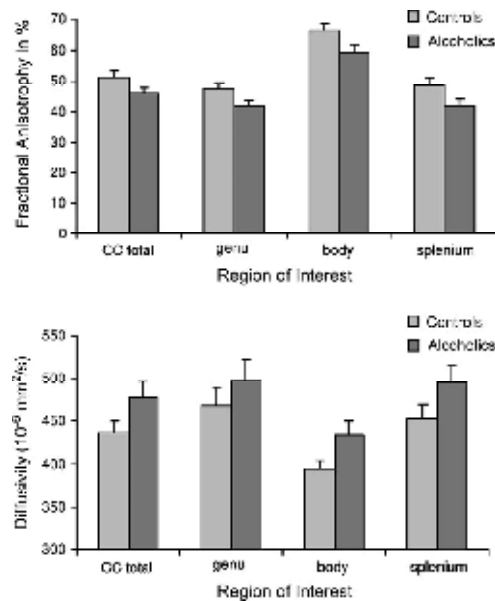

Top: expanded midsagittal view of the fractional anisotropy image of the corpus callosum. The outline was manually drawn on the b 5 0 image and superimposed onto the FA image for quantitation. Geometric lines divide the total corpus callosum into the genu (left), body (middle) and splenium (right). Bottom: full midsagittal FA (left) and $<D>$ (right) image of a 61-year-old healthy man.

in alcoholics and healthy controls. FA of the full extent of the corpus callosum (genu, body and splenium) was abnormally low in alcoholics whereas $<D>$ tended to be greater in all callosal regions in alcoholics than controls. The relationship between DTI and behavioral measures of interhemispheric processing seen in alcoholics provide evidence that subtle but significant microstructural disruption of white fiber tracts linking the hemispheres may be a significant neural mechanism underlying reduced response facilitation in this patient group. Furthermore, even though DTI is normally sensitive to aging, lifetime alcohol consumption had a demonstrably greater effect than aging on disruption of brain white matter microstructure in alcoholics.

Conclusions

DTI is a suitable method for detecting of subtle functional disorders not attributable to classical syndromes arising from disconnection of the hemispheres. The results of the present study provide in vivo evidence for disruption of white matter microstructure in alcoholism and suggest that interruption of white matter fiber coherence contributes to mild yet detectable disturbance in interhemispheric processing.

Raw values (± SEM bars) for FA and $<D>$ of the total callosum and regional of the genu, body and splenium. Controls showed in all corpus callosum regions higher FA than alcoholics (top panel) and alcoholics had higher $<D>$ than controls (bottom panel).

Disruption of Brain White Matter Microstructure by Excessive Intracellular and Extracellular Fluid in Alcoholism: Evidence for Diffusion Tensor Imaging

[1,2]Adolf Pfefferbaum, [1]Edith V. Sullivan, – [1]Neuroscience Program, SRI International, Menlo Park, CA, [2]Department of Psychiatry and Behavioral Sciences, Stanford University

Introduction

Magnetic resonance diffusion tensor imaging (DTI) has revealed disruption of brain white matter microstructure in normal aging and alcoholism undetectable with conventional structural MR imaging. Metrics of DTI can be useful in establishing the nature of the observed microstructural aberrations. Abnormally low fractional anisotropy (FA), a measure of diffusion orientation and coherence, may result from increased intracellular or extracellular fluid, which would be reflected in complementary high apparent diffusion coefficients (bulk mean diffusivity) and low FA, or from disorganization of fiber structure, which would be reflected in low FA but with a lack of the inverse FA and diffusivity relationship.

Materials and Methods

To test these competing possibilities, we examined 15 alcoholic men and 31 control men with DTI to quantify diffusivity in the genu and splenium of the corpus callosum and centrum semiovale.

Results

In addition to the previously observed FA deficits in all three brain regions, the alcoholics had abnormally high white matter diffusivity values in the genu and centrum. Further, inverse correlations between FA and diffusivity were significant in the genu ($r=-.52$, $p<.05$) and centrum ($r=-.92$, $p=.0001$). Multiple regression analyses examining diffusivity and age as predictors of FA identified diffusivity as a significant unique contributor to FA in both regions.
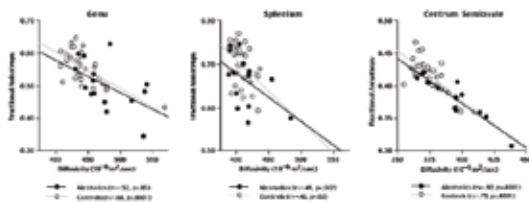
Lower FA and higher mean diffusivity were related to each other in controls and alcoholics.
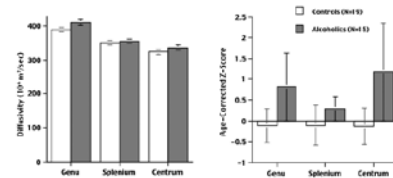
Raw values and age-corrected Z-scores (±SEM bars) of regional callosal and centrum trace. Alcoholics had higher mean diffusivity than controls despite equivalent tissue volumes of the regional samples. The alcohol effect was most profound in the centrum (>1 S.D.).
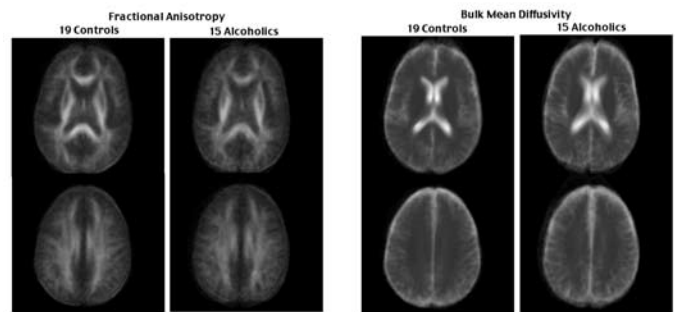
Averaged images at two levels in the brains of the 15 alcoholics and 19 controls for FA (left panel of four images) and mean diffusivity (right panel of four images).

Conclusion

These results suggest that decreased orientational coherence of brain white matter in alcoholism is attributable, at least in part, to the accumulation of intracellular and extracellular fluid in excess of that occurring in aging and that the differential influence of these fluid compartments can vary across brain regions.

88

Cortical NAA deficits in HIV infection without dementia: influence of alcoholism comorbidity

[1,2]Adolf Pfefferbaum, [3]Elfar Adalsteinsson, [1]Edith V. Sullivan,– [1]Neuroscience Program, SRI International, Menlo Park, CA; [2]Department of Psychiatry and Behavioral Sciences, [3]Department of Radiology, Stanford University

INTRODUCTION

Alcoholism comorbidity is highly prevalent in individuals infected with human immunodeficiency virus (HIV). Each condition is known to affect brain structure, function, and metabolism, but the combined effects on the brain have only recently been considered. Single-voxel, proton MR spectroscopy (MRS) has yielded sensitive measures of early brain deterioration in the progression of HIV but has limited coverage of neocortex, whereas MRS imaging (MRSI) can simultaneously interrogate large regions of cortex.

MATERIALS AND METHODS

We tested 15 men with HIV+alcoholism, 9 men with HIV alone, 8 men with alcoholism alone (abstinent for 3 to 17 months), and 23 controls. The two HIV groups were matched in T-cell count and were not demented; the two alcoholism groups were matched in lifetime alcohol consumption. We used MRSI with a variable density spiral sequence to quantify major proton metabolites, N-acetylaspartate (NAA), creatine (Cr), and choline (Cho), in the superior parietal-occipital cortex. Metabolites were expressed in absolute units and as the NAA/Cr ratio.

RESULTS

Significant group effects were present for NAA and Cr. Only the HIV+alcoholism group was significantly affected, exhibiting a 0.8 standard deviation deficit in NAA and a 1.0 standard deviation deficit in Cr. The deficits were not related to HAART status.
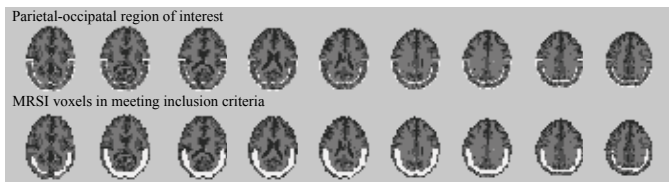
CONCLUSION

Neither HIV infection nor alcoholism independently resulted in parietal-occipital cortical metabolite abnormalities, yet each disease carried a liability that put affected individuals at a heightened risk of neuro-

Representative example (34 year old man with HIV infection and alcohol dependence) of the parietal-occipital cortical region of interest used in MRSI metabolite quantification. Top row: 9 axial slices, segmented in to compartments of gray matter (dark gray), white matter (light gray), and CSF (black), with the region of interest outlined in white. Bottom row: The same axial slices as in the top row now display the MRSI voxels meeting inclusion criteria.
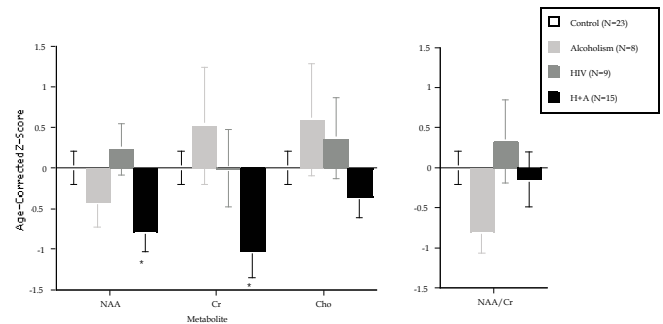
nal compromise when the diseases were compounded. Further, the use of absolute measures revealed deficits in NAA and creatine that would have gone undetected if these metabolites were expressed as a ratio.

Grand average spectra from the four study groups

Mean (±S.E.M. bars) of the three metabolites (left) and the NAA/Cr ratio (right) measured in each of the four study groups. The metabolites are absolute values expressed as age-corrected standardized Z-scores. The expected mean values of the controls=0±1 S.D. Negative values are in the direction of deficit. *p≤05.

Striatal and Forebrain Nuclei Volumes: Contribution to Motor Function and Working Memory Deficits in Alcoholism

[1]Edith V. Sullivan, [2]Anjali Deshmukh, [1]Eve De Rosa, [1,2]Margaret J. Rosenbloom, [1,2]Adolf Pfefferbaum, – [1]Department of Psychiatry and Behavioral Sciences, Stanford University; [2]Neuroscience Program, SRI International, Menlo Park, CA

Introduction

Striatal structures are involved in dopaminergic alcohol reward mechanisms and aspects of motor control. Basal forebrain structures hold cholinergic mechanisms influencing memory formation, vulnerable to chronic alcoholism. However, alcoholism's effect on volumes of these structures has seldom been considered with in vivo measurement.

Materials and Methods

We measured bilateral volumes of caudate nucleus, putamen, nucleus accumbens, and medial septum/diagonal band (MS/DB) in 25 men with alcohol dependence and 51 age-matched control men. Six alcoholics had been drinking recently while 19 had been sober.

Results

Volumes of caudate and putamen were smaller in the alcoholics than the controls, regardless of length of sobriety. Recent drinkers showed greater deficits in nucleus accumbens than sober alcoholics. Putamen volume was positively correlated with grip strength; MS/DB volume was positively correlated with verbal working memory independently of the negative association between age-standardized MS/DB and age in alcoholics.

Discussion

This study reports on the in vivo volume of striatal structures, functionally implicated in the development and maintenance of alcohol addiction, in a group of men with chronic alcohol dependence. To our knowledge, this is the first in vivo neuroimaging study to demonstrate that the caudate and putamen are significantly smaller (mean volume deficits of ~0.8 and ~0.7 standard deviations respectively) in alcoholic adult men than non-alcoholic control men. The nucleus accumbens was smaller by ~.5 standard deviation in patients with alcoholism than control men, but this difference did not attain statistical significance. When we subdivided alcoholics into recent drinkers and sober alcoholics, based on whether they had been drinking within the last 3 weeks, we found no difference between recent drinkers and sober alcoholics in deficits for putamen and caudate, while the nucleus accumbens was reduced by 1.2 standard deviations in recent drinkers but only 0.3 in sober alcoholics. One interpretation of this finding is that the nucleus accumbens, part of the extended amygdala identified as critically involved in the reinforcing effects of alcohol and other drugs of abuse is particularly susceptible to the recent effects of drinking and may show recovery with sobriety, whereas the caudate and putamen show volume deficits that persist even after more extended sobriety.

Conclusion

Caudate and putamen volume deficits occur and endure in chronic alcoholism. Nucleus accumbens may be especially sensitive to recent alcohol exposure. Striatal volumes should be considered in functional imaging studies of alcohol craving that target striatal brain regions. The age-alcohol interaction for MS/DB volumes is consistent with a cholinergic mechanism for observed working memory impairment in the alcoholics.
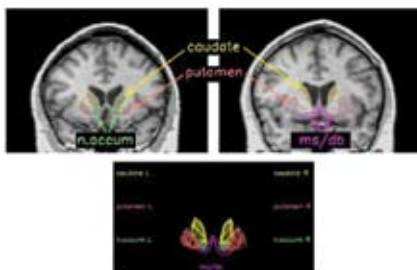
Example of manual outlining of caudate, putamen, nucleus accumbens, and medial-septum/diagonal band on 2 coronal slices, 11 mm apart shown for a 54-year old healthy control subject (upper panel). Outlines of each structure across all additional slices where they appear are represented by color-coded wire drawings in the lower panel.
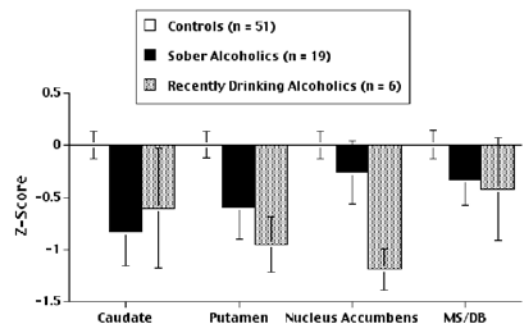
Volume measures (expressed as age- and ICV-corrected Z-scores) for mean bilateral volumes of caudate, putamen, nucleus accumbens, and the medial septum/diagonal band for 51 controls, 6 alcoholics who had been drinking in the past 3 weeks and 19 alcoholics with a median sobriety of 1 year.

Striatal and Forebrain Nuclei Volumes: Contribution to Motor Function and Working Memory Deficits in Alcoholism

[1]Anjali Deshmukh, [1,2]Margaret J. Rosenbloom, [2]Eve De Rosa, [2]Edith V. Sullivan, [1,2]Adolf Pfefferbaum – [1]Neuroscience Program, SRI International, Menlo Park, CA, [2]Department of Psychiatry and Behavioral Sciences, Stanford University, CA.

Introduction

Alcohol comorbidity has a high prevalence in schizophrenia, an adverse impact on its clinical course and can also compound or account for brain volume abnormalities of schizophrenia in cortical, cerebellar, pontine, and thalamic sites. Striatal structures are of considerable relevance to the study of alcoholism and its comorbidity with schizophrenia. In alcoholics they are the site of preferential alcohol-related dopamine release and lower dopamine D2 receptor levels. In schizophrenia, dysmorphology of striatal brain structures is attributable both to intrinsic pathology and to the effects of antipsychotic medication. It has been hypothesized that abnormalities of the reward-related neural circuitry found in schizophrenia may render patients vulnerable to addictive behavior.

Materials and Methods

We examined the separate and combined effects of schizophrenia and alcoholism and effects of medication type and drinking recency on striatal volumes. Accordingly, we measured caudate nucleus, putamen, and nucleus accumbens in 27 schizophrenic, 25 alcohol-dependent, 19 comorbid (schizophrenia and alcohol dependence or abuse), and 51 age-matched control men. Schizophrenics were classified by antipsychotic medication (typical or atypical), and alcoholics were classified by recency of sobriety.

Results

All measured structures were smaller in the patient groups than the control group. The caudate deficit was comparable across groups, whereas putamen and nucleus accumbens deficits were greater in schizophrenia than alcoholism; comorbids fell between these groups. Schizophrenic patients treated with atypical medication showed greater volume deficits in the putamen than those treated with typical medication. Recently sober (< 3 weeks) alcoholics had greater deficits in nucleus accumbens than longer sober drinkers.

Conclusion

Alcoholism comorbidity in these patients with schizophrenia neither exacerbated striatal volume deficits associated with schizophrenia alone nor altered the regional striatal profile of deficits that differentiates patients with alcoholism alone from those with schizophrenia alone. Further, patients with chronic schizophrenia had more marked deficits in putamen and nucleus accumbens than caudate, and those on typical medications showed more modest deficits in the putamen than those on atypical medications. Finally, deficits associated with chronic alcohol use, with or without schizophrenia comorbidity, are more likely to resolve with sobriety for the nucleus accumbens than for the caudate or

Example of manual outlining of caudate, putamen, and nucleus accumbens on 16 consecutive coronal slices, for a 37-year old comorbid man. Color-coded outlines from manual scoring are presented for the putamen, caudate and nucleus accumbens on each slice where they appear.
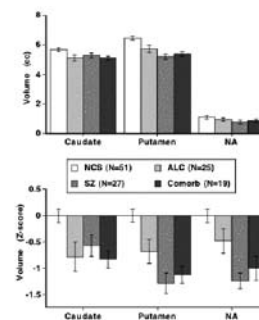
Mean and standard error (SE) volume measures, expressed both as cc (upper panel) and as age and intracranial volume corrected Z-scores (lower panel) for bilateral volumes of caudate, putamen, and nucleus accumbens for healthy control subjects, patients with alcoholism only, patients with schizophrenia only, and patients comorbid for both disorders.

Resting-sate Functional MRI in Major Depression: Abnormally Increased Activity in the Subgenual Cingulate Cortex and Thalamus

Michael D. Greicius[1,2], Benjamin H. Flores[2]; Vinod Menon[2]; Gary H. Glover[3]; Hugh B. Solvason[2]; Heather Kenna[2]; Allan L. Reiss[2]; Alan F. Schatzberg[2] - [1]Department of Neurology and Neurological Sciences, [2]Department of Psychiatry and Behavioral Sciences, [3]Radiological Sciences Laboratory, Department of Radiology

Introduction

Positron emission tomography (PET) studies of major depression have revealed resting-state abnormalities in the prefrontal and cingulate cortices. Recently, fMRI has been adapted to examine connectivity within a specific resting-state neural network—the default-mode network—that includes the medial prefrontal and anterior cingulate cortices. In this study we used fMRI to examine default-mode network activity in major depression compared to healthy controls.

Methods

28 subjects with major depression and 21 healthy control subjects underwent 6-minute fMRI scans while resting quietly. Independent component analysis was used to isolate the default-mode network in each subject. Group

maps of the default-mode network were generated and compared between the two groups. A within-group analysis was performed in the depressed group to explore effects of depression refractoriness on network activity.

Results

Resting-state subgenual cingulate and thalamic activity was significantly greater in the depressed subjects compared to the control group (Figure 1). Within the depressed group, the length of the current depressive episode (a surrogate for refractoriness) was positively correlated with activity in the subgenual cingulate.
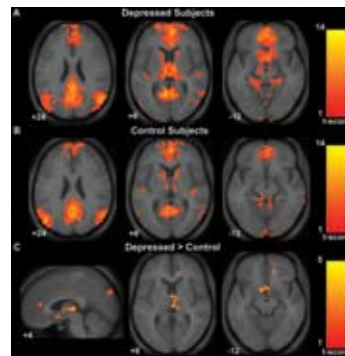

Figure 1: Increased default-mode network activity in subjects with major depression. Axial images of group default-mode activity in depressed subjects (A) and in healthy controls (B). The contrast map in (C) demonstrates clusters in the subgenual cingulate, thalamus, and precuneus where resting-state activity was greater in depressed subjects versus controls. T-score bars are shown at right. Numbers at the bottom left of the images refer to the z-coordinates (and for the sagittal image the x-coordinates) in the standard space of the Montreal Neurological Institute (MNI) template. The left side of the image corresponds to the left side of the brain.

Conclusions

This is the first study to explore default-mode fMRI activity in subjects with major depression. The findings provide cross-modality confirmation of PET studies demonstrating abnormally increased thalamic and subgenual cingulate activity in major depression. The correlation between refractoriness and subgenual cingulate activity raises the possibility that a quantitative, resting-state fMRI measure could be used to guide therapy on an individual subject basis.

Hippocampal Volume Predicts the HPA-axis Response to Stress

David M. Lyons, Karen J. Parker, Jamie M. Zeitzer, Christine L. Buckmaster, Alan F. Schatzberg – Department of Psychiatry and Behavioral Sciences

Introduction

Increased secretion of hypothalamic-pituitary-adrenal (HPA)-axis stress hormones (i.e., CRH, ACTH, and cortisol) is thought to diminish human hippocampal volumes in neuropsychiatric disorders. Here, we show that hippocampal volume instead predicts the HPA-axis response to stress due, in part, to impaired glucocorticoid feedback inhibition in adult monkeys.

Materials and Methods

In early adulthood, T1-weighted brain images (Fig. 1a) were acquired at high-resolution (voxel size = 0.312 x 0.312 x 1.0 mm) on a 1.5 Tesla GE Signa system. To investigate the hypothesis that hippocampal volume predicts the HPA-axis response, monkeys were administered standard stress tests 3.5 years after brain imaging (i.e., at 8.5 years of age). In humans, this period of the life span corresponds to ~35 years of age.

Results

Post-stress levels of ACTH were significantly greater after saline pretreatment compared to mean baseline ACTH levels measured in homecage conditions (Fig. 1b). ACTH at baseline did not correlate with hippocampal volume, but monkeys with smaller hippocampi responded to stress after saline pretreatment with greater time-integrated ACTH levels controlling for intracranial volume ($r = -0.43$, $P = 0.009$; Fig. 1c). Similar predictive relationships were discerned for diminished glucocorticoid feedback indicated by greater time-integrated levels of post-stress ACTH after pretreatment with exogenous cortisol ($r = -0.42$, $P = 0.009$; Fig. 1d).

Conclusion

These findings suggest that small hippocampi may be a cause, and not just an effect, of stress-related psychopathology.
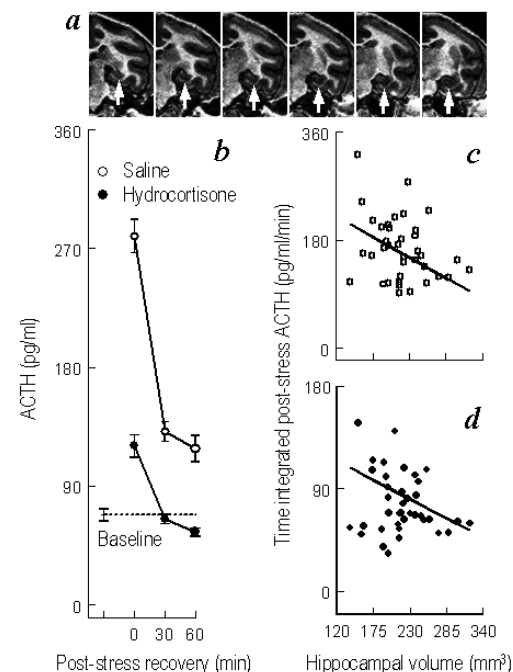

Figure 1. Hippocampal volume predicts the HPA-axis response to stress. (a) Representative images of the squirrel monkey hippocampus (arrows) at 1 mm intervals in the coronal plane. (b) Post-stress ACTH levels are presented after pretreatment with saline or exogenous cortisol (mean $\pm$ SEM). Bilateral hippocampal volumes are regressed on time-integrated levels of post-stress ACTH after pretreatment with (c) saline or (d) exogenous cortisol.

Extended Concepts of Occipital Retinotopy

C. W. Tyler, L. T. Likova, C.C. Chen, Leonid L. Kontsevich, M.M. Schira, A. R. Wade - Smith-Kettlewell Eye Research Institute, San Francisco

Introduction

The retinotopic organization of early visual areas V1-3 is well established, although anatomical landmarks can help to resolve ambiguities in poorly-defined functional maps. In the dorsal occipital regions, there is fair agreement that area V3A should be split into separate V3A and V3B maps, and that beyond them lies a further area, V7. Ventrally, V4 is generally agreed as a hemifield map, but the organization of adjacent areas is under dispute.

Materials and Methods

The fMRI responses were collected with 2D spiral acquisition from a custom occipital surface coil in a GE Signa 3T scanner. There were 23 coronal slices at 3 s TR, with TE of 30 ms and flip angle 90°, providing 2 x 2 x 3 mm voxels through the occipital cortex. Retinotopic octant wedge and logarithmic rings were run for 10 blocks each.

Results

We specify the eccentricity mapping of both V3B and V7 for the first time, showing the paradoxical behavior of V7 with roughly parallel eccentricity and meridian maps. In ventral occipital cortex, we support Press et al. (2001) and Wade et al. (2002) in seeing that a full hemifield map for V4, and show the existence of two more areas, a VentroMedial Occipital map of the lower quadrant, emphasizing the upper vertical meridian, and an adjacent area VOF with a dominant foveal representation. A dorsolateral map between the motion area and V3B, which represents the lower quadrant with an emphasis the foveal part of the lower vertical meridian, may be a counterpart to the ventromedial map. The basic layout of this conceptualization is schematized in a dual-flatmap representation centered on the two occipital poles.

Conclusion

The difficulty with extending retinotopic representation beyond areas V1-3 is that the mapping principles propagate with a different logic from first tier areas. The present analyses coordinate concepts from previous work into an integrated scheme for the third-tier retinotopic representation in lateral occipital cortex, offering novel interpretations in many details.

Supported by NHI/NEI EY 7890 and EY 13025.

References

Press et al. (2001) Vision Res. 41, 1321-32.
Tyler. et al.. Current Medical Imaging Reviews (in press)
Wade et al.. (2002). Phil. Trans. R. Soc. Lond. B 357, 963–973

Rotating wedges

Expanding rings

| V1 | V2 d/v | V3 d/v | V3 A/B | V4 | V5 | V7 | DLO/VMO | VOF |

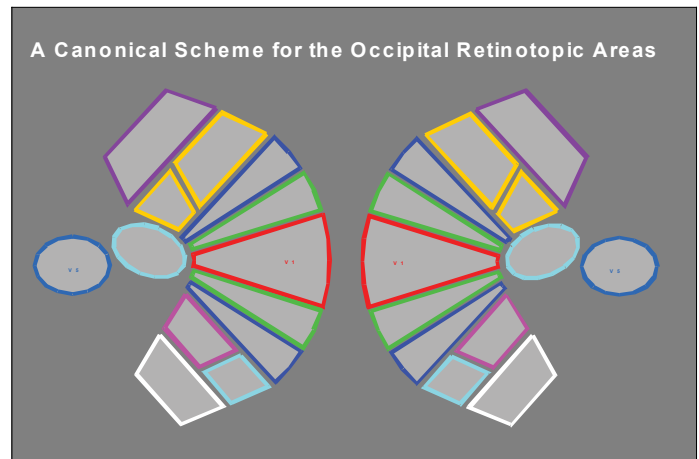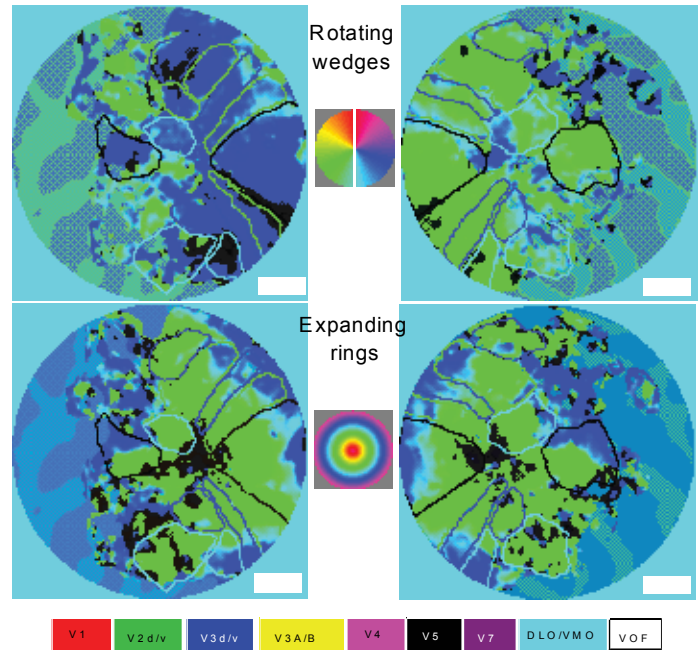A Canonical Scheme for the Occipital Retinotopic Areas

Figure-Ground Organization: Top-Down Suppression of the Background in Early Retinotopic Areas

Lora T. Likova, Christopher W. Tyler - Smith-Kettlewell Eye Research, San Francisco, CA

Introduction

Segmentation and figure-ground organization are basic mechanisms involved in the perception of visual scenes. Strong image segmentation can be generated from transient asynchronies in fields of homogeneous visual noise. We term this novel phenomenon 'Structure-from-Transients' (SfT). This study sought to determine the neural correlates for figure/ground and dissociate it from the segmentation mechanism with a SfT figure/ground paradigm.

Materials and Methods

We used a GE Signa 3T scanner at the Lucas Center with 2D spiral acquisition. There were 23 coronal slices at 3 s TR, with TE of 30 ms and flip angle 70°, 2.5 x 2.5 x 3 mm voxels through the occipital cortex. The stimuli were random dot fields of 30 x 40°, replaced by uncorrelated dots every 500ms. Asynchronous updates in subregions of random-dot fields result in structure-from-transients. Exp.1: SfT with figure/ground organization was generated in the test stimuli by introducing asynchrony in the figure area (central horizontal strip 8 x 40°) versus its surround. The transient changes in the null stimuli however were synchronized, generating no structure from transients. Thus the global percepts switched from figure/ground (test) to a homogeneous field (null) every 9 sec**.** Exp.2: Figure/ground organization was eliminated by segmenting the test stimuli into a SfT structure of multiple equivalent parts. The null stimulus was the same as in Exp.1.

Results

Our data show dramatic reorganization of the cortical activation pattern with manipulation of the perceptual organization. Exp. 1. The data revealed a retinotopic figure/ground-specific suppression (blue coloration) of the background regions in areas V1/V2, accompanied by a strong excitation (greenish coloration) localized to hMT+ (Fig. 1). The location of the figure/ground border representation in V1 is marked by a white dash line.

Exp.2. Both the hMT+ activation an V1/V2 suppression were abolished by eliminating the figure/ground organization, while the increased number of borders and equivalent segments increased the activation in V3A, together with most of the higher retinotopic areas, both dorsal and ventral (Fig. 2).

Conclusion

By means of fMRI, we have revealed for the first time the mechanism of figure/ground organization by top-down suppression of the background region in the human brain (Fig. 3).

The pattern of activation was dramatically changed by varying the perceptual organization of the segmented stimuli. The activation pattern implies a crucial role of hMT+ in (dynamic) figure/ground classification and segmentation. The results support a view of a recurrent architecture with functional feedback loops, exhibiting complex spatiotemporal behavior in the case of a figure/ground organization.
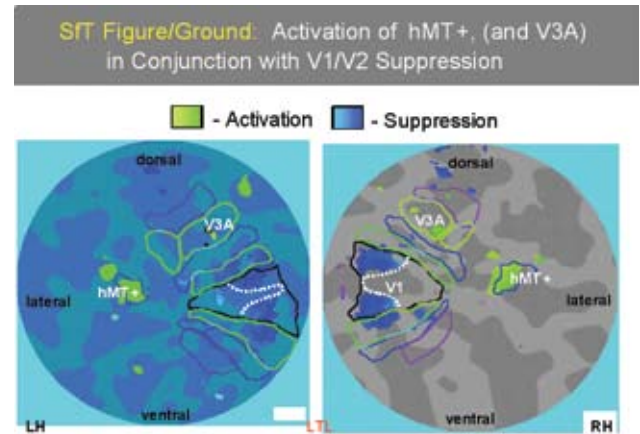
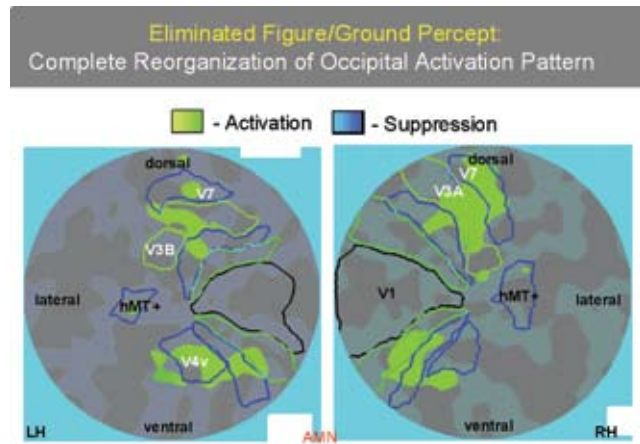*Fig. 1: Occipital flatmaps for SfT figure/ground in Exp. 1*

Fig. 2: Occipital flatmaps for multiple SfT borders in Exp. 2
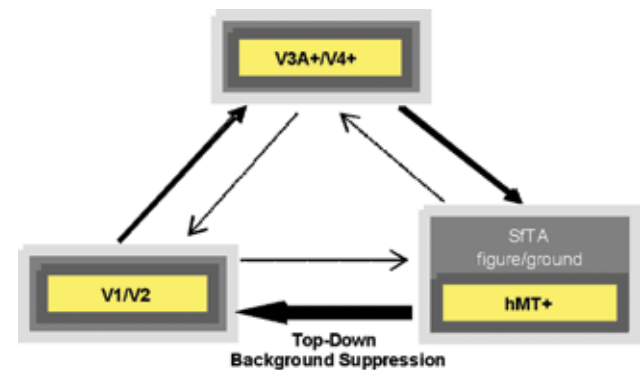

Fig. 3: Proposed model for neural processing of (dynamic) figure/ground in the occipital cortex

Cortical Evaluation of a Rule-based Trajectory Revealed by fMRI

Steven Heinen, Jess Rowland, Anva Velisar, Alex Wade – Smith-Kettelwell Eye Research Institute, 2318 Fillmore St, San Francisco CA

Introduction

Kim and Heinen (2001) introduced a novel paradigm for investigating rule-based eye movements in awake behaving monkeys. In this "ocular baseball" task, monkeys either executed or withheld eye movements to a moving spot target depending on whether or not the target crossed a visible "strike zone." They found neurons in supplementary eye fields (SEF) that signaled early the target state (Kim et al., 2005). Here, we show neural correlates of this task in humans using event-related fMRI. Consistent activity related to the baseball task was found in three areas: inferior parietal lobule (IPL), dorsolateral prefrontal cortex (DLPFC), and ventrolateral prefrontal cortex (VLPFC). This study represents a first step in elucidating the network involved in interpreting the trajectory of a moving target within the context of a rule in humans.

Materials and Methods

Three subjects were scanned on a 3T GE Signa system with 23 functional slices covering the entire head at a resolution of 3x3x5mm. Event-related design was used to measure activity in four within-block conditions: always fixate in which subjects maintained fixation throughout the trial; always go in which subjects executed eye movements to the target; baseball, decided go; and baseball, decided no go. In the baseball task, subjects pursued the target only if they thought it would cross the plate. Eye movements were measured using a video eye-tracking system. MR signals were analyzed using Stanford's Vistasoft package (white.stanford.edu/software/).

Results

Block-design eye-motion localizer scans identified two regions corresponding to the human supplementary eye fields (SEF) and frontal eye fields (FEF). In addition, three loci were activated consistently across all subjects when comparing the baseball task to either "always fixate" or "always go": right IPL, right DLPFC, and right VLPFC. For the subject shown (JB), activity was also found in the parietal-occipital region and the medial-temporal area (MT). Plots show mean timecourses for these regions of interest (ROIs). Time zero represents the start of a trial. BA = Brodmann area. In these areas, we measured significantly greater activity during tasks involving saccade suppression compared tasks requiring an eye movement.
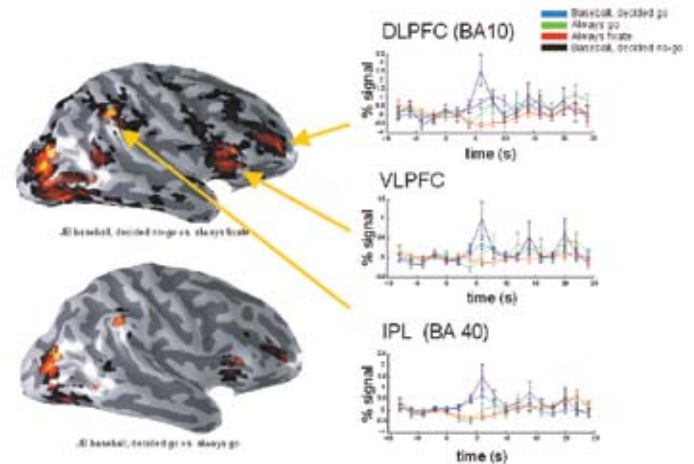
Single subject responses for baseball 'decide fixate' and 'decide saccade' ('nogo' and 'go'). Active regions include the IPL, the DLPFC and VLPFC as well as accipital cortex.

Conclusion

This study, combining high spatio-temporal resolution eye tracking in the scanner and a novel experimental design is the first to demonstrate a link between macaque single-unit eye movement rule evaluation studies and human imaging data. The network we identify as being involved in this task has components that have previously been linked to spatial imagery (IPL), rule evaluation (DLPFC) and maintenance of goal-related representations in working memory (VLPFC). The fact that we see higher activation for saccade suppression is intriguing given that single unit measurements using this experimental task indicate a larger population of inhibitory compared to excitatory neurons in the SEF. In future studies, we will aim to dissect this network more precisely by breaking down responses according to response (as well as task) type, error rates and spatial direction.

3D CINE SSFP Breath-hold Imaging Using a Spiral Acquisition

MARCUS ALLEY, FRANDICS CHAN, BOB HERFKENS – DEPARTMENT OF RADIOLOGY

INTRODUCTION

Our group has been quite active in the development of "fast" 3D cine MR imaging. Coupled with the use of a fully refocused steady-state acquisition (SSFP or True FISP), high SNR images can be produced without the need for additional contrast agents. However due to the long scan times respiratory compensation must be used to produce reasonable image quality. We have addressed this problem using spiral readouts, which allows the entire acquisition to be done in a single breath-hold.

MATERIALS AND METHODS

A typical scan prescription included a 128x128 in-plane resolution over a 30 cm field-of-view. This could be achieved with 40 spiral interleaves and a receiver bandwidth of 250 kHz. Coverage in the slice direction was prescribed with 10 sections of 10 mm thickness. The sequence TR and TE was 3.4 and 0.6 ms, respectively, and the true temporal resolution of the data was 34 ms. This prescription resulted in a total scan time of 24 secs, which can be reasonably performed in a single breath-hold.

DISCUSSION

Representative images showing both the diastolic and systolic phases from one section of the study are shown in Figure 1. The acquisition was done after the administration of an external contrast agent, which helps in further boosting the SNR from the SSFP acquisition. While the resolution of the study is limited due to the need to keep the acquisition time below 30 seconds, adequate coverage is easily obtained.

CONCLUSION

We have presented a technique that allows 3D, temporally-resolved coverage of the cardiac anatomy using a spiral SSFP acquisition in a breath-hold. Eliminating the need for multiple 2D acquisitions leads to a faster acquisition time and greater patient comfort. The acquisition of a 3D volume reduces the chance of misregistration errors.
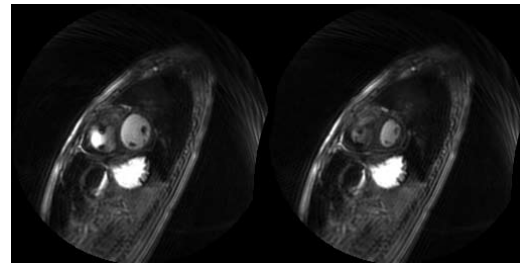

Figure 1: Diastolic (left) and systolic (right) images from a breath-held 3D SSFP spiral cine exam.

3D MRA with Parallel Imaging: A Comparison of Grappa and mSense

MARCUS ALLEY, FRANDICS CHAN, ROLAND BAMMER – [1]DEPARTMENT OF RADIOLOGY, STANFORD UNIVERSITY

INTRODUCTION

Recent advances in parallel imaging have made it possible to greatly reduce scan times in MR when imaging with multiple coil arrays. In order to assess the feasibility of these techniques for use in MRA, we have developed an offline reconstruction that can produce both Grappa and mSense images from an appropriate data set [1, 2].

MATERIALS AND METHODS

The comparison data were acquired in a post-injection phase. A conventional MRA was first acquired with a scan prescription that included an in-plane resolution of 384x192 over a 35 cm field-of-view. Coverage in the section direction was done with 48 2.4 mm sections. An 8-channel cardiac phased-array coil was used for signal reception. With a scan TR and TE of 3.6 and 0.8 ms, respectively, this acquisition could be completed in 25 sec. This was followed by a second scan using the same parameters in which only a fraction of the number of in-plane phase-encodes were acquired. Specifically, the scan collected the 24 most central k-space lines and then every other line outside this region. This corresponds to a nominal reduction factor of 2, and the resulting scan time was 14.5 sec. The data from this acquisition were reconstructed using both the Grappa and mSense algorithms.

DISCUSSION

Figure 1 shows a section from the conventional acquisition on the left, and the Grappa and mSense reconstructions in the center and on the right, respectively. Both parallel reconstruction techniques exhibit greater noise due to the decreased acquisition time, and generally the overall image quality from the Grappa and mSense reconstructions is quite similar. The mSense reconstruction tends to show more structured artifacts, which could be problematic if they were to be subsequently misinterpreted.

CONCLUSION

The substantial scan time reductions with parallel imaging can be used in MRA to achieve better temporal resolution and thus better capture the arterial phase after contrast injection. However, the question remains as whether or not the resulting image quality is still diagnostically useful. Our ongoing study will attempt to assess this issue and further qualify the differences between the Grappa and mSense reconstructions.

[1] Griswold, MA, et al., Magn Reson Med, **47**, ppgs. 1202-1210 (2002)
[2] Pruessmann, KP, et al., Magn Reson Med, **42**, ppgs. 952-962 (1999)

Figure 1: *The image on the left shows one section from a conventional 3D MRA acquired in 25 sec. The images in the center and on the right show the GRAPPA and mSense reconstruction, respectively, from a subsequent 14.5 sec scan.*

Parallel Imaging Accelerated Single Acquisition Water-Fat Separation for Dynamic Imaging

Huanzhou Yu[1], Charlie A. McKenzie[2], Ann Shimakawa[3], Anja C.S. Brau[3], Angel R. Pineda[1], Norbert J. Pelc[1], Jean H. Brittain[3], Scott B. Reeder[1] – [1]Department of Radiology, Stanford University; [2]Radiology Department, Beth Israel Deaconess Medical Center and Harvard Medical School; [3]GE Healthcare, Applied Science Lab-West

Introduction

The perfect fat suppression or water-fat separation method should not only achieve robust and uniform fat suppression despite the presence of field inhomogeneities, but also introduce minimum scan time overhead. Achieving these goals has been difficult for past techniques. We recently proposed a single acquisition water-fat separation method for dynamic imaging [1] that achieves uniform separation while maintaining scan times comparable to conventional non-fat suppressed acquisitions.

Parallel imaging techniques [2, 3], such as ASSET (Array Spatial Sensitivity Encoding Technique), allow the acquisition of fewer phase encoding lines and thus shorter scan times. In this work, the single acquisition water-fat separation method, or "1+pt" dynamic imaging method, is refined and combined with parallel imaging to provide further scan time reduction.

Materials and Methods

The echo time TE is chosen such that phase shift of fat relative to water at TE is $(1/2 + k)\pi$, where k is any integer. Signal with water (W) and fat (F) is described by: $S(TE) = (W \pm jF) \times e^{j2\pi\phi(TE)}$, where $\phi(TE)$ denotes additional spatially dependent phase shifts from B_0 field inhomogeneity and other system imperfections. If $\phi(TE)$ is known, water and fat can be obtained from real and imaginary channels of the $\phi(TE)$-corrected signals. To obtain $\phi(TE)$, we first perform a low resolution 3pt "calibration scan". An iterative method similar to IDEAL (Iterative Dixon water-fat separation with Echo Asymmetry and Least-squares estimation) [4] is used to estimate $\phi(TE)$, which is then repeatedly used in subsequent scans of the same location during a dynamic acquisition to calculate water and fat images, based on the assumption that phase is relatively stable in these situations.

To truly combine parallel imaging and 1+pt separation, we use one calibration scan for both ASSET and 1+pt method. The scheme is illustrated in Figure 1. We acquire low-resolution images (S_1, S_2, S_3) at 3 echo times. In particular, S_1, acquired with no ASSET acceleration, is also used for ASSET calibration, which enables unwrapping of the accelerated S_2 and S_3. $\phi(TE)$ is then estimated from ASSET-reconstructed images at the 3 echo times. During the dynamic portion of the study, full-resolution, accelerated images are acquired with phase $(1/2+k)\pi$. The reconstruction unwraps these images to full FOV, demodulates them by $\phi(TE)$, and finally separates them into water and fat images.

Liver imaging was performed to demonstrate the feasibility of this method. A modified 3pt SPGR sequence was used in both shared calibration scan and 1pt separation scan. Echo times were [2.0, 3.6, 5.2] ms. In the 1pt separation scan, only the signal at echo shift = $3\pi/2$ was used, simulating the single acquisition data. An 8-channel cardiac coil was used. Other imaging parameters included: TR = 20ms, FOV = 36cm, BW = ±83.3kHz, acquisition matrix = 256x256. All volunteer scanning
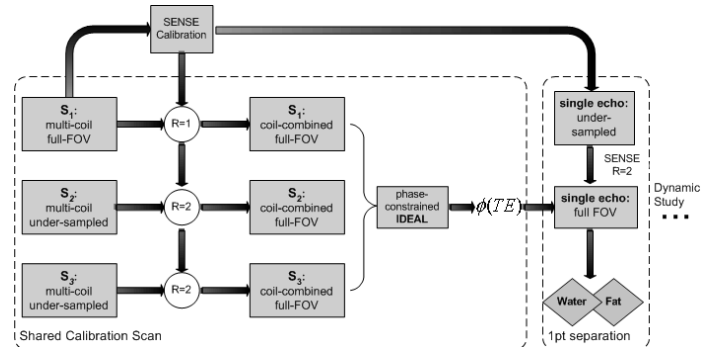

Figure 1: Schematic diagram of combining ASSET with 1+pt separation method. R=2 (reduction factor) is used as the example.
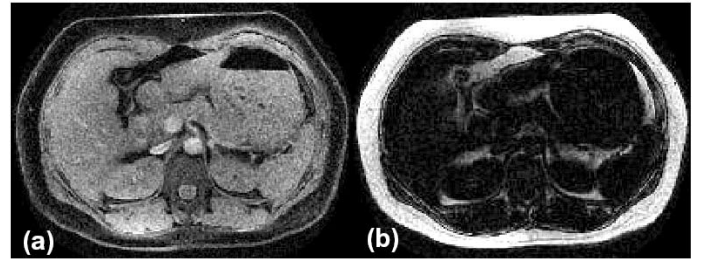

Figure 2: 1+pt separated (a) water and (b) fat. ASSET R=2 is used for the 1pt scan and S_2, S_3 of the calibration scan.

was approved by our IRB and informed consent was obtained prior to imaging.

Results

Fig. 2 shows 1+pt images of the abdomen of a normal volunteer. Excellent and uniform separation of water and fat was achieved.

Discussion and Conclusion

In clinical dynamic imaging situations, the calibration scan can be performed intermittently to update the $\phi(TE)$ if needed. The results in liver imaging demonstrate excellent water-fat separation. This method may be valuable for dynamic imaging to provide both high temporal resolution and uniform fat suppression.

References
[1]. Yu et al, ISMRM 2004; p263
[2]. Pruessmann et al, MRM 1999; 42(5): 952-962
[3]. Sodickson et al, MRM 1997; 38(4):591-603
[4]. Reeder et al, MRM in press

Segmentation and Characterization of Vortical Flow Patterns in MRI Phase-contrast Velocity Data

L Wigström[1,4], T Hope[1], MT Draney[2], E Heiberg[4], AF Bolger[4,5], MT Alley[1], NJ Pelc[1], DC Miller[3], RJ Herfkens[1] – Departments of [1]Radiology, [2]Mechanical Engineering, [3]Cardiothoracic Surgery, Stanford University; [4]Linköping University, Sweden; [5]University of California, San Francisco.

Introduction

Phase-contrast magnetic resonance imaging (PC-MRI) provides a unique method to accurately estimate velocities within a 3D region during the complete cardiac cycle. This 4D-flow technique enables studies of flow patterns in the heart and great vessels to provide new physiological insights. Based on the acquired velocity data, particle trace visualization can be used to create an informative display of the velocity field. Still, this visual approach requires a lot of experience to locate and describe flow structures of interest, and searching through the complete dataset for any unknown flow patterns is extremely time consuming. An automatic and objective characterization of flow patterns would be of great importance for the definition of normal and abnormal flow, and to subsequently make 4D-flow studies more applicable in a clinical setting. In this project new image processing tools are being developed in order to locate and quantify flow patterns of interest.

Materials and Methods

A set of vector valued filters are applied on each time-frame of the acquired PC-MRI data. Since no a-priori information exists regarding the orientation of the flow structures, 6 differently oriented filters are used. The filter responses are combined using a tensor representation. The largest Eigenvalue or the tensor norm is used to find the similarity between the used filter and the actual velocity data [1]. Using a range of filter diameters, the best match is computed and the corresponding region in 3D space is marked. From the best matching filter in each voxel, a number of parameters can be derived, including vortex size and pitch. Within the segmented regions, additional parameters can subsequently be estimated based on the original velocity data. Parameters of interest for objective characterization of vortical flow are vorticity, angular velocity, helicity and kinetic energy.
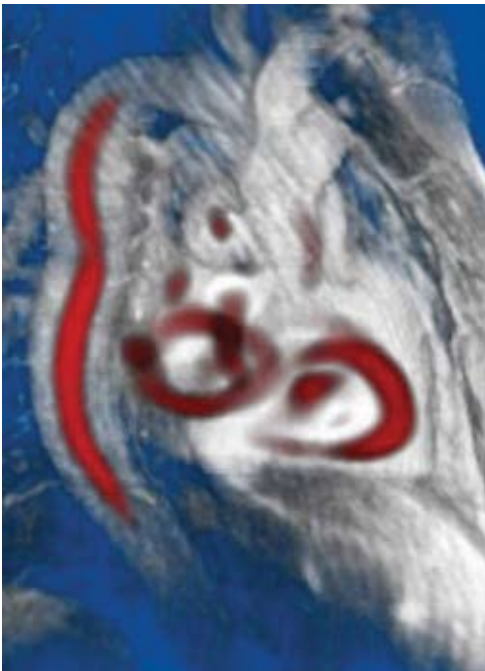

Figure 1: Volume rendering of the vortex core similarity showing ring vortices in both the left and right ventricles of the heart and the swirling flow in the descending aorta.

A volume rendering tool was develop to visualize the resulting flow feature parameters. The commercially available EnSight software also gives the possibility to compare the derived parameters with particle traces calculated from the velocity data.

Results

An example of a volume rendering of vortex core similarity is shown in Figure 1. Further calculations based on a range of filter diameters are subsequently combined and results in a scalar volume that in each voxel contains the probability of being part of a vortical flow structure (see Figure 2). Figure 3 shows a comparison with streamlines calculated from the same velocity data.
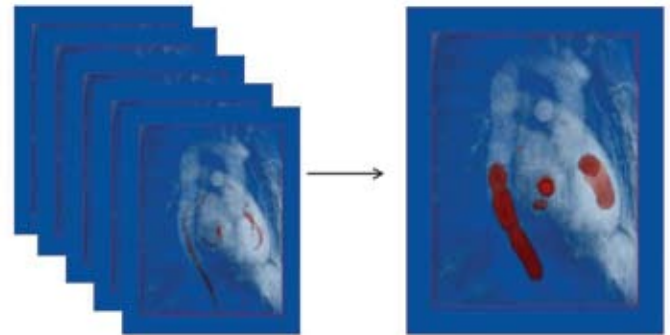

Figure 2: Vortex core similarities from a range of filter diameters are combined in order to estimate the regions occupied by vortex like flow.
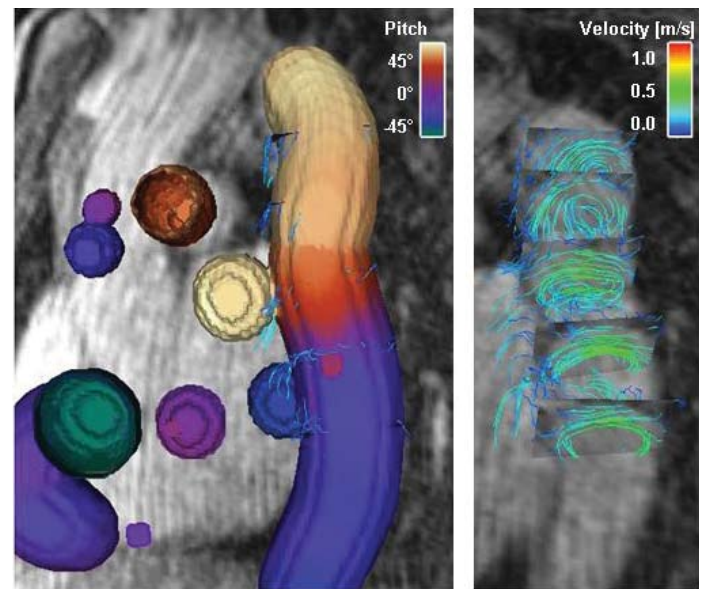

Figure 3: Left: Detected regions with vortical flow (surface renderings color coded according to pitch angle). Right: Streamline visualization of the same region in the descending aorta in late systole also shows a rotating flow pattern.

Conclusion

Automatic segmentation of vortical flow patterns provides an objective approach to characterization of 4D-flow data. Volume rendering of the results gives a quick overview, where regions of vortical flow can be easily identified. Further studies using for example streamline visualization can be performed in these regions to display more details of the flow field.

References

1. Heiberg E, Ebbers T, Wigström L, Karlsson M. Three-dimensional flow characterization using pattern matching. IEEE Transactions on Visualization & Computer Graphics 2003; 9(2)

Validating 4D-flow MRI Using a Human Thoracic Aorta Phantom

Christopher Elkins[1], Mary Draney[1], Marcus Alley[1], Robert Herfkens[1], Ananth S. Iyengar[2], Francisco Medina[2], Ryan B. Wicker[2] – [1]Department of Radiology, Stanford University; [2]W.M. Keck Border Biomedical Manufacturing and Engineering Laboratory, University of Texas at El Paso

Introduction

Hemodynamics is thought to play a major role in the development of vascular diseases. Accurate in vivo measurements of blood flow are important clinically for diagnosis and treatment of these diseases. 4D-flow MRI measures time-dependent blood flow in three-dimensional volumes in the body. Therefore, it is an ideal technique for acquiring hemodynamic information in the human vascular system. To date, though, its accuracy has not been fully quantified. This objective of this experiment is to characterize the 4d-flow accuracy by comparing the MRI measurements with particle image velocimetry (PIV) measurements made in the same phantom with the same flow conditions.

Materials and Methods

A CT scan of a healthy human was used to create a computer model of the thoracic aorta. Using this computer model with rapid prototyping manufacturing, we created the optically clear, MR compatible polyurethane aorta phantom shown in Figure 1.

Figure 1. MRV compatible, optically clear polyurethane thoracic aorta phantom.

2D PIV measurements are made by illuminating a plane in the model with two laser sheets pulsed in quick succession. Small, neutrally buoyant particles in the flow reflect the laser light, and a camera captures the particle images from each laser pulse. The two images are processed to determine the motion of the particles and create velocity vector maps. For this experiment, velocities were measured with resolution of 1.2 mm in a 2D plane. Because the flow is physiologic and pulsatile, the PIV measurements were phase locked to 10 time points along the flow waveform. 500 image pairs at each time point were analyzed to produce the average velocities for comparison with the 4D-flow results.
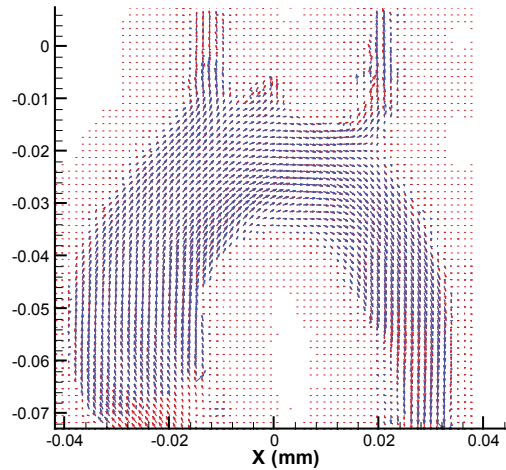
4D-flow measurements were performed in the

Figure 2. Direct comparison between 4D-flow (red) and PIV (blue) velocity vectors in one plane of the phantom.

Lucas 1.5T magnet. The imaged measurement volume was 83 mm by 300 mm by 300 mm with the resolution of 1.6 mm by 1.2 mm by 1.2 mm. Data were acquired at 8 different phases in the waveform and reconstructed to 20 phases. In order to compare directly to PIV results, 2D planes of velocity data were extracted for the phase most closely corresponding to the phase of the PIV data.

Results

Figure 2 shows a direct comparison between velocity vectors for PIV (blue) and 4Dflow (red) during a peak flow of 14 L/min. The agreement is excellent.

Conclusion

The accuracy of the 4D-flow MRI technique is excellent during the peak flow phase of the heart beat. The accuracy during the diastolic phases is currently being evaluated.

# Cardiac Heterotaxy: Emerging State of the Art Evaluation Using Cardiac-Gated MDCT and MRI

Scott K. Nagle, Frandics P. Chan – Department of Radiology

Cardiac isomerism or heterotaxy refers to the spectrum of congenital cardiac anomalies in which both atria are of either right or left morphology. The importance of correctly and thoroughly evaluating the thoracic and abdominal anatomy of patients with these abnormalities is due to (1) the association of these cardiac abnormalities with extra-cardiac malformations having serious clinical sequelae, (2) the complexity of the necessary surgical repairs, and (3) the distinct clinical trajectories of each group of patients. In this exhibit, we will illustrate how emerging cardiac-gated MDCT and MRI techniques, with an emphasis on their high-resolution three-dimensional imaging capabilities, can be used to describe the complex cardiovascular anatomy as well as the myriad of visceral abnormalities encountered in these conditions, even in very young children. These new techniques have the potential to markedly improve the medical and surgical management of these patients.

Double-oblique reformated retrospectively ECG-gated CT image of the atrial appendages in a different patient with right isomerism.
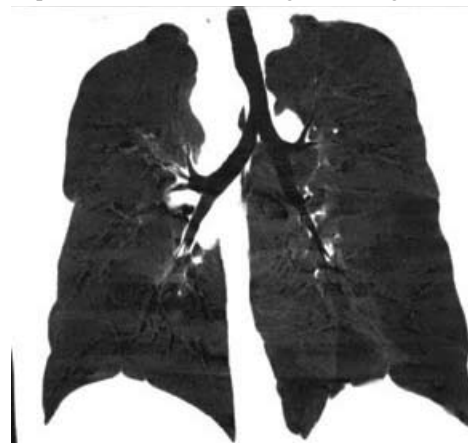
A thin slab minimum intensity projection from a CT exam, demonstrating thoracic situs inversus by bronchial morphology criteria.

Quantification of Hemodynamic Conditions in the Human Abdominal Aorta under Resting and Simulated Exercise Conditions

Beverly Tang[1], Mary Draney[1], Christopher Cheng[1], Philip Tsao[2], Charles Taylor[1,3] – Departments of [1]Mechanical Engineering, [2]Medicine, [3]Bioengineering & Surgery

Introduction

Elevated blood flow associated with exercise has been hypothesized to result in hemodynamic conditions that inhibit atherosclerosis. Computational flow simulations, using MRA data to construct anatomically representative models and PC-MRI to specify inlet and outlet boundary conditions, provide a means to quantify and visualize complex hemodynamic conditions along the entire abdominal aorta. The results from these flow simulations provide a subject-specific, three-dimensional description of the flow patterns present in the human abdominal aorta under both resting and simulated exercise conditions.

Materials and Methods

MRA scans of five healthy subjects (age 20-30) were obtained in a 1.5T GE Signa. Coronal slices of 4 mm thickness were obtained in a 40 cm x 40 cm FOV. 3D, subject-specific solid models were created from the MRA images using custom software and discretized. Cine PC-MR images taken perpendicular to the vessels of interest were used to calculate *in vivo*, time-varying volumetric flow, which served as inlet and outlet boundary conditions.

Results

Results from one subject-specific simulation are shown on the right. Note that regions of low flow velocities and recirculation zones that exist under resting conditions are replaced by higher flow velocities and more laminar flow under simulated exercise conditions.
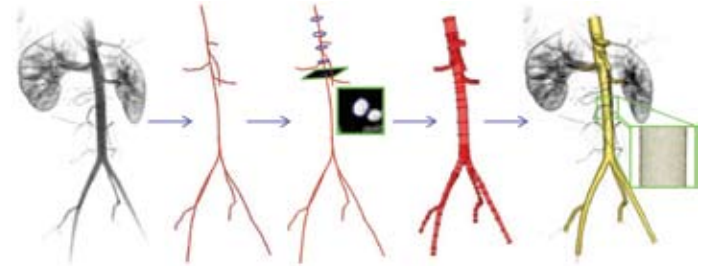
Geometric model construction from 3D MRA data.
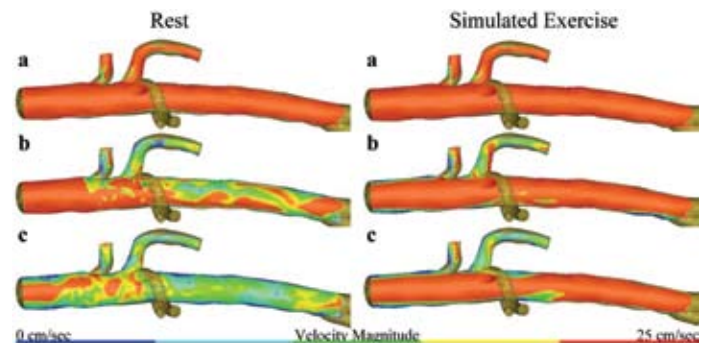
Velocity magnitude plotted along midplane slice of abdominal aorta under resting (left) and simulated exercise (right) conditions at peak systole (a), end systole (b), and mid-diastole (c).

Multi-Scale Vascular Geometry Construction and Hemodynamic Quantification from Medical Images

Erik Bekkers, Charles Taylor – Departments of Mechanical Engineering & Bioengineering, Stanford University

Abstract

Computational fluid dynamics (CFD) modeling of blood flow from image-based patient specific models can provide useful physiologic information for guiding clinical decision making. Current research focuses on i) the construction of three dimensional (3D) multi-scale CFD vascular models from time dependent medical imaging data and ii) the quantification of hemodynamic parameters from four dimensional phase contrast imaging (4DPC-MRI).

Methods

Model construction utilizes current 3D image filtering and level set segmentation methods to generate an initial uniform sized triangulated surface representation. By estimation of the local surface 3D curvature tensor, the uniform triangulated surface is converted to a multi-scale triangulated surface which can be further converted to a globally smooth non-uniform rational b-spline (NURB) representation. This surface remeshing method is particularly suited for CFD modeling of very large vascular models (as from CT data) with wide ranges in vasculature size scale, where initial surface mesh density is an important consideration for balancing accuracy with manageable size volumetric meshes. In addition, the underlying smooth surface representation allows for stable adaptive mesh refinement during CFD computation.

Left: Multi-resolution computational model of diseased aorta constructed from CT data. Triangulated mesh (black) and NURB surface (red).
Right: Analysis of one time point of a 4DPC-MRI data set of a healthy aorta. A) Computational tetrahedral mesh B) Interpolation of velocity data onto mesh C) Wall velocity D and E) Shear stress with least squares fitting of velocity field at coarser (D) and finer (E) mesh resolution. F) Relative pressure field.

Quantification of hemodynamic parameters occurs through the generation of a time-dependent series of computational meshes from a 4DPC-MRI data set. The blood velocity field is interpolated onto the computational mesh and standard finite element methods are used for noise suppression (through least squares fitting of the velocity field), elimination of divergence in the velocity field, and the computation of shear stress, relative pressure field and flow streamlines. Examples of both areas of research are shown in the above figure.

Age and Gender Related Differences in Thoracic Aortic Wall Motion and Strain

MARY T. DRANEY[1], MICHAEL MARKL[2], ROBERT J. HERFKENS[2], CHRISTOPHER K. ZARINS[4], CHARLES A. TAYLOR[1,3,4] – [1]DEPARTMENT OF MECHANICAL ENGINEERING, [2]DEPARTMENT OF RADIOLOGY, [3]DEPARTMENT OF BIOENGINEERING, [4]DEPARTMENT OF SURGERY

INTRODUCTION

Mechanical behavior of the thoracic aorta is largely unknown, including how the magnitude of wall motion varies along the length of the aorta, and how this changes with age and gender. It is known that women are less likely to develop abdominal aortic aneurysms than men, but they are equally prone to develop thoracic aortic aneurysms. For both genders, the incidence of aneurismal disease increases with age. The objective of this study is to evaluate age and gender related differences in descending thoracic aorta wall motion and strain using non-invasive cardiac-gated magnetic resonance imaging.

MATERIALS AND METHODS

Young (27+/-4 years) and older (61+/-5 years) women (n=9) and men (n=10) volunteers with no evidence of cardiovascular disease were studied using a GE Signa 1.5 T MR scanner. A contrast-enhanced MR angiogram (MRA) was acquired in a single breath hold during bolus IV administration of 40 cc of a gadolinium contrast agent. Following the MRA, a bright-blood, cardiac-gated sequence was used to acquire a series of 2D slices, perpendicular to the aorta, between the left subclavian and celiac arteries. Each slice was centered between intercostal arteries, and was acquired during a single breath hold. 20-32 time frames through the cardiac cycle were acquired for each slice. All imaging was done under resting conditions in the supine position. Centerline paths of each aorta, spanning from the left subclavian artery to the celiac artery, were constructed from the MRA data and the luminal boundary of the descending thoracic aorta was segmented for each time frame of each slice using custom software (Aspire2, Stanford University); this is illustrated in Figure 1. Mean aortic diameter and circumferential strain were then calculated along the length of the thoracic aorta.

RESULTS

For all subjects, the diameter of the thoracic aorta decreased with distal position. Young women had smaller aortas than young men at all levels of the thoracic aorta, but aortic diameter was the same in older women and older men at all levels of the thoracic aorta (Figure 2, left). Thus, women experienced considerably greater enlargement of the thoracic aorta with age. Contrary to the change in aortic diameter, circumferential strain either increased or remained constant in the distal thoracic
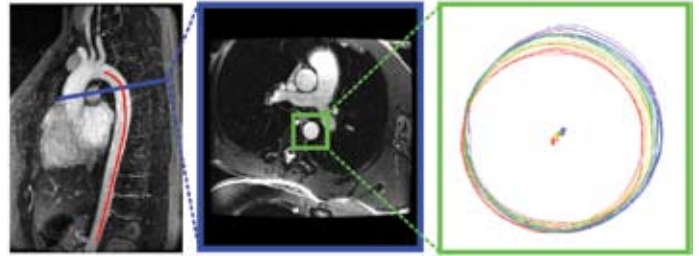

Figure 1: Left: Image from MRA illustrating location of left subclavian and celiac arteries. The red curve represents the centerline path and the blue line illustrates the location of a 2D slice perpendicular to the aorta. Middle: a representative slice at one point in the cardiac cycle. The green box highlights the location of the descending thoracic aorta. Right: Luminal boundary segmentations for all time frames of the aorta shown in the middle image.
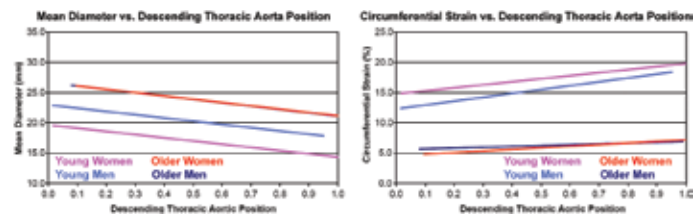

Figure 2: Mean diameter(left) and circumferential strain (right) along the descending thoracic aorta for each age and gender group. Position is relative to the left subclavian artery (position = 0.0) and the celiac artery (position = 1.0).

aorta for all subjects. Aortas in young women demonstrated greater circumferential strain than in young men, however, the gender difference was not evidenced in the older aortas (Figure 2, right). Thus, women demonstrated a larger decrease in circumferential strain with age than men.

CONCLUSIONS

There is significant variation in mechanical behavior along the length of the descending thoracic aorta. These variations are both age and gender dependent, with evidence of gender differences only in the younger age group. Women experience greater age-related thoracic aortic enlargement than men and a greater age-related reduction in circumferential strain.

Patient-Specific Modeling of Altered Hemodynamics and Arterial Deformation Induced by Aortic Coarctation and Subsequent Stent Implantation

JOHN F. LADISA, JR.[1], C. ALBERTO FIGUEROA[2], IRENE E. VIGNON-CLEMENTEL[2], FRANDICS P. CHAN[3], CHARLES A. TAYLOR[2], JEFFREY A. FEINSTEIN[1] - DEPARTMENTS OF [1]PEDIATRICS, [2]MECHANICAL ENGINEERING,[3]BIOENGINEERING, [4]RADIOLOGY

INTRODUCTION

Stents are playing an increasing role in the alleviation of pressure gradients caused by aortic coarctation (CoA). However, morbidity (hypertension, aneurysms, stroke) persists and may be attributed to abnormal hemodynamics in the aorta and its branches. We hypothesize that computational fluid dynamics (CFD) modeling can be used to quantify alterations in blood pressures (BP), flow and vascular deformation introduced by CoA, and stent implantation.

METHODS

CFD modeling was performed using magnetic resonance (MR) angiography and phase contrast (PC) data obtained before and after stent implantation in a 13 year old patient with severe CoA. A PC-MR flow waveform was mapped to the aortic inlet and resistance boundary conditions were imposed at the descending aorta, innominate, left common carotid (LCCA) and subclavian arteries (LSA) based on observed BP and flow.
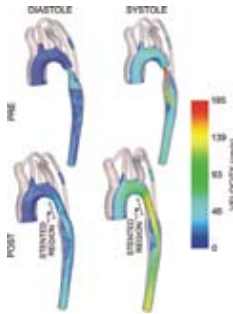

Figure: Wall deformation (opaque shells) and axial velocity during diastole (left) and systole (right) before (pre) and after (post) rigid stent implantation.

RESULTS

CoA caused hypertension (134-142 mmHg) and elevated pulse BP (66-73 mmHg) in arteries proximal to the stenosis consistent with measured data. Pronounced deformation (21%) occurred in the LCCA and LSA with concomitant increases in left collateral artery flow. SBP rescinded after stenting (111-112 mmHg) and collateral artery flow was attenuated by 56%.

CONCLUSION

These temporal and spatial alterations demonstrate that CFD modeling can reproduce hemodynamic waveforms in patients with CoA. These results may provide insight into sources of morbidity and offer quantitative assessment of treatment options such as stent implantation.

Image-Based Modeling of Abdominal Aortic Blood Flow in Spinal Cord Injury Patients

Hyun Jin Kim[1], Irene E. Vignon[1], Janice J. Yeung[2], Ronald L. Dalman[2,4], Charles A. Taylor[1,2,3] – Departments of [1]Mechanical Engineering, [2]Surgery, [3]Bioengineering,Stanford, [4]Veterans Affairs Palo Alto Health Care System

INTRODUCTION

Spinal cord injury (SCI) patients have atrophied lower extremity vessels, but, paradoxically, have a 3-fold greater risk of abdominal aortic aneurysms (AAA). We propose that increased incidence of AAA in SCI patients is due to slower decay of the pressure wave and lower wall shear stress in the abdominal aorta of SCI patients compared to normal subjects. We test this hypothesis using image-based modeling.

MATERIALS AND METHODS

Five SCI patients and six age and risk-factor matched control subjects were recruited from the Veterans Affairs Palo Alto Health Care system and underwent magnetic resonance angiographic (MRA) examinations. Imaging was conducted using a 1.5T GE Signa magnet. Cine phase-contrast MR imaging (PC-MRI) was also used to acquire time-resolved through-plane blood flow velocity maps perpendicular to the aorta at the supraceliac and infrarenal levels. Patient-specific computer models were generated from MRA data using custom software. The nonlinear 1D equations governing blood flow in deformable arteries were solved for flow rate and pressure using a space-time finite element method. A stabilized finite element method was used to solve the Navier Stokes equations for the 3D simulations.

DISCUSSION

The solutions of the 1D equations of blood flow showed that diastolic pressure decays slowly due to the higher resistance downstream. Daily averaged wall shear stress acquired using 3D simulations shows that SCI patients exhibit low wall shear stress in the infrarenal abdominal aorta.
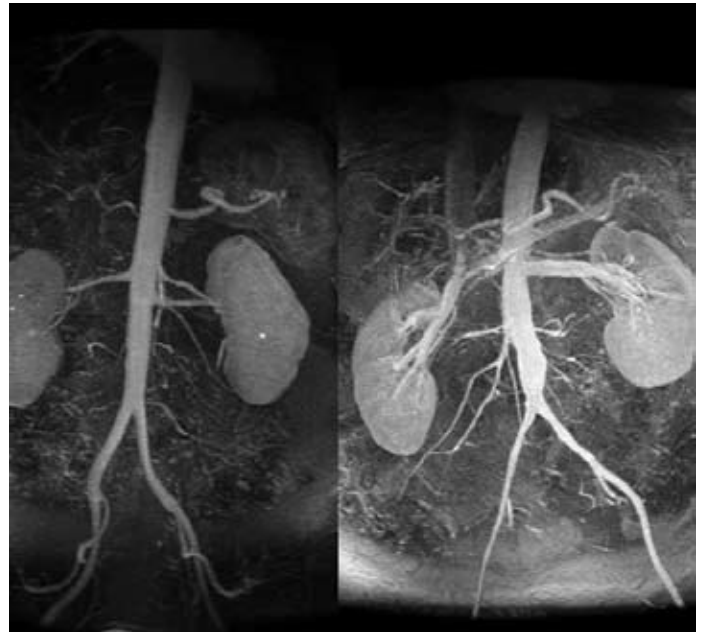
MRA data for one control subject(left) and one SCI patient (right).

CONCLUSION

We believe that slowly decaying diastolic pressure and lower daily averaged wall shear stress in the abdominal aorta can contribute to the increased risk of AAAs in SCI patients.

Superficial Femoral Artery Deformations Due to Maximal Hip and Knee Flexion

Christopher P. Cheng[1], Nathan M. Wilson[2], Robert J. Herfkens[3], Charles A. Taylor[1,2,4] –Departments of [1]Mechanical Engineering, [2]Surgery, [3]Radiology, [4]Bioengineering

INTRODUCTION

Recent studies have estimated that stents deployed in the SFA to treat atherosclerotic lesions fracture at a rate of 15 to 20%, and that these fractures may be correlated with restenosis and the return of clinical symptoms. This high rate of fracture has been hypothesized to be partially due to large, non-pulsatile deformations from repetitive body movement, including axial compression and extension, bending, and torsion.

MATERIALS AND METHODS

Eight young, healthy adults (16 lower limbs) were imaged in a GE Signa 1.5T scanner in the supine and fetal positions using contrast-enhanced MRA. A 3D gradient-recalled MRA sequence was performed in approximately 40 seconds with the following parameters: 5.1 ms TR, 1.2 TE ms, 25 degree flip angle, 448 by 256 acquisition matrix per slice, and 3 mm slices with 1.5 mm overlap. Using the MRA data, centerline spline paths for the iliofemoral, profunda femoris, and descending genicular arteries were constructed for each limb using custom software. SFA arc lengths and angle of separation between the two branches of the main axis of the SFA were quantified for both body positions and each limb. SFA arc length change, and angle of twist were calculated between supine and fetal positions.

DISCUSSION

Substantial axial and torsional deformations were measured in the SFA, however, very little bending was detected due to maximal hip and knee flexion. Axial deformations of the SFA were large and variable between

| A | B | C |
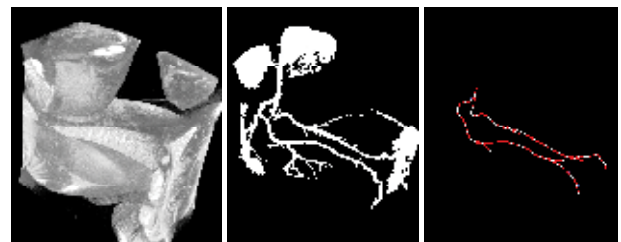
(A) Volume-rendering of a 27 y.o. healthy male subject in the fetal position in a GE Signa Excite 1.5T scanner. (B) Thresholded point cloud of the gadolinium-enhanced MRA of the lower extremity vasculature. (C) Corresponding centerline paths of the iliofemoral artery and the profunda femoris and descending genicular artery branches.

subjects, with greatest measured shortening of 25% and elongation of 17%. Although SFA length was only weakly correlated with subject height, SFA length and axial deformation for the left and right legs of the same subject were highly correlated, suggesting bilateral symmetry in the axial direction. Twisting of the SFA, however, while also exhibiting large variations in magnitude and direction, showed no evidence of bilateral symmetry or antisymmetry. The deformation data acquired in this study will help elucidate SFA stent fracture mechanisms as well as describe mechanical loading boundary conditions to guide the design of future stents and develop mechanical fatigue tests.

Comparison of Hemodynamic Parameters Across Species in Normal Abdominal Aortas Using Magnetic Resonance Imaging and Computational Fluid Mechanics

Andrea Les[1,2] , Joan Greve[1], Mary O'Connell[2], Nathan Wilson[3], Irene Vignon[2], Eiketsu Sho[4], Ronald Dalman[3,4], Charles Taylor[1,2,3] — [1]Department of Bioengineering, [2]Department of Mechanical Engineering, [3]Department of Surgery, Stanford University; [4]Palo Alto Veteran's Affairs Health Care System, Palo Alto, CA

Introduction

Abdominal Aortic Aneurysms (AAA)—the local enlargement of an artery, whose rupture can lead to hemorrhage and death—represent the 13th leading cause of death in the United States. Mice and rats are often used as models for human AAA's, however very little is known about the hemodynamic conditions of these animals. With the ability to easily manipulate the genome of the mouse in order to study the influence of specific genes to normal and pathological states, it is becoming increasingly important to understand how to scale from mouse to human when investigating physiology, pathogenesis, and therapeutic development.

The work presented here has combined Magnetic Resonance Imaging (MRI) and Computational Fluid Dynamics (CFD) to obtain spatially and temporally resolved data in order to investigate how regional hemodynamic parameters vary from mouse to rat to human in normal and pathogenic states in the abdominal aorta.

Materials and Methods

Male 8-12 week old Sprague Dawley rats and male 8-12 week old 129/SV mice were used. To create the AAA, animals were anesthetized via IP injection of 40-mg/kg sodium pentobarbital. A midline incision was made to isolate the infrarenal aorta and infuse 15U/mL of porcine pancreatic elastase for 1 hour for rats and 5 minutes for mice. The incision was closed in two layers, and animals recovered in their own cages with free access to food and water.

MRI was performed at 4.7T (Varian, Inc., Palo Alto, CA) using a 6cm inner diameter RF volume coil. Animals were anesthetized using 2% isoflurane in 1L/min of O2 and body temperature was maintained at 37°C. To quantify the geometry of the aorta, we implemented a 2D time-of-flight magnetic resonance angiography (TOF-MRA) sequence with a saturation pulse placed distal to the acquisition slice in order to null signal from venous blood (TR/TE 40/5ms, FOV 5.5cm^2, matrix 256^2, slice thickness 1mm, NEX 6).

In order to provide a non-invasively derived inlet boundary condition, a phase contrast MRI (PCMRI) sequence was implemented (TR/TE 13/3.2ms, FOV 6cm^2, NEX 8, slice thickness 2mm, flip angle 30°, matrix 128^2 zero-filled to 256^2). Volumetric flow measurements appropri-ate for use as boundary conditions for CFD simulations were obtained by integrating the velocity over the vessel cross-section. Validation included testing the sequence at 5 different velocities using a steady flow phantom and using a pulsatile flow phantom with a sinusoidal waveform (period of 200 ms) and velocities near expected systolic and diastolic values in a rat aorta. All phantom studies were done in a 3mm tube using in-line transonic flow probes as the comparison method.

Three dimensional geometric models were constructed from the 2D TOF-MRA data using custom software. A Womersley velocity profile was assigned to the inlet boundary based on the average volumetric flow rate obtained from PCMRI measurements. Resistance boundary conditions were prescribed at the iliac and sacral arteries and a stabilized finite element method was used to compute three-dimensional velocity fields and wall shear stress assuming a Newtonian fluid and rigid wall models.

Discussion

Volumetric flow rates calculated from PCMRI data (3 subjects per species) and representative plots of mean wall shear stress for each species are shown below.

Results demonstrate that PCMRI and CFD can be successfully extended to both a rat and mouse model to provide the spatial resolution and longitudinal capability to quantify hemodynamics across species. We believe the MR measurements of volumetric flow and derived hemodynamic parameters more properly reflect the in vivo conditions because the technique is completely non-invasive, unlike transonic flow probe data acquisition.

Conclusion

Small animals such as mice and rats are often used as models for human illness such as cardiovascular disease. This work contributes to understanding how hemodynamic conditions such as shear stress—important in the localization of vascular disease—scale from mouse to rat to human. It agrees with the allometric law for shear stress in blood vessels that predicts that wall shear stress will be inversely related to body size ($\tau \propto M^{-0.2}$) but proposes a coefficient of -0.37 to more accurately predict aortic shear stress values.
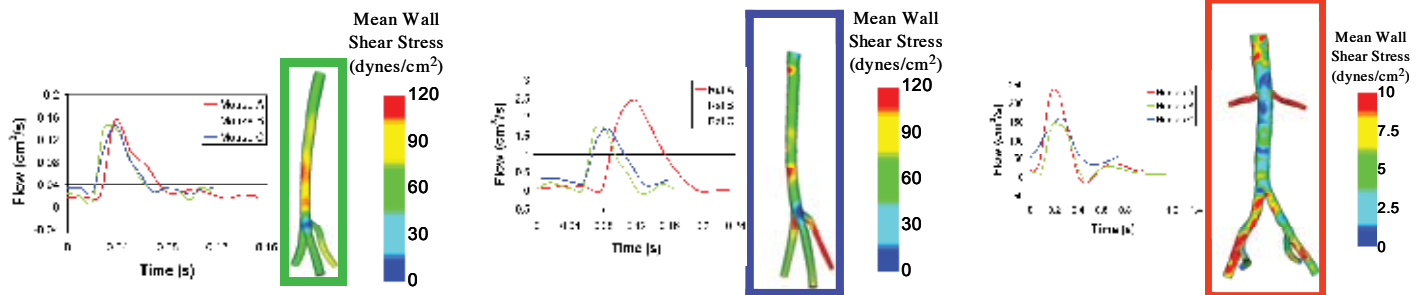
Development of Methods to Non-invasively, Longitudinally Quantify Hemodynamics in a Rat Model of Abdominal Aortic Aneurysm Using Magnetic Resonance Imaging and Computational Fluid Dynamics

Joan Greve[1], Andrea Les[1,2], Mary O'Connell[2], Nathan Wilson[3], Eiketsu Sho[4], Ronald Dalman[3,4], Charles Taylor[1,2,3] – [1]Department of Bioengineering, [2]Department of Mechanical Engineering, [3]Department of Surgery, Stanford University; [4]Palo Alto Veteran's Administration, Palo Alto, CA

Introduction

An abdominal aortic aneurysm (AAA) is defined as an increase of vessel diameter of ~150%. The fact that 98% of aortic aneurysms occur in the infrarenal aorta strongly suggests that localized factors contribute to AAA pathogenesis. However, most recent investigations have focused on systemic risk factors for developing AAA, not localized risk factors.

Ideally, longitudinal studies in human subjects at risk for AAA could be conducted to elucidate the important hemodynamic variables. Due to the long time-course of AAA, these studies are impractical in human subjects. Small animal models with induced aneurysms represent a viable means to investigate longitudinal hemodynamic conditions with the progression of AAA. Noninvasive methods to quantify aortic hemodynamics in small animals are needed for such studies.

We have combined an *in vivo* technique, magnetic resonance imaging (MRI), with an *in silico* technique, computational fluid dynamics (CFD), to provide a non-invasive, longitudinal methodology to quantify the geometric and hemodynamic changes that occur in a rat model of AAA. These methods can be extended to correlate changes in hemodynamic parameters with physiological alterations, e.g. inflammation, hypothesized to contribute to the development of AAA.

Materials and Methods

Male 8-12 week old Sprague Dawley rats were utilized. To create the AAA, animals were anesthetized via IP injection of 40-mg/kg sodium pentobarbital. A midline incision was made to isolate the infrarenal aorta and infuse 15U/mL of porcine pancreatic elastase for 1 hour. The incision was closed in two layers, and animals recovered in their own cages with free access to food and water.

MRI was performed at 4.7T (Varian, Inc., Palo Alto, CA) using a 6cm inner diameter RF volume coil. Animals were anesthetized using 2% isoflurane in 1L/min of O2 and body temperature was maintained at 37°C. To quantify the geometry of the aorta, we implemented a 2D time-of-flight magnetic resonance angiography (TOF-MRA) sequence with a saturation pulse placed distal to the acquisition slice in order to null signal from venous blood (TR/TE 40/5ms, FOV 5.5cm^2, matrix 256^2, slice thickness 1mm, NEX 6).

In order to provide a non-invasively derived inlet boundary condition, a phase contrast MRI (PCMRI) sequence was implemented (TR/TE 13/3.2ms, FOV 6cm^2, NEX 8, slice thickness 2mm, flip angle 30°, matrix 128^2 zero-filled to 256^2). Volumetric flow measurements appropriate for use as boundary conditions for CFD simulations were obtained by integrating the velocity over the vessel cross-section. Validation included testing the sequence at 5 different velocities using a steady flow phantom and using a pulsatile flow phantom with a sinusoidal waveform (period of 200 ms) and velocities near expected systolic and diastolic values in a rat aorta. All phantom studies were done in a 3mm tube using in-line transonic flow probes as the comparison method.

Three dimensional geometric models were constructed from the 2D TOF-MRA data using custom software. A Womersley velocity profile was assigned to the inlet boundary based on the average volumetric flow rate obtained from PCMRI measurements. Resistance boundary conditions were prescribed at the iliac and sacral arteries and a stabilized finite element method was used to compute three-dimensional velocity fields and wall shear stress assuming a Newtonian fluid and rigid wall models.

Discussion

The velocities and calculations of volumetric flow rate measured using the PCMRI sequence matched flow meter measurements made from all five steady-state velocities and the pulsatile phantom, respectively, Figure 1. A typical velocity image from the abdomen of a rat and mean velocity values at 12 timepoints through the cardiac cycle for six rats are shown in Figure 2. The 2D TOF-MRA data was successfully reconstructed into 3D geometric models for all rats at all timepoints. Veloci-

ties at peak systole and mean wall shear stress values for the rat with the largest aneurysm are shown in Figure 3.
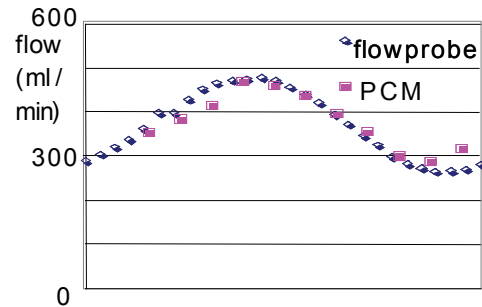

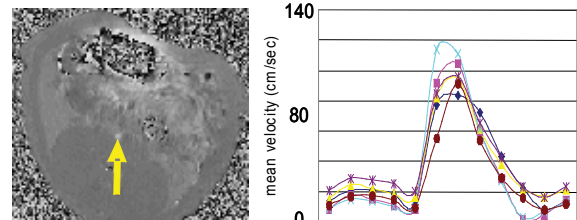*Figure1: PCMRI volumetric flow calculated from a pulsatile flow phantom.*

Figure 2: Velocity image of rat abdominal aorta (left arrow). Mean velocities through cardiac cycle for six rats.
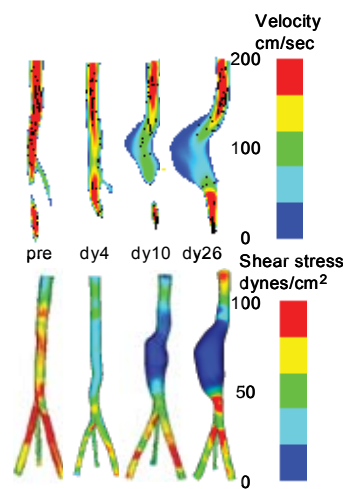

Figure 3: Velocity fields at peak systole (top) and mean wall shear stress (bottom) in a rat model of AAA.

Conclusion

Longitudinal investigation of AAA in human patients is infeasible. Small animal models of AAA represent an alternative, especially in light of the extensive manipulation of the mouse genome. The PCMRI technique presented here provides a non-invasive method to measure hemodynamic conditions *in vivo*, a preferred alternative to the more common techniques (e.g. transonic flow probes) that require perturbing the vessel of interest. PCMRI data can be coupled with anatomical MRI data and CFD in order to quantify the changing hemodynamic state during AAA progression. Future work will implement *in vivo* MR methods for visualizing inflammation with the goal of providing a completely non-invasive methodology to quantify and correlate geometric, hemodynamic, and pathogenic changes in a small animal model of AAA in order to develop novel therapeutic approaches.

Reducing Gradient Imperfections for Spiral CSI

D. Kim[1], E. Adalsteinsson[2,3], D. M. Spielman[1] - [1]Department of Radiology, Stanford University; [2]Division of Health Sciences and Technology, [3]Electrical Engineering and Computer Science, MIT

Introduction

Spiral readout based CSI (Chemical Shift Imaging) [1] offers several potential advantages over conventional phase encoded CSI. The minimum total scan time to collect the data is dramatically reduced due to the k-space coverage method of the spirals. This characteristic enables spiral CSI to be used for applications such as full volumetric coverage CSI or spatially resolved two-dimensional spectroscopy [2,3]. However, using time varying gradients during the readout period are susceptible to system imperfections such as eddy current effects or maxwell fields, which can lead to a discrepancy between the desired and actual k-space trajectory. This can ultimately limit the performance and thereby restrict the usefulness of the spiral CSI sequence. Although the nature of these imperfections are pretty well understood, the effect on the spiral CSI seqeunce both spatially and spectrally is nonintuitive. This abstract illustrates the effects on spiral CSI resulting from the presence of the nonideal time varying readout gradient.

Methods

All data acquisition and simulations were performed with the following spiral CSI sequence at 1.5 T: 32x32 cm FOV inplane, single slice acquisition, 4 spatial interleaves to cover the required k-space, 256 spiral lobes per readout which resulted in 0.54 sec readout time, each spiral 2.096 ms long. Data reconstruction consisted of gridding in kx and ky and inverse FFT. The spectral bandwidth after reconstruction was 477 Hz with 1.85 Hz resolution. K-space trajectories were measured for each interleave and for the whole duration of the readout using the technique by Duyn [4] (16 nex, 1:48 minute scan). Data were reconstructed assuming desired k-space trajectory as well as actual measured trajectories. Also, simulations were performed assuming ideal k-space data collection with reconstruction based on actual measured k-space trajectory to illustrate the effect when there is a discrepancy.

Results and Discussion

Figure 1 shows an illustration of a spiral readout trajectory drifting off from the actual trajectory during the readout interval. The amount of drift depends on the gradient system and can be significant. Figure 2 shows the desired versus the measured k-space trajectory. To illustrate the discrepancy more pronouncely, the plot shows the 64 th spiral lobe of the total 256 lobes. The accumulation of the drift can be seen in Fig. 3. Desired
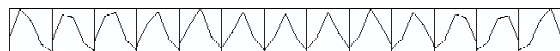
Fig. 4 Simulation across a 16 cm phantom assuming discrepancy in desired and measured k-space trajectory. The data is shown between a +- 3 Hz region.

Fig. 5 Spectra from phantom data reconstructed with the measured trajectory. Each voxel has spectra of +- 7 Hz from the water peak. The peak shifts are mostly due to B_0 inhomogeneity.
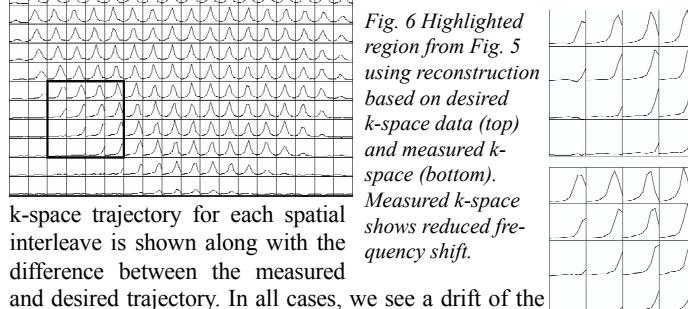
Fig. 6 Highlighted region from Fig. 5 using reconstruction based on desired k-space data (top) and measured k-space (bottom). Measured k-space shows reduced frequency shift.

k-space trajectory for each spatial interleave is shown along with the difference between the measured and desired trajectory. In all cases, we see a drift of the trajectory along k_x to be the most significant feature.

Figure 4 shows simulated results obtained assuming data collection from ideal k-space versus reconstruction with the measured trajectory. The plot shows a spatially dependant frequency shift of the peak which correlates to the k_x drift of the measured trajectory. The amount of frequency shift from left to right is approximately 4 Hz. Figure 5 shows phantom data reconstructed with the measured k-space trajectory. The inherent B_0 inhomogeneity can be observed from the spatially dependant frequency shift of the peak. If the data were reconstructed assuming the desired k-space trajectory, this can lead to additional frequency shifts as seen in Fig. 4. This is illusrated in Fig. 6 where data were reconstructed assuming desired k-space trajectory (top) and measured k-space trajectory (bottom). As can be seen, using the measured k-space trajectory for the reconstruction reduces the amount of frequency shifts compared to desired k-space trajectory. The amount of frequency shift difference was approximately 2 Hz within the illustrated region.

Conclusion

Gradient imperfections resulting in k-space trajectory discrepancy can lead to spatially varying frequency shifts for spiral based CSI. In addition, we have observed minor spatially varying amplitude modulations. Measurement error can lead to decreased SNR or other types of effects. If the trajectory was designed to critically sample the k-space region, aliasing artifacts can be present when measured k-space trajectory does not critically. A simple method to overcome this is to apply a 2x gridding algorithm to move the aliasing artifact to outside the field of view. Misadjusted gradient timing can also cause frequency dependant phase shifts in the presence of B_0 inhomogeneity.

References

[1] E. Adalsteinsson, et al., MRM,1998;39:889-898
[2] E. Adalsteinsson, et al., MRM 1999;41:8-12
[3] B Hiba, et al., MRM 2004;52:658-662 [4] J. Duyn, et al., MRM 1998;132:150-153.

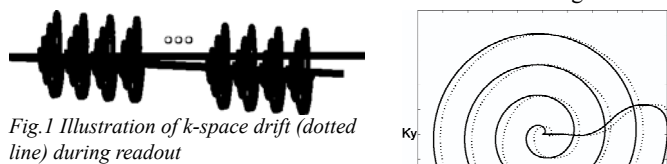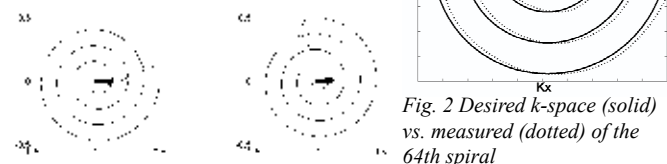Fig.1 Illustration of k-space drift (dotted line) during readout

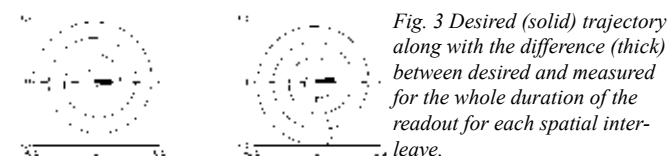Fig. 2 Desired k-space (solid) vs. measured (dotted) of the 64th spiral

Fig. 3 Desired (solid) trajectory along with the difference (thick) between desired and measured for the whole duration of the readout for each spatial interleave.
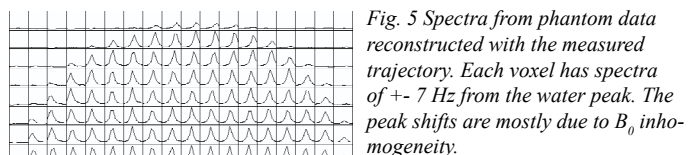
Brain 3D MRSI using Dualband Spectral-Spatial Excitation and k-Space Corrected Spiral Readout

M. Gu[1], D.H. Kim[1], E. Adalsteinsson[2], D. M. Spielman[1] - [1]Department of Electrical Engineering, Department of Radiology, Stanford University; [2]Harvard-MIT Division of Health Sciences and Technology, EECS Department, MIT

INTRODUCTION

Brain magnetic resonance spectroscopic imaging (MRSI) has demonstrated its usefulness in diagnosing and monitoring brain illness. To obtain high fidelity metabolite spectra, it is critical to suppress water and lipids. Instead of having complete water suppression, partial water signal can provide valuable phase and frequency reference for subsequent signal processing. In order to utilize full capacity of the gradient system and reduce imaging time, spiral k-space trajectory is generally applied. However, gradient imperfection caused by eddy currents would result in distortion or drift in k-space. To address these issues, in this paper, we present an MRSI sequence based on PRESS [1] technique at 1.5T with additional VSS suppression of lipids, dualband spectral-spatial excitation and k-space corrected spiral readout.

METHODS

Three spectral-spatial RF pulses were incorporated into a PRESS sequence to form a spin echo [2]. The 90 degree pulse is designed to fully excite both water and metabolites. To retain partial water signal, dualband spectral-spatial 180 degree pulses were designed and implemented. At 1.5T, the spectral profile is designed to excite metabolites that resonant from 3.2ppm (Choline) to NAA(2.02ppm) with 15Hz margin on both sides. A partial passband of about 70 Hz that has amplitude of 0.08 was centered on water resonance. The spectral-spatial pulses also suppress lipids below 1.4ppm as opposed to the non-selective inversion recovery technique that normally leads to 30% metabolite signal loss [3]. A minimum-phase spectral profile was chosen to retain a sharp transition band. Before excitation, VSS pulses were prescribed for outer volume lipid suppression. During readout, spirals with 4 interleaves were played out for spatial and spectral encoding. Actual k-space trajectories were calculated by measuring the different phase accrued between signals with gradients on and off before they were used in reconstruction [4]. The final imaging sequence has the following characteristics: outer volume suppression, dualband spectral-spatial PRESS RF pulse for metabolite excitation, partial water suppression and further lipid suppression, TR/
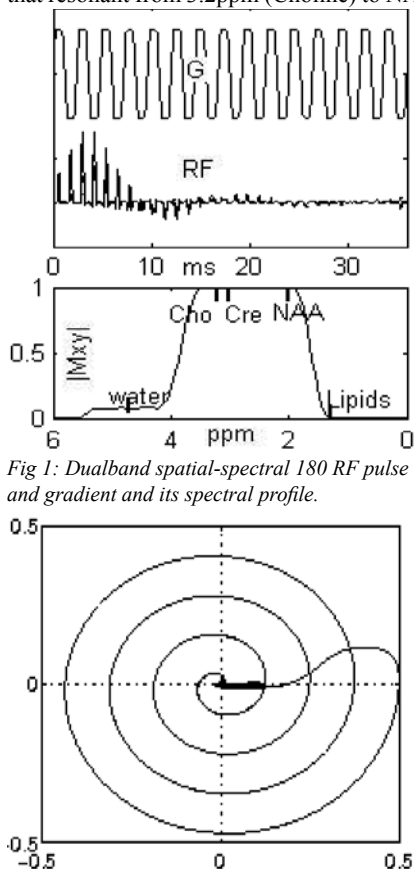

Fig 1: Dualband spatial-spectral 180 RF pulse and gradient and its spectral profile.

Fig 2: One interleave of ideal spiral trajectory and its difference from the measured ones for one TR. The dense dots near the origin represent differences between the ideal spiral and 256 measured ones.

Fig 3. Metabolite spectra from a volumetric ^{1}H MRSI in vivo brain study. The white bars on the grid represent the VSS region and the gray box represents the PRESS box.

TE=1500/144ms, 4 spatial interleave spiral readout gradients, 256 spirals per readout, 500 Hz spectral bandwidth, 32/32/16 matrix size, 1cc voxel, 8 NEX with phase cycling and 13 minute acquisition time.
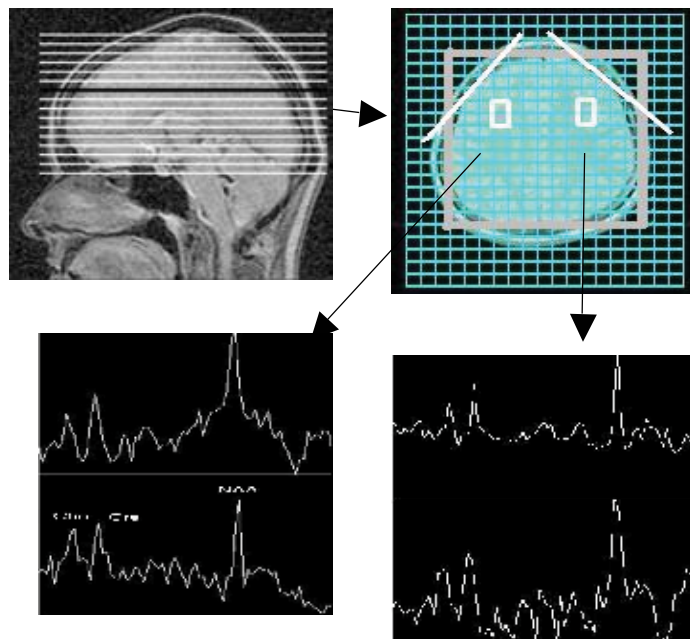
RESULTS

The dualband RF, gradient waveforms and its spectral profile are shown in Figure 1. The ripple magnitude in the pass and stop bands are 1% and the transition bandwidth on the lipid side is about 30 Hz. Figure 2 shows one interleaf of an ideal spiral trajectory and its difference from 256 measured ones in one TR. Spectra from voxels in one of 16 slices from an in vivo study, after rephasing with water signal, are shown in Figure 3. The enlarged spectra from 4 representative voxels clearly show well phased spectra. The reconstructed data were reordered to generate DICOM compatible data and put back to the scanner database to be viewed using standard GE spectroscopic tools (Functool).

CONCLUSION

A 3D MRSI sequence based on PRESS localization with outer-volume lipid suppression, dualband excitation and k-space corrected spiral readout has been implemented at 1.5T for brain imaging. Its capability of obtaining high quality metabolite spectra with water reference has been demonstrated from an in vivo study. Ongoing studies are being performed to evaluate if the lipid suppression provided by the spectral-spatial pulse is sufficient to eliminate the need for the VSS pulses and the PRESS box.

REFERENCES

[1] Bottomley, P. A. Ann N Y Acad Sci, 508, 333, 333-348, 1987
[2]A. A. Schricker, et al, MRM 46:1079-1087, 2001
[3] E. Adalsteinsson, et al, MRM 33:461-466, 1995
[4] J. H. Duyn, et al, Journal of Magnetic Resonance 132, 150-153, 1998

Effectively Decoupled Spiral CSI with Frequency-Selective Lipid Suppression at 3 T

Dirk Mayer[1], Meng Gu[1], Donghyun Kim[2], Elfar Adalsteinsson[3], Daniel M. Spielman – [1]Department of Radiology, Stanford University; [2]Department of Radiology, UC San Francisco; MIT, Cambridge, MA

Introduction

Fast Constant Time (CT)-PRESS based spiral chemical shift imaging (CSI) [1,2] has been introduced as an alternative to short TE CSI. By using effective homonuclear decoupling [3] it allows the detection of coupled resonances such as glutamate (Glu) and myo-inositol (mI) with improved signal separation and high signal-to-noise ratio (SNR). The PRESS pre-localization is advantageous for lipid suppression when pre-selecting a volume entirely within the brain. But it also increases the minimum evolution time (t_c, echo time at the central CS encoding step), which can be used to optimize the SNR of a particular coupled resonance. Using a PRESS module also potentially increases the signal loss due to transverse relaxation. Therefore, the aim of this work was to implement a fast effectively decoupled CSI sequence without PRESS pre-localization in order to reduce the minimum t_c. A frequency-selective inversion pulse was used to suppress lipid signals from the scalp.

Materials and Methods

All measurements were performed on a GE 3 T MR scanner equipped with self-shielded gradients (40 mT/m, 150 mT/m/ms). A quadrature bird-cage coil was used for both RF excitation and signal reception.

The implemented sequence consists of six parts: (a) a frequency-selective inversion pulse (b) two CHESS pulses for water suppression, (c) an outer volume suppression (OVS) module, (d) a slice(z)-selective excitation pulse, (e) a slice-selective(x) refocusing pulse (167°) for CS encoding in f_1, and (f) a spiral readout gradient for combined spatial(xy)-spectral(f_2) encoding. The inversion pulse (20 ms) was designed with a pass band of 500 Hz and a transition band of only 50 Hz [4]. The pulse was applied with a frequency offset of -285 Hz relative to the singlet resonance of N-acetyl-aspartate (NAA) at 2 ppm. The CS encoding pulse was shifted in increments of 6.4 ms in 17 steps leading to a spectral width SW_1 of only 78.125 Hz. Therefore, the 2D spectra are severely aliased in f_1. But as the signals occur close to the spectral diagonal, the aliasing does not lead to signal overlap. By eliminating the y-selective refocusing pulse and using the x-selective pulse for CS encoding t_c could be reduced from 146 ms to 125 ms. The spatial-spectral encoding was performed with 12 spatial interleaves for an oversized FOV of 48×48 cm² with a 32×32 matrix (2×1.5×1.5 cm³ nominal voxel size) and SW_2 of 1050 Hz. Due to hardware restrictions the number of data points acquired continuously at the readout bandwidth of 250 kHz was 7168. Therefore, each readout consisted of 10 blocks of 7168 points to increase the nominal spectral resolution in f_2. The readout was repeated with the start of data acquisition shifted by 1.3 ms to fill the resulting gaps in the acquisition. The spiral CSI module was shifted together with the CS encoding pulse in order to increase the SNR. With a TR = 2s, T_{meas} was 13:44 min. If the experiment is not limited by SNR, a variation of the spiral design (24×24 cm², 16×16 matrix) can be used leading to a T_{meas} of 4:40 min.

The data post-processing comprised gridding, apodization in the spectral dimensions (multiplication with sine-bell functions and zero-filling), and FFT. A t_1-dependent linear phase correction was performed
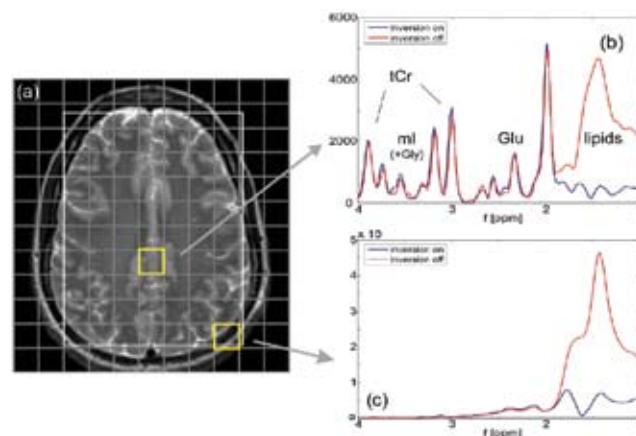

Fig. 1 Effectively decoupled spectra from voxels from a healthy volunteer containing predominantly gray matter (b) and subcutaneous fat (c), respectively. The location of the voxels is indicated in the water MRI (a). Also shown is the volume as defined by OVS and the x-selective refocusing pulse. For each voxel the spectra acquired with inversion (blue) and without inversion (red) are shown.

along f_2 to correct for the differences of the start of data acquisition. After unwrapping the 2D spectra in f_1 diagonal spectra were calculated by integrating the signal along f_2 within a ±13 Hz interval around the spectral diagonal.

Results

For the in vivo application of the method a 20×107×142 mm³ volume (axial slice orientation) was selected by OVS just above the ventricles of a healthy volunteer as shown in Fig. 1a. The TI was 190 ms. Both spectra from voxels containing predominantly gray matter (Fig. 1b) and subcutaneous fat (Fig. 1c), respectively, demonstrate that the spectral region downfield of 2 ppm is not affected by the inversion pulse. The suppression factor for the lipids is about 7. Figure 1b also shows the good separation of the Glu C4 resonance due to effective decoupling

Discussion and Conclusion

The presented data show the feasibility of effectively decoupled fast spiral based CSI. This implementation allows the reduction of the minimum tc of the sequence. An inversion pulse with a sharp transition band of 50 Hz was used to suppress lipid signals from the scalp. By using effective decoupling this work demonstrates that compounds such as Glu and mI can be reliably measured without water or lipid baseline artifacts which typically hamper short TE CSI. Further improvement in lipid and water suppression can be achieved by using a spatial-spectrally selective refocusing pulse which pass band does not include these resonances.

References

1. Mayer, D., et al., Proc. ISMRM 2004, 678.
2. Dreher, W., Leibfritz, D., Magn. Reson. Imag., 17, 141-150, 1999.
3. Bax, A., Freeman, R., J. Magn. Reson., 44, 542, 1981.
4. Gu, M., et al., Proc. ISMRM 2004, 2293.

Matched Phase Dualband Spectral-Spatial RF Pulse Sequence for Spectroscopic Imaging of the Breast at 3T

Priti Balchandani[1], John Pauly[2], Daniel Spielman[1] — [1]Department of Radiology, [2]Department of Electrical Engineering

Introduction

[1]H MR spectroscopic imaging (MRSI) may be used to detect the presence of cancerous tissue in the breast. In breast MRSI studies, an elevated level of the metabolite, choline, relative to normal breast tissue is used as the main indicator of cancer. MRSI usually suffers from: 1) Inadequate water or lipid suppression; 2) Low SNR of metabolite signals and 3) Spatially varying phase profiles due to B1 inhomogeneities. In addition, a reference is required for proper phase and frequency correction. The pulse sequence developed in this study attempts to address these problems by: 1) using spectral-spatial pulses to suppress lipids while fully exciting metabolites; 2) Using dualband pulses to partially suppress water so that it may be used as a phase and frequency reference and 3) Using a phase matched 90º and 180º pulse pair so that the final echo has a flat phase profile that is as immune to spatially varying B1 as possible. In addition the sequence is being developed for use at 3T so that higher SNR and frequency separation can be possible as compared to 1.5T. However, moving to higher fields requires increased RF peak power to achieve the same frequency coverage. This problem will be addressed by using the technique of root flipping to find RF pulses with identical excitation profiles but different RF power distributions.

Materials and Methods

Initially a maximum phase 180º dualband spectral-spatial pulse was designed. Twenty linear phase subpulses were used to excite an 8 cm slab in the spatial direction. The passband for the pulse encompassed the choline resonance at 3.2 ppm while suppressing the lipid resonances at 1.5 ppm and below. The partial water band was designed to excite 10% of the water signal at 4.7 ppm. Ripple in the water passband was limited to less than 1%. After designing the maximum phase 180º pulse, every possible root flipped configuration was traversed to find the one that results in the lowest RF peak power. The final pulse was below RF peak power limitations. The beta polynomial from the 180º pulse was then used to create a phase matched beta polynomial for the 90º pulse. No root flipping was required to bring the 90º pulse below RF peak power limitations. The 90º and 180º pulses were both designed to excite a slab in the z-direction and have the same spectral excitation profile, resulting in increased selectivity.

Discussion

The optimized dualband 180º and 90º RF pulses are shown in figures 1 and 2. The spectral profile of the final echo with choline centered at 0 Hz is shown in figure 3. It can be seen in figure 3 that the lipid resonances have been suppressed. In order to stay within RF peak power limitations, only 96% excitation was possible for the metabolite passband, resulting in lower than maximum achievable SNR. This was a necessary tradeoff. Water has been partially suppressed with low ripple. This may allow for the use of water for quantification as well as phase and frequency correction. The phase profile across the water and metabolite passbands still has about a 0.4 radian variation across it. This is due to the fact that there is still some phase contribution from the alpha polynomial which has to be removed in order to achieve a completely flat phase profile.

Conclusions and Future Work

A 3T spectroscopic imaging pulse sequence has been designed that successfully excites the metabolite of interest, choline, in the breast while
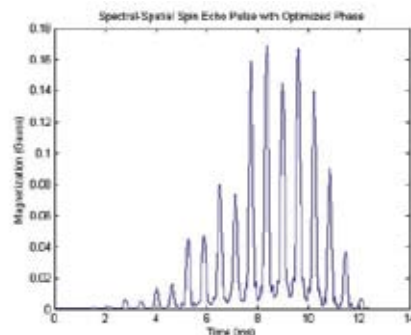

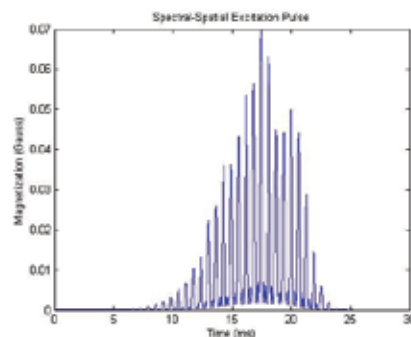Figure 1: Spectral-Spatial dualband phase optimized 180° RF pulse

Figure 2: Spectral-Spatial 90° pulse matched in phase to 180° pulse
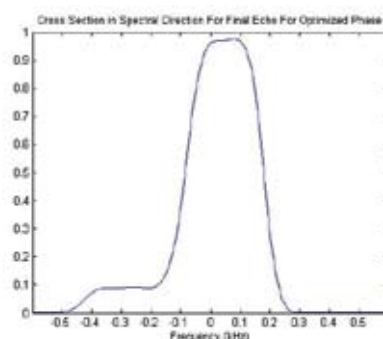

Figure 3: Spectral excitation profile for final echo

suppressing water and lipids and remaining under RF peak power limitations. Data has yet to be collected from phantom and patient studies on the 3T scanner (Echospeed Whole Body Magnet, GE Healthcare, Waukesha, WI). This pulse sequence can be easily extended for use in the brain by adjusting the metabolite passband to encompass metabolites from myoinositol to NAA. In addition, the fact that this pulse sequence, unlike PRESS, utilizes only two pulses instead of three makes it more amenable to short echo times. Work is currently underway to adjust this sequence to excite the full range of metabolites in the brain at 3T, including short T_2 metabolites such as glutamate and glutamine.

Spectroscopic Imaging of Hyperpolarized ^{13}C-labelled Metabolites

Yakir Levin[1], Dirk Mayer[1], Ralph Hurd[2], Yi-Fen Yen[2], Daniel Spielman[1] – [1]Department of Radiology, Stanford University; [2]ASL-West, GE Healthcare

Introduction

The development of hyperpolarized MRI agents presents both unprecedented opportunities as well as new technical challenges. With SNR enhancements on the order of 100,000-fold, dynamic nuclear polarization (DNP) of metabolically active substrates (e.g. ^{13}C-labelled pyruvate or acetate) theoretically permits in vivo imaging the injected agent and downstream metabolic products. This feature of hyperpolarized MRS provides an opportunity to noninvasively monitor dynamic metabolic processes in vivo under normal and pathologic conditions. Important applications include tumor diagnosis as well as treatment monitoring and assessment of cardiac function. Finite relaxation times (pyruvate in vivo T1/T2s are approximately 60/2 s respectively) necessitate rapid spectroscopic imaging. While a number of fast spectroscopic imaging methods have been proposed for general in vivo MRS applications, the relatively sparse spectrum resulting from the bolus injection of a high SNR substrate such as hyperpolarized ^{13}C-labelled pyruvate can be exploited by focusing on imaging methods that achieve high spatial resolution in exchange for relatively modest spectral resolution and bandwidth requirements.

Materials and Methods

A small phantom (Figure 1a) of cylindrical tubes containing 13C1-alanine, 13C1-lactate, and a pyruvate-pyruvate C1-C2 ester was constructed in order test our imaging sequence. Figure 1b depicts structures and the biochemical relationships among pyruvate, alanine, and lactate. The structure of the ester is also depicted. Figure 1c depicts the spectra, obtained from the phantom tubes, of all of the labelled carbons. The pulse sequence, depicted in figure 2a, takes advantage of the sparsity of the spectrum by allowing peaks to "alias" into a narrow spectral width. Because kf (= t) is undersampled, higher spatial resolution can be achieved in a single readout, thus allowing faster imaging. The sequence is capable of spatial interleaving (rotating the gradient waveforms) and spectral interleaving (delaying the gradient waveforms for additional readouts). The latter option allows the user to trade spectral width for temporal resolution in analysis of data.

Results

Figure 2b depicts alanine, lactate, and pyruvate metabolic images along with a color overlay on the corresponding 1H MRI images obtained using FIDCSI, single-shot spiral MRSI , and thrice interleaved spiral MRSI acquisitions, respectively. The minimum acquisition time for the single-shot version of the spiral MRSI sequence was approximately 160 ms (8 cm FOV, 5 mm isotropic voxels), although 64 averages were used for these initial phantom experiments. With the use of hyperpolarized agents, the additional averaging should be unnecessary.

Discussion and Conclusion

Metabolic images compare favorably with the much more time consuming traditionally phase-encoded acquisition (FIDCSI). Additional experimentation will compare the performance of this sequence with other fast imaging sequences (EPSI, Multi-Point Dixon) in dynamically assessing in vivo metabolism for a variety of metabolic pathways.

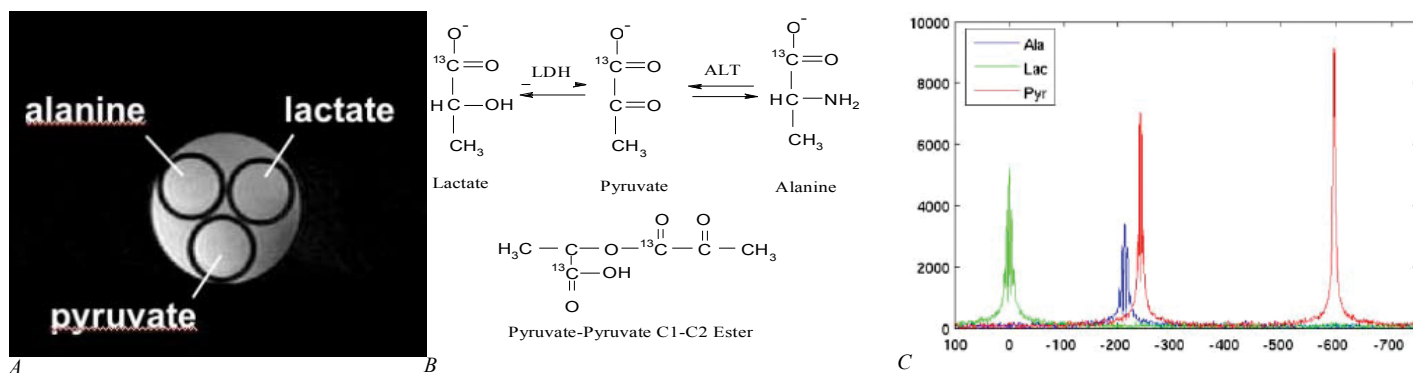*Fig. 1 A: 1H image of phantom B: Chemical structures of relevant molecules. C: 13C spectra of molecules in the phantom*
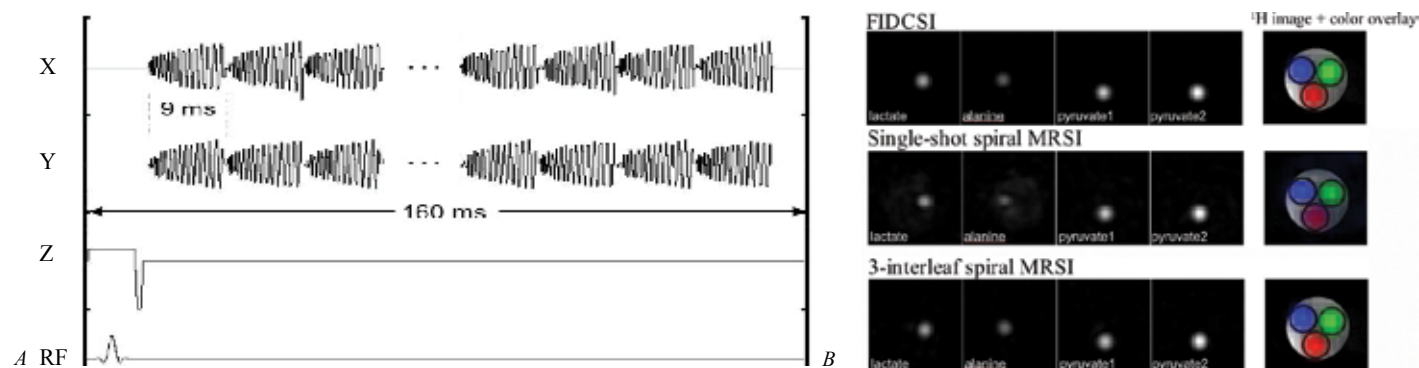

Fig. 2. A: Sample Spiral MRSI pulse sequence B: , lactate, and pyruvate metabolic images along with a color overlay on the corresponding 1H MRI images obtained using FIDCSI, single-shot spiral MRSI , and thrice interleaved spiral MRSI acquisitions, respectively.

Referenceless Thermometry in the Presence of Phase Discontinuities Between Water and Fat

Viola Rieke[1], Anthony Ross[2], William Nau[2], Chris Diederich[2], Graham Sommer[1], Kim Butts Pauly[1] - [1]Department of Radiology, Stanford University; [2]Department of Radiation Oncology, UCSF.

Introduction

Referenceless proton resonance frequency (PRF) shift thermometry [1] is inherently robust to tissue motion because the subtraction of a baseline phase image acquired prior to heating is not necessary. Instead, the background phase is estimated in every individual image from a frame region of interest (ROI) surrounding the heating region. In the simple approach, only aqueous tissue is present in the frame ROI.

For thermal ablation of the prostate, both adipose and aqueous tissues are present in the frame ROI. Referenceless temperature estimation still works when the echo time TE is chosen such that water and fat are exactly in-phase in order to prevent phase discontinuities between the two tissue types which would distort the phase estimation. However, determination of the exact in-phase TE is difficult in practice since it depends on the body temperature of the subject and the spectral components of the fat.

We propose an extension to referenceless thermometry where the background phase is estimated from water and fat, allowing for a constant phase offset between the two tissues and thereby eliminating the constraint of an in-phase echo time TE. The method is demonstrated during in vivo canine prostate ablation.

Methods

Images at three different echo times (14.3 ms, 21.4 ms, 28.6 ms) are acquired in two acquisitions. Corresponding to phase angles between water and fat of 2π, 3π and 4π at 0.5T. From a 3pt-Dixon decomposition, binary masks of regions that contain water or fat are created.

For referenceless temperature mapping, a frame region of interest is selected around the prostate, as seen in Fig. 1. The unwrapped phase in aqueous tissue in this region is approximated by a polynomial, P_W. The phase in adipose tissue is described by the same polynomial, but has a constant phase offset from water that varies with echo time, such that $P_W = P_F + c$. With the binary fat/water maps, the polynomial coefficients including the offset c are determined in the least squares sense using a weighting by the image magnitude squared. The extrapolation of the fitted polynomial to locations within the prostate serves as an estimation of the baseline phase.

Images were acquired during thermal ablation of the prostate in a canine model using a transurethral ultrasound applicator [2] on a 0.5T GE Signa SP scanner. Imaging parameters were TR/BW1/BW2/flip/FOV/slice = 150 ms/12.5 kHz/12.5 kHz/60/20x16 cm/5 mm. Temperature maps were reconstructed with referenceless reconstruction with and without the described phase offset correction and compared to those obtained with conventional baseline phase subtraction.

Results

Figure 2 shows a comparison of the three temperature maps. Conventional baseline subtraction (left) gives reasonable temperature maps, but suffers when tissue motion is present. Although an in-phase echo time was chosen for referenceless reconstruction (middle), small phase discontinuities between water and fat (seen in Fig. 1, right) cause errors in the temperature estimation (dashed arrows). Allowing for an offset between water and fat in the phase estimation with referenceless reconstruction (right) improves the quality of the temperature maps.
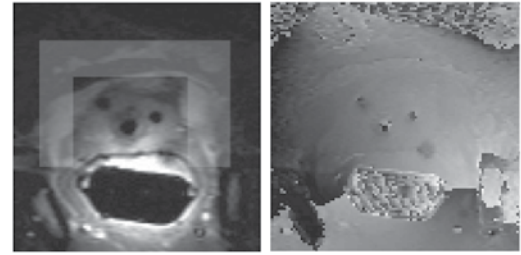

Figure 1: Magnitude image (left) showing the frame region around the prostate and unwrapped phase image (right). Note the small phase discontinuities between the water and fat regions in the unwrapped phase image.
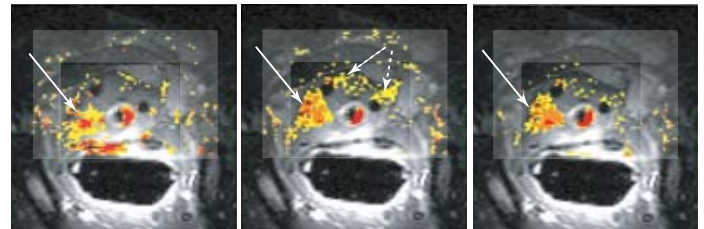

Figure 2: Temperature maps generated with conventional baseline subtraction (left), and referenceless reconstruction without (middle) and with (right) phase offset correction showing heating from the transurethral applicator in the right part of the prostate (solid white arrows). Without phase offset correction, temperature errors occur near the interface between prostate and fatty tissue (dashed arrows). Phase offset correction eliminates these errors.

Discussion

This referenceless method allows temperature estimation with any echo time and takes advantage of both aqueous and adipose tissues present in the frame ROI. In the current implementation, two image acquisitions are needed to acquire all necessary echoes for the 3pt-Dixon decomposition, such that the binary masks are updated every other image. However, since motion experienced during prostate ablation is small from image to image, the same binary mask can be used for the reconstruction of two consecutive temperature maps. The temperature measurements can be made from each acquisition, so that the temporal resolution of the thermal measurements is not compromised. Since fat and water areas are handled separately in the reconstruction, it is also possible to correct the phase in fatty regions for chemical shift before the polynomial fit [3].

Using binary maps to locate water and fat regions works well in the prostate images, since the regions are discrete and most pixels contain only either water or fat. Use of the method in more heterogeneous tissues, where the majority of pixels contain varying amounts of water and fat (e.g. breast tissue) will require further development of the reconstruction algorithm.

References

[1] Rieke V., et al, Magn Res Med. 51(6):1223-31 (2004).
[2] Ross A.B., et al, Phys Med Biol. 49(2):189-204 (2004).
[3] Rieke V., et al, Proc. IEEE EMBS, 2004.

Echo Combination to Reduce Temperature Measurement Errors in the Presence of Small Fractions of Fat

Viola Rieke, Kim Butts Pauly – Department of Radiology

Introduction

Lipids create errors in temperature quantization with the proton resonant frequency shift method (PRF). Normal liver tissue can contain more than 6% lipid while diseased liver may consist of lipid signal on the order of 20% or more. Fat suppression is commonly used, but increases imaging time and is difficult at low field strengths. In this study, we investigate a simple method to substantially reduce these errors by refocusing several gradient echoes and combining them. This echo combination technique then eliminates the need for fat suppression in tissues such as the liver.

Methods

Simulation of temperature errors were made as a function of echo time (TE) and fat percentage. Data acquired at echo times corresponding to 2π, 3π, and 4π phase shifts between fat and water were combined. Experiments were performed in pure water and a mixture of 80% water and 20% fat that were heated to 90°C and imaged during cooling to room temperature.

Results and Discussion

Figure 1 shows simulated errors as a function of echo time in a mixture of 80% water and 20% fat. Due to the cyclic nature of the error, measurements at different TEs can cause either overestimation or underestimation of the temperature. Therefore, echo combination, indicated by the dotted line, can substantially reduce the error. Absolute errors after echo combination are close to 1°C compared to up to 10°C in the individual echoes for this water and fat ratio. Experimental results verified simulation.
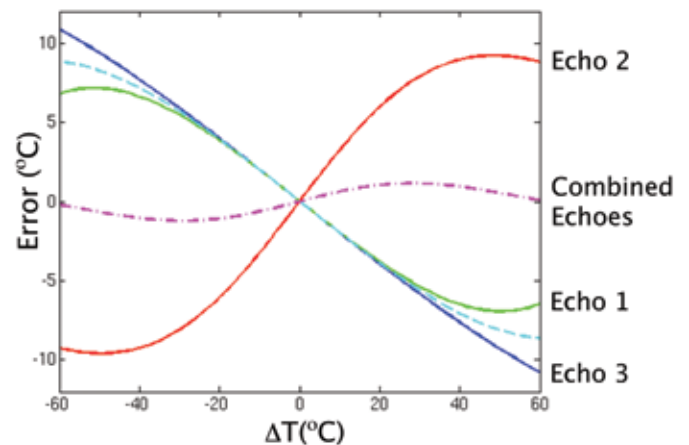

Figure 1: Temperature error as a function of temperature change for three different echo times. Combining the echo times substantially reduces the error (dotted pink line).

Conclusion

The results show that echo combination successfully reduces errors caused by low fractions of fat (20% fat). The method can be used to replace other fat suppression techniques or it can be combined with existing techniques for temperature measurements with improved accuracy.

Eddy Current Characterization with a Simple Gradient Measuring Approach

Aiming Lu, Kim Butts Department of Radiology

Introduction

Eddy currents induced by varying gradients can result in image artifacts or degrade RF excitation profile especially when half RF pulse is used to achieve short echo times [1]. Correction of these effects can significantly improve the system performance. However, accurately measuring eddy currents is often not a trivia task. Here we present a simple method to characterize the B0 and linear eddy currents at the same time.

Materials and Methods

Eddy currents were measured in a way similar to that used by Gurney [2]. On each axis, a total of 4 acquisitions were performed on two opposite off-isocenter thin slices with either a positive or a negative readout gradient under test. Since phase accumulations due to both B0 and linear eddy currents are linear with the applied gradient, and B0 eddy currents is independent of position, linear combinations of the signal phases from the four acquisitions can then be used to derive B0 and linear eddy gradients separately.

The eddy currents were modeled as a convolution of the gradient slew-rate with a sum of decaying exponentials. The amplitudes and time constants are found using a non-linear least squares fitting algorithm in Matlab.

Results and Discussion

Data were collected on a 0.5T GE scanner. The first 3 rows in Figure 1 show the gradient slew rate (1st row), exponential fitting for linear (2nd row) and B0 (3rd row) eddy currents, both with three time constants, respectively. It takes ~3 ms for the eddy currents to die away in this particular case. The calculated parameters were then used to predict the
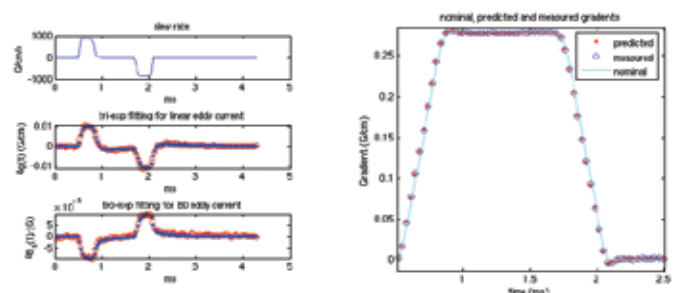
Figure 1. Eddy current characterization. Both B0 eddy current and linear eddy current can be fitted with a convolution of the gradient slew rate and several exponential decay terms.

system output from the input gradients, as shown at the bottom, which traces the measured gradient nicely. It is therefore possible to calculate gradients that give a desired output gradient.

Conclusion

A simple method was presented to characterize the B0 and linear eddy currents separately. The obtained parameters can then be potentially used to calculate the pre-emphasized gradients and/or to correct for k-space trajectory deviation during reconstruction.

References

1. Pauly et al, PROC 8th SMRM, #28 (1989).
2. Gurney et al, PROC 13rd ISMRM, #866 (2005)

Optimized MR-guided Biopsy with SSFP and a Hybrid Injection Scheme

JING CHEN[1,2], BRUCE DANIEL[2] AND KIM BUTTS PAULY[2] – [1]DEPT. OF ELECTRICAL ENGINEERING, [2]DEPT. OF RADIOLOGY

INTRODUCTION

MR-guided breast biopsy is limited in time by the contrast kinetics of the tumor and surrounding tissues. A prolonged period of lesion enhancement would be preferable in order to provide the means to target and biopsy multiple lesions. The purpose of this work was to optimize MR-guided biopsy by optimizing the MR sequence and the timing of the contrast injection.

MATERIALS AND METHODS

The first improvement is to employ an SSFP sequence A phantom study was designed to demonstrate the increase in CNR-efficiency of SSFP over 3pt Dixon GRE (TE/TR = 21/200 ms), which is the current standard sequence for MR-guided core biopsy on our 0.5T GE Signa SP MRI scanner. CNR efficiency was measured and compared with computer simulation in Figure.1.The second improvement is to adopt a hybrid injection scheme to tradeoff CNR gained by SSFP for a longer period of contrast enhancement. For simulation, a rapidly vanishing lesion was picked from the clinical patient studies acquired on a 1.5T scanner. The signal time courses of the tumor and fibroglandular tissue were fit to Tofts' model, and using the fit parameters k and Vl, the tumor's visibility during the biopsy is predicted. The contrast is simulated with the SSFP and the GRE sequences for both coventional bolus injection and hybrid injection, where a fraction of the contrast is given in an initial bolus and the remaining fraction is given evenly spaced through the 30-min procedure.
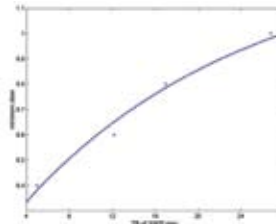

Fig.1 Reduction of contrast material allowed by imaging with SSFP compared to a GRE sequence.
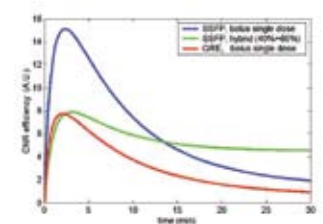

Fig.2 Comparison of contrast time course of GRE and SSFP.

RESULTS

The simulated contrast enhancement curves is demonstrated in Figure.2. With conventional imaging methods, this tumor will lose conspicuity in 15 min. Better contrast is obtained with the SSFP sequence. Spreading the improvement over 30 minutes with the hybrid injection provides a stable and sufficient contrast enhancement through-out the 30-min procedure.

DISCUSSION AND CONCLUSION

In this work we present a technique that combines SSFP imaging with a hybrid injection of contrast material to optimize MR-guided core biopsy. By acquiring pre-contrast T1/T2 and pharmacokinetic parameters in diagnostic MRI, the contrast enhancement time course could be tailored for the procedure individually. Future research includes in vivo experiments and better fat/water separation techniques.

RF Coil for Mouth and Throat MR Imaging

ELENA KAYE[1], KIM BUTTS PAULY[2] – [2]DEPARTMENTS OF RADIOLOGY AND [1]ELECTRICAL ENGINEERING

INTRODUCTION

To evaluate the swallowing disorders (*dysphagia*) of the oral and pharyngeal phases cineradiography and upper endoscopy are commonly used. Working in collaboration with Dr.Gerald Popelka in the department of Otolaryngology, we are using the 0.5T Signa SP MR scanner to study swallowing and speech. For both studies we need a coil to image the mouth and throat of a subject in upright position, without affecting the swallowing process and speech quality.

The purpose of this work was to design and build an optimal RF coil for the swallowing and speech studies.

MATERIALS AND METHODS

Governed by the anatomy that we wish to image (the area from the upper half of the neck to the top of the oral cavity) and the restrictions of the experiment, we chose a phased array coil design. This coil was designed and built to combine two solenoid coils of different diameters shown in Fig. 1. The neck coil was designed with an opening to ensure its ability to fit every person. A cardboard tube was used as a frame for this coil: 8" in diameter and 2" tall. One half of the coil circuit was built using copper tape; the second half was built with 9-wire cable and a 9-pin connector. A "gate" was cut into the cardboard tube in order that the coil could go around a person's neck. The mouth coil was built on a plexiglass tube: 4" in diameter and 0.5" tall. Copper tape was used for the circuit. Both coils were tuned to the resonant frequency of 21.285MHz and the input impedance was matched to 50Ω.

RESULTS

Fig. 2 shows the image taken with the phased array coil (FGR, TR/TE/flip/BW40ms/5.5ms/30/31kHz). The neck coil alone provided a satisfactory image of the upper part of esophagus, but not of the oral cavity and epiglottis, which are all of equal interest to this study. When combined into the phased array, the two coils provided an image with a higher SNR in the latter two areas. SNR of the soft plate and hard plate area of the mouth was improved by a factor of 5, and in the epiglottis region SNR was improved by a factor of 2, compared to the case of using the neck coil only.

Figure 1. Phased array coil.

CONCLUSION

The phased array coil built specifically for the swallowing and speech studies demonstrated a satisfactory performance. It provided a high SNR of the areas of interest and gave a sufficient field of view. In the future this coil may be used for other applications where access to neck or mouth during imaging process may be important.

Figure 2. Image acquired with phased array coil. Dashed lines indicate the coil location.

Catheter-based Ultrasound Applicators for MR-Guided Prostate Thermal Therapy

Chris Diederich[1], Tony Ross[1], Will Nau[1], Adam Kinsey[1], Kim Butts[2], Viola Rieke[2], Graham Sommer[2] – [1]Department of Radiation Oncology, UCSF Cancer Center, [2]Radiology Department, Stanford Medical Center

Introduction

We are developing miniature high-intensity ultrasound applicators that can deliver very precise or targeted thermal therapy to the prostate while avoiding or reducing damage to surrounding structures. These catheter-based devices are designed to be compatible with MR thermal imaging to improve control and verify treatment.

Applicators and Evaluation

Two types of transurethral applicators are currently being investigated. One is a curvilinear device with lightly-focused transducer segments to provide narrow but penetrating heating patterns. The transducers can be precisely rotated via an MR-compatible motor. The second consists of multi-sectored tubular transducers, with three or four sectors of angular heating control so that complete or conformal ablation of the target region can be achieved without mechanical manipulation (inducing movement artifact) during heating. Interstitial needle-like devices have been devised with angular heating control to selectively heat target regions and avoid heating the rectum. MR temperature imaging in dog prostate and simulation studies have been used to evaluate these devices.

Discussion

The transurethral devices are very selective in their ability to target regions of the prostate gland, with the multi-sectored devices offering
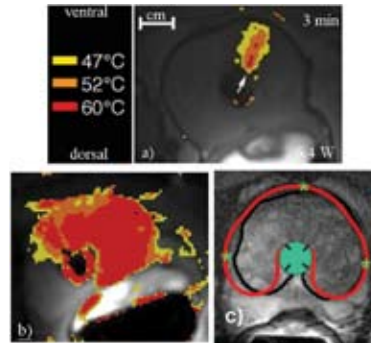
MR temperature maps of heating in canine prostate with the transurethral curvilinear applicator sonicating in (a) a single position and (b) cumulative max temperature produced during180° sequential rotation. (c) Simulated(red) thermal destruction of prostate using tri-sectored applicator with dynamic angular control.

faster yet less selective treatment. The effective heating penetration is between 1.5 to 2.0 cm extending from the urethra to the outer prostate capsule. A modified endorectal coil provides cooling of the rectum. Multiple applicator implants (n=3), similar to HDR brachytherapy treatments, can effectively ablate the peripheral gland while avoiding the rectum. The MR thermal imaging and dose maps are useful for controlling therapy delivery (rotation, power levels) and assessing treatment.

Correlation of Real-time MRTI and Post-treatment MRI with Histologic Depiction of Prostatic Ablation using High-intensity Ultrasound

Graham Sommer[1], Kim Butts[1], Bruce Daniel[1], Donna Bouley[2], Tony Ross[3], Will Nau[3], Chris Diederich[3] - [1]Departments of Radiology, [2]Comparative Medicine, Stanford University; [3]Department of Radiation Oncology, University of California, San Francisco

Introduction

We are continuing our work on prostate tissue ablation using high-frequency ultrasonic applicators and MRI for both monitoring of tissue heating, and delineation of prostate tissue ablation post-treatment. The specially-designed applicators are designed and constructed by our collaborators at UCSF, and deliver ultrasonic energy with varying degrees of directionality. The ultimate goal of these studies is the development of a technique for ablation of prostate cancer in vivo in humans, and we are performing a wide variety of studies using a canine model to define the best techniques.

Materials and Methods

We are currently evaluating the effectiveness of a variety of ultrasonic applicator designs for the precise ablation of prostate tissue. In the example shown below, an applicator radiating through an angle of 90 degrees is shown ablating 2 regions of canine prostate. In figure 1, the distribution of heating in the prostate is shown quantitatively via MRTI (MR thermal imaging). In the detailed histologic studies performed following ablation, an interesting and unexpected finding of the presence of 2 distinct zones of ablation, a central "heat-fixed" zone subjected to the highest temperatures, and a peripheral zone of coagulative necrosis.

In Figure 1 below, the 2 left images demonstrate the real-time monitoring of temperature using MR during heating of the canine prostate in vivo; the two right images obtained after ablation indicate that contrast-enhanced T1-weighted imaging (d) is best for demonstrating zones of ablated tissue

In the figure (2) below, the actual histology of ablated tissue is seen in an overall section of prostate corresponding to the plane of imaging in Figure 1, and the high-power appearance of the 2 zones of prostate ablated with ultrasound is demonstrated.
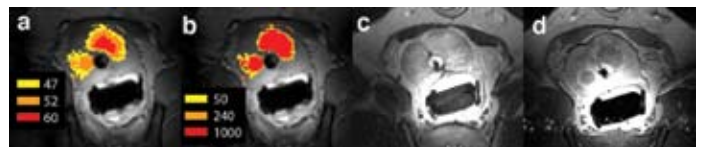

Figure 1: *(a) Cumulative temperature map (°C) and (b) t_{43} equivalent map with correlative T2-weighted (c) and post-contrast T1-weighted (d) MR images following ablation.*
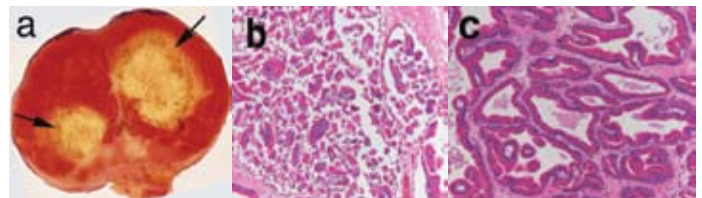
Figure 2: *(a) TTC-stained histologic section of ablated canine prostate at the level demonstrated in the MR images of Figure 1. Viable tissue is stained red-orange, and the ablated regions are pale, with the "perimeter zone" of ablation indicated with arrows. Low-power magnification (H+E) of the prostate shows (b) marked tissue destruction in the perimeter zone and (c) relatively normal-appearing "heat-fixed" prostate centrally*

Discussion

We have shown the feasiblity of precise in vivo ablation of prostate tissue under MR guidance, and are in the process of defining the optimal heating and MR monitoring techniques to allow the eventual in vivo of human prostate cancer.

MR Imaging of Cartilage Stress Under Load in Patellofemoral Pain

Garry Gold, Kim Butts, Thor Besier, Christie Draper, Michael Fredericson, Gary Beaupre, Scott Delp – Departments of Radiology, Orthropedics, Mechanical Engineering, and Bioengineering

Introduction

Patellofemoral pain or anterior knee pain is common in adults, and may be the result of mal-tracking of the patella or excessive cartilage stress. This pain can lead to prolonged periods of inactivity, accelerated onset and progression of osteoarthritis, and obesity. This research uses a combination of unique MR methods to determine a scientific basis for patellofemoral pain.

Materials and Methods

Conventional MRI is useful for evaluation of cartilage thickness and volume, but is unable to apply significant loads while imaging. Using the open 0.5T Signa SP and a custom back support, we are able to acquire three-dimensional images of the patellofemoral cartilage under upright, weight-bearing conditions. Combining this data with data from a finite element model, we can estimate cartilage stress in the patellofemoral compartment of individual patients. Increased cartilage stress is a major reason for pain in these patients.

Discussion

We have studies 30 pain-free control subjects and 30 subjects with patellofemoral pain. Application of advances such open MRI and fi-
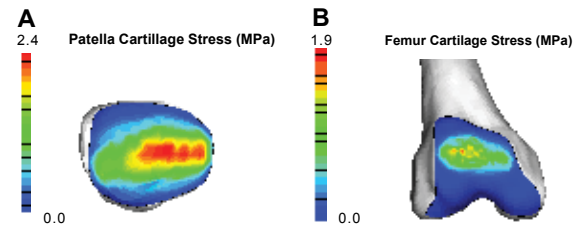

Figure 1. Results from a subject-specific FE model, simulating a static squat at 60 degrees knee flexion. Contact stresses were estimated for the patellar (A) and femoral cartilage (B).

nite element modeling have allowed us to develop a scientific basis for understanding increased cartilage stress due to poor tracking, decreased contact area, or increased forces. This information allows us to improve treatment decisions, both surgical and non-surgical, for these patients.

Conclusion

Measurement of cartilage stress under load is possible in open MRI systems like the Signa SP.

Improved MR Imaging of Cartilage with IDEAL Water/Fat Separation at 3.0T

Garry Gold, Scott Reeder, Brian Hargreaves – Department of Radiology

Introduction

Osteoarthritis is very prevalent in our society and a frequent cause of joint pain and disability. New treatment methods demand sensitive methods for detection of early cartilage and joint pathology. 3.0T MRI improves signal-to-noise and spatial resolution of images, allowing more rapid diagnosis and evaluation of therapy.

Materials and Methods

MRI is useful for evaluation of cartilage thickness and volume. Conventional MRI methods at 1.5T are slow and take up to nine minutes to acquire volume data. We have developed a method known as IDEAL (Iterative Decomposition of water and fat with Echo Asymmetry and Least Squares) that allows us to acquire fat and water images with high signal-to-noise and a variety of sequences. We have implemented IDEAL for cartilage imaging at 3.0T with SPGR, GRE, and SSFP sequences.

Discussion

IDEAL fat/water separation is useful in cartilage imaging because it provides images that are water only (cartilage), fat only (marrow) and combined images free of chemical shift artifact. This allowed us to collect information on cartilage thickness and volume much more rapidly than before. The short echo shift employed in IDEAL work well for

Water and fat images of knee cartilage at 3.0T using IDEAL SSFP. Acquisition time is about 3 minutes.

3.0T imaging, and correction of chemical shift is useful to evaluated the thickness of the sub-chondral bone.

Conclusion

IDEAL water/fat separation allows improved imaging of articular cartilage at 3.0T.

MR Imaging and 3-D Articular Cartilage Thickness Mapping of a Mechanically Loaded Knee Joint with and without Meniscectomy

Yongnam Song[1,3], Joan Greve[1], Nicholas Giori[2,3] – [1]Department of Mechanical Engineering, [2]Department of Orthopedic Surgery, Stanford University; [3]VA Palo Alto Rehabilitation Research Center

Introduction

High resolution MR imaging of an entire joint under physiologic load will allow one to determine articular cartilage deformation and will contribute to our understanding of the mechanical basis of osteoarthritis. Meniscectomy has been shown in the sheep and in humans to lead to osteoarthritis of the knee. Previous studies have examined the effects of meniscectomy on the contact stress distribution of the knee, but three-dimensional mapping of the changes in articular cartilage deformation due to meniscectomy have never been measured. In this study, we hypothesize that an entire knee joint can be loaded to a physiologic level inside a high resolution 4.7T MRI scanner, and that entire knee joint articular cartilage thickness maps before and after meniscectomy can be generated using a 3D reconstruction process. We also hypothesized that meniscectomy results in greater loss of articular cartilage thickness centrally, and less change peripherally.

Materials and Methods

Sample Preparation: Four sheep (2 years old, 50kg) hind limbs were frozen at a 45 degree knee flexion angle. The entire knee joint was then cored with a 4.5cm hole-saw from the medial to the lateral side. This cylindrical specimen, which contained the entire tibio-femoral joint, the menisci, and the collateral and cruciate ligaments, remained frozen during the coring process and until testing.

Loading Device: A custom MR compatible pneumatic loading device and a custom air flow control box were designed and fabricated. The cored tissue specimen was placed into the bore of the device. Compressed air inflates the air bladder between upper shell and outer cylinder applying uniaxial compressive force across the tibio-femoral joint (Figure 1). We applied two times of body weight across the tibio-femoral joint which corresponds to 980N of knee joint reaction force.

MR Imaging: Prior to imaging, the sample was bathed in 5mmol/L gadolinium (Magnevist, Schering Ag, Berlin, Germany) and proteinase inhibitors solution for 12 hours. The intact knee sample was then scanned. Following this, a 2xBW static compressive force was applied across the joint. After two hours of loading to achieve steady-state deformation, the statically loaded knee sample was scanned. The load was then removed, and after 24 hours to allow for full cartilage thickness recovery, only medial meniscus was carefully removed, the joint was again loaded as before, and scanning was performed. Imaging was performed on a Unity Inova console (Varian, Inc., Palo Alto, CA) controlling a 4.7T. T1-weight 3D gradient echo sequence (TR/TE 22/6ms; matrix 1024 x 1024 x 128; FOV 6cm x 6cm) was used providing 58um x 58um in plane resolution.
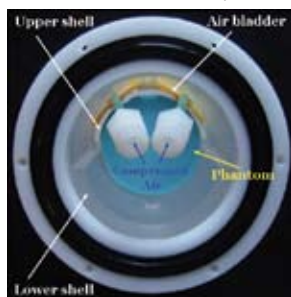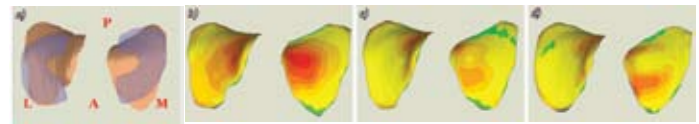

Figure 1. Pneumatic loading device

Figure 2. (a)3D model of Tibial cartilage (orange) with meniscus (blue), (b)Cartilage thickness map for the uncompressed intact knee, (c)the statically loaded intact knee, (d)the statically loaded meniscectomized knee. (P: posterior, A: Anterior, M: Medial, L: Lateral)

3D Reconstruction: Custom software and GeoMagic (Raindrop Geomagic, Inc., Research Triangle Park, NC) were used for image segmentation, 3D surface generation, and cartilage thickness mapping. Only the tibial articular cartilage was mapped in this study.

Results

Figure 2 shows the cartilage thickness maps for the intact knee without loading, with static loading, and with meniscectomy and static loading. With the meniscus intact (Figure 2b), a broad area of articular cartilage is deformed under load, and this area corresponds to the area of meniscal contact. In contrast, when the medial meniscus is removed (Figure 2c), a smaller area of cartilage on medial side is deformed to a greater extent due to direct contact with the femoral condyle, while the tibial articular cartilage that would have been in contact with the meniscus remains relatively undeformed. However, the cartilage thickness on the lateral tibial plateau, where the meniscus remained intact, is relatively unchanged (Figure 2C) with meniscectomy.

Discussion

We have demonstrated that an entire joint can be loaded to physiologic levels and imaged under load in a high field MRI scanner and that three dimensional maps of the articular cartilage deformation can be obtained. In this preliminary study, a static load was selected. The static loading condition of this study resulted in a greater magnitude of cartilage thickness loss than has been seen in patellar cartilage after cyclic loading. Future work will incorporate cyclic loading, numerical modeling of the articular cartilage layer, and an investigation into the regional structural and biological changes under normal and meniscectomy conditions.

We found that the meniscus causes a broad area of articular cartilage to be deformed. Removal of the meniscus results in a smaller area of articular cartilage deformation and higher peak deformation. This novel technique involving three dimensional imaging and direct measurement of an intact and mechanically loaded joint will be useful in studying the mechanical etiology of osteoarthritis. Alteration in the normal pattern of articular cartilage deformation with meniscectomy may be responsible for the development of osteoarthritis.

Quadratic Fat-Water Separation in Balanced-SSFP

Brian A. Hargreaves[1], Scott B. Reeder[1] and Dwight G. Nishimura[2] – Departments of [1]Radiology and [2]Electrical Engineering

Introduction

Balanced steady-state free precession (SSFP) imaging suffers from bright fat signal and sensitivity to off-resonance [1,2]. Of the numerous proposed fat/water separation techniques for balanced SSFP, two are very SNR-efficient: Dixon SSFP [3] offers high image quality, but demands three or more acquisitions with varying echo times and a non-trivial reconstruction. Conversely, phase-sensitive SSFP [4] requires only one acquisition, but suffers from partial-volume effects. Neither method addresses the off-resonance sensitivity of balanced SSFP. Here we present a novel 2 point fat/water separation technique that (a) uses a simple reconstruction to separate water and fat, (b) avoids partial volume effects and (c) correctly identifies fat and water in the presence of SSFP signal nulls.

Methods and Results

Two signals S_1 and S_2 can be acquired with relative phase differences of 180° and 90° respectively between water and fat. The refocusing properties of balanced SSFP provide signal S_1 naturally with appropriate selection of TE and $TR=2TE$. Phase variations ϕ in S_1 are small and can easily be removed with simple algorithms, resulting in a water-fat difference image. In a water vs fat coordinate space, a given water-fat difference represents a line of slope 1, while a given magnitude of S_2 gives a circle (Figure 1). The intersection of the line and circle, easily found with a quadratic equation gives the water and fat quantities in a voxel with no need for a field map.

In balanced SSFP, the use of multiple echo times can significantly reduce efficiency, so this method was explored with both signals S_1 and S_2 acquired with different RF phase increments so that dark bands can also be removed. Using a 1.5T GE Excite scanner and a transmit/receive extremity coil, images were acquired with $TR = 2TE_1 = 13.8$ ms, $TE_2 = 6.75$ ms, and 30° flip angle, was repeated twice, first with RF phase alternating by 180°, then with constant RF phase [6,7] for 4 total signals. The total scan time was 15:05 for a 256x256x64 matrix over a 16x16x12.8 cm³ FOV. Water and fat values were calculated for both phase cycling schemes, and images combined to remove the dark band artifacts as shown in Figure 2.

Discussion

We have presented a quadratic water/fat separation technique for balanced SSFP that is simpler and requires fewer acquisitions than recent Dixon methods, while eliminating the partial-volume effects of phase-sensitive SSFP. This method is similar to that shown by Xiang [8], but also exploits the refocusing effect of balanced SSFP. The 90° signal (S_2) can be replaced by any non-zero angle, but will, along with fat/water fraction, affect the propagation of noise. Extending TR minimizes efficiency loss from use of multiple echo times, and the multiple-phase-cycle approach here enables accurate fat/water separation for high-field or high-resolution SSFP in reasonable scan times.

References

1. Oppelt A, *et al.* Electromedica 54:15, 1986.
2. Freeman R and Hill HDW. JMR 4:366, 1971
3. Reeder S, *et al.* AJR 180(2): 357, 2003.
4. Hargreaves BA, *et al.* MRM 50: 210, 2003.
5. Ma J, MRM 52(2): 415, 2004.
5. Zur Y, *et al.* MRM 6(2): 175, 1988.
6. Haacke, et al. Radiology 175: 545, 1990.
7. Xiang QS. 11th ISMRM, p. 1130, 2003.
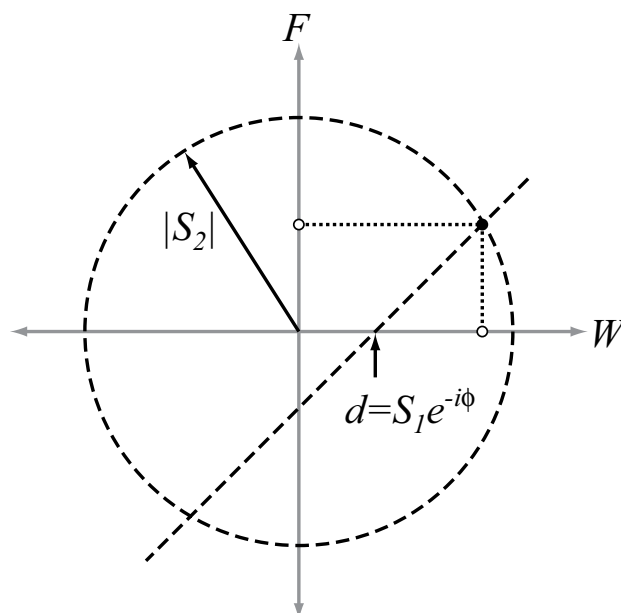
Figure 1. Geometric interpretation of the water and fat values obtained from the intersection in W-F space of a line of slope 1 and W-intercept d, with a circle of radius |S2|.
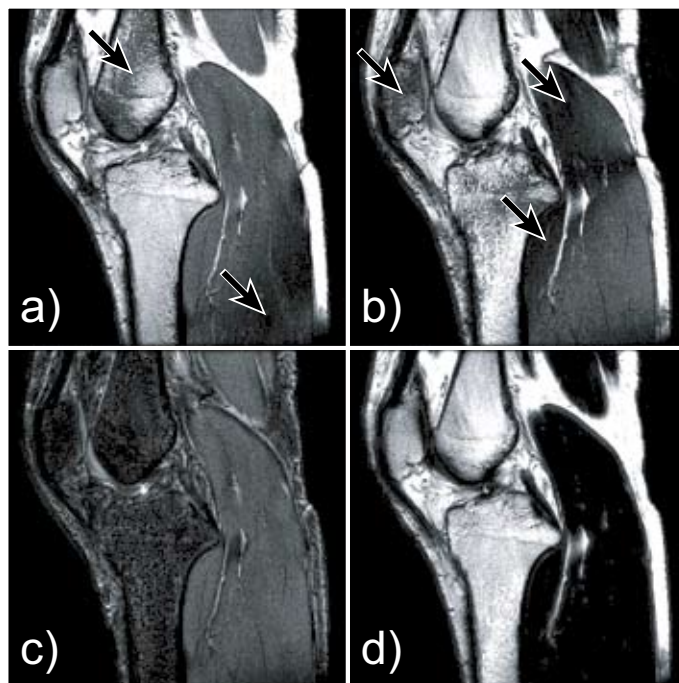
Figure 2. Sagittal knee images for TR=2TE=13.8 ms. Source S2 images (a) and (b) with alternating and non-alternating RF phase have null-signal areas (arrows). Water (c) and fat (d) images after maximum-combination of separated images for each RF phase scheme. Note that the dark signal bands (arrows) are removed in the combined water and fat images.

Artifact Reduction in Dynamic Contrast-Enhanced Breast Imaging: Fly-back EPI vs Spiral Imaging

Brian Hargreaves[1], Rebecca Rakow-Penner[1], Jin Hyung Lee[2], Charles Cunningham[2], John Pauly[2,] Bruce Daniel[1] – Departments of [1]Radiology and [2]Electrical Engineering

INTRODUCTION

Breast cancer is a leading cause of death among women in developed countries. Dynamic contrast-enhanced (DCE) MRI is an important diagnostic tool in the evaluation of patients at risk for breast cancer, or with known breast cancer. Spiral and echo-planar imaging (EPI) both acquire image data very efficiently, but can result in certain image artifacts. Fly-back EPI can almost completely eliminate EPI artifacts, and is an attractive option for DCE imaging, where quantitative measurements will be made.

METHODS AND RESULTS

We implemented both variable-density spiral and fly-back EPI (See Fig. 1) sequences with a spectral-spatial excitation to excite only water. Image resolution was 1 x 1 x 2.5 mm for both sequences, with the spiral scan acquiring about 2.5 times as many 3D sections. Sample images from a patient with breast cancer are shown in Fig. 2. As expected, the fly-back EPI images have reduced artifact levels, but lower SNR than the spiral scans.

DISCUSSION

Spiral images can be affected by "swirl" artifacts due to cardiac and respiratory motion. Though small, these artifacts can be noticeable when analyzing time-course contrast curves. Fly-back EPI has no significant artifacts due to motion or off-resonance effects, and thus is a promising method for DCE imaging. Future work will include optimizing the efficiency of the EPI trajectory, and comparing the quality of the contrast curves that result from fly-back EPI with those of spiral imaging.

REFERENCES
1. Tsai CM, Nishimura D. Magn Reson Med 2000; 43:452–458.
2. Meyer C, et al. Magn Reson Med 1990; 15:287–304.
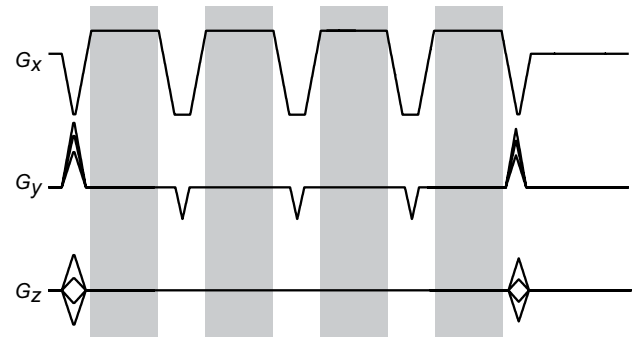3. Hulka CA, et al. Radiology 1997; 205:837–842.

Figure 1. Fly-back EPI imaging gradients. When a moderate readout bandwidth is used, the acqusition efficiency (gray) is almost as efficient as standard EPI.
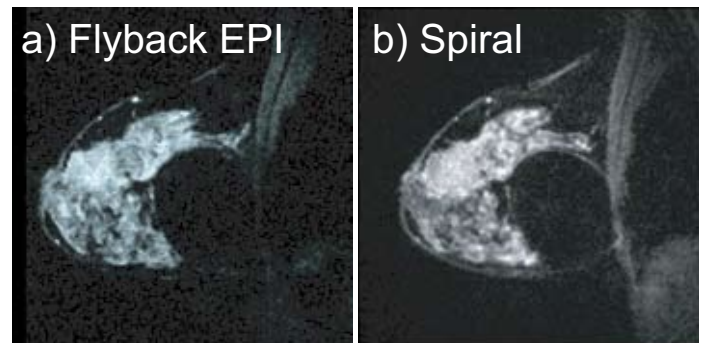

a) Flyback EPI   b) Spiral

Figure 2. Late-enhancement breast images using fly-back EPI (a) and variable-density spiral (b). The fly-back EPI image shows slightly less image blurring than the spiral, as well as reduced artifact levels, but lower SNR due to reduced acquisition efficiency.

IDEAL Gradient-Echo Imaging for Knee Cartilage Segmentation

Misung Han[1], Anne Muendermann[2], Chris Dyrby[2], Lise Worthen[2], Scott B. Reeder[1], John M. Pauly[3], Garry E. Gold[1] and Brian A. Hargreaves[1]– Departments of [1]Radiology [2]Mechanical Engineering and [3]Electrical Engineering

INTRODUCTION

Osteoarthritis is a leading cause of disability in developed nations. MRI of cartilage can depict morphologic information such as thickness, surface detail and lesions, as well as structural information. Typically T_2-weighted multislice imaging is used for overall knee assessment, while T_1-weighted 3D imaging is used for segmentation of cartilage. The goal of this project is to validate IDEAL gradient-echo imaging [1,2], a robust 3D sequence with "T_2-like" contrast, for imaging cartilage morphology as well as measurement of cartilage volumes.

METHODS AND RESULTS

Using a 1.5 T MRI scanner, and an 8 channel phased-array knee coil, we have scanned a total of 14 knees using 3D SPGR (TR=38ms, TE=6ms) and 3D IDEAL gradient echo (GRE) (TR=12.2ms, TE=4, 6 and 8 ms). Both methods have similar scan times of approximately 9 minutes. All images are 256x256x64 matrix over a 14x14x9.6 cm FOV for 0.55x0.55x1.5 mm³ resolution. SNR values in cartilage are typically within 10% between the two imaging sequences. However, the "T_2-like" contrast of IDEAL GRE shows synovial fluid in addition to cartilage, with excellent contrast between the two tissue types, as shown in Fig. 1. The bright synovial fluid can be useful in depicting surface irregularities, cartilage fissures or meniscal tears.

DISCUSSION

Early results from this study show that IDEAL GRE is a promising sequence for studying knee cartilage, and provides T_2 weighted 3D imaging that provides improved robustness compared with other 3D

a) SPGR   b) IDEAL GRE
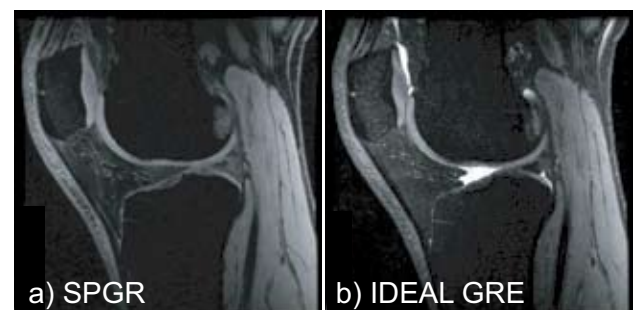
Figure 1. Sagittal slices from (a) 3D SPGR volume and (b) 3D IDEAL gradient echo (GRE) volume in the knee of a healthy volunteer. The cartilage SNR values are comparable, but the IDEAL GRE image shows very bright synovial fluid that can be very useful in diagnosing surface lesions.

T2-weighted methods [3,4]. In future work, we will compare measurements of cartilage volumes and signal-to-noise ratios from the different sequences using advanced segmentation techniques.

REFERENCES
1. Reeder SB, et al. AJR Am J Roentgenol 2003; 180:357–362.
2. Reeder SB, et al. Magn Reson Med 2004; 51:35–45.
3. Kornaat PR, et al. Osteoarthritis Cartilage 2005; 13:338–344.
4. Hargreaves BA, et al. Magn Reson Med 2003; 49:700–709.

Extrapolating Truncated Projections in Cone-Beam CT using 0th and 1st Moment Constraints

Jared Starman[1], Norbert Pelc[1,2], Norbert Strobel[2], Rebecca Fahrig[2] – Departments of [1]Electrical Engineering and [2]Radiology

Introduction

C-Arm CT systems suffer from artifacts due to truncated projections caused by a finite detector size. The goal of this project is to determine a simple and computationally efficient method of extrapolating truncated projections to minimize reconstruction errors for cone-beam CT.

Materials and Methods

Our proposed extrapolation algorithm makes use of the 0th and 1st moments of the projection data. The goal of the algorithm is to extrapolate the projections in such a manner that the 0th and 1st moments of the extrapolated projections are equal (or as close as possible) to the ideal, non-truncated projection 0th and 1st moment values. This is an appropriate extrapolation strategy because, according to Lewitt [1] for a parallel geometry, reconstructed CT values in the center of reconstruction are only sensitive to the average value for objects past the edge of the field of view (FOV). The 0th moment constraint forces the average value of the extrapolated projection to equal the true average value of the ideal, non-truncated projection. We further assume that this relationship holds for divergent cone-beam geometry. For 2D cone-beam projections, the extrapolation algorithm also assumes it is operating on a stack of fan-beam projections and treats each detector row as an independent fan-beam projection.

The algorithm contains two main steps. The first is an estimation stage, where the 0th and 1st moment estimates for each detector row must be determined. This information can be obtained in multiple ways. Two possible estimation methods have been investigated. 1.) The moment values of the ideal, non-truncated projections can be estimated directly from the truncated dataset. If some non-truncated views exist in the measured projection dataset, those non-truncated projections can be used to estimate globally what the 0th and 1st moments are for each projection. However, if all, or most, projections exhibit truncation, the moment values can be estimated by assuming a simple model for the ideal projection data, and then the estimated moment values can be calculated from the model. It was found that for many areas of clinical relevance, a simple elliptical profile to model the true projection data for each detector row was adequate for significant artifact reduction. 2.) If a previous, non-truncated dataset exists for the object being imaged, the 0th and 1st moments of the measured projection data can be estimated from the previous reconstruction. The second step of the algorithm is to perform the actual extrapolation of the projection. First order polynomials (straight lines) are used to perform the extrapolation. Given desired 0th and 1st moment values for a projection, and the constraint that projections are continuous, line equations can be solved that extrapolate the projections with the proper moment values.
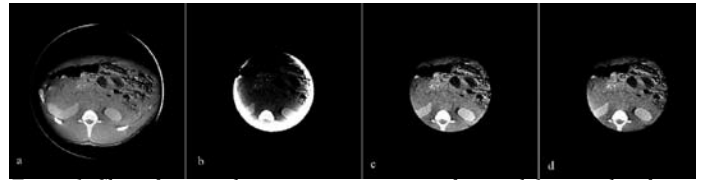

Figure 1: Slices from a volumetric reconstruction of a pig abdomen taken from a Siemens Axiom Artis dTA flat panel C-arm system. a) full-width projections, b) artificially truncated projections, c) symmetric mirrored projections, and d) moment extrapolated projections. All images have a window width of 250 gray levels (GL). Images a, c, and d are centered at 730 GL and image b is centered at 950 GL.

Results

Figure 1 shows results from a volume reconstruction of a pig abdomen from a Siemens AXIOM Artis dTA flat panel C-Arm system. Figure 1a) shows the reconstruction of the full-width projections, which are taken as a gold-standard. 1b) clearly shows the bright artifact at the FOV edge for truncated (artificially in this case) projections. 1c) and 1d) show extrapolated projections using symmetric mirroring by Ohnesorge et al [2] and the moment extrapolation algorithm respectively. The moment extrapolation algorithm estimated the moments directly from the dataset. Both extrapolation algorithms have eliminated the majority of the artifact. Preliminary results for volume reconstructions of a thorax phantom (not shown) show that even more accurate reconstructions can be achieved by using a previous CT reconstruction to estimate moment parameters. For a small region of interest (ROI) at the center of a slice, this technique produced an error of 9 Hounsfield Units (HU), while symmetric mirroring had an error of 32 HU.

Discussion

Moment extrapolation for reducing truncation artifacts is as effective as symmetric mirroring for most cases in cone-beam CT. Moment extrapolation offers a further advantage of easily being able to incorporate data from a previous scan. Preliminary results from a thorax phantom show significantly more accurate HU estimation in this case than symmetric mirroring.

References

[1] Lewitt R. Processing of incomplete measurement data in computed tomography. Medical Physics (**5**), 412-417, 1979.
[2] Ohnesorge B, Flohr T, Schwarz K, Heiken JP, Bae KT. Efficient correction for CT image artifacts caused by objection extending outside the scan field of view. Medical Physics (**27**), 39-46, 2000.

Fusing Intrinsically Registered 3D Cone-Beam Data Sets acquired using X-ray C-arm Devices

Norbert Strobel[1,2], Teri Moore[2], Hideki Arakawa[1], Michael Marks[1], Rebecca Fahrig[1] - [1]Department of Radiology, [2]Siemens Medical Solutions

Introduction

Due to their excellent spatial resolution, interventional X-ray C-arm systems have been used to obtain high-resolution 3D isotropic data sets of vascular structures. Modern C-arm devices based on flat-panel detector technology now also facilitate improved 3D contrast resolution. Using C-arm cone-beam image reconstruction techniques, we can generate intrinsically registered, fused 3D data sets simultaneously depicting vessels and surrounding organ tissue.

Materials and Methods

A series of 2-D X-ray mask and fill projections is acquired by rotating a C-arm around a subject before and during injection of contrast. Two such mask and fill images are shown in Figs. 1(a) and (b). Mask or fill volumes are then reconstructed using the related projections. Figs. 2(a) and 2(b) show associated coronal slices through 3D mask and fill data sets, respectively.
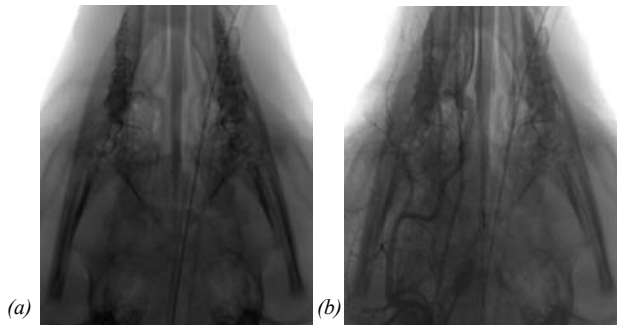

(a) *(b)*

Fig.1(a) X-ray baseline image acquired during the mask run of a C-arm around a pig's head (AP view) (b) associated fill image after injection of iodinated contrast (300mg/ml, at 4ml/sec)
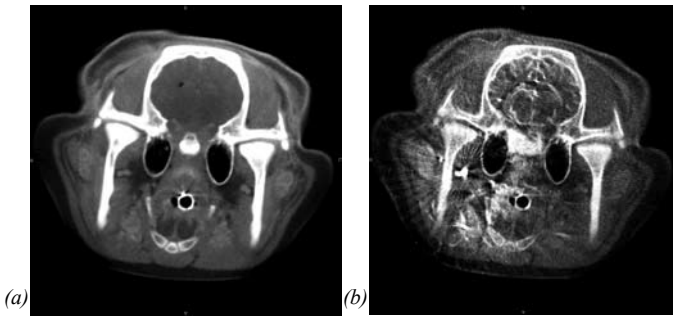

(a) *(b)*

Fig.2(a) Coronal slice through a baseline volume based on mask projections, (b) associated slice through (unsubtracted) fill volume. Highly opacified vessels and a limited number of 2D projections generate beam hardening and streak artifacts that are absent in Fig. 2(a).

To opacify even small vessels, we need to inject dense contrast at high flow-rates. Since the amount of contrast is limited by patient tolerance, the total acquisition time is restricted, which in turn limits the number of projections. Together, high vessel contrast and too few 2D views impair 3D image quality after tomographic reconstruction due to beam-hardening and streak artifacts. The artifacts severely reduce soft-tissue detectability as shown in Fig. 2(b).

Alternatively, if mask and fill volumes are reconstructed with respect to the same world coordinate system, they are intrinsically registered. We can exploit this property to isolate the vessel tree, and fuse it into the baseline (non-contrast enhanced) volume. We subtract the mask volume from the fill volume first and obtain a vessel tree as shown in Fig. 3(a). Then, we may apply a noise reduction technique. Finally, we can generate a compound data set by fusing the vessel tree with the baseline (mask) volume. This volume can now be visualized in many ways. In

(a) *(b)*
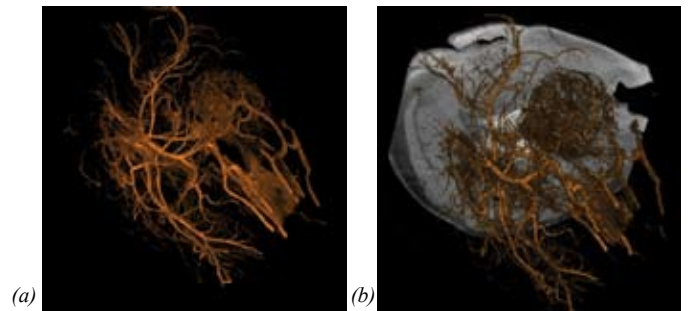
Fig.3(a) Commonly used 3D vessel tree representation obtained by subtracting a mask volume from a fill volume. (b) 3D fusion of the vessel tree with the soft tissue baseline volume, e.g., displayed as a soft tissue cut plane around the 3D vasculature .

Fig. 3(b), for example, we use a VR plane cut method to highlight vessel details.

Discussion

Although modern C-arm devices facilitate both high isotropic 3D resolution and good 3D soft tissue detectability, injecting contrast can significantly impair low contrast resolution. Nevertheless, both vasculature and surrounding organ tissue can still be visualized together by fusing appropriately reconstructed 3D data sets. They are intrinsically registered by design of the C-arm cone-beam image reconstruction algorithm.

Conclusions

Medical applications that can benefit from this fused reconstruction and visualization method involve guidance, e.g., for surgery, radiation therapy treatment, ablations, biopsies, and interventional procedures such as TIPS.

Direct Comparison of 3D Image Data from a Flat Panel Detector (FD) C-arm system versus clinical CT in an In Vivo Model

Rebecca Fahrig[1], Norbert Strobel[1,2], Jeff C. Hellinger[1], Joan K. Frisoli[1], Hideki Arakawa[1], Michael Marks[1], Stephen Kee[1], Teri Moore[2], Gary Glazer[1] – [1]Department of Radiology, Stanford University; [2]Siemens Medical Solutions, AX Division

Introduction

A new C-arm system, shown in Fig. 1, (Siemens AXIOM Artis dTA DynaCT, 30x40 cm FD) with enhanced 3D functionality extends the capabilities of 3D C-arm imaging to soft-tissue applications by facilitating the detection of low-contrast objects. We report on a direct comparison with conventional CT in a porcine model for a range of in vivo imaging applications.

Materials and Methods

Fourteen animal investigations compared 3D C-arm image quality to conventional CT. Each animal was imaged using a Siemens SOMATOM Sensation-16 scanner (80kVp, 100-150mAs, 1mm slice) before and 70s after an injection into the vena cava (30s injection, 3ml/s, 300mg/ml Iodine). The FD C-arm system was used to generate 3D liver volumes during intravenous injection and during selective hepatic artery injection (10s rotation, 0.25-0.5mm slice, 70-80kVp, 247 views). Injection of autologous blood into the brain over 15min (1.5cc's, 2.5cc's and 5cc's, hematocrit between 18 and 24%) to produce fresh bleed was imaged using a 20s C-arm rotation (494 views). Intraperitoneal leak was created during a mock-TIPS procedure, and a covered stent placed. Pre-stent and follow-up 3D images were acquired to verify leak location and stent placement.

Discussion

In the liver, the C-arm results clearly depicted the major portal and hepatic veins to 200 micron level comparable to conventional CT; 3D C-arm images obtained during hepatic arterial injection showed vessels below 100 microns. Images acquired during the venous phase demonstrated the increased resolution and artifact level of the C-arm CT images relative to the conventional CT (fig. 3). In the brain, autologous blood clot was seen for both 1.5 and 5cc's. Injection of 2.5cc's into the ventricles could be detected in 3D C-arm images. Local beam hardening artifact peculiar to porcine anatomy in the posterior region of the cranium could be sometimes mistaken for bleed (Fig. 2). Intraperitoneal leak following TIPS puncture was easily detected using 3D C-arm imaging, and individual struts of the abdominal stent could be seen.

Conclusion

Enhanced C-arm volume reconstruction using a C-arm with FD has demonstrated good low contrast detectibility. It can now be used to guide a wide range of challenging interventional procedures including subselective chemoembolization in the liver, detection of intracranial hemorrhage during aneurysm treatment and endoleak detection. Further improvement in image quality is expected as new correction algorithms for beam hardening, truncation and scatter are implemented.

Fig. 1 The Axiom Lab in the Grant Building, showing the Siemens AXIOM dTA C-arm system used for acquisition of the in vivo C-arm-based CT images.

Fig. 2 Comparison of 3-mm slices through the head of the porcine model showing (left) C-arm CT and (right) conventional clinical CT. The presence of beam hardening and other artifact is evident in the c-arm CT data.
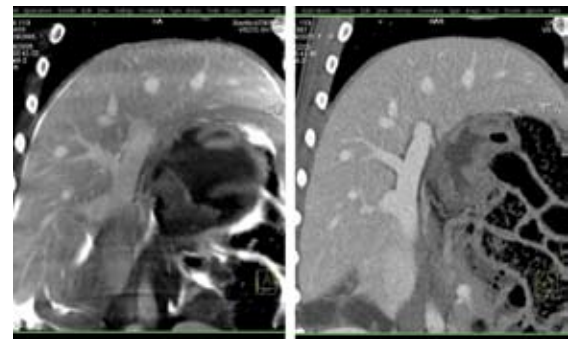

Fig. 3 Comparison of the venous phase following venous injection of contrast (same injection protocol for (left) C-arm CT and (right) conventional CT. Note the increased resolution of the C-arm image, as well as the increased artifact.

Characterization of Dose Distribution and Image Quality in 3D Volume Images Reconstructed from Data acquired on a Flat-panel-based C-arm Angiography System

Rebecca Fahrig[1], Robert L. Dixon[2], J. Thomas Payne[3], Richard L. Morin[4], Arundhuti Ganguly[1] and Norbert Strobel[1,5] –
[1]Department of Radiology, Stanford University; [2]Wake Forest University School of Medicine, NC; [3]Abbot Northwestern Hospital, Minnesota [4]Department of Radiology, Mayo Clinic Jacksonville, [5]Siemens Medical Solutions, AX.

Introduction

C-arm based 3D imaging has seen significant improvements in the recent years, with the transition from XRII to flat panel enabling the acquisition of high-quality 3D volumes with good low-contrast resolution. The availability of the technology in the interventional suite may lead to changes in the way interventional procedures are carried out by providing both real-time 2D projection images as well as 3D images *during* treatment. The additional dose to the patient must, however, be assessed, and trade-offs between dose and image quality evaluated and optimized. We present an investigation of the dose distribution and image quality in such 3D C-arm CT images.

Materials and Methods

A Siemens AXIOM Artus dTA C-arm system was used to acquire 2D projections during rotation around the object of interest. Using a CTDI phantom (cylinder of 16-cm diameter, with a length of 14 cm) and a 0.6 cc Farmer chamber, the exposure was measured at the center of the phantom, and at 12 points around the periphery. Meaurements were repeated at 3 kVp, 70, 81 and 109, during a partial circle-scan over ~ 200 degrees. This represents the acquisition protocol in standard use for the side position (sleeve rotation) of the C-arm system. In addition, using the same protocol, images of the low-contrast insert of the CatPhan phantom (also 16-cm diameter) were obtained at several dose settings ranging from 0.36 uGy to 1.2 uGy for the same range of applied kilovoltages.

Volume data sets were reconstructed using enhanced C-arm CT reconstruction software including correction for ring artifacts and scatter (DynaCT). Contrast-to-noise ratio (CNR) was calculated for the 10 Hounsfield Unit (HU) 10-mm-diameter disk using a region of interest (ROI) in the disk and an equivalent ROI in the background at the same radius. Measuring both ROIs at the same radial distance from the center of the volume ensured that uncorrected cupping due to scatter did not affect the CNR measurements. A Siemens SOMATOM Sensation-16 scanner was used to obtain standard reconstructe images of the same CatPhan at 80 kVp and 120 kVp for purposes of comparison.

The resolution of the C-arm CT system was measured in reconstructions of a 100 um wire at three detector zoom formats: 32, 42 and 48 cm. Limiting resolution of the system could then be calculated using standard Fourier techniques.

Discussion

We list here only a subset of our results at 81 kVp. First, the peripheral dose measured using the pencil chamber varied from 39% to 184% of the dose measured at the center of the CTDI phantom (see Fig. 1). A modification of the standard CT dose volume calculation technique (1/3 center + 2/3 periphery) was used by averaging over all the measured points at the periphery to give (1/3 center + 2/3 *mean* periphery) as an estimate of dose when using the short-scan acquisition technique (ie. 200 rather than 360 degrees) of the C-arm system. The CTDIvol was 27 and 49 mGy for the low and high dose settings of the CatPhan images. This compares with CTDIvol of 41.5 mGy in the same phantom for the Sensation-16 clinical CT scanner at 120kVp, 250mAs, using a pitch of 1.

Contrast-to-noise ratios measured in the phantom were 1.65 and 0.91 for high and low-dose protocols respectively (see Fig. 2). This compares with a CNR of 1.21 for the 80 kVp Sensation-16 scan.

Fig.1 Graphical representation of the variability of dose measured around the periphery of the phantom using the pencil chamber. All peripheral doses are relative to the center value, set to 100 on a 0-255 gray scale.
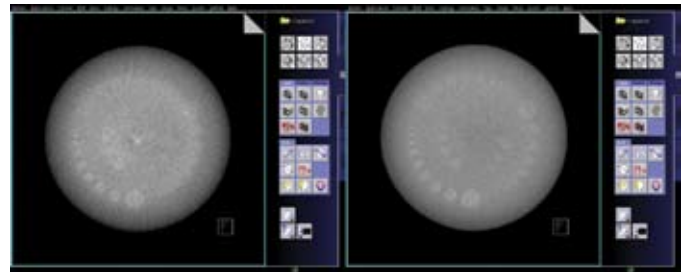
Fig. 2 Reconstructed C-arm CT slice through the low-contrast portion of the CatPhan phantom. The objects are 3, 5 and 10 HU above background. The effect of dose is clearly seen when comparing the low-dose acquisition of 0.36 uGy (left) to the high dose acquisition of 1.2 uGy (right).

Interestingly, the best MTF of the system was seen for a zoom of 42 cm, which is not the highest zoom available for the system. This is due to the fact that at this zoom factor, a second interpolation of the data, as is required for presentation on a 1kx1k matrix, is avoided. The limiting resolution of the system is 10% at 1.75 cycles/mm.

Conclusion

Low-contrast detectability within C-arm CT slices approaches that of clinical CT for 80 kVp acquisitions. We expect that at 120 kVp, clinical CT will continue to outperform C-arm CT since the flat-panel detector on the C-arm system is optimized for low-kVp operation in the range of 70-90 kVp. Limiting through-plane resolution of the C-arm CT system currently exceeds that of clinical CT. The excellent image quality expands the opportunities for new applications of C-arm based 3D imaging in the interventional suite.

C-arm CT Imaging of the Kidney for Accurate Stenosis Quantification, Calcification Detection and Functional Assessment

Rebecca Fahrig[1], Robert Bennett[1], Donna Bouley[2], Eric Olcott[3] and Graham Sommer[1] − [1]Department of Radiology, [2]Department of Comparative Medicine, Stanford University; [3]Department of Radiology, Palo Alto VA

Introduction

The ability to acquire 3D volume images in the interventional suite, using a C-arm mounted flat panel imaging system (Siemens AXIOM Artis dTA), permits increased accuracy in the measurement of arterial stenosis, increased discrimination between calcification types, and assessment of renal function during an interventional procedure. We have carried out a combination of phantom and *in vivo* studies to investigate the potential of this new imaging modality in the area of renal diagnosis and intervention.

Materials and Methods

Renal Artery Stenosis Measurement To compare the ability of C-arm CT vs. clinical CT to assess the diameter of renal arteries, a custom phantom was designed and built that permitted orientation of vessel-simulating tubes (1-6 mm diameter) within the plane of acquisition of the CT systems (see Figure 1). The phantom was filled with iodinated contrast to a CT number of ~ 330 HU, and was imaged on a Siemens Sensation 16 MDCT scanner (120 kV) and the Artis system (125 kV). Slices were reconstructed at 1 mm and 0.323 mm respectively, and vessel length, diameter and cross-sectional area were measured.
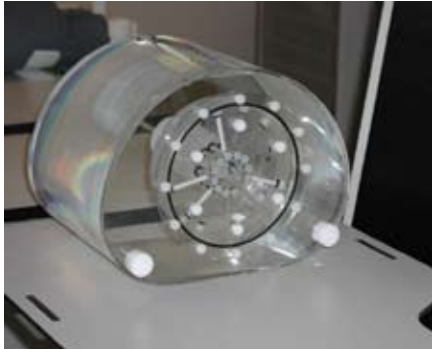

Figure 1. Renal artery phantom used for comparison of accuracy of 3D measurements in volumes acquired using CT and C-arm CT.

Imaging of Urinary Calculi Twenty-two radio-opaque (calcium) and 17 non-radio-opaque (urate) calculi were encapsulated within soft-tissue density material (agar), placed within an anthropomorphic phantom abdomen, and scanned as above with both the MDCT and C-arm CT systems. Detectibility and visibility of margins were assessed in reconstructed volumes.

Renal Functional Parameters Three Yorkshire pigs were scanned using the MDCT scanner and using the C-arm CT system. Using comparable scan parameters, abdominal CT images were obtained pre-contrast injection, and at 10 s, 90 s, and 470 s following IV contrast injection. In addition, images were obtained during a selective arterial injection of dilute contrast into the renal arteries during imaging using the C-arm CT system (see Figure 2). Renal cortical, medullary and overall volumes were calculated for acquisition with both scanners and compared to histologic results. Single-kidney renal extraction fractions were determined using a previously described technique.

Figure 2. MIP image through the C-arm CT volume acquired during a selective injection into the left renal artery. Difference between inflow and outflow HU values is used to assess renal function.

Results

Renal Artery Stenosis Measurement Rendered volumes of the C-arm CT data were somewhat noisier than the corresponding CT volumes, in part due to the smaller voxel size of the reconstructions. Vessel tracking using Vitrea2 was more successful on the C-arm CT data, allowing vessels of **all** diameters to be measured. The MDCT system could not resolve the smallest structures at the HU investigated here due to the effects of partial volume signal loss.

Imaging of Urinary Calculi All urinary calculi could be clearly distinguished using both 3D CT systems. The C-arm CT system subjectively achieved higher spatial resolution, supporting the findings of the artery stenosis phantom studies. Although truncation of projection images occurred for C-arm CT acquisitions (detector size 40x30 cm, magnification 1.5), the correction algorithms prevented cupping and calcification visualization was not impaired in the 3D reconstructions.

Renal Functional Parameters After optimization of injection protocol using the first two animals, renal extraction fraction values of 20.8% and 25.0% were obtained for the left and right kidneys respectively using MDCT and an intra-venous injection of contrast, compared to corresponding values of 19.6% and 18.6% using the C-arm CT system and intra-arterial injections. Actual zonal and overall renal volumes were in excellent agreement with volumes determined using both scanners.

Conclusion

Accurate determination of renal artery diameter, visualization of renal calculi and measurement of functional reserve are possible with both MDCT and C-arm CT systems. These measurements are of considerable prognostic importance during interventional procedures since it has been shown that only those ischemic kidneys with a moderate degree of dysfunction respond well to angioplasty. The advent of C-arm CT means that planning and intervention can be readily performed using the guidance of the same system, exploiting the fluoroscopic capabilities of the C-arm system for catheter placement and the 3D CT capabilities of the same system for accurate stenosis sizing, calculi visualization and renal function evaluation.

Methods for Imaging and Quantifying Stent Deformation in the Superficial Femoral Artery

Bonita Song[1], Robert Bennett[2], Nathan Wilson[3], Jeffrey Simons[4], Donald Shockey[4], Charles Taylor[1,3,5], Rebecca Fahrig[2]

Departments of [1]Mechanical Engineering, [2]Radiology, [3]Surgery & [5]Bioengineering, Stanford University; [4]Center for Fracture Physics, SRI International

Introduction

Several studies have shown a significant fracture rate in stents deployed in the superficial femoral artery (SFA). Biomechanical forces imparted on the SFA by the musculoskeletal system during leg flexion and extension may play a critical role in the fracture of SFA stents. We have previously investigated the motion of the SFA during leg flexion using MRI. In this work, we describe methods to image an SFA stent in several bending conformations *in vitro* (using a rotational C-arm computed tomography (CT) machine) and quantify the resulting deformation. Two custom test devices were used to produce repeatable deformations and apply known loads to a stent. Custom software was then utilized to visualize the CT images and to track trajectories of the specific points on the stent across deformations. The methods developed will be used to image implanted SFA stents *in vivo* and quantify the resulting deformation.

Materials and Methods

Twelve x-ray attenuating markers made from solder and copper wire were affixed to a 6 mm by 40 mm nickel titanium alloy ("Nitinol") stent (Figure 1a). These markers were used as landmarks to simplify image processing for this pilot study. A rotational C-arm CT system (Siemens dTA, Siemens Medical Solutions) (Figure 1b), was used to image the stent during bending in air at 70 kVp. The C-arm CT system uses a new state-of-the-art digital detector (30 cm x 40 cm, 154 µm x 154 µm pixels) to provide CT volumes with isotropic resolution as high as 0.15 mm, while allowing flexible patient positioning and scan plane orientation.
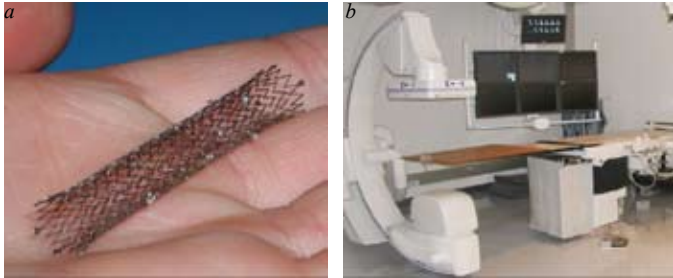

Figure 1. Nitinol stent tagged with markers; and as imaged on the Siemens Axiom dTA C-arm CT system.

For this *in vitro* study, the stent was first deformed using a cantilever bending apparatus and then an apparatus constructed to subject the stent to a pure bending moment. Since one end of the stent is fixed in the cantilever bending apparatus, a common reference point is attained for all subsequent deformations. The pure bending test apparatus has an integrated load cell and is ideal for validating finite element simulations of stent deformation. Both test devices were constructed out of low x-ray attenuating materials in order to minimize introduction of artifacts into the image data. After a stent was loaded and several image data sets were acquired, the reconstructed volumes were imported into custom software for visualization and analysis. A surface representation of the stent in each volume was created by choosing an appropriate threshold intensity value and creating an iso-surface. In the software, multiple iso-surfaces can be visualized in the same rendering window simultaneously. The user can then interactively select points in the volume and generate the trajectory of an individual marker throughout the deformation. This was done for several markers and cubic splines were fit to the selected points.

Results

Two imaging studies were performed (Figure 2). The first consisted of acquiring seven 3-D volumetric scans for a stent deformed using the cantilever bending device. In the second study, seventeen 3-D volumetric scans were acquired loading the stent using the pure bending moment

device. In the volumes, the markers were clearly visible. In addition, the images had sufficient resolution to identify the stent struts. For the pure bending tests, loading information was obtained during the deformation. Figure 3 shows the load vs. average deflection angle for each of the deformations imaged.
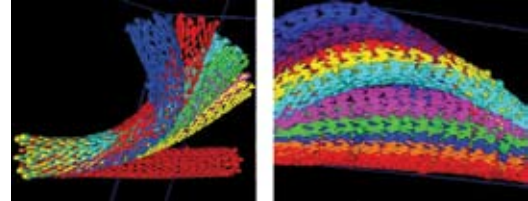

Figure 2. Visualizations of the deformed stent geometry, showing deformations due to cantilever and pure bending.
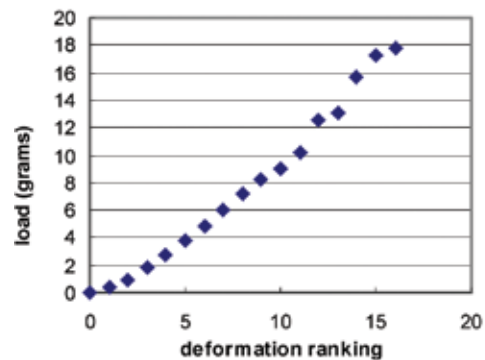

Figure 3. Load vs. deflection angle during pure bending.

Discussion

Future *in vitro* studies will focus on additional important modes of stent deformation including tension, torsion and radial compression. The methods discussed herein should be applicable to *in vivo* imaging and analysis. Two additional significant challenges will be present in the future *in vivo* studies. First, clinically implanted stents will not have special markers attached to facilitate motion tracking. Second, due to patient health concerns the number of acquisitions in patients and volunteer subjects will be limited. Although direct loading information will not be acquired *in vivo*, we believe that measured displacement trajectories obtained using high-resolution CT data can be used together with finite element analysis to estimate the forces deforming the stents and provide insight into stent fracture.

Conclusion

We have demonstrated a technique for imaging the three-dimensional deformation of a stent subject to cantilever and pure bending using a C-arm CT system. Using markers, the displacement of several points along a stent were successfully tracked as it was systematically deformed. In addition, image quality was found to be sufficient such that an unmarked point on the stent was identified and the trajectory was calculated. The tracking was simplified by the large number of image volumes acquired (7 to 17) since the displacements between individual time points were small.

First 3D Cardiac Images on a C-arm Angiography System Reconstructed with Retrospective Gating

Rebecca Fahrig[1], Jan Boese[2], Guenter Lauritsch[2], Norbert Strobel[1,2], Amin Al-Ahmad[3], Dominique Sandner-Porkristl, Teri Moore[2], Frandics P. Chan[1] − [1]Department of Radiology, [2]Siemens Medical Solutions and [3]Department of Cardiology

Introduction

We are investigating the visualization of cardiac structures in volumes reconstructed from projections acquired on an interventional C-arm flat-panel detector (FD) imaging system.

Materials and Methods

An interventional C-arm system (AXIOM Artis dTA FD, Siemens Medical Solutions, Forchheim, Germany) was modified to allow acquisition of several bi-directional sweeps through 200 degrees during synchronized acquisition of the ECG signal. Protocols with 4 to 6 sweeps were investigated, with the number of images per sweep from 96 to 247, and total acquisition time from 16 to 40 seconds. Our software for retrospective gating allows specification of cardiac phase for reconstruction, selecting for each angle the image that is closest to this cardiac phase. Enhanced C-arm CT reconstruction software is used to reconstruct at the chosen cardiac phase. Four-D image quality was tested in two *in vivo* porcine models (heart rate ~ 90 bpm) for data acquired during injection of 2 cc/s and 3 cc/s of iodinated contrast into the inferior vena cava. These images were compared to the gold standard clinical CT images of the same animal on the same day using clinical gated cardiac MDCT on the Siemens Sensation 16 CT scanner. Curved planar reformations were performed in the most motionless data (ie. at the most motionless point in the cardiac cycle) through the vessel of interest, and the 2D projected length as determined by the visibility of the most distal vessel structure was measured. The lengths of the right coronary (RCA), left anterior descending (LAD) and left circonflex (LCx) were measured in the clinical CT and 3D C-arm volumes.
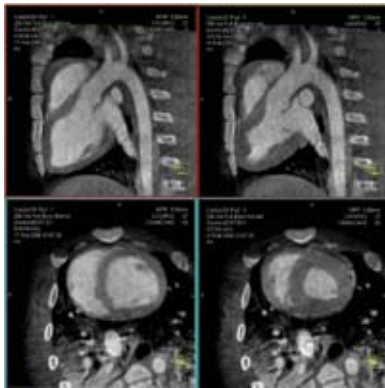

Figure 1 Representative images acquired using the C-arm system and retrospective cardiac gating (left) long and short axis MPRs through the heart during diastole (right) long and short axis MPRs through the heart at systole.
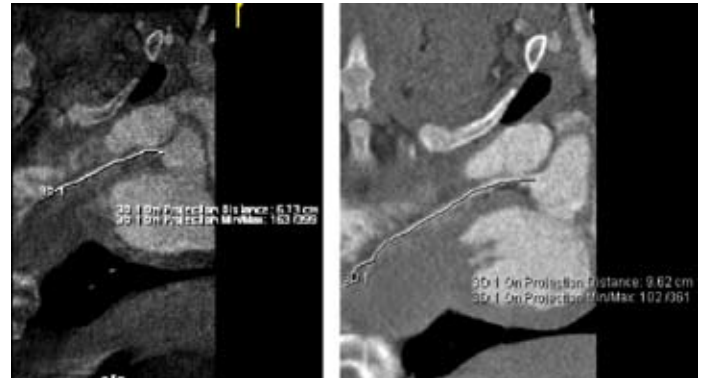
Figure 2 (left) C-arm CT-based measurement of the length of the LAD as compared to (right) clinical 16-slice CT measurement of the same vessel.

Discussion

Figure 1 shows long and short axis cuts through the heart at two points during the cardiac cycle. The temporal resolution achieved with retrospective gating on the C-arm system is clearly sufficient for clear visualizatiton of the chambers of the heart. Figure 2 shows a direct comparison of vessels on the C-arm and clinical CT scanners. Length measurements of the RCA, LAD and LCx showed that for experiment #1, 35%, 64% and 98% of the vessels respectively could be seen in the reconstructed 3D C-arm images relative to the CT images. For experiment #2, 85%, 65% and 45% of the vessels could be seen in the C-arm results. All four heart chambers are well seen through out the cardiac cycle. The coronary veins, pulmonary arteries and veins are best seen at 80% RR-interval.

Conclusions

For the first time, it was possible to visualize cardiac anatomy in 3D using a C-arm CT system and intravenous contrast injection. Further optimization to reduce radiation dose and acquisition time is underway. Providing cardiac volume reconstructions during interventional proce-

Mathematical Models for Detection of Lung Nodules in Tomosynthetic Images

Angel R. Pineda, Sung-Won Yoon, David S. Paik, Rebecca Fahrig - Department of Radiology

Introduction

Optimization of medical imaging systems ultimately attempts to improve system performance on clinical tasks. Since it is impractical to evaluate every hardware design decision with a clinical study, a number of physical characterizations of the system such as resolution or variance serve as surrogates of image quality. Another approach to evaluating image quality is to subjectively evaluate the quality of the images. By combining a task that is specific to the application and mathematical predictors of human performance, we attempt to achieve the convenience of the physical descriptors and remove the subjective nature of the human evaluation.

Our overall goal is the optimization of a new, real-time tomosynthesis system for the detection of lung nodules. Our primary objective in this work is to optimize the tomosynthetic angle of the system with respect to detection of lung nodules while validating mathematical models that will allow us to minimize the number of future human observer studies.

Methods and Results

One 3.6 mm, 40 HU nodule was smoothly integrated into a high resolution (150 micron) CT volume of a dog lung in 46 non-overlapping locations of the parenchyma. Simulated radiographs and tomosynthetic reconstructions were produced using the CT volume data. Sub-regions of the radiographic and tomographic images, either centered on the nodule or not containing any nodule, were used in the two-alternative forced

Figure 2. The mathematical models for human observer detectability are compared with the average human observer results from the psychophysical experiments. Both the Eye and Channelized Hotelling models are calibrated at 0 degrees and their prediction of human performance tested for the other tomosynthetic angles. Both mathematical models follow the same trend as human studies but the Eye model has better agreement with the human data.

choice (2-AFC) study (Figure 1). The clinical detection task of possibly finding multiple lesions over an entire image is simplified to determining whether one lesion is in one of two distinct locations. The observer is forced to choose between the two locations. We used a set of 46 image pairs to estimate each percent correct for each of our 4 human observers. The detectability measure shown in Figure 2 is a monotonic transformation of the percent correct which quantifies the separability of the ensemble of images with and without a nodule. On that scale, 0 maps to random chance and 3 is close to perfect detection.

We used two mathematical observers to model the improvement in detection observed in the psychophysical studies. The Channelized Hotelling observer used the Laguerre-Gauss basis expansion to estimate the ideal linear observer. The Eye model used a parametric representation of the human sensitivity function to modify the matched filter. In both cases, parameters in mathematical models were picked to match the human observer performance for the 0 degree tomosynthetic angle (projection radiography). The models trained on the projection data were then tested on the remaining tomosynthetic angles. The mathematical observers were rank-ordered in the same way as the 2-AFC studies. The Eye model had better agreement with the human data.

Conclusion

We verified the benefit of tomosynthesis for very small tomosynthetic angle in the detection of lung nodules in anatomical backgrounds. The largest increase occurs in the detectability of a 3.6 mm lung nodule when comparing the projection image to the tomosynthetic reconstruction with an angle of only 3 degrees. The channelized Hoteling observer and the eye filter were shown to track human performance as the tomosynthetic angle changed. These results validate and extend the use of mathematical observers to evaluate and optimize the choice of tomosynthetic angle with a finite number of non-stationary images.
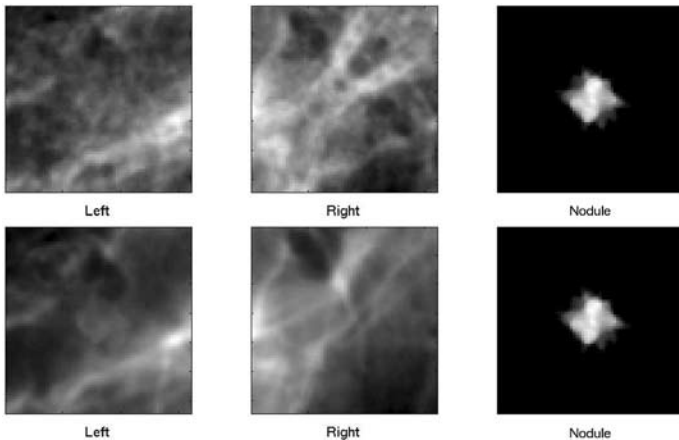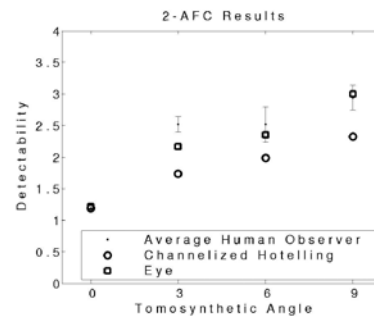

Figure 1. Sample images used in the 2-AFC study of lung nodule detectability. The images labeled "left" and "right" represent two different locations in the lung. The right most images show the nodule, which for the images shown is present in the "left" image. The top row is for projection radiography and the bottom row for tomosynthesis with an angle of 3 degrees.

Tomosynthesis Reconstruction from Real NexRay System Acquisitions

Sungwon Yoon[1], Angel R. Pineda[2], Josh Starlack, Rebecca Fahrig[2] – [1]Department of Electrical Engineering, Stanford University; [2]Department of Radiology, Stanford University

Introduction

X-ray detection of lung nodules is a challenging task due to the complex over- and under-lying anatomical structures that confound the visualization. For this application, we are investigating the use of a tomosynthesis system that uses a large area scanned X-ray source and a small area digital detector array. Such a system currently available has 230*mm* by 230*mm* square source area and a 54*mm* by 54*mm* detector area. From previous analysis, it is desirable to have a larger detector to achieve a higher half-tomographic angle, which enables better plane-to-plane separation in the reconstruction, than the currently achievable angle of 1.5°. To investigate the effect of larger tomographic angle in the reconstructions, we acquired real data from the NexRay system at 9 different configurations to simulate a virtual larger detector.

Materials and Methods

By tiling the 54*mm* by 54*mm* detector in a 3x3 matrix format, we could theoretically achieve a virtual detector that is 3 times longer in length in both dimensions. Due to the smaller field of view and the physical limitations of the system, only a 3x3 overlapping acquisition was possible which could provide half-tomographic angle of < 3°. Since the 9 configuration geometries could not be known exactly in advance, we inserted fiducial markers into the chest phantom (which had lung nodule inserts). Data at each of the 9 acquisition geometries was reconstructed followed by inverse solution of the 9 configurations from the reconstruction data of the fiducial markers.

Figure 1 shows the reconstructions for the 9 independent NexRay acquisition configurations. Due to the imperfect nature of the detector elements and source point distributions, the acquisition data had to be corrected (flat field correction and source point validity detection, respectively) before being used in the reconstruction. Note that all views see the 3 markers which will be essential in the registration algorithm.

Figure 2 shows the comparison between two different reconstruction methods for the same chest phantom data. On the left, a radiographic projection image is shown, and on the right, tomosynthesis reconstruction at a particular plane is shown. The effect of tomosynthesis is noticeable in the blurring of the spine and rib bones which are located farther away from the focal plane. More importantly, lung nodules are more discernible in the tomographic reconstruction compared to the projection.

Discussion

We are in the process of registering the reconstructions from the 9 different configurations to inversely solve for the exact amount of overlap of the detectors to simulate a "virtual" detector. Using this extended detector, we will be able to understand the effects of a larger half-tomographic angle in visualizing lung nodules in the tomosynthesis system.
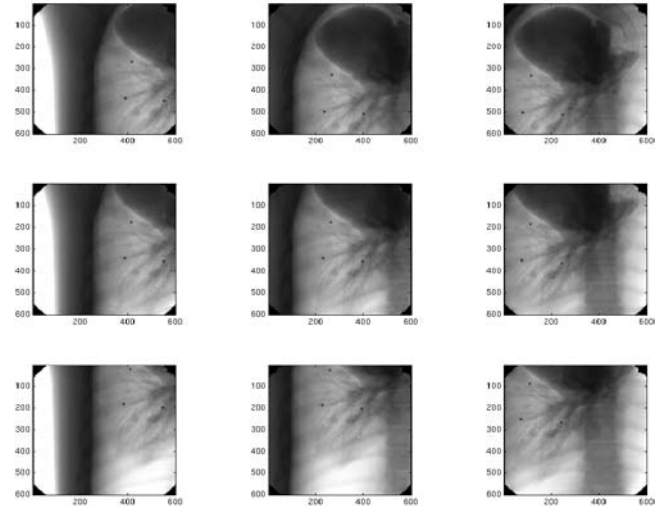
Figure 1. Reconstructions for the 9 different acquisition geometries at the same plane focusing on the fidcial markers.
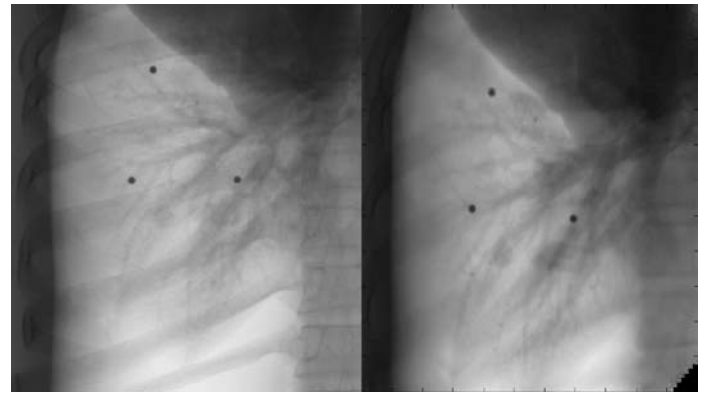
Figure 2. Comparison between the radiographic projection (left) and tomosynthetic reconstruction at the currently available system configuration (half-tomographic angle = 1.5°). Note the difference in the conspicuity of the nodules between the two images.

Conclusion

To investigate the effects of larger tomographic angle than what is currently available, we created a "virtual" extended detector by setting up 9 different acquisition geometries. We corrected the raw acquisition data and reconstructed tomosynthetic images at various planes. Although the current system provides better detectibility than the traditional projection data, we hope to show from the reconstructions of the virtually augmented data that an further improvements are possible for a larger tomographic angle.

Investigation of Increase in Radiation When an X-ray Tube Is Placed in a Magnetic Field

Zhifei Wen[1,2], Norbert Pelc[1], Walter Nelson[3], Rebecca Fahrig[1] —Departments of [1]Radiology and [2]Physics, Stanford University; [3]Stanford Linear Accelerator Center

Introduction

Previous work has shown that when an x-ray tube is placed inside a magnetic field (B) that is parallel to the tube axis, the x-ray exposure increases with increasing B. It was hypothesized that the increase was caused by back-scattered electrons which were constrained by B and re-accelerated by the electric field (E) onto the x-ray tube target. We performed computer simulations and physical experiments to study the behavior of the backscattered electrons in a magnetic field, and their effects on radiation output, x-ray spectrum and off-focal radiation.

Materials and Methods

A Monte-Carlo program (EGS4) was used to generate the combined energy and angular distribution of the back-scattered electrons. The electron trajectories were traced and their landing locations back on the anode were calculated. Radiation emission from each point was modeled with published data (IPEM Report 78), and thus the dose rate and x-ray spectrum with the contribution of backscattered electrons could be predicted. The point spread function for a pencil beam of electrons was generated and then convolved with the density map of primary electrons incident on the anode as simulated with a finite element program (Opera-3d, Vector Fields, UK). Therefore, the total spatial distribution of x-ray emission could be calculated. Experimental measurements used an x-ray tube (10° anode), a 30μm pinhole, a flat panel x-ray detector, a calibrated dosimeter, and a 0.5T magnet (Signa-SP, GE Healthcare, Milwaukee, WI). Measurements of the dose rate, half value layer and focal spot images were acquired as functions of B. Alignment between the cathode-anode axis and B was maintained for all experiments.

Results

Simulations showed that at 65keV about 54% of the electrons incident on the target were backscattered. Fig. 1 shows the combined energy and angular distribution of these backscattered electrons. Predicted dose rates as functions of field strength agreed well with measured data points at different tube voltages (Fig. 2). At 0.5T when the magnetic field was strong enough to constrain all backscattered electrons within the target area, the x-ray half value layer (HVL) was reduced by about 6% as a re-

Fig. 2. Plot of radiation dose rates v.s. magnetic field strengths at different tube voltages. Solid lines are simulation results and discrete points are experimental data.
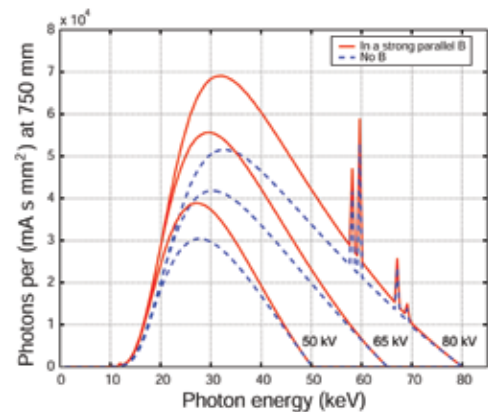
Fig. 3. Predicted x-ray spectra with and without a parallel strong magnetic field at different tube voltages.
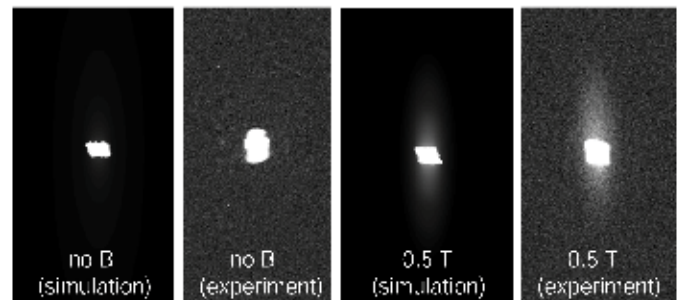
Fig. 4. Comparison of focal spot images with no field and with a field of 0.5 T.

sult of the x-ray spectrum being shifted to the left (Fig. 3). Calculations showed that the exposure would be increased by 33%, and around 39% of the increase was within an area twice the size of the focal spot.

Conclusion

Computer simulations strongly support the hypothesis that the increased emission from an x-ray tube placed within a strong B is caused by backscattered electrons. The x-ray spectrum is slightly shifted to the low energy end and the change in HVL is not significant. A majority of the increased radiation is off-focal when B≤0.5T (Fig. 4).
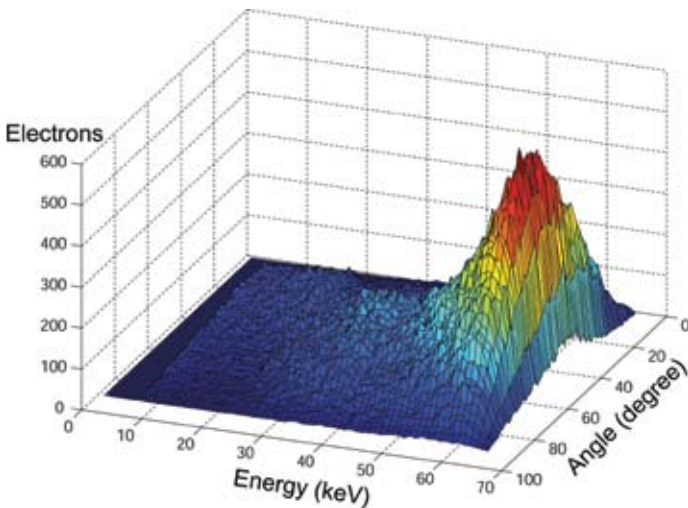

Fig. 1. The combined energy and angular distribution of backscattered electrons simulated with EGS4 for 10[6] primary electrons incident at 65keV.
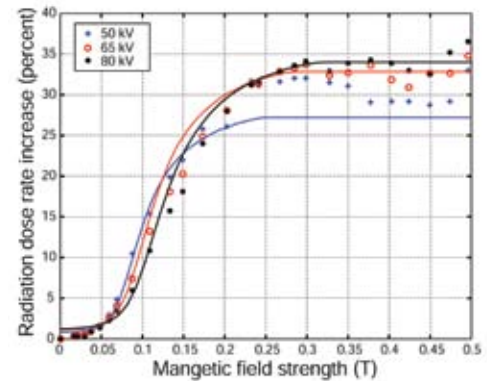
Truly Hybrid X-ray/MR System: Expanding Clinical Applications

Arundhuti Ganguly[1], Zhifei Wen[1,2] Bruce Daniels[1], Richard Barth[3], William Kennedy[4], Kate Stevens[1], Kim Butts[1], Norbert Pelc[1], Rebecca Fahrig[1] - Department of: [1]Radiology, [2]Physics, [3]Pediatric Radiology, [4]Urology

Introduction

We have previously reported on the development of our x-ray/MR hybrid system for image guided procedures, . This system combined an x-ray fluoroscopy unit within the bore of a 0.5T GE Signa-SP interventional magnet (GE Medical Systems, Milwaukee, WI). Here we describe the recent clinical applications of this system for two diagnostic procedures: voiding cysto-urography (VCUG) and dynamic hip MR arthrography.

Materials and Methods

The x-ray/MR hybrid system consists of a fixed anode x-ray tube with a maximum power of 510W (GE OEC, Salt Lake City, UT). It uses a flat panel detector (FPD) connected to a modified mobile C-arm system GE-OEC 9800. The x-ray tube and detector are mounted in the 60 cm gap between the double-donuts of the 0.5T open magnet. Following system modifications including RF shielding and filtration, magnetic compatibility, field inhomogeneity compensation, and x-ray transparency of MR coils, the present system allows easy switching between imaging modes.

VCUG: This procedure is per-formed in children with urinary tract infections or prenatal hydronephrosis (diagnosed in up to 4% of all pregnancies). Typically, it consists of inserting a catheter in to the bladder, filling the bladder with iodinated saline and imaging the flow of urine during voiding to look for any reflux. This procedure is typically performed under x-ray fluoroscopic guidance in pediatric patients for quantifying the degree of reflux. Using the x-ray/MR hybrid system, the procedure is first conducted under MR guidance with gadolinium (Gd) agent for contrast enhancement of urine. A thick slice of about 2 cm is selected and a fast GRE sequence is used. The x-ray fluoroscopy then provides the routine diagnostic images, while the MRI provides additional data for verification without relocating the patient.

Hip Arthrography: This procedure involves placing a needle in the hip joint under x-ray guidance, followed by injection of Gd contrast agent. The hip joint is then imaged dynamically with MR to examine for labral tears and femoral acetabular impingement. Needle placement using MR guidance is time consuming and complex but is easily performed under x-ray fluoroscopy. Imaging the joint in the open magnet configuration allows freedom in terms of flexing and rotating the hip for improved diagnosis. Therefore, conducting this procedure under x-ray/MR hybrid guidance allows quick needle placement and flexibility in patient positioning. Typically, spin-echo (SE) imaging of the joint following administration of Gd contrast is performed.
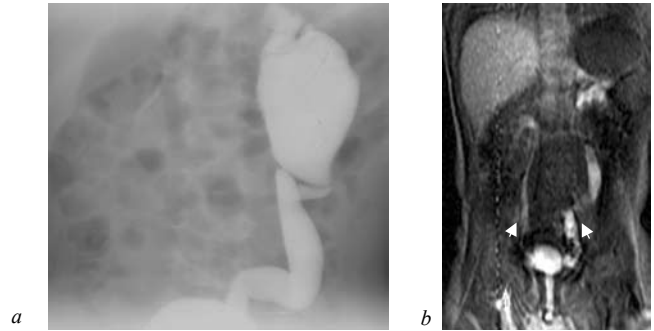
Fig.1(a) X-ray image showing reflux of iodinated urine from the bladder towards the left kidney (65 kVp, 3 mA) (b) MR image showing GDTPA enhanced urine reflux towards both left and right kidneys (FSPGR sequence, TE/TR 4/12 ms, FA 54, slice thickness 2 cm)
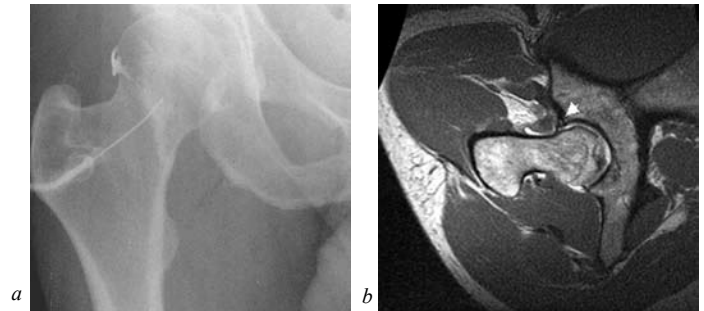
Fig.2(a) X-ray image showing positioning of needle in pelvic joint for injecting contrast agent (85 kVp, 3 mA) (b) MR image showing labrum tear (arrow) (SE. sequence, TE/TR 20/567 ms, slice thickness 3mm)

Discussion

The VCUG is a commonly performed procedure in children which exposes them to radiation. Hybrid technology is facilitating research to develop cystogram using MRI, which could significantly reduce radiation to children. For hip arthrography, the hybrid system may reduce overall procedure time and the accuracy of the diagnosis.

Conclusions

So far we have performed 4 VCUG procedures and three hip arthrograms. The truly hybrid x-ray/MR system has allowed increased efficacy in several standard clinical interventions by effectively combining two complimentary imaging modalities within one unit.

Determination of Electronic and Quantum Noise Dominated Regions in a CT System

J.H. Dormo, Jongduk Baek, Norbert J. Pelc - Departments of Radiology and Electrical Engineering

Introduction

There is great interest in reducing the dose of CT examinations. Theory predicts that the dependence of noise variance on flux should change from linear at high dose (due to quantum noise), to quadratic at low dose (due to electronic noise). Knowledge of this transition is important in protocol design and system comparisons. A robust measurement method must be independent of reconstruction kernel. We developed a technique to explore this behavior, and examine the location where a CT scanner transitions from an electronic noise dominated region to a quantum noise dominated region.

Materials and Methods

Some CT systems smooth the projection data when the photon flux is low, making parameters such as the noise variance inappropriate measures for this analysis. We used the slope of the low frequency portion of the Noise Power Spectrum (NPS) as a metric that is independent of smoothing or reconstruction bandwidth.

Polyethylene phantoms (35 and 48 cm diameter) were scanned on a single slice CT scanner (GE, Milwaukee WI) using a 1 s rotation time. To get a wide range in detected flux we used eight mA settings (10 – 100 mA) and three slice thicknesses (1.5 – 10 mm). Ten scans were performed at each combination. The spectra calculated for each image were averaged, producing one NPS for each combination. The slope of the low frequency portion of the NPS was used as a measure of the noise at each setting, and all the values were combined into a single curve of noise vs. flux.

Discussion

The slope of log (noise) versus log (flux) should be -2 and -1 when performance is limited by electronic noise and quantum noise, respectively. The experimental results showed a slope of -1.06 for thick slices and high mA and –2.28 for thin slices and low mA. The transition from an electronic noise dominated region to a quantum noise dominated region was evident.

Conclusion

The slope of the NPS at low frequency provides an index of fundamental noise performance that is independent of reconstruction kernal and data smoothing. Measurements at a wide range of detected photon flux appear capable of locating the electronic noise floor in CT systems, which can aid in the development of low dose applications.

Calibration Method for an Inverse Geometry Volumetric CT System

Jongduk Baek, Norbert J. Pelc - Departments of Radiologya and Electrical Engineering

Introduction

For high resolution CT image reconstruction, accurate scanner geometric calibration is important. The purpose of this work is to describe a new method for calibration of an IGCT scanner. In order to do this, 4 parameters are determined by using a non-linear least square method.

Materials and Methods

We assume an IGCT system with a 71×71 x-ray source and a 48×48 array detector. We assume that the only misalignment is the orientation and location of the axis of rotation with 4 parameters, two angles and two distances. The two distance parameters, x_offset and y_offset, define where the axis crosses the z=0 plane. ζ is the rotation about the z-axis and $\square$ is the angle of the axis of rotation about the y-axis. We define the axis of rotation as the z axis, and acquire projections of a calibration phantom. The data are path-lengths of rays through beads. The phantom contains 6 beads and the minimum distance between each bead in the z direction is 20 mm to avoid projection image overlap.

We collect data at 8 view angles equally spaced over 360 degrees. For each bead, our system provides ray measurements and bead locations are calculated from these data by using a non-linear iterative least square method. In each iteration, we used the estimated positions and computed projection data to refine the position using a non-linear least square method again. From 48 bead locations(6 beads×8 views) , we find 6 circle centers and get the equation 3 dimensional line through circle centers. From the line equation, the 4 parameters are determined. The method was treated with computer simulated data containing noise.

Discussion

In the simulation, the true x_offset and y_offset were 0.5mm and the ξ and ζ were 4 degrees. We compared results at SNR = 23 and SNR = 10. For each, the simulation was performed 50 times and the mean and standard deviation were calculated..

Conclusion

The results shows that very accurate calibration is possible in the IGCT system. The advantage of this approach is that even if it is necessary to increase the number of unknown parameters(i.g. source or detector tilt), we can get the parameters by using the same approach.

	SNR=23		SNR=10	
	MEAN	STD	MEAN	STD
X_OFFSET	0.4974	0.0007	0.5027	0.0159
Y_OFFSET	0.5	1.0115×10-4	0.5	3.2445×10-4
ζ	4.018	0.1068	3.8461	0.4817
ξ	4.0002	5.9121×10-4	3.9992	0.0024

Wider Field-of-view Inverse-geometry CT with Multiple Detector Arrays

Samuel R. Mazin[1,2], Josh Star-Lack[3], N. Robert Bennett[1], Taly Gilat Schmidt[1,2], Norbert J. Pelc[1] – [1]Department of Radiology, [2]Department of Electrical Engineering, Stanford University; [3]NexRay, Inc., Los Gatos, CA

Introduction

Inverse-geometry CT (IGCT) is being investigated for its ability to acquire a cylindrical volume in a single rotation without cone-beam artifacts. If a single small detector array is used, the FOV of an IGCT system is limited by the source size. By using multiple detector arrays, the FOV becomes suitable for human applications. A feasibility demonstration was performed and the first images have been reconstructed to demonstrate the large FOV.

Materials and Methods

The prototype consists of an inverse-geometry C-arm fluoroscopy system (NexRay, Inc). The C-arm employs a large transmission target that is rapidly scanned by an electron beam which dwells behind each of an array of collimators. Opposite the source array is a much smaller area photon-counting detector array that is read out for each source spot position. With a single detector array, the in-plane FOV is limited by the source array size (16 cm for a 25 cm wide source). The FOV can be substantially increased, without having to increase the source array size, by adding detector arrays suitably separated in the transverse plane. To demonstrate the feasibility of the multiple detector array IGCT geometry, the C-arm was placed in a horizontal orientation with a rotating stage placed in between the source and the single detector array. The rotating stage was mounted onto a precision translation stage. A human torso phantom, which contained an iodinated real porcine heart, was placed on the rotating stage and scanned in step-and-shoot mode with 120 views over 360 degrees. To generate the data that would be acquired by an outer detector array, a second scan was done using the same setup but with the rotating stage displaced laterally by 15 cm. A calibration scan was performed to measure the geometric alignment. The data for a single axial slice were resampled into parallel rays and reconstructed using a standard 2D algorithm.

Discussion

A full chest axial slice can be observed including the arms, with an in-plane FOV of 48 cm. Bones, lungs, spine and cardiac anatomy can be seen clearly. Image artifacts are mainly due to view aliasing and geometric misalignment. It should be noted that cross-plane rays (i.e. rays that are not parallel to the image plane) were not used for reconstruction due to the 2D nature of the algorithm. Making use of these extra rays could help increase the SNR of the reconstructed image. View aliasing can be seen which is due to the acquisition of only 120 projections.

Conclusion

The results demonstrate that the in-plane FOV of the IGCT system can be increased by a factor of three using three detector arrays. Further work is needed to optimize image quality.
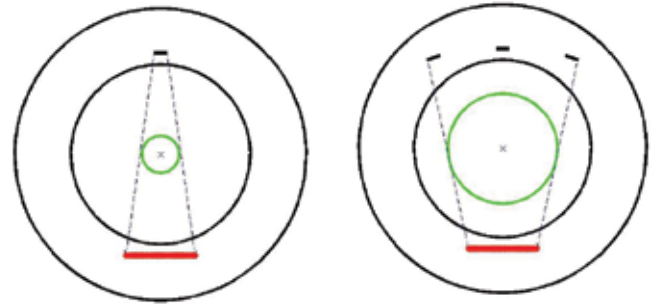
The in-plane FOV of an IGCT system with a single detector array is limited by the source size. Adding multiple detector arrays can increase the FOV without changing the source size.

A human torso phantom containing an iodinated porcine heart was scanned using the NexRay C-arm system as a table-top IGCT system. A second scan was done with the center of rotation translated to simulate data from an outer detector array.
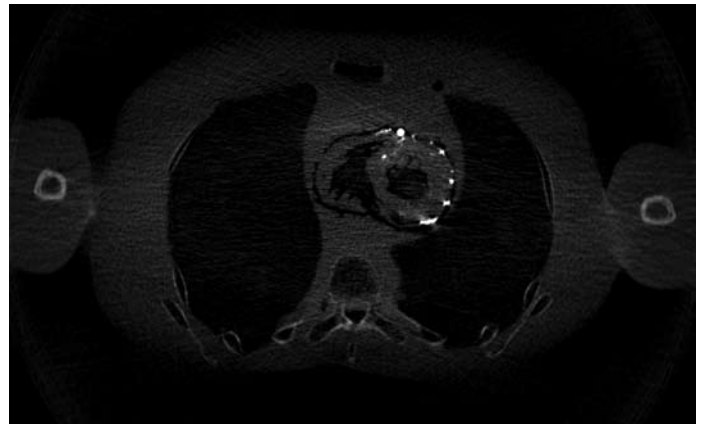
Reconstructed image of an axial slice using a 2D reconstruction algorithm. The in-plane FOV is 48 cm. View aliasing streaks are a result of an insufficient number of acquired projections.

Investigation of a Prototype Table-top Inverse-geometry Volumetric CT System

Taly Gilat Schmidt[1,2], Josh Star-Lack[3], N. Robert Bennett[1], Samuel R. Mazin[1,2], Edward G. Solomon[3], Rebecca Fahrig[1], Norbert J. Pelc[1] – [1]Department of Radiology, Stanford University; [2]Department of Electrical Engineering, Stanford University; [3]NexRay, Inc., Los Gatos, CA

Introduction

We have previously proposed the inverse-geometry CT (IGCT) concept for complete volumetric scanning in one fast circular scan with isotropic, high resolution and good low contrast detectability. This work investigated the implementation and performance of a prototype table-top IGCT system capable of acquiring a 5-cm thick volume in one circular scan. The noise, resolution, and artifact performance of the system was investigated through experiments, theoretical predictions, and comparisons to conventional CT systems.

Materials and Methods

The prototype system, shown in Figure 1, consists of a C-arm gantry with a 23 x 23-cm scanned-source opposite a 5.4 x 5.4-cm detector (NexRay, Inc). During an acquisition, the electron beam is rapidly steered across the transmission target, dwelling behind each of an array of collimator holes which limits the x-ray beam to illuminate the detector while ray measurements are made. A rotating stage simulated gantry rotation. Ideally the source and detector would have the same axial (z) extent to provide a sufficient dataset. For the prototype system, the axial FOV was restricted to 5-cm to meet this requirement. Each CT acquisition consisted of 125 views, each view containing all rays from one source scan. The data were acquired at 120 kVp, 60 mA, and were corrected for geometric misalignment and incident intensity. The MTF was measured using a 76-micron tungsten wire. The noise was predicted by modeling the source flux and experimentally measured using an 11-cm-diameter water sphere. The measured resolution and noise values were compared to analytical predictions and computer simulations. A "Defrise" phantom, composed of alternating Teflon and balsa wood disks, each 0.8 mm thick, was scanned on both the IGCT system and a cone-beam micro-CT system to test for cone-beam artifacts. The cone-beam system had a +/- 5 degree cone angle for the 4.5 cm volume thickness. To examine the IGCT performance for complex objects, a cadaveric inner ear specimen was imaged using the prototype system and a clinical scanner.
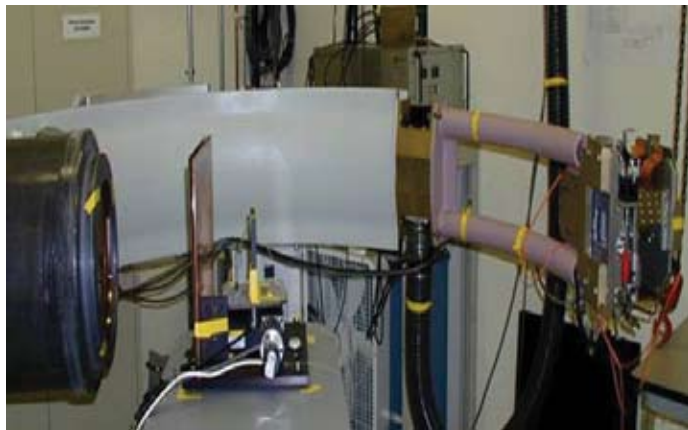
Figure 1: The prototype table-top IGCT system

Results

A comparison of the measured, simulated, and theoretically predicted in-plane MTF curves is plotted in Figure 2. The prototype IGCT system demonstrated 0.25-mm isotropic limiting resolution. The measured noise at the center of the water sphere was 80 HU, compared to a predicted 74 HU, and the models predict that noise comparable to a con-
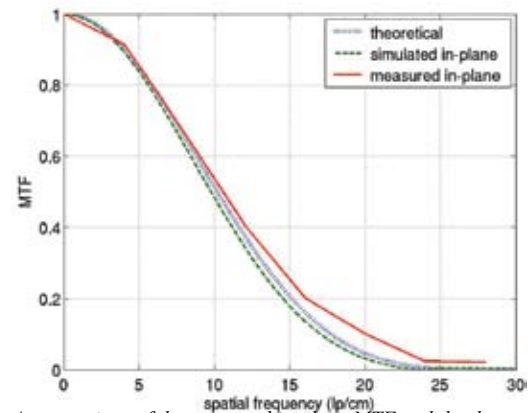
Figure 2: A comparison of the measured in-plane MTF and the theoretically predicted and simulated MTF curves.
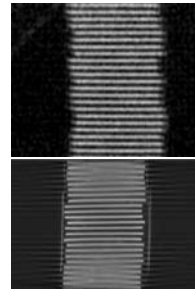
Figure 3: A coronal image of the "Defrise" phantom acquired by the IGCT system (top) and a cone-beam micro-CT system (bottom). Severe cone-beam artifacts are visible in the cone-beam reconstruction.
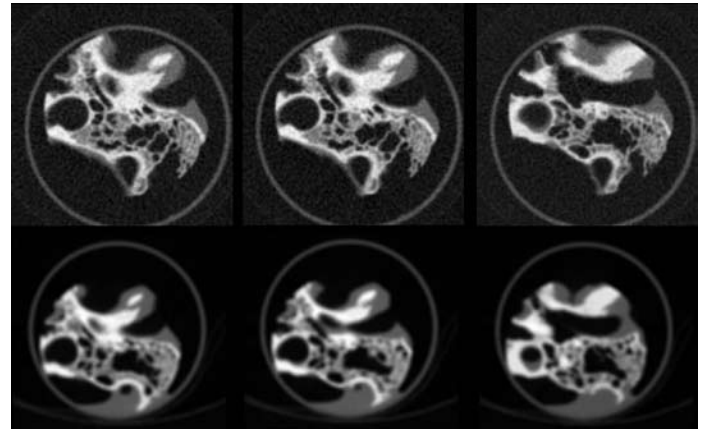
Figure 4: A comparison of three axial images of the inner ear specimen acquired by the IGCT system (top) and the clinical CT scanner (bottom).

ventional system is achievable. As shown in Figure 3, the IGCT images of the Defrise phantom were free of cone-beam artifacts while severe artifacts were present in the cone-beam images. The IGCT inner ear images, displayed in Figure 4, were visually sharper than those from a conventional scanner.

Conclusion

The successful implementation of the table-top IGCT scanner supports the inverse-geometry concept for high-resolution, volumetric scanning without cone-beam effects.

CT Colonography: Influence of 3D Viewing and Features of Polyp Candidates on Interpretation using Computer Aided Detection

Rong Shi[1], Pam Schraedley-Desmond[1], Sandy Napel[1], Eric Olcott[1, 2], R. Brooke Jeffrey[1], Jr., Judy Yee[3, 4], Michael Zalis[5], Daniel Margolis[1], David Paik[1], Anthony Sherbondy[1], Padmavathi Sundaram[1], Christopher F. Beaulieu[1] – [1]Department of Radiology, Stanford University; [2]Veterans Affairs Palo Alto Health Care System; [3]Department of Radiology, University of California, San Francisco; [4]San Francisco Veterans Affairs Medical Center; [5]Department of Radiology, Massachusetts General Hospital

Introduction

To determine if 3D viewing improves radiologists' accuracy in classifying true positive (TP) and false positive (FP) polyp candidates identified by computer aided detection (CAD), and to determine candidate features that are associated with classification accuracy, using known polyps as the reference standard.

Materials and Methods

We selected 47 CT colonography (CTC) datasets from a group of 26 men and 10 women, age 42-76 years old. Four radiologists classified 705 polyp candidates (53 TP, 652 FP) identified by CAD, initially with 2D images only, then supplemented by 3D renderings. Another radiologist unblinded to colonoscopy characterized each candidate for its features and assessed colon distension and preparation, in addition to defining the truth of FP candidates (stool, fold, etc). Receiver operator characteristic (ROC) curves were used to compare readers' performance, and repeated-measures of variance were done to test how features affect interpretation.

Discussion

The addition of 3D improved classification accuracy for three of the four readers, increasing the area under ROC curve from 0.93-0.95 (2D) to 0.96-0.97 (2D3D; p < 0.001). For TP candidates, three features significantly affected reader accuracy: maximum polyp width (p = 0.038), polyp height (p = 0.019), and preparation (p = 0.004). For FP candidates, six features significantly affected accuracy: colonic segment (p = 0.007), attenuation (p < 0.001), surface smoothness (p < 0.001), disten-

SURF interface showing an experimental polyp candidate (here a colonoscopy-confirmed polyp) in the center of the red bounding box on magnified transverse (A) and coronal (B) sections. (C) Volume rendering window, showing a subvolume surrounding the polyp candidate. The arrow indicates a polyp and arrowheads indicate a haustral fold. (D) Polyp CAD manager, used for establishing the reference standard and for the blinded reader trial.

sion (p = 0.034), preparation (p < 0.001) and the truth of the candidate lesion (p < 0.001).

Conclusion

3D viewing increases reader accuracy beyond 2D in classifying CAD identified polyp candidates. Features such as polyp size and exam quality are significantly associated with reader accuracy.

Rapid Prototyping and Development of Visualization/CAD Interaction Studies using SURF

Bindi Pankhudi[1], Anthony Sherbondy[2], Ajay Joshi[1], Christopher F. Beaulieu[3], Sandy Napel[3] – Departments of [1]Computer Science, [2]Electrical Engineering, [3]Radiology

Introduction

Our lab develops new visualization tools and Computer-aided Detection (CAD) techniques for medical image data. Assessment of these developments generally requires users (*e.g.*, radiologists) interacting with them and comparing them to existing methods. The Stanford University Radiology Framework (SURF) is a programmer's toolkit that aids the setup of these studies, by providing programmer with visualization tools (called plug-ins) that can be arranged on the computer screen as an interface to observe and examine medical data. We improved the original SURF design to provide more flexibility and convenience on part of the programmer and hence to facilitate rapid prototyping and design of interfaces for studies of new visualization and Computer-aided Detection (CAD) techniques.

Materials and Methods

The original SURF design required the programmer to assemble and arrange the code manually, resulting in excessive code duplication and long development cycles. In order to overcome these obstacles and expedite the process of developing new interfaces, we introduced the use of script files, wherein developing a new interface only requires knowledge of the plug-ins involved.

Discussion

Plug-ins can now be directly invoked from the script file and arranged arbitrarily on the computer's display by simply passing parameter lists, as opposed to re-assembling the code for the new interface. We have
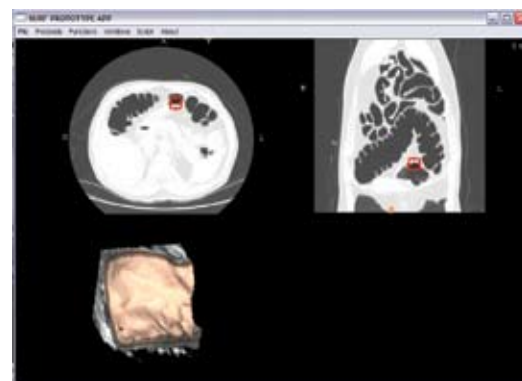
SURF example for studies of CT colonography, showing interactive axial (top left), coronal (top right) and subvolume rendering (lower left) within red bounding box.

tested the concept by using scripts to setup two separate interfaces we had made previously, one for studies of CT colonography visualization and CAD, and one for lung nodule detection.

Conclusion

The new SURF design is extremely programmer-friendly and intuitive, and does not assume any prior knowledge about SURF. Scripting greatly simplified the process of developing new interfaces and thereby improved the ease of future changes to SURF as well.

Classification and Volume Rendering Using Neural Networks

Ajay Joshi[1], Anthony Sherbondy[2], Bindi Pankhudi[1], Christopher F. Beaulieu[3], Sandy Napel[3] — Departments of [1]Computer Science, [2]Electrical Engineering, [3]Radiology

Introduction

Visualizing volume data consists of classification and rendering steps. Traditionally, manually edited transfer functions are used for classification. We have developed software that permits interactive classification using an intuitive "painting" interface and machine learning neural networks.

Materials and Methods

Our software allows the user to paint on regions of the data, thereby selecting them as being examples of various tissue types. These regions are input to a classifier that extracts image statistics (e.g scalar values, gradient magnitudes, locations, texture features) under the painted regions to learn how to classify unpainted regions prior to rendering.

Discussion

This type of volume visualization user interface allows the users to specify the regions in a volume that they would like to visualize by simply painting on a few slices from that volume, resulting in an automatically constructed classification function that makes use of many local image properties.

Conclusion

This new method greatly simplifies the task of designing transfer functions for volumetric rendering.
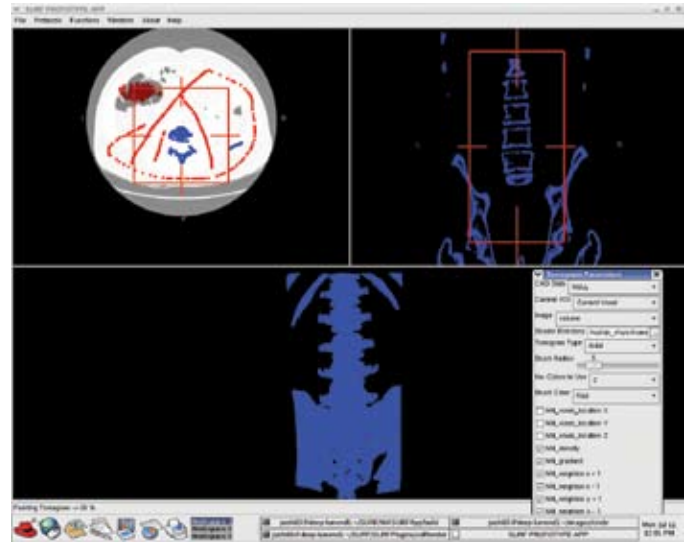
By painting on an axial image (upper left), classified volumes can be visualized, e.g., coronal (upper right) showing bones in blue, and subvolume rendering (lower right), showing bones within red bounding box (upper images) in blue.

Anatomically Selective Morphological Enhancement and Suppression in CT Colonography

David Paik, Padma Sundaram, Christopher Beaulieu, Sandy Napel — Department of Radiology

Introduction

The surface of the colon is very complex, making the search for polyps in CT colonography volumes very difficult. Prior approaches to unrolling or unfolding the colon straighten out the curves in this tubular structure and even unroll it to perform "virtual pathology." However, these methods have not attempted "intelligent" subtraction of the complex but normal background anatomy. Our approach to polyp detection simplifies interpretation by removing the complex undulations of haustral folds, thereby leaving behind only polyps on a flat sheet.

Materials and Methods

We start by reconstructing a surface model of the colon (pink). For the sake of the subtraction process, we selectively remove polyps from this surface by removing transverse but not longitudinal shape variation (yellow). Then, these two surfaces are geometrically subtracted, leaving behind a flat sheet with bumps corresponding to polyps (green).

Discussion

Our initial results with this method have been promising as shown with the above example. However, some difficulties still remain in that sometimes, the folds are not fully subtracted. We plan to continue refining this algorithm before performing a larger evaluation.

Conclusion

This subtraction method represents a significant departure from previous methods for aiding the interpretation of CT colonography data. It aids both human interpretation, by allowing the entire surface to be rapidly visualized, and CAD, by suppressing haustral folds, which can serve as sources of false positive CAD detections.

Folds + Polyps — Folds — Polyps
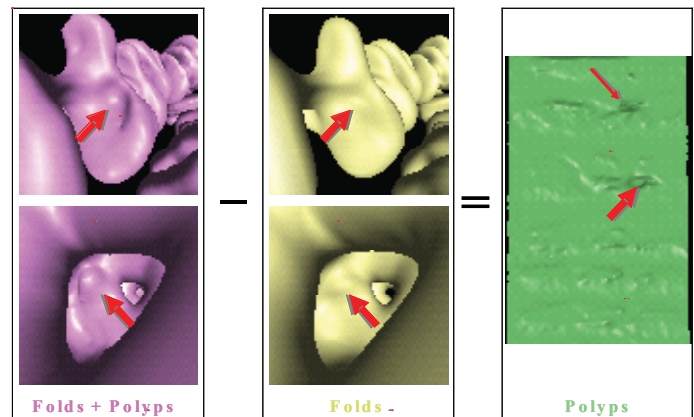
Geometric subtraction of haustral folds: Original surface (pink). Surface with polyps (red arrows) selectively removed (yellow). Geometric subtraction of these two surfaces (green) leaves primarily polyps protruding from an otherwise flat sheet.

133

Fold Removal in CT Colonography (CTC): A Physics-based Approach

P. Sundaram[1,3], E. Sifakis[2], D. Paik[1], C. F. Beaulieu[1], S. Napel[1] – [1]Departments of Radiology, [2]Computer Science, [3]Electrical Engineering

Introduction

Normal haustral folds complicate both visual and computer-aided detection (CAD) of polyps in Computed Tomography Colonography (CTC) data. We present a method to straighten and flatten the colon by simulating stretching of the colonic surface using a quasistatic Finite Element Model (FEM). The output of our algorithm is a 3D fold-free surface that can be displayed as a single image and/or subjected to a CAD algorithm.

Materials and Methods

We created several mathematical phantoms using MATLAB 7.0.1, with folds and polyps modeled as half sine functions and hemispheres, respectively. The phantoms had folds, polyps on flat regions and polyps on folds, as shown in Figure 1(a) and 1(d). We also tested our algorithm on a subvolume of actual patient data, acquired from a research CTC scan at our institution, containing a 6.9 mm polyp, as shown in Figure 1(g). Our algorithm stretches the surface in a direction normal to the direction of the folds, resulting in flattening the folds, with minimal distortion to polyps. A spatially invariant response to pulling from both ends is essential, otherwise structures closer to the edges being pulled will be more distorted than those farther away. We neglected inertial effects in our FEM implementation in order to achieve this. Figure 2 illustrates the importance of the quasistatic assumption. To evaluate our methods we measured the curvature and size of the polyps (diameters) and folds (heights) before and after simulated stretching.

Results

On phantom and patient data, our method shows reductions in fold height and curvature ranging from 54.4% to 70.3%, and 36.3% to 86.1% respectively. Polyp size and curvature were reduced by only 0% to 16%, and 0% to 20%, respectively. The output of our algorithm is a 3D surface that can be viewed as a single image.

Conclusion

Our physics-based method to flatten the colonic surface using a quasistatic finite element model suppresses folds while leaving polyps relatively undistorted, and has the potential to improve the efficiency of interpretation by reducing visual clutter and sources of false positive detections by CAD. Continued development is warranted.
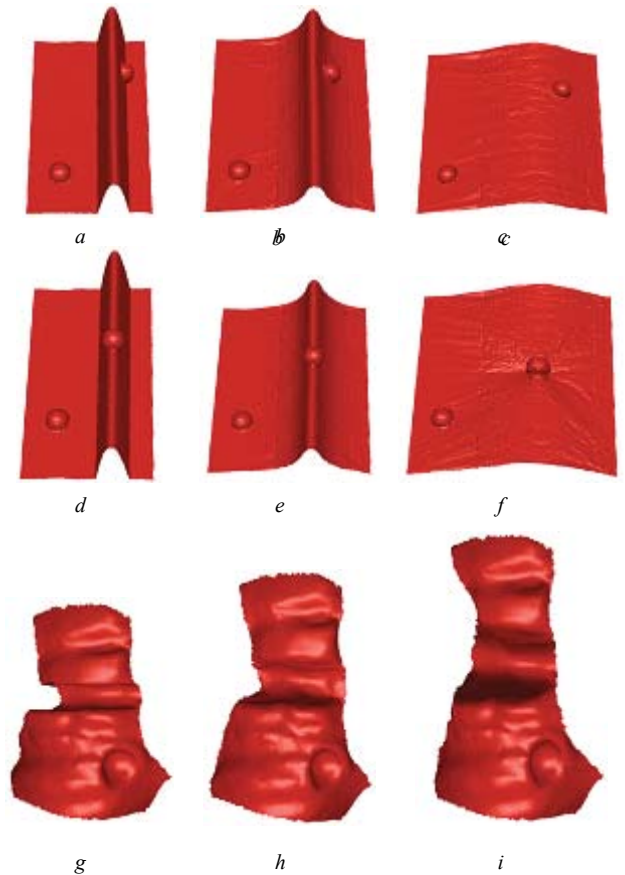
Figure 1: Results from phantom and actual patient experiments. Figures (a)-(c), (d)-(f) and (g)-(i) show steps in the deformation of a phantom or actual patient data. Figures (a), (b) and (c) show a phantom with a polyp on a flat portion in addition to one on top of a fold, while figures (d), (e) and (f) show a polyp on a flat portion, as well as one on the side of the fold. Figures (g), (h) and (i) show a subvolume of actual patient data being stretched. In all cases, folds were attenuated and relatively undistorted polyps remained.

Figure 2: Illustration of what can go wrong if a quasistatic assumption is not made, comparing single time points in the simulated stretching of a phantom with polyps and folds, with inertial effects neglected in (a), but not in (b). In (b), polyps at different spatial locations were distorted by different amounts. This is undesirable.

Rotational Roadmapping: A Contrast- and Time-efficient Navigation Technique Based on a Single Acquisition of Multiple Views

Markus Kukuk[1,2], Hideki Arakawa[2], Michael Marks[2], Huy Do[2], Sandy Napel[2] – [1]Siemens Medical Solutions; [2]Department of Radiology, Stanford University

Introduction

To date, conventional 2D-roadmapping (Ro) is the technique of choice for instrument navigation in neuroendovascular procedures. Two newer techniques capable of replacing 2D-Ro are 3D RA- and 3D CTA-Ro. The first requires the acquisition of about 400 projections from the interventional suite's C-arm scanner for an accurate 3D reconstruction of the vasculature, thus resulting in a considerable amount of radiation exposure. The second is derived from a pre-procedural CT scan, which, compared to 3D RA-Ro, suffers from limited spatial resolution, venous-phase artifacts and an increased amount of iodinated contrast needed. Both techniques suffer from streak artifacts in the presence of embolic agents such as metallic coils and stents. As a response to this need, we have developed a novel technique called Rotational Roadmapping (RoRo).

Materials and Methods

The RoRo navigation technique provides the following functionality: neurovascular anatomy from a rotational angiographic acquisition; projectional display of the vasculature as a "rotatable roadmap" to allow for interactive selection of the best working view; automatic movement of the C-arm into the selected working position; ability to subtract the selected projection from the live fluoroscopic images, thus displaying any medical device within the context of the vasculature; and the ability to return to the rotatable roadmap if a new working view is needed. RoRo was compared to 2D-Ro in 3 pre-clinical experiments in the swine model on a Siemens Axiom Artis dTA system.

Discussion

Using conventional 2D-Ro, a senior interventionalist required 6 minutes and a total of 16cc of iodine to navigate a guidewire into a pre-selected branch of the external carotid artery. By comparison, a less experienced interventionalist only needed 5 minutes for the same task using RoRo.

Siemens C-arm with flat panel detector.

The rotatable roadmap consisted of 40 projections covering 180deg and was acquired in 5s, using 15.7cc of iodine. Note that the same rotatable roadmap can be used for further navigation without the need for additional iodine.

Conclusion

In this preliminary investigation, RoRo appears to be a simple yet powerful navigation technique that is superior to conventional 2D-Ro. Similar to other 3D-Ro techniques, RoRo allows for visual selection of the best working view, but does not suffer from their respective shortcomings.

Vascular Centerline Restoration using Knowledge Based Interpolation

Tejas Rakshe[1], Dominik Fleischmann[2], Justus Roos[2], Sandy Napel[2] – [1]Departments of Electrical Engineering and [2]Radiology

Introduction

Efficient and accurate interpretation of CT angiograms through the peripheral arteries requires construction of Curved Planar Reformations (CPR), in which, curved vessel paths are flattened for viewing in a plane. This, in turn, requires the tracking of vascular centerlines, but existing density- and gradient-based algorithms cannot track arterial centerlines through occluded vessel segments. We attempted to solve this problem by making use of a database of vascular centerlines.

Materials and Methods

We built a database of 30 centerlines of each of the internal and external iliac and the femoropopliteal arteries on the right side. Common vascular landmarks (e.g., bifurcations) were used to register the datasets with each other. The centerlines were sampled regularly along between two consecutive landmarks. We performed Principle Component Analysis (PCA) on these arteries separately and extracted eigen-curves of the centerlines. We then simulated occlusions of different lengths in new cases by deleting portions of their centerlines at various locations. We project the incomplete curve on some of the most prominent eigen-curves and obtain an estimate of the missing segments. We compared the results of this with the known centerlines.

Discussion

For an occlusion length of 100mm in the femoropopliteal artery, the maximum deviation had a mean of 2.2mm and the average deviation had a mean of 1.2mm. The standard deviations were 1.4mm and 0.8mm respectively. For simulated occlusions of lengths up to 100mm, the method estimated centerlines that generated CPRs of diagnostic quality.

Conclusion

Knowledge based methods can be used for estimating missing segments of centerlines in CTA data. Database building, and application and testing of this technique in diseased vessels are in progress.
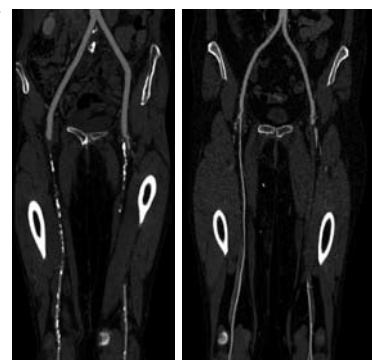
Two examples of manually obtained CPRs through occluded arteries. We propose to automate the process by knowledge-based centerline estimation.

Robust Quantification of Arterial Calcium Independent of Lumen Intensity

Raghav Raman, Bhargav Raman, Sandy Napel, Geoffrey D. Rubin – Department of Radiology

Introduction

We have previously developed and tested a system for automatic detection and localization of calcium fragments. However, quantification of the actual mass of the detected fragments was subject to underestimation due to the threshold used to segment the fragment. The threshold applied reduced the apparent volume and therefore the apparent mass of the fragment. Fragments in the wall of contrast-enhanced arteries were particularly susceptible due to the higher thresholds used to differentiate luminal contrast from the fragment. We have developed a method that corrects for this underestimation and renders mass quantification independent of the level of luminal contrast enhancement and independent of the intensity of the tissues surrounding the fragment being quantified.

Materials and Methods

The mass of each fragment is calculated as follows. First, we define the brightness-volume product (BVP) for a fragment as the average intensity of the voxels in the fragment above a threshold multiplied by the volume of the fragment above a threshold. We then calculate the BVP at thresholds between 130 HU and 390 HU every 10 HU. For fragments within the luminal VOI, contrast material present in the lumen is excluded by adaptively increasing the minimum threshold in this series to one standard deviation above the intensity of the central vessel lumen near the fragment. From the series of BVP measurements thus obtained, a best-fit line is calculated and extrapolated to calculate the theoretical BVP that would be obtained at a threshold of 0 HU (BVP_0, Fig. 1). To calculate the fragment mass from BVP_0, four homogeneous cylindrical standards of known calcium density of 0 mg/ml (water intensity), 50 mg/ml, 100 mg/ml, and 200 mg/ml are inserted under the patient and thus included in the scan field. The densities of the standards expressed in mg/mm^3 are plotted against the intensity in HU of each standard. The gradient G of the best-fit line is used to derive the mass of each fragment from BVP_0 as follows:

$$Mass\ (mg) = G\ (mg/(HU*mm^3)) * BVP_0\ (HU*mm^3)$$

Validation

Three homogeneous standard materials with elemental calcium densities of 0.15, 0.30 and 0.45 mg/mm^3 were created. 24 fragments (0.4-50 mg, mean 15.12 mg) were randomly chipped from these solids and placed on the walls of four "aortic" phantoms composed of low-density polyethylene. The phantoms were filled alternately with water and a dilute iodine solution (1:30 dilution of Omnipaque/Iohexol 300 mg/mL, 200-250 HU). 3 cylindrically shaped standards were then machined from the same materials. A 4th standard was made from epoxy resin that contained no calcium (40 HU). The phantoms and standards were scanned on an GE Medical Systems (Milwaukee, WI) 16-row CT scanner (1.25mm thickness, 0.625mm section spacing, pitch 1.7, 0.5s rotation at 120 kV and 440 mA.) The mass for each fragment in each scan was quantified using the algorithm described above and compared to the actual mass of each fragment.

Results

When our algorithm was used to calculate fragment mass, the R^2, absolute error, and relative error for actual *vs.* measured mass over both
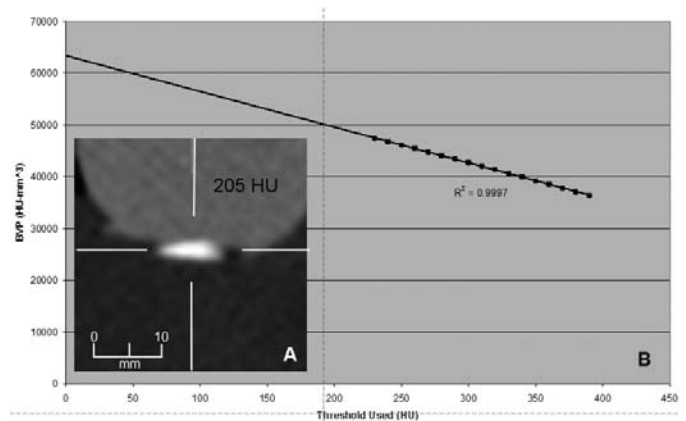
An example 31 mg fragment on the inferior surface of an aortic phantom. The minimum threshold used was one standard deviation higher than the intensity of the contrast material in the lumen. BVP was calculated at several thresholds (black dots), from which a best fit line was calculated and extrapolated back to determine the theoretical BVP of the fragment at a threshold of 0 HU.

unenhanced and contrast-enhanced scans was 0.98, 1.2 ± 1.6 mg, and 9.1 ± 5.9 %, respectively. The R^2, absolute error, and relative error for actual *vs.* measured mass for the unenhanced scan was 0.99, 1.0 ± 1.4 mg, and 9.1 ± 5.1 %, respectively, and the R^2, absolute error, and relative error for actual *vs.* measured mass for contrast-enhanced scans was 0.95, 1.4 ± 1.9 mg, and 9.1 ± 7.0 %, respectively. The difference between contrast-enhanced and unenhanced scans was not significant. Fragments more than 4 mg in mass had an error of 1.7 ± 1.8 mg (8.6 ± 4.5 %) while fragments less than 4mg in mass had an error of 0.21 ± 0.26 mg (9.8 ± 7.8 %). The difference in percentage error between large and small fragments was not significant (p=0.58). The average variability of mass measurements for the same fragments between unenhanced and contrast-enhanced scans was 1.8 ± 2.0 mg (13.0 ± 7.2 %). There was no statistical difference between mass measured using unenhanced and contrast-enhanced scans (p=0.35). Variability for fragments more than 4 mg was 2.3 ± 2.2 mg (11.9 ± 7.1 %) and variability for fragments more than 4 mg was 0.5 ± 0.3 mg (16.1 ± 7.3 %). The difference in percentage variability between large and small fragments was not significant (p=0.28).

Conclusion

The results obtained using our algorithm exhibited excellent correlation between the actual and measured calcium mass. The algorithm can be used in unenhanced and contrast-enhanced (200-250 HU) scans without a significant increase in error. Our method for determining the actual mass of calcium fragments gives accurate and reproducible measurements in phantom scans. These results are preliminary, but our algorithm showed promise for use as a tool to facilitate quantitative studies of the relationship between the quantity and distribution of systemic arterial calcification in a variety of patient subtypes.

An Abdominal Aortic Aneurysm Segmentation Method: Level Set with Region and Statistical Information

Feng Zhuge[1], Geoffrey D. Rubin[2], Shaohua Sun[1], and Sandy Napel[2] – Departments of [1]Electrical Engineering, [2]Radiology

Introduction

We present a fully automatic system for segmenting the human aorta, including the flow channel, thrombus, calcifications, and the outer wall, in CT Angiograms (CTA) of patients with aortic aneurysm.

Materials and Methods

The system estimates a rough "initial surface," and then refines it using a level set segmentation scheme augmented with two external analyzers: The Global Region Analyzer, which incorporates a priori knowledge of the intensity, volume and shape of the aorta and other structures, and the Local Feature Analyzer, which uses voxel location, intensity, and texture features to train and drive a Support Vector Machines classifier. Each Analyzer outputs a value that corresponds to the probability that a given voxel is part of the aorta, which is used during level set iteration to control the evolution of the surface.

Discussion

We tested our system using a database of twenty CTA scans of patients with aortic aneurysms. The mean and worst case number of falsely included and excluded voxels relative to human tracing was 0.049 ± 0.025 (s.d.); worst case=0.10, and 0.047 ± 0.023 (s.d.); worst case=0.10, respectively.

Conclusion

This algorithm shows promise to allow quantitative accurate, precise, and efficient measurement of aortic aneurysm volume and morphology and, thereby, to improve treatment planning and follow-up for patients with aortic aneurysms.
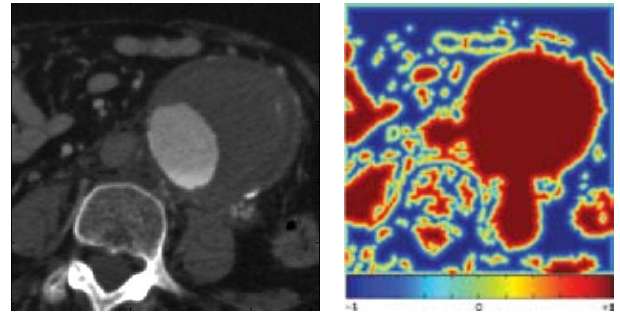
Sample axial cross-section slices. Left: Original CTA image. Right: The speed map generated using both global region and local statistical information, which is used as level set external force.
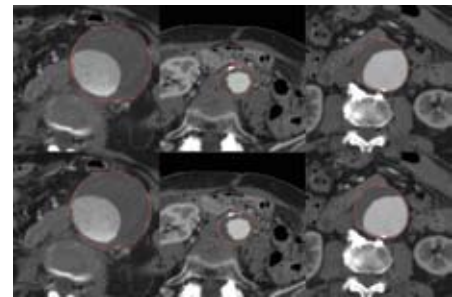
Example slices of the segmentation results. Top row: automatic segmentation results. Bottom row: manual segmentation results.

Flattening of the Abdominal Aortic Vascular Tree for Effective Visualization

Joong Ho Won[1], Geoffrey D. Rubin[2], Bhargav Raman[3] and Sandy Napel[2] – [1]Departments of Electrical Engineering, [2]Radiology, [3]Computer Science

Introduction

Visualization of a 3D vascular structure is difficult because its complex tree-like geometry often causes perceived intersections of vessels when the tree is projected onto a 2D display. The goal of this research is to provide a single, 2D overview of the vascular tree without intersections with minimal user input.

Materials and Methods

A vascular structure is modeled as a geometric binary tree, where each branch consists of a piecewise linear three-dimensional curve that represents the vessel centerline. A first-order approximation of a projected tree is obtained by replacing each branch with a straight line edge connecting its two endpoints. Next, starting at the root, edges are drawn at each depth in turn and their intersections are found. The innermost intersection of each edge, if any, is taken and the edge is shrunk to remove intersections up to the given depth. This results in a layout with no intersections. Next, a force-directed graph drawing algorithm that preserves edge crossings is applied so as to relax the structure towards its original shape while avoiding the introduction of new intersections.

Discussion

We tested the algorithm with abdominal aortic trees obtained using custom software from multidetector CT scans of 6 patients with abdominal vascular disease. For each patient, we chose anterior-posterior and left-to-right views for projection so as to introduce severe false intersections in the renal artery region. The algorithm resolved all false intersections for all cases. For shape conservation, 10 of 12 cases showed less than 0.25 of length distortion, defined as a weighted average of branch length
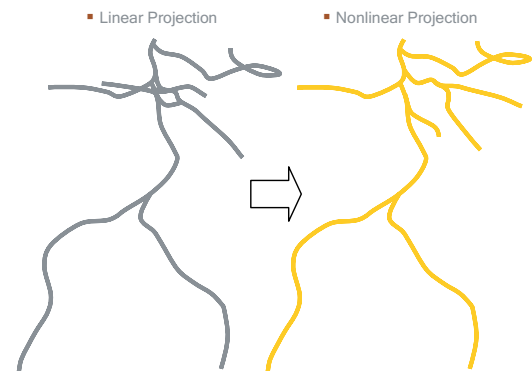
Example of intersection-free nonlinear projection. The goal is to provide a complete 2D overview of the vasculature with minimum distortion in geometry.

change ratios, and less than 0.05 shape distortion, defined as relative change of sample point locations. 2 cases showed moderate (less than 0.40) length distortion primarily due to the aggressive untangling step.

Conclusion

Our algorithm flattens tree-like vascular structures using graph drawing algorithms, conserving overall shape while eliminating misleading intersections, and can be combined with curved planar reformation methods to visualize large portions of the human aortic vascular tree in a single image.

Patient Data Base for Knowledge-based Classification and Visualization of Lower Extremity Arteries

Justus Roos, D. Fleischmann, Tejas Rakshe, GD Rubin, Sandy Napel – Department of Radiology

Introduction

Identification of vascular centerlines is a prerequisite for advanced vessel analysis and visualization, such as the generation of curved planar reformations (CPR). While automated extraction of vascular centerlines has been successful in normal or mildly diseased vessels, standard density- and threshold-based algorithms have failed to extract centerlines through occluded arterial segments and segments with advanced atherosclerotic disease. We hypothesize that this limitation can be overcome by the development of new knowledge-based algorithms, which take the three-dimensional shape information of the peripheral arterial tree into account, and are thus independent of local density and gradient information. One prerequisite for the development of such algorithms is the generation of a knowledge-base. To this end, the purpose of this work is to generate an initial database of vessel trees extracted from existing CT angiographic datasets of the lower extremities.

Materials and Methods

144 consecutive patients (74 women and 80 men, mean age 63 years, age range 16-80 years) who underwent MDCT angiography of the lower extremities between September 2003 and May 2005 were identified in the hospital's electronic records. Cases were reviewed by a vascular radiologist to identify disease categories, notably a subset of subjects with femoro-popliteal arterial occlusions. Vessel trees, including lumen areas as functions of location, were extracted using a semi-automated vessel tracking algorithm (based on a cost-function and using density information) and a separate centering algorithm. Centerlines for severely diseased and occluded segments were added or edited manually by placing control-points in the vessel center (See Figure). Bony landmarks (hip-joint, knee joint, ankle joint) were also registered in each patient for use as size reference.

Results

Out of the 144 patients, 50 patients had normal arterial findings, 60 patients had stenotic diseased vessels, 8 patients had iliac occlusions and 36 patients had crural occlusions. A total of 40 femoropopliteal occlusions were present in 34 patients. In 3 patients, multiple-, and in 7 patients bilateral-femoropopliteal occlusions were present. The femoropopliteal occlusions were distributed in the following anatomic locations: superficial femoral artery (right, n = 7; left, n= 16), popliteal artery (right, n=4, left, n=5) and overlapping superficial femoral and popliteal artery (right, n= 5; left, n=3). The mean length of the occlusions was 10.1cm with a range of 1-35 cm. Based on the TransAtlantic Inter-Society Consensus (TASC – guidelines) for management of peripheral arterial disease, the occlusions could be morphologically stratified in 4 different types: Type A (n=5), type B (n=2), type C (n=23) and type D (n=10).

Conclusion

We have created a database of peripheral arterial trees, extracted from 144 CT angiographic datasets. This database will serve as the source for generating statistical shape descriptions of arterial tree geometry. In addition, we plan to explore any relationships between shape and subject categories, such as normal versus diseased arterial trees, subject age, sex, etc. It is hoped that this knowledge-base will help to interpolate 'missing centerlines' of occluded and severely diseased arteries, or serve as an alternative vessel segmentation tool in the future.
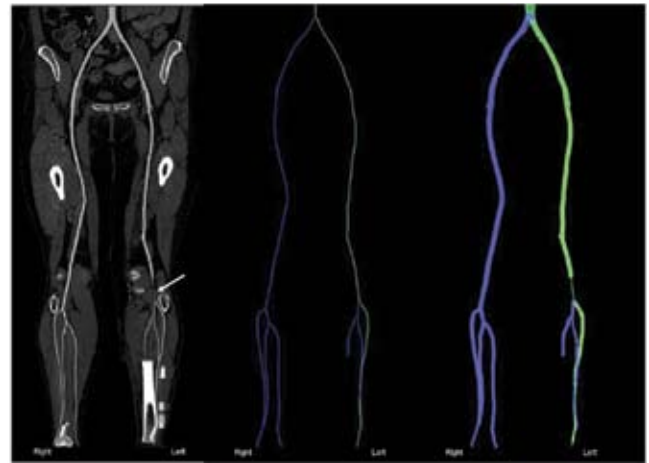
Vessel tree extraction: Multi-path CPR (left image) shows the vessel lumens of the peripheral arteries from the aortic bifurcation down to the three main arteries of each calve. Note a focal occlusion of the left popliteal artery (arrow). The corresponding computed 3D centerlines (middle image) provide an overview of the geometric information of the peripheral arterial tree. Adding the information of the local arterial radius (right image) provides additional characteristics of the artherosclerotic changes in the vessels.

Registration of Lung Nodules over Time in Sequences of CT Scans

SHAOHUA SUN[1], GEOFFREY RUBIN[2], SANDY NAPEL[2] – DEPARTMENTS OF [1]ELECTRICAL ENGINEERING, [2]RADIOLOGY

INTRODUCTION

Lung nodule growth over time is a strong indicator of malignancy. Thus, our purpose was to develop a system to facilitate matching lung nodules detected in serially-acquired CT scans.

MATERIALS AND METHODS

We propose two methods to achieve our goal. First, we propose to maximize a Weighted Correlation Coefficient, using a hybrid optimization framework, under a rigid transformation, that aligns a sphere centered on a source nodule in one scan to another in a second scan. We matched 93 nodules in 12 pairs of sequentially acquired patient scans and compared our results to a radiologist's visual determination. This method may have problems when a nodule undergoes substantial changes in shape and/or size, or even resolves. Therefore, we developed second method, which is more robust to changes in nodule characteristics with time. This method extracts principal structures around the nodule, treats them as independent rigid bodies, allows relative movement among them, and aligns them with their appearances in the second scan. We tested this method with above patient dataset as well as simulation experiments that simulate 10 nodules that resolve, that grow and shrink uniformly by a factor of 2, and that grow non-uniformly over time.

DISCUSSION

For the first method, the mean distance registration error for the 12 pairs patient scans was 1.1 mm ± 0.62 mm (s.d.). For the second method, the results for the patient experiments were 1.2 mm ± 0.8 mm (s.d.). The re-
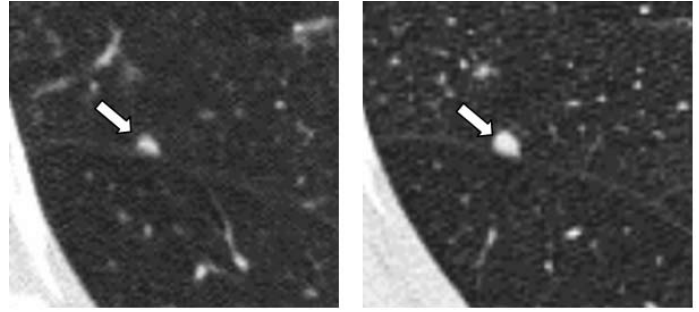
An example of matching a nodule in one scan (left) with its counterpart, which appears to have grown in size in a subsequent scan (right).

sults for the 4 cases of simulation experiments were 1.13mm ± 1.08mm (s.d.), 0.97mm ± 1.09mm (s.d.), 0.72 mm ±0 .73mm (s.d.), and 1.09mm ± 1.36mm (s.d.), respectively. All were registered to within the nodule radius. However, execution time for the second method was about 10 times longer than for the first.

CONCLUSION

Our preliminary results suggest that accurate nodule matching can be achieved to aid qualitative and quantitative evaluation of nodule growth. Continued refinement, speed improvement, and evaluation on a more extensive database are warranted.

Real World Usage Patterns of a Computer Aided Detection Scheme for Lung Nodules in Chest CT

DAVID PAIK[1], EMILY LIU[1], SANDY NAPEL[1], GEOFF RUBIN[1] – [1]DEPARTMENT OF RADIOLOGY

INTRODUCTION

Computer Aided Detection (CAD) algorithms are an important method for reducing the workload of radiologists who are interpreting ever larger volumetric datasets. Detecting small lung nodules in chest CT volumes is particularly tedious and so we have developed a novel CAD algorithm for this task. In this study we examined how radiologists interpret the candidate lesions presented by CAD.

MATERIALS AND METHODS

Three radiologists interpreted the results of the CAD algorithm on 20 chest CT volumes. There were a total of 217 nodules distributed among 19 of the 20 CT volumes. The radiologists first read the CT images without the aid of a CAD algorithm to establish a baseline performance (pink line). Then, they interpreted the CAD output and each response was timed. Their average performance was calculated in 10-second increments (blue dots). For reference, a hypothetically optimum interpretation was computed by assuming they perfectly determined whether each CAD result was a nodule or a false positive (green line).

DISCUSSION

Many studies of CAD algorithms assume that radiologists will make nearly perfect interpretations once directed to a potential lesion (i.e., that finding the lesion in the first place is the only difficult task). However, our study indicates that radiologists initially perform well as the blue dots climb in sensitivity adding few false positives. But then, a "knee" in their performance is found where they begin to accept many false positive CAD findings and ignore the nodules found by CAD.
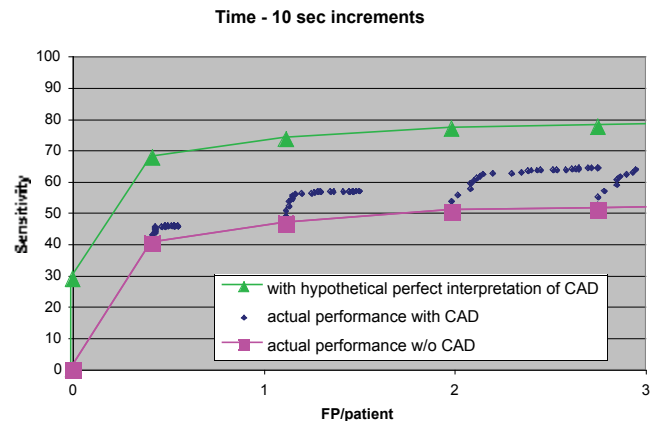
The change in detection performance as radiologists use more time to look at CAD results.

CONCLUSION

This preliminary analysis of the temporal nature of radiologist performance with CAD algorithms has not been done before. It demonstrates an interesting phenomenon that we will further study and hope to address so that radiologists are able to perform closer to their hypothetical optimal performance with CAD.

139

New Directions for Tractography Algorithms for Diffusion Tensor Imaging

Anthony Sherbondy[1], David Akers[2], Robert Dougherty[3], Michal Ben-Shachar[3], Pat Hanrahan[2], Brian Wandell[3], and Sandy Napel[4] – Departments of [1]Electrical Engineering, [2]Computer Science, [3]Psychology, [4]Radiology

INTRODUCTION

Neuroscientists use Magnetic Resonance Diffusion Tensor Imaging (DTI) to attempt to understand connections within the human brain. Due to limited spatial resolution and noise, existing algorithms for extracting these "pathways" from the DTI data may miss smaller connections due, in part, to overwhelming signal from larger, adjacent paths. More robust path tracing (tractography) algorithms may recover these connections.

MATERIALS AND METHODS

The imaging data we used was generated from a DTI scan sequence used to produce images of a 35 year old neurologically normal human male. For a baseline in tractography performance, we chose to use the Streamlines Tracing Technique (STT) first developed by Mori, et al.

DISCUSSION

The green lines in Figure (a) suggest particular neuronal connections that intersect the two red boxes, which were placed to elucidate cross-hemispherical connections between some of the primary visual areas. Figure (b) shows the two red boxes moved slightly to now cover specific visual areas known as the Middle Temporal regions (MTs). The absense of green lines implies there are no connections between them, despite strong evidence from other types of studies to the contrary. We hypothesize that the STT algorithm fails to find the connections between the MTs because the other, higher-density pathways hide this secondary pathway from the tractography algorithm.
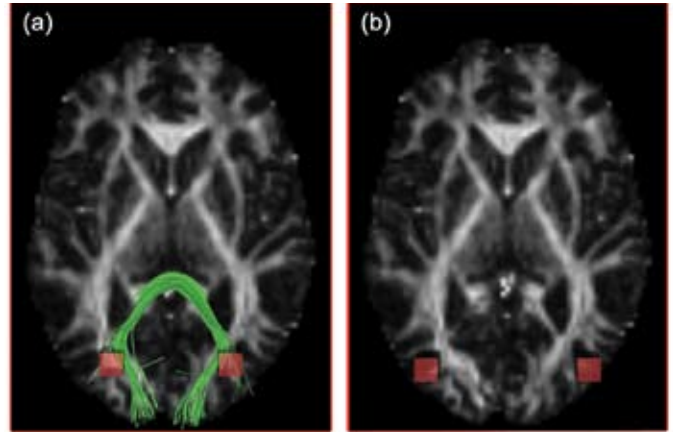
Tractography study suggesting (a) connections between some primary visual areas, and (b) no connections between others.

CONCLUSION

Our research is investigating methods for producing pathway estimates between any specific combinations of target regions for the purpose of finding these highly plausible secondary connections that may be suggested by the DTI data.

Numerical Simulation of Wavefront Propagation along Anatomic Surfaces

David Paik[1], Sandy Napel[1] – [1]Department of Radiology

INTRODUCTION

Simulating wavefront propagation is a very general purpose technique that can be used for biological simulations (e.g., cardiac electrophysiology), robotics (e.g., motion planning and path finding) and computer vision (e.g., image segmentation). Toward this end, so called "Fast Marching" methods are often used to solve the Eikonal equation, which defines the behavior of a moving wavefront. These methods have been studied and used for over 15 years but suffer some problems, especially when the wavefronts are constrained to move along surfaces.

MATERIALS AND METHODS

Kimmel et al. have described a mathematical method for wavefront propagation along triangulated surfaces. This method works well on surfaces where the triangles are all acute, but uses special case handling when the triangles are obtuse. Unfortunately, obtuse triangles are very commonly encountered on surfaces derived from medical imaging via the well-known Marching Cubes algorithm. We have demonstrated significant numerical inaccuracies in these cases on very simple surfaces with obtuse triangles. In order to address this problem, we have improved these Fast Marching methods so that they more accurately simulate wavefronts on *any* type of triangulated surface. Our method is well-grounded in physical principles using Huygen's Principle as a basis for these calculations.

DISCUSSION

The initial analysis of this new algorithm indicate that there are improvements in accuracy for even such a simple case of a single point source traveling across a flat triangulated plane with a small section of sheared and, therefore, obtuse triangles.
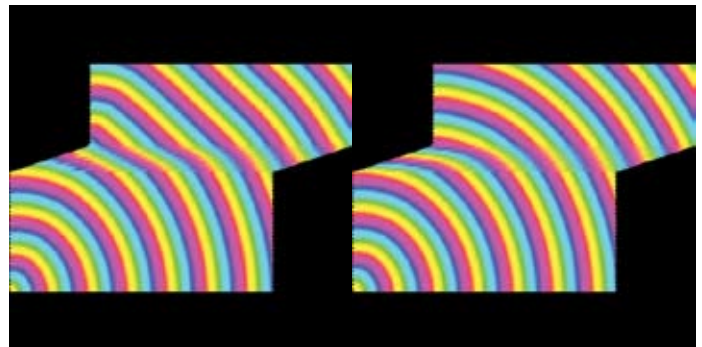
Fast marching methods for propagating a wavefront from a single point source (lower left corner) across a triangulated plane where the triangles in the middle section have been sheared by a factor of 3:1. Note distortions and slowing of the wavefront caused by obtuse triangles with previous algorithm (left) compared to new algorithm (right).

CONCLUSION

This algorithm has the potential to improve upon numerical simulations in a wide variety of situations, particularly in the simulation of wavefronts along complex anatomic surfaces where obtuse triangulations may be encountered regularly.

Estimating the Impact of Screening Mammography And Adjuvant Therapy on US Breast Cancer Mortality from 1975 to 2000

Sylvia K. Plevritis[1], Bronislava M. Sigal[1], Peter Salzman[1,2], Peter Glynn[2] - [1]Department of Radiology, [2]Department of Management, Science and Engineering

INTRODUCTION

In 1975, breast cancer mortality among women aged 30-79 was 48.3 deaths per 100,000 women and 2000 it decreased to 38.0 death per 100,000 women. The contributions of screening mammography and adjuvant therapy to this decline are not known. We have been part of an NCI-sponsored consortium entitled "Cancer Intervention and Surveillance Network," whose goal is to quantify the relative and absolute contributions of screening and adjuvant therapy on breast cancer mortality rates.

METHODS AND MATERIALS

We developed a Monte Carlo simulation model that reproduces the life history of individual women in the United States who were born since the calendar year 1890 and outputs population level statistics from 1975 onward. The simulation tracks the life history of individual women and records the following information for each breast cancer patient with invasive disease: her date of birth, her screening schedule (based on from the National Health Interview Survey), when and how she was detected, her tumor size and stage at detection stage, ER status at detection (based on data from SEER), what treatment she received (based on from the Patterns of Care Registry), and her survival time from diagnosis and her cause of death (based on SEER). While several of the model inputs were developed by the CISNET consortium, a key component of our simulation is a natural history model of breast cancer that we developed and presented in earlier reports.

RESULTS

Figure 1 illustrates our predictions for breast cancer incidence under the following hypothetical scenarios: (1) screening and adjuvant therapy were not offered, (2) adjuvant therapy was offered but not screening, and (3) screening and adjuvant therapy were offered. Under scenario 3, which mimics reality, we demonstrate that simulation closely matches the trends observed in the SEER database. In the absence of screen-
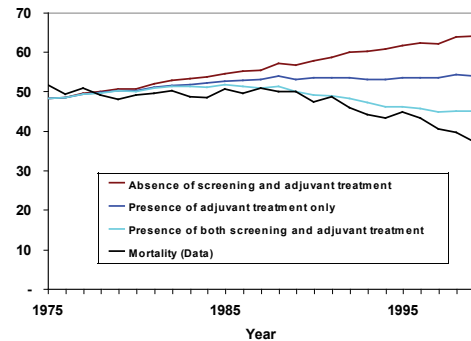

Figure 1. US breast cancer mortality predicted in the absence of screening and adjuvant therapy, the presence of adjuvant therapy alone, and the presence of both screening and adjuvant therapy. These predictions are contrasted against the observed US breast cancer mortality.

ing and treatment, we predict a steady increase in age-adjusted breast cancer mortality due to the secular trend in incidence. Compared to the predicted mortality rate in the absence of screening and adjuvant therapy in the year 2000, the mortality rate in the presence of both screening and adjuvant therapy is reduced by a total of 29.9%, which is decomposed as follows: 16.9% due to screening, 6.9% due to chemotherapy and 8.9% due to adjuvant therapy. The estimated relative contributions of screening and adjuvant therapy to the mortality reduction were similar in magnitude: 53% due to screening versus 47% due to adjuvant therapy.

CONCLUSION

Our model predicts that both screening mammography and adjuvant therapy have been contributing to the decline in US breast cancer mortality and their impact was similar in magnitude.

Predicting the Health Benefit Due to Screening BRCA1/2 Mutation Carriers for Breast Cancer with Magnetic Resonance Imaging

Sylvia Plevritis[1], Allison Kurian[1,2], Bronislava Sigal[1] – [1]Department of Radiology, [2]Division of Oncology

INTRODUCTION

Women with inherited mutations in the BRCA1 or BRCA2 genes have a lifetime breast cancer risk in the 45-65% range; recent publications estimate greater than 250,000 female BRCA1/2 mutation carriers in the United States. Although multiple studies have reported earlier cancer detection in high-risk women when screening magnetic resonance imaging (MRI) is added to mammography, no resulting survival benefit has been demonstrated. Moreover, the high false-positive biopsy rate and increased costs of MRI screening may have adverse psychological and economic consequences. We performed a model-based analysis of screening breast MRI as an adjunct to annual mammography in BRCA/12 mutation carriers, in order to estimate associated survival benefit.

METHOD

A Monte Carlo computer simulation model was used to reproduce the life histories of individual women with BRCA1/2 mutations. Women were assumed to undergo annual screening mammography from ages 25-70, with or without the addition of screening breast MRI. Screening by either mammography or MRI was assumed to increase the probability that a woman's breast cancer would be detected at a less advanced stage and age. The model was based on breast cancer survival curves in the absence of screening from the United States Surveillance, Epidemiology and End Results (SEER) database, and incorporated characteristics of screening techniques, cancer risk and tumor characteristics associated with BRCA1 and BRCA2 mutations derived from published literature. Breast cancer survival was estimated according to tumor characteristics

and patient age at detection, and incorporated the effects of primary and adjuvant therapy.

RESULTS

Adding MRI to mammography increased screening sensitivity from 35% to 84% for BRCA1 mutation carriers and from 55% to 88% for BRCA2 mutation carriers, the proportion of local stage disease from 57% to 81% for BRCA1 carriers and 66% to 82% for BRCA2 carriers, and the average leadtime by almost 1.5 years. With MRI screening, life expectancy (LE) increased from 71.9 to 73.3 years for BRCA1, and from 78.8 to 79.6 years for BRCA2, mutation carriers. Annual screening mammography provided a 14% and 16% breast cancer mortality reduction for BRCA1 and BRCA 2 mutation carriers, respectively; adding MRI increased each reduction to 38%.

CONCLUSION

Adding annual screening breast MRI to mammography is estimated to reduce breast cancer mortality in women with inherited mutations in BRCA1/2. Given the low likelihood that any randomized trial will assess the contribution of MRI screening to breast cancer survival in high-risk women, these results may help to guide clinical practice and health policy. An analysis of the cost-effectiveness of breast MRI screening in BRCA1/2 mutation carriers is ongoing. Future research will include evaluation of the quality of life associated with breast MRI screening in high-risk women and its impact on cost-effectiveness, and analysis of screening MRI's benefit to women at various levels of increased breast cancer risk.

Simulating Chest X-Ray Screening Under the Mayo Lung Project

YenLin Chia[1,2], Bronislava Sigal[1], Sylvia Plevritis[1] – [1]Department of Radiology, [2]Department of Management Science and Engineering

Introduction

Lung cancer is the leading cause of cancer death for both men and women in the United States. Screening for lung cancer, particularly among the high risk population of current and former smokers, promises to yield substantial health benefits by detecting lung cancer at an earlier stage and hence a better prognosis. However, several randomized controlled trials conducted in the 1960's and 1970's of chest radiography as a screening test did not demonstrate a reduction in lung cancer mortality, even though they did demonstrate increased rates of earlier stage, resectable disease and increased 5-year survival. One such trial was the Mayo Lung Project (MLP), which randomized 9211 men, composed of heavy-smokers and former heavy smokers, into an intervention arm and acontrol arm. The intervention arm was offered screening by chest X-Ray and sputum cytology every four months for six years, while the control arm only received a prevalence screen. To this day, advocates of chest-radiology as a lung cancer screening test, claim that the MLP and the other trials were flawed. With respect to the MLP, they argue that the trial was poorly designed and should not have allowed any screening in the control group, and that the trial was poorly executed due to the amount of contamination from screening studies outside of the trial in both the intervention and control arms. Our goal is to simulate the MLP under ideal conditions of no screening in the control group and no outside contamination, in order to determine whether the predicted lung cancer mortality reduction would have been significantly impacted.

Methods

We modeled the intervention and control arms of the MLP via Monte Carlo simulation, in which we reproduce the life history of individual men, from the birth cohorts of the MLP, undergoing various screening strategies, including no screening. The model has six underlying components: (1) incidence of lung cancer among heavy smokers, (2) compliance probability to the screening schedule of the MLP, (3) the natural history of lung cancer for different histologies, (4) the tumor detection characteristics of chest radiography, (5) post-detection survival from lung cancer, and (6) other cause mortality among heavy smokers. The natural history model of lung cancer assume that the tumor grows exponential in its preclinical but screen detectable phase, and use mean doubling times reported for the four main histologies: 88 days for squamous carcinoma, 161 days for adenocarcinoma, 86 days for large cell carcinoma, and 29 days for small cell carcinoma.

Results

The simulation model closely reproduce tshe incidence by trial arm as demonstrated in Table 1. It also closely reproduced the stage distributions observed in the trial, as well as the survival curves. At the end of 7 years of follow-up, the MLP showed an 8% increase in incidence of the intervention arm as compared to the control arm, while the simulation produced a 9% increase in incidence. However, the lung cancer mortality in MLP increased by 4% while the simulation model predicted a 4% lung cancer mortality reduction. We predict if the intervention arm were compared to a hypothetical unscreened control arm, there would be a 25% increase in incidence and significant improvement in 5-year survival due to screening, but only a 5% lung cancer mortality reduction.

Conclusion

We predict that had the Mayo Lung Project been conducted under optimal conditions, there would have been a lung cancer mortality reduction due to screening. However, the mortality reduction would have been 5% after 7 years of follow-up, and would likely not have been detected with the sample size of the trial. It is possible that if the MLP were conducted today, the mortality reduction could be larger since the detection characteristics of chest radiography have improved over the past 30 years.

Mode of detection	Intervention Arm Data	Model	Control Arm Data	Model
Prevalence Screen	1.21 [0.85, 1.67]	0.96	1.27 [0.91, 1.74]	0.96
Repeat Screen	2.42 [1.89, 3.05]	2.90	-	-
External Screening	0.74 [0.46, 1.12]	0.86	1.13 [0.78, 1.58]	1.21
Symptoms	1.31 [0.93, 1.79]	1.12	2.87 [2.29, 3.54]	3.00
Total	5.68 [5.10, 6.89]	5.84	5.27 [4.75, 6.48]	5.16

Table 1. Comparison of lung cancer incidence rate per 1000 person-years between the Mayo Lung Project and the simulation model, at 7 years since randomization.

Comprehensive Breast Screening in Women at High Inherited Risk

Allison Kurian[1,2], Anne-Renee Hartmann [5], Bruce Daniel[1], Mills Meredith[2], Kent Nowels[3], Margo Jaffee[2], Nicole Chun [2], Kerry Kingham [2], Frederick Dirbas, Robert Herfens[1], Judy Garber [5], James Ford [2+], Sylvia Plevritis[1+] – [1]Department of Radiology, [2]Division of Oncology, [3] Department of Pathology, [4]Department of Surgery, [5] Dana Farber Cancer Institute, [+]Co-Principal Investigators

Introduction

About 9,000-18,000 breast cancer cases yearly in the United States (U.S.) are attributable to high inherited risk; greater than 500,000 people in the U.S. carry such risk. Screening mammography often performs poorly in high-risk women, and the only proven method of breast cancer prevention is prophylactic mastectomy. There is an urgent need for more effective and tolerable methods of breast cancer screening and prevention in this population; moreover, techniques found to be effective in high-risk women may benefit those at lower risk. The purpose of this research is to evaluate the combination of two emerging breast cancer screening techniques, breast magnetic resonance imaging (MRI) and ductal lavage (DL), for early detection of breast cancer in high-risk women

Methods

122 women with high inherited breast cancer risk, either because of an inherited mutation in the cancer susceptibility genes BRCA1/2, p53, or CDH1, or because of a strong family history, were enrolled in a protocol of yearly breast MRI, mammogram, and DL, with clinical breast examination (CBE) semi-annually. Women were advised to perform breast self-examination monthly. Follow-up MRI or mammograms were performed at 6 months if abnormal results were found on prior imaging or DL. A questionnaire was administered to assess patient tolerance of this protocol.

Results

118 women have undergone at least one round of screening, resulting in 35 breast biopsies in 28 women. Five malignant lesions have been found: 3 cases of high-grade ductal carcinoma in situ (DCIS) found by MRI only, and 2 invasive breast cancers, one by mammogram only and one by CBE only. There was a trend toward a lower positive predictive value of MRI in women who underwent treatment likely to reduce breast cancer risk (0% vs. 30%, p=0.07). DL was attempted in 79 women, and succeeded in 64 (81% [71.0-88.3%]). Atypical cells were found in 18 women (28.1% [18.9-40.3%]), and were more common from ducts which did not produce fluid (72.2% vs. 27.8%, p=0.02). In one woman, atypical cells on DL prompted a follow-up MRI and subsequent breast biopsy, yielding high-grade DCIS. This protocol was well tolerated, with 85.3% (p=0.017) willing to continue after at least one round of screening.

Conclusion

Breast MRI screening can find early malignant lesions, including DCIS, in high-risk women; however, it has a high false-positive rate, especially in women whose risk has been somewhat reduced. Longer follow-up is necessary to determine the clinical significance of atypical cells on DL. Future study will include 1) optimization of MRI screening guidelines, incorporating patient preferences, through computer modeling and 2) exploration of breast duct cell analysis for studies of risk assessment and chemoprevention.

Breast Cancer Risk Management Choices by Women with Inherited Breast Cancer Predisposition: A Preliminary Analysis

Allison Kurian[1,2], Anne-Renee Hartmann [3], Meredith Mills [2], Nicole Chun [2], Judy Garber [3], James Ford[2], Sylvia Plevritis [1] – [1]Department of Radiology, [2]Division of Oncology, [3] Dana Farber Cancer Institute

Introduction

More than 250,000 women in the United States are estimated to have a high inherited risk of breast cancer. Genetic counseling and testing permits identification of such women, and options for management of their breast cancer risk include prophylactic mastectomy (PM) or intensive screening, incorporating mammography and breast magnetic resonance imaging (MRI). Factors predicting women's choices for breast cancer risk management have not been fully characterized.

Methods

Women at high risk for breast cancer, either because of a documented mutation in BRCA1/2 or another cancer susceptibility gene, or because of a greater than 10% predicted chance of BRCA mutation carriage based on clinical and familial characteristics, were evaluated in cancer genetics clinics and educated about options for breast cancer risk management, including PM or screening with annual mammography plus breast MRI. After genetic counseling and testing, they were mailed an 11-item questionnaire about their intended management of their breast cancer risk, and the Revised Impact of Event Scale (RIES), a validated measure of breast-cancer related anxiety. Statistical analysis used Fisher's exact test, 2-sided for categorical variables and t-test or Wilcoxon Rank Sum test for continuous variables.

Results

55 women were sent a questionnaire, and 36 have responded to date, yielding a response rate of 65.5%. The median age of responders was 40.5 years; 50% were mutation carriers and 50% at high risk due to family history. Thirteen (36.1% [22.5-52.6%]) women declared a low, 16 (44.4% [29.6-60.5%]) a moderate, and 7 (19.4% [9.5-35.5%]) a high likelihood of choosing PM. There was a non-significant trend toward increase in median RIES score from low (18) to moderate (21) to high (25) PM likelihood groups (p=0.56). Compared to moderate and low PM likelihood groups combined, the high likelihood group had a greater proportion of patients with prior personal cancer history (100% vs. 44.8%, p=0.01). Low PM likelihood patients had a significantly lower proportion of mutation carriers (23.1% vs. 65.2%, p=0.04) and a non-significantly higher median age (46 vs. 38 years, p=0.17) than high and moderate likelihood groups combined.

Conclusion

In a clinic-based sample of women at high inherited breast cancer risk, personal cancer history, BRCA or other high-risk mutation carriage, and higher breast cancer-related anxiety as measured by RIES score, showed a trend toward greater frequency among women likely to choose PM versus intensive screening including breast MRI. Evaluation of a larger number of high-risk women is ongoing, and updated data will be presented. Future study will include follow-up questionnaire administration after women have chosen either PM or breast screening, permitting identification of patient characteristics which predict risk management choices.

Identification of Genomic Profiles Associated with High Vascular Permeability in Human Glioblastoma Multiforme Through MRI-Guided Sampling

Yi-Shan Yang[1], Yingyung Wang[1], Mike Lim[2], Griff Harsh[2], Scott Atlas[1], Mark Bednarski[1], Samira Guccione[1] – [1]Department of Radiology, Stanford University; [2]Department of Neurosurgery

Introduction

Glioblastoma multiforme (GBM) is a primary brain tumor with poor prognosis and low survival rate. Similar to other types of solid tumors, GBM is heterogeneous in morphology with high angiogenesis activity. Thus tissue sampling for further analysis from these tumors are difficult yet critical. Contrast-enhanced MRI (CE-MRI) using Gd(DTPA) has been demonstrated to be a powerful technique to identify regions with increased vascular permeability and vessel density. In this study we proposed that CE-MRI can be used to guide tissue sampling for genomic analysis. A series of genes with high expression level on the regions having high vascular activity, such as integrin or growth factor family, have been identified and can be used for development of therapeutic agents.

Materials and Methods

Patients diagnosed with GBM, without any prior surgical, chemotherapy or radiotherapy procedures were scanned on a GE 1.5T MRI scanner using standard T1- and T2-weighted pulse sequences and Magnevist (Gd(DTPA), Berlex Inc., NJ) as contrast agent. Samples from regions that have contrast agent accumulation (contrast-enhancing, CE) and regions that do not take up contrast agent (non-enhancing, NE) were collected for gene expression profiling using oligonucleotide microarray (Figure 1). Genomic data was analyzed using a probe-level normalization packge, Bioconductor, to minimize variability, followed by a modified t-test via Significance Analysis of Microarray (SAM) for identifying significant expression levels.
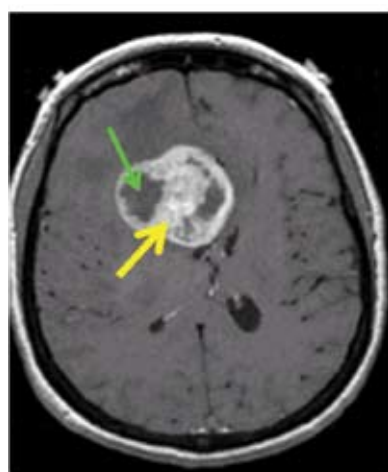

Figure 1. T-1 weighted CE-MRI of representative patient with GBM. The thick (yellow) and thin (green) arrows indicate the contrast-enhanced (CE) and non-enhanced (NE) regions, respectively.

Results

Tissue samples from the CE and NE regions of 13 patients reveal significantly distinct gene expression patterns. Genes with high expression level in the CE region that are associated with angiogenesis and growth factor family are selectively shown in Figures 2A and B. These results show that integrin α_{IIb}, α_v and β_5, laminin receptor, insulin growth factor binding protein 3 (IGFBP-3), IGFBP-5, all up-regulated in the CE regions as compared to the NE region. Immunohistochemical staining confirmed correlation of protein expression patterns with the observed genomic profile.
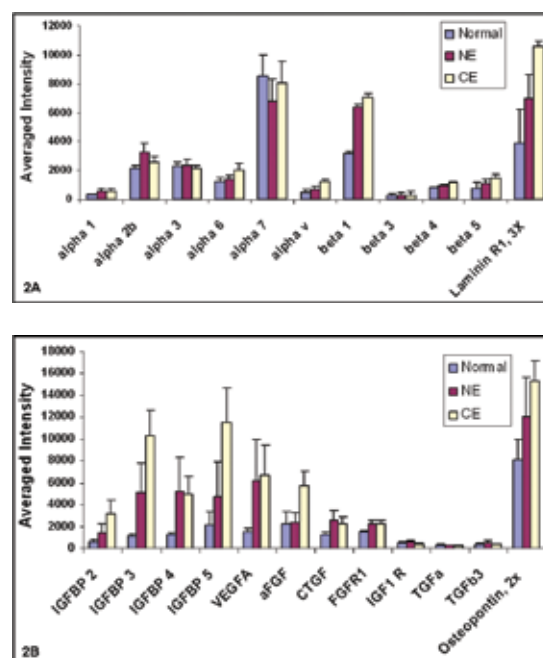
Figure 2. Average gene expression level for the contrast-enhanced (CE) and non-enhanced (NE) regions of the GBM patients (n=13) and for the normal brain (n=5) on genes from (A) integrin and (B) growth factor families.
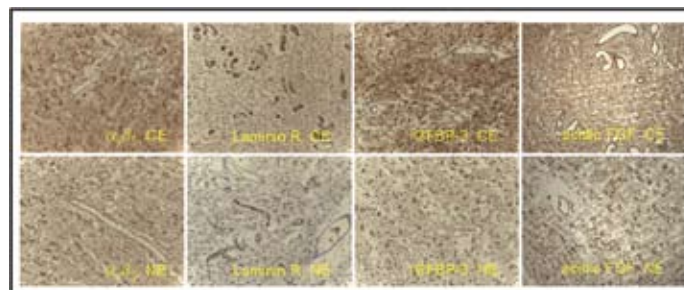
Figure 3. Immunohistochemical staining of the contrast-enhanced (CE) and non-enhanced (NE) regions of the GBM patients on selected proteins that have a higher expression level in the CE region from the microarray analysis.

Conclusion

We have found that CE-MRI can serve as a powerful tool for characterizing different regions of heterogeneous solid tumors for microarray analysis. CE-MRI using the clinical MRI agent Gd(DTPA) can reveal imaging features associated with increased vascular permeability and vessel density, and areas of fluid accumulation and necrosis. We have observed that differences in spatial resolution in the tumor correlate to changes in gene expression profiles. We conclude CE-MRI guided sampling and microarray analysis can be used to evaluate targets in permeable regions of the tumor. These targets can be further screened to identify serum profiles for diagnostic and clinical monitoring of the patient before and after therapeutic intervention.

MRI-Guided Genomic Analysis: Temporal Changes in Genomic Expression Pattern in Contrast-Enhancing and Non-Enhancing Regions of Squamous Cell Carcinomas

Yi-Shan Yang[1], Yen Lin Chia[2], Sylvia Plevritis[1], Samira Guccione[1] – [1]Department of Radiology, [2]Department of Statistics

Introduction

Gene expression profiles in tumors can vary with temporal progression and spatial distribution. In this study, contrast-enhanced Magnetic Resonance Imaging (MRI) was used to non-invasively characterize solid tumors, to delineate the spatial heterogeneity and temporal changes of tumor progression, and to guide tissue sampling for genomic analysis. Genes identified to have differential expression level among different stages of tumor progression can be potential targets for diagnostics and therapeutics.

Materials and Methods

C3H/K mice bearing squamous cell carcinoma VII (SCC VII) were imaged with GE clinical 1.5T MR using spin-echo (T1-weighted) and fast spin echo (T2-weighted) pulse sequence. Images were obtained pre- and post-contrast agent (Gd(DTPA)) administration starting 1-2 weeks after tumor implantation. Tumors show differential uptake of contrast agent and distinct imaging patterns in both T1 and T2-wt images spatially and temporally (Figure 1), and three different stages were defined based on changes in the T1- and T2-weighted MRI features. Rim and center regions from Stage 1 tumors, and regions associated with contrast enhancing and non-enhancing from Stage 2 and 3 tumors were collected for H&E staining and genomic study.

Results

Two sets of comparison for (1) rim/CE and (2) center/NE regions across the 3 stages were conducted to obtain genes with statistically significant changes (Figure 2). Table 1 presents genes from comparisons for rim/CE and center/NE regions with differential expression level (fold change, FC) among the three stages to be larger than approximately 2. These genes fall into 6 different function catagories. Total of 5 genes have significant changes on both comparisons.

Conclusion

Genes that have significant fold change in both comparisons are listed in Table 1. For SWI/SNF that acts as tumor suppressor, the expression level is the lowest in the CE area of Stage 2 where growth activity is the highest, and in the NE area of Stage 3 where tumor is no more viable. For genes related to cell proliferation (KDEL and DDR2), the expression level reaches the highest in the CE area of Stage 2, and the lowest in the NE area of Stage 3. With CE-MRI, we have observed that differences in spatial and temporal resolution in the tumor correlate to changes in gene expression profiles. This methodology can be used to identify potential targets playing different roles in tumor development. These targets can be further validated and developed for diagnosis and therapy.
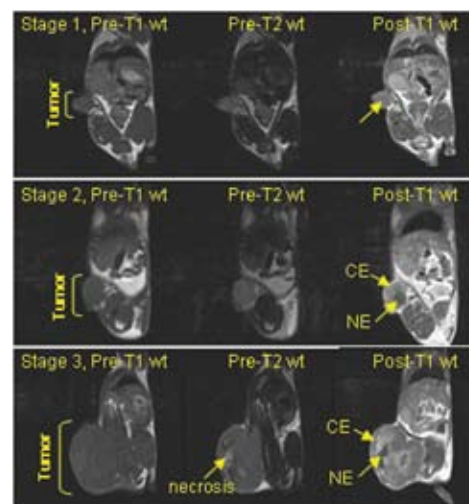

Figure 1. MR images for tumor mice. Three stages were defined based on their contrast enhancement patterns. Post-contrast T1-wt image is homogenous for Stage 1, and heterogeneous for Stage 2 and 3. Stage 3 also show heterogeneity in the T2-wt image.
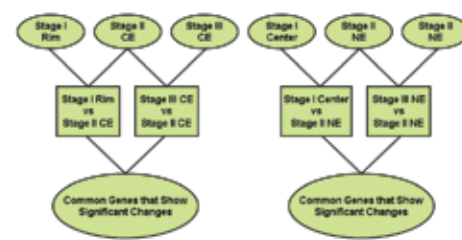
Figure 2. Strategy for microarray analysis. Mouse tumor samples were grouped to different stages based on their T1- and T2-weighted MR imaging characteristics. The oval modules in the top represent microarray data from different regions of the tumor. The rectangular modules represent the comparison studies between two stages using Significant Analysis for Microarray.

CE/Rim comparison			NE/Center comparison		
	Fold Change	Fold Change		Fold Change	Fold Change
Gene Title	Stage 1 vs 2	Stage 3 vs 2	Gene Title	Stage 1 vs 2	Stage 3 vs 2
Translation/Transcription Factors			**Translation/Transcription Factors**		
SWI/SNF complex 1	3.2	2.0	SWI/SNF complex 1	1.9	0.8
Ion Transport			**Ion Transport**		
Cu++ transporting ATPase alpha	2.9	2.0	Cu++ transporting ATPase alpha 7	2.2	2.0
Metabolism: biosynthesis/proteolysis			**Metabolism: biosynthesis/proteolysis**		
NMDA receptor-regulated gene 1	3.3	2.2	NMDA receptor-regulated gene 1	4.7	0.6
KDEL endoplasmic reticulum protein retention receptor 2	0.2	0.5	KDEL endoplasmic reticulum protein retention receptor 2	11.3	0.5
Signal Transduction			**Signal Transduction**		
DDR2 discoidin domain receptor 2	0.4	0.7	DDR2 discoidin domain receptor 2	2.4	0.6

Table 1. Summary of genes with significant expression difference for CE/Rim (left) and NE/Center (right) comparison. In both comparisons, normalized PM values of each gene in each stages were used to calculate the fold change (FC), and Stage 2 was used as baseline.

Vasculature Development of Human Cancer Cell Lines in Xenograph Mouse Model: A Comparison to Syngeneic Mouse Model

Yi-Shan Yang, Samira Guccione – Department of Radiology

Introduction

Research in tumor angiogenesis often relies on tumor bearing animal models. In order to understand the angiogeneic behavior, and the contribution of the microenvironment to tumor progression, we have designed a study to monitor tumor growth based on their MR imaging patterns in both xenograph and sygeneic mouse models. The purpose of this study is to (1) characterize the tumor growth and vasculature development of human cancer cell lines on xenograph mouse model, and mouse cancer cell line on sygeneic mouse model using contrast-enhanced magnetic resonance imaging (CE-MRI); and (2) to validate the hypothesis that the host environment can significantly alter the vascularization of human cancer cells grown in mouse model.

Materials and Methods

Mice were implanted subcutaneously in the rear flank with ~10^6 human glioblastoma U87 cells, a highly vascularized tumor type, as the xenograph model, or with ~10^6 murine glioma GL261 cells, or with ~2×10^5 murine squamous cell carcinoma VII cells as the sygeneic model. Animals were imaged at 1.5T MRI starting when the tumors reached a diameter of about 5 mm. T1 (spin-echo) and T2 (fast spin-echo) weighted images were acquired pre- and post- contrast agent (Gd(DTPA), gadopentetate dimeglumine) administration. Image acquisition stopped when significant mass of central necrosis was observed from the MR images. T1- and T2-wt MR contrast-enhancing (CE) and non-enhancing (NE) imaging features were used to characterize tumors to differential temporal stages. Histological staining was used to characterize the pathological features of these tumors.

Results

Xenograph model: Human tumors grown on 4 different strains of nude mice reached 5 mm in diameter about 4 weeks after tumor implantation. Post-contrast T1- and T2-wt MR images were completely homogeneous throughout the tumors (Stage 1). Tumors then progressed to Stage 2, in which post-contrast T1-wt MR images showed a rim-enhancement pattern while T2-weighted images remained homogeneous. These features correspond to an increasing activity of vascularization on the periphery of viable tumors. Each of these two viable stages lasted for a few days only. By week 5, the T2-weighted images showed elevated signal intensity in the area where it was not enhanced in the post-contrast T1-weighted im-

Figure 1. MR images for (A) xenograph and (B) syngeneic tumor mice. Three stages were defined based on their contrast enhancement patterns. Post-contrast T1-wt image is homogenous for Stage 1, and heterogeneous for Stage 2 and 3. Stage 3 also show heterogeneity in the T2-wt image.
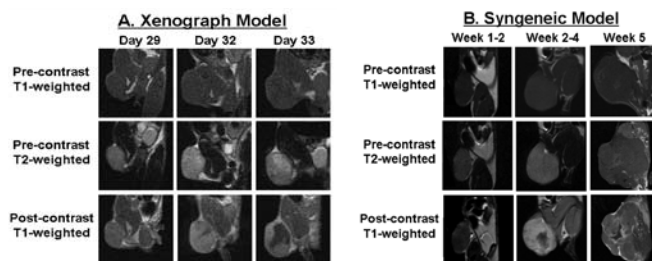
ages (Stage 3). These features correlate with the development of the necrosis. The results were confirmed by histological staining.

Sygeneic model: Murine tumors grown on C3K mice reached Stage 1 with MR imaging patterns as described above about 1-2 weeks after tumor implantation. Stage 2 imaging patterns were observed at about 2-4 weeks, and Stage 3 at about 4-5 weeks of tumor implantation.

Three differential observations were identified between the xenograph and syngeneic models: (1) Initial rate of tumor growth is much delayed in xenograph model; (2) The absolute MR intensity in the homogeneous post-contrast T1 image associated with Stage 1 is brighter in the xenograph model; (3) Stage 2 tumor progression in xenograph model was extremely short. The results were also confirmed by histological staining.

Conclusion

Human cancer cell lines grown as xenograph mouse models require recruitment of mouse vasculature and construction of appropriate microenvironment for the tumor to progress. This is likely to result in the slow initial growth of the tumor. In addition, due to the nature of vascularity of these tumors, as reflected by contrast-enhancing MRI and histologic features, tumor progression may be altered compared to those in sygeneic models, giving a very rapid transition to Stage 3 where significant central necrosis persists.

Diagnostic and Prognostic Serum Markers for Glioblastoma Multiforme

Yingyun Wang[1], Yi-Shan Yang[1], Michael Lim[2], Griffith Harsh[2], Samira Guccione[1] – [1]Department of Radiology, [2]Department of Neurosurgery.

Introduction

Glioblastoma Multiforme (GBM) is a high grade brain tumor, with poor prognosis and a median survival of 14 months. The purpose of this study is to find diagnostic and prognostic serum markers for this disease.

Materials and Methods

Tumor samples within the same patient were obtained from contrast-enhanced (CE) and non-enhanced (NE) regions as identified by contrast-enhanced MR imaging. Genomic microarray studies were completed on the two different regions of the patient's tumor samples by first extracting RNA from these tumor samples. Patients' blood samples were collected at time of surgery. These blood samples are then processed and the serums were analyzed using Enzyme-Linked Immunosorbent Assay (ELISA). Normal volunteers' blood samples were also collected for comparison.

Discussion

Since the blood-brain barrier is broken in the CE regions of this tumor, we hypothesized that some of the gene products maybe upregulated in the serum. Using ELISA, we evaluated the following protein concentrations in the patient serum samples: Insulin-like Growth Factor Binding Protein
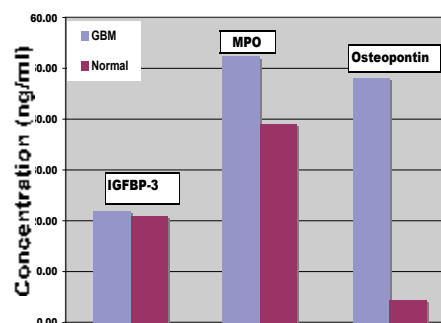
(IGFBP)-2, IGFBP-3, acidic fibroblast growth factor (aFGF), myeloperoxidase (MPO), andosteopontin among others. Most of these markers were elevated in GBM patients as compared to normal adult serum.

Conclusion

This study is ongoing. We aim for these ELISA results to help us to diagnose GBM and also determine the patients' outcome after surgical removal of tumor.

146

Effects of Targeted Nanoparticle-Based Antiangiogenic Therapy on Brain Tumor Metabolism and Progression - MicroPET and MRI Study on a Rat Glioblastoma Model

Yi-Shan Yang, Leroy Sims, Steven Choi, Yingyun Wang, Samira Guccione – Department of Radiology

Introduction

Glioblastoma is a primary brain tumor with poor prognosis and low survival rate. The purpose of this study is to monitor metabolic changes during tumor progression with or without anti-angiogenic treatment in a rat glioma model. This novel nanoparticle (NP)-based anti-angiogenic approach is a non-viral gene delivery system using $\alpha_v\beta_3$ to target tumor vasculature. A mutated raf gene is delivered to cause apoptosis in tumor endothelium. PET imaging with radio-tracer ^{18}F-FDG has been widely used in clinical practice to monitor glucose metabolism; while T2-weighted MRI provide high quality brain tumor anatomy. Combination of these two imaging modalities on the time course along tumor growth allows one to monitor the effect of our therapeutic NP on tumor progression.

Materials and Methods

Fisher rats were divided into 3 groups. Treated (Group 1, n=5) and control groups (Groups 2, n=5) received RT2 tumor cells implanted intracranially into the striatum. Normal group (Group 3, n=3) received no tumor cells or treatment. Group 1 received an $\alpha_v\beta_3$ targeted NP that carried a mutated Raf gene (NP-ATP$^\mu$-Raf) complex. This gene disrupts the VEGF and FGF mediated signaling pathway. Group 2 received saline. Three treatments with targeted NP (Group 1) or saline (Group 2) were conducted starting day 6 after tumor implantation. Animals in both groups were imaged with ^{18}F-FDG PET to monitor glucose uptake, and with T2-weighted MR sequences to record tumor on the days they received treatments and two time points after the treatments were finished. Animals in the control and normal groups were imaged on microPET and MR on the same dates when the treated animals were imaged.

Results

Figure 1 and Table 1 summarize the results of the PET study. Treated animals showed an increased FDG uptake in brain early in the treatment period. A constant decrease of PET signal in the tumor area was observed starting day 10 after tumor implantation and lasted until the end of the study. Control animals had a high FDG uptake over the course of the study. All the control animals died between 15 to 27 days post tumor implantation. Figure 2 summarizes the results of the MR imaging. Both the treatment group and the control group demonstrated tumors in the beginning of the treatment. Tumors in the treated group showed reduction in tumor size after the treatment period. The tumor in the controls continued to increase in size and signal intensity. Animals with no tumor had normal PET and MRI images (data not shown).

Conclusion

MR images showed that the NP slowed tumor progression with subsequent encephalomalacia, while PET images showed that this agent caused an initial increase then a significant decrease in metabolic activity in brain tumors. We hypothesize that two factors may be involved in the increasing PET signal in the beginning of the treatment: (1) vessel normalization prior to vascular apoptosis and (2) hypoxia and subsequent vessel apoptosis caused by the destruction in vasculature caused by NP therapy. Signal drop on both PET and MR toward to the end of study indicates destruction of the tumor mass. We conclude that MRI and PET imaging combined can be powerful to monitor tumor progression and to follow therapy.

Figure 1. Representative serial T-2 weighted MR (top) and ^{18}F-FDG microPET images (bottom) of Group 1 (treated) animals from day 6 to day 24 after tumor implantation. Treatments were conducted using $\alpha_v\beta_3$-targeted nanoparticle at days 6, 8, and 10. Brightness on the rim of the tumor shown on Day14 MR indicates the development of necrosis associated with a signal decrease in the corresponding PET images. Dark area in the center of the tumor on Days 20 and 24 MR images represent tumor shrinkage, observed also in the corresponding PET images.
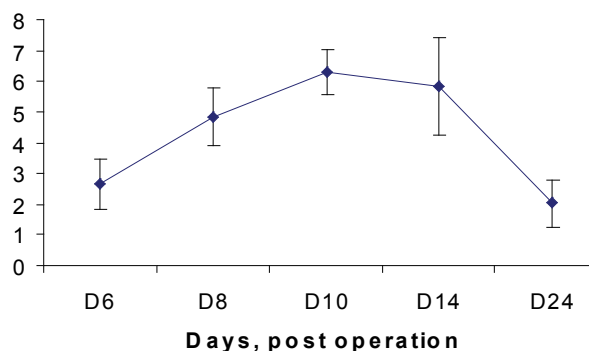
Table 1. Standard Uptake Value (SUV) of 18F-FDG in rat brain tumor with treatment of $\alpha_v\beta_3$ targeted nanoparticles (Group 1). SUV increases up to day 10 followed by a continuous decrease till the end of the study.
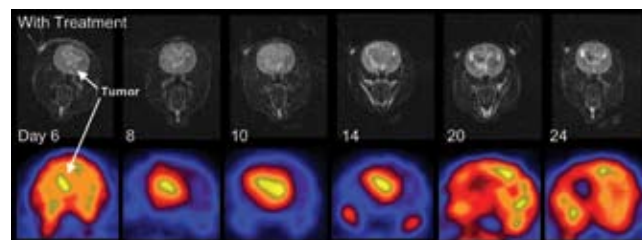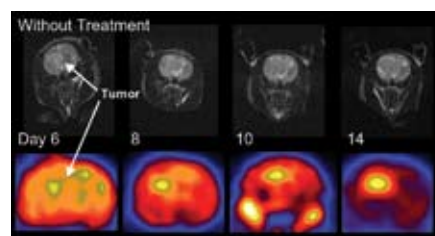

Figure 2. Representative serial T-2 weighted MR (top) and ^{18}F-FDG microPET images (bottom) of Group 2 (untreated) animals from day 6 to day 14 after tumor implantation. Signal intensity and tumor volumes remain increasing till the end of time course when the animal died.

Antiangiogenic Dual Modality Nanoparticle Platform for Imaging and Therapy

Steven Choi[1], Mike Lim[2], LeRoy Sims[1], Yingyun Wang[1], Griff Harsh[2], Samira Guccione[1],- [1]Department of Radiology, [2]Department of Neurosurgery

Introduction

Glioblastoma is a primary brain tumor with poor prognosis and low survival rate. The purpose of this study is to determine the optimum therapeutic window for vascular targeted non-viral gene therapy using an integrin targeted nanoparticle (NP) platform with the use of $\alpha_v\beta_3$ targeted molecular imaging

Materials and Methods

Fisher rats were divided into 3 groups. Treated (Group 1, n=5) and control groups (Groups 2, n=5) received RT2 tumor cells implanted intracranially into the striatum. Normal group (Group 3, n=3) received no tumor cells or treatment. Group 1 received an $\alpha_v\beta_3$ targeted NP that carried a mutated Raf gene (NP-ATP$^\mu$-Raf) complex. This gene disrupts the VEGF and FGF mediated signaling pathway. Group 2 received saline. Three treatments with targeted NP (Group 1) or saline (Group 2) were conducted starting day 6 after tumor implantation. Additionally, T2-weighted MR imaging was used to determine the size of tumors.

Results

Both the treatment group and the control group demonstrated 3 mm tumors prior to the start of treatment. The tumor in the controls continued to increase in size and signal intensity. Most of the controls died between days 10 and 21. The tumors in the treated group showed significant reduction in tumor size by day 24. These tumors demonstrated signs of encephalomalacia and significant reduction in vessel density by histologic analysis. 80% of all treated animals have survived, while 100% of untreated tumor-bearing animals died.

Conclusion

Dual modality targeted probes are a powerful way of separating patient population based on treatment responders vs. non-responders through molecular imaging.
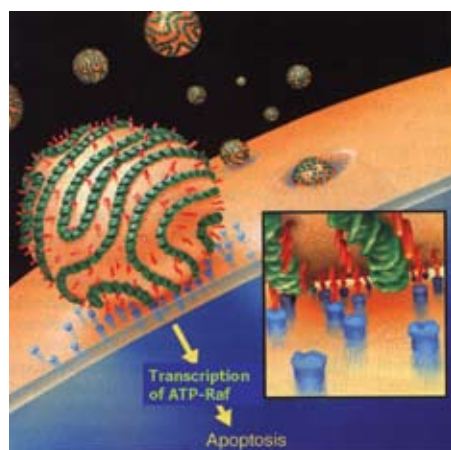
Fig. 1 Lipid-based nanoparticle that accumulates in the tumor by targeting integrin $\alpha_v\beta_3$ on the surface of cells. These nanoparticles delivers a gene that destroys tumor vessels
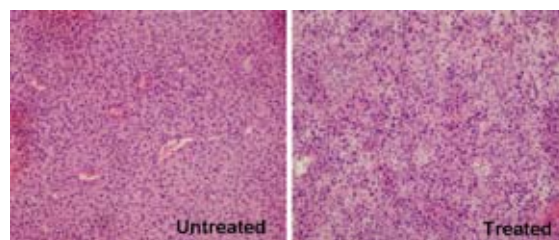
Fig 2. H&E staining of treated tumors demonstrate markedly reduced vessel density implying ongoing tumor death. H&E stainging of untreated tumors show expected high vessel density.
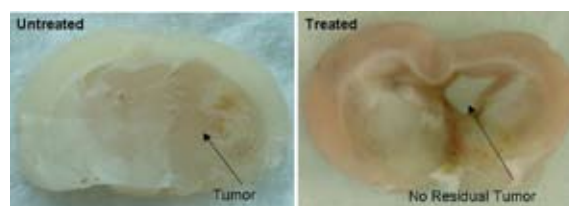
Fig. 3 Post treatment with nanoparticles, observed complete regression of tumor with only remaining scar tissue
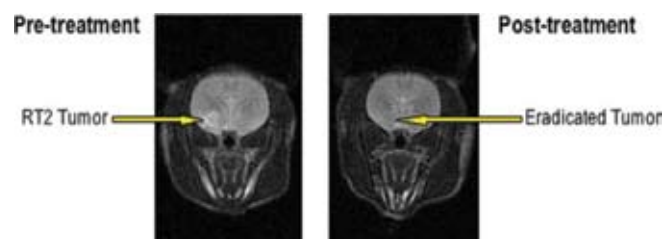
Fig. 4 Demonstrates tumor regression after treatment with integrin targeted nanoparticles
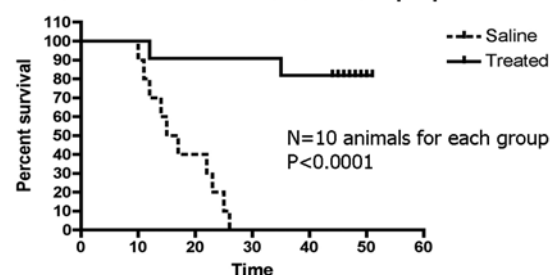
Fig. 5 A longer survival time was observed after treatment. 80% survival in treated group compared to 100% mortality in untreated group.

Characterization of a Time-Domain Fluorescence Imaging System with Cy5.5 and Qdot Probes

S. KEREN, O. GHEYSENS, C.S. LEVIN, S.S. GAMBHIR, MOLECULAR IMAGING PROGRAM AT STANFORD (MIPS), DEPARTMENT OF RADIOLOGY AND BIO-X PROGRAM

OBJECTIVES

Time-domain based optical imaging can quantitatively recover depth, volume, concentration, and fluorescent lifetime of different light-emitting molecular probes, using both photon temporal distribution and intensity data. Here we present initial phantom study results that assess the performance capabilities of the ART-GE optical imaging system, eXplore Optix.

MATERIALS AND METHODS

A diode laser source generates short pulses (<100ps) at 670nm that excite fluorescent probes. A 96 well plate and a liquid phantom, filled with 1% liposyn (simulating tissue), were used to evaluate surface sensitivity, depth sensitivity and depth estimation of the system with Cy5.5 (Amersham Bioscience) and Qdot 705 PEG conjugated (Quantum Dot Inc.) as fluorescent probes.

RESULTS

Serial dilutions of Cy5.5 and Qdot 705 placed in a well plate showed that concentrations as low as 0.1nM (50ul volume) of both probes could be detected. Fluorescence intensity varied linearly for more than 3 log orders of magnitude of fluorophore concentration with excellent correlation (r^2>0.99). Depth sensitivity assessed with liquid phantom showed 62.5nM (5ul volume) could be resolved at 11mm, with good correlation (r^2>0.98) to a mono-exponential decay of intensity as a function of depth. Depth estimation of probe using time shift in peak fluorescence intensity gave results within 10% accuracy of actual depth for up to 10mm.

CONCLUSIONS

The eXplore Optix time-domain optical imaging system can detect sub-nanomolar concentrations, image deeper than 10mm, and accurately estimate depth. Accompanied with a rigorous tomographic reconstruction model this system should recover the shape, location and concentration of fluorescent inclusions in three-dimensions

Improved Mutants of Renilla Luciferase for Imaging Applications in Living Subjects

ANDREAS M. LOENING, ANNA M. WU, SANJIV S. GAMBHIR - MOLECULAR IMAGING PROGRAM AT STANFORD (MIPS), DEPARTMENT OF RADIOLOGY AND BIO-X PROGRAM, STANFORD UNIVERSITY; CRUMP INSTITUTE FOR MOLECULAR IMAGING, DEPARTMENT OF MOLECULAR & MEDICAL PHARMACOLOGY, UCLA SCHOOL OF MEDICINE

Bioluminescent proteins have become essential tools for molecular imaging, primarily as reporter genes in the context of small animal imaging. Recently, their use has been expanded to include bioluminescent tagging, in which the protein itself is conjugated to a ligand and the resultant fusion protein is used as an imaging probe. We have been developing mutants of Renilla luciferase (RLuc) that possess improved characteristics for both reporter gene applications and bioluminescent tagging.

Candidate mutations were chosen using a consensus driven approach, via homology to bacterial haloalkane dehalogenases, and screened for light output and stability. A mutant (RLuc8) combining a total of 8 mutations exhibited a 150-fold in vitro serum stability increase compared to RLuc (>100 hrs versus 0.7 hrs) and a 4-fold increase in light output. Transient transfection of RLuc8 in mammalian cells showed a 15-fold increase in signal compared to RLuc after 24 hours. A double mutant (RLuc-M185V/Q235A) was developed that exhibited a 50 percent reduction in stability compared to RLuc but increased light output 4-fold. When used with the substrate analogs coelenterazine-cp, coelenterazine-n, and bisdeoxycoelenterazine (DeepBlueC), RLuc8 showed 6, 9, and 60-fold increases in light output, while RLuc-M185V/Q235A showed 14, 7, and 20-fold increases. Only a portion of these increases could be explained by enhancements in quantum yield.

Ongoing work is attempting to alter the emission spectrum of RLuc, by targeting mutations based on a homology model and an estimate of the substrate orientation in the active site. One mutant with a 10 nm red shifted emission showed little drop in light output, while another mutant showed a 20 nm red shift but with a large drop in output.

In summary, RLuc8 represents a significant improvement for the bioluminescent tagging of ligands, and both RLuc8 and RLuc-M185V/Q235A are significant improvements over the native luciferase for reporter gene applications.

A Fusion Protein Approach for Imaging Drug Mediated Protein-Protein Interactions in Living Animals

R. Paulmurugan and S. S. Gambhir - Molecular Imaging Program at Stanford (MIPS), Department of Radiology and Bio-X - Program

BACKGROUND

The split luciferase complementation system often has low sensitivity for studying weakly interacting proteins. We constructed a fusion protein approach and compared this using a rapamycin mediated protein-protein interaction system.

METHODS

Vectors expressing fusion proteins containing both interacting proteins and the split fragments of renilla luciferase with proper linker *(screened from six peptide linkers)(NhRL-FRB-E-FKBP12-ChRL)*, and the split fragments of enhanced green fluorescent proteins *(NEGFP-FRB-E-FKBP12-CEGFP)* were constructed. 293T cells transfected with the fusion vector system and a two-vector system were analyzed by luminometer (luciferase) and FACS (EGFP). Imaging of mice (N=6) implanted with 293T cells stably expressing the fusion and two-vector system was performed before and after injecting rapamycin.

RESULTS

The peptide linker with 2 and 4 repeats of amino acids EAAAR are efficient in producing a low background and higher complementation signal. The cells transfected with the fusion system show signal that is significantly higher (8±2 fold; p<0.001) than the cells transfected with the two-vector system. The cells transfected with the fusion vector system shows significantly (p<0.01) rapid protein-protein interaction even with very low concentrations of rapamycin (0.004 nM). Imaging of animals shows significantly higher level of signal (6±3 fold; p<0.01) from the site implanted with the cells expressing the fusion protein than the cells expressing proteins from the two-vector system when given rapamycin. The FACS analysis of the system with split EGFP shows similar results.

CONCLUSION

The developed fusion protein strategy has high sensitivity and should be useful in studying drug-mediated protein -protein interactions in living animals.

Optical Imaging of Ligand Induced Estrogen Receptor Intramolecular Folding in Living Animals

Ramasamy Paulmurugan and Sanjiv S. Gambhir - Molecular Imaging Program at Stanford (MIPS), Department of Radiology and Bio-X Program

OBJECTIVES

The estrogen receptor (ER) controls many key downstream pathways in response to the hormone estrogen. We have developed a new strategy in which split reporters complement as ER protein folds in response to drug binding.

METHODS

We constructed vectors that express fusion protein with wild (w) *(binds estradiol)* and mutant (m) (*doesn't bind estradiol*) estrogen receptor alpha Ligand Binding Domain (ERα-LBD) with NhRL and ChRL (*split renilla luciferase fragments*) in the N- and C- terminus respectively *(NhRL-ER(w)-ChRL and NhRL-ER(m)-ChRL)* and studied the intramolecular folding in ER positive (293T, MCF7) and ER negative (MDA-MB435) cell lines with known antagonists and agonists. Anticancer drugs that use different pathways (*other than ER mediated*) served as negative controls. The drug induced intramolecular folding was imaged in living mice (N=6) implanted with 293T cells stably expressing *NhRL-ER(m)-ChRL using a cooled CCD camera*.

RESULTS

The cells transfected with the vector expressing *NhRL-ER-ChRL* shows ligand *(antagonist)* specific intramolecular folding associated complementation only in ER positive (293T and MCF7) cells and ranges from 30±5 to 50±5 fold more than the cells not exposed to drug. There is no significant level of complementation from ER negative MDA-MB435 cells. Optical bioluminescence imaging of the cell implants of 293T stable cells expressing fusion protein of *NhRL-ER(m)-ChRL* shows significant *(p<0.05)* signal upon injecting antagonist raloxifene (12±4 X 10^3 p/sec/cm2/sr) than animals receiving agonist estradiol (1.5±2 X 10^3 p/sec/cm2/sr).

CONCLUSION

This is an entirely new class of molecular "switch" that can be used for imaging drug-receptor interaction in living subjects.

Self Complementing Firefly Luciferase Enzyme Fragments for Imaging Intracellular Events in Cells and Living Animals

RAMASAMY PAULMURUGAN AND SANJIV S. GAMBHIR - MOLECULAR IMAGING PROGRAM AT STANFORD (MIPS), DEPARTMENT OF RADIOLOGY AND BIO-X PROGRAM, STANFORD UNIVERSITY

BACKGROUND

Split fragments of luciferase reporter proteins that do not self-complement have been successfully used for studying protein-protein interactions in cells and living animals. We now report the development and characterization of self-complementing fragments of firefly luciferase enzymes split by selecting different sites based on crystal structure. These self-complementing fragments can be used for studying cellular localization of proteins, identifying macromolecular delivery vehicles (e.g., TAT), and other intracellular events.

METHODS

We constructed N- and C- fragments of luciferase selected from 10 different split sites (10 Nfluc and 7 Cfluc) with and without overlapping combinations. These were studied using transient transfection in 293T cells to identify the combination that produces efficient self-complementation. We also constructed N- and C- fragments with nuclear localization signal peptides (NLS) and TAT peptides with the most efficient self-complementing combination *(Nfluc-475/Cfluc-265)* in order to study protein localization and TAT-mediated cell delivery.

RESULTS

The transient transfection study shows significant level *(p<0.05)* of complemented luciferase self-complementation from 18 of 63 combinations, and the recovered enzyme activity ranges from 0.01 to 4% when compared to the intact luciferase enzyme activity. The highest signal was achieved from the combination of fragments with Nfluc-475 and Cfluc-265. This combination shows cellular compartment specificity when expressed one with NLS and another without NLS signal peptide. The stable 293T cells expressing Nfluc-475 shows 10±2 fold higher signal *(p<0.05)* upon delivery of TAT-Cfluc-265.

CONCLUSION

These developed self-complementing fragments will be very useful for imaging many intracellular events including protein compartmentalization and TAT mediated protein delivery.

A New Intracellular Sensor for Optical Imaging of Protein Phosphorylation in Living Subjects

RAMASAMY PAULMURUGAN AND SANJIV S. GAMBHIR - MOLECULAR IMAGING PROGRAM AT STANFORD (MIPS), DEPARTMENT OF RADIOLOGY AND BIO-X PROGRAM

BACKGROUND

Protein phosphorylation plays a key role in controlling many cellular processes, and has been limited to cell culture studies by using phospho-specific antibodies. We have developed a new sensor that uses self-complementing firefly luciferase fragments for studying insulin receptor substrate 1(IRS-1) phosphorylation. We validate this system in cells and also with optical imaging of living mice.

METHODS

A vector carrying the fusion proteins with split firefly luciferase fragments, IRS-1 signal peptide, linker and PI-3kinase-SH2 domain *(Nfluc-475-Y941-E2-SH2-Cfluc-265)* was created. Transient transfections of insulin receptor (IR) positive (CHO-IR and 3T3-L1) and negative (293T) cells were studied by inducing with 100nM insulin for 24 h. The system was also studied in living mice (N=3) implanted with the cells expressing the fusion protein before and after intraperitoneal injection of 4 IU human long-acting insulin by optical CCD camera imaging.

RESULTS

The linker peptide $(EAAAR)_2$ is efficient in preventing the self-complementation between the luciferase fragments before an induced interaction occurs between the phosphorylated-IRS-1 peptide and its counterpart SH2 domain. The cells expressing the fusion protein show 3 ± 1.5 fold more signals upon induction with IR positive cells, and 1 ± 0.5 fold more signals from IR negative cells. The mice implanted with IR positive (CHO-IR) and IR negative (293T) cells expressing the fusion protein show significant *(p<0.05)* signal from the site implanted with IR positive cells upon insulin induction as compared to the IR negative cells ($1.0 \pm 0.2 \times 10^4$ p/sec/cm2/sr vs $4.0 \pm 1.2 \times 10^3$ p/sec/cm2/sr).

CONCLUSION

This work validates a new molecular switch that can be used to image protein phosphorylation in living subjects and should be useful for accelerating the testing of new drugs targeted against modulating phosphorylation events.

Reproducibility of 3′-Deoxy-3′-^{18}F-Fluorothymidine MicroPET Studies in Mouse Tumor Xenografts

Jeffrey R. Tseng[1], Mangal Dandekar[1], Murugesan Subbarayan[1], Zhen Cheng, Jinha M. Park[1,2], Stan Louie,[3], Sanjiv S. Gambhir [1]
[1]Molecular Imaging Program at Stanford, Bio-X Program, and Department of Radiology, Stanford University School of Medicine; [2]Department of Radiology, University of California at Los Angeles; [3]Department of Pharmacy, University of Southern California

Introduction

3'-deoxy-3'-^{18}F-fluorothymidine (FLT) has been used to image tumor proliferation in pre-clinical and clinical studies. Serial microPET studies may be useful to follow therapy response or for drug screening, however the reproducibility of serial scans has not been determined. The purpose of this study was to determine the reproducibility of ^{18}F-FLT microPET studies.

Methods

C6 rat glioma xenografts were implanted into 9 nude mice and grown to a mean diameter of 5-17 mm for 2 weeks. A microPET scan was performed 1 hour after ^{18}F-FLT (50-200 μCi) injection via the tail vein. A second microPET scan was performed 6 hours later after re-injection of ^{18}F-FLT. Most of the mice were studied twice within the same week (total studies n = 17). Regions of interest (ROI) were drawn around images of tumor activity, and mean percent injected dose per gram (%ID/g) values were calculated. Coefficients of variation and differences for the %ID/g between studies from the same day were calculated to determine the reproducibility after subtracting away the estimated residual tumor activity from the first ^{18}F-FLT injection.

Results

The coefficient of variation ± sd for %ID/g between ^{18}F-FLT microPET scans performed on the same day 6 hours apart was 14 ± 10 %. The mean difference for %ID/g between scans was 0.06 ± 1.3 %ID/g. Serum thymidine levels were mildly correlated with %ID/g ($R^2 = 0.40$). The tumor size, body weight, injected dose, and fasting state did not contribute to the variability of the scans, however consistent scanning parameters were necessary to ensure accurate studies, particularly controlling the body temperature, the time of imaging after injection, and the ROI size.

Conclusion

^{18}F-FLT microPET xenografted mice studies are reproducible with moderately low variability. Serial studies may be performed to assess for significant changes to follow therapy response or for pre-clinical drug development.

Near-Infrared Fluorescent Dye Conjugated D-Glucosamine as a Novel Probe for Tumor Optical Imaging in Cell Culture and in Living Mice

Z. Cheng, S. Keren, X. Chen, S.S. Gambhir - Molecular Imaging Program at Stanford (MIPS), Department of Radiology, Bio-X Program

Objectives

2-deoxy-2-[^{18}F]fluoro-D-glucose ([^{18}F]FDG) has been used extensively for the clinical diagnosing and staging of cancer and other diseases. Non-radioactive glucose analogs with ability to screen the glucose metabolic rate of tumors are particular interesting for anticancer drug development, because this type of molecular probe may have many applications for optical imaging of tumors and monitoring therapeutic efficacy of drugs in living animals. We therefore synthesized and tested the feasibility of D-glucosamine-Cy5.5 conjugate (CyDG) for near-infrared (NIR) fluorescence imaging of tumor in a pre-clinical xenograft model.

Methods

CyDG was prepared by conjugating Cy5.5-mono-NHS ester and D-Glucosamine followed by RP-HPLC purification. The *in vitro* accumulation of CyDG in tumor cell lines at 37 °C and 4 °C was imaged using a fluorescence microscope and tumor targeting and retention of CyDG in subcutaneous U87MG glioma model was visualized and quantified by a Xenogen IVIS 200 optical CCD system (n=3).

Results

Fluorescence microscopy imaging shows that CyDG is taken up and trapped by a variety of tumor cell lines at 37 °C incubation, while it exhibits marginal uptake at 4 °C. U87MG tumor localization is clearly visualized in living mice with NIR fluorescent probe. Tumor/Muscle contrast shows up at as early as 30 min, and the highest tumor/muscle ratio of 2.34±0.03 are achieved at 18 hr postinjection.

Conclusion

The NIR fluorescence glucose analog, CyDG demonstrates tumor targeting ability both *in cell culture* and *in living mice*. More studies are warranted to further explore this strategy for optical tumor imaging including direct comparisons to [^{18}F]FDG.

MicroPET Imaging of Melanoma Using Cu-64 Labeled alpha-Melanocyte Stimulating Hormone Peptide Analogue

Z. Cheng, Z. Xiong, Y. Wu, X. Zhang, X. Chen, S.S. Gambhir Molecular Imaging Program at Stanford (MIPS), Department of Radiology, Bio-X Program

Objectives

Alpha-melanocyte stimulating hormone (α-MSH) analogs can specifically bind with α-MSH receptors that are present on the most murine and human melanoma, rendering them excellent carriers for delivering radioisotopes and small molecules for melanoma detection and treatment. Herein we evaluate a Cu-64 labeled α-MSH analog, DOTA-MSH1, as a potential molecular imaging agent for microPET imaging of melanoma using a B16F10 xenograft model.

Methods

1,4,7,10-tetraazacyclododecane-1,4,7,10-tetraacetic acid (DOTA) conjugated MSH1 was synthesized and it was radiolabeled with ^{64}Cu in NH$_4$OAc (0.1 M; pH 5.5)-buffered solution for 60 min at 50 °C. The biodistribution of both ^{64}Cu-DOTA-MSH1 and 2-deoxy-2-[^{18}F]fluoro-D-glucose ([^{18}F]FDG) were investigated in C57BL/6 mice (n=4) bearing subcutaneous B16F10 melanoma tumors. MicroPET imaging of the mice at different times post tail vein injection of radiolabeled probes was also performed.

Results

Biodistribution experiments show that tumor uptake values of ^{64}Cu-DOTA-MSH1 are 4.55±0.49 %ID/g, 4.41±0.93 %ID/g, and 1.48±0.36 %ID/g in C57BL/6 mice bearing B16F10 xenografts at 2 h, 4 h, and 24 h postinjection, respectively. The tumor uptake is inhibited with a coinjection of excess α-MSH peptide, NDP. Comparing to the biodistribution of [^{18}F]FDG, ^{64}Cu-DOTA-MSH1 exhibits significantly higher tumor/muscle (T/M) ratio, while lower tumor/blood (T/B) ratio at all the times examined in this study. For example, T/M 10.92±1.17 vs 2.57±0.64 and T/B 5.99±2.61 vs 29.2±4.99 is observed for ^{64}Cu-DOTA-MSH1 and [^{18}F]FDG at 2 hr postinjection, respectively. MicroPET imaging of ^{64}Cu-DOTA-MSH1 in B16F10 tumor mice clearly shows good tumor localization.

Conclusion

Cu-64 labeled DOTA-MSH1 is a promising imaging agent for α-MSH receptor positive melanoma PET imaging.

Firefly Luciferase (fLuc) Does Not Induce Photodynamic Toxicity of Rose Bengal (RB) and Hypericin (Hy)

Meike L. Schipper, MR Patel, Sanjiv Sam Gambhir - Molecular Imaging Program at Stanford (MIPS), Department of Radiology, Bio-X

Abstract

It has been proposed that cancer cells can be killed with sufficient light and a photosensitizer (photodynamic toxicity). Our goal was to determine if cancer cells expressing firefly luciferase produce enough light to induce cell death in the presence of photosensitizers.

Methods

Light emission of fLuc expressing/control cells was assessed by CCD camera. C6fLuc, N2afLuc, and controls were exposed to RB (0-50 μM) or Hy (0-100 μM) (3h), incubated with D-Luciferin (0-6 mg/ml) (24h), and assessed for cell death by MTT assay. C6fLuc, C6, N2afLuc, N2a, NIH3t3, MCF7, 3T3, CHO, 293T, and A375 were incubated with RB/Hy (3h), exposed to darkness/sunlight (1h), and incubated (23h) before MTT assays. A375 and 293T were exposed to lamp light (0-120 min) after RB/Hy, and incubated (24 h) before MTT assays. Experiments were conducted in darkness with an infrared camera.

Results

Maximal light levels of N2afLuc (2.26×10^8 photons/s/cm^2/steridian angle) and C6fLuc (1.6×10^6 p/s/cm^2/sr) were reached within 25 min and fell to background levels within 19 h. Survival of cells exposed to RB/Hy did not differ significantly from unexposed cells. D-Luciferin levels above 1.2 mg/ml decreased cell survival regardless of photosensitizer. Hy above 10 μM decreased survival regardless of D-Luciferin. Sunlight after nontoxic concentrations of RB/Hy reduced cell survival in 8/10 cell lines. Lamp light did not reduce survival.

Conclusion

In contrast to recent reports, we do not observe a phototoxic effect of RB or Hy on fLuc expressing cells. Light levels that reduced cell survival were significantly higher than generated by fLuc.

Count Rate Studies of a PET Breast Imaging System Comprised of PSAPDs Utilizing Monte Carlo Simulation

Angela Foudray[1,2], Frezghi Habte[1], Garry Chinn[1], Jin Zhang[1] and Craig Levin[1] - [1]Molecular Imaging Instrumentation Laboratory, Department of Radiology, Stanford University; [2]University of California, San Diego, Department of Physics

Introduction

We are investigating a high-sensitivity, high-resolution positron emission tomography (PET) system for clinical use in the detection, diagnosis and staging of breast cancer. Using conventional figures of merit, design parameters were evaluated for count rate performance, module dead time, and construction complexity. The detector system modeled comprises extremely thin PSAPDs coupled to LSO scintillation crystals. Previous investigations of detector geometries with Monte Carlo indicated that one of the largest impacts on sensitivity is local scintillation crystal density when considering systems having the same average scintillation crystal.

To evaluate the performance of new detector systems used in applications such as high-energy physics and nuclear medicine, Monte Carlo is one of the first tools utilized [1]. Sensitivity, count rate performance, and reconstructed spatial resolution are a few of the characteristics of the modeled system that can be measured. The modeling capabilities of GATE were verified by comparing simulation to built system results.

Method

A. NEC and Count Rate

The simulated position sensitive avalanche photodiodes (PSAPDs) were modeled based on 11mm x 11mm x 230μm prototypes from RMD, Inc. An 8x3 array of 1mm x 1mm x 3mm LSO scintillation crystals were sandwiched between a reflector and optically coupled to the PSAPDs. The PSAPDs are mounted on a thin (50 μm) flex cable for signal acquisition and delivering power. The total thickness of the flex cable, PSAPD, crystals and reflector was 1.3mm. The crystal array-PSAPD structures were configured edge-on with respect to incoming 511 keV photons and were repeated trans-axially to form four heads. This four-headed or "box" system was found to be the configuration with the highest sensitivity [2].

Signal to noise (SNR) was estimated for the system using the NEMA standard: noise equivalent counts:

$$NEC = \frac{T^2}{T + S + 2R}$$

Equation 1

where T, S and R are true, scatter and random events respectively. NEC rates were calculated for the worst-case scenario of a uniformly filled cylindrical phantom, with diameter 16cm and length 12cm, which almost completely fills the detector inner volume.

The amount of injected activity that accumulates in the breast is ~ 200 μCi. The other regions of high uptake such as the heart and lungs that contribute to background are not simulated in this study.

B. Count Rate vs. EW, CTW, and Concentration

To assess the count rate performance of the system, we use the same 16cm diameter cylindrical water phantom described in the previous section and filled it uniformly with a range of activities of ^{18}F that include those pertinent to the application of breast imaging.
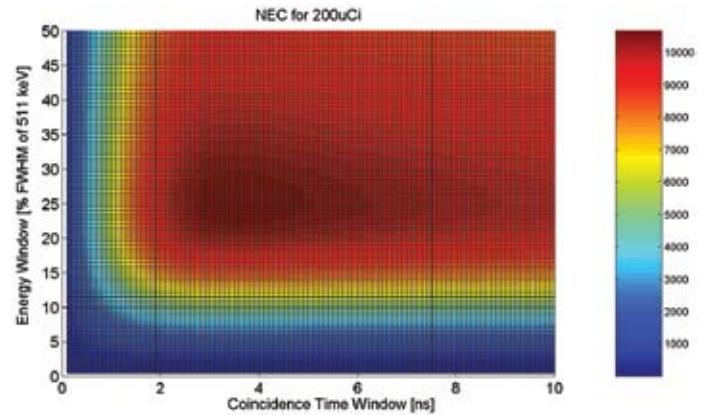
Results

Figure 1. NEC count rates versus energy window and coincidence time window. The maximum NEC rate was observed for a 24% energy window and 3-4 ns coincidence time window.
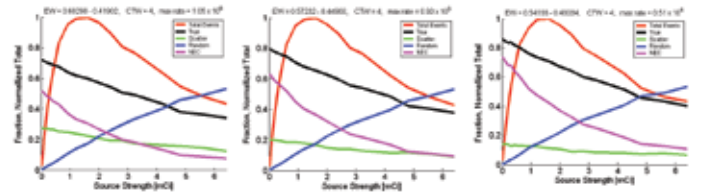
Figure 2. Count rate vs. concentration for various energy windows: a) EW: 12% CTW: 4ns, b) EW: 24% CTW: 4ns, c) EW: 36% CTW: 4ns. The total counts are plotted normalized to the peak total counts. The trues, scatters and randoms are plotted as their fraction of the total. NEC is also scaled to the total counts.

Conclusions

We found 24% energy window, twice the energy resolution, and 3ns or 4ns time window, 1.5 or 2 times the coincidence time resolution, to give the best NEC rate. Looking at system performance in the activity range in the application of dedicated breast imaging (a few hundred micro-Curie), the slope of total count rate vs. activity is still linearly increasing, so we are not operating near the system counting limitations due to multiples rejection and module dead-time.

References

1. Strul, D, et al, "GATE (Geant4 Application for Tomographic Emission):a PET/SPECT general-purpose simulation platform" Nucl. Phys. B (Proc. Suppl.) 125 (2003)75 –79.

2. A. M. K. Foudray, F. Habte, G. Chinn , J. Zhang, C. S. Levin, P. D. Olcott, "Optimization of a PET Breast Imaging System Comprised of Position Sensitive Avalanche Photodiodes Utilizing Monte Carlo Simulation" Presented at the 2004 IEEE Breast Imaging Workshop, Oct 22-24, 2004, Roma, Italy

Positioning Annihilation Photon Interactions in a Thin LSO Crystal Sheet with a PSAPD

Angela Foudray[1,2], Frezghi Habte[1], Craig Levin[1], Peter Olcott[1] - [1]Molecular Imaging Instrumentation Laboratory, Department of Radiology, Stanford University; [2]University of California, San Diego, Department of Physics

Introduction

We are developing a high-sensitivity, high-resolution small animal positron emission tomography (PET) system for studying the kinetics and mechanisms of human disease in small laboratory animal models. Most high-resolution imaging systems in use and in development are incorporating increasingly smaller pixellated scintillation crystals to try to improve system resolution [1]. In order to increase the detection efficiency of the annihilation photons, the crystals are made long in the direction of the incoming photons. In standard PET detector designs, the thin crystals are coupled to the photodetector on the side with the smallest cross-sectional area, giving them an aspect ratio that does not promote optimal light output [2]. This results in a compromise between high system resolution, high light output (effectively energy resolution) and sensitivity in several research efforts.

Recently developed detectors such as very thin position-sensitive avalanche photodiodes (PSAPDs) and cadmium zinc telluride (CZT) blocks allow a very compact detector system with more advantageous scintillator coupling geometries and detector orientations, which significantly improve the sensitivity, energy resolution and spatial resolution (figure 1). With such small detectors, the packing fraction does not change significantly for different detector orientations. Crystals can then be coupled so that the aspect ratio is high (higher energy resolution) without a reduction in annihilation photon interaction by orienting the detectors edge on (the PSAPD surface normal is perpendicular to the incoming photon direction).

Methods

The PSAPD being characterized was developed by RMD, Inc. with an active region of 8mm x 8mm[2]. An 8mm x 8mm x 1mm LSO continuous crystal is coupled to the PSAPD with silicone optical grease. A LabView controlled, motorized National Aperture MM-4M-EX-140 micro-stage was used to automate and accurately control the positioning steps across the detector. ^{57}Co (122 keV gamma) and ^{22}Na (511 keV annihilation photons) sources were used to observe the point spread function and spatial linearity of the PSAPD.

To collimate the highly energetic 511 keV photons from the 10μCi ^{22}Na source, a coincidence setup was constructed using a Hamamatsu H3164 photomultiplier tube (PMT) that was coupled to a Teflon-wrapped 5mm x 5mm x 10mm LSO crystal with silicone optical grease. The LSO-PMT detector was mechanically coupled to the source at a distance of 190mm and moved with the micro-stage in 160μm steps. The ^{57}Co source was collimated using a 30mm x 30mm x 10mm block of lead with a 500μm hole.

Positions were calculated from the four digitized PSAPD channels using Anger-type logic. Position is calculated from the four digitized voltages from the corner anodes of the PSAPD.

To compare the results with theory, we utilized two standard simulation packages to model both the high energy and light photon interactions in the LSO scintillation crystal. The interaction mechanisms of the high-energy annihilation photon were simulated with GATE. The scintillation photon transport and interaction statistics were carried out using DETECT2000.

Results
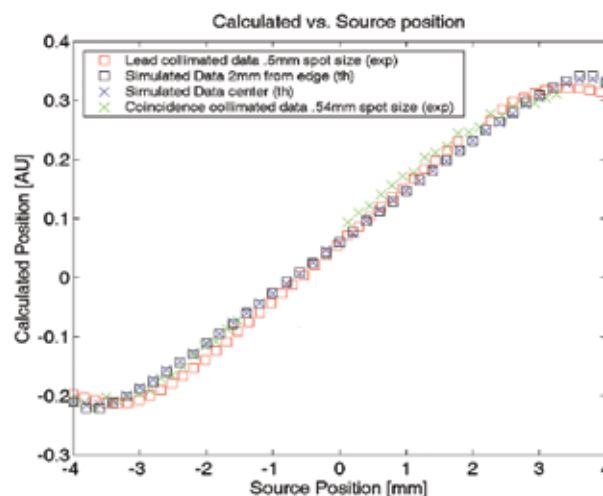
Figure 1. Comparison of 22Na and 57Co experimental (exp) and simulated (th) positioning along a line across the face of the detector.
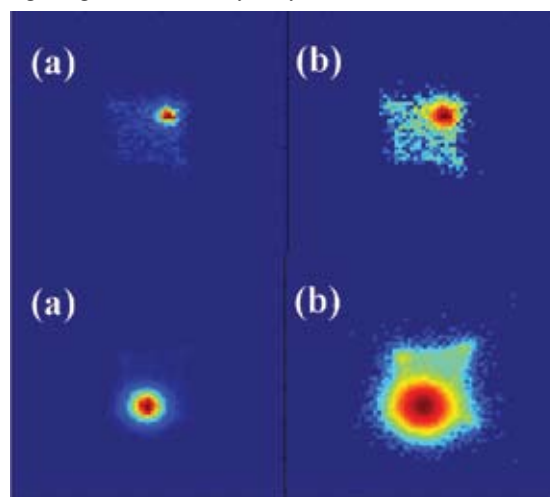
Figure 2. For a single source position, a) the histogrammed centroid of the light spread b) the log of the histogram values (enhance the visualization of the dynamic range). Top: ^{22}Na and bottom: ^{57}Co

Conclusions

The experimental and simulated results agree quite well – both show that the calculated positions from events whose centroid are in the first 1.2 mm near the edge of the sheet crystal are degenerate. This is most likely due to a sizable portion of the scintillation photons reflecting off the surface of the crystal sides.

References

1. C.S. Levin, A.M.K. Foudray, P.D. Olcott, F. Habte. "Investigation of Position Sensitive Avalanche Photodiodes for a New High Resolution PET Detector Design." *IEEE Transactions on Nuclear Science 51 (3) 805 – 810, June 2004*
2. C.S. Levin, F. Habte, and A.M. Foudray. "Methods to Extract More Light from Minute Scintillation Crystals Used in an Ultra-High Resolution Positron Emission Tomography Detector." *Nucl Instr and Meth in Phys Res Sect A (in press, 2004).*

Investigating Positioning and Scatter Rejection Algorithms in a High Resolution PET System Capable of Depth of Interaction Measurement

Angela Foudray[1,2], Garry Chinn[1], Craig Levin[1] and Peter Olcott[1] - [1]Molecular Imaging Instrumentation Laboratory, Department of Radiology, Stanford University; [2]University of California, San Diego, Department of Physics

Introduction

We are investigating the accuracy of positioning algorithms and event filtering using Monte Carlo simulation. We are also developing maximum likelihood techniques for data reconstruction and scatter and random rejection. The techniques, though applicable to any system, were used here for data acquired in simulation by a small animal imaging system under development.
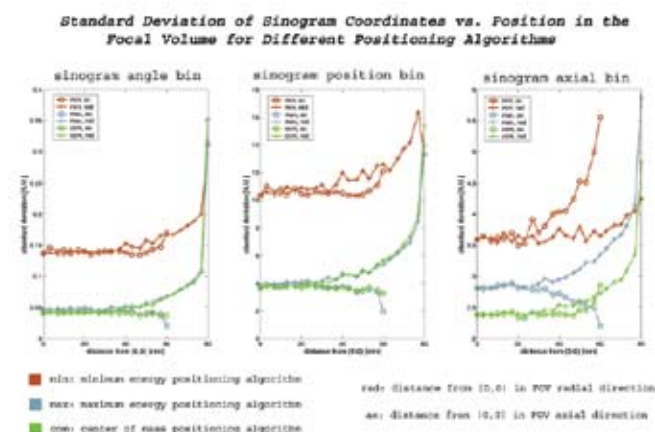
Methods

A. Positioning Algorithm

Using the Monte Carlo package GATE, the modeled system comprises edge-on oriented modules formed from an 8x3 array of 1x1x3 mm3 LSO crystals coupled to an 11 x 11 x 0.2 mm3 position-sensitive avalanche photodiode (PSAPD). Details of each Compton scatter interaction and photoelectric absorption in the scintillation crystals, for every annihilation photon, were written to a file. Coincidence events were energy gated using a symmetric 24% energy window around 511 keV. To assess the positioning algorithms, the ideal (correct) line of response (LOR) was calculated from the first simulated interaction position. In the actual system however, all Compton and photoelectric interactions from one annihilation photon which occur in one PSAPD cannot be resolved as separate interactions; only their center of mass (COM) position and energy are determined by the PSAPD. Therefore, all subsequent positioning calculations (except for the ideal position) were performed on the data after an intra-PSAPD COM calculation.

For a particular positioning algorithm, the calculated position was compared to the ideal position, and for each sinogram coordinate; $\square$, t or z, the standard deviation was found. Three positioning algorithms were investigated: the position of the interaction with the (1) minimum energy deposited, (2) maximum energy deposited and (3) the center of mass of the energy deposited.

B. Event Filtering Algorithm

A maximum likelihood approach was taken to predict the position and incident angle of an event with interactions in two or more PSAPDs. Multiple interactions that occur in only one PSAPD are not individually resolvable by the detector and look the same as a photoelectric interaction. The maximal probability in (location, angle) space was calculated from the product of the probabilities of the COM location, interaction locations and energies. These probabilities were calculated by constructing the probability density function (PDF) of the COM of an event and the PDF of the interaction locations and energies for each training incident location and angle using Bayes equation.

Results

Standard Deviation of Sinogram Coordinates vs. Position in the Focal Volume for Different Positioning Algorithms

	center (0,0,0)	edge – axial dir. (4cm)	edge – radial dir. (4cm)
Interactions occur in:	coincidence fraction	coincidence fraction	coincidence fraction
1 PSAPD	0.509	0.639	0.486
2 PSAPDs	0.376	0.306	0.390
3 PSAPDs	0.0991	0.0556	0.102
4 or more PSAPDs	0.0159	<0.001	0.0220
Type of interactions			
Photoelectric only (PE)	0.365	0.385	0.358
1 scatter + PE	0.370	0.363	0.365
2 scatters + PE	0.155	0.144	0.158
3 scatters + PE	0.0660	0.0647	0.0693
4 or more scatters + PE	0.0450	0.0433	0.0498

Table 1. The number and types of interactions happening in the detector for emission sources throughout the field of view.
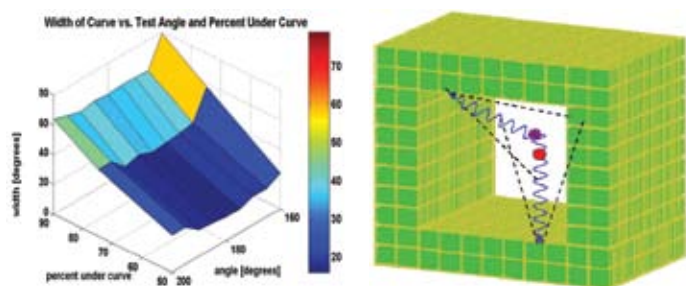
Figure 2. left: The width of the gaussian fitted to testing data (angle resolution) for differing amounts of data included. right: an illustration of the rejection mechanism (red: annihilation, blue: annihilation photons, purple: scatter event, black: bounds of angular resolution) .

Conclusions

Ninety percent or more of the events have interactions that stay within 1 or 2 PSAPDs, with a 10keV threshold throughout the detector. This coupled with the fact that the center of mass locations are tightly distributed about the incident direction (as seen by the COM being a good predictor of true line of response), gives the maximum likelihood estimation algorithm enough information to predict the incident angle to within 20 degrees (for 50% of the events). More training events brought the predicted angle closer to the correct angle. Using a maximum likelihood approach, we were able to predict incident angle to within ten degrees (50% of events). This information will provide a means to reject non-true coincidences that fall outside of our incident angle resolution.

Component-based Normalization for PET Systems with Depth of Interaction Measurement Capability

Angela Foudray[1,2], Garry Chinn[1], Craig Levin[1] – [1]Molecular Imaging Instrumentation Laboratory, Department of Radiology, Stanford University; [2]University of California, San Diego, Department of Physics

Introduction

In order to achieve quantitation in reconstructed images, the sensitivity of each detector line of response (LOR) must be normalized. There are two commonly used methods for calculating a weighting factor to apply to binned data before reconstruction: direct normalization and component-based normalization. Direct normalization is time consuming and does not account for the difference between the normalization factors for scatter and true coincidence events [1]. Also, direct normalization assumptions break down when the useful field of view (FOV) becomes a significant portion of the viewable area of the system. To take advantage of the sensitivity increase, the detectors in the system in this study were moved in close to the object being imaged, giving us a usable FOV equal to the dimensions of the interior of the system. Component based normalization was introduced to take all the factors into account that contribute to the efficiency of a particular LOR. Here we propose a method to adapt the component-based normalization model to include depth of interaction (DOI) and large FOV considerations without an order of magnitude increase in computational resources.

Theory

Component-based normalization models compute the activity within a LOR The normalization coefficient can be broken down into components based on intrinsic efficiencies ($\square$) such as crystal properties, which vary for each crystal, and geometric efficiencies (g) such as solid angle variation versus annihilation location along the LOR. With depth of interaction measurement capability, the number of lines of response can very quickly become overwhelming for any conventional memory and computation resource. For instance, the number of independent LORs in the small animal imaging system investigated here is about $3*(6*70*62)^2$, or about 2 billion. To reduce the matrix sizes involved in normalization and reconstruction, LORs involving detectors beyond those closest to the center of the detector system can be re-binned to detectors nearest to the FOV.

Methods

The Monte Carlo package GATE (GEANT4) was used to generate the data reported in this study. The imaging system simulated is a box-shaped small animal PET system constructed of thin (~300 μm) position-sensitive avalanche photodiodes (PSAPDs) coupled to 1mm x 1mm x 3mm Lutetium Oxyorthosilicate (LSO) scintillation crystals forming an 8x3 array (dimensions 8mm x 9mm), giving the system ~ 1mm trans-axial, 1.3 mm axial and 3mm depth of interaction positioning capability.

The intrinsic efficiency variation in the detector pairs were not modeled in the Monte Carlo data, so the normalization coefficient reduces to the following geometric factors:

$$g_i = (g_{rad})_i (g_{ax})_i (g_{int})_i \qquad (4)$$

where g_{rad} are the 'radial geometric factors', g_{ax} are the 'axial geometric factors', and g_{int} are the 'interference geometric factors'. These are the factors that will be included in this study and will be compared to a direct normalization technique.

Preliminary Results
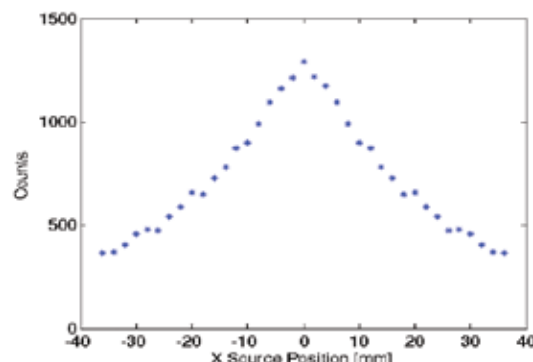
Figure 1. Radial geometric factor: counts plotted vs. source location in the field of view. The source was moved along the line of response between two crystals.
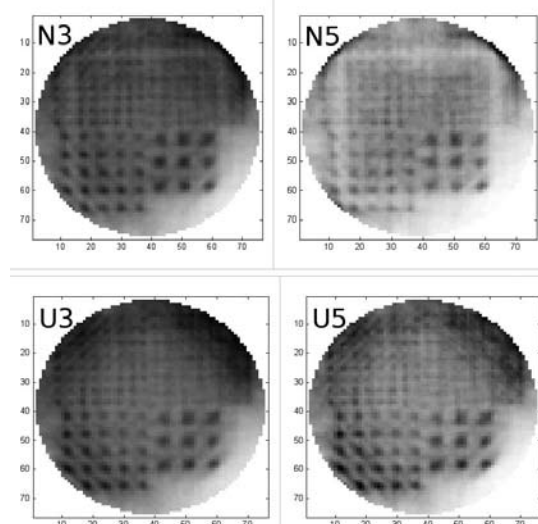
Figure 2. ML-EM reconstructed images of resolution phantom with and without normalization for iteration 3 and 5. U: un-normalized, N: normalized, 3 or 5: number of iterations of reconstruction performed.

Conclusions

Separating the factors of the normalization coefficients can be used not only to accurately determine the amount that a particular line of response must be adjusted to obtain quantitative reconstructed images, but also helps to illuminate the design factors affecting construction of a detector system. We have observed the large effect of radial geometric factors (3.25 center to edge count ratio).

References

1. Ollinger, JM, "Detector Efficiency and Compton Scatter in Fully 3D PET" *IEEE TNS Vol 42, No 4 (1995)*

Simulation and Measurement of Gamma Ray and Annihilation Photon Imaging Detectors

F. Habte[1], P. D. Olcott[1], A. M. K. Foudray[1,2], C. S. Levin[1] - [1]Molecular Imaging Instrumentation Laboratory, Department of Radiology, Stanford University; [2]Department of Physics, University of California at San Diego

Introduction

To model the performance of nuclear medicine imaging instrument, Monte-Carlo simulation packages are used to generate particles (photons) and to calculate the probability distribution of photoelectric or Compton interactions in tissue or scintillation crystal. The propagation of light photons generated from each interaction of gamma ray or annihilation photon within the scintillation crystals is also simulated. The time, energy, and position of each interaction are processed according to the physical, observable detector response. Most simulation tools assume an ideal position sensitive detector surface and the actual physical geometry and sensitivity variation of each detector are generally not modeled. To recover the actual signal response of a detector from simulation, the physical geometry and sensitivity variation of each position sensitive detector has to be modeled. In this work, we modified and incorporated photodetector response in the Detect2000 simulation package [1] that models optical photon transport in scintillation material to include typical detector parameters such as anode plane dead area and spatial non-linearity to realistically compare simulation results to experimental data.

Material and methods

Flood irradiation measurements were performed for two detector systems. The first uses Lutetium oxyorthosilicate (LSO) and NaI(Tl) crystal arrays that are coupled to a position sensitive photomultiplier tube (PSPMT). The LSO crystal array consists of 23x23 crystals each of 2x2x3 mm^3 and the NaI(Tl) crystal array is packaged with 29x29 crystals each 1.5x1.5x6 m^3 on a 1.7 mm pitch. A white reflector was applied between each of the crystals. Both LSO and NaI(Tl) crystal arrays were irradiated using Co-57 (122 keV) source. The second detector system uses 4x3 array of 2x2x3mm^3 LSO crystals and PSAPD photodetector. Flood measurement is performed using a Na22 (511keV) annihilation photon source. The simulation software developed combines two Monte-Carlo simulation codes to generate interaction gamma photons and to simulate light transport of optical photons generated from each interaction in the defined crystal geometry. DETECT2000 is used to simulate the light transport for a given crystal array. The input and output parameters of DETECT2000 have been modified to include physical characteristics of a particular photodetector (PSPMT or PSAPD).

Results

Fig. 1 shows the comparison of [57]Co flood images from simulation and measurements using LSO crystal array and a PSPMT detector. After the size and dead spaces between each anode of the 8x8 anode PSPMT has been modeled, the simulation result (Fig. 1b) better matched experimental measurements (Fig. 1c). In both cases, 21 x 21 crystal array could be resolved when energy gating is applied, while the "ideal" detector (Fig.1a) resolved 22x22 crystals that cover the sensitive 5x5cm^2 area of the PSPMT. The peak location of the flood images from simulation and measurement matched very well (Fig.1d). Similarly, simulation and
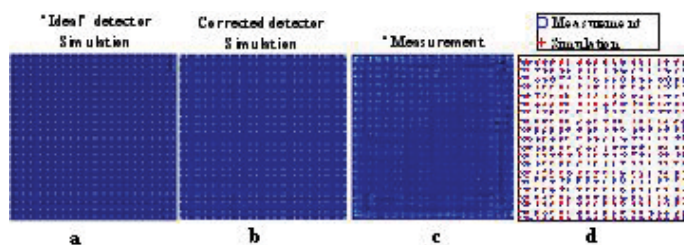

Fig. 1 Flood images of LSO crystal array (23x23) coupled to 5x5cm^2 FOV PSPMT: a) Simulation assuming an "ideal" detector, b) Simulation after the size and dead area has been modeled, c) Measurement using Co-57 single photon source and d) Peak coordinates of flood images of LSO crystal array coupled to PSPMT from corrected simulation (red) and measurement (blue).
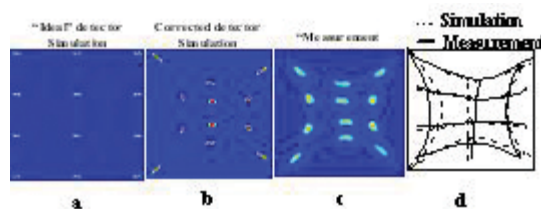
Fig. 2, Flood image using LSO coupled to PSPAD of a) "Ideal" detector simulation, b) Corrected simulation, c) Measurement and d) Peak coordinates of simulation and measurement of PSAPD detector

measurement with the NaI(Tl) crystal array also resolved 27x27 crystals after energy gating was applied. Both simulated and measured data showed near perfect match with similar edge effect.

Fig. 2 shows the flood images obtained from simulation and measurement using the 4x3 LSO crystal array coupled to a PSAPD. A third order polynomial fit to the PSAPD finite element model is applied to map the simulation data to the actual detector response (Fig. 3b). The result provided a better match to the measured data (Fig. 3c) compared to the "ideal" detector model (Fig. 3a). Peak coordinate location are plotted (Fig. 3d) to show the match between the simulation and measurement.

Conclusion

Accurate simulation data generally lead to a more accurate design of imaging systems. Accurate modeling of crystal identification and edge effects of each detector in simulation allows one to easily study the detector performance when two or more detectors are combined together. We have developed more accurate model of a scintillation detector array that compares very well to measured flood data.

Reference

1. F. Cayouette, et al., IEEE Trans. Nucl. Sci, Vol. 49, No 3, June 2003.

Light Multiplexing Techniques for 1 mm Resolution Positron Emission Tomography Detectors

F. Habte, P. Olcott, J. Zhang, C. S. Levin - Molecular Instrumentation Laboratory, Department of Radiology

Introduction

Dedicated compact PET systems for breast and small animal imaging are being developed based on Lutetium oxyorthosilicate (LSO) scintillation crystals coupled to position sensitive avalanche photodiodes (PSAPDs). The design goals are 1 mm^3 volumetric spatial resolution and >12% coincidence detection efficiency (system sensitivity). Thousands of highly compact PSPADs (~200μm thick and 8x8 mm^2 active area) will be needed to densely pack arrays of 1x1x3 mm^3 LSO crystal in novel detector configurations that allow high photon detection efficiency, ~ 3 mm interaction depth resolution, and at the same time >95% light collection efficiency that is independent of light origin. The PSPADs used in our system dominate the total system cost. In this work, methods to multiplex scintillation light from LSO array crystals are investigated to reduce the number of PSAPDs at least by a factor of two without significantly compromising the system performance.

Material and Methods

Experiments have been performed to read two layers of LSO arrays using only one PSAPD (Figure 1). A 3x3 array of polished 1x1x3 mm^3 LSO crystals was optically coupled to the PSAPD and a 2x3 array of the same LSO crystals was offset by 0.5 mm and placed on the top of the 3x3 array.
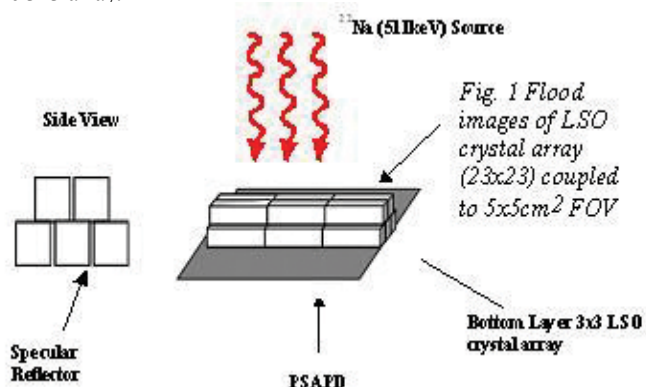

Figure 1: Right: Two layers of LSO arrays, 3x3 bottom layer and 2x3 top layer arranged to be read by a single PSAPD. Top layer is offset by half of the width along the 1mm dimension of the 1x1x3 mm^3 LSO crystals. Left: side view showing the 25micron thick spectral reflector placed between the crystals along the 1x3mm long side of the crystal array.

A 25-micron thick specular reflector was placed between crystals to reduce the light sharing between adjacent sides and guide the light from the top crystals uniformly between the bottom crystals into the PSAPD. A flood image was taken using a ^{22}Na (511 keV) source with and without top crystals.

Results

Figure 2 shows flood images for two array layers (Left) and single array layer (middle) of the LSO crystal arrays using a ^{22}Na source after energy gating of individual crystals was applied. All crystals are resolved. Figure 2 (Right) shows the middle column profile for both images. An average peak to value ratio of 3:1 is obtained for the two-layer LSO array and 8:1 peak to valley ratio for the single layer.
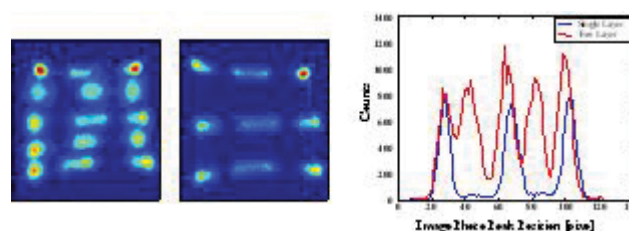
Figure 2: Left: Energy gated flood image for two layer LSO crystal arrays, Middle: Single layer energy gated flood image, and Right: Profile through middle columns.

The individual crystal energy spectra were extracted from the flood images after image segmentation is applied to individual crystal. An average energy resolution of 15.5±2.5% for bottom layer and 16.9±3.5 top layer was obtained. Calculations predict that the average energy resolution of the two layer arrangement is expected to improve to 13% when a continuous double layer LSO crystals is used with cuts offset with respect to top and bottom layer. For the two-layer LSO crystal array, a systematic photopeak pulse height difference between the top and bottom layers is clearly seen (Figure 3).
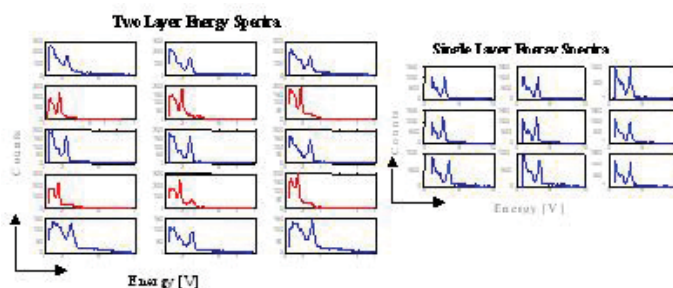
Figure 3: Energy Spectra, Left: for two layers LSO array, Right: for single array. Pulse heights were clearly resolved between top (red) and bottom (blue) spectra

Conclusion

Results show that multiplexing scintillation light from two 1 mm thick crystal layers to only one PSAPD is possible using two layers of LSO crystal arrays offset to each other by half the crystal width and separated by a specular reflector. Work is in progress to optimize the system by performing experimental and simulation studies considering additional factors such as crystal surface treatments, reflectors, and crystal arrangements.

Effect of Detector Configuration and Physical Factors on Sensitivity of a High-Resolution Positron Emission Tomography

F. Habte[1], A. M. K. Foudray[1,2], and C. S. Levin[1], J. Zhang[1] - [1]Molecular Imaging Instrumentation Laboratory, Department of Radiology, Stanford University; [2]Department of Physics, University of California at San Diego

Introduction

For practical reasons in most PET systems, rectangular block detectors (detector modules) consisting of arrays of scintillation crystals are used in a cylindrical geometry (Figure 1). For PET systems with small diameter (8 cm) small detector modules are used, which produces significant number of inter-module gaps. Simulations showed that for small system diameter, arranging rectangular detectors in a cylindrical geometry is not optimal. This is due to the inter-detector module gaps allowing significant number of detector scattered photons to escape, limiting the system sensitivity. The effects of detector configuration and other physical parameters are studied to optimize the sensitivity of a small animal PET system, which is being developed.

Figure 1: Cylindrical detector configuration

Materials and Methods

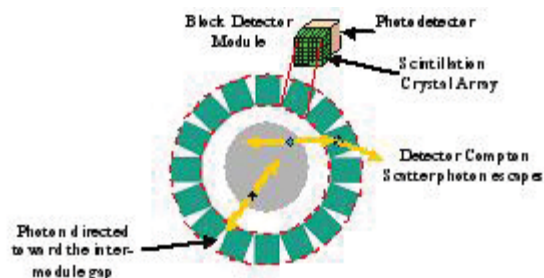Two new high-resolution PET detectors are being considered for developing small animal PET system. The first is based on pixellated Lutetium Oxyorthosilicate (LSO) crystals coupled to a position sensitive photodiodes (PSAPD). The second uses Cross strip Cadmium Zinc Telluride (CZT) semiconductor detector. Rectangular detector modules were formed using arrays of LSO-PSAPD or CZT detectors allowing different detector configurations (Figure 2). Simulation is performed using Gate (GEANT4 Application for Tomographic Emission), a validated software package for PET/SPECT [1].

Results

Figure 3a compares the sensitivity of different detector configurations using LSO-PSAPD detectors for a fixed 8 cm diameter. It shows that the Compton scatter plays a major role in limiting the sensitivity of a particular detector configuration. The sensitivity due to direct photoelectric absorption remains nearly constant independent of system geometry. An average geometric efficiency of 78% was calculated for detector configuration that use six or more detector modules showing that the geometric sensitivity does not improve significantly as the number of detector modules increase towards a cylindrical geometry (Figure 3b).

Discussion and Conclusion

A maximum sensitivity of ~ 11% was obtained using LSO-PSPAD, when using only four detector modules with four corner gaps in box geometry (Figure 2). This is due to the relatively high geometric effi-
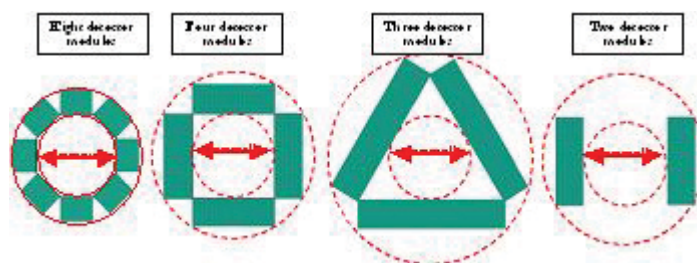
Figure 2: Illustration of detector configuration using Eight, four, three and two detector-modules (or Heads) in an 8 cm Field of View (FOV)
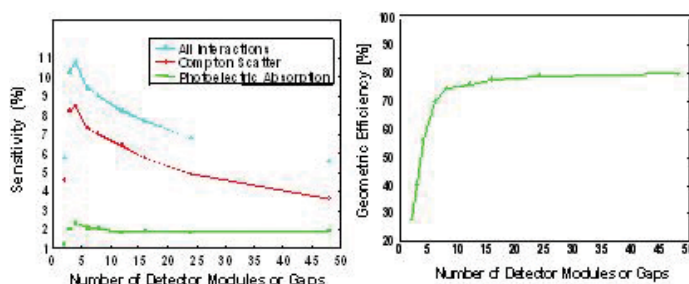
Figure 3: Sensitivity (a) and Geometric Efficiency (b) for different number of detector-modules using LSO-PSPAD detectors.

ciency and fewer inter-detector gaps, which improves the probability of photon interactions in the detectors. As the number of detector modules increases the sensitivity drops due to increased number of inter-module gaps, which provide a path for direct or scatter photons to escape. A similar result was also obtained using a CZT detector. Maximum sensitivity of ~14% is obtained for a box detector geometry using only four detector modules with four corner gaps. To optimize the sensitivity the four corner gaps of a box geometry was filled with detectors forming "Full Box" geometry that provided better than 17% sensitivity for point source at the center of field of view. Simulated sensitivity of "Full-Box" geometry as function of coincidence time and energy window was also evaluated. The sensitivity saturates at the coincidence time window greater or equal to twice the time resolution of the detectors used (2 ns FWHM for LSO-PSAPD and 8 ns CZT). Simulation also verified that increasing the energy window for CZT detector has less effect on sensitivity compared to using LSO-PSAPD detectors due to good energy resolution of CZT (3%) compared to LSO (12%). Compared to standard cylindrical geometry, the "Full Box" geometry showed more than 4 and 7 fold improvement in sensitivity using LSO-PSAPD and CZT detectors in an 8 cm FOV.

Reference

1. D. Strul, et. al. " *Nucl. Phys. B (Proc. Suppl.)* 125 (2003) 75-79

Comparing Geometries for PET Systems with Depth of Interaction

Garry Chinn, Angela Foudray, and Craig Levin – Molecular Imaging Instrumentation Laboratory

Introduction

A box geometry has been shown to have twice the sensitivity of a ring geometry system for a comparable FOV [1]. However, the box system also has non-uniform depth-of-interaction artifacts. In this study, we compared the resolution and signal-to-noise ratio (SNR) of reconstructed images for a ring system and a box system. A computer observer ROC study was also performed to compare the systems for lesion detection applications.

Method

The SNR for Bayesian (or penalized maximum likelihood) reconstruction can be estimated by using the Fisher information matrix (FIM) for a Gaussian approximation of the measurement noise model. The direct normalization method was used for these calculations. A ring source was used for the ring system and a box source was used for the box system. GATE (Monte Carlo software) was used to simulate the normalization scans. Computations were performed for a two-dimensional system because of the high computational costs involved in inverting the FIM and error covariance matrix.

Non-prewhitening (npw) and prewhitening (pw) computer observers [2,3] were used for the ROC study. A human observer is likely to perform between these computer observers. If the reconstructed image is Gaussian distributed, the SNR of the test statistic is directly related to the area under the ROC curve (AUC) [3].

To compare the SNR and lesion detection performance, a series of single lesion phantoms were simulated with Gate. A 2 mm diameter cylindrical rod was placed inside a 5 cm water cylinder with a 5:1 contrast ratio (lesion to background). The lesion was placed at a radial position of 0 cm (center) and 2 cm. Because of the asymmetries of the box, lesions were also placed along a diagonal as shown in Figure 2. To compare the resolution of the system, a phantom with 1.5, 2, 3, and 4 mm diameter rods was used.

Results

The MSE and CRC are presented in Table 1. The box geometry produced a lower MSE than the ring geometry with only a slight loss of contrast recovery. With normalization, the box system is expected to be comparable to the ring geometry.

Figure 1 shows images reconstructed without normalization. Component based normalization is being developed in a separate study and is expected to reduce the artifacts caused from positioning the detectors close to the animal subject.

Table 2 compares the systems for lesion detection using computer observer models. Again, the box geometry was shown to be superior to the ring geometry.

Conclusions

The box geometry has superior MSE. For lesion detection SNR, the ring geometry is superior near the center of the field of view. For lesions away from the center, the box geometry has a better lesion detection SNR than the ring geometry.
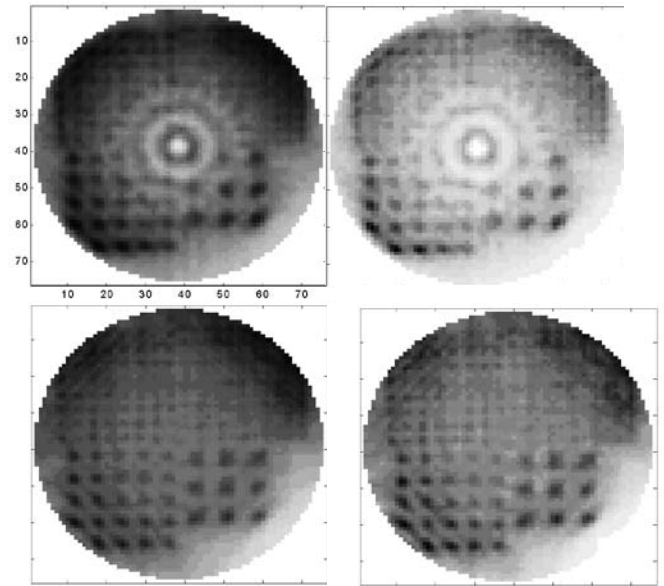
Figure 1. A low-count resolution phantom was reconstructed using the ML-EM algorithm and 1 mm pixels for the ring (top row) and box (bottom row)) for 3 (left column) and 5 (right) iterations without normalization. The rods in the four quadrants (1 to 4) were 1.5, 2, 3, and 4 mm diameter spaced center-to-center at twice the diameter of the rods.

	Ring geometry		Box geometry		
	(0,0)	(2,0)	(0,0)	(1.4,1.4)	(2,0)
MSE	1	1.39	.14	.11	.10
CRC	1	0.98	0.92	1	0.99

Table 1. The mean square error (MSE) and contrast recovery coefficient (CRC) were calculated for single lesion phantoms in both the ring and the box geometry. The MSE was normalized to the (0,0) lesion for the ring geometry. The box geometry showed 7-14 times improvement in MSE over the ring geometry. The CRC was more uniform for the ring geometry.

	Ring geometry		Box geometry		
	(0,0)	(2,0)	(0,0)	(1.4,1.4)	(2,0)
SNR pw	1	0.57	.84	.75	.77
SNR npw	0.02	0.01	0.13	0.11	0.10

Table 2. The computer observer signal-to-noise ratio for the prewhitening filter test statistic (SNR pw) and the non-prewhitening filter test statistic (SNR npw) for the single lesion phantoms were computed. The SNR has been normalized to the (0,0) lesion SNR_pw for the ring geometry. It appears that the box geometry provides a higher detection SNR for lesions away from the center of the field of view.

References

1. A. M. K. Foudray, F. Habte, G. Chinn , J. Zhang, C. S. Levin, P. D. Olcott, "Optimization of a Cylindrical PET Breast Imaging System Comprised of Position Sensitive Avalanche Photodiodes Utilizing Monte Carlo Simulation" Presented at the 2004 IEEE Breast Imaging Workshop, Oct 22-24, 2004, Roma, Italy.
2. H.H. Barrett, "Objective assessment of image quality: effects of quantum noise and object variability," JOSA A, vol. 7, pp. 1266-1278, July 1990.
3. J. Qi and R.H. Huesman, "Theoretical study of lesion detectability of MAP reconstruction using omputer observers," *Trans. Med. Imaging*, vol. 20, pp. 815-822, 2001.

Iterative Reconstruction Methods for Depth of Interaction PET Systems

Garry Chinn, Angela Foudray, Frezghi Habte, Jin Zhang, and Craig Levin - Molecular Imaging Instrumentation Laboratory, Department of Radiology

Introduction

The conventional ring geometry does not optimize performance for specialized positron emission tomography (PET) applications. In the Molecular Imaging and Instrumentation Lab, we are developing detector modules with depth of interaction capabilities. These detector modules can be brought in close to the animal or patient in order to increase sensitivity. In this project, we are developing iterative image reconstruction for three-dimensional data sets from systems with depth of interaction capabilities.

Methods

Data sets were simulated using the Monte Carlo simulation software called GATE. Two systems were simulated using PSAPD (position sensitive avalanche photodiode) detector modules: a dual panel system and a small animal box system. Also a CZT (cadmium zinc telluride) box system was also simulated.

Histogram reconstruction [1-2] and list-mode [3] reconstruction methods are being implemented using the maximum-likelihood expectation maximization (ML-EM) approach. For depth of interaction systems, there are a very large number of different lines of responses measured by the system. The histogram data set is prohibitively large. In these experiments, events at greater depths of interaction are rebinned to the inner diameter of the system to reduce the data size; this is called the *reduced histogram data set*.

List-mode reconstruction can be used to preserve the full sampling of depth of interaction systems. However, list-mode reconstruction is slower than reconstruction using the reduced histogram data set for high count studies. We intend to compare the performance of the two approaches for various geometry systems.

Preliminary Results

A resolution phantom was simulated for the animal system using a box configuration for both PSAPD detector modules and CZT detector modules. A high resolution rod phantom was simulated for the CZT system. Images were reconstructed using both filtered backprojection and the ML-EM algorithm and are shown in Figure 1.

The PSAPD-based animal system was simulated using a simple phantom containing multiple point sources of varying sizes and positions. Images were reconstructed by the ML-EM algorithm are shown in Figure 2. Shown are nine different slices of the phantom. Each slice is 1 mm thick. In the first two slices at the top of the figure, there are two point sources. Because of partial volume effects, one of the point sources is barely visible. In the next frame, one of the point sources is barely perceptible because of partial volume effects. The next two frames are blank. the final four frames contain a larger point sources. Because of partial volume effects, the intensity of the point source appears to be different at each slice.

Conclusions

We have developed a general-purpose three-dimensional image reconstruction package that supports both histogram and list-mode reconstruction for arbitrary geometry systems. We have reconstructed images
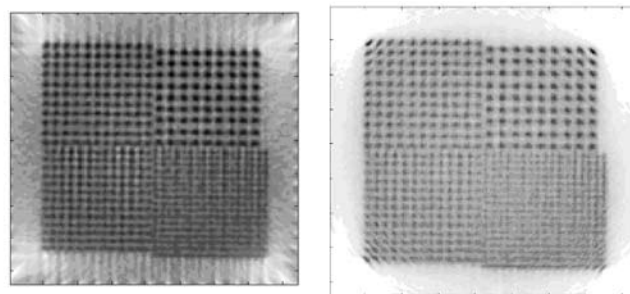
Figure 1. A high-resolution rod phantom reconstructed by (left) filtered backprojection using a Hanning filter and (right) 40 iterations of ML-EM for the CZT box system. The rods 1.75, 1.5, 1.25 and 1.0 cm in diameters.
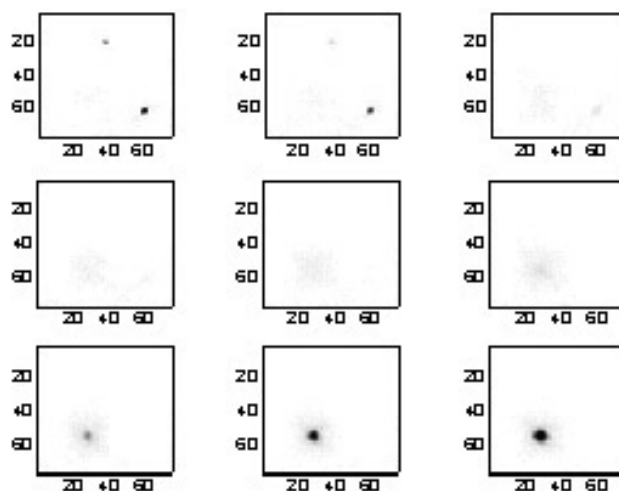
Figure 2. The PSAPD animal system was simulated with GATE using a multiple point sources of varying sizes and positions. Shown are nine 1.0 mm (slices) planes of a phantom with various point sources were reconstructed by 4 iterations of list-mode EM reconstruction. In the first two frames, two small point sources are visible with partial volume effects. In the last four frames, a larger point source is visible with varying degrees of partial volume effects.

for Monte Carlo simulated data for three geometric PET configurations: box, ring, and parallel slab.

References

1. Y. Vardi, L. A. Shepp, and L. Kaufman, "A statistical model for positron emission tomography," *J. Amer. Stat. Assoc.*, vol. 80, pp. 8-37, 1985.
2. P. J. Green, "Bayesian reconstructions from emission tomography data using a modified EM algorithm," *IEEE Trans. Med. Imaging*, vol. 1, pp. 113-122, 1982.
3. A. Rahmim, M. Lenox, A.J. Reader, C. Michel, Z. Burbar, T.J. Ruth, and V. Sossi, "Statistical list-mode image reconstruction for high resolution research tomography," Physics Med. Bio., vol. 49, pp. 4239-4258, 2004.

Finite Element Model Based Spatial Linearity Correction for Scintillation Detectors that use Position Sensitive Avalanche Photodiodes

Peter D. Olcott, Jin Zhang, Craig S. Levin - Molecular Imaging Instrumentation Laboratory, Department of Radiology

Abstract

We have developed a method using polynomial correction derived from a finite element model (FEM) to correct spatial linearity of scintillation detectors that use Position Sensitive Avalanche Photodiodes (PSAPD). A PSAPD is a planar avalanche photodiode with a resistive coating that allows continuous, but non-linear, positioning of scintillation light pulses over the entire active area. The spatial response of a scintillation crystal array coupled to a PSAPD shows a characteristic pincushion distortion. A finite element simulation was used to derive the spatial response function for the PSAPD detector, and then used to calculate a polynomial linearity correction function. The pincushion distorted peaks in the 2-D crystal positioning histogram make it difficult to segment corner array crystals. The derived polynomial correction will remove the pincushion distortion and improve the accuracy of crystal segmentation that is used to generate a positioning lookup table. After correction, the pincushion distortion was removed and we were able to segment all 24 crystals of an 8x3 array of 1x1x3 mm3 crystals correctly versus only 20 when uncorrected. This spatial linearity correction is useful for both discrete arrays and continuous crystals coupled to the PSAPD.

Methods

We are building a PET detector that uses pixellated scintillation crystals coupled to PSAPDs. Using a flood-field image of the crystals one generates a linear spatial map of a non-linear response through segmentation of the crystal pattern seen in the image. Simple segmentation algorithms have problems correctly segmenting distorted crystals in the corners of the array because of very large non-linearity in the spatial response of the PSAPD and the non-circularly symmetric light distribution.

A finite element simulation used a 100x100 element approximation of the resistive sheet connected by finite impedance at the four corners of the array. A steady state test current was injected at each node of the finite element and a vector value function that mapped the <X,Y> location of the point current to the <X,Y> position recorded at the detector was determined. A two dimensional, 3rd order polynomial was fit to the simulated data. The inverse of the coefficient matrix of the polynomial was used to map the vector valued spatial <X,Y> position recorded on the detector to a linear <X,Y> square An 8x3 array of 1x1x3mm3 lutetium oxyorthosilicate (LSO) crystals was placed on a 8x8 mm2 active area PSAPD. A 10uCi 22Na source flood irradiated the array at 1cm and a crystal flood histogram with approximately 250k events was segmented using a minimum distance-to-peak segmentation algorithm before and after polynomial correction.
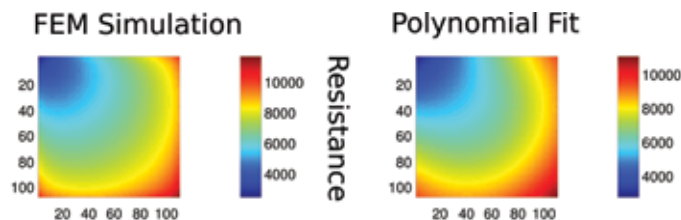
Figure 1. (A) Simulation and (B) 3rd order polynomial fit showing the resistance of one corner as a function of input current. The third order polynomial approximates the surface well, except for at the edges and the corners due to singularities in the boundary conditions.
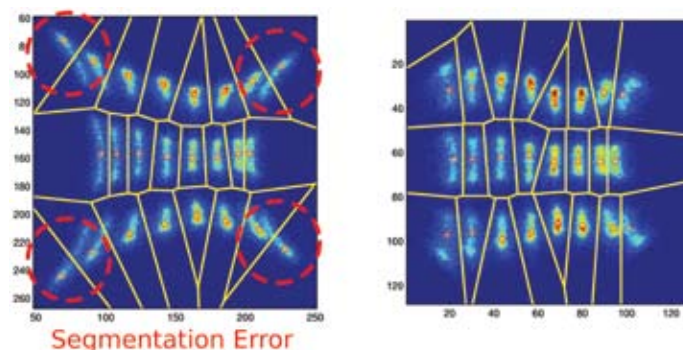
Figure 2. Segmentation of a flood histogram of a uniform irradiation of a 1x1x3 mm3 LSO crystal array before and after polynomial correction.

Results

The PSAPD spatial position vector valued function is not truly invertible because of the singularities in the 4 corners. A polynomial must be rational to perfectly fit the surface that is in the form of $A<x,y>/B<x,y>$. Fortunately complete inversion is not necessary to correct for most of the spatial non-linearity of the PSAPD, and a polynomial of the form $A<x,y>$ is all that is necessary.

Conclusions

The polynomial correction was enough to correct the non-linear spatial response function of the PSAPD to allow for correct segmentation of all 24 crystals. We are also exploring the use of this correction technique for continuous crystal sheets instead of discrete crystal arrays.

Charge Multiplexing Readout for Position Sensitive Avalanche Photodiodes

Peter D. Olcott, Craig S. Levin, Jin Zhang - Molecular Imaging Instrumentation Laboratory, Department of Radiology

Abstract

A novel technique to charge-multiplex multiple position sensitive avalanche photodiodes (PSAPD) has been studied. We have observed that with multiplexing the spatial resolution is slightly degraded, but the energy and time resolution are not affected. This charge multiplexing technique will reduce the number of readout channels required by a factor of two. A PSAPD is a new silicon semiconductor photodetector that may be used to replace a photomultiplier tube in PET or SPECT systems. It is a planar avalanche photodiode with a resistive coating that allows continuous positioning over the entire active area. PSAPDs are currently fabricated with active areas that range from 8x8mm^2 and higher. The proposed PET system detectors comprise 1mm lutetium-oxyorthosilicate (LSO) crystals coupled to extra thin PSAPDs. Non-multiplexed, these detectors have achieved excellent spatial resolution (<1mm^2), energy resolution (<10%), and time resolution(<2ns). Unlike a position-sensitive PMT, the electronic amplification of a PSAPD is only on the order of 1000, which makes it challenging to charge multiplex multiple devices. We measured the effects of charge multiplexing using a 3x3 array of 2x2x3mm3 LSO crystals coupled to one PSAPD that was capacitively coupled to a second PSAPD device. Measured peak-to-valley ratios in the crystal flood histogram were 2.5:1 before and 2.0:1 after multiplexing; energy resolution at 511keV was 11.9+/-0.2 before and 11.8+/-0.2 after.

Methods

A 3x3 array of 2x2x3mm2 lutetium-oxyorthosilicate (LSO) crystals (ground on all sides except for a polished bottom) were coupled end-on to a 8x8mm2 PSAPD device. Flood acquisitions with a 10 uCi 22Na source (511keV and 1275keV) placed at 1cm distance were taken before and after adding a second 8x8mm2 PSAPD device to the multiplexed socket. Each PSAPD device was biased with -1740V and was connected to charge multiplexed Cremat110 low noise preamplifiers for the spatial readout channels and independent energy and time readout channel. Only three of the spatial channels and the common preamplifier signals were fed into an Ortec Gaussian shaping amplifiers (500ns shaping constant) and digitized using a National Instruments 12-bit 4-channel simultaneous sampling ADC. The individual crystals seen in raw flood acquisitions were segmented using a minimum distance-to-peak qualifier algorithm and energy gated to produce the final crystal positioning histogram.

Results

Peak-to-valley before multiplexing was 2.5:1 versus 2.0:1 after. Mean energy resolution before multiplexing was 11.9+/-0.2% while after multiplexing was 11.8+/-0.2%. Best single crystal energy resolution for the center crystal was 11.3+/-0.5 % before versus 11.8+/-0.5% after multiplexing.
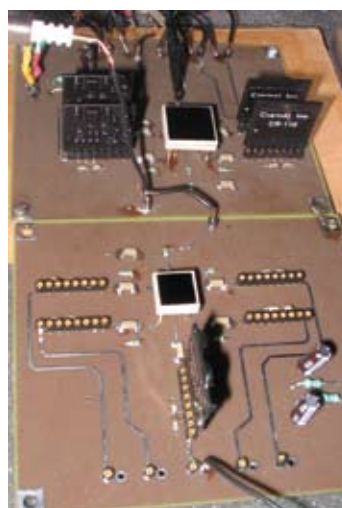
Figure 1. Charge multiplexing readout prototype board with two PSAPD devices populated in separate sockets. The PSAPDs are shown in two different sizes, 14x14mm^2 (top) and 8x8 mm^2 (bottom). The 4 spatial channels are connected together underneath the PCB board), while the common energy and time channel connection is independent.
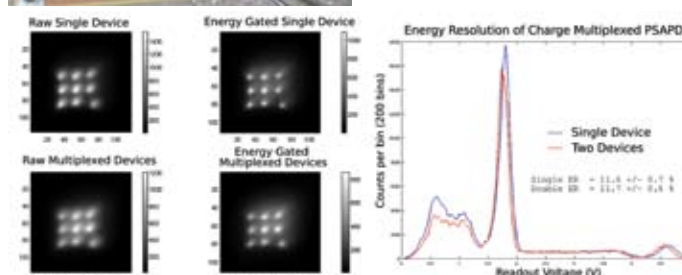
Figure 2. (left) Raw and 2xFWHM energy gated 2-D Flood histograms for a 3x3 LSO array with 2x2x3mm3 crystals with no inter-crystal reflector or gaps. The 9th crystal is offset from the array because of poor reflector coverage in the corner, not from the readout. The decreased crystal identification performance of the device does not prevent segmentation of the crystals. (right) Energy resolution for the center crystal before and after multiplexing two devices. The energy resolution is virtually unchanged.

Conclusion

Using multiplexing, the spatial degradation did not significantly degrade our ability to segment the 3x3 LSO crystal array for crystal identification. At the same time, the charge multiplexing technique did not degrade the energy resolution of either of the two multiplexed devices.

Design of a Data Acquisition System for Position Sensitive Avalanche Photodiode 3D-PET Systems Using Event-based Simulations

PETER D. OLCOTT, CRAIG S. LEVIN, JIN ZHANG - MOLECULAR IMAGING INSTRUMENTATION LABORATORY, DEPARTMENT OF RADIOLOGY

ABSTRACT

We have developed a time accurate event simulation and visualizations of software package for the data acquisition (DAQ) system used in a dual panel lutetiem-oxyorthosilicate (LSO) position sentive avalanche photodiode (PSAPD) positron emission tomography (PET) scanner for dedicated breast cancer imaging. We are using this simulation to design a listmode DAQ system that uses a highly multiplexed ASIC to reduce the number of readout channels. Using a monte carlo simulated positron source in air, our DAQ architecture simulation predicts that we should be able to detect 1.4 million coincident annihilation photons/sec with a 16% system sensitivity using an open energy window while over 600 million photon interactions/sec on are ocurring. Our simulation predicts that the bottleneck that determines DAQ throughput has moved from the front-end electronics to the backend ADCs.

INTRODUCTION

A PET data acquisition system converts the scintillation light recorded from a pair of high energy (511 keV) annihilation photon interactions into a single coincident event localized to a line of response (LOR). We are developing a system comprised of densly packed LSO scintillation crystals coupled to PSAPDs that have a full 3D detection volume (2D plus depth of interaction) for high energy photon photoelectric and Compton interactions. By correcting parallax error from the recorded depth of interaction location, the detector panels can be brought into close proximity to the patient which significantly increases the sensitivity (the fraction of coincident photons detected). High sensitivity will generate a very large photon interaction event rate that a PET DAQ system must process to extract the coincident interactions.

METHODS

An accurate event simulation models the time dependent behavior of events that flow through a finite number of connected components. The connected components represent the actual physical elements of the DAQ system. Events represent the physical state of each component as a function of time. Only a single event or state can exist on any one component at any instant in time. Visualizing the collisions, the mechanisms that lead to the pile-up and saturation can be corrected by different hardware configurations or improved software algorithms.
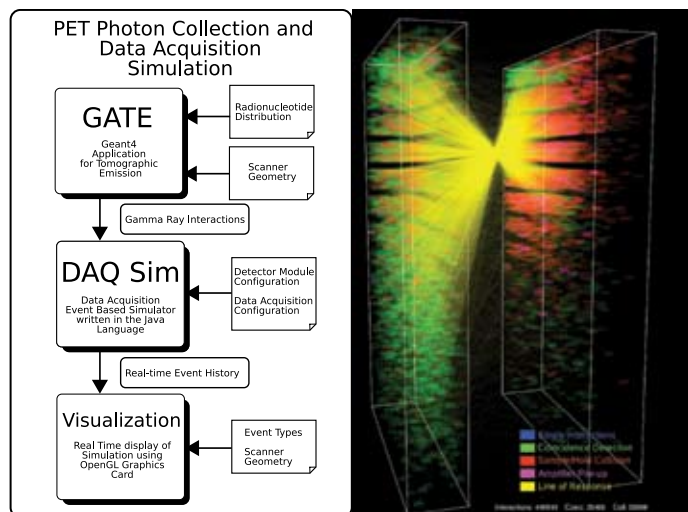
Figure 1. (left) Block diagram of the simulation package. (right) A simulated 200uCi point source is in close proximity to a panel to illustrate the high collision rate (red and magenta boxes). The DAQ system is able to resolve the coincident lines of response (yellow lines connecting green boxes).

RESULTS

The peak coincident event rate is 1.4 million events/second with over 600 million interactions events/per second at 4 cm and 8 cm of panel separation when using a wide 150keV – 650keV (12% FWHM simulated detector energy resolution at 511 keV) open energy window and a 6 ns time window (2 ns FWHM simulated detector time resolution). A wide energy window is used to maximize the event rate, and allow for better offline software energy gating and advanced positioning algorithms.

CONCLUSION

Our DAQ architecture can handle the extremely high event rates that are experienced when bringing PET detectors into close proximity of the activity.

The feasibility of a List mode PET data acquisition will allow for advanced positioning algorithms and for very accurate time correlated data for dynamic PET protocols.

Performance Characterization of a Miniature, High Sensitivity Gamma Ray Camera

P. D. Olcott, F. Habte, Member, C. S. Levin, A. M. Foudray - Molecular Imaging Instrumentation Laboratory, Department of Radiology

Abstract

A compact, hand-held gamma camera with excellent intrinsic and extrinsic performance has been developed for the rapid identification and localization of the sentinel lymph node during the surgical staging of cancer. A goal for this device is an image acquisition time of five seconds or less to allow the surgeon to easily search for points of interest without excessive motion blurring. The camera comprises a 5x5 cm2 field of view NaI (Tl) pixellated crystal array, a high sensitivity (2.0 cm thick) hexagonal parallel-hole collimator, a position sensitive photomultiplier tube (PSPMT), and a novel highly multiplexed electrical readout. The good intrinsic energy resolution (12.1±2.0%) at 140 keV including edge crystals, extrinsic sensitivity (5 cps/µCi with 24% energy window) and extrinsic spatial resolution (1.81+/-0.02 mm at 0.5 cm) facilitate rapid identification of a hot node. Using a node phantom we performed an ideal observer study to estimate the detectability of sentinel lymph nodes with different exposure times. The camera can detect a 3 mm diameter sphere phantom at a depth of 3.6 cm with 1µCi of Tc-99m in a cold background, and a 4 mm diameter sphere with 2µCi at 2.6 cm with a warm background in a 5 second exposure duration.

Methods

Simulated frames of different exposure times were derived from the 120-second acquisitions taken at different depths and different background contamination concentrations. The lambda parameter of a Poisson distribution was estimated with 95% confidence intervals from the frames for each sphere phantom size and at each depth.

Results

A 3 mm sphere was detectable at 3.6 cm depth in 5 seconds with approximately a 1 µCi total activity in a cold background with a 78+/-6 % true positive probability. In a warm background of 160 µCi total, a 4 mm sphere could be detected at 2.6 cm of depth with 85+/-1 % true positive probability.

Conclusion

This hand-held scintillation camera has good intrinsic and extrinsic performance. The pixellated scintillation crystal array provides good spatial resolution, sensitivity, and energy resolution. Using an ideal observer, the camera was able to resolve 3 mm diameter spheres with sufficient detectability for it to be useful tool for locating a sentinel lymph node during the surgical staging of cancer.
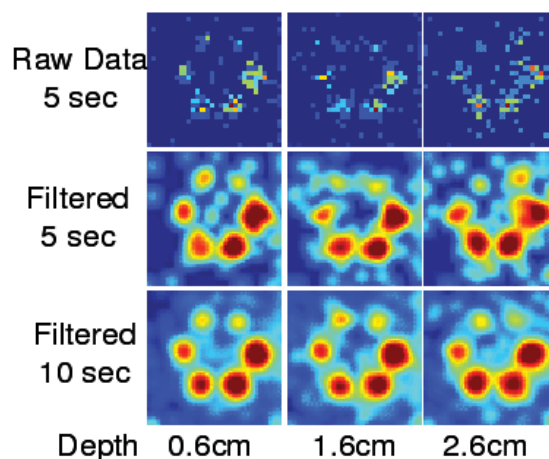
Figure 1. Sphere phantoms were placed at different depths in a water scattering medium. Acquisitions were taken with only 5 or 10 second frames

Figure 2. Conceptual rendering of the hand-held Gamma Camera.

Performance Characterization of a Novel Thin Position-sensitive Avalanche Photodiode for a 1 mm³ Resolution PET Camera

Jin Zhang, Angela M.K. Foudray, Peter D. Olcott, and Craig S. Levin, – Department of Radiology and Molecular Imaging Program

Introduction

Semiconductor based photodetectors show promise to improve performance of ultra-high resolution positron emission tomography (PET) systems due to their high quantum efficiency and compactness. A novel, extremely thin (230 micron) silicon based position-sensitive avalanche photodiode (PSAPD) has been developed and compared to a standard PSAPD device using an array of 1x1x3 mm³ Lutetium Oxyorthosilicate (LSO) scintillation crystals. The PSAPD is a novel position sensitive photodetector manufactured by RMD, Inc.

Materials and Methods

We are building a PET detector configuration that will achieve 1 mm³ intrinsic spatial, <12% FWHM energy, and 2 ns FWHM temporal resolutions, with 2 cm effective LSO crystal thickness, and 3 mm directly measured photon depth-of-interaction (DOI) resolution[1]. This is achieved by placing the PSAPD photodetector on the long sides of the crystal array ("side-on") with the PSAPD surface parallel to incoming photons, see Figure 1. To maintain 70% crystal packing fraction in this new configuration, ultra-thin (<300 μm) PSAPDs are required. New PSAPD chips mounted on 50-μm-thick polyimid flex circuit were designed and fabricated, as shown in Figure 1. Changing the thickness of the chip, the substrate, and the production process can lead to degraded device performance. In this paper, we present performance comparison of the standard (ceramic substrate mounted) PSAPD and thin, flex mounted PSAPDs with regards to their energy resolution (ER), coincidence time resolution (CTR) and spatial resolution (SR).

Results and Discussion

Figure 2 shows the flood images taken with a 3x4 LSO crystal array coupled "side-on" to both PSAPD devices (both have an 8x8 cm² sensitive area). Each crystal for this measurement has a size of 2x2x3 mm³. For the standard PSAPD, the average crystal ER at 511 keV is 10.81±0.63%, the best ER is 9.89±0.55% and the worst ER is 11.44±0.5%, as shown in the top row of Fig. 2. For the thin flex circuit PSAPD, the average ER at 511keV for the 12 crystals is 10.89±0.68% with the best ER of 9.94±0.58% and the worst ER of 11.88±0.83%. Also notice that the flex PSAPD has about 40% higher pulse height (photopeak position in energy spectrum).

CTR was also measured for both PSAPDs. A LSO coupled PMT was used as the start channel to the TAC (time-to-amplitude converter) and signals from the sum energy channel of the PSAPD was used as the stop channel. The measured CTR of standard and thin devices is 2.01±0.22 ns and 1.97±0.25 ns, respectively.

In the measurement of the coincidence SR, the same LSO crystal coupled to a PMT used for the TCR measurement was mounted rigidly on a motor-driven stage with a 10 μCi 22Na source. Then this stage was scanned along the edge of an 8x3 LSO crystal array of 1x1x3 mm³ LSO crystals along the 8 crystal edge with a 511 keV photon beam size of about 0.6 mm. There were no inter-crystal reflectors or gaps. To evaluate the performance of different crystal surface finish, the 8x3 LSO array contains 12 crystals with polished surface on all sides, and another 12 crystals with all ground surfaces. Analysis showed the polished crys-
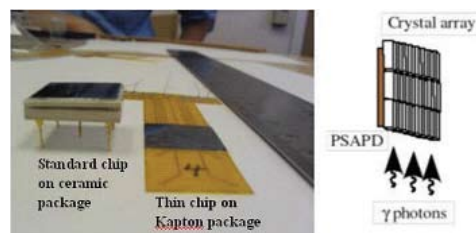
Figure 1: Picture of standard (left) and new thin (right) PSAPD devices. The new thin design is only 220 microns thick.
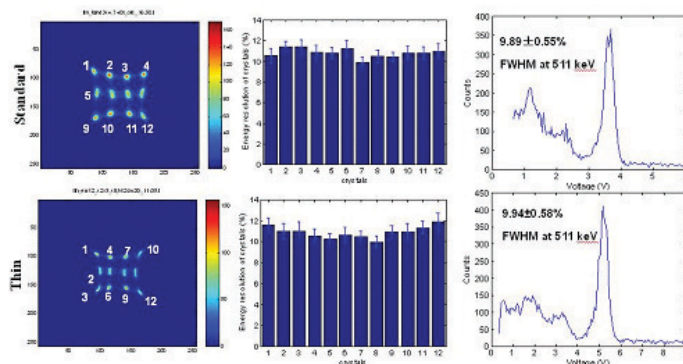
Figure 2: Flood images and energy resolution for twelve 2x2x3mm³ LSO crystals coupled to (top) standard and (bottom) thin flex-mounted PSAPD. (Left) flood image; (Middle) bar plot of energy resolution vs. crystal number; (Right) best energy spectra for each device.

tals have better average ER of 12.5%±1.2% vs 14.7±1.3% for ground crystals. The point spread functions (PSF) of the eight crystals closest to the scanning source are also studied. The average FWHM of raw PSFs for the standard and flex PSAPD is 1.25±0.1 and 1.29±0.09 mm, respectively. With photon beam size deconvolution, the intrinsic SR is1.09±0.1 and 1.14±0.09 mm FWHM, respectively for the standard and thin PSAPD.

Conclusion

The recently developed thin polyimid flex circuit mounted PSAPD has comparable energy and time resolutions to the ceramic packaged standard PSAPD, but it generates ~40% higher photopeak pulse height. This extremely thin PSAPD is essential for achieving 70% crystal packing fraction with a PET system design with 1 mm³ intrinsic spatial, <12% FWHM energy, and 2 ns FWHM temporal resolutions, 2 cm effective LSO crystal thickness, and 3 mm photon DOI resolution. The new thin PSAPD allows us to achieve the design specifications for the proposed 1 mm³ spatial resolution PET systems.

[1] C.S. Levin, A.M.K. Foudray, P.D. Olcott, F. Habte. IEEE Transactions on Nuclear Science 51 (3): 805-810, 2004

Study of Count Performance, Lesion Visualization and Contrast Resolution as a Function of Crystal Resolution for a Dual-plate PET Camera Dedicated to Breast Cancer Imaging

Jin Zhang, Peter D. Olcott, Angela M.K. Foudray, Garry Chinn, Craig S. Levin, – Department of Radiology and Molecular Imaging Program

Introduction

We are developing a portable, dual-plate, positron emission tomography (PET) camera dedicated to breast cancer imaging. This camera, with a field of view (FOV) of 15x10 mm^2 with variable plate separation, is designed to achieve >10% sensitivity [Jin Zhang, *et al*, AMI annual conference, 2005], ~1 mm^3 intrinsic spatial resolution, < 12% energy resolution at 511 keV, and 2 ns coincidence time resolution [1,2]. These performance parameters are achieved using a recent new technology development of extremely thin (<300 μm) position-sensitive avalanche photodiode (PSAPD) devices. In this paper, we present results from a detailed Monte Carlo simulation study of the expected dual-plate PET camera count performance, lesion visualization, and contrast resolution. The latter two parameters were studied for various crystal resolutions. All of the simulation parameters for different crystals are summarized in Table 1.

Table 1: Parameters used in Monte Carlo simulation for different crystal resolutions for 15x10 cm2 plates.

LSO crystal size (mm3)	1x1x3	2x2x10	3x3x30	4x4x20
Effective thickness (mm)	18 (six layers)	10	30	20
Energy resolution (%)	12%	16%	25%	20%
Time resolution (ns)	2	2	2	2
DOI resolution (mm)	3	10	10	20

Materials and Methods

Figure 1 schematically shows the geometry of the dual-plate PET camera. A source phantom with various radius spheres, each size sphere in a separate quadrant, were distributed with a separation of two times the sphere diameter. Focal plane tomography was used for the image reconstruction. We expect improved results with an iterative image reconstruction algorithm under development.
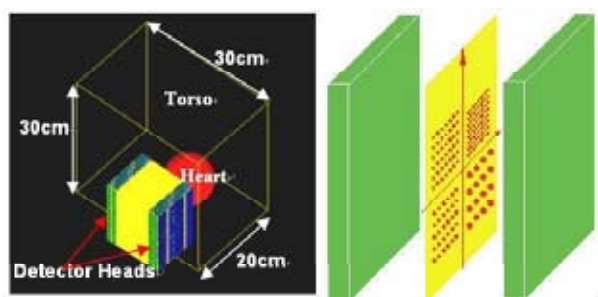
Figure1: (Left) Dual-plate geometry PET camera with breast, heart and torso background present; (right) four quadrants of tumor spheres (2.5, 3.0, 3.5, and 4.0 mm diameter with separation of twice the diameter) placed in between plates inside breast tissue. The positron activity concentration ratio: tumors: breast:heart:torso=10:1:10:1.

Results and discussion

Figure 2 (with only breast background) show the reconstructed images with 1-D profiles. The lesion visualization of the 1x1x3mm^3 crystal system is significantly better. For the 4-mm diameter sources in Figure 2, the mean peak-to-valley ratio is 1.7 compared to 1.2 for the 2x2x10 mm^3 crystal resolution). As also shown in Figures 2, the superior intrinsic spatial resolution (1 mm in plane, 3 mm into crystal) leads to tumor foci appearing brighter, narrower and better separated. The superior energy resolution (12% FWHM) combined with better spatial resolution leads to superior tumor to background contrast in the presence of strong background from the adjacent heart and torso activity. A dual-plate system comprising 1x1x3mm^3 crystals can resolve 2.5 mm diameter (8μl) tumors in only 30 seconds acquisition time. This is markedly improved capability compared to existing clinical systems which typically require 45 minutes to visualize 1 cm diameter (500μl) lesions.
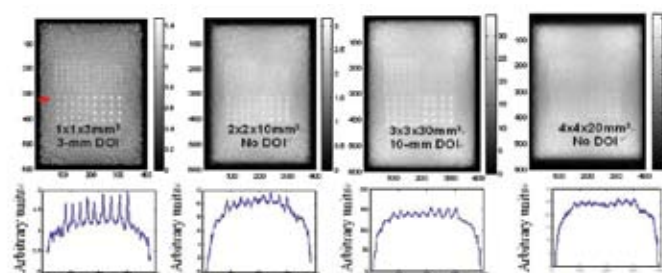
Figure 2: (Top) Data acquired for 30 seconds, with hot tumors in center plane, warm breast tissue background (10:1 concentration ratio), and 4 cm plate separation for different LSO crystals size, DOI resolution and energy resolution (see Table 1). Images are reconstructed with solid angle and photon attenuation correction. (Bottom) Plots of 1-D profiles through the top row of 3.5 and 4.0 mm diameter tumors as indicated by the arrow in the top left image.

Conclusion

The design of a dual-plate PET camera with 1x1x3mm^3 LSO crystals, 3 mm DOI, allows superior visualization of minute lesions. The 12% energy and 2ns time resolution, allows one to use narrow energy window settings (24%) to significantly reduce both random and scatter coincidence background, in order to improve lesion contrast resolution, while still maintaining high >10% coincidence detection sensitivity. This high sensitivity facilitates image reconstruction at the desired 1 mm^3 spatial resolution.

[1] C.S. Levin, A.M.K. Foudray, P.D. Olcott, F. Habte. IEEE Transactions on Nuclear Science 51 (3): 805-810, 2004.
[2] Jin Zhang, et al, presentation on the conference, IEEE 2005 annual meeting-MIC.

Development of Near Infrared Fluorogenic Probes for Imaging Gene Expression

Bengang Xing and Jianghong Rao - Department of Radiology & Bio-X Program, Molecular Imaging Program at Stanford

TEM-1 β-lactamase (Bla) is a sensitive reporter for detecting biological processes and interactions in vivo, and has been applied for monitoring the promoter/regulatory elements activity, protein-protein interactions, and ribozyme in vivo splicing reactions. There are several reported fluorogenic substrates for β-lactamase, but none of them are suitable for animal imaging. Infrared/near infrared (NIR) light has deep tissue penetration because of its long wavelength, less scattering and less absorption by water and hemoglobin, and thus is suitable for in vivo living animal imaging. Here we present a design and synthesis of a membrane-permeable near infrared fluorogenic substrate for β-lactamase, and its application in imaging gene expression in vivo.

Based on fluorescence energy resonance transfer (FRET), we designed and prepared a novel β-lactam-based probe (CNIR2) consisting of a NIR fluorescent donor (Cy5), and an accepter (QSY21) to sense Bla activity in vivo. QSY21 efficiently quenches the emission of Cy5 through FRET, resulting in very low fluorescent background. Cleavage by β-lactamase led to a large increase (~50-fold) in the fluorescence emission at 660 nm. The kinetics of the Bla hydrolysis was determined as k_{cat} = 0.8 ±0.2 s^{-1} and K_m = 7.83±1.5 μM. β-lactamase concentrations down to 400 fM are readily quantifiable with CNIR2 in vitro. To deliver the probe into cells, D-glucosamine derivative was used as the transporter. The uptake pathway appeared to be consistent with endocytosis, and the hydrolysis fluorescent product appeared to accumulate in the nuclei of cells after internalization. This probe is to be used in an in vivo imaging study of β-lactamase expression.

CNIR2

CMV-Bla C6 Glioma cell Excitation filter, 650/20; Emission filter, 675/35; 500 ms exposure time; 40X magnification

Wild type C6 Glioma cell

Ribozyme-mediated Imaging of Endogenous Gene Expression In Vivo

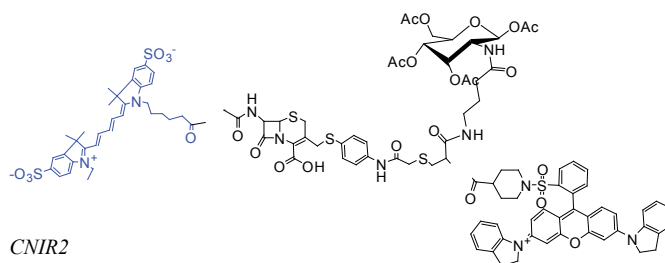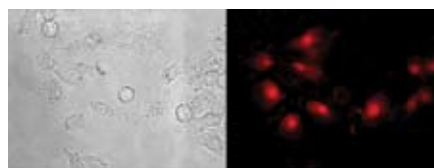Sumitaka Hasegawa and Jianghong Rao - Department of Radiology & Bio-X Program, Molecular Imaging Program at Stanford

Few methods exist to image endogenous mRNAs within intact cells or intact living subjects. Radiolabeled antisense oligonucleotides have been developed for this goal but with limited successes in living subjects. One of the main difficulties encountered in this task is the limited number of copy of mRNA for a given gene target. Here we present a novel target mRNA dependent signal amplification strategy to achieve the imaging of endogenous mRNA in vivo.

Our approach is based on the trans-splicing Tetrahymena ribozymes and a reporter enzyme, beta-lactamase. We have designed a reporter construct encoding a trans-splicing ribozyme and beta-lactamase to report the expression of p53 gene in vivo. This construct can recognize the p53 transcript and produce a trans-spliced mRNA product that can be translated into a fusion reporter enzyme. Cells expressing p53 have much higher (>30-fold) beta-lactamase activity than cells without the p53 expression. We have confirmed that this beta-lactamase activity is dependent on both p53 expression and the trans-splicing activity of ribozyme. Such p53-expressed cells can be easily imaged optically using beta-lactamase fluorogenic substrates. This genetically encoded imaging system offers exciting opportunity of imaging endogenous gene expression, especially over-expressed tumor-specific gene expression in living subjects.
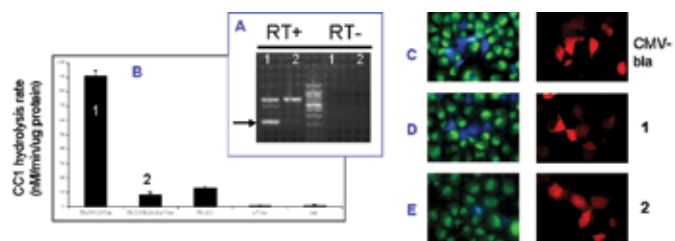
Figure 1: A) RT-PCR analyses or RNA extracts from Cos-7 cells transiently cotransfected with TRz200 (a trans-splicing ribozyme carrying Bla gene and targeting sequence against p53mt) and p53mt (2). The expected splicing product Bla was as indicated by arrow. The top bring band was unspliced complex. B) In vitro Bla assay using CC!. Hydrolysis rates were normalized against total lysates protein content in a unit of nM/min/ug protein. C-E) Fluorescence microscopy images of the Cos-7 cells transiently transfected with CMV-bla ©. 1 (D), or 2(E). Left images in C-E were an overlay of frames captured at 530 nm (green emission) and 460 nm (blue emission), and right images were dsRed emission at 605 nm with excitation at 560 nm. Nontransfected cells show no Bla activity (green in left images and black in right images).

Quantitative PET Imaging Of Tumor Integrin $\alpha_v\beta_3$ Expression With [18F]FRGD2

Xianzhong Zhang, Zhengming Xiong, Yun Wu, Jeffery R. Tseng, Sanjiv S. Gambhir, and Xiaoyuan Chen – Molecular Imaging Program at Stanford (MIPS) and Bio-X Program, Department of Radiology

Introduction

Cell adhesion receptors of the integrin family, which are responsible for a wide range of cell-extracellular matrix (ECM) and cell-cell interactions, have been well studied in many tumor types. One of the most prominent members of this receptor class is $\alpha_v\beta_3$ integrin which is related to several pathological processes and is being investigated intensively. The cell adhesion molecule integrin $\alpha_v\beta_3$ is highly expressed on activated endothelial cells and solid tumor cells, particularly in pathways stimulated by VEGF. It is not expressed on mature vessels or on non-neoplastic epithelium. The expression of integrin adhesion molecule $\alpha_v\beta_3$ on sprouting capillary cells and its interaction with specific matrix ligands has been shown to play a key role in angiogenesis and metastasis. The ability to non-invasively visualize and quantify $\alpha_v\beta_3$ integrin expression level will provide new opportunities to document tumor receptor expression, more appropriately select patients considered for anti-integrin treatment and monitor treatment efficacy in integrin-positive patients. We and others have developed a series of RGD peptide based probes for multimodality imaging of integrin expression in vivo. In this study, we would like to introduce a dimeric RGD peptide tracer [18F]FB-E[c(RGDyK)]$_2$ (abbreviated as [18F]FRGD$_2$) and fully characterize the pharmacokinetics, pharmacodynamics and PET imaging properties.

Materials and Methods

The RGD dimer E[c(RGDyK)]$_2$ was labeled with 18F by conjugation coupling with N-succinimidyl-4-[18F]fluorobenzoate ([18F]SFB) under slightly basic condition. The octanol/water partition coefficient (log$P$) and in vivo metabolic stability of [18F]FRGD2 was determined. Estimated human dosimetry was calculated from tracer distribution in mice. The diagnostic value after injection of [18F]FRGD2 was evaluated in various xenograft models by dynamic microPET imaging followed by ex vivo quantification of tumor integrin level.

Results

Starting from 18F- Kryptofix 2.2.2/K$_2$CO$_3$ solution, the total reaction time for [18F]FRGD2 including final HPLC purification is about 200 ± 20 min. Typical decay-corrected radiochemical yield is 23 ± 2 % (n = 20). The title compound (Figure 1) is relatively hydrophilic (log$P$ = -1.65 ± 0.06) and metabolically stable. According to the residence times in female athymic nude mice, the effective dose in human was calculated to be 1.26 × 10^{-2} mGy/MBq, which is significantly lower than [18F]FDG. The highest radiation dose was found for the urinary bladder wall, reflecting rapid clearance of most of the injected [18F]FRGD2 into the bladder and making it the dose limiting organ which will assist in the determination of an appropriate amount of [18F]FRGD2 to inject into a human. The binding potential (BP) extrapolated from graphical analysis of PET data
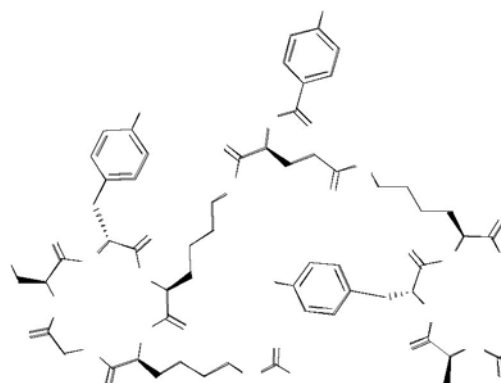
Figure 1: Schematic structure of [18F]FB-E[c(RGDyK)]$_2$ ([18F]FRGD2).
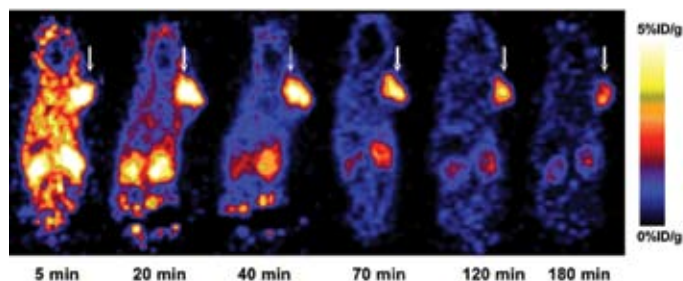
Figure 2: Dynamic microPET study of U87MG tumor bearing mouse over 60 min after injection of [18F]FRGD2 (100 μCi), static scans at 2 h and 3 h time points were also conducted to complete the tracer kinetic study. Decay-corrected whole-body coronal images that contain the tumor were shown

(Figure 2) and Logan plot correlates well with the receptor density measured by SDS-PAGE and autoradiography in various xenograft models. Tumor/background ratio at 1 h postinjection of [18F]FRGD2 also gives a good linear relationship with tumor tissue integrin level.

Conclusion

The dimeric RGD peptide tracer [18F]FRGD2 with high integrin specificity and favorable excretion profile may be translated into clinic for imaging integrin $\alpha_v\beta_3$ expression. The binding potential calculated from simplified tracer kinetic modeling such as Logan plot appears to be an excellent indicator of tumor integrin density.

References

1. Chen X, et al. Mol. Imaging., 3:96-104 (2004)

MicroPET Imaging of Glioma Integrin $\alpha_v\beta_3$ Expression Using ^{64}Cu-Labeled Tetrameric RGD Peptide

Yun Wu[1], Xianzhong Zhang[1], Zhengming Xiong [1], Zhen Cheng[1], Darrell R. Fisher[2], Shuang Liu[3], Sanjiv S. Gambhir[1], Xiaoyuan Chen[1] - [1]Department of Radiology & Bio-X, Stanford University; [2]Radioisotopes Program, Pacific Northwest National Laboratory; [3]Industrial and Physical Pharmacy, School of Pharmacy and Pharmaceutical Sciences, Purdue University

INTRODUCTION

Cell adhesion molecule integrin $\alpha_v\beta_3$ is up-regulated in association with tumor angiogenesis and metastasis. The unique and/or overexpression of this G-protein receptor on sprouting endothelial cells in growing tumors and on tumor cells of various origins provides a robust platform for anti-angiogenic and anti-metastatic strategy. We and others have reported radiolabeled RGD-containing peptides as radiopharmaceuticals for diagnosis of rapidly growing solid tumors. In this project we applied the polyvalency principle and developed a novel tetrameric RGD peptide using glutamate as the branching unit. The resulting RGD peptide tetramer was conjugated with the macrocylic chelator 1,4,7,10-tetraazacyclododecane-N, N', N'', N'''-tetraacetic acid (DOTA) and labeled with ^{64}Cu for microPET imaging of integrin expression in a subcutaneous U87MG glioblastoma xenograft model in female athymic nude mice. The aim of this study was to investigate integrin targeting characteristics of ^{64}Cu-DOTA-E{E[c(RGDyK)]$_2$}$_2$ (Figure 1) as a potential agent for diagnosis and receptor mediated internal radiotherapy of integrin receptor expressing tumors.
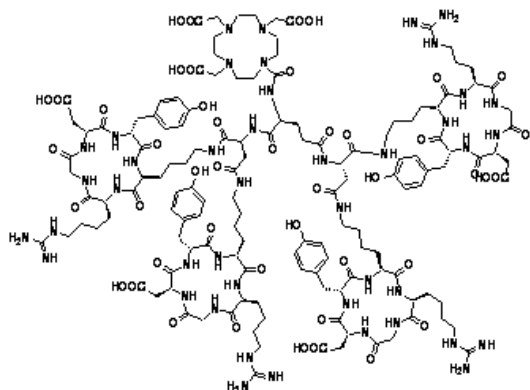
Figure 1: Schematic structure of ^{64}Cu-DOTA- E{E[c(RGDyK)]$_2$}$_2$.
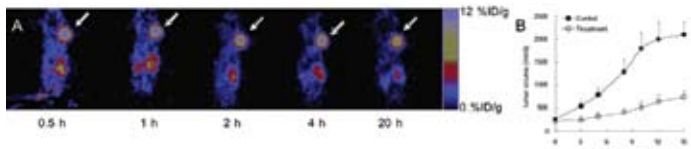
Figure 2: A). Serial static microPET scans of U87MG tumor bearing mouse over 20 h after injection of ^{64}Cu-DOTA-E{E[c(RGDyK)]$_2$}$_2$ (200 µCi). Decay-corrected whole-body coronal images that contain the tumor are shown. B). Growth curves of subcutaneous U87MG tumors in two groups of nude mice after injection of 37 MBq of ^{64}Cu-DOTA-E{E[c(RGDyK)]$_2$}$_2$ (°) or PBS (•).

MATERIALS AND METHODS

The synthesis of DOTA-E{E[c(RGDyK)]$_2$}$_2$ was carried out through an active ester method by coupling Boc-Glu(OSu)-OSu with dimeric RGD peptide E[c(RGDfK)]$_2$ followed by TFA deprotection. In aqueous solution, DOTA was activated with SNHS/EDC, and the resulting DOTA-OSSu ester was conjugated with tetrameric cyclic RGD peptide. ^{64}Cu-labeling of DOTA-RGD tetramer conjugate was performed using ^{64}Cu having a measured specific activity of 1 Ci/µmol (37 MBq/nmol) at greater than 95% radiochemical purity as determined by analytical HPLC (decay corrected). The ^{64}Cu-DOTA-E{E[c(RGDyK)]$_2$}$_2$ was purified by semi-preparative HPLC.

RESULTS

The title compound displayed rapid blood clearance. Tumor uptake in the $\alpha_v\beta_3$-positive U87MG tumor was significantly higher than other organs at any time point examined. The highest activity accumulation in tumor was found at 30 min time p.i., which decreased slowly with time, resulting in excellent tumor contrast (Figure 2A). The tracer showed good stability in blood and urine but quickly degraded in the liver and kidneys. The decay characteristics of ^{64}Cu allows the radiopharmaceutical chemistry for both PET imaging and internal radiotherapy, we thus assessed the therapeutic efficacy of ^{64}Cu-DOTA-E{E[c(RGDyK)]$_2$}$_2$ in a subcutaneous U87MG tumor model. The growth curves of the two groups of mice that received the ^{64}Cu-labeled RGD tetramer and the control group are shown in Figure 2B. A time-related increase in tumor volume was observed in the control group (saline treatment only) in which the tumors showed an average fractional tumor volume (V/V_0) = 7.6 on day 15. A single dose of 37 MBq of ^{64}Cu-labeled RGD tetramer on day 1 resulted in a V/V_0 = 3.4 on day 15. This represents a tumor growth inhibition (TGI) of 55%. Throughout the study, the weights of all the treated animals were monitored. There was no significant change (> 10%) in weight when compared to control. In a separate experiment, it was established that an i.v. injection with the unlabeled DOTA-E{E[c(RGDyK)]$_2$}$_2$ did not have any therapeutic effect in this model.

CONCLUSION

In summary, ^{64}Cu-DOTA-E{E[c(RGDyK)]$_2$}$_2$ was shown to bind with high affinity and specificity with integrin positive U87MG glioma cells *in vitro* and *in vivo* and has the right characteristics for further pursuit as an imaging agent with PET. The presumed polyvalency effect and suitable apparent size of this tetrameric RGD peptide tracer make it a superior ligand for integrin targeting *in vivo*. The effectiveness of this copper complex to eradicate integrin positive tumors was also tested. As DOTA is a universal chelator capable of forming stable complexes with a variety of metals such as ^{111}In, [67/68]Ga, [64/67]Cu, [86/90]Y and ^{177}Lu, the same peptide conjugate used for ^{64}Cu-labeling in this study can also be applied to label other radiometals for tumor localization and therapy.

RGD Peptide-labeled Quantum Dots for Integrin $\alpha_v\beta_3$ Targeting

Weibo Cai[1], Xianzhong Zhang[1], Yun Wu[1] and Xiaoyuan Chen[1] – [1]Molecular Imaging Program at Stanford, Department of Radiology

Introduction

Adhesion receptors of the integrin family (18 α and 8 β subunits, 24 different receptors) are responsible for a wide range of cell-ECM and cell-cell interactions. Integrin signaling plays a key role in tumor angiogenesis and metastasis (1). Integrin $\alpha_v\beta_3$ which binds to Arginine-Glycine-Aspartic acid (RGD)-containing components of the interstitial matrix (e.g. vitronectin, fibronectin and thrombospondin) is significantly upregulated on endothelium during angiogenesis but not in quiescent endothelium (2). The ability to non-invasively visualize and quantify integrin $\alpha_v\beta_3$ expression level will provide new opportunities to document tumor (tumor cells and sprouting tumor vasculature) integrin expression, to more appropriately select patients for anti-integrin treatment and to monitor treatment efficacy in integrin-positive patients. Quantum dots (QDs) with size- and composition-tunable fluorescence emission have high quantum yields and photostability suitable for optical imaging and multiplexing (3). Quantum dot-based probes will have great potential in imaging-guided surgery and therapy.

Materials and Methods

We have labeled QD705 (emission wavelength 705 nm) with monomeric RGD peptide c(RGDyK) (potent integrin $\alpha_v\beta_3$ antagonist, see Figure 1) and the resulting conjugate QD705-RGD was tested for *in vitro* staining of several cancer cell lines (U87MG glioblastoma, MDA-MB-435 breast cancer, MCF-7 breast caner and C6 rat glioma which have decreasing levels of integrin $\alpha_v\beta_3$ expression, see Figure 2). The *in vitro* cell staining experiments successfully demonstrated the integrin targeting ability of QD705-RGD, as the QD705 stained cells showed no visible fluorescence signal while the cells with high integrin $\alpha_v\beta_3$ expression level (U87MG & MDA-MB-435) were lit up by QD705-RGD and the fluorescence could be effectively blocked when unconjugated c(RGDyK) was added (see Figure 3). Moreover, the fluorescence intensity correlated well with the integrin expression level of the cell lines. *Ex vivo* and *In vivo* experiments are currently under way.
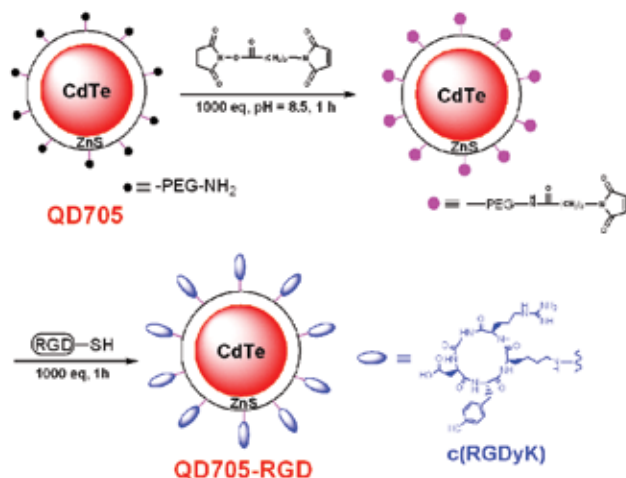
Figure 1. The synthesis of QD705-RGD conjugate. The final product was purified by size exclusion chromatography.

Figure 2. Receptor number per cell of the four cell lines tested.

Cell Line	U87MG	MDA-MB-435	MCF-7	C6
Receptor # per Cell	$(1.28 \pm 0.46) \times 10^5$	$(1.99 \pm 0.26) \times 10^4$	$(3.24 \pm 0.45) \times 10^3$	$(1.48 \pm 0.28) \times 10^3$
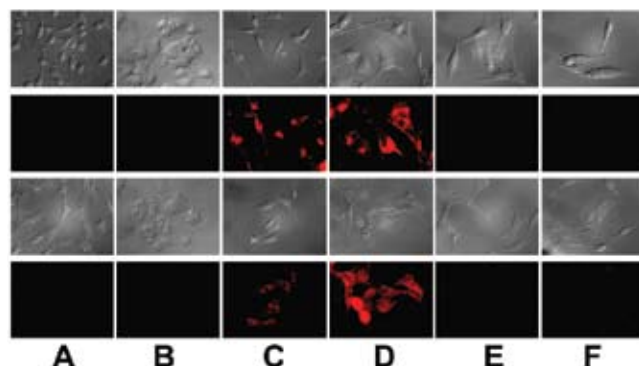
Figure 3. Staining of four cell lines. A-D: C6, MCF-7, MDA-MB-435 and U87MG cells stained with 1 nM QD705-RGD. E: U87MG cell stained with 1 nM QD705. F: U87MG cell stained with 1 nM QD705-RGD with 2 μM c(RGDyK).Top two rows are live cells while the bottom two rows are fixed cells.

Discussion

Based on the initial results shown here, a combinatorial approach which takes advantage of the multiplexing ability of the quantum dots, high integrin targeting efficacy of the cyclic RGD peptides, and emission wavelength in the near infrared window (700 - 900 nm) will have great potential in cancer diagnosis and imaging as well as imaging-guided surgery and therapy.

Conclusion

For the first time, we demonstrated that suitably labeled quantum dots are capable of specific integrin $\alpha_v\beta_3$ targeting. This will have great potential and may open up new perspectives in integrin-targeted optical imaging.

References

1. Hood, J. D.; Cheresh, D. A., *Nat. Rev.Cancer* **2002,** 2, (2), 91-100.
2. Ruoslahti, E., *Annu. Rev. Cell Dev. Biol.* **1996,** 12, 697-715.
3. Michalet, X.; et al., *Science* **2005,** 307, (5709), 538-44.

MicroPET Imaging of Human Integrin $\alpha_v\beta_3$ Expression by Using 64Cu-labeled Humanized Monoclonal Antibody - Vitaxin

Yun Wu[1], Xianzhong Zhang[1], David Tice[2], Xiaoyuan Chen[1] – [1]Department of Radiology, Stanford University; [2] MedImmune, Inc.

Introduction

Angiogenesis is crucial for the tumor development and progression. A growing tumor needs an extensive network of capillaries to provide nutrients and oxygen. Antiangiogenic therapy aimed at interfering with tumor blood supply represents a promising approach for cancer treatment. One important approach is to inhibit the adhesive interactions required by angiogenesis vascular endothelial cells. The cell adhesion receptor - integrin $\alpha_v\beta_3$ plays a key role in this process. RGD peptide antagonists of $\alpha_v\beta_3$ have been found to inhibit adhesion-dependent signal transduction by angiogenic factors, leading to apoptosis within the angiogenic blood vessels. Vitaxin, the humanized form of the anti- $\alpha_v\beta_3$ antibody, has also been shown to target angiogenic blood vessels and cause suppression of tumor growth in various animal models. The aim of this project was to develop a radiolabeled analogue of Vitaxin that was suitable to image human integrin $\alpha_v\beta_3$ expression.

Materials and Methods

Antibody was conjugated with 1,4,7,10-tetraazacyclododecane-N,N',N'',N'''-tetraacetic acid (DOTA) by in situ activation method. The resulting DOTA-OSSu ester (1000 equivalent) was conjugated with antibody (pH was adjusted to 5.5 by addition of 1N NaOH). Following conjugation, the DOTA-Vitaxin was purified and concentrated by using Centricon filter tube. ^{64}Cu-labeling of Vitaxin was performed in NH$_4$OAc buffer (0.25 M, pH 6.3). Vitaxin (40 µg) was incubated with 1 mCi of carrier-free ^{64}Cu-chloride for 1 hr at 40 °C. The reaction was then terminated and purified by PD-10 desalting column. MicroPET imaging was employed to evaluate the in vivo receptor targeting ability of the humanized antibody. For this purpose, athymic nude mice carrying $\alpha_v\beta_3$-positive (U87MG glioblastoma) and $\alpha_v\beta_3$-negative control (PC-3 prostate cancer) tumors were injected with ^{64}Cu-DOTA-Vitaxin (ca. 100 µCi). The tumor-bearing mice were imaged via the Concorde microPET R4 system. All images were reconstructed using an OSEM algorithm and displayed by the VISPro VM software. The same color threshold was applied to all images.

Results

The ratio of functional DOTA chelators per antibody molecule was determined by an isotopic dilution assay. At DOTA-OSSu : mAb conjugation ratio of 1000:1, approximately 12 DOTA chelators are available for complexing ^{64}Cu. The ^{64}Cu-radiolabeling efficiency for Vitaxin ranged
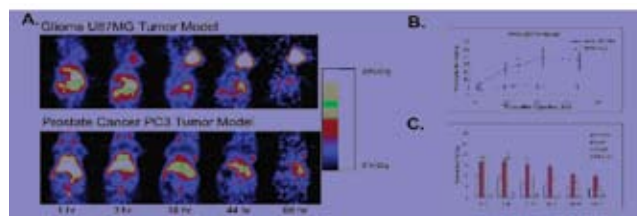
Figure 1: (A) Decay-corrected whole-body coronal microPET images of nude mouse bearing human U87MG and PC3 tumor over 68 h after injection of ^{64}Cu-DOTA-Vitaxin (100 µCi). All the images had been modified by decay correction; (B) Comparison of kinetics of tumor clearance in human glioma U87MG and prostate cancer PC3 xenograft models for ^{64}Cu-DOTA-Vitaxin; (C) Comparison of tissue uptake (kidney, liver, heart and muscle) at 1 h, 3 h, 18 h, 25 h, 44 h, and 68 h in human glioma U87MG xenograft models.

from 65 to 80% and specificity activity of ^{64}Cu-DOTA-Vitaxin reached a maximum of 20 mCi/mg. The immunoreactivity of ^{64}Cu-DOTA-Vitaxin was determined under conditions of antigen excess in $\alpha_v\beta_3$ -expressing U87MG cells. Under these conditions, the immunoreactivity of the conjugate was about 75%. Whole-body microPET scans were obtained at 1, 3, 18, 44, and 68 hours post injection. Representative coronal images of the same tumor mouse were illustrated in Figure 1. As expected, the radiolabeled conjugate cleared relatively slowly from blood as evidenced by prominent heart uptake visualized from the microPET images. U87MG tumor uptake of ^{64}Cu-DOTA-Vitaxin was initially low (4.9 ± 1.4 %ID/g at 1 hr p.i., and 6.5 ± 1.3 %ID/g at 3 hr p.i., respectively) and reached a maximum of 24.3 ± 6.0 %ID/g at 44 h. As expected, tumor uptake in U87MG tumor was significantly higher than that in PC-3 tumor at all time points measured ($P < 0.001$), reflecting integrin specificity of this radiolabeled antibody. The nonspecific accumulation of the radioconjugate in normal organs (liver, heart and kidneys) was expected for intact radiolabeled antibody.

Conclusion

In summary, this study demonstrates that ^{64}Cu-DOTA-Vitaxin binds to human integrin $\alpha_v\beta_3$ receptor with high affinity and specificity. The sustained activity accumulation in human integrin $\alpha_v\beta_3$ expressing tumors suggests that further evaluation of the diagnostic and therapeutic efficacy of this radioconjugate is warranted.

Imaging Chemically Modified Adenovirus for Targeting Tumor Expressing Integrin $\alpha_v\beta_3$ in Living Mice with Positron Emission Tomography

Zhengming Xiong, Zhen Cheng, Xianzhong Zhang, Manish Patel, Joseph C. Wu, Sanjiv S. Gambhir, Xiaoyuan Chen - Department of Radiology

Introduction

Recombinant adenovirus (Ad) has been widely used as an attractive gene delivery vehicle to mammalian cells because of its unparalleled efficacy in accomplishing gene transfer in vivo. The virus can stably incorporate relatively large insertions of foreign DNA (<7.5 kb) into the genome. It can be concentrated to high titers from infected cells, and it has high transduction efficiency in many cell types. Furthermore, DNA of Ad cannot be integrated into host genome, thus it does not infect oocytes and consequently female germline transduction. Currently about 25-30% gene therapy studies in pre-clinical trials are based on using Ad vectors. There are, however, some limitations associated with the use of Ad for gene delivery. One such disadvantage is related to the wide native tropism of Ad, which often results in high accumulation in non-targeting tissues. Vector targeting to a specific tissue of cell type would enhance gene therapy efficacy and permit the delivery of lower doses, which would consequently result in reduced toxicity. In this study, a replication-deficient Ad was modified with bifunctional PEG and then conjugated with cyclic RGD peptide (Figure 1). We hypothesize that surface modification of Ad fiber knobs with PEGylated-RGD peptide will ablate the normal tropism (CAR recognition) and reduce transduction of nontarget tissues in vivo; incorporation of integrin $\alpha_v\beta_3$ specific RGD peptides will enhance the gene delivery to tumor neovasculature and integrin positive tumor cells. In order to monitor the localization and expression of the chemically modified virus we packed the HSV1-sr39tk mutant as a reporter gene under the control of cytomegalovirus (CMV) promoter. The kinetics, homing selectivity and transgene expression after intravenous administration of integrin-directed adenovirus were studied by microPET imaging using [18F]FHBG as a reporter probe.

Materials and Methods

The first generation Ad vector, which expresses mutant herpes simplex virus type 1-sr39tk (HSV1-sr39tk) gene (Adtk) under the control of cytomegalovirus (CMV) promoter was conjugated with poly(ethylene glycol) (PEG) or PEGylated Arg-Gly-Asp (RGD) peptide (RGD-PEG). The transduction efficiency of Ads (non-modified Ad: Adtk; PEGlyated Ad: PEG-Adtk; and RGD-PEG modified Ad: RGD-PEG-Adtk) into different types of cells (293T, MCF-7, MDA-MB-435, and U87MG) were analyzed and quantified by thymidine kinase (TK) assay using 8-[3H]-penciclovir (8-[3H]-PCV) as radioligand. The in vivo infectivity of the Ad vectors after intravenous administration into U87MG and MDA-MB-435 tumor bearing athymic nude mice were measured by both non-invasive microPET imaging using 9-[4-[18F]fluoro-3-(hydroxymethyl)butyl]guanine ([18F]FHBG) as a reporter probe and ex vivo TK assay of the tumor and tissue homogenates.

Results and Discussion

Using 10^5 PEG or RGD-PEG per virion, about 55-60% of the reactive groups on the viral caspid were modified by these ligands. PEGylation completely abrogated CAR-knob interaction and the infectivity of PEG-Adtk is significantly lower than that of unmodified Adtk in CAR positive cells. RGD-PEG-Adtk had significantly higher infectivity than PEG-Adtk but the extent of increase is related to both CAR and integrin $\alpha_v\beta_3$ expression levels. [18F]FHBG had minimal non-specific uptake in
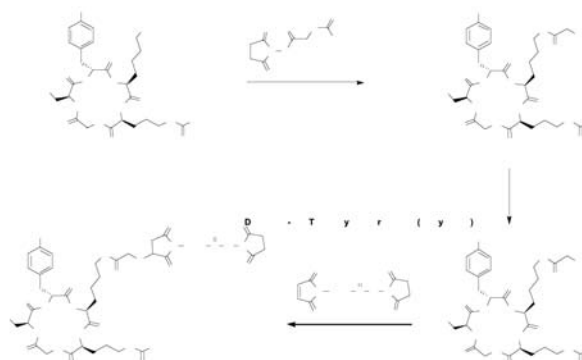
Figure 1. Schematic representation of the synthesis of RGD-PEG-NHS.
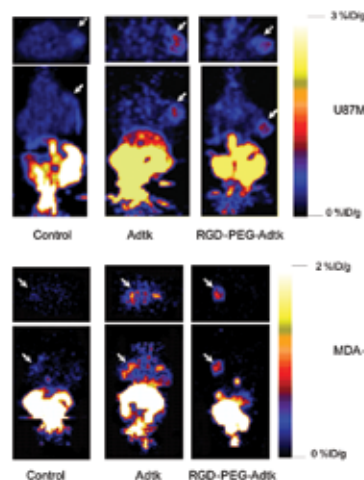
Figure 2: MicroPET imaging of tumor bearing mice (top: subcutaneous U87MG tumor on the right shoulder, bottom: orthotopic MDA-MB-435 tumor on the left mammary fat pad) after 1 h injection of [18F]FHBG (10 min static scan). The images (both transaxial and coronal) were normalized to the same scale.

the liver and tumors that are void of sr39tk. Mice pre-injected intravenously with unmodified Adtk resulted in high hepatic uptake and moderate tumor accumulation of the tracer. RGD-PEG-Adtk administration resulted in significantly lower liver uptake without compromising the tumor accumulation of [18F]FHBG (Figure). Expression of TK in the liver and tumor homogenates evaluated 12 h after PET scans corroborated with the magnitude of [18F]FHBG uptake quantified by non-invasive microPET imaging. Analysis of liver and tumor tissue integrin level confirmed that RGD-integrin interaction is responsible for the enhanced tumor infectivity of RGD-PEG-Adtk.

Conclusion

The results of this study suggest that RGD-PEG conjugation is an effective way to modify adenoviral vector tropism for improved systemic gene delivery. Non-invasive PET imaging and [18F]FHBG is able to monitor in vivo transfectivity of both Adtk and RGD-PEG-Adtk vectors in the liver and tumors after intraveous injection.

PUBLICATIONS and PRESENTATIONS

STANFORD UNIVERSITY
100
A Century
of Discovery,
Diagnosis and
Treatment
RADIOLOGY & RADIATION ONCOLOGY

Medical Physics

AVAILABLE ONLINE—See http://www.medphys.org   June 2005   Volume 32, Number 6

AAPM Annual Meeting Issue
Seattle, Washington

NeuroImage

2005 RELEASE
Volume 23, Number 3 April 18, 2005

Editors-in-Chief

John C. Mazziotta   Arthur W. Toga

ELSEVIER

Also available on
SCIENCE@DIRECT
www.sciencedirect.com

Science

22 January 2005

VOL 307   PAGES 405-628 $10

AAAS

125

Published Papers, Book Chapters and Books

Allexander JO, Bednarski MD, Guccione S, Yao J, Menard C, Li K, Choyke P. Systemic prostate specific antigen (PSA) is a measure of vascular permeability: A study of dynamic contrast-enhanced magnetic resonance imaging (DCE-MRI). AJR Am J Roentgenol 2004; 182:97.

Aziz N, Lenzi TA, Jeffrey RB, Jr., Lyell DJ. Postpartum uterine atrio-venous fistula. ObAllexander JO, Bednarski MD, Guccione S, Yao J, Menard C, Li K, Choyke P. Systemic prostate specific antigen (PSA) is a measure of vascular permeability: A study of dynamic contrast-enhanced magnetic resonance imaging (DCE-MRI). AJR Am J Roentgenol 2004; 182:97.

Aziz N, Lenzi TA, Jeffrey RB, Jr., Lyell DJ. Postpartum uterine atriove-nous fistula. Obstet Gynecol 2004; 103:1076-1078.

Bammer R, Schoenberg SO. Current concepts and advances in clinical parallel magnetic resonance imaging. Top Magn Reson Imaging 2004; 15:129-158.

Bammer R, Skare S, Newbould R, Liu C, Thijs V, Ropele S, Clayton DB, Krueger G, Moseley ME, Glover GH. Foundations of advanced magnetic resonance imaging. NeuroRx 2005; 2:167-196.

Bangerter NK, Hargreaves BA, Vasanawala SS, Pauly JM, Gold GE, Nishimura DG. Analysis of multiple-acquisition SSFP. Magn Reson Med 2004; 51:1038-1047.

Barnea-Goraly N, Menon V, Eckert M, Tamm L, Bammer R, Karchemskiy A, Dant CC, Reiss AL. White Matter Development During Childhood and Adolescence: A Cross-sectional Diffusion Tensor Imaging Study. Cereb Cortex 2005.

Barnes P. Child abuse: Cerebral Trauma. In:The Pediatric Radiology Curriculum: The Cleveland Clinic Foundation Division of Radiology, 2004.

Beaulieu CF, Paik DS, Napel S, Jeffrey RB, Jr. Advanced 3D Display Methods. In: Dachman AH, ed. Fundamentals of Virtual Colonoscopy. New York: Springer Verlag, 2005; 53-64.

Bentolila LA, Michalet X, Pinaud FF, Tsay JM, Doose S, Li JJ, Sundaresan G, Wu AM, Gambhir SS, Weiss S. Quantum dots for molecular imaging and cancer medicine. Discovery Medicine 2005; 5:213-218.

Bergman AG, Fredericson M, Ho C, Matheson GO. Asymptomatic tibial stress reactions: MRI detection and clinical follow-up in distance runners. AJR Am J Roentgenol 2004; 183:635-638.

Besier TF, Draper CE, Gold GE, Beaupre GS, Delp SL. Patellofemoral joint contact area increases with knee flexion and weight-bearing. J Orthop Res 2005; 23:345-350.

Bilello M, Gokturk SB, Desser T, Napel S, Jeffrey RB, Beaulieu CF. Automatic detection and lassification of hypodense hepatic lesions on contrast-enhanced venous-phase CT. Med Phys 2004; 31:2584-2593.

Blankenberg FG. Molecular imaging with single photon emission computed tomography. How new tracers can be employed in the nuclear medicine clinic. IEEE Eng Med Biol Mag 2004; 23:51-57.

Bogdan MA, Klein MB, Rubin GD, McAdams TR, Chang J. CT angiography in complex upper extremity reconstruction. J Hand Surg [Br] 2004; 29:465-469.

Butts K, Pauly JM, Gold GE. Reduction of blurring in view angle tilting MRI with multiple view angle tilting readouts. Magn Reson Med 2005; 53:418-424.

Chan FP, Rubin GD. MDCT angiography of pediatric vascular diseases of the abdomen, pelvis, and extremities. Pediatr Radiol 2005; 35:40-53.

Chen K, Bird L, Barnes P, Barth R, Hudgins L. Lateral meningocele syndrome: Vertical transmission and expansion of the phenotype. Am J Med Genet 2005; 133:115-121.

Chen SH, Desmond JE. Cerebrocerebellar networks during articulatory rehearsal and verbal working memory tasks. Neuroimage 2005; 24:332-338.

Chen SH, Desmond JE. Temporal dynamics of cerebro-cerebellar network recruitment during a cognitive task. Neuropsychologia 2005; 43:1227-1237.

Chen X, Conti PS, Moats RA. In vivo near-infrared fluorescence imaging of integrin alphavbeta3 in brain tumor xenografts. Cancer Res 2004; 64:8009-8014.

Chen X, Hou Y, Tohme M, Park R, Khankaldyyan V, Gonzales-Gomez I, Bading JR, Laug WE, Conti PS. Pegylated Arg-Gly-Asp peptide: 64Cu labeling and PET imaging of brain tumor alphavbeta3-integrin expression. J Nucl Med 2004; 45:1776-1783.

Chen X, Hui L, Foster DA, Drain CM. Efficient synthesis and photodynamic activity of porphyrin-saccharide conjugates: targeting and incapacitating cancer cells. Biochemistry 2004; 43:10918-10929.

Chen X, Liu S, Hou Y, Tohme M, Park R, Bading JR, Conti PS. MicroPET imaging of breast cancer alphav-integrin expression with 64Cu-labeled dimeric RGD peptides. Mol Imaging Biol 2004; 6:350-359.

Chen X, Park R, Hou Y, Khankaldyyan V, Gonzales-Gomez I, Tohme M, Bading JR, Laug WE, Conti PS. MicroPET imaging of brain tumor angiogenesis with 18F-labeled PEGylated RGD peptide. Eur J Nucl Med Mol Imaging 2004; 31:1081-1089.

Chen X, Park R, Hou Y, Tohme M, Shahinian AH, Bading JR, Conti PS. microPET and autoradiographic imaging of GRP receptor expression with 64Cu-DOTA-[Lys3]bombesin in human prostate adenocarcinoma xenografts. J Nucl Med 2004; 45:1390-1397.

Chen X, Park R, Shahinian AH, Bading JR, Conti PS. Pharmacokinetics and tumor retention of 125I-labeled RGD peptide are improved by PEGylation. Nucl Med Biol 2004; 31:11-19.

Chen X, Park R, Shahinian AH, Tohme M, Khankaldyyan V, Bozorgzadeh MH, Bading JR, Moats R, Laug WE, Conti PS. 18F-labeled RGD peptide: initial evaluation for imaging brain tumor angiogenesis. Nucl Med Biol 2004; 31:179-189.

Chen X, Park R, Tohme M, Shahinian AH, Bading JR, Conti PS. MicroPET and autoradiographic imaging of breast cancer alpha v-integrin expression using 18F- and 64Cu-labeled RGD peptide. Bioconjug Chem 2004; 15:41-49.

Chen X, Plasencia C, Hou Y, Neamati N. Synthesis and biological evaluation of dimeric RGD peptide-paclitaxel conjugate as a model for integrin-targeted drug delivery. J Med Chem 2005; 48:1098-1106.

Chen X, Sievers E, Hou Y, Park R, Tohme M, Bart R, Bremner R, Bading JR, Conti PS. Integrin alpha v beta 3-targeted imaging of lung cancer. Neoplasia 2005; 7:271-279.

Chen X, Tohme M, Park R, Hou Y, Bading JR, Conti PS. Micro-PET imaging of alphavbeta3-integrin expression with 18F-labeled dimeric RGD peptide. Mol Imaging 2004; 3:96-104.

Chen X, Yao G, Hou Y. Pentachlorophenol reduces B lymphocyte function through proinflammatory cytokines in Carassius auratus. Food Chem Toxicol 2005; 43:239-245.

Cheng Z, Subbarayan M, Chen X, Gambhir SS. Synthesis of (4-[14F]fluorophynl)Triphenylphoshponium as a potential imaging agent for mitochondrial dysfunction. J Labelled Comp Radiopharm 2005; 48:131-137.

Cheng Z, Winant RC, Gambhir SS. A new strategy to screen molecular imaging probe uptake in cell culture without radiolabeling using matrix-assisted laser desorption/ionization time-of-flight mass spectrometry. J Nucl Med 2005; 46:878-886.

Chung C, Mohana-Borges A, Gold GE, Resnick D. Musculoskeletal imaging: Exploring new limits - bone and cartilage injury: Pathogenesis an MR imaging. In:RSNA Categorical Course Syllabus, 2004.

Coert BA, Chang SD, Marks MP, Do HM, Schraedley-Desmond PK, Steinberg GK, Tong DC, Albers GW. Revasuclarization of the posterior circulatioin. Skull Base 2005; 50:43-62.

Craft N, Bruhn K, Nguyen B, Prins L, Liau L, Collisson E, De A, Kolodney M, Gambhir SS, Miller J. Bioluminescent imaging of melanoma in live mice. J Invest Dermatol 2005; 125:159-165.

D'Arceuil HE, de Crespigny AJ, Pelc L, Howard D, Alley M, Seri S, Hashiguchi Y, Nakatani A, Moseley ME. An MRA study of vascular stenosis in a pig model using CH3-DTPA-Gd (NMS60) and Gd-DTPA. Magn Reson Imaging 2004; 22:1243-1248.

Daniel BL, Freeman LJ, Pyzoha JM, McCoy TD, Birdwell RL, Bouley DM, Movius B, Hibner JA. An MRI-compatible semiautomated vacuum-assisted breast biopsy system: initial feasibility study. J Magn Reson Imaging 2005; 21:637-644.

Daniel BL, Ikeda DM. Magnetic resonance imaging of breast cancer and MRI-guided breast biopsy. In:Breast Imaging: The Requisites: Elsevier, 2004.

Deutsch GK, Dougherty RF, Bammer R, Siok WT, Gabrieli JD, Wandell BA. Children's reading performance is correlated with white matter structure measured by diffusion tensor imaging. Cortex 2005; 41:354-363.

Diederich CJ, Nau WH, Ross AB, Tyreus PD, Butts K, Rieke V, Sommer G. Catheter-based ultrasound applicators for selective thermal ablation: progress towards MRI-guided applications in prostate. Int J Hyperthermia 2004; 20:739-756.

Do HM, Kim BS. Percutaneous vertebroplasty for painful vertebral body compression fracture. In: Kim D, Fessler R, Regan J, eds. Endoscopic Spine Surgery and Instrumentation and Percutaneous Procedures. New York: Thieme, 2005.

Dong D, Dubeau L, Bading J, Nguyen M, Luna M, Yu H, Gazit-Bornstein G, Gordon M, Gomer C, Hall F, Gambhir SS, Lee A. Spontaneous and controllable activation of suicide gene expression driven by the stress-inducible Grp 78 promoter resulting in eradication of sizable human tumors. Hum Gene Ther 2004; 15:553-561.

Dougherty RF, Ben-Shachar M, Bammer R, Brewer AA, Wandell BA. Functional organization of human occipital-callosal fiber tracts. Proc Natl Acad Sci U S A 2005; 102:7350-7355.

Fahrig R, Wen Z, Ganguly A, DeCrescenzo G, Rowlands JA, Stevens GM, Saunders RF, Pelc NJ. Performance of a static-anode/flat-panel x-ray fluoroscopy system in a diagnostic strength magnetic field: a truly hybrid x-ray/MR imaging system. Med Phys 2005; 32:1775-1784.

Federle MP, Jeffrey RB, Jr., Desser TS, Anne VS, Eraso A. Diagnostic Imaging: Abdomen. Salt Lake City: Amirsys Inc., 2004.

Fleischmann D. Contrast medium delivery for vascular MDCT: principles and rationale. In: Reiser MF, Takahashi M, Modic M, Becker CR, eds. Multislice CT. 2nd rev. ed. New York: Springer, 2004; 27-33.

Fleischmann D. Priniciples of contrast medium delivery of computed tomography angiogrphy. In: Saini SJ, Bonomo L, Teasdale E, White R, eds. Yearbook in MDCT. Oxford: Clinical Publishin Serviced Limited, 2005; 323-336.

Fleischmann D. Contrast-medium administration. In: Catalano C, Abe H, eds. Multidetector Row CT Angiography. Berlin; Heidelberg; New York: Springer, 2005; 41-54.

Fleischmann D, Hellinger JC, Napoli A. Multidetector-row CT angiography of peripheral arteries: Imaging upper-extremity and lower-extremity vascular disease. In: Catalano C, Abe H, eds. Multidetector Row CT Angiography. Berlin; Heidelberg; New York: Springer, 2005; 187-198.

Fleischmann D, Rubin GD. Quantification of Intravenously Administered Contrast Medium Transit through the Peripheral Arteries: Implications for CT Angiography. Radiology 2005.

Forero A, Weiden PL, Vose JM, Knox SJ, LoBuglio AF, Hankins J, Goris ML, Picozzi VJ, Axworthy DB, Breitz HB, Sims RB, Ghalie RG, Shen S, Meredith RF. Phase I trail of a novel anti-CD20 fusion protein in pretargeted radioimmunotherapy for B-cell non-Hogdkin's lymphoma. Blood 2004; 104:227-236.

Franc B, Yoshida E, Herfkens R, Goris M. Pericardial lymph node involvement in lymphoma as identified on PET. Clin Nucl Med 2004; 29:741-742.

Fredricson M, Jang KU, Bergman AG, Gold GE. Femoral diaphyseal stress fractures: Results of a systematic bone scan and magnetic resonance imaging evaluation in 25 runners. Phys Ther Sport 2004; 5.

Frisoli JK, Sze DY, Kee S. Transcatheter embolization for the treatment of upper gastrointestinal bleeding. Tech Vasc Interv Radiol 2004; 7:136-142.

Ganaha F, Ohashi K, Do YS, Lee J, Sugimoto K, Minamiguchi H, Elkins CJ, Sameni D, Modanlou S, Ali M, Kao EY, Kay MA, Waugh JM, Dake MD. Efficient inhibition of in-stent restenosis by controlled stent-based inhibition of elastase: a pilot study. J Vasc Interv Radiol 2004; 15:1287-1293.

Ghaznour S, Desser T, Jeffrey RB, Jr. Increased through-transmission in abdominal tuberculous lymphadenitis. J Ultrasound Med 2004; 23:837-841.

Gold GE. MR imaging of articular cartialge. In:Magnetic Resonance Update, 2004.

Gold GE, Beaulieu C. Musculoskeletal imaging: Exploring new limits - MRI ON THE Fringe: Musculoskeletal MR imaging at 3.0 Tesla. In: RSNA Categorical Course Syllabus, 2004.

Gold GE, Besier TF, Draper CE, Asakawa DS, Delp SL, Beaupre GS. Weight-bearing MRI of patellofemoral joint cartilage contact area. J Magn Reson Imaging 2004; 20:526-530.

Gold GE, Fuller SE, Hargreaves BA, Stevens KJ, Beaulieu CF. Driven equilibrium magnetic resonance imaging of articular cartilage: initial clinical experience. J Magn Reson Imaging 2005; 21:476-481.

Gold GE, Han E, Stainsby J, Wright G, Brittain J, Beaulieu C. Musculoskeletal MRI at 3.0 T: relaxation times and image contrast. AJR Am J Roentgenol 2004; 183:343-351.

Gold GE, Hargreaves BA, Reeder SB, Vasanawala SS, Beaulieu CF. Controversies in protocol selection in the imaging of articular cartilage. Semin Musculoskelet Radiol 2005; 9:161-172.

Gold GE, Suh B, Sawyer-Glover A, Beaulieu C. Musculoskeletal MRI at 3.0 T: initial clinical experience. AJR Am J Roentgenol 2004; 183:1479-1486.

Green LA, Nguyen K, Berenj B, Bauer E, Barrio J, Namavari M, Satyamurthy N, Gambhir SS. A tracer kinetic model for FHGB for quantitating herpes simplex virus type I thymidine kinase reporter gene expressionin living animals using positron emission tomography. J Nucl Med 2004; 45:1560-1570.

Gross M, Stevens K. Sunburst periosteal reaction in osteogenic sarcoma. Pediatr Radiol 2005; 35:647-648.

Habte F, Levin CS. Study of low noise multichannel readout electronics for high sensitivty PET systems based on Avalanche Photodiode Arrays. IEEE Trans Nucl Sci, Nucl Med, Imaging Sci 2004; 51:764-769.

Hellinger JC. Evaluating mesenteric ischemia with multidetector-row CT angiography. Tech Vasc Interv Radiol 2004; 7:160-166.

Hiatt MD. Malpractice issues in radiology. J Am Coll Radiol 2004; 1:789.

Hiatt MD, Rubin GD. Surveillance for endoleaks: how to detect all of them. Semin Vasc Surg 2004; 17:268-278.

Hope MD, Levin JM, Markl M, Draney MT, Alley M, Herfkens RJ. Images in cardiovascular medicine. Four-dimensional magnetic resonance velocity mapping in a healthy volunteer with pseudocoarctation of the thoracic aorta. Circulation 2004; 109:3221-3222.

Horning SJ, Younes A, Kroll S, Jain V, Lucas J, Podoloff D, Goris M. Efficacy and Safety of Tositumomab and Iodine-131 Tositumomab (Bexxar) in B-cell Lymphoma Progressive after Rituximab. J Clin Oncol 2005; 23:712-719.

Hundt W, Siebert K, Wintersperger BJ, Becker CR, Knez A, Reiser MF, Rubin GD. Assessment of global left ventricular function: comparison of cardiac multidetector-row computed tomography with angiocardiography. J Comput Assist Tomogr 2005; 29:373-381.

Hwang B, Fredericson M, Chung CB, Beaulieu CF, Gold GE. MRI findings of femoral diaphyseal stress injuries in athletes. AJR Am J Roentgenol 2005; 185:166-173.

Hwang GL, Leung AN, Zinck SE, Berry GJ. Recurrent lymphoma of the lung: computed tomography appearance. J Comput Assist Tomogr 2005; 29:228-230.

Ihnken K, Sze D, Dake MD, Fleischmann D, Van der Starre P, Robbins R. Successful treatment of a Stanford type A dissection by percutaneous palement of a covered stent graf in the ascending aorta. J Thorac Cardiovasc Surg 2004; 127:1808-1810.

Illes J, Atlas SW, Raffin TA. Imaging neuroethics for the imaging neurosciences. Neuroscience Imaging 2005; 1:5-18.

Illes J, Kann D, Karetsky K, Letourneau P, Raffin TA, Schraedley-Desmond P, Koenig BA, Atlas SW. Advertising, patient decision making, and self-referral for computed tomographic and magnetic resonance imaging. Arch Intern Med 2004; 164:2415-2419.

Illes J, Racine E. Imaging or imagining? A neuroethics challenge informed by genetics. American Journal of Bioethics 2005; 5:1-14.

Iyer M, Bergara F, Lewis X, Zhang J, Carey M, Wu L, Gambhir SS. Non-invasive imaging of enhanced prostate-specific gene expression using a two-step transcriptional amplification based lentivirus vector. Mol Ther 2004; 10:545-552.

Iyer M, Salazer FB, Lewis X, Zhang L, Wu L, Carey M, Gambhir SS. Non-invasive imaging of a transgenic mouse model using a prostate-specific two-step transcriptional amplification strategy. Transgenic Res 2005; 14:47-55.

Jeffrey RB, Jr. Pancreatic Malignancy. In:Imaging in Oncology. 2nd ed. London, England: Taylor and Francis, 2004.

Jeffrey RB. Book review. Abdom Imaging 2005.

Joon Yun A, Bazar KA, Lee PY. Tumors may modulate host immunity partly through hypoxia-induced sympathetic bias. Med Hypotheses 2004; 63:352-356.

Jun P, Chow LC, Jeffrey RB. The sonographic features of papillary thyroid carcinomas: pictorial essay. Ultrasound Q 2005; 21:39-45.

Karanas YL, Antony A, Rubin G, Chang J. Preoperative CT angiography for free fibula transfer. Microsurgery 2004; 24:125-127.

Kee ST, Ganguly A, Daniel BL, Wen Z, Butts K, Shimikawa A, Pelc NJ, Fahrig R, Dake MD. MR-guided transjugular intrahepatic portosystemic shunt creation with use of a hybrid radiography/MR system. J Vasc Interv Radiol 2005; 16:227-234.

Kenanova V, Olafsen T, Crow DM, Sundaresan G, Subbarayan M, Carter NH, Ickle DN, Yazaki PJ, Chatziioannou AF, Gambhir SS, Williams LE, Shively JE, Colcher D, Raubitschek AA, Wu AM. Tailoring the pharmacokinetics and positron emission tomography imaging properties of anti-carcinoembryonic antigen single-chian FvFv antibody fragments. Cancer Res 2005; 65:622-631.

Kim BS, Do HM, Razavi M. N-butyl cyanoacrylate glue embolization of splenic artery aneurysms. J Vasc Interv Radiol 2004; 15:91-94.

Kim DH, Margolis D, Xing L, Daniel B, Spielman D. In vivo prostate magnetic resonance spectroscopic imaging using two-dimensional J-resolved PRESS at 3 T. Magn Reson Med 2005; 53:1177-1182.

Kim F, Barnes P. Epilepsy in Children. In: Latchaw RE, Kucharczyk J, Moseley ME, eds. Diagnostic and Therapeutic Imaging of the Nervous System. Philadelphia: Elsevier Publishers, 2004.

Kim YJ, Dubey P, Ray P, Gambhir SS, Witte O. Multimodality imaging of lymphocyte migration using lentiviral-based transduction of a fusion reporter gene. Mol Imaging Biol 2004; 6:331-340.

Kirschen MP, Chen SH, Schraedley-Desmond P, Desmond JE. Load- and practice-dependent increases in cerebro-cerebellar activation in verbal working memory: an fMRI study. Neuroimage 2005; 24:462-472.

Koo S, Gold GE, Andriacchi TP. Considerations in measuring cartilage thickness using MRI: factors influencing reproducibility and accuracy. Osteoarthritis Cartilage 2005.

Kornaat PR, Reeder SB, Koo S, Brittain JH, Yu H, Andriacchi TP, Gold GE. MR imaging of articular cartilage at 1.5T and 3.0T: comparison of SPGR and SSFP sequences. Osteoarthritis Cartilage 2005; 13:338-344.

Kuo MD, Bright IJ, Wang DS, Ghafouri P, Yuksel E, Hilfiker PR, Miniati DN, Dake MD. Local resistance to oxidative stress by overexpression of copper-zinc superoxide dismutase limits neointimal formation after angioplasty. J Endovasc Ther 2004; 11:585-594.

La Cruz A, Straka M, Koechl A, Sramek M, Groeller E, Fleischmann D. Non-linear model fitting to parameterized diseased blood vessels. In: Rushcmeier H, Turk G, van Wick JJ, eds. IEEE Visualization 2004. Houston: IEEE Computer Society, 2004; 393-400.

Latchaw R, Moseley ME, Kucharczyk J, eds. Imaging of the Nervous System. Philadelphia: Elsevier, 2004.

Levin CS. Basic physics of radioisotope imaging. In: Aarsvold J, Wernick M, eds. Emission Tomography: The Fundamentals of PET and SPECT: Elsevier-Academic Press, 2004.

Levin CS. Application-specific small field-of-view nuclear emission imagers in medicine. In: Aarsvold J, Wernick M, eds. Emission Tomography: The Fundamentals of PET and SPECT: Elsevier-Academic Press, 2004.

Levin CS, Foudray AMK, Olcott PD, Habte F. Investigation of position sensitive avalanche photodiodes for a new high resolution PET detector design. IEEE Trans Nucl Sci Nucl Med Imaging Sci 2004; 51:805-810.

Levin CS, Habte F, Foudray AM. Methods to extract more light from minute scinitillation crystals used in an ultra-high resolution positron emission tomography detector. Nucl Instrum Methods Phys Res A 2004; 527:35-40.

Levin YS, Chow LC, Pelc NJ, Sommer FG, Spielman DM. Estimation of renal extraction fraction based on postcontrast venous and arterial differential T1 values: an error analysis. Magn Reson Med 2005; 54:309-316.

Li P, Napel S, Acar B, Paik DS, Jeffrey RB, Jr., Beaulieu CF. Automatic registration of colonic polyps between supine and prone scans in CT colonography. Med Phys 2004; 31:2912-2923.

Li TQ, Kim DH, Moseley ME. High-resolution diffusion-weighted imaging with interleaved variable-density spiral acquisitions. J Magn Reson Imaging 2005; 21:468-475.

Lian J, Xing L. Incorporating model parameter uncertainty into inverse treatment planning. Med Phys 2004; 31:2711-2720.

Lian J, Xing L, Hunjan S, Dumoulin C, Levin J, Lo A, Watkins R, Rohling K, Giaquinto R, Kim D, Spielman D, Daniel B. Mapping of the prostate in endorectal coil-based MRI/MRSI and CT: a deformable registration and validation study. Med Phys 2004; 31:3087-3094.

Lilienstein J, Daniel BL, Ikeda DM. In vivo sonography through an open MRI breast coil to correlate sonographic and MRI findings. AJR Am J Roentgenol 2005; 184:S49-52.

Lin AH, Luo J, Mondshein LH, Ten Dijke P, Vivien D, Contag CH, Wyss-Coray T. Global Analysis of Smad2/3-Dependent TGF-{beta} Signaling in Living Mice Reveals Prominent Tissue-Specific Responses to Injury. J Immunol 2005; 175:547-554.

Liu C, Bammer R, Kim DH, Moseley ME. Self-navigated interleaved spiral (SNAILS): application to high-resolution diffusion tensor imaging. Magn Reson Med 2004; 52:1388-1396.

Liu C, Bammer R, Moseley ME. Limitations of apparent diffusion coefficient-based models in characterizing non-gaussian diffusion. Magn Reson Med 2005; 54:419-428.

Marchal G, Vogl TJ, Heiken JP, Rubin GD, eds. Multidetector-Row Computed Tomography: Scanning and Contrast Protocols. Milan: Springer, 2005.

Margolis DJ, Bammer R, Chow LC. Parallel imaging of the abdomen. Top Magn Reson Imaging 2004; 15:197-206.

Markl M, Draney MT, Hope MD, Levin JM, Chan FP, Alley MT, Pelc NJ, Herfkens RJ. Time-resolved 3-dimensional velocity mapping in the thoracic aorta: visualization of 3-directional blood flow patterns in healthy volunteers and patients. J Comput Assist Tomogr 2004; 28:459-468.

179

Markl M, Draney MT, Miller DC, Levin JM, Williamson EE, Pelc NJ, Liang DH, Herfkens RJ. Time-resolved three-dimensional magnetic resonance velocity mapping of aortic flow in healthy volunteers and patients after valve-sparing aortic root replacement. J Thorac Cardiovasc Surg 2005; 130:456-463.

Markl M, Pelc NJ. On flow effects in balanced steady-state free precession imaging: pictorial description, parameter dependence, and clinical implications. J Magn Reson Imaging 2004; 20:697-705.

Marks MP, Marcellus ML, Do HM, Schraedley-Desmond PK, Steinberg GK, Tong DC, Albers GW. Intracranial angioplasty without stenting for symptomatic atherosclerotic stenosis: long-term follow-up. AJNR Am J Neuroradiol 2005; 26:525-530.

Mayer D, Spielman DM. Detection of glutamate in the human brain at 3 T using optimized constant time point resolved spectroscopy. Magn Reson Med 2005; 54:439-442.

Medina D, Detoledo-Morrell L, Urresta F, Gabrieli JD, Moseley ME, Fleischmann D, Bennett DA, Leurgans S, Turner DA, Stebbens GT. White matter changes in mild cognitive impairment and AD: A diffusion tensor imaging study. Neurobiol Aging 2005; Jul 6; [Epub ahead of print].

Michalet X, Pinaud FF, Bentolila LA, Tsay JM, Doose S, Li JJ, Sundaresan G, Wu AM, Gambhir SS, Weiss S. Quantum dots for live cells, in vivo imaging, and diagnostices. Science 2005; 307:538-544.

Miller KL, Hargreaves BA, Gold GE, Pauly JM. Steady-state diffusion-weighted imaging of in vivo knee cartilage. Magn Reson Med 2004; 51:394-398.

Mirmiran M, Barnes PD, Keller KA, Constantinou JC, Fleisher BE, Hintz SR, Ariagno RL. Neonatal brain MRI before discharge is better than serial cranial US in predicting cerebral palsy in VLBW preterm infants. Pediatrics 2004.

Miyagawa M, Anton M, Haubner R, Simoes MV, Stadele C, Erhardt W, Reder S, Lehner T, Wagner B, Noll S, Noll B, Grote M, Gambhir SS, Gansbacher B, Schwaigner M, Bengel FM. PET imaging of cardiac transgen expression comparison of two approaches based on herpesviral thymidine kinase reporter gene. J Nucl Med 2004; 45:1917-1923.

Mlynash M, Eyngorn I, Bammer R, Moseley M, Tong DC. Automated method for generating the arterial input function on perfusion-weighted MR imaging: validation in patients with stroke. AJNR Am J Neuroradiol 2005; 26:1479-1486.

Mogensen M, Nino-Murcia M. Idiopathic granulomatous epididymo-orchitis: Sonographic appearance. J Ultrasound Med 2005; 24:1007-1010.

Moseley M, Bammer R. Tracking Cognition and Learnin with MRI Sequencing Tool. In:Stanford Center Focus, 2005.

Moseley M, Donnan G. Multimodality Imaging: Introduction. Stroke 2004; 35:2632-2634.

Moseley ME, Bammer R, Rother J. Techniques for the Detection of Cerebral Ischemia. In: Nowak H, ed. Handbook of "Magnetism in Medicine": Wiley-VCH, 2005.

Na DG, Thijs VN, Albers GW, Moseley ME, Marks MP. Diffusion-weighted MR imaging in acute ischemia: value of apparent diffusion coefficient and signal intensity thresholds in predicting tissue at risk and final infarct size. AJNR Am J Neuroradiol 2004; 25:1331-1336.

Napel S. Basic Principles of MDCT. In: Fischman E, Jeffrey RB, Jr., eds. Multidetector CT, Principles, Techniques, and Clinical Applications. Philadelphia, PA: Lippincott Williams and Wilkins, 2004; 3-13.

Napoli A, Fleischmann D, Chan FP, Catalano C, Hellinger JC, Passariello R, Rubin GD. Computed tomography angiography: state-of-the-art imaging using multidetector-row technology. J Comput Assist Tomogr 2004; 28 Suppl 1:S32-45.

Nau WH, Diederich CJ, Ross AB, Butts K, Rieke V, Bouley DM, Gill H, Daniel B, Sommer G. MRI-guided interstitial ultrasound thermal therapy of the prostate: a feasibility study in the canine model. Med Phys 2005; 32:733-743.

Offodile RS, Daniel BL, Jeffrey SS, Wapnir I, Dirbas FM, Ikeda DM. Magnetic resonance imaging of suspicious breast masses seen on one mammographic view. Breast J 2004; 10:416-422.

Olcott PD, Talcott JA, Levin CS, Habte F, Foudray AMK. Compact readout electronics for positron sensitive photomulplier tubes. IEEE Trans Nucl Sci Nucl Med Imaging Sci 2005; 52:21-27.

Paik DS, Beaulieu CF, Rubin GD, Jeffrey RBJ, Yee J, Napel S. A computer aided detection algorithm for colonic polyps and lung nodules in helical CT. IEEE Trans Med Imaging 2004; 23:661-675.

Panuelas I, Mazzolini G, Boan JF, Sangro B, M-Climent J, Ruiz J, Ruiz M, N. S, Qian C, Barrio J, Phelps MD, A. RJ, Gambhir SS, Prieto J. Positron emission tomography imagin of adenoviral-mediated transgene expression in living cancer patients. Gastroenterology 2005; 128:1787-1795.

Paulmurugan R, Gambhir SS. Firefly luciferase enzyme fragment complementation for imaging in cells and living animals. Anal Chem 2005; 77:1295-1302.

Pereira J, Sirlin C, Pinto P, Jeffrey RJ, Stella D, Casola G. Disproportionate Fat Stranding: A Helpful CT Sign in Patients with Acute Abdominal Pain. Radiographics 2004; 24:703-715.

Pfefferbaum A, Adalsteinsson E, Sullivan EV. Dysmorphology and microstructural degradation of the corpus callosum: Interaction of age and alcoholism. Neurobiol Aging 2005.

Pfefferbaum A, Adalsteinsson E, Sullivan EV. Frontal circuitry degradation marks healthy adult aging: Evidence from diffusion tensor imaging. Neuroimage 2005; 26:891-899.

Pfefferbaum A, Adalsteinsson E, Sullivan EV. Cortical NAA deficits in HIV infection without dementia: influence of alcoholism comorbidity. Neuropsychopharmacology 2005; 30:1392-1399.

Pfefferbaum A, Sullivan EV. Disruption of brain white matter microstructure by excessive intracellular and extracellular fluid in alcoholism: Evidence from diffusion tensor imagin. Neuropsychopharmacology 2005; 30:423-432.

Pisani LJ, Ross AB, Diederich CJ, Nau WH, Sommer FG, Glover GH, Butts K. Effects of spatial and temporal resolution for MR image-guided thermal ablation of prostate with transurethral ultrasound. J Magn Reson Imaging 2005; 22:109-118.

Quon A, Gambhir SS. FDG-PET and beyond: molecular breast cancer imaging. J Clin Oncol 2005; 23:1664-1673.

Racine E, Bar-Ilan O, Illes J. FMRI in the public eye. Nature Reviews Neuroscience 2005; 6:159-164.

Ray S, Paulmurugan R, Hildebrandt I, Iyer M, Wu L, Carey M, Gambhir SS. A novel bi-directional vector strategy for amplification of therapeutic and reporter gene expression. Hum Gene Ther 2004; 15:681-690.

Reeder SB, Herzka DA, McVeigh ER. Signal-to-noise ratio behavior of steady-state free precession. Magn Reson Med 2004; 52:123-130.

Reeder SB, Markl M, Yu H, Hellinger JC, Herfkens RJ, Pelc NJ. Cardiac CINE imaging with IDEAL water-fat separation and steady-state free precession. J Magn Reson Imaging 2005; 22:44-52.

Rieke V, Ganguly A, Daniel BL, Scott G, Pauly JM, Fahrig R, Pelc NJ, Butts K. X-ray compatible radiofrequency coil for magnetic resonance imaging. Magn Reson Med 2005; 53:1409-1414.

Rosenberg J, Chia YL, Plevritis S. The effect of age, race, tumor size, tumor grade, and disease stage on invasive ductal breast cancer survival in the U.S. SEER database. Breast Cancer Res Treat 2005; 89:47-54.

Ross AB, Diederich CJ, Nau WH, Gill H, Bouley DM, Daniel B, Rieke V, Butts RK, Sommer G. Highly directional transurethral ultrasound applicators with rotational control for MRI-guided prostatic thermal therapy. Phys Med Biol 2004; 49:189-204.

Ross AB, Diederich CJ, Nau WH, Rieke V, Butts RK, Sommer G, Gill H, Bouley DM. Curvilinear transurethral ultrasound applicator for selective prostate thermal therapy. Med Phys 2005; 32:1555-1565.

Rubin GD. CT angiography of the thoracic aorta. In: Schoepf UJ, ed. Multidetector-Row CT of the Thorax. Berlin: Springer-Verlag, 2004; 287-306.

Rubin GD, Lyo JK, Paik DS, Sherbondy AJ, Chow LC, Leung AN, Mindelzun R, Schraedley-Desmond PK, Zinck SE, Naidich DP, Napel S. Pulmonary nodules on multi-detector row CT scans: performance comparison of radiologists and computer-aided detection. Radiology 2005; 234:274-283.

Saket RR, Razavi MK, Sze DY, Frisoli JK, Kee ST, Dake MD. Stent-graft treatment of extracranial carotid and vertebral arterial lesions. J Vasc Interv Radiol 2004; 15:1151-1156.

Saket RR, Sze DY, Razavi MK, Kee ST, Frisoli JK, Semba CP, Dake MD. TIPS reduction with use of stents or stent-grafts. J Vasc Interv Radiol 2004; 15:745-751.

Sato M, Johnson M, Zhang L, Gambhir SS, Carey M, Wu L. Functionality of angrogen receptor-based gene expression imaging in hormone refractory prostate cancer. Clin Cancer Res 2005; 11:3743-3749.

Schmidt TG, Fahrig R, Pelc NJ, Solomon EG. An inverse-geometry volumetric CT system with a large-area scanned source: a feasibility study. Med Phys 2004; 31:2623-2627.

Schreibmann E, Lahanas M, Xing L, Baltas D. Multiobjective evolutionary optimization of the number of beams, their orientations and weights for intensity-modulated radiation therapy. Phys Med Biol 2004; 49:747-770.

Schreibmann E, Xing L. Feasibility study of beam orientation class-solutions for prostate IMRT. Med Phys 2004; 31:2863-2870.

Schreibmann E, Xing L. Narrow band deformable registration of prostate magnetic resonance imaging, magnetic resonance spectroscopic imaging, and computed tomography studies. Int J Radiat Oncol Biol Phys 2005; 62:595-605.

Schulte T, Sullivan EV, Muller-Oehring EM, Adalsteinsson E, Pfefferbaum A. Corpus Callosal Microstructural Integrity Influences Interhemispheric Processing: A Diffusion Tensor Imaging Study. Cereb Cortex 2005.

Sen L, Gambhir SS, Furukawa DB, Stout AL, Laks H, Cui G. Noninvasive imaging of ex vivo intracoronary delivered nonviral therapeutic transgene expression in heart. Mol Ther 2005; 12:49-57.

Sherbondy AJ, Holmlund D, Rubin GD, Schraedley PK, Winograd T, Napel S. Alternative input devices for efficient navigation of large CT angiography data sets. Radiology 2005; 234:391-398.

Shou Z, Yang Y, Cotrutz C, Levy D, Xing L. Quantitation of the a priori dosimetric capabilities of spatial points in inverse planning and its significant implication in defining IMRT solution space. Phys Med Biol 2005; 50:1469-1482.

Smith WS, Sung G, Starkman S, Saver JL, Kidwell CS, Gobin YP, Lutsep HL, Nesbit GM, Grobelny T, Rymer MM, Silverman IE, Higashida RT, Budzik RF, Marks MP. Safety and efficacy of mechanical embolectomy in acute ischemic stroke: results of the MERCI trial. Stroke 2005; 36:1432-1438.

Sommer G, Olcott EW, Chow LC, Saket RR, Schraedley-Desmond P. Measurement of Renal Extraction Fraction with Contrast-enhanced CT. Radiology 2005.

Song Y, Boyer A, Ma C, Jiang S, Xing L. Modulated electron beam therapy. In: Mundt AF, Roeske JC, eds. Intensity Modulated Radiation Therapy: A Clinical Perspective. Hamilton, Canada: BC Decker Inc. Publisher, 2005; 327-336.

Spencer DC, Szumowski J, Kraemer DF, Wang PY, Burchiel KJ, Spielman DM. Temporal lobe magnetic resonance spectroscopic imaging following selective amygdalohippocampectomy for treatment-resistant epilepsy. Acta Neurol Scand 2005; 112:6-12.

Straka M, Cervenansky M, La Cruz A, Koechl A, Sramek M, Groeller E, Fleischmann D. The vesselglyph: focus and context visualization in CT-angiography. In: Rushcmeier H, Turk G, van Wick JJ, eds. IEEE Visualization 2004. Houston: IEEE Computer Society, 2004; 385-392.

Sullivan EV, Deshmukh A, De Rosa E, Rosenbloom MJ, Pfefferbaum A. Striatal and forebrain nuclei volumes: Contributions to motor function and working memory deficits in alcoholism. Biolog Psychiatr 2005; 57:768-776.

Sullivan EV, Sable HJ, Strother WN, Friedman DP, Davenport A, Tillman-Smith H, Kraft RA, Wyatt C, Szeliga KT, Buchheimer NC, Daunais JB, Adalsteinsson E, Pfefferbaum A, Grant KA. Neuroimaging of rodent and primate models of alcoholism: initial reports from the integrative neuroscience initiative on alcoholism. Alcohol Clin Exp Res 2005; 29:287-294.

Sze DY, Magsamen KE, McClenathan JH, Keeffe EB, Dake MD. Portal hypertensive hemorrhage from a left gastroepiploic vein caput medusa in an adhesed umbilical hernia. J Vasc Interv Radiol 2005; 16:281-285.

Tang XW, Yang Y, Kim W, Wang Q, Qi P, Dai H, Xing L. Measurement of ionizing radiation using carbon nanotube field effect transistor. Phys Med Biol 2005; 50:N23-31.

Tolwani R, Hagan C, Runstadler J, Lyons H, Green S, Bouley D, Rodriguez L, Schendel S, Moseley M, Daunt D, Otto G, Cork L. Magnetic resonance imaging and surgical repair of cleft palate in a four-week-old canine (Canis familiaris): an animal model for cleft palate repair. Contemp Top Lab Anim Sci 2004; 43:17-21; quiz 58.

van den Bosch MA, Daniel BL, Mariano MN, Nowels KN, Birdwell RL, Fong KJ, Desmond PS, Plevritis S, Stables LA, Zakhour M, Herfkens RJ, Ikeda DM. Magnetic resonance imaging characteristics of fibrocystic change of the breast. Invest Radiol 2005; 40:436-441.

Vasanawala SS, Desser TS. Accommodation of requests for emergency US and CT: applications of queueing theory to scheduling of urgent studies. Radiology 2005; 235:244-249.

Vasanawala SS, Hargreaves BA, Pauly JM, Nishimura DG, Beaulieu CF, Gold GE. Rapid musculoskeletal MRI with phase-sensitive steady-state free precession: comparison with routine knee MRI. AJR Am J Roentgenol 2005; 184:1450-1455.

Versnick EJ, Do HM, Albers GW, Tong DC, Marks MP. Mechanical thrombectomy for acute stroke. AJNR Am J Neuroradiol 2005; 26:875-879.

Vidarsson L, Conolly SM, Lim KO, Gold GE, Pauly JM. Echo time optimization for linear combination myelin imaging. Magn Reson Med 2005; 53:398-407.

Wallace AM, Daniel BL, Jeffrey SS, Birdwell RL, Nowels KW, Dirbas FM, Schraedley-Desmond P, Ikeda DM. Rates of reexcision for breast cancer after magnetic resonance imaging-guided bracket wire localization. J Am Coll Surg 2005; 200:527-537.

Wang Q, Contag CH, Ilves H, Johnston BH, Kaspar RL. Small Hairpin RNAs Efficiently Inhibit Hepatitis C IRES-Mediated Gene Expression in Human Tissue Culture Cells and a Mouse Model. Mol Ther 2005.

Wang SL, Sze DY, Busque S, Razavi MK, Kee ST, Frisoli JK, Dake MD. Treatment of hepatic venous outflow obstruction after piggyback liver transplantation. Radiology 2005; 236:352-359.

Wang XY, Manjili MH, Park J, Chen X, Repasky E, Subjeck JR. Development of cancer vaccines using autologous and recombinant high molecular weight stress proteins. Methods 2004; 32:13-20.

Wang Y, Iyer M, Annala AJ, Chappell S, Mauro V, Gambhir SS. Noninvasive monitoring of target gene expression by imaging reporter gene expression in living animals usin improved bicistronic vectors. J Nucl Med 2005; 46:667-674.

Wapnir IL, Goris M, Yudd A, Dohan O, Adelman D, Nowels K, Carrasco N. The Na+/I- symporter (NIS) mediates iodide uptake in breast cancer metastases and can be selectively downregulated in the thyroid. Clin Cancer Res 2004; 10:4294-4302.

Weinreb JD, Larson PA, Woodard PK, Stanford W, Rubin GD, Stillman AE, Bluemke DA, Duerinckx AJ, Dunnick NR, Smith GG. American College of Radiology Clinical Statement of Noninvasive Cardiac Imaging. Radiology 2005; 235:723-727.

Wexler L. Invited Commentary. Radiographics 2005; 25:438-440.

Wooton-Gorges SL, Buonocore MH, Kupperman N, Marcin J, DiCarlos J, Neely EK, Barnes PD, Glaser N. Detection of cerebral b-hydroxy butyrate, acetoacetate, and lactate in children with diabetic ketoacidosis. AJNR Am J Neuroradiol 2005; 26.

Xing B, Khanamiryan A, Rao J. Cell-permeable near-infrared fluorogenic substrates for imaging beta-lactamase activity. J Am Chem Soc 2005; 127:4158-4159.

Xing L, Wessels B, Hendee WR. Point-Counterpoint Debate: The value of PET/CT is bein oversold as a clinical tool in radiation oncology. Med Phys 2005; 32:1457-1459.

Xing L, Wu Q, Yong Y, Boyer AL. Physics of IMRT and inverse treatment planning. In: Mundt AF, Roeske JC, eds. Intensity Modulated Radiation Therapy: A Clinical Perspective. Hamilton, Canada: BC Decker Inc. Publisher, 2005; 20-51.

Xing L, Yang Y, Spielman D. Molecular/functional image-guided intensity modulated radiation therapy. In: Bortfetld T, Schmidt-Ullrich R, de Neve W, eds. IMRT Handbook and Clinical Applications. Heidelberg, Berlin: Springer-Verlag.

Yaghoubi SS, Barrio JR, Namavari M, Satyamurthy N, Phelps ME, Herschman HR, Gambhir SS. Imaging progress of herpes simplex virus type I thymidin kinase suicide gene therapy in living subjects with positron emission tomoraphy. Cancer Gene Ther 2005; 12:329-339.

Yang Y, Xing L. Clinical knowledge-based inverse treatment planning. Phys Med Biol 2004; 49:5101-5117.

Yang Y, Xing L. Inverse treatment planning with adaptively evolving voxel-dependent penalty scheme. Med Phys 2004; 31:2839-2844.

Yang Y, Xing L. Quantitative measurement of MLC leaf displacements using an electronic portal image device. Phys Med Biol 2004; 49:1521-1533.

Yang Y, Xing L. Towards biologically conformal radiation therapy (BCRT): selective IMRT dose escalation under the guidance of spatial biology distribution. Med Phys 2005; 32:1473-1484.

Yuh EL, Shulman SG, Mehta SA, Xie J, Chen L, Frenkel V, Bednarski MD, Li KC. Delivery of systemic chemotherapeutic agent to tumors by using focused ultrasound: study in a murine model. Radiology 2005; 234:431-437.

Yun AJ. The intellectual lineage of paradoxical pharmacology strategy. Med Hypotheses 2005.

Yun AJ, Bazar KA, Gerber A, Lee PY, Daniel SM. The dynamic range of biologic functions and variation of many environmental cues may be declining in the modern age: implications for diseases and therapeutics. Med Hypotheses 2005; 65:173-178.

Yun AJ, Bazar KA, Lee PY, Gerber A, Daniel SM. The smoking gun: many conditions associated with tobacco exposure may be attributable to paradoxical compensatory autonomic responses to nicotine. Med Hypotheses 2005; 64:1073-1079.

Yun AJ, Lee PY. Maldaptation of the link between inflammation and bone turnover may be a key determinant of osteoporosis. Med Hypotheses 2004; 63:532-537.

Yun AJ, Lee PY. Enhanced fertility after diagnostic hysterosalpingography using oil-based contrast agents may be attributable to immunomodulation. AJR Am J Roentgenol 2004; 183:1725-1727.

Yun AJ, Lee PY. The link between T helper balance and lymphoproliferative disease. Med Hypotheses 2005; 65:587-590.

Yun AJ, Lee PY, Bazar KA. Modulation of autonomic balance by tumors and viruses. Med Hypotheses 2004; 63:344-351.

Yun AJ, Lee PY, Bazar KA. Modulation of host immunity by HIV may be partly achieved through usurping host autonomic functions. Med Hypotheses 2004; 63:362-366.

Yun AJ, Lee PY, Bazar KA. Clinical benefits of hydration and volume expansion in a wide range of illnesses may be attributable to reduction of sympatho-vagal ratio. Med Hypotheses 2005; 64:646-650.

Yun AJ, Lee PY, Bazar KA. Can thromboembolism be the result, rather than the inciting cause, of acute vascular events such as stroke, pulmonary embolism, mesenteric ischemia, and venous thrombosis?: a maladaptation of the prehistoric trauma response. Med Hypotheses 2005; 64:706-716.

Yun AJ, Lee PY, Bazar KA. Paradoxical strategy for treating chronic diseases where the therapeutic effect is derived from compensatory response rather than drug effect. Med Hypotheses 2005; 64:1050-1059.

In Press Papers, Book Chapters and Books

Barnes P, Levine D. Fetal brain imaging. In: Levine D, ed. Atlas of Fetal MR Imaging.

Barnes P. Neuroimaging of the spine and spinal neuraxis in childhood. In Kim D, Betz R, Huhn S, Newton P. Surgery of the Pediatric Spine.

Besier TF, Gold GE, Delp SL, Beaupre GS. specific modeling to estimate patellofemoral joint cartilage. stress. Med Sci Sports Exer.

Birdwell RL, Bandodkar P, Ikeda DM. Computer-aided detection with screening mammography in a university hospital setting. Radiology.

Caffarelli AD, Banovac F, Cheung SC, Fleischmann D, Mitchell RS. Unusual case of later thoracic stent graft failure after cardioversion. J Thorac Cardiovasc Surg.

Chen X, Park R, Khankaldyyan V, Gonzales-Gomez I, Tohme M, Moats R, Bading JR, Laug WE, Conti PS. Longitudinal microPET imaging of brain tumor growth with ^{18}F-Labeled RGD Peptide. Mol Imaging Biol.

Chen X. Multimodality imaging of tumor integrin expression. Mini-Reviews in Med Chem.

Chow LC, Napoli A, Klein MB, Chang J, Rubin GD. Vascular mapping with multidetector CT angiography prior to free-flap reconstruction. Radiology.

Conaghan P, Felson D, Gold GE, Lohmander D, Totterman S, Altman R. MRI of non-cartilaginous structures in the knee in OA. Osteoarthritis Cartilage

Dhanasopon AP, Levin CS, Foudray AMK, Olcott PD, Habte F. Scintillation crystal design features for a miniature gamma ray camera. IEEE Trans Nucl Sci, Nuclear Medical Imaging Sciences.

Do HM, Kim BS, Marcellus ML, Curtis L, Marks MP. Prospective analysis of clinical outcomes after percutaneous vertebroplasty for painful osteoporotic vertebral body fractures. AJNR

Espinosa L, Daniel BL, Nowels K, Jeffrey S, Ikeda DM. Magnetic resonance imaging features of mucosa-associated lymphoid tissue lymphoma in the breast, A Case Report. AJR.

Espinosa L, Daniel BL, Vidarsson L, Herfkens RJ, Zakhour M, Ikeda DM. Contrast–enhanced MRI of the lactating breast: Findings of normal lactation and breast cancer. Radiology

Fleischmann D. Contrast medium application in multislice CT. In: Brüning R, Flohr T, Küttner A, eds. Protocols for Multislice CT. Springer

Frates MC, Benson CB, Charboneau JW, et al. Management of thyroid nodules detected at sonography – Society of Radiologists in Ultrasound consensus conference statement. Radiology

Frates, MC, Benson CB, Charboneau JW, et al. Management of thyroid nodules detected at sonography – Society of Radiologists in Ultrasound consensus conference statement. Ultrasound Quarterly.

Gallelli KA, Wagner C, Karchemskiy A, Howe M, Spielman D, Reiss A, Chang KD, N-acetylaspartate levels in bipolar offspring with and at high-risk for bipolar disorder. Journal Bipolar Disorders.

Ganguly A, Wen Z, Daniel B, Butts, K, Kee S, Rieke V, Do H, Pelc N, Fahrig R, Truly hybrid X-ray/MR imaging: Towards a streamlined clinical system, Acad Radiol,

Gold GE, D. Burstein, B. Dardzinski, P. Lang, F. Boda, T. Mosher. MRI of articular cartilage in OA: Novel pulse sequences and compositional/functional markers. Osteoarthritis Cartilage

Gold GE, Hargreaves BA, Vasanawala SS, Webb JD, Brittain JH, Shimakawa AS, Beaulieu CF. Fluctuating equilibrium MR imaging of articular cartilage in the knee: initial experience in 10 healthy volunteers. Radiology.

Gold GE, Reeder SB, Yu H, Kornaat HP, Shimakawa AS, Johnson JW, Beaulieu CF, Brittain JH. Rapid 3D cartilage MR imaging at 3.0T with IDEAL (Dixon) SSFP. Radiology.

Hellinger JS, Rubin GD. CT angiography. In: Baum S ed., Abram's Angiography. Philadelphia: Lippincott Williams & Wilkins,

Illes J, DeVries R, Cho MK, Schraedley-Desmond P. ELSI priorities for brain imaging. Am J Bioethics

Illes J, Gallo M, Kirschen MP. An ethics perspective on the use of transcranial magnetic stimulation (TMS) for human neuromodulation, In A. Pascual-Leone (Ed). TMS: Disrupting the brain to enhance human cognitive abilities. Special Issue of Behav Neurol

Illes J, Racine E, Kirschen MP. A picture is worth 1000 words, but which 1000? In, J. Illes (Ed). Neuroethics: Defining the Issues in Theory, Practice and Policy. Oxford, UK: Oxford University Press.

Illes J, Racine E. (Eds.) Neuroethics: From neurotechnology to healthcare. Camb Q Healthc Ethics.

Illes J, Racine E. Neuroethics: Dialogue on a continuum from tradition to innovation. Am J Bioethics

Illes J, Raffin TA. No child left without a brain scan? Cerebrum.

Illes J. Neuroethics: In, Illes J (ed). Neuroethics: Defining the Issues in Theory, Practice and Policy. Oxford, UK: Oxford University Press.

Kang KW, Min J-J, Chen X, Gambhir SS. Comparison of [^{14}C]FMAU, [^{3}H]FEAU, [^{14}C]FIAU, and [^{3}H]PCV for monitoring reporter gene expression of wild type and mutant herpes simplex virus type 1 thymidine kinase in cell culture. Mol Imaging Biol.

Ketchum ES, Zamanian RT, Fleischmann D. CT-angiography of pulmonary artery aneurysms in Hughes-Stovin syndrome. AJR Am J Roentgenol.

Kim BS, Do HM, Marks MP. Diagnosis and management of cerebral sinus and venous thrombosis. In: Seminars in Cerebrovascular Disease: Cerebrovenous Diseases. Brewster R (ed).

Kurian AW, Hartman AR, Mills MA, Ford JM, Daniel BL, Plevritis SK. Opinions of women with high inherited breast cancer risk about prophylactic mastectomy: An initial evaluation from a screening trial including magnetic resonance imaging and ductal lavage. Health Expect.

Kwan SW, Partik BL, Zinck SE, Chan FP, Kee ST, Leung AN, Voracek M, Rubin GD. Primary interpretation of thoracic multidetector-row CT images using coronal reformations. AJR.

Levin CS, Habte F. Initial studies of a new detector design for ultra-high resolution positron emission tomography. IEEE Trans Nucl Sci, Nuclear Medical Imaging Sciences.

Li, Xing L, Radiation dose planning, computer-aided. In: Webster JG (ed). Encyclopedia of Medical Devices and Instrumentation. John Wiley & Sons, .

Illes J. (ed.) Neuroethics: Defining the Issues in Theory, Practice and Policy, Oxford, UK; Oxford University Press.

Mariano M, Van den Bosch M, Ikeda DM, Daniel BL, Nowels KW, Birdwell RL, Fong KJ, Desmond PS, Plevritis S, Stables LA, Zakhour M, Herfkens R. Contrast-enhanced MR imaging of ductal carcinoma in situ: Characteristics of a new intensity-modulated parametric mapping technique correlated to histopathologic findings. JMRI

Nino-Murcia M, Jeffrey RB Jr. McGahan JP. Gastrointestinal tract and peritoneal cavity. In: McGahan JP, Goldberg BB, eds. Diagnostic Ultrasound: A Logical Approach. Philadelphia: Lippincott-Raven Publishers.

Nino-Murcia M, Jeffrey RB Jr. Radiology of the appendix. Radiology, Diagnosis, Imaging and Intervention.

Pappas GP, Blemker SS, Beaulieu CF, McAdams TR, Whalen ST, Gold GE. In vivo anatomy of the Neer and Hawkins sign positions for shoulder impingement. J Shoulder Elbow Surg.

Peterfy C, Gold GE, Eckstein F, Cicuttini F, Dardzinski B, Stevens R. MRI protocols for whole-organ assessment of the knee in OA. Osteoarthritis Cartilage

Pineda AR, Reeder SB, Wen Z, Pelc NJ. Cramér-Rao bounds for 3-Point Dixon imaging. Magn Reson Med.

Racine E, Bar-Ilan O, Illes J. A decade of brain imaging coverage in the print media. Sci Commun.

Rakow-Penner R, Daniel B, Yu H, Sawyer-Glover A, Glover GH. Relaxation times of breast tissue at 1.5T and 3T using 3 point Dixon. J Magn Reson Imaging

Rand T, Basile A, Cejna M, Fleischmann D, Funovics M, Gschwendtner M, Haumer M, Von Katzler I, Kettenbach J, Lomoschitz F, Luft C, Minar E, Schneider B, Schoder M, Lammer J. PTA versus Carbofilm coated stents in infrapopliteal arteries: Pilot study. J Vasc Intervent Radiology

Reeder SB, Hargreaves B, Yu H, Brittain JH. Homodyne reconstruction for IDEAL water-fat decomposition. Magn Reson Med.

Reeder SB, Pineda AR, Wen S, Shimakawa A, Yu H, Brittain JH, Gold GE, Beaulieu CF, Pelc NJ. Iterative decomposition of water and fat with echo asymmetry and least-squares estimation: Application to fast spin-echo imaging. Magn Reson Med.

Reeder SB, Wintersperger BJ, Dietrich O, Lanz T, Greiser A, Reiser MF, Glazer GM, Schoenberg SO. Practical approaches to the evaluation of SNR performance with parallel imaging: Application with cardiac imaging and a 32-channel cardiac coil. Magn Reson Med

Robinson TE, Goris ML, Zhu HJ, Chen X, Bhise P, Sathi A, Sheikh F, Moss RB. Dornase Alpha reduces air trapping in children with mild CF lung disease: A quantitative analysis. CHEST.

Roos JE, Hellinger JC, Hallet RL, Fleischmann D, Zarins CK, Rubin GD. Detection of endograft fractures with multi-detector row CT (MDCT). J Vasc Surg.

Shi C, Jeffrey RB Jr. CT Colonography: Influence of 3D viewing and features of polyp candidate on interpretation using computer aided detection. Radiology.

Stebbins G, Urresta F, Gabrielli J, Moseley M, Bennett D, Turner D, Medina DM, deToledo-Morrell L. White matter changes in mild cognitive impairment and AD: A diffusion tensor imaging study. Neurobiol Aging.

van den Bosch M, Daniel BL. MR-Guided Interventions of the Breast. Magnet Reson Imaging Clin N Am.

van den Bosch M, Ikeda DM, Daniel BL, Nowels KN, Birdwell RL, Fong KJ, Desmond PS, Plevritis L, Stables LA, Zakhour M. Magnetic resonance imaging characteristics of fibrocystic changes of the breast. , Invest Radiol.

Vasanawala S, Desser TS, Jeffrey RB Jr. Pictorial essay: Value of delayed imaging in MDCT of the abdomen and pelvis. AJR.

Vasanawala SS, Hargreaves BA, J. M. Pauly, D. G. Nishimura, Beaulieu CF, Gold GE. Rapid musculoskeletal MR imaging with phase-sensitive steady state free precession. AJR Am J Roentgenol.

Venook RD, Hargreaves BA, Gold GE, Connolly SM, Scott GC. Automatic tuning of flexible interventional RF receiver coils. Magn Reson Med.

Weinstein S, Desser, TS, Jeffrey RB Jr. Intraoperative ultrasound of the pancreas – pictorial essay. AJR.

Wu QW, Xing L, Ezzel G, Mohan R, Inverse treatment planning. In: Modern Technology of Radiation Oncology: II. Van Dyk J, (ed). Madison, WI: Medical Physics Publishing

Wu Y, Zhang X, Xiong Z, Cheng Z, Fisher Dr, Liu S, Gambhir SS, Chen X. MicroPET Imaging of glioma alpha(v)-integrin expression using ^{64}Cu-labeled tetrameric RGD peptide. J Nucl Med

Peer-reviewed Presentations at Scientific Meetings
RSNA 2004
90TH SCIENTIFIC MEETING
CHICAGO, IL DECEMBER 2004

Antonios VP, Silverman NH, Chan FP. Effectiveness of cardiac-gated MDCT for the diagnosis of congenital heart disease in small children with high heart rates

Biswal S, Thomas R, Padmanabhan P, Lee S-W. Using molecular imaging techniques to monitor stem cell-based therapy for skeletal injury

Busse R, Brittain J, Johnson J, Hura S, Daniel B, Herfkens R. MRCP with 3D-FSE: How view order and T2-decay signal correction affect image quality

Chan FP, Narayan G, Napoli A, Choi B, Chun SH, Pretreatment planning for biventricular pacemaker placement using MDCT: effectiveness and findings

Davis TA, Kaminsky MS, Leonard JP, Wahl RL, Kroll S, Coleman M et al. Randomized trial assessing the contribution of Iodine-131 conjugation to Tositumomab compared with Tositumomab alone in patients with relapsed or refractory low-grade or transformed low-grade non-Hodgkin's lymphoma.

Desser TS, Kirkpatrick ID, Mindelzun RE. Dynamic MDCT Evaluation of suspected small bowel obstruction

Desser TS, Margolis D, Shelton A, Welton M, Jeffrey RB. MDCT for local staging of rectal cancer: comparison with endoscopic ultrasound

Gilat Schmidt T, Bennett R, Mazin S, Star-Lack J, Solomon E, Pelc N. First images from a table-top inverse geometry volumetric CT system with a large-area scanned source

Gold G, Besier T, Draper C, Asakawa D, Delp S, Beaupre G. Upright weight bearing MRI of patellofemoral joint cartilage contact area

Hellinger J, Napoli A, Schraedley-Desmond P, Fleischman D, Rubin G. Multi-detector row CT angiography (MDCTA) of the upper extremity (UE): Comparison with digital subtraction angiography (DSA)

Hellinger J, Napoli A, Williamson E, Fleischman D, Rubin G. Upper extremity (UE) multi-detector row CT (MDCT) angiography: Clinical experience in 100 examinations

Hellinger J, Raman R, Raman B, Raman L, Beaulieu C. Mobile image interpretation using handheld personal digital assistants: preliminary clinical validation using head and chest CT

Hellinger J, Reeder S, Markl M, Herfkens R. Combined "Dixon" water-fat separation and steady state free precession cardiac cine imaging: clinical application

Hiatt MD, Stockton CG. The impact of the flexner report on the fate of medical schools in north america after 1909

Hiatt MD. The relationship between physician supply and per capita income in counties across the united states

Hollingsworth C, Chan FP, Yoshizumi TT, Frush DP, Nguyen G, Lowry CR. Pediatric gated cardiac CT angiography: what is the radiation dose?

Hundt W, Guccione S, Mayer D, Bednarski M. In vivo assessment of gene expression ability after application of focused ultrasound

Ikeda D, Birdwell R, Hancock S. Imaging results in women treated for hodgkin disease (HD) invited for late-effects of HD

Jude C, Sherbondy AJ, Schraedley-Desmond P, Napel S, Rubin GD. Radiologist characterization of lung nodule candidates detected by computer aided detection (CAD): Comparison of visualization methods

Kim D-H, Margolis D, Daniel B, Xing L, Spielman D. Magnetic resonance spectroscopic imaging of the human prostate using spiral based j-resolved technique at 3 Tesla main magnetic field

Kirkpatrick ID, Desser TS, Nino-Murcia M, Jeffrey RB. Small cystic lesions of the pancreas: Clinical significance and findings at follow-up

Kornaat, Reeder SB, Koo S, Bloem J, Gold GE. Comparison of articular cartilage MR imaging at 1.5T and 3.0T using SPGR and SSFP sequences

Mazin SR, Schmidt T, Pelc NJ Collimator for a multiple-eye inverse-geometry volumetric CT system

Nagle SK, Chan FP. Cardiac heterotaxy: Emerging state-of-the-art evaluation using cardiac-gated MDCT and MRI

Napoli A, Helinger J, Fleischmann D, Rubin G. Multi-detector row spiral CT pulmonary angiography (CTPA): Diagnostic performance of 4, 8, and 16 row ct scanners

Paik DS, Sundaram P, Beaulieu CF, Napel S. Anatomically selective morphological enhancement and suppression in CT colonography: initial experience with a Lagrangian approach

Pineda A, Pelc N. To bin or not to bin? A question regarding the noise properties of CT reconstructions with or without binned projections

Quon A, Taira A, Herfkens R, Goris M, Kalinyak J, Gambhir S. Assessment of integrated FDG PET/CT imaging in the detection of bone metastases

Reeder SB, Beaulieu C, Johnson J, Yu H, Brittain J, Gold G, et al. T1 and T2 weighted brachial plexus imaging with fast spin-echo and "Dixon" Fat-water separation: comparison with STIR and fat saturation

Reeder SB, Pineda AR, Y H, Wen Z, Shimakawa A, Brittain JH, Gold GE, Pelc NJ. Asymmetric echoes for optimal SNR performance of "Dixon" water-fat separation with fast spin-echo imaging

Reeder SB, Yu H, Johnson J, Shimakawa A, Brittain JG, Pelc NJ, Beaulieu CH, Gold GE. T1 and T2 weighted brachial plexus fast spin-echo imaging with "Dixon" fat-water separation: A comparison with STIR and fat saturation

Rubin DL, Desser TS. Building an open-architecture integrated data warehouse for radiology using public domain tools

Rubin DL, Desser TS. Radbank: Evaluating an integrated data warehouse for radiology research and teaching

Starman J, Strobel N, Pelc N, Fahrig R. Extrapolating truncated projections using 0th and 1st moment constraints

Sun S, Rubin GD, Napel S. A simulated annealing-based algorithm for lung nodule registration in CT scans

Sundaram P, Sifakis E, Paik DS, Beaulieu CF, Napel S. Removal of folds in CT colonography using level sets and physically-based simulation: Proof of concept

Wang D, Bryant C, Lin C, Waugh J, Kuo M, Dake M. Optical molecular imaging of targeted cancer antigens after transdermal or transepithelial delivery using a HIV tat-peptide derivative

Balci SK, Acar B, Paik DS, Beaulieu CF, Napel S. Registration of supine and prone CT colonography data using dynamic time warping: Method and evaluation.

Burnside ES, Sisney GA, Rubin DL, Ochsner JE: The ability of microcalcification descriptors in the BIRADS 4th edition to stratify the risk of malignancy

Gold GE, Fuller SE, Shimakawa A, Yu H, Johnson JW; Beaulieu CF, Brittain J, Reeder S. MR imaging of the ankle: Comparison of FS-FSE with IDEAL-FSE

Iagaru A, Masamed R, Singer PA, Conti PS. Detection of occult medullary thyroid cancer with FDG PET and PET/CT.

Iagaru A, Quan V, Silberman H, Conti PS. Sentinel lymph node scintigraphy and FDG PET in the diagnosis and management of breast cancer.

Konukoglu E, Acar B, Paik DS, Beaulieu CF, Napel S. Polyp enhancement scheme for improved detection of colonic polyps in CT colonography.

Kukuk M, Arakawa H, Marks MP, Do HM, Napel S. Rotational Roadmapping: A contrast- and time-efficient navigation technique based on a single acquisition of multiple views.

Lee S-W, Leaffer D, Greve JM, Lollini L, Manning A, Gold GE , Biswal S. Early histological changes seen in a murine model of rheumatoid arthritis can be detected with micro-computed tomography and micro-magnetic resonance imaging

Leung W, Burnside ES, Rubin DL: Using a probabilistic expert system to determine the likelihood of malignancy for microcalcifications on mammography: performance and examples

Li T, Schreibmann E, Yang Y, Xing L. Reconstruction-based respiratory motion correction for improved target localization with on-board cone-beam CT imaging

Mazin SR, Star-Lack J, Bennett NR, Gilat Schmidt T, Pelc NJ. Wider field-of-view inverse-geometry CT with multiple detector arrays: initial experimental results

Quon A, Margolis DJ, Napel S, Beaulieu CF, S. S. Gambhir. Pilot study to develop and evaluate integrated FDG PET/CT scanning to perform 3D virtual colonscopy and bronchoscopy.

Rakshe T, Fleischmann D, Roos JE, Napel S. Automated tracking of vascular centerlines through CTA data: A knowledge-based approach.

Reeder SB, Hargreaves BA, Johnson, JW, Brittain JH, Gold GE. Water-fat separation with IDEAL-GRE and IDEAL-SPGR: Comparison to FS-SPGR for cartilage imaging in the knee at 3.0T.

Rubin DL, Fergerson R, Musen MA: Protégé: An open-source tool for managing and analyzing radiology vocabularies and knowledge

Rubin DL, Grossman D, Dameron O, Musen MA. Toward virtual humans: creating models from images incorporating anatomic and physiological knowledge for simulating the consequences of trauma.

Rubin DL. Improving RadLex using terminological analysis with ontology models

Rubin DL. Managing data explosion in radiology: using ontologies to facilitate information retrieval

Rubin DL. What are ontologies, and how are they useful to radiology?

Schmidt TG, Star-Lack H. Bennett R, Solomon E; Mazin SR, Fahrig R, Pelc NJ. Investigation of a prototype table-top inverse-geometry volumetric CT system

Shi R, Schraedley-Desmond P, Napel S, Margolis DJ, Yee J, Beaulieu CF, et al. Computer aided polyp detection in CT colonography: Influence of 3D viewing and features of polyp candidates on interpretation

Sun S, Rubin GD, Napel S. A semi-rigid model for lung nodule registration in computed tomography (CT) scans.

Sundaram P, Sifakis E, Paik DS, Beaulieu CF, Napel S. Fold Removal in CT colonography (CTC): A physics-based approach.

Wen Z, Pelc N, Nelson W, Fahrig R, Investigation of increase in radiation when an x-ray tube is placed in a magnetic field

Won J, Rubin GD, Raman B, Napel S. Flattening of the abdominal aortic vascular tree for effective visualization.

Blatnik D, Butts K. Motion compensation in mri temperature imaging

Blemker SS, Sherbondy AJ, Akers DL, Bammer R, Delp SL, Gold GE. Characterization of skeletal muscle fascicle arrangements using diffusion tensor tractography

Brau ACS, McKenzie CA, Shimakawa A, Yu H, Johnson JW, Brittain JH, Reeder SB. Accelerated IDEAL water-fat separation techniques for single- and multi-coil applications

Brittain JH, Shimakawa A, Johnson JW, Dharmakumar R, Gold GE, Hu B, Wright GA, Hargreaves BA. SSFP non-contrast-enhanced MR angiography at 3.0T: improved arterial-venous contrast with increased TR

Busse RF, Johnson JW, Brittain JH, Matthias S, Herfkens R. Suppression of artifacts caused by loss of breath hold

Chen J, Daniel BL, R. Butts K. Optimized MR-guided biopsy with SSFP and a hybrid injection scheme

Cheng CP, Wilson NM, Herfkens RJ, Taylor CA. Superficial femoral artery deformations due to maximal hip and knee flexion: Implications for stent design

Clayton DB, Bammer R. Methods for SENSE reconstruction with partial k-space acquisition

Clayton DB, Skare S, Golub GH, Modarresi M, Bammer R. Augmented SENSE reconstruction by an improved regularization approach

Dietrich O, Reeder SB, Reiser MF, Schoenberg SO. Influence of parallel imaging and other reconstruction techniques on the measurement

Draper C, Beseier T, Santos J, Blemker S, Pauly J, Beaupre G, Delp S, Gold G. Estimation of patellar tendon strain in vivo during static and dynamic loaded knee flexion

Ennis DB, Kindlmann G. Orthogonal tensor decomposition for analysis of DTMRI anisotropy

Fuller SE, Reeder SB, Shimakawa A, Yu H, Johnson JW, Beaulieu CF, Gold GE. IDEAL-FSE Imaging of the ankle: initial clinical experience

Gold G, Hargreaves B, Han E, Pauly J, Wright G, Beaulieu C, Brittain J. Rapid measurement of cartilage T1 and T2 relaxation times at 3.0T with spiral

Gold G, Reeder S, Yu H, Shimakawa A, Johnson J, Pelc N, Beaulieu C, Brittain J. Cartilage morphology at .5T: Comparison of 3D FS-SPGR and IDEAL SPGR imaging

Gu M, Kim DH, Adalsteinsson E, Spielman DM, Brain 3D MRSI using Dualband Spectral-Spatial Excitation and k-Space Corrected Spiral Readout

Guccione S, Yang Y-S, Chia YL, Wang Y, Lim M, Homer R, Harsh G, Atlas C, Bednarski M. Growth factors and integrins associated with contrast-enhancing regions of GBM

Hsu J-J, Glover GH. Rapid method for mapping the longitudinal relaxation time

Hsu J-J, Glover GH. Towards Dynamic Shimming for fMRI

Hu Y, Glover GH. Conjugate Kz 3D spiral-in/out sequence

Hu Y, Glover GH. Reduce physiological noise with multi-slab technique

Josan S, Butts K, Pauly J. Effect of constant frequency noise in half-echo radial sampling

Kim D, Adalsteinsson E, Spielman DM. Reducing gradient imperfections for spiral CSI

Law CS, Glover GH. New Interleaved spiral in/out fMRI method

Lew C, Bammer R, Spielman D, Chan F. Challenges with coil calibrations in in-vivo phase contrast SENSE

Lew C, Spielman D, Chan F, Bammer R. Effects of phase perturbations in SENSE coil calibration

Lew C, Spielman D, Chan F, Bammer R. Improved turbo SENSE with iterated conjugate gradient phase refinement

Liu C, Bammer R, Moseley ME. High resolution multi-shot SENSE DTI using self-navigated interleaved spirals (SNAILS)

Liu C, Bammer R, Moseley ME. Limitations of ADC-based models in characterizing non-gaussian diffusion

Liu C, Moseley ME, Bammer R. Fast SENSE reconstruction using linear system transfer function

Liu C, Moseley ME, Bammer R. Iterative phase correction of multi-shot DWI using conjugate gradient method

Liu C, Moseley ME, Bammer R. Simultaneous off-resonance and phase correction for multi-shot DWI

Margolis D, Daniel B, Glover G, Kim D, Spielman D, Sommer G. Clinical Evaluation of 3T prostate magnetic resonance imaging and spectroscopy with spiral J-resolved PRESS,

Margolis DJ, Daniel BL, Glover G, Herfkens RJ, Pal S, Plevritis S, Sigal B, Ikeda D. Kinetic and morphologic parameters on MRI predict response to neoadjuvant chemotherapy in locally advanced breast cancer

Mayer D, Gu M, Kim D-H, Adalsteinsson E, Spielman DM. Effectively decoupled spiral CSI with frequency-selective lipid suppression at 3 T

McKenzie CA, Reeder SB, Yu H, Brau ACS, Shimakawa A, Johnson JW, Farrar N, Daniel B, Rofsky NM, Brittain JH. IDEAL breast MRI

McKenzie CA, Reeder SB, Yu H, Brau ACS, Shimakawa A, Johnson JW, Farrar N, Rofsky NM, Brittain JH. Dynamic contrast enhanced IDEAL with parallel imaging

Newbould RD, Gold GE, Alley MT, Bammer R. Quantified T1, T2, and PD mapping in cartilage with 3D IR-trueFISP

Pineda AR, Reeder SB, Wen Z, Pelc NJ. Optimization of echo time shifts for 3-Pt fat/water separation

Pisani LJ, Bammer R, Glover GH. Feasibility of inner volume excitation for fetal fMRI (f-fMRI)

Po J, Margolis DJ, Cunningham CH, Herfkens RJ, Ikeda DM, Daniel BL. Water-selective spectral-spatial contrast-enhanced breast MRI for cancer detection in patients with extracapsular and injected free silicone

Rakow-Penner R, Daniel BL, Gold G, Pauly JM, Mazin SR, Glover GH. Correction of 3D truncation artifacts in knee and breast imaging

Rakow-Penner R, Daniel BL, Po J, Sawyer-Glover AM, Bammer R. Viable b-value range for diffusion weighted imaging of the breast at 1.5T

Reeder SB, Hargreaves BA, Yu H, Brittain JH. Homodyne reconstruction and IDEAL (Dixon) water-fat decomposition

Reeder SB, Pineda AR, Yu H, McKenzie CA, Brau AC, Gold GE, Johnson JW, Pelc NJ, Brittain JH. Water-fat separation with IDEAL-SPGR

Reeder SB, Wintersperger BJ, Dietrich O, Lanz T, Greiser A, Reiser MF, Glazer GM, Schoenberg SO. Cardiac CINE SSFP imaging with a 32-channel cardiac coil: Evaluation of SNR performance for parallel imaging at 1.5T

Ress D, Glover GH, Liu J. Gray-matter morphometry using high-resolution fMRI

Rieke V, Ross AB, Nau WH, Diederich CJ, Sommer G, Butts K. Referenceless thermometry in the presence of phase discontinuities between water

Santos JM, Gold G, Beseier T, Hargreaves BA, Draper C, Beaupre GS, Delp SL, Pauly JM. Ptellofemoral joint kinematics with real-time MRI at 0.5T

Schroeder JL, Spielman DM, Adalsteinsson E, Hurd RE, Gold GE. $_1$H-MRS of muscle at 3.0T in endurance-trained subjects before and after exercise

Skare S, Bammer R. Spatial modeling of the GRAPPA weights

Takehara Y, Isoda H, Hirano M, Takeda H, Yamashita S, Nozaki A, Nagasawa K, Alley MT, Markl M, Pelc NJ, Sakahara H. Time-resolved 3D velocity mapping for the abdominal aorta and its branches

van den Bosch MA, Daniel BL, Nowels KW, Jeffrey SS, Pal S, Ikeda DM. MRI-guided needle localization of suspicious breast lesions: Results of a freehand technique

Vance CJ, Newbould RD, Ames BN, Bammer R. Placental imaging and relaxation parameter mapping at 1.5 Tesla

Vidarsson L, Cunningham C, Lim KO, Pauly JM. Myelin imaging with matched spin-echo pulse pairs

Vidarsson L, Daniel BL, M. Zakhour, Pauly JM. DCE breast MRI: How fast is fast enough?

Wintersperger BJ, Reeder SB, Dietrich O, Huber A, Lanz T, Greiser A, Reiser MF, Schoenberg SO. Multi-slice TSENSE cardiac CINE SSFP imaging with a 32-channel cardiac coil

Yu H, Fahrig R, Butts K, Ganguly A, Adalsteinsson E, Mayer D, Pelc NJ. MR Imaging for polymethylmethacralate during a percutaneous vertebroplasty procedure

Yu H, McKenzie CA, Shimakawa A, Brau AC, Pineda AR, Pelc NJ, Brittain JH, Reeder SB. Parallel imaging accelerated single acquisition water-fat separation for dynamic imaging

OTHER SCIENTIFIC MEETINGS

Arakawa H, Davis C, Howard D, Baumgardner W, Marks MP, Do HM. Embolization of swine retia mirabilia (RMs) experimental arteriovenous malformation (AVM) models with non-adhesive liquid embolic material: Eudragit polymer. 8th Joint Annual Meeting of AANS/CNS Cerebrovascular Section and the American Society of Interventional and Therapeutic Neuroradiology (ASITN), New Orleans, LA, February 2005.

Barnes P, Lertvananurak R, Hahn J, DiDomenico P. Leukoencephalopathy: An unusual pattern in infantile hypoxia-ischemia. 48th Annual Meeting, Society for Pediatric Radiology, New Orleans, LA, May 7, 2005

Barnes P, Lertvananurak R, Hahn J, DiDomenico P. Leukoencephalopathy: An unusual pattern in infantile hypoxia-ischemia. American Society of Pediatric Neuroradiology, American Society of Neuroradiology, Toronto, Ontario, May 25, 2005.

Barnes P. Cerebral venous thrombosis: A mimic of nonaccidental injury. American Society of Pediatric Neuroradiology, American Society of Neuroradiology, Toronto, Ontario, May 25, 2005

Bell-Stephens TE, Garrett L, Marcellus ML, Marks MP, Nicolas LE, Steinberg GK, Vavao J, Albers GW. Developing a stroke code. International Stroke Conference 2005, New Orleans, LA, February 2005.

Besier T, Gold GE, Draper C, Powers C, Delp S, Beaupre G. Methods to determine in vivo cartilage stress in the patellofemoral joint from weight-bearing MRI. Proceedings of the American Society of Biomechanics, September 2004.

Breen MS, Butts K, Chen L, Saidel GM, Wilson DL. MRI-guided laser thermal ablation: Model to predict cell death from MR thermometry images for real-time therapy monitoring. Proceedings of the 2004 IEEE Engineering in Medicine and Biology Society International Conference. San Francisco, California, September 2004.

Breen MS, Butts K, Chen L, Saidel GM, Wilson DL. MRI-guided laser thermal ablation: Model and parameter estimates relating MR thermometry images to cell death. Proceedings of IEEE International Symposium on Biomedical Imaging: From Nano to Macro. Arlington, Virginia, April 2004.

Butts K, Rieke V, Pisani L, Sommer G, Diederich C, Ross A, Kinsey A, Nau W, Dumoulin K, Watkins R, Bouley D. Assessment of MR thermometry during high intensity ultrasound ablation of the canine prostate, International Symposium on Therapeutic Ultrasound, October 2005

Cai W, Chen X. GD peptide-labeled quantum dots for optical imaging of integrin $\alpha_v\beta_3$ expression. The 4th Annual Meeting of the Society for Molecular Imaging, Cologne, Germany, September 2005

Cai W, Chen X. PET Imaging of tumor integrin expression. 2005 IEEE Computational Systems Bioinformatics Conference, Stanford, CA, August 2005

Cai W, Chen X. RGD-labeled quantum dot for imaging tumor cells overexpressing $\alpha_v\beta_3$ integrin. 19th American Peptide Symposium, San Diego, June 2005

Chen X. 18F-labeled cyclic RGD peptides for non-invasive PET imaging of tumor integrin expression. NIBIB - Annual Grantee Meeting, Washington, D.C., August 2005

Chen X. PET imaging of tumor integrin expression: From bench to bed-side. 2005 Molecular Imaging International Symposium, Taipei, ROC, November, 2005

Chen X. α_v integrin targeted delivery of Paclitaxel. Era of Hope Department of Defense Breast Cancer Research Program Meeting, 2005 Proceedings, June 8-11, Philadelphia, PA

Cheng Z, Keren S, Chen X, Gambhir SS. Near-infrared fluorescent dye conjugated D-glucosamine as a novel probe for tumor optical imaging in cell culture and in living mice. AMI International Conference 2005, Orlando, FL, March 2005.

Cheng Z, Subbarayan M, Chen X, Gambhir SS. (4-[18F]fluorophenyl) triphenylphosphinium as a potential imaging agent for mitochondrial dysfunction. AMI International Conference 2005, Orlando, FL, March 2005.

Cheng Z, Wu Y, Xiong Z, Gambhir SS, Chen X. Cyanine Dye Conjugated RGD monomer, dimer, tetramer for optical imaging of integrin alpha(v)beta(3) in living Mice. AMI International Conference 2005, Orlando, FL, March 2005.

Cheng Z, Xiong Z, Wu Y, Zhang X, Chen X, Gambhir SS. MicroPET Imaging of melanoma using Cu-64 labeled alpha-melanocyte stimulating hormone peptide analogue. AMI International Conference 2005, Orlando, FL, March 2005.

Chinn G, Foudray A, Levin C. Comparing geometries for PET systems with depth of interaction. 2005 IEEE Medical Imaging Conference. Puerto Rico, October 23-29, 2005.

Coert BA, Dodd RL, Marcellus ML, Do HM, Marks MP, Chang SD, Steinberg GK. Posterior circulation fusiform aneurysms: results of surgical, endovascular and combined treatment. 8th Joint Annual Meeting of AANS/CNS Cerebrovascular Section and the American Society of Interventional and Therapeutic Neuroradiology (ASITN), New Orleans, LA, February 2005.

Coert BA, Dodd RL, Marcellus ML, Do HM, Marks MP, Chang SD, Steinberg GK. Posterior circulation fusiform aneurysms: results of surgical, endovascular and combined treatment. 2005 American Association of Neurologic Surgeons, New Orleans, LA, April 2005.

Fields JD, Lansberg M, Albers G, Jayaraman MV, Do HM, Marks MP. Intravenous thrombolysis followed by mechanical thrombectomy in the treatment of acute stroke. 57th Annual Meeting of the American Academy of Neurology. Miami Beach, FL, April 2005.

Forero-Torres A, Besh, Knox S, Micallef I, Wiseman G, Witzig T, LoBuglio A, Shen S, Goris M, Carpenter M, Meredith R. Pharmacokinetics and biodistribution of ibritumomab-tiuxetan(Zevalin) after 4 weeks of rituxan: Early report of a phase I study for treatment of CD20+ B-cell follicular/transformed non-Hodgkin's lymphoma: ASTRO 2004

Foudray AMK, Chinn G, Levin CS. Component-based normalization for PET systems that use detectors with depth of interaction measurement capability. 2005 IEEE Medical Imaging Conference. Puerto Rico, October 23-29, 2005.

Foudray AMK, Habte F, Chinn G, Zhang J, Levin CS, Olcott PD. Optimization of a cylindrical PET breast imaging system comprised of position sensitive avalanche photodiodes utilizing monte carlo simulation. Presented at the 2004 Workshop on the Nuclear Radiology of Breast Cancer, Rome, Italy, October 22-23, 2004.

Foudray AMK, Habte F, Chinn G, Zhang J, Levin CS. Optimization of a novel advanced positron emission tomography system for imaging mouse models of human disease. Presented at the Bio-X Program at Stanford, Watching Life Symposium, Stanford University Fairchild Auditorium Friday March 25, 2005.

Foudray AMK, Levin CS, Habte F, Olcott PD. Positioning Annihilation photon interactions in a thin LSO crystal sheet with position-sensitive avalanche photodiodes. Presented at the 2004 IEEE Nuclear Science Symposium and Medical Imaging Conference, Rome, Italy, October 16-22, 2004.

Foudray AMK, Levin CS, Olcott PD. Investigating positioning algorithms for a high resolution positron emission tomography system capable of depth of interaction measurement. 2005 Society of Nuclear Medicine Meeting, Toronto, Canada, June 18-22, 2005.

Gheysens O, Keren O, Levin CS, Gambhir SS. Comparison of time-domain versus continuous wave fluorescence imaging using Cy 5.5 and quantum dots. Accepted for presentation at the 2005 Academy of Molecular Imaging Meeting, Orlando, FL, March 19-23, 2005.

Gold GE, Hargreaves B, Vasanawala S, Webb S, Shimakawa A, Brittain J, Pauly J, Beaulieu C. Knee cartilage volume with fluctuating equilibrium mri. Proceedings of the Osteoarthritis Society International, December 2004.

Goris ML, Zhu HJ, Schipper ML. A method for dosimetry in small animals, using a segmented mouse phantom and convolution filters based on the dose distribution of point sources. Presented at the 52nd Annual meeting of the Society for Nuclear Medicine, Toronto, Canada, June18-22, 2005.

Guzman R, Bliss T, Greve J, Palmer T, Sun GH, Moseley M, Steinberg G. Stroke initiates targeted migration of transplanted iron-labeled neural progenitor cells as revealed by MRI. AHA "Stroke", San Diego, February 2005.

Habte F, Foudray AM, Levin CS. The effect of photon compton scatter on sensitivity in high resolution positron emission tomography. Presented at the Bio-X Program at Stanford, Watching Life Symposium, Stanford University Fairchild Auditorium Friday March 25, 2005.

Habte F, Levin CS, Foudray AMK. The optimal configuration of detectors for highest coincidence detection efficiency in high-resolution positron emission tomography. Accepted for presentation at the 2005 Academy of Molecular Imaging Meeting, Orlando, FL, March 19-23, 2005.Habte F, Olcott P, Zhang J, Levin CS. Investigation of scintillation light multiplexing techniques for 1 mm resolution Positron Emission Tomography detectors. Submitted to the 2005 IEEE Medical Imaging Conference. Puerto Rico, October 23-29, 2005.

Habte F, Olcott PD, Foudray AMK, Levin CS. Simulation and measurement of gamma ray and annihilation photon imaging detectors. Presented at the 2004 IEEE Nuclear Science Symposium and Medical Imaging Conference, Rome, Italy, October 16-22, 2004.Hallett RL, Chan FP, Fleischmann D, Hellinger JC, Rubin GD, Hiatt MD. Imaging of atrioventricular septal defect with multidetector-row CT angiography. 17th European Congress of Radiology, Vienna, Austria, March 3-8, 2005.

Horst KC, Birdwell RL, Ikeda DM, Goffinet DR, Daniel BL, Nowels K, Dirbas FM. Breast imaging characteristics seen in patients receiving accelerated partial breast irradiation with intraoperative radiotherapy for early-stage breast cancer. ARRS, New Orleans LA, May 15-20, 2005,

Horst KC, Daniel BL, Ikeda DM, Jeffrey SS, Carlson RC, Stockdale FE, Goffinet DR, Birdwell RL, Dirbas FM. Breast MRI findings following neoadjuvant chemotherapy for breast cancer. American Society of Breast Disease, Las Vegas NV, April 14-16, 2005,

Jayaraman MV, Marcellus ML, Do HM, Chang SD, Steinberg GK, Marks MP. Hemorrhage rate in patients Spetzer-Martin Grade IV and V AVMs: Is treatment justified? 8th Joint Annual Meeting of AANS/CNS Cerebrovascular Section and the American Society of Interventional and Therapeutic Neuroradiology (ASITN), New Orleans, LA, February 2005.

Jayaraman MV, Marcellus ML, Do HM, Steinberg GK, Chang SD, Marks MP. Hemorrhage rate in patients with Spetzler-Martin Grade IV and V Arteriovenous Malformations: Is Treatment Justified? 43rd Annual Meeting of the American Society of Neuroradiology (ASNR), Toronto, Canada, May 2005.

Kalinyak JE, Steinmetz N, Vanderheiden J-L, Goris ML, Blankenberg F. Annexin V Imaging in human stroke. Presented at the 52nd Annual meeting of the Society for Nuclear Medicine, Toronto, Canada, June 18-22, 2005

Kalinyak JE, Zhu HJ, Goris ML. Characterizing thyroid malignancies: Fusion of FDG-PET/CT images with whole body images. Presented at the 52nd Annual meeting of the Society for Nuclear Medicine, Toronto, Canada, June 18-22, 2005

Kalinyak JE, Zhu HJ, Goris ML. Utility of Fusion of FDG-PET images dor the analysis of disease progression. Presented at the 52nd Annual meeting of the Society for Nuclear Medicine, Toronto, Canada, June 18-22, 2005

Kang K, Min J, Chen X, Gambhir SS. Comparison of ^{14}C]FMAU, [^{3}H]FEAU, [^{14}C]FIAU, [^{3}H]PCV Accumulation in cells expressing wild type or mutant herpes simplex virus type 1 thymidine kinase receptor genes. AMI International Conference 2005, Orlando, FL, March 2005.

Keren S, Gheysens O, Levin CS, Gambhir SS. Characterization of a time-domain fluorescence imaging system with cy5.5 and qdot probes. Accepted for presentation at the 2005 Academy of Molecular Imaging Meeting, Orlando, FL, March 19-23, 2005.

Knox SJ, Fisher GA, Wessels BW, Cho C, Hernandez, MC, Street H, Nangiana J, Shan J, Goris ML. Phase I study of ^{131}I-Chimeric (ch) TNT-1/B antibody for the treatment of advanced colorectal cancer. Presented at the 10th Conference on Cancer Therapy with Antibodies and Immunoconjugates, Princeton, N.J. October 21-23, 2004.

Konukoglu E, Acar B, Paik DS, Beaulieu DF, Napel S, Heat Diffusion Based Detection Of Colonic Polyps In Ct Colonograph. accepted 13th Annual European Signal Processing Conference, Antalya, Turkey, Sept. 4-8, 2005.

Koo S, Gold G, Andriachi T. Factors Influencing the Accuracy of Articular Cartilage thickness Measurement from MRI. Proceedings of the American Society of Biomechanics, September 2004, P. 291.

Kornaat P, Reeder SB, Koo S, Bloem J, Andriacchi T, Gold GE. MR Imaging of Articular Cartilage at 1.5T and 3.0T: Comparison of SPGR and SSFP sequences. Proceedings of the Osteoarthritis Society International, December 2004.

Langer S, Horst K, Ikeda DM, Daniel B, Dirbas F. Pathologic correlates of false-positive MRI lesions. Which lesions warrant biopsy? American Society of Breast Surgeons, March 16-20, 2005, Los Angeles CA.

Levin CS, Habte F, Foudray AMK, Zhang J, Chinn G. Impact of High Energy Resolution Detectors on the Performance of a PET System Dedicated to Breast Cancer Imaging. Oral presentation at the 2004 Workshop on the Nuclear Radiology of Breast Cancer, Rome, Italy, October 22-23, 2004.

Levin CS, Matteson JL, Skelton RT, Pelling MR, Duttweiler F. Promising Characteristics and Performance of Cadmium Zinc Telluride Detectors for Positron Emission Tomography. Presented at the 2004 IEEE Nuclear Science Symposium and Medical Imaging Conference, Rome, Italy, October 16-22, 2004.

Levin CS, Zhang J, Habte F, Foudray AMK, R. Farrell, Foudray AMK, Olcott PD, McClish M, Shah KS. A Thin Position Sensitive Avalanche Photodiode Has Been Fabricated for Ultra-High Resolution Positron Emission Tomography. Presented at the 2004 IEEE Nuclear Science Symposium and Medical Imaging Conference, Rome, Italy, October 16-22, 2004.

Levin CS. A Miniature Gamma Ray Scintillation Camera for Improved Surgical Staging of Cancer. Presented at the 2004 Whitaker Foundation Biomedical Engineering Research Conference, La Jolla, CA, August 12-15, 2004

Levin CS. In Vivo Bioluminescence Imaging. Presented at the Annual Academy of Molecular Imaging Conference, Institute of Molecular Imaging Training Session, Orlando, FL, Wednesday March 23, 2005,.

Marks MP, Wojak JC, Al-Ali F, Jayaraman MV, Marcellus ML, Connors JJ, Do HM. Angioplasty of intracranial stenosis: long-term clinical outcome. 43rd Annual Meeting f the American Society of Neuroradiology (ASNR), Toronto, Canada, May 2005.

Nicolas LE, Bell-Stephens TE, Marcellus M, Marks MP, Steinberg GK, Vavao JA, Albers GW. JACHO Stroke Center Certification: A Team Approach. International Stroke Conference 2005, New Orleans, LA, February 2005.

Nyenhuis DL, Stebbins GT, Wang C, Freels S, Shah N, Johnson J, Moseley M, Gorelick PB. The Influence of White Matter Classification Probability on the Relation of Fractional Anisotropy and Cognitive Function in Ischemic Stroke. ISMRM Workshop on DTI, Lake Louise, March 2005.

Olcott PD, Habte F, Levin CS. Miniature Gamma Ray Camera for Localization of the Sentinel Lymph Node During Surgical Staging of Cancer. Presented at the Bio-X Program at Stanford, Watching Life Symposium, Stanford University Fairchild Auditorium Friday March 25, 2005.

Olcott PD, Levin CS, Habte F, Foudray AMK. Characterization of Performance of a Miniature High Sensitivity Gamma Ray Camera. Presented at the 2004 IEEE Nuclear Science Symposium and Medical Imaging Conference, Rome, Italy, October 16-22, 2004.

Olcott PD, Levin CS, Zhang J. Design of data acquisition architecture for position sensitive avalanche photodiode-based 3D-PET systems using event-based simulation. Accepted for presentation at the 2005 Society of Nuclear Medicine Meeting, Toronto, Canada, June 18-22, 2005.

Olcott PD, Levin CS. Charge multiplexing techniques for position sensitive avalanche photodiodes. Submitted to the 2005 IEEE Medical Imaging Conference. Puerto Rico, October 23-29, 2005.

Olcott PD, Levin CS. Finite Element Modeling Based Spatial Linearity Correction for Scintillation Detectors that use Position Sensitive Avalanche Photodiodes. Submitted to the 2005 IEEE Medical Imaging Conference. Puerto Rico, October 23-29, 2005.

Olcott PD, Levin CS. Image Processing Algorithms to Facilitate and Enhance Sentinel Node Detection Using a Hand-Held Gamma Ray Camera in Surgical Breast Cancer Staging. Presented at the 2004 Workshop on the Nuclear Radiology of Breast Cancer, Rome, Italy, October 22-23, 2004.Paik DS, Acar B, Konukoglu E, Beaulieu CF, Napel S, Computer-aided detection of polyps in virtual colonoscopy using 3D heat diffusion fields. Fifth International Symposium on Virtual Colonoscopy, Boston, MA, October 28-29, 2004.

Paik DS, Sundaram P, Beaulieu CF, Napel S, Anatomically-selective morphological enhancement and suppression in CT colonography: initial experience," Fifth International Symposium on Virtual Colonoscopy, Boston, MA, October 28-29, 2004.

Poplaw S, Hellinger JC, Hiatt MD, Chan FP, Fleischmann D. Imaging of atrial septal defects with multidetector-row CT angiography. 17th European Congress of Radiology, Vienna, Austria, March 3-8, 2005.

Reeder SB, Herfkens, RJ, Daniel, BL. 3D-spiral mr imaging for dynamic contrast enhanced imaging of the breast: applications for tumor characterization and therapy monitoring. 2005 MRI Symposium, Garmisch-Partenkirchen, Germany, January 29, 2005

Reeder SB, McKenzie CA, Brau ACS, Hargreaves BA, Yu H, Shimakawa A, Brittain JH, Gold GE, Johnson JW, Rofksy NM, Herfkens RJ, Rapid body MRI using IDEAL water-fat separation and parallel imaging. 28th SCBT/MR Meeting, Miami Beach, 2005.

Rieke V, Ganguly A, Scott GC, Daniel BL, Pauly JM, Pelc NJ, Fahrig R, Butts K. X-ray compatible RF-coil for integrated x-ray/MR imaging systems. 5th Interventional MRI Symposium, Boston, MA, 2004.

Rieke V, Ross A, Nau A, Diederich C, Sommer G, Butts K. MRI-temperature mapping duing ultrasound prostate ablation using fat for phase estimation, IEEE EMBS, San Francisco, Sept 2004.

Shi R, Margolis D, Napel S, Jeffrey RB Jr, Olcott E, Schraedley-Desmond P, Beaulieu CF. CAD in colonography: Influence of polyp features and 3D viewing on interpretation. Fifth International Symposium on Virtual Colonoscopy, Boston, MA October 28-29, 2004.

Smith CA, Stebbins G, Bartt RE, Kessler H, Bammer R, Moseley ME. Effects of HIV-1 Infection and Aging on Normal Appearing White Matter Integrity. ISMRM Workshop on DTI, Lake Louise, March 2005.

Smith CA, Stebbins GT, Bartt RE, Kessler H, Bammer R, Moseley ME. Reaction Time And Whole-Brain Radiologically-Defined Normal Appearing White Matter: Impact Of HIV-Infection On Speed. OBHM, December 2004.

Stebbins G, Berry-Kravis E, Nyenhuis D, Freels D, Johnson J, Wang H, de Toledo-Morrell L, Sripathirathan V, Bammer R, Moseley M. ApoE 4 Associated Decline in White Matter Integrity in Ischemic Stroke. Vascular Cognitive Meeting. November 2004.

Stebbins G, Berry-Kravitz L, Nyenhius DL, Freels S, Johnson J, Wang C, Bammer R, Moseley ME. Interaction of longitudinal changes in fractional anisotropy and ApoE status in ischemic stroke patients ISMRM Workshop on DTI, Lake Louise, March 2005.

Stebbins G, Smith CA, Bartt RE, Kessler H, Martin E, Bammer R, Moseley M. HIV Associated Regional Decrease in Normal Appearing White Matter Integrity: A Diffusion Tensor Imaging Study. ANA International Meeting, Gothenburg, March 2005.

Stevens K, Bammer R, Gold G, Careagee E, Alamin T. High-resolution MR imaging of paraspinal muscle injury following minimally invasive and conventional open posterolateral lumbar fusion. Proceedings of the Orthopedic Research Society, February 2005.

Sundaram P, Paik DS, Sifakis ED, Beaulieu CF, Napel S, Selective fold removal in CT colonography using physically-based simulation. Fifth International Symposium on Virtual Colonoscopy, Boston, MA, October 28-29, 2004.

Whale RL, Kostakoglu L, Divgi C, Goris M, Vallabhajosula S, Goldsmith S. Factors influencing total body clearance in 1247 patients treated with Tositumomab and Iodine 131 Tositumomab. Presented at the 52nd Annual meeting of the Society for Nuclear Medicine, Toronto, Canada, June 18-22, 2005

Wootton-Gorges S, Buonocore M, Kupperman N, Marcin J, Barnes P, Glaser N. Detection of cerebral beta-hydroxy butyrate, acetacetate, and lactate by proton MR spectroscopy in children with diabetic ketoacidosis. 48th Annual Meeting, Society for Pediatric Radiology, New Orleans, LA, May 7, 2005.

Wu Y, Chen X. In Vivo Near-Infrared Fluorescent Imaging of $\alpha_v\beta_3$ Integrin Expression in Brain Tumor Xenografts by Cy7-labeled Multimeric RGD Peptides. The 4th Annual Meeting of the Society for Molecular Imaging, Cologne, Germany, September 2005

Wu Y, Chen X. RGD-Cy7 Conjugate as NIR Fluorescence Probe to Image $\alpha_v\beta_3$ Integrin Expression in Brain Tumor Xenografts. 19th American Peptide Symposium, San Diego, June 2005

Wu Y, Fisher DR, Liu S, Chen X. Evaluation of Copper-64 Labeled Tetrameric RGD Peptide for Tumor Imaging. SNM 52th Annual meeting, Toronto, Canada, June 2005

Wu Y, Zhang X, Xiong Z, Yang Y, Cheng Z, Liu S, Chen X. MicroPET Imaging of Brain Tumor Angiogenesis with ^{64}Cu-Tetra-c(RGDfK) Peptide. AMI International Conference 2005, Orlando, FL, March 2005.

Xing L, Spielman D, MRI and MRSI in Radiation Treatment Planning, AAPM, 2005.

Xiong Z, Cheng Z, Zhang X, Wu Y, Subbarayan M, Wu JC, Gambhir SS, Chen X. MicroPET Imaging of Chemically Modified Adenovirus for Integrin $\alpha_v\beta_3$ Retargeting. AMI International Conference 2005, Orlando, FL, March 2005.

Yang Y, Wu Y, Zhang X, Chen X. NIR Fluorescence Imaging of Gastrin-Releasing Peptide Receptor Expression in Androgen-Independent Prostate Cancer Tumor Model. AMI International Conference 2005, Orlando, FL, March 2005.

Yang Y, Zhang X, Cheng Z, Chen X. MicroPET Imaging of Gastrin-Releasing Peptide Receptor Expression with 64Cu-Labeled Bombesin Analogs in a Mouse Model of Human Prostate Adenocarcinoma. AMI International Conference 2005, Orlando, FL, March 2005.

Zhang J, Chinn G, Foudray AMK, Habte F, Olcott PD, Levin CS. Evaluation of a Dual-Head PET Camera Design Dedicated to Breast Cancer Imaging. Presented at the 2004 Workshop on the Nuclear Radiology of Breast Cancer, Rome, Italy, October 22-23, 2004.

Zhang J, Foudray A, Olcott P, Chinn G, Habte F, Levin CS. Development of a dual-panel Positron Emission Tomography camera dedicated to breast cancer imaging. Presented at the Bio-X Program at Stanford, Watching Life Symposium, Stanford University Fairchild Auditorium, Friday, March 25, 2005.

Zhang J, Foudray AMK, Chinn G, Levin CS. Development of Compact PET Camera Based Upon New Detectors for Dedicated Breast Cancer Imaging. Accepted for presentation at the 2005 Academy of Molecular Imaging Meeting, Orlando, FL, March 19-23, 2005.

Zhang J, Foudray AMK, Olcott PD, Levin CS. Coincidence measurements with a 1 mm^3 resolution avalanche photodiode-based scintillation detector for ultra-high resolution PET. Accepted for oral presentation at the 2005 Society of Nuclear Medicine Meeting, Toronto, Canada, June 18-22, 2005.

Zhang J, Foudray AMK, Olcott PD, Levin CS. Performance characterization of a novel thin position-sensitive avalanche photodiode for a 1 mm^3 resolution PET camera. 2005 IEEE Medical Imaging Conference. Puerto Rico, October 23-29, 2005.

Zhang J, Olcott PD, Foudray AMK, Chinn G, Levin CS. Study of count performance, lesion visualization and contrast resolution as a function of crystal resolution for a dual-plate PET camera dedicated to breast cancer imaging. Submitted to the 2005 IEEE Medical Imaging Conference. Puerto Rico, October 23-29, 2005.

Zhang X, Wu Y, Chen X. ^{18}F-Labeled Bombesin Analogs for Targeting GRP Receptor-Expressing Tumors. SNM 52th Annual meeting, Toronto, Canada, June 2005

Zhang X, Wu Y, Chen X. Evaluation of ^{18}F-Labeled Dimeric RGD Peptide for PET Imaging of Tumor $\alpha_v\beta_3$-Integrin Expression. SNM 52th Annual meeting, Toronto, Canada, June 2005

Zhang X, Wu Y, Xiong Z, Yang Y, Cheng Z, Chen X. Preparation and Characterization of $^{99m}Tc(CO)_3$-Bpy-RGD Complex as $\alpha_v\beta_3$ Integrin Receptor Targeted Imaging Agent. AMI International Conference 2005, Orlando, FL, March 2005.

Zhu HJ, Goris ML. Display of myocardial motion by projecting specific components of the 3D motion of myocardial elements on the plane of origin. PRESENTED AT: 7th International Conference of Nuclear Cardiology. Lisbon Portugal, 8-11 May 2005.